NNT : 2024AIXM0000

THÈSE DE DOCTORAT

Soutenue à Aix-Marseille Université
le 11 Décembre 2024 par

Antonello TANGREDI

Mechanisms of interactions between organic and mineral matter (phosphates) during hydrothermal liquefaction of residual biomass: application to digestate from anaerobic digestion

Discipline
Sciences pour l'ingénieur

Spécialité
Génie des procédés

École doctorale
ED 353 Sciences pour l'ingénieur : mécanique, physique, micro et nanoélectronique

Laboratoire/Partenaires de recherche
Laboratoire de mécanique, modélisation & procédés propres, M2P2 (UMR CNRS 7340)

Composition du jury

Benedetta DE CAPRARIIS	**Rapporteuse**
Associate professor, Université de Rome La Sapienza	
Véronique DELUCHAT	**Rapporteuse**
Professeure des universités, Université de Limoges	
Anthony DUFOUR	**Président du jury**
Directeur de recherche, CNRS LRGP	
Jean Henry FERRASSE	**Examinateur**
Professeur des universités, Aix Marseille Université	
Mathieu GAUTIER	**Examinateur**
Professeur des universités, INSA Lyon	
Elsa WEISS	**Examinatrice**
Maitresse assistante, IMT Mines Albi	
Olivier BOUTIN	**Directeur de thèse**
Professeur des universités, Aix Marseille Université	
Cristian BARCA	**Co-directeur de thèse**
Maitre de conférences, Aix Marseille Université	

Affidavit

I, undersigned, Antonello Tangredi, hereby declare that the work presented in this manuscript is my own work, carried out under the scientific supervision of Olivier Boutin and Cristian Barca, in accordance with the principles of honesty, integrity and responsibility inherent to the research mission. The research work and the writing of this manuscript have been carried out in compliance with both the French national charter for Research Integrity and the Aix-Marseille University charter on the fight against plagiarism.

This work has not been submitted previously either in this country or in another country in the same or in a similar version to any other examination body.

Aix-en-Provence, 26 septembre 2024

Signature:

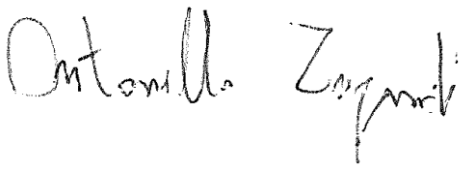

Cette œuvre est mise à disposition selon les termes de la Licence Creative Commons Attribution - Pas d'Utilisation Commerciale - Pas de Modification 4.0 International.

List of publications and/or patents and participation in conferences

1) List of publications and/or patents produced as part of the thesis project:

    1. A. Tangredi, C. Barca, J.-H. Ferrasse, O. Boutin, Effect of process parameters on phosphorus conversion pathways during hydrothermal treatment of sewage sludge: A review, Chem. Eng. J. 463 (2023) 142342. https://doi.org/10.1016/j.cej.2023.142342.
    2. A. Tangredi, C. Ochoa, O. Boutin, J.-H. Ferrasse, C. Barca, Phosphorus Recovery from Sewage Sludge Digestate and Pig Manure by Hydrothermal Treatments, in: G. Mannina, A. Cosenza, A. Mineo (Eds.), Resour. Recovery Wastewater Treat., Springer Nature Switzerland, Cham, 2024: pp. 181–186. https://doi.org/10.1007/978-3-031-63353-9_32.
    3. A. Tangredi, C. Barca, J.-H. Ferrasse, O. Boutin, , Combining process severity and response surface methodology: a comprehensive approach to phosphorus speciation in sewage sludge hydrothermal treatment, Journal of Environmental Management. **(under review)**

2) Participation in conferences and summer schools during the thesis period:
    1. A. Tangredi, C. Barca, J.-H. Ferrasse, O. Boutin, Valorisation du phosphore des digestats des boues de STEP par liquéfaction hydrothermale, 30ème Congrès école doctorale science de l'environnement 251, 3-4 mai 2023, Marseille, France. **(Poster)**
    2. A. Tangredi, C. Barca, J.-H. Ferrasse, O. Boutin, Phosphorus conversion pathways during hydrothermal liquefaction of sewage sludge digestate, 14th European Congress of Chemical Engineering and 7th European Congress of Applied Biotechnology, 17-21 septembre 2023, Berlin, Germany. **(Oral)**
    3. A. Tangredi, C. Barca, J.-H. Ferrasse, O. Boutin, Phosphorus conversion pathways during hydrothermal liquefaction of sewage sludge digestate, V Congreso International en Tecnologias Limpia, 2-3 novembre 2023, Bogotá, Colombia. **(Oral)**
    4. A. Tangredi, C. Ochoa, O. Boutin, J.-H. Ferrasse, C. Barca, Phosphorus Recovery from Sewage Sludge Digestate and Pig Manure by Hydrothermal Treatments, International Conference On Wider- Uptake Of Water Resource Recovery From Wastewater Treatment, 18-21 juin 2024, Palermo, Italy. **(Oral)**
    5. A. Tangredi, C. Barca, J.-H. Ferrasse, O. Boutin, Phosphorus conversion pathways during hydrothermal liquefaction of sewage sludge digestate, 32nd European Biomass Conference and Exhibition, 24-27 juin 2024, Marseille, France. **(Poster)**

6. A. Tangredi, C. Barca, J.-H. Ferrasse, O. Boutin, Voies de conversion du phosphore lors de la liquéfaction hydrothermale du digestat des boues de station d'épuration, 19eme congrès de la société française de génie des procèdes, 15-17 octobre 2024, Deauville, France. **(Oral)**

Résumé

Le phosphore (P) est un nutriment essentiel à la production alimentaire mondiale, mais l'agriculture intensive perturbe son cycle naturel et accroît la dépendance aux sources non renouvelables. Une alternative durable est de récupérer le P contenu dans les déchets organiques renouvelables comme les boues d'épuration. Cette thèse de doctorat étudie le traitement hydrothermal des boues d'épuration pour explorer la conversion et la spéciation du P, visant à valoriser la phase minérale en engrais et la phase organique en biohuile. Deux boues, différentes en teneur en solides et composition, ont été prélevées d'une station d'épuration dans le sud de la France. Les boues ont été traitées dans un réacteur batch à des températures variant de 250 à 350 °C pendant 5 à 45 min. Les produits ont été centrifugés en une pastille solide et de l'eau procédé et entièrement caractérisés. Les résultats montrent que des températures plus élevées et des durées prolongées augmentent le rendement en biohuile. Les traitements à 250-300 °C favorisent la minéralisation du P organique, tandis qu'à 350 °C conduisent à un meilleur rendement de récupération du P dans la pastille solide (> 90%). Un taux élevé de calcium et fer dans les boues favorise la précipitation des phosphates, et l'ajout d'oxyde de calcium améliore la récupération de P sous forme de phosphate de calcium. Cette recherche propose un cadre pour une récupération durable du P, proposant les produits solides des traitements hydrothermaux comme engrais à libération lente de P. Les travaux futurs devraient se concentrer sur la caractérisation de la biohuile pour mieux évaluer le potentiel de récupération d'énergie.

Mots clés : biomasses résiduaires, récupération du phosphore, liquéfaction hydrothermale, boues de station d'épuration, économie circulaire.

Abstract

Phosphorus (P) is an essential nutrient for global food production, but intensive agriculture disrupts its natural cycle, increasing reliance on non-renewable sources. A sustainable alternative is recovering P from renewable organic waste streams such as sewage sludge and digestate. This PhD thesis investigates the hydrothermal treatment of sewage sludge to explore P conversion and speciation, aiming to valorize the mineral phase as fertilizer and the organic phase as bio-oil. Two types of sludge, differing in solids content and composition, were sampled from a wastewater treatment plant in southern France. The sludge was treated in a batch reactor at temperatures varying from 250 to 350 °C for 5 to 45 min. Products were centrifuged into a solid pellet and process water, followed by characterization of their physicochemical properties. Results show that temperature and treatment duration significantly impact by-product characteristics, including their P content and speciation. Higher temperatures and longer times improve bio-oil yield. Treatments at 250-300 °C promote organic P mineralization and increase soluble phosphate concentration in the process water, while treatments at 350 °C lead to greater P recovery yield in the solid pellet (> 90%). Higher calcium and iron contents of sludge improve orthophosphate precipitation, and calcium oxide addition enhances P recovery in the solid pellet as calcium phosphate. This research provides a framework for sustainable P recovery, suggesting hydrothermally treated pellets as potential slow-release fertilizers. Future work should include detailed bio-oil characterization to better assess the energy recovery potential.

Keywords : residual biomass, phosphorus recovery, hydrothermal liquefaction, sewage sludge, circular economy.

Acknowledgments

This work received support from the French National Research Agency, France (ANR) for the Project D2LIFE under the reference number ANR-21-CE43-0013-01.

I would like to begin by expressing my heartfelt gratitude to my supervisor, Olivier Boutin, and my co-supervisor, Cristian Barca, for their unwavering support throughout these three years. Their insightful guidance has been vital in optimizing both my research results and the time spent on this journey. I am truly grateful for the opportunity they provided by selecting me as a candidate for this PhD, allowing me to grow both personally and as a researcher.

I also wish to thank Jean-Henry Ferrasse for his guidance and assistance, particularly in studying the thermal profile of the hydrothermal process. His interest in my work and his expertise have been incredibly supportive throughout my research.

I would like to sincerely thank the examiners—Anthony Dufour, Mathieu Gautier, and Elsa Weiss—and the reviewers, Benedetta De Caprariis and Véronique Deluchat. I appreciate their willingness to evaluate my work and participate as committee members during my PhD defense. I look forward to their constructive feedback and insights.

My thanks extend to the M2P2 laboratory, where I conducted all my research and experimental work. In particular, I am grateful to the members of my team, TED, for creating a professional and enthusiastic environment filled with harmony and mutual understanding. I also want to thank the technical staff of the laboratory, especially Emmanuelle, for their support and assistance throughout my research.

I would like to acknowledge Alessio, Alex, Abdoul, Aymeric, Carolina, Emilie, Fatimatou, Guillaume, Hugo, Jeanne, Katharina, Laurie, Laura, Man Nghi, Maryse, Rachel, Rosario, Shuxin, Stacy and Zohra for sharing both the hardships and joys of this journey over the past three years. I am thankful for all my PhD colleagues, post-docs, engineers, professors, and interns with whom I had the privilege of sharing the office, laboratory, kitchen, and meeting room.

I am especially grateful to my friends Fiona, Giovanni, and Giulia for their companionship during these three years. Looking back on this period in fifty years, the wonderful moments we shared will undoubtedly be the first to come to mind. Thank you for the kind words, deep conversations, walks in the calanques, movie nights, breakfasts, lunches, dinners, beach days, concerts, discussions, misunderstandings, and exchanges. Thank you for listening and for sharing your thoughts with me, for your patience, and for your kindness.

Finally, I would like to express my deepest gratitude to my family, without whom I could never have achieved such remarkable results. I thank my grandparents for their constant presence, kindness, and generosity. I am also grateful to my sisters, Asia and Sara, for their unwavering support. Most importantly, I thank my parents for instilling in me a love of knowledge and encouraging my curiosity and critical thinking. I appreciate all the Focus Junior magazines you bought for me when I was a child.

List of abbreviations

AD	Anaerobic digestion
Ag	Silver
AIP	Apatite inorganic phosphorus
Al	Aluminum
ANOVA	Analysis of variation
As	Arsenic
Ca	Calcium
Cd	Cadmium
COD	Chemical oxygen demand
Cr	Chrome
Cu	Copper
DOE	Design of experiments
DSC	Differential scanning calorimetry
Fe	Iron
Hg	Mercury
HT	Hydrothermal
HTC	Hydrothermal carbonization
HTG	Hydrothermal gasification
HTL	Hydrothermal liquefaction
ICP-AES	Inductively Coupled Plasma Atomic Emission Spectroscopy
ICP-MS	Inductively Coupled Plasma Mass Spectrometry
IP	Inorganic phosphorus
K	Potassium
Mg	Magnesium
Mn	Manganese
N	Nitrogen
NAIP	Non apatite inorganic phosphorus
NH_4-N	Ammonium nitrogen
Ni	Nickel
NMR	Nuclear magnetic resonance
NO_3-N	Nitrate nitrogen
O	Oxygen
OA/A	O-alkyl/alkyl
OP	Organic phosphorus
P	Phosphorus
Pb	Lead
PO_4-P	Soluble orthophosphate phosphorus

S	Sulfur
SLR	Solid-to-liquid ratio
SMT	Standard measuring and testing
SRY	Solid recovery yield
SS	Sewage sludge
TC	Total carbon
TDS	Total dissolved solids
TIC	Total inorganic carbon
TN	Total nitrogen
TOC	Total organic carbon
TP	Total phosphorus
TS	Total solids
TSRY	Total solid recovery yield
TSS	Total suspended solids
V	Vanadium
WWTP	Wastewater treatment plant
Zn	Zinc

Table of contents

Affidavit **II**
List of publications and/or patents and participation in conferences **III**
Résumé **V**
Abstract **VI**
Acknowledgments **VII**
List of abbreviations **VIII**
Table of contents **X**
List of figures **XIV**
List of tables **XXII**
General introduction **1**
1. State of the art **2**
1.1. Global phosphorus framework 2
1.2. Sewage sludge 3
1.3. Hydrothermal treatments 5
1.4. Fate of organic matter: reaction pathways to hydrochar formation 7
1.4.1. Hydrolysis 7
1.4.2. Dehydration and decarboxylation 8
1.4.3. Polymerization, condensation and aromatization 8
1.5. Selected studies of sewage sludge hydrothermal treatments 11
1.5.1. Sewage sludge type and composition 11
1.5.2. Hydrothermal process parameters 14
1.5.3. Main results of selected studies 16
1.6. Effect of hydrothermal process parameters on phosphorus conversion pathways 18
1.6.1. Temperature, reaction time, and pressure 18
1.6.2. Solid-to-liquid ratio 24
1.6.3. Acidic and basic treatments 24
1.6.4. Use of additives 27
1.6.5. Proposed mechanism for phosphorus conversion 30
1.7. Perspectives and conclusions 30
2. Materials and methods **35**
2.1. Sewage sludge digestate 35
2.1.1. Wastewater treatment plant 35
2.1.2. Digestate pre-treatment 36
2.2. Hydrothermal treatment 37

2.2.1. Experimental reactor 37
2.2.2. Reactor loading and reaction monitoring 40
2.2.3. By-products recovery and separation 40
2.3. Characterization of liquid phases 42
2.3.1. General characteristics 42
2.3.2. Total alkalinity 42
2.3.3. Solid content 42
2.3.4. Total and ammonia nitrogen 43
2.3.5. Chemical Oxygen Demand 43
2.3.6. Dissolved carbon 44
2.3.7. Free orthophosphates 44
2.3.8. Inductively Coupled Plasma Atomic Emission Spectroscopy (ICP – AES) 44
2.4. Characterization of solid phases 45
2.4.1. Lyophilization 45
2.4.2. Elemental CNHS analysis 45
2.4.3. Aqua regia extraction 46
2.4.4. Inductively Coupled Plasma Spectroscopy 46
2.4.5. Nuclear magnetic resonance spectroscopy 47
2.4.6. Extraction methods for phosphorus speciation 48
2.5. Hydrothermal treatment thermal profile investigation 53
2.6. Statistical analysis 56
2.6.1. Design of experiments methodology 56
2.6.2. Error propagation 61
2.6.3. Ruyter severity function 62
2.7. Conclusions 63
3. Sewage sludge digestate feed characterization 64
3.1. Introduction 64
3.2. Materials and methods 65
3.3. Feed characterization 65
3.3.1. Sludges characterization 65
3.3.2. Centrates characterization 74
3.4. Environmental compatibility 78
3.5. Conclusion 79
4. Effect of temperature and treatment duration on by-products characteristics and phosphorus speciation 81
4.1. Introduction 81
4.2. Materials and methods 82
4.3. Mass balances and by-products distribution 83
4.4. Process water characterization 88
4.4.1. Soluble nitrogen 89
4.4.2. Soluble carbon 91

4.4.3. Dissolved metallic species 93
4.4.4. Experimental design analysis results 94
4.5. Solid by-product characterization 96
4.5.1. Ultimate analysis 96
4.5.2. Fate of organics 99
4.5.3. Metals and heavy metals 103
4.6. Phosphorus speciation and distribution 107
4.7. Options for products valorization and disposal 118
4.8. Thermal profile investigation 120
4.9. Conclusion 127
5. Effect of feed characteristics on by-products characteristics and phosphorus speciation 130
5.1. Introduction 130
5.2. Materials and methods 130
5.3. By-products distribution and general characteristics 131
5.4. Process water characterization 134
5.5. Solid by-products characterization 138
5.6. Conclusions 143
6. Effect of Calcium oxide addition on by-products characteristics and phosphorus speciation 145
6.1. Introduction 145
6.2. Materials and methods 147
6.3. By-products distribution and mass balances 148
6.4. Process water characterization 155
6.5. Solid by-products characterization 166
6.6. Integration of bio-oil production and solid pellet exploitation as fertilizer 173
6.7. Conclusions 176
General conclusion 179
Résumé en français 184
I. Etat de l'Art 184
II. Matériel et méthodes 188
III. Caractérisation des boues 192
IV. Effet de la température et du temps 195
V. Effet des caractéristiques de l'alimentation 201
VI. Effet de l'ajout d'oxyde de calcium 203
References 205
ANNEXES 225
A. Supplementary Figures and Tables: State of the Art 226
B. Ammonium molybdate-ascorbic acid method for orthophosphate concentration 235
C. Methods for design of experiments 236

D. Statistical validation of experimental design models 241
E. Supplementary figures: phosphorus quantification and speciation 255
F. Supplementary elements for thermal profile investigation 258
G. Supplementary elements for the investigation of feed properties on HT products 262
H. Supplementary elements for the investigation of CaO addition on HT products 266

List of figures

Figure 1.1 - Distribution of phosphate rock reserves around the world. Data from [7]. 3

Figure 1.2 - (a) Sewage sludge annual production expressed in kt of dried sludge per year. (b) sewage sludge annual per capita production expressed in kg of dried sludge per year. Data from Eurostat[17]. 4

Figure 1.3 - Water phase diagram with regions typically associated with HT carbonization (HTC), liquefaction (HTL) and gasification (HTG). 6

Figure 1.4 - Overview of the mechanisms and reactions which the organic matter undergoes during the hydrothermal treatment of sewage sludge, leading to the carbonization of biomass and the formation of hydrochar. 10

Figure 1.5 - Box distributions of P, N, Fe, Ca, Al, Mg, K contents in sewage sludge expressed as mg g^{-1} of dry sewage sludge. Average values are underlined. Data collected from works listed in Table A.1. For each distribution, the number of experimental data is shown in brackets in the legend. 12

Figure 1.6 - Box distributions of Fe/P, Ca/P, Al/P, Mg/P, K/P and N/P molar ratios in sewage sludge. Average values are underlined. Data collected from works listed in Table A.1. For each distribution, the number of experimental data is shown in brackets in the legend. N/P molar ratio values can be read in the left axis. 13

Figure 1.7 - Box distribution of the apatite inorganic P (AIP), non-apatite inorganic P (NAIP), and organic P (OP) relative amounts in sewage sludge. expressed as a fraction of the total P content. Average values are underlined. Data from [10,77–94]. 14

Figure 1.8 - Temperature and reaction time of hydrothermal studies listed in Table A.1. Pink points (274) correspond to typical hydrothermal carbonization temperatures, blue points (49) to hydrothermal liquefaction temperatures, red points (45) to hydrothermal gasification temperatures, and green points (90) to hydrothermal treatments at relatively low temperatures (T < 180 °C). 15

Figure 1.9 - Box distributions of P, Fe, Ca, Al, Mg contents in solid products of hydrothermal treatment (expressed as mg g^{-1} of dry solid product). Average values are underlined. Data collected from works listed in Table A.1. For each distribution, the number of experimental data is shown in brackets in the legend. Data from solid products include only hydrothermal treatments without pH adjustments or addition of additives. 17

Figure 1.10 - Box distribution of the apatite inorganic P (AIP), non-apatite inorganic P (NAIP), and organic P (OP) relative amounts in solid products of HT process expressed as a fraction of the total P content. Average values are underlined. Data from [10,77–94]. Data from hydrochar include only hydrothermal treatments without pH adjustments or addition of additives. 17

Figure 1.11 - Solid product mass yield as a function of process severity expressed with the Ruyter severity factor f(T,t) (Equation 1.4). Each color represents a different study listed in Table A.1 19
Figure 1.12 - P recovery yield in the solid product as a function of process severity expressed with the Ruyter severity factor f(T,t) (Equation 1.4). The color scale represents the treatment duration expressed in minutes. Data collected from works listed in Table A.1. 20
Figure 1.13 - Non-apatitic inorganic P (NAIP) (green points) and apatitic inorganic P (AIP) (orange points) fractions over total inorganic P (IP) as a function of the process severity expressed by the Ruyter severity factor f(T,t) (Equation 1.4). Data from [10,77–81,83,85–94]. Points in a dashed rectangle are related to a FeCl3-assisted process[86]. Points marked by arrows are characterized by a relatively high Ca/(Fe+Al) molar content[79,92]. 22
Figure 1.14 - Sum of the H_2O- and $NaHCO_3$- extracted P fractions (blue points), and the NaOH-, HCl- and residual- P fractions (orange points) as a function of the process severity expressed by the Ruyter severity factor f(T,t) (Equation 1.4). Data from [62,82,106,109,122,124]. 23
Figure 1.15 - P recovery yield in the solid product as a function of water process pH, each color represents a different acidic or basic species used to adjust the feed or feed water pH. Data from [10,62,84,85,87,91,108,126]. 25
Figure 1.16 - Solubility of the metal phosphates. Adapted from [134] and [72]. 26
Figure 1.17 - Apatite inorganic P (AIP) fraction over total inorganic P (IP) as a function of the Ca/P molar ratio of the feedstock. Color represents process severity expressed by the Ruyter severity factor f(T,t) (Equation 1.4). Data from [10,77–81,86,88,89,91–93]. ... 28
Figure 2.1 - Diagram of the physical, chemical, and biological processes that wastewater undergoes at the Aix-La Pioline wastewater treatment plant. 36
Figure 2.2 - Left: appearance of the small batch reactor used for the SS HT treatment. Right: technical scheme of the reactor body. 38
Figure 2.3 - Schematization of the experimental setup. PI: pressure indicator; PT1: pressure transmitter (P inside the reactor); TC1: reactor internal temperature; TS1: temperature of the heating coil; TS1: mixer motor temperature. 39
Figure 2.4 - Experimental protocol scheme for reactor loading and product recovery and separation 41
Figure 2.5 - The SMT extraction method for Total P (TP) quantification (a) and Non-Apatite Inorganic P (NAIP) and Apatite Inorganic P (AIP) quantification (b). Adapted from Ruban et al. [74]. 49
Figure 2.6 - Adjusted Hedley fractionation method. Adapted from [121]. 52
Figure 2.7 - Experimental setup used for high-pressure DSC analysis. 54
Figure 2.8 - DSC thermal procedure as proposed by Pecchi et al.[158], consisting of two consecutive runs realized without opening the cell. 55
Figure 2.9 - Ruyter[101] severity function (Equation 2.34) as a function of temperature (°C) and treatment duration (min). 63

Figure 3.1 - Visual presentation of Sludge A (left) and Sludge B (right). 65
Figure 3.2 - Sludge A and Sludge B ultimate analysis results in terms of C, N, H, S, O and ash contents expressed as % of total dry matter. Error bars representing standard deviation. Box plots report distributions of the works listed in Table A.1. 67
Figure 3.3 - Van Krevelen diagram for Sludge A and Sludge B, and for sludges used in works listed in Table A.1. Error bars representing standard deviation. Adapted from [163,164]. 68
Figure 3.4 - P, Ca, Fe, Al, Mg and K content in Sludge A and B expressed as mg g^{-1} of dried sludge. Box plots represent the general content distributions observed for SS used in HT treatments and listed in Table A.1. Error bars represent standard deviation. 69
Figure 3.5 - Heavy metals contents in Sludge A and B expressed as mg kg^{-1} of dried sludge. Error bars represent standard deviation. 70
Figure 3.6 - (a) NAIP, AIP and OP absolute contents in Sludge A and B, expressed as mg P g^{-1} of dried sludge. (b) Relative NAIP, AIP and OP amounts as fraction of TP (SMT method)[74]. Error bars represent standard deviation. Box plots represent P speciation distribution in SS form previous studies[10,77–94]. 71
Figure 3.7 - Results of Hedley extraction method[121] for Sludge A and B. Each fraction is expressed as the ratio of the sum of all fractions. Error bars represent standard deviation. 72
Figure 3.8 - Comparison between the total P values obtained with four different quantification techniques for Sludge A and B expressed as mg P g^{-1} of dried sludge. Error bars represent standard deviation. 74
Figure 3.9 - Microscopic examination of Centrate A. 75
Figure 3.10 - P, Ca, Fe, Mg and K concentration in Centrate A and B. Error bars represent propagated uncertainty. 77
Figure 4.1 - Global mass yield as a function of severity f(T,t): Error bars representing propagated uncertainty. 83
Figure 4.2 - (a) Solid pellet by-product dry mass (%) (b) Process water TDS (c) Total Solids Recovery Yield (as defined by Equation 2.8) evolutions as a function of HT severity f(T,t). 84
Figure 4.3 - Mass distribution in HT treatment by-product for carbon (a), nitrogen (b), phosphorus (c), calcium (d), iron (e), magnesium (f) and potassium (g). Error bars represent propagated uncertainty. 85
Figure 4.4 - Second-degree polynomial surface response for TSRY% based on the experimental design reported in Table 2.1, as a function of temperature (°C) and treatment duration (min) as expressed by Equation 4.1. 88
Figure 4.5 - Process water pH and total alkalinity evolutions as a function of HT severity f(T,t). Error bars represent propagated uncertainty. Dashed lines are included to help data interpretation. 89
Figure 4.6 - Concentration of ammonium N (NH_4-N) in process water (g L^{-1}) and its relative proportion in relation to total soluble N. Error bars represent propagated uncertainty. Dashed lines are included to help data interpretation. 90

Figure 4.7 - (a) COD concentration (g O_2 L^{-1}) and TC concentration (g C L^{-1}) in process water by-product as a function of increasing severity. (b) TIC and TOC concentration (g C L^{-1}) in process water by-product as a function of increasing severity. (c)correlation between TOC concentration (mol C L^{-1}) and COD content (mol O_2 L^{-1}). (d) correlation between TIC concentration (mol C L^{-1}) and alkalinity expressed in mol C L^{-1}. Error bars represent propagated uncertainty. Dashed lines are included to help data interpretation. 91

Figure 4.8 - Process water by-products under progressively more severe treatments. 92

Figure 4.9 - Concentration of Ca, Fe, Mg (a), P and K (b) in process water by-products as a function of severity f(T,t). Error bars represent propagated uncertainty. Dashed lines are included to help data interpretation. 94

Figure 4.10 - Second-degree polynomial surface response for soluble Fe concentration (mg L^{-1}) in process water, based on the experimental design reported in Table 2.1, as a function of temperature (°C) and treatment duration (min) as expressed by Equation 4.5. 96

Figure 4.11 - Ultimate analysis results for solid pellet by products. (a) Ash, C, O (b) N, H, S contents as a function of HT severity f(T,t). Error bars represent propagated uncertainty. Dashed lines are included to help data interpretation. 97

Figure 4.12 - Van Krevelen diagram for the solid pellet by-products. Color bar represent HT severity f(T,t). 98

Figure 4.13 - ^{13}C solid-state NMR analysis results. 100

Figure 4.14 - (a) Organic C species aromaticity index, (b) O-Alkyl/alkyl ratio and (c) hydrophobicity index as a function of increasing HT severity f(T,t). Dashed lines are included to help data interpretation. 103

Figure 4.15 - (a) P, Ca, Fe, Mg, (b) Al, K, Zn, Cu content in solid pellet by-product, expressed as mg g^{-1} of dry solid, as a function of HT severity f(T,t). Error bars represent propagated uncertainty. Dashed lines are included to help data interpretation. 104

Figure 4.16 - (a) Cr, Pb, Ni, V, Ag, (b) As, Cd, Hg content in solid pellet by-product, expressed as mg kg^{-1} of dry solid, as a function of HT severity f(T,t). Error bars represent the propagated uncertainty combined with the relative standard deviation associated with the spectrometric intensity measurement (3). Dashed lines are included to help data interpretation. 105

Figure 4.17 - P relative repartition in the two by-products (solid pellet and process water). P fraction in the solid pellet is calculated by difference under the hypothesis that no gaseous or volatile P species are formed during the SS HT treatment. Error bars represent propagated uncertainty. 108

Figure 4.18 - P speciation in the solid pellet as a function of HT severity f(T,t). Error bars represent propagated uncertainty. 110

Figure 4.19 - Ca/P, Fe/P and Mg/P (a) K/P (b) and N/P (c) molar ratios in process water by-product as a function of severity f(T,t). Error bars represent propagated uncertainty. Dashed lines are included to help data interpretation. 111

Figure 4.20 - Ca/P, Fe/P, Mg/P, K/P and N/P molar ratios in solid pellet by-product as a function of severity f(T,t). Error bars represent propagated uncertainty. Dashed lines are included to help data interpretation. 112

Figure 4.21 - Second-degree polynomial surface response for P concentration in process water (mg P L^{-1}), based on the experimental design reported in Table 2.1, as a function of temperature (°C) and treatment duration (min) as expressed by Equation 4.6, with the coefficients reported in Table D.6. 114

Figure 4.22 - Second-degree polynomial surface response for P recovery yield in solid pellet (%), based on the experimental design reported in Table 2.1, as a function of temperature (°C) and treatment duration (min) as expressed by Equation 4.7, with the coefficients reported in Table D.8. Solid pellet P fraction is calculated by difference under the hypothesis that no gaseous or volatile P species are formed during the SS HT treatment. 115

Figure 4.23 - Second-degree polynomial surface response for AIP in solid pellet (% TP), based on the experimental design reported in Table 2.1, as a function of temperature (°C) and treatment duration (min), expressed by Equation 4.8 (coefficients reported in Table D.10). 116

Figure 4.24 - Proposed P mechanism. (I) OP mineralization to soluble PO_4^{3-} (II) Dissolution of Fe and Al P phosphates to soluble PO_4^{3-} (III) PO_4^{3-} (re)-precipitation with Ca^{2+} cations under the form of Ca phosphates. For less severe reactions (250 °C) (I) and (II) are prevalent. At more severe conditions (350 °C) reaction (III) is prevalent. 117

Figure 4.25 - Reactor internal temperature and heating rate (as defined in Equation 4.9) for three HT treatments realized with the same feed mass (110 g), same mixing rate (700 rpm), same initial temperature (17 °C) and same target temperature (250 °C), at three increasing initial pressures (0 MPa, 2 MPa, 7 MPa). 121

Figure 4.26 - Heat flux (W kg^{-1}) of a DSC experience realized on a 20% DM sample (400 mg dried sludge + 1600 mg water) with an initial pressure of 4.7 MPa, using the "exhaust method" described in Section 2.5. 122

Figure 4.27 – Heat flux of three DSC analysis realized using 2 g of sludge 20% DM with respectively no pressurization, 4.7 MPa and 9.4 MPa of N_2. q_{HT} is expressed as W kg^{-1} of dry matter. 123

Figure 4.28 - Results of three DSC analysis realized using 2 g of sludge with varying solid loading (10%, 20%, 30% DM) with 9.4 MPa of N_2. q_{HT} is expressed as W kg^{-1} of dry matter. 123

Figure 5.1 - Balances for total mass and P, Ca, Fe, Mg and K, for Sludge A and B HT treatments. 132

Figure 5.2 - Mass distribution of the HT products from Sludge A and Sludge B showing the repartition of water and TS between the pellet and the process water after centrifugation. 133

Figure 5.3 - HT products TSRY (Equation 2.8) for both sludges, compared with SS HT treatments Solid Recovery Yield (SRY) results from literature (works listed in Table A.1). 133

Figure 5.4 - Main physico-chemical properties of the two sludges HT process waters (a) pH, (b) alkalinity (g $CaCO_3$ L^{-1}), (c) NH_3-N (g N L^{-1}), (d) Total soluble N (g N L^{-1}), (e) COD (g O_2 L^{-1}), (f) Total soluble C (g C L^{-1}), (g) TIC (g C L^{-1}), (h) TOC (g C L^{-1}). pH measurement accuracy: ±0.01. Dashed lines are included to facilitate data interpretation. Error bars represent propagated uncertainty. 135

Figure 5.5 – Concentration (mg L^{-1}) of soluble P (a), Ca (b), Fe (c), Mg (d) and K (e) after HT process water of Sludge A and B. Error bars represent propagated uncertainty. 137

Figure 5.6 - Van Krevelen diagram for Sludge A (◆)and Sludge B (●) HT pellets. .. 138

Figure 5.7 - P(a), Ca (b), Fe (c), Al (d), Mg (e) and K (f) contents (mg g^{-1} of dry matter) in Sludge A and B HT solid pellets as function of severity. Error bars represent propagated uncertainty..... 140

Figure 5.8 - P recovery yield in solid pellet by-product for both Sludge A and Sludge B, compared to experimental results available in literature (from studies listed in Table A.1). 141

Figure 5.9 - SMT method NAIP and AIP relative fractions, expressed as fraction of TP, alongside the box distribution of the experimental results available in literature for NAIP (green) and AIP (orange) fractions distributions [10,77–94]. Error bars represent propagated uncertainty. 142

Figure 5.10 - Effects of using Sludge B instead of Sludge A on by-products physico-chemical characteristics..... 144

Figure 6.1 - Global mass (a), P (b) and Ca (c) mass distribution as a function of HT severity f(T,t), for the three investigated Ca/P molar ratios. Error bars represent propagated uncertainty. 148

Figure 6.2 - Fe (a), Mg (b) and K (c) mass distribution as a function of HT severity f(T,t), for the three investigated Ca/P molar ratios. Error bars represent propagated uncertainty. 149

Figure 6.3 - Total dissolved solids in process water as a function of HT severity f(T,t), for the three investigated Ca/P molar ratios. Error bars represent propagated uncertainty. Dashed lines are included to help data interpretation. 150

Figure 6.4 - Bio-oil yield (calculated according to Equation 2.2) expressed as % of total dry feed mass, as a function of HT severity f(T,t), for the three investigated Ca/P molar ratios. Error bars represent propagated uncertainty. Dashed lines are included to help data interpretation. 151

Figure 6.5 - Second-degree polynomial surface response for bio-oil yield expressed as % of dry feed matter, based on the experimental design reported in Table 2.4, as a function of temperature (°C) and treatment duration (min), for Ca/P molar ratio of 0.70 (a), 1.15 (b) and 1.60 (c), as expressed by Equation 6.3 with the coefficients reported in Table D.12. 153

Figure 6.6 - Solid pellet by-product dry mass (%) as a function of severity f(T,t) for different Ca/P molar ratios. Error bars represent propagated uncertainty. Dashed lines are included to help data interpretation. 154

Figure 6.7 - Process water pH (a), alkalinity (b), NH_4-N (c), COD (d), TOC (e) and TIC (f) as a function of severity f(T,t) for different Ca/P molar ratios. Error bars represent propagated uncertainty. Dashed lines are included to help data interpretation. 156

Figure 6.8 - Process water soluble P (a), Ca (b), Fe (c), Mg (d) and K (e) concentrations (mg L^{-1}) as a function of severity f(T,t) for different Ca/P molar ratios. Error bars represent propagated uncertainty. Dashed lines are included to help data interpretation. 158

Figure 6.9 - Second-degree polynomial surface response for soluble P in process water (mg L^{-1}), based on the experimental design reported in Table 2.4, as a function of temperature (°C) and Ca/P molar ratio (-), for treatment duration of 5 min(a), 15 min(b) and 45 min (c), as expressed by Equation 6.6 with the coefficients reported in Table D.14. 159

Figure 6.10 - Response surfaces for soluble Ca (a), Fe (b), Mg (c) and K (d) concentrations in process water based on the experimental design reported in Table 2.4, as a function of temperature and Ca/P molar ratio. Treatment duration is fixed at 15 min. Ca, Fe and Mg color scales are logarithmic. 162

Figure 6.11 - Response surface for P yield in process water based on the experimental design reported in Table 2.4, as a function of Temperature and Ca/P molar ratio for three treatment durations (5, 15, 45 min). 164

Figure 6.12 – Ca/P molar ratio (a) and Fe/P molar ratio (b) in process water as a function of severity f(T,t) for the three different feed Ca/P molar ratios (0.70, 1.15, 1.60). Error bars represent propagated uncertainty. Dashed lines are included to help data interpretation. 165

Figure 6.13 - P (a), Ca (b), Fe (c), Al (d), Mg (e) and K (f) contents in solid pellet expressed as mg g^{-1} (on a dry basis) as a function of severity f(T,t) for different Ca/P molar ratios. Error bars represent propagated uncertainty. Dashed lines are included to help data interpretation. 166

Figure 6.14 - NAIP (a) and AIP (b) fractions expressed as % of TP in solid pellet, as a function of severity f(T,t) for the three different Ca/P molar ratios. Error bars represent propagated uncertainty. Dashed lines are included to help data interpretation. 167

Figure 6.15 - AIP fraction expressed as % of total P in solid pellet by-product based on the experimental design reported in Table 2.4, as a function of temperature and treatment duration for three Ca/P molar ratios (0.70, 1.15, 1.60). 169

Figure 6.16 - Comparison between AIP fraction (% of IP) in this study (★), with data points from various studies available in literature(●) [10,77–81,86,88,89,91–93]. 169

Figure 6.17 – Ca/P (a), Fe/P (b), and Al/P (c) molar ratio in solid pellet as a function of severity f(T,t) for the three different feed Ca/P molar ratios (0.70, 1.15, 1.60). Error bars represent propagated uncertainty. Dashed lines are included to help data interpretation. 171

Figure 6.18 - (a) Global desirability color map obtained with specification described in Table 6.6 (bio-oil yield oriented). (b) global desirability color map obtained with specification described in Table 6.7 (AIP oriented). Desirability expressed as function of feed Ca/P molar ratio and temperature. Treatment duration is fixed at 45 min. 176

Figure 7.1 - schematic summary of the chemical reactions and physical mechanisms interesting the organic components of the biomass, along with the general pathways related to P conversion and speciation. ……183

List of tables

Table 1.1 - Additives used in the selected works and their effects on solid recovery yield, P partition among solid product and process water, and P speciation in solid product. 29

Table 1.2 - State of knowledge on HT Treatment of SS for P Recovery. On the right there are the elements on which this work will focus, and the corresponding chapter(s) in which each element is discussed. 33

Table 2.1 - List of the conditions selected for the temperature/time design of experiments 58

Table 2.2 - Values assumed by the five coefficients constituting the screening design of experiments model described by Equation 2.24. 58

Table 2.3 - Temperature and duration values used in the second-degree polynomial model along with their corresponding normalized values in the range -1 to 1. 59

Table 2.4 - 18 experiments constituting the surface response DOE for studying temperature, duration and Ca/P molar ratio effects on HT by-products characteristics. 60

Table 2.5 - Ca/P molar ratio values used in the second-degree polynomial model along with their corresponding normalized values in the range -1 to 1. 61

Table 3.1 - Main physico-chemical characteristics for Sludge A and Sludge B obtained with methods and techniques described in Section 2.4. Reported values are in the form a ± s (n), where a is the average of the different measurements, s the standard deviation, and n the number of measurements. 66

Table 3.2 - Main physico-chemical characteristics for Centrate A and Centrate B. Reported values are in the form a ± s (n), where a corresponds to the average of the different measurements, s is the standard deviation, and n is the number of measurements. 75

Table 3.3 - European[179] and French national[180] limits for heavy metals in sludge in the perspective of an agricultural application, compared to Sludge A and B actual values (on a dry basis). 78

Table 3.4 - Comparison between the macronutrients and organic carbon contents guidelines and the heavy metals limits prescribed by the 2019/1009 regulation[181], and the respective values for both Sludge A and B. **X** = it does not respect the guidelines. ✓ = it respects the guidelines. 79

Table 4.1 - Screening analysis results on by products distribution and mass balances based on the experimental design reported in Table 2.1. Statistical validation is reported in Table D.20 (Annex D). Positive effects are expressed through one or two positive signs (**+**), negative effects through one or two negative signs (**-**). Effects are indicated with a double sign if the effect is three times more significant than the smallest significant effect. The absence of symbols indicates that the effect is not significant. 86

Table 4.2 - Screening analysis results for process water properties based on the experimental design reported in Table 2.1. Statistical validation is provided in Table D.21 (Annex D). Positive effects are expressed through one or two positive signs (**+**), negative effects through one or two negative signs (**-**). Double sign means that the effect is three times more significant than the smallest significant effect. The absence of symbols indicates that the effect is not significant. 94

Table 4.3 - Screening analysis results for solid by-product ultimate analysis based on the experimental design reported in Table 2.1. Statistical validation is provided in Table D.22 (Annex D). Positive effects are expressed through positive signs (**+**), negative effects through negative signs (**-**). Double sign indicates that the effect is three times more significant than the smallest significant effect. The absence of symbols indicates that the effect is not significant. 98

Table 4.4 - Integration values of peaks corresponding to each family of organic compounds (% of total area). 101

Table 4.5 - Screening analysis results for metals and heavy metals contents in solid pellet (expressed on a dry basis) based on the experimental design reported in Table 2.1. Statistical validation is provided in Table D.23 (Annex D). Positive effects are expressed through one or two positive signs (**+**), negative effects through one or two negative signs (**-**). Double effects are three times more significant than the smallest significant effect. The absence of symbols indicates that the effect is not significant. 106

Table 4.6 - Screening analysis results for P distribution and speciation based on the experimental design reported in Table 2.1. Statistical validation is provided in Table D.24 (Annex D). Positive effects are expressed with positive signs (**+**), negative effects with negative signs (**-**). Double effects are three times more significant than the smallest significant effect. The absence of symbols indicates that the effect is not significant. Contents in pellets are expressed on a dry basis. 113

Table 4.7 - Comparison between the macronutrients guidelines and the heavy metals limits prescribed by the 2019/1009 regulation[181], and the respective ranges observed for solid pellet by-products. **X** = it does not respect the guidelines. ✓ = it respects the guidelines. Compositions in solid pellets are expressed on a dry basis 119

Table 4.8 - Enthalpy, peak temperature, time and intensity for the DSC experiences realized at three different initial pressures (0, 4.7, 9.4 MPa) and solid loading (10%, 20%, 30%). Enthalpy and heat flux are expressed as kJ kg^{-1} and W kg^{-1} of dry matter. 124

Table 4.9 - Energy analysis of DSC experiments. First column: total energy required to heat the sample. second column: reaction enthalpy; third column: energy supplied to the system in the form of reaction heat (%). 126

Table 5.1 - HT parameters for Sludge B treatments selected to compare the results with Sludge A products. 130

Table 6.1 - Screening analysis results on by products distribution and mass balance based on the experimental design reported in Table 2.4. Statistical validation is provided in Table D.25 (Annex D). Positive effects are expressed through one or two positive signs (**+**), negative effects through one or two negative signs (**-**). Double effects are three times

more significant than the smallest significant effect. The absence of symbols indicates that the effect is not significant. 155
Table 6.2 - Results of the screening analysis on process water characteristics based on the experimental design reported in Table 2.4. Statistical validation is provided in Table D.26 (Annex D). Positive effects are expressed through one or two positive signs (**+**), negative effects through one or two negative signs (**-**). Double effects are three times more significant than the smallest significant effect. The absence of symbols indicates that the effect is not significant. 157
Table 6.3 - Results of the screening analysis on process water composition based on the experimental design reported in Table 2.4. Statistical validation is provided in Table D.27 (Annex D). Positive effects are expressed through one or two positive signs (**+**), negative effects through one or two negative signs (**-**). Double effects are three times more significant than the smallest significant effect. The absence of symbols indicates that the effect is not significant. 165
Table 6.4 - Screening analysis results on solid pellet by-products characteristics based on the experimental design reported in Table 2.4. P, metals and heavy metals contents are expressed on a dry basis. Statistical validation is provided in Table D.28 (Annex D). Positive effects are expressed through one or two positive signs (**+**), negative effects through one or two negative signs (**-**). Double effects are three times more significant than the smallest significant effect. The absence of symbols indicates that the effect is not significant. 172
Table 6.5 - Comparison between the macronutrients guidelines and the heavy metals limits prescribed by the 2019/1009 regulation[181], and the respective ranges observed for solid pellet by-products. *guidelines and limits from [181]. P_2O_5 = P/0.436; K_2O = K/0.830; MgO = Mg/0.603; CaO = Ca/0.715; SO_3 = S/0.4. **expressed as mg kg^{-1} P_2O_5. Composition expressed on a dry basis. 173
Table 6.6 - Specifics of the first desirability study and relative results. 174
Table 6.7 - Specifics of the second desirability study and relative results. 175

General introduction

Phosphorus is an essential element for the survival of all living beings as it constitutes a fundamental block for the construction of some biomolecules essential for the proper functioning of metabolism (ATP), the construction of cellular structures (phospholipids), and the encoding of genetic information (DNA). Plants absorb phosphorus from soil, while animals and humans need to consume plants or smaller animals to obtain essential phosphorus intake. This indicates that phosphorus is a crucial nutrient for modern agriculture and food production. In recent decades, due to the application of intensive crop production, the natural phosphorus cycle has been broken. The production of phosphorus-based fertilizers is not sustainable, since it is based almost exclusively on the extraction of natural phosphate minerals deposits, which are running out. Global food security depends on the development of a sustainable model for phosphorus production, use, and recovery that gradually reduces the dependence on finite reserves. This strategy requires the development of large-scale methods to recover phosphorus from waste streams, include wastewater, sewage sludge, human excreta, animal manure, and urban waste. There are various processes for recovering the main macronutrients (nitrogen, phosphorus, potassium) from different waste streams. These include gas-liquid stripping, precipitation as salts and minerals, ion exchange, and adsorption. Additionally, some thermal treatments (incineration, pyrolysis, gasification) can produce solid products in which most of phosphorus is collected. A specific category of thermochemical treatments, known as hydrothermal processes, consist in treating biomass in a subcritical or supercritical aqueous environment at high temperatures and autogenous pressure. This PhD thesis aims to investigate the mechanisms of phosphorus conversion and speciation during the hydrothermal treatment of sewage sludge, to define how the main process parameters influence the pathways and the recovery of phosphorus. A detailed knowledge of the chemical-physical mechanisms driving phosphorus transformation under hydrothermal conditions will support the integration of mineral phase recovery (macronutrients) in the form of solid fertilizer, with a simultaneous energy exploitation in the form of bio-oil. This approach can open the way to new value chains, making the process more economically attractive and facilitating its large-scale implementation at an industrial level.

Chapter 1 will examine the current research on phosphorus conversion during hydrothermal treatment of sewage sludge. It will address the global phosphorus framework, including production and scarcity, and propose phosphorus recovery from sewage sludge as a solution. This discussion will be supported by an overview of global sewage sludge production and a critical analysis of its potential for macronutrient recovery.

1. State of the art

This first chapter presents a comprehensive overview of the current state of research about phosphorus conversion during sewage sludge hydrothermal treatment.

First, the global phosphorus (P) framework will be described, detailing the current state of P production and the worsening issue of global P scarcity. Some options that have been proposed to solve or mitigate this issue will then be presented, including P recovery from sewage sludge (SS) from wastewater treatment plants (WWTP). Subsequently, an overview of the global SS production and a critical analysis of how it can be used as a resource for macronutrients recovery will be presented. After a brief overview of the main processes currently used for the treatment and disposal of SS, the chapter will focus on hydrothermal (HT) treatments and their advantages.

In the second part of the chapter, the results from over 65 studies in the literature on the HT treatment of SS will be critically analyzed. After a statistical analysis of the general characteristics of SS and HT products, the investigation will focus on how HT treatment parameters affect product characteristics, particularly P speciation and conversion pathways.

This focus will provide a general overview of the already well-known phenomena that have been widely discussed over the past few years, but it will also allow to identify which elements have been poorly characterized and require further study. Large part of this overview has been published in Tangredi et al., 2023[1].

1.1. Global phosphorus framework

Phosphorus (P) is an essential nutrient constituting key biomolecules in all living organisms, such as phospholipids, adenosine triphosphate, and nucleic acids[2].

The natural biogeochemical P cycle starts in the phosphate rocks and minerals, in which P is generally found in apatite complexes (Ca-phosphate minerals). Erosion and weathering of these rocks lead to phosphates release into soil and water[3]. P is then absorbed by plants from the soil for energy transfer, photosynthesis and tissue construction. Animals take in P by consuming plants or smaller animals, which is then excreted as waste or returned to the environment when the organism dies. Fungi and bacteria decomposers are then able to break down P releasing it back into the soil. Part of soil P can then be subjected to leaching and runoff, in other words carried away by water, ending up in water bodies and finally into the ocean. Over long periods of time, P in water can finally sediment producing new phosphate minerals and rocks, closing the cycle[3].

Since the industrial revolution, the anthropogenic factor has disrupted the natural P cycle[4]. P is in fact crucial for modern agriculture and food production: in order to sustain intensive crop yields production, P-based fertilizers are added to soil. In the last century,

P-based fertilizers have been affected by a growing demand related to the world's population growth[2,5] and nowadays, P-fertilizer production primarily depends on P extraction from natural deposits of phosphate minerals[6].

As shown in Figure 1.1, apatite rocks reserves are not evenly distributed across the globe. More than 70% of the global reserves of apatite rocks in 2020 are in fact located in Morocco and Western Sahara[2], and the reserves of the most populous countries are expected to run out over the next few decades at the current extraction rate[7,8]. Apatite rock scarcity and geopolitical tensions can impact P-fertilizers production and distribution, affecting agriculture product costs and threatening the global food supply. Therefore, it is necessary and of high importance to develop P recovery from P-rich waste streams at a large scale.

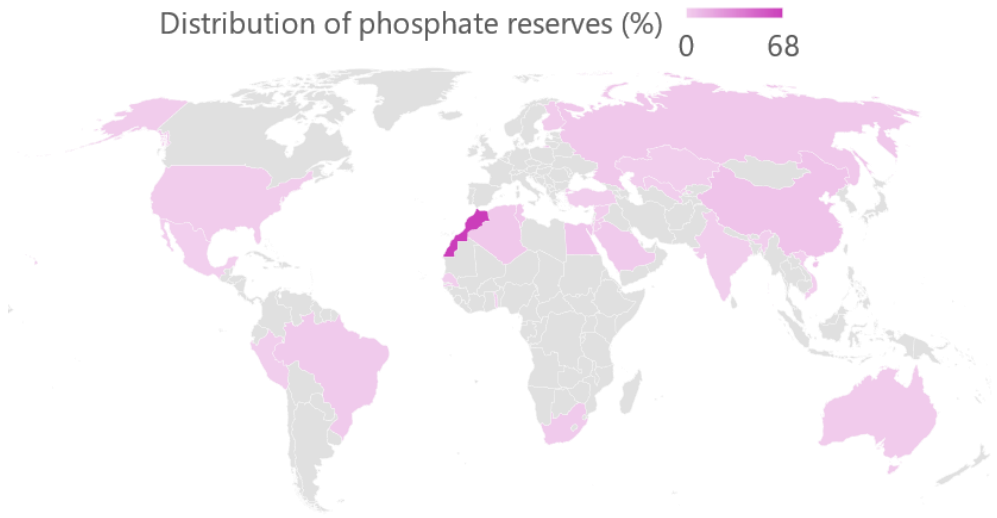

Figure 1.1 - Distribution of phosphate rock reserves around the world. Data from [7].

1.2. Sewage sludge

Sewage sludge (SS) is a heterogeneous liquid-solid suspension continuously generated in WWTP that is mainly composed of water (up to 98%)[6], organic matter (dissolved and particulate organic compounds), dangerous compounds (heavy metals, pathogens, and micropollutants)[9] and important amounts of P and other nutrients such as nitrogen (N) and potassium (K)[10], which, if not recovered, can end up in rivers, lakes, water basins, and finally in the sea, contributing to eutrophication.

SS composition and properties, including P amount and speciation, strongly depend on the sources and the type of processes exploited in the WWTP[9,11–15].

Large amounts of SS are produced globally every year. With an estimation of around 5.0 Mt y^{-1} of dried sludge in the United States, 4.4 Mt y^{-1} in India, 11.2 Mt y^{-1} in China, 2.5 Mt y^{-1} in Brazil, 2.2 Mt y^{-1} in Japan, 0.4 Mt y^{-1} in Australia, 0.1 Mt y^{-1} in Mexico[16], 1.1 Mt y^{-1} in the UK, 0.3 Mt y^{-1} in Turkey and 8.2 Mt y^{-1} in the 27 EU states[17].

Figure 1.2 presents Europe countries SS annual production expressed in kt of dried matter.

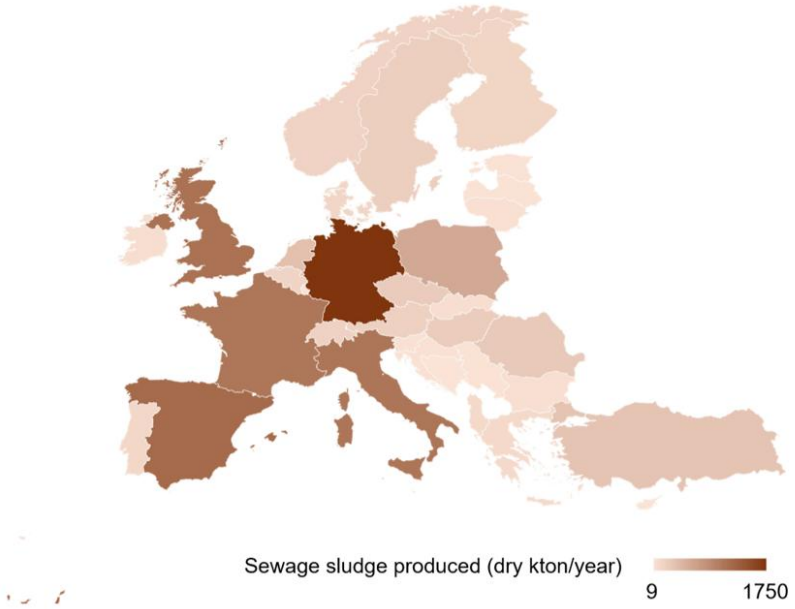

Figure 1.2 - (a) Sewage sludge annual production expressed in kt of dried sludge per year. (b) sewage sludge annual per capita production expressed in kg of dried sludge per year. Data from Eurostat[17].

SS global production rate is rising, due to world population growth and wastewater volumes increase, this trend is linked to the fact that an expanding share of global population is now connected to wastewater treatment facilities. Because of these reasons, the use of SS as a resource for P recovery becomes an important tool to support the global food supply and limit eutrophication[2,18]. In some countries, SS could be the largest P waste stream source[18], making P recovery from SS a crucial step to realize the perspective of a sustainable cycle. Previous researches[18] have shown how P recovery and reuse from various waste streams, including SS, can partially contribute in meeting the growing global P demand if integrated with improved efficiency of the anthropogenic P cycle, through enhanced agricultural efficiency and diet changes.

Besides, water scarcity and quality degradation is an escalating issue in various parts of the planet, including Europe[19], making wastewaters reclamation central in a sustainable circular approach. In response, there has been a notable shift in the scientific community's approach to wastewater management, moving away from conventional waste treatment methods, towards recognizing wastewater and SS as valuable resources[20]. Moreover, WWTP are increasingly viewed as important hubs for the recovery of different resources beyond water, such as energy, nutrients, heavy metals, cellulose, volatile fatty acids, and CO_2 [20], which are generally concentered in SS and can be recovered by subjecting SS to various treatment technologies.

Over the last two decades, SS anaerobic digestion (AD) has become increasingly widespread in Europe and USA[21]. In this process, organic waste is broken down by anaerobic bacteria, producing biogas (mainly CH_4 and CO_2) and a by-product called digestate[22], rich in minerals and organic matter. The energy transition promotes an increased biogas production via AD, resulting in more and more digestate. Thus, efficient management of digestate (and SS in general) is crucial to prevent disposal issues from becoming a major bottleneck and hindering biogas production[23].

All types of sludges must be subjected to treatments to reduce their dangerousness to the environment and human health before being released into the environment. Currently, SS treatments for safe disposal can account for up to 60% of the total costs of WWTP[24]. In the past, raw sludge application on agricultural lands has been the most popular SS disposal method, but due to increasingly strict legislation [25,26] and the reduction of available land space[27], this application is now generally avoided.

Several methods are available for SS treatment and disposal. Dewatering (SS water content reduction) can be realized by different techniques: solid-liquid mechanical separation[28], evaporation[29], and membrane treatments[30] are possible alternatives to reduce the SS water content and individually exploit the liquid and solid phases. Gas-liquid ammonia stripping, struvite ($NH_4MgPO_4 \cdot 6H_2O$), calcium phosphate or hydroxyapatite precipitation, ion exchange and adsorption are all available processes for recovering nutrients (P, N, K) from SS[31]. All these techniques have some technical limitations at the current state of the art. Membrane separation, ion exchange and adsorption technologies are still in a development phase and are characterized by high operation costs (membrane fouling, desorption, regeneration) and low removal efficiency. Both gas-liquid ammonia stripping and the chemical precipitations are effective exclusively on aqueous phases (SS leachate), and only if P or N are present in ionic form. Moreover, struvite precipitation requires an equimolar N/P ratio, which is often not present, and therefore does not allow the complete precipitation of both elements. Additionally, it is often necessary to add Magnesium (Mg) in the form of MgO.

Thermal treatments allow to destroy organic pollutants and pathogens, while yielding valuable by-products including chars, biofuel and syngas[32]. Among the possible thermal treatments, the most applied ones are dry processes such as incineration, pyrolysis, and gasification[33–35]. These treatments differ in temperature, pressure, and oxygen conditions[31], but they are all performed at high temperatures (>300 °C) to decompose organic pollutants and reduce pathogens[36]. Most of the nutrients (especially P and K) are generally retained in the solid residues (biochars and ashes)[6], and, therefore, these by-products are directly used as fertilizers, or subjected to chemical leaching to recover the nutrients[31,37]. However, these treatments usually require an energy-intensive pre-drying step that can affect operative costs[27,38].

1.3. Hydrothermal treatments

During the last decade, an increasing number of international studies has investigated the applicability of HT processes (HT carbonization, liquefaction, and gasification) for the

treatment and valorization of various types of residual biomasses, including algae, animal manure, SS, and anaerobic digestates[39–42].

HT treatments consist in exposing the wet biomass to high temperatures and autogenous pressures[43,44] to convert the biomass into high-value by-products (biofuels and chemicals)[45,46] through energy densification, carbon concentration, and oxygen elimination[5]. The by-products' characteristics and distribution depend on various factors, including biomass composition, water content, presence or absence of a catalyst, temperature, and process duration[9].

One of the advantages of HT treatments is that they do not require a pre-drying step, which could make them more economically attractive than dry processes[46]. Indeed, water has a central role in HT treatments acting both as a reaction medium and as a reagent, promoting the polymerization, decarboxylation, dehydration, and hydrolysis reactions that characterize the HT conversion process[38]. With increasing temperature, the water dielectric constant decreases[47], allowing water to better dissolve organic molecules. Besides, a temperature increase leads to a viscosity reduction, which increases the diffusion coefficient and mass transfer coefficients, and increases the ionic product, making sub-critical water an optimal medium for catalyzing acid/base reactions[48].

HT treatments can be classified based on the nature of the product present in a higher quantity or which is the object of practical interest, as follows: hydrothermal carbonization (HTC) produces mainly a solid product, the hydrochar, and it is operated between 180 and 280 °C with a slow heating rate[49]; hydrothermal liquefaction (HTL) is realized at 250 - 400 °C with a faster heating rate and a shorter residence time[49], and the target product is the bio-oil; finally hydrothermal gasification (HTG), realized at temperatures higher than 400 °C and in supercritical water conditions, yields a high CH_4 and H_2-rich syngas [45,50]. Figure 1.3 shows the water phase diagram, and the temperature/pression regions typically associated with HTC, HTL and HTG.

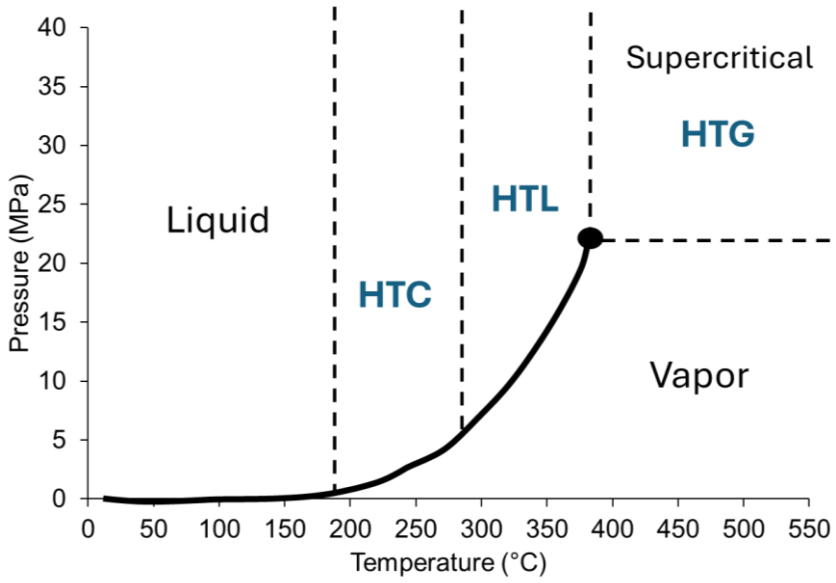

Figure 1.3 - Water phase diagram with regions typically associated with HT carbonization (HTC), liquefaction (HTL) and gasification (HTG).

HT treatment of SS is the subject of numerous studies and many reviews in the literature[2,5,6,9,11,27,33,38,44,49]. To date, there is a quite clear understanding of the mechanisms behind the degradation of organic species in biomass subjected to HT treatment. An analysis of these mechanisms will be described in Section 1.4.

On the other hand, to the best of our knowledge, the effect of the main HT process parameters on the mineral phase, and more specifically on P distribution and speciation in the byproducts, have not been characterized comprehensively, and the main P conversion pathways during HT treatment of SS are still poorly understood. In Section 1.5 the results of a relevant number of recent studies will be analyzed. These studies have investigated P conversion during HT treatments of SS, providing a critical reading of the collected results, and suggesting some physicochemical mechanisms underlying the P conversion pathways. The influence of the main process parameters, including temperature, pressure, reaction time, liquid-to-solid ratio, acidic-basic treatment, and addition of additives, on the distribution and speciation of P in the HT by-products is also investigated by a in depth critical analysis of the literature data, providing a comprehensive overview to elucidate the main P conversion pathways.

1.4. Fate of organic matter: reaction pathways to hydrochar formation

The organic matter present in the biomass undergoes various transformations during HT treatment, constituting a relatively complex reaction pathways scheme which have been the subject of numerous studies[51–53]. These studies have provided a definite overview of the mechanisms leading to the carbonization of biomass and the formation of hydrochar which is reported in the next three paragraphs and resumed in Figure 1.4.

1.4.1. Hydrolysis

Hydrolysis is favorized by the presence and the properties of HT water (sub-critical conditions). In these conditions, water molecules break more easily the ester and ether bonds constituting the main organic macromolecules.

- The hemicellulose present in the biomass is generally the one that hydrolyses first, starting already at 180 °C[54], yielding xylose[52], glucose, mannose, galactose and acetic acid[51].
- Cellulose starts to hydrolyze at 230 °C[54]. Glycosidic 1→4 bonds are broken down by water molecules to form various oligomers constituted by 2 to 6 units of glucose[55,56].
- Lignin is the last one to be hydrolyzed (T>260 °C)[54], due to the prevalence of ether bonds which are more difficult to break[57]. Lignin hydrolysis leads to the release of various phenolic compounds[51–53], polyhydroxyalkanoates[52] and catechol[53].
- Sucrose and starch are hydrolyzed into the respective monomers (glucose and fructose)[58].

- Protein hydrolysis leads to the production of polypeptides, further broken into oligopeptides and dipeptides and finally amino acids[52]. Due to the higher stability of peptide bonds, protein hydrolyze at a slower rate and at more severe conditions compared to carbohydrates[59].
- Lipids hydrolysis leads to the release of triglycerides and phospholipids, further hydrolyzed into glycerol, orthophosphates and various long chain fatty acids[60].

1.4.2. Dehydration and decarboxylation

Dehydration denotes the set of reactions that leads to water removal from a molecule, usually by attacking a hydroxyl group. Decarboxylation consists of a carboxyl group loss. During HT treatment of biomass, carboxyl groups are attacked at relatively low temperatures (150 °C)[51].

Subjected to dehydration and decarboxylation, monosaccharides gets fragmented to form various soluble intermediates[52,60], such as furans, furfurals, aldehydes and organic acids (acetic, lactic, propionic and formic acid)[61]. The latter lead to a decrease in the reaction medium pH[62]. Phenolic structures derived from lignin are less influenced by dehydration and decarboxylation, due to their higher stability[52,63]. Some amino acids can be subjected to decarboxylation to form organic acids, amines and CO_2[52,64]. Dehydration and decarboxylation of fatty acids leads to the formation of alkane and alkene intermediates[60]. The further dehydration/decarboxylation of all these intermediates leads to the formation of CO_2 and H_2O. While dehydration and decarboxylation usually occur together, the rate of dehydration is always higher that the rate of decarboxylation[65].

Fatty acids, fatty acids esters and alkenes resulting from lipids hydrolysis, aldehydes and ketones from monosaccharides decarboxylation and dehydration, and phenols produced by lignin degradation are all components of the so called “bio-crude” or “bio-oil” product which is mainly produced during HTL[66,67].

1.4.3. Polymerization, condensation and aromatization

Phenolic derivatives, monosaccharides intermediates, alkanes and alkenes, are all subjected to polymerization and condensation reactions that lead to the formation of soluble polymers[52] and aromatic clusters[52,60] (aromatization). At the basis of the polymerization there are reactions such as intramolecular dehydration and aldol condensation[52,68,69] which lead to the formation of C=O and C=C bonds[58]. Lignin derivatives are highly reactive species, and their polymerization is characterized by a fast kinetic at T > 300 °C. Monosaccharides intermediates are subjected to a much slower polymerization, due to competing recondensation to oligosaccharides[51,52]. Amines can react with sugars following Maillard reactions to produce N-containing heterocycles that can polymerize into melanoidins[52,60]. All these aromatic polymerized compounds containing C=O, C=C and C=N bonds structurally reorganize to form N-containing

monocyclic and dicyclic aromatic structures, which are at the bases of the hydrochar[52]. Additionally, the formation of these structures is enhanced by alkaline conditions[69].

Aromatic clusters start to grow in the reaction medium until the formation of hydrochar nuclei, then microspheres, that increase in size with temperature and time[58].

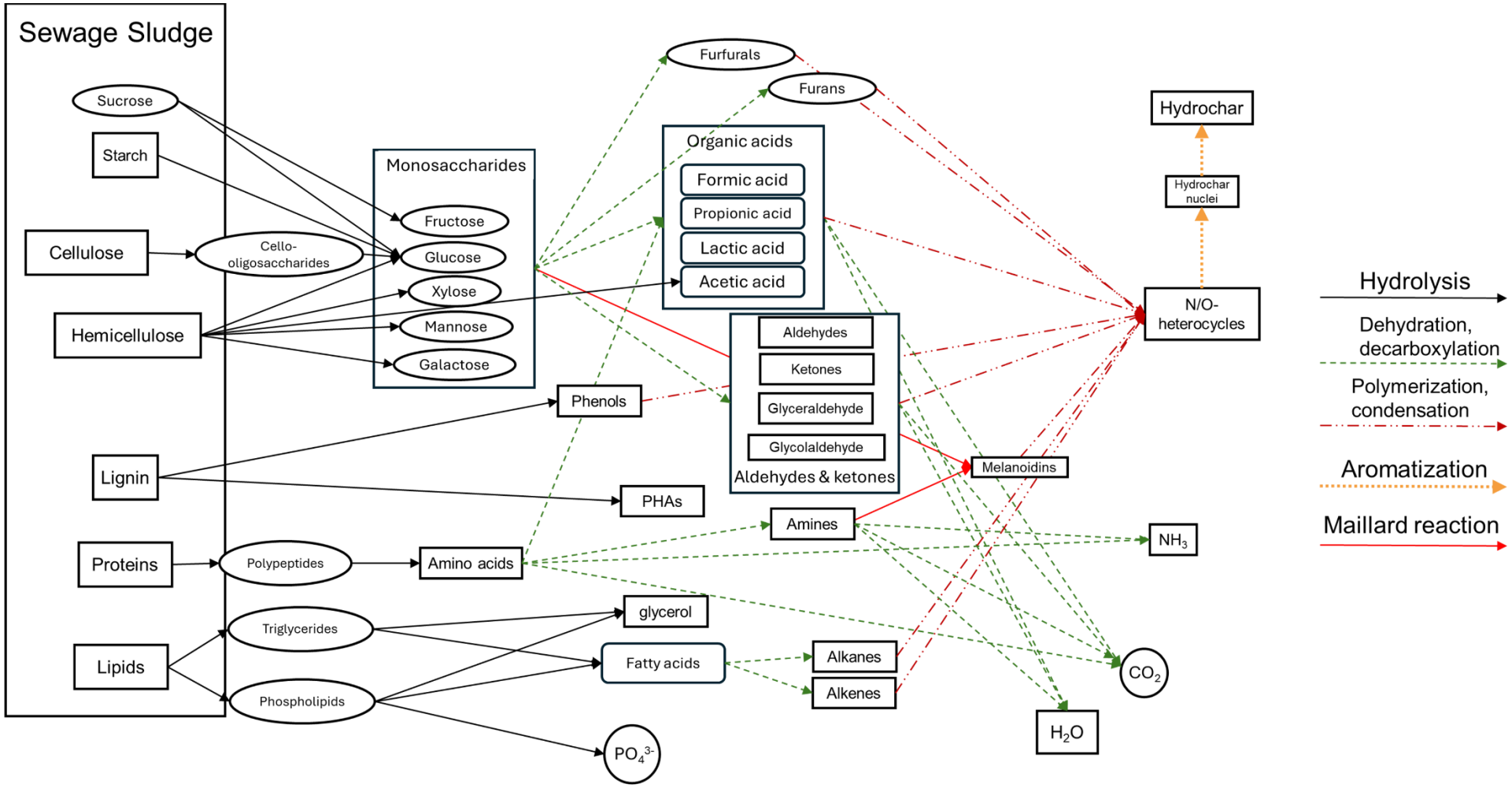

Figure 1.4 - Overview of the mechanisms and reactions which the organic matter undergoes during the hydrothermal treatment of sewage sludge, leading to the carbonization of biomass and the formation of hydrochar.

1.5. Selected studies of sewage sludge hydrothermal treatments

1.5.1. Sewage sludge type and composition

A critical classification and analysis of published studies in the literature allowed the selection of over 60 works that investigate P conversion during HT treatments of SS. The studies were selected using Web of Science (Clarivate) by using the combination of different keywords (hydrothermal, phosphorus, nutrients, speciation, fate, carbonization, liquefaction, gasification). All selected studies have been published in the last 10 years, 40 of which after 2020. Table A.1 shows the studies that provide information on the main HT process parameters and experimental results on P speciation and migration in HT treatment by-products.

The main parameters that were considered for the characterization of the SS used as feedstock are their geographical origin and production process, as well as physical-chemical parameters such as pH, water content, nutrient content (P, N, and K), and metal content, in particular Calcium (Ca), Iron (Fe), Aluminum (Al), and Magnesium (Mg), which are elements with high affinity to P binding.

The SS presented in Table A.1 have been categorized into four main categories according to their production process:

i) Primary SS, that are generated by mechanical treatments, in which solid particles and oils are separated from wastewater.
ii) Secondary SS, that result from biological treatments in which various microorganisms degrade the organic fraction.
iii) Digested SS, that represents the product of AD in which SS is stabilized with a simultaneous biogas production[70].
iv) Mix or not specified sludge, that represent mixtures of different types of sludges, or in case there was not enough information to identify the sludge nature.

Among the selected works, digested SS constitutes the main SS type used as feedstock (40%). As shown in Table A.1, most of the studies are from Europe (39%), China (31%), USA (11%), and Japan (8%).

Figure 1.5 presents a statistical analysis on the contents of P, N, Fe, Ca, Al, Mg, and K among the SS used as HT feedstock in the selected studies (mg element g^{-1} dried SS). The results indicate that P content varies between 2.8 and 56.2 mg P g^{-1} SS, with an average value of 27.4 mg P g^{-1} SS and a median value of 22.7 mg P g^{-1} SS. This P distribution, obtained by combining the data of 65 different sludges, is in good agreement with the findings of Liu et al. [11]. P concentration in raw SS presents a certain variability, due to several factors, including wastewater origin and SS production process. For most studies in Table A.1, SS derives from municipal WWTP, which usually treats domestic effluents. However, the treated wastewater is not always specified, and some of the SS reported in

Table A.1 could derive from a mixture of domestic and (agro)-industrial effluents, which can affect P content variability.

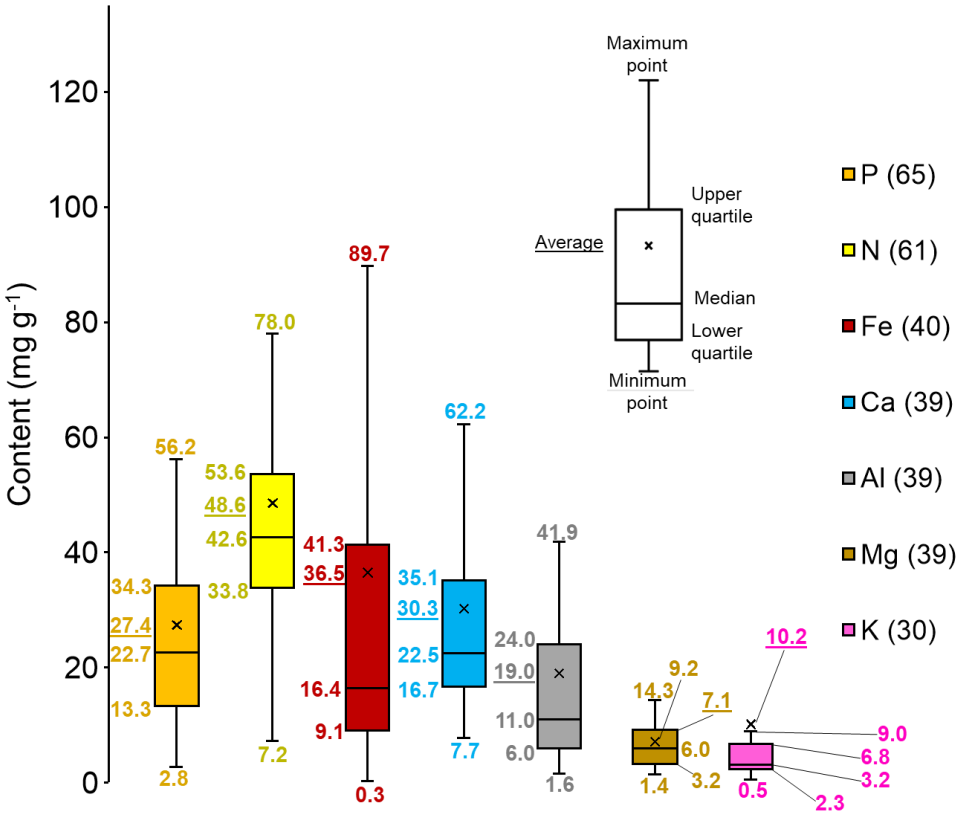

Figure 1.5 - Box distributions of P, N, Fe, Ca, Al, Mg, K contents in sewage sludge expressed as mg g^{-1} of dry sewage sludge. Average values are underlined. Data collected from works listed in Table A.1. For each distribution, the number of experimental data is shown in brackets in the legend.

The average contents of Fe, Ca, Al, and Mg in SS used as feedstock in the selected studies were 36.5 mg Fe g^{-1} SS, 30.3 mg Ca g^{-1} SS, 19.0 mg Al g^{-1} SS, and 7.1 mg Mg g^{-1} SS, respectively. It is important to consider these elements, as under HT conditions they may form stable solid precipitates such as Ca and Mg phosphates, but also Fe and Al (hydro)-oxides which can adsorb phosphates in solution (P-ferrihydrite, P-alumina, P-Al hydroxide)[71]. Fe, Al, Mg, and Ca-P complexes are known to present lower solubility compared to other compounds such as K and Na-P salts[72,73]. This property together with the prevailing amounts of these elements over other metals in wastewater treatment systems[11] makes Fe, Al, Mg, and Ca-P complexes the main precipitate forms controlling P recovery in the solid product. The average contents of N and K in SS used in the selected studies are 48.6 mg N g^{-1} SS and 10.2 mg K g^{-1} SS, respectively (Figure 1.5). It is also interesting to characterize N and K contents, because they can react with P to form stable precipitates with strong practical interest (two commercialized fertilizers), namely struvite and K-struvite ($KMgPO_4 \cdot 6H_2O$).

Figure 1.6 shows the molar ratios Fe/P, Ca/P, Al/P, Mg/P, N/P, K/P in the SS that were used as HT feed. Average molar ratios of Fe/P, Ca/P, and Al/P were 1.00, 1.47, and 0.93,

respectively. These values are very close to those of the most commons Fe, Ca, and Al phosphates that can precipitate in water solutions ($FePO_4$, $CaHPO_4$, $Ca_5(PO_4)_3(OH)$, $AlPO_4$)[72], suggesting that, in most SS, Fe, Ca, and Al contents are not limiting for phosphate precipitation. Indeed, N is nearly always present in higher stoichiometric quantities than those required for struvite precipitation, as shown by the average N/P molar ratio of 6.3 (Figure 1.6). This suggests that struvite precipitation is not an effective way for N recovery from SS, as only a small fraction of the total N in SS would be recovered. Moreover, it should also be noticed that Mg is present in stoichiometric defect (average Mg/P molar ratio in SS is 0.56), and it would be necessary to add Mg salts to allow complete P recovery by struvite precipitation. The results in Figure 1.6 also indicate that K is always present in stoichiometric defect (average K/P molar ratio in SS is 0.37) compared to the amounts required for K-struvite precipitation.

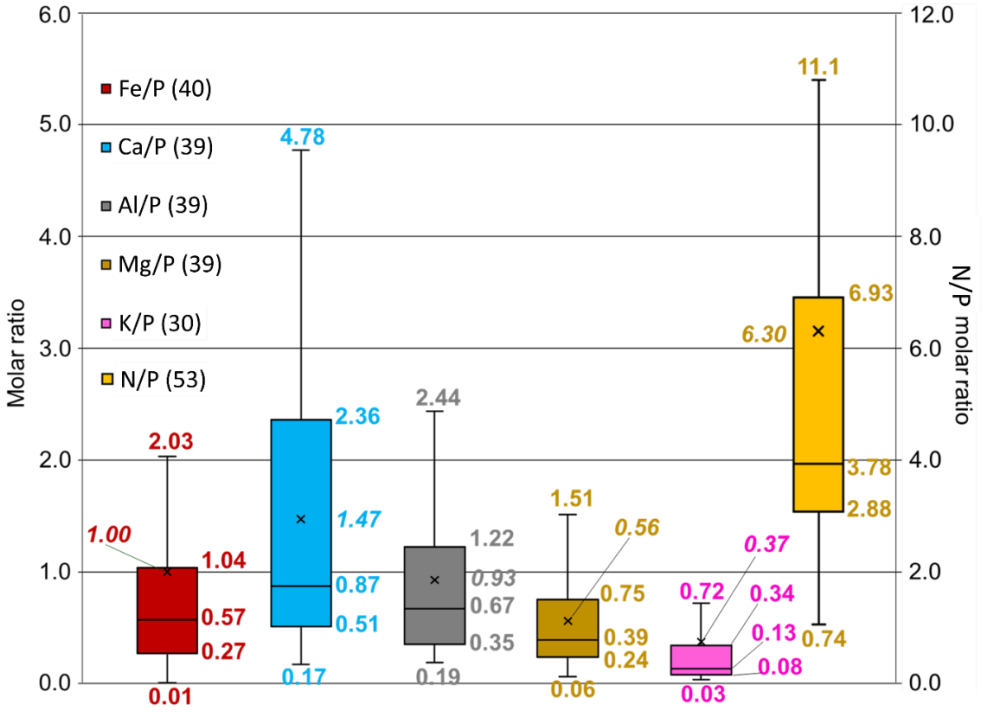

Figure 1.6 - Box distributions of Fe/P, Ca/P, Al/P, Mg/P, K/P and N/P molar ratios in sewage sludge. Average values are underlined. Data collected from works listed in Table A.1. For each distribution, the number of experimental data is shown in brackets in the legend. N/P molar ratio values can be read in the left axis.

Figure 1.7 presents a statistical analysis on the contents of Non-Apatite Inorganic P (NAIP), Apatite Inorganic P (AIP), and Organic P (OP) compared to the total P contents (TP) in SS used as feedstock for the selected studies. These P fractions were determined by Standard Measurements and Testing method[74,75]. TP represents total P, which includes OP and inorganic P (IP). The latter can be further classified in AIP and NAIP. OP is referred to P present in organic compounds such as DNA, phospholipids, and ATP. AIP represents P associated with various Ca compounds, whereas NAIP is inorganic P that is not associated with Ca compounds[76]. The average values in Figure 1.7 indicate that NAIP usually represents the highest P fraction in SS (57% of TP), followed by AIP (24% of

TP) and OP (16% of TP)[10,77–80]. However, it should be noticed a high variability on P fractions between the different SS. Indeed, the original Ca, Al, Fe, and Mg contents in wastewater, as well as the addition of $FeCl_3$ or $Al_2(SO_4)_3$ as reagents to improve P precipitation in WWTP can affect the distribution of P fractions in SS.

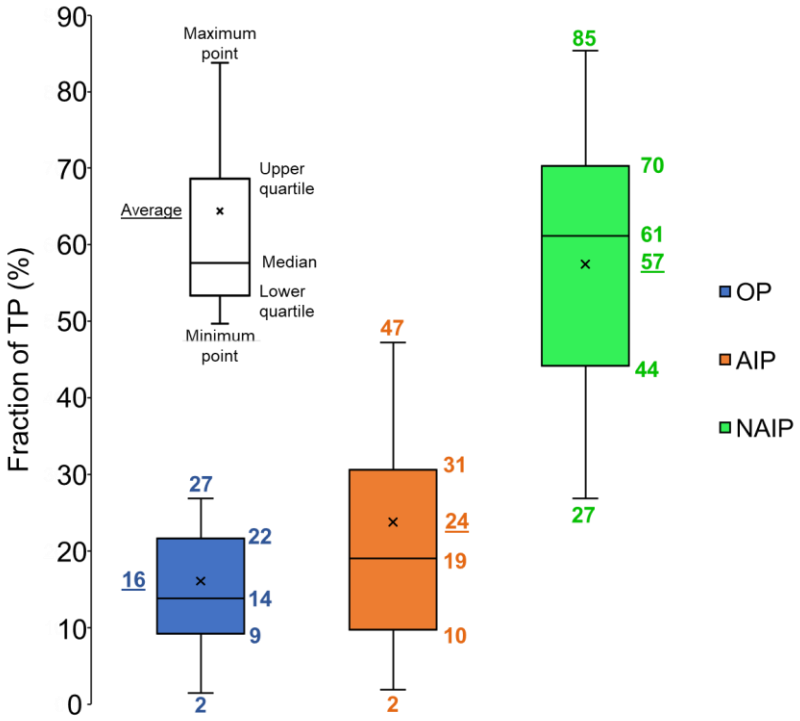

Figure 1.7 - Box distribution of the apatite inorganic P (AIP), non-apatite inorganic P (NAIP), and organic P (OP) relative amounts in sewage sludge. expressed as a fraction of the total P content. Average values are underlined. Data from [10,77–94].

It has been suggested that the geographical origin could reflect some of SS physicochemical characteristics, because of local differences in people's diets and/or WWTP sizes and technologies. Nevertheless, according to the results of this study, no specific trend was observed between SS composition, P speciation and its geographic origin, probably because of the small number of selected samples, the strong variability on production processes and WWTP process parameters among the same geographical areas.

1.5.2. Hydrothermal process parameters

The main HT process parameters that have been investigated in the selected studies from the literature (Table A.1) are the temperature and duration of the HT process, and the solid-to-liquid ratio (SLR), which is defined as the mass ratio of the dry matter to water of the SS solution used as HT feedstock (Equation 1.1).

$$SLR = \frac{m_{dry}}{m_{water}} \quad (1.1)$$

For this review, 580 experimental points (temperature and time pairs) have been collected and analyzed from the selected studies summarized in Table A.1. As shown in Figure 1.8, many of the temperature-time pairs are within the temperature range associated with HTC (60%) or lower temperatures (18%), and only a small fraction is within the temperature ranges associated with HTL (12%) or HTG (10%). Moreover, data in Figure 1.8 indicates that relatively longer reaction times (> 120 min) are usually associated with lower temperatures (< 250 °C), while at higher temperatures usually correspond to shorter reaction times. Importantly, the distinction between HTC, HTL, and HTG is not unambiguously defined, and slightly different alternative temperature ranges are often suggested in the literature. What defines whether the HT treatment is carbonization, liquefaction, or gasification, is above all the nature of the target product (solid, liquid, or gaseous). For this reason, some of the studies that carry out HTC, also apply temperatures above 280 °C, which are generally associated with HTL.

The SLR values for the different HT treatment studies summarized in Table A.1 range from 0.02 to 0.34 kg L^{-1} (70% wt to 98% wt of water content), with a median value of 0.11 kg L^{-1} (90% wt of water content). This large range of SLR values may indicate that solid/liquid pretreatment, such as centrifugation or drying, was applied to raw SS before performing HT experiments.

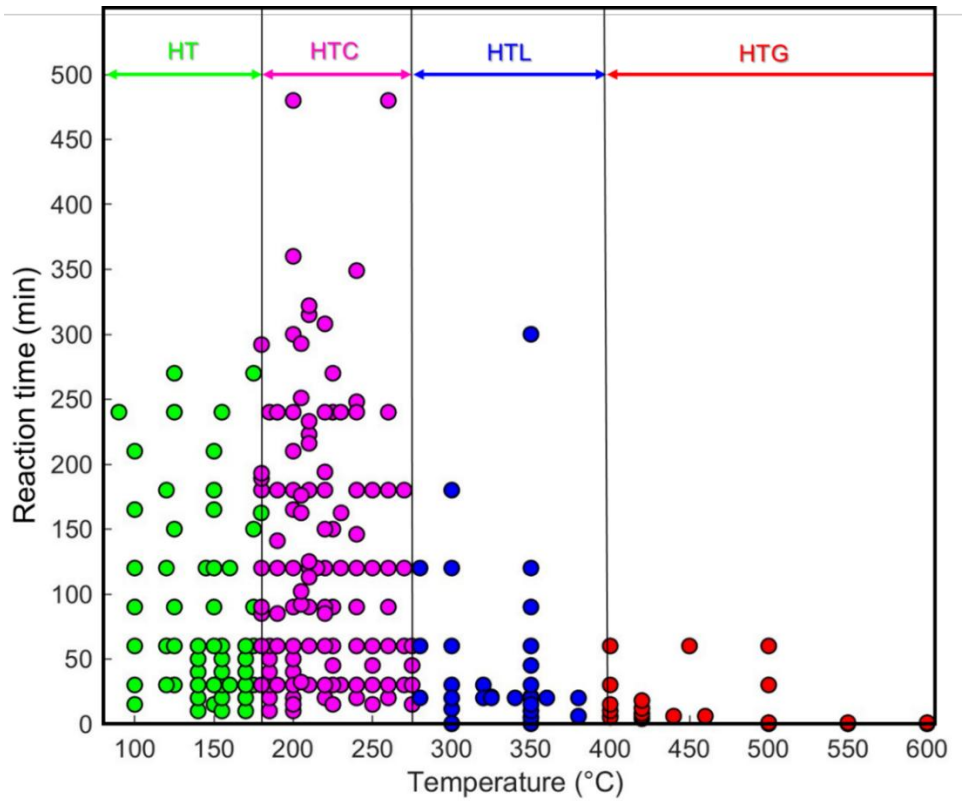

Figure 1.8 - Temperature and reaction time of hydrothermal studies listed in Table A.1. Pink points (274) correspond to typical hydrothermal carbonization temperatures, blue points (49) to hydrothermal liquefaction temperatures, red points (45) to hydrothermal gasification temperatures, and green points (90) to hydrothermal treatments at relatively low temperatures (T < 180 °C).

1.5.3. Main results of selected studies

The main results of HT treatments, including Solid Recovery Yield (SRY) (%), P recovery yield in the solid product (%), P content in the solid product (mg P g^{-1} dried hydrochar), and P concentration in process water (mg P L^{-1}), for all the selected studies are summarized in Table A.1.

The Solid Recovery Yield (SRY) (%) is defined by Equation 1.2, where $m_{SP,dry}$ is the solid product dry mass (g), and $m_{SS,dry}$ the feed SS dry mass (g).

$$\text{Solid product recovery yield (\%)} = \frac{m_{SP,dry}}{m_{SS,dry}} \cdot 100 \quad (1.2)$$

The solid product recovery yield from the selected studies varies from a minimum of 27% up to 100%, with an average value of 67%. Generally, most of the works report a solid product recovery yield between 60% and 80% (Table A.1). P recovery yield in the solid product (%) is defined by Equation 1.3, where $C_{P,SP}$ and $C_{P,SS}$ are the total P content in the solid product and in the SS (mg P g^{-1} dried mass).

$$\text{P recovery yield in solid product (\%)} = \frac{C_{P,SP}}{C_{P,SS}} \cdot 100 \quad (1.3)$$

The P recovery yield in the solid product from the selected studies varies from a minimum of 6% up to 100%, most probably because of the large range of temperature and duration of the HT treatment process among the different studies (Table A.1).

According to the data in Table A.1, total P content in the solid product vary from 3.3 to 178.6 mg P g^{-1} dried hydrochar, whereas P concentration in process water varies from 0.2 mg L^{-1} up to 5160 mg P L^{-1}, with an average value of 442 mg P L^{-1} and a median value of 130 mg P L^{-1}. This high variability in P concentration could be partially explained by the large discrepancies on SLR used for HT experiments in the different studies, as higher SLR may give higher P concentrated liquid effluents.

Figure 1.9 summarizes the statistical distribution of total P, Fe, Ca, Al, and Mg contents in the solid products from the HT treatments (mg g^{-1} dried hydrochar) for the selected studies in Table A.1. The average contents in hydrochars were 41.1 mg P g^{-1}, 51.3 mg Fe g^{-1}, 39.8 mg Ca g^{-1}, 19.7 mg Al g^{-1}, and 7.1 mg Mg g^{-1}, respectively, thus indicating that all these elements tend to be concentrated in the HT solid product[5].

Figure 1.10 summarizes the distribution of OP, AIP, and NAIP fractions (%) compared to the total P content in the solid products from the HT treatments for the selected studies in Table A.1. The average values in Figure 1.10 indicate that NAIP represents the highest P fraction in the HT solid products (52% of TP), followed by AIP (40% of TP) and OP (5.5% of TP). Interestingly, NAIP and OP fractions in HT solid residues are significantly lower than those of SS before HT treatment (Figure 1.7). Most probably, the high temperature of the HT process promotes OP mineralization to phosphate[65,71,87], followed by Ca-phosphate precipitation, thus reducing OP and increasing AIP fractions.

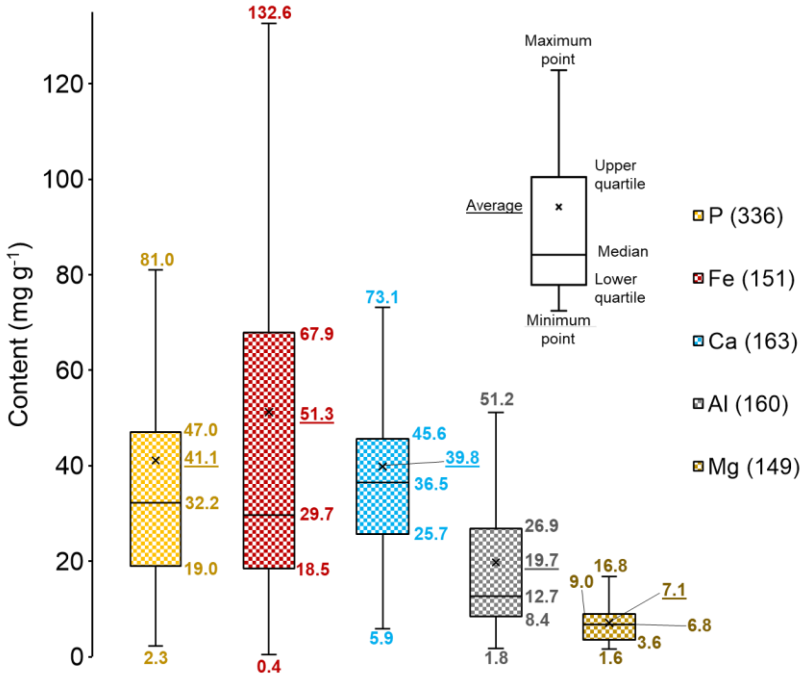

Figure 1.9 - Box distributions of P, Fe, Ca, Al, Mg contents in solid products of hydrothermal treatment (expressed as mg g^{-1} of dry solid product). Average values are underlined. Data collected from works listed in Table A.1. For each distribution, the number of experimental data is shown in brackets in the legend. Data from solid products include only hydrothermal treatments without pH adjustments or addition of additives.

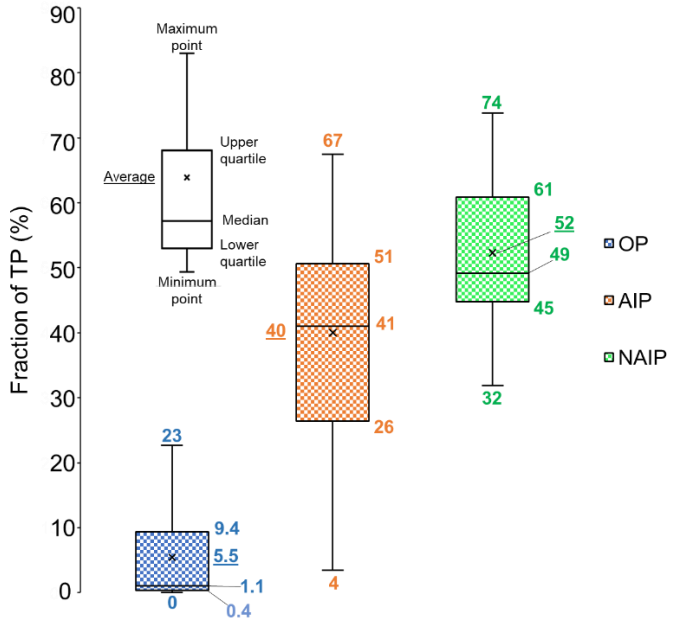

Figure 1.10 - Box distribution of the apatite inorganic P (AIP), non-apatite inorganic P (NAIP), and organic P (OP) relative amounts in solid products of HT process expressed as a fraction of the total P content. Average values are underlined. Data from [10,77–94]. Data from hydrochar include only hydrothermal treatments without pH adjustments or addition of additives.

The characterization of P species in the products from HT process is very important to predict their P bioavailability. Indeed, plants can directly only sorb inorganic P anions, such as orthophosphates[95]. P bioavailability is a complex topic that depends on different factors, such as temperature, P distribution between OP, NAIP, and AIP fractions, presence of Fe and Al oxides, amount of $CaCO_3$, P adsorption-desorption rates, pH, and humidity[73,74].

Therefore, several studies have further characterized P contents in SS and HT products by Liquid ^{31}P NMR. The most commonly analyzed compounds are orthophosphate, orthophosphate monoester and diester, pyrophosphate, and polyphosphate[10,82,86,96]. Orthophosphate and pyrophosphate are considered IP, while monoester-P and diester-P are major constituents of OP[10]. The results indicate that orthophosphate is the dominant species in SS before HT treatment[10,82,96], with smaller proportions of monoester-P[10,82,86], diester-P[82,86] and pyrophosphate[10,86]. Indeed, OP species (monoester and diester) are usually not present in the HT products[10,82], making orthophosphate the only detectable P form in the hydrochars[43]. Shi et al.[10] observed a stronger pyrophosphate signal in hydrochars compared to raw SS, suggesting that OP (monoester-P) is hydrolyzed and converted into pyrophosphate during the HT treatment.

1.6. Effect of hydrothermal process parameters on phosphorus conversion pathways

1.6.1. Temperature, reaction time, and pressure

Temperature and reaction time are the most investigated HT process parameters among the selected studies presented in Table A.1. Temperature variation has a strong effect on the products from HT processes, directly related to the physical properties of water[77,79].

Reaction time is another important parameter that impacts product yields, properties, and nutrient migration. It has a decisive effect when physical phenomena and chemical reactions have relatively slow kinetics, thus requiring more time to reach thermodynamic equilibrium.

Most studies in Table A.1 indicate that solid recovery yield (Equation 1.2) decreases with increasing temperature, as clearly shown in Figure A.1 (Annex A). Indeed, temperature increase enhances organic matter dissolution and degradation by dehydration and decarboxylation reactions[80,81,97–99], and leads to biopolymers[39,91] and inorganic species solubilization in process water[97].

As shown on Figure A.2 the effect of reaction time on solid product recovery yield is usually less straightforward than temperature[65]. However, it has been observed that the solid recovery yield decreases with increasing reaction time[71,81,82,100].

To better understand the combined effects of temperature and reaction time, many authors use a parameter called HT *severity factor* f(T,t), which is function of time and temperature. According to the literature, the *Ruyter coalification model* [101] is the mostly used severity function to calculate the severity factor f(T,t) of HT processes[11,81,102] (Equation 1.4):

$$f(T,t) = 50\, t^{0.2}\, e^{-\frac{3500}{T}} \tag{1.4}$$

where t represents the reaction time (s) and T the temperature (K).

Figure 1.11 shows the solid recovery yield (%) as a function of the HT severity factor f(T,t) for the studies listed in Table A.1. The results indicate that higher f(T,t) (>0.5) can lead to lower solid product mass yield (< 55%), with the only exception of two experimental points by Fei et al.[103] and Ekpo et al.[39]. This reduction in solid recovery yield by increasing f(T,t) has been already observed in previous studies[9,11]. It was primarily attributed to cell rupture, biopolymers degradation and solubilization into the aqueous phase at high f(T,t). Accordingly, the minimum value for the solid product recovery yield would correspond to the ash content of the feedstock[9,104], which would indicate the total conversion and/or transfer of organic carbon to the liquid and gaseous phases.

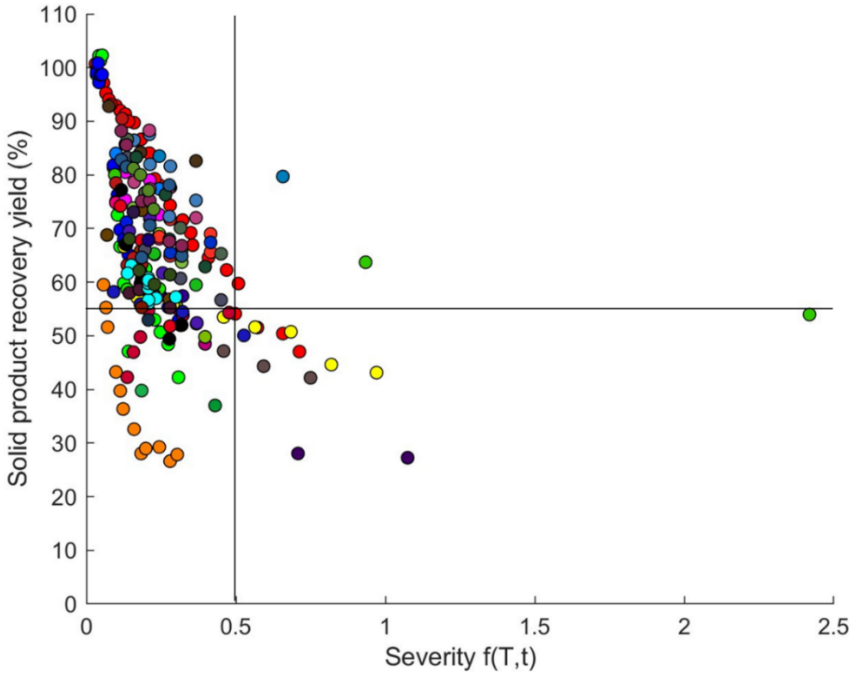

Figure 1.11 - Solid product mass yield as a function of process severity expressed with the Ruyter severity factor f(T,t) (Equation 1.4). Each color represents a different study listed in Table A.1.

Many studies presented in Table A.1 have also found that P content in the solid product increases with increasing temperature[62,77,79–82,89,91,98,105–109] and/or with increasing reaction time[71,77,81,82,100,107,110]. However, the results of comparative

studies indicate that temperature has a more relevant effect on solid product P content rather than reaction time[78,81]. These findings suggest that, although the increase in temperature and/or reaction time process promotes solid organic matter solubilization and decrease in solid product recovery yield, P tends to remain preserved in the solid fraction, and therefore its content in the solid product increases[81,88,103,105,110].

Figure 1.12 shows the P recovery yield in the solid product (%) as a function of severity f(T,t) and reaction time. A positive trend between the increase in f(T,t), and the increase in P recovery yield in the solid product, has been observed for many studies[10,39,77,80,81,85,88,96,98,99,103,111,112], indicating that higher temperature and/or higher reaction time usually promote P recovery in the solid product rather than in the process water. As already found for P content in solid product, temperature seems to have a more relevant effect also on P recovery yield in the solid product compared to the duration of the HT process.

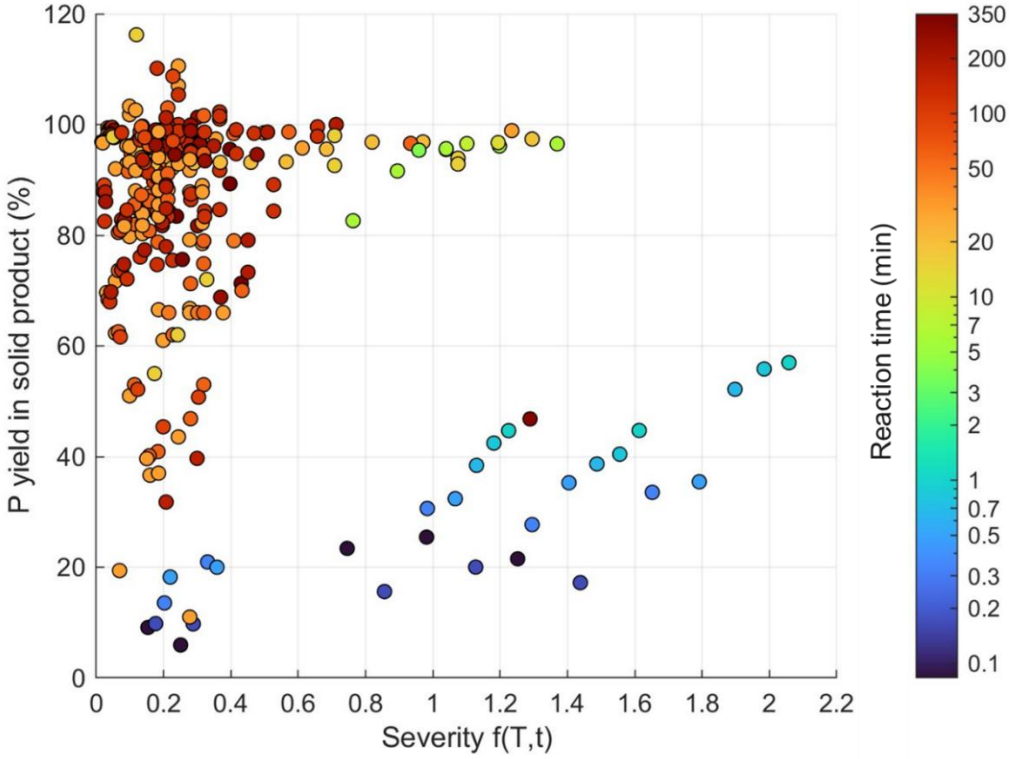

Figure 1.12 - P recovery yield in the solid product as a function of process severity expressed with the Ruyter severity factor f(T,t) (Equation 1.4). The color scale represents the treatment duration expressed in minutes. Data collected from works listed in Table A.1.

The effect of HT reaction time on P recovery yield in the solid product is often more relevant when working at low temperature (< 180 °C), probably because of the influence of temperature on the kinetic of OP mineralization to soluble orthophosphates. Indeed, previous studies have found that the kinetic of OP mineralization during HT processes is primarily controlled by the temperature according to an Arrhenius kinetic law[113]: lower temperature may result to slower kinetics, thus requiring a longer time to mineralization OP to orthophosphates[82]. This is in agreement with the finding of

various authors who observed that OP fraction decreases with increasing reaction time[81,82,114]. The findings of several studies indicate that OP is completely mineralized to orthophosphates in less than 60 min, in particular at temperatures above 175 °C[10,77,78,82,114,115], whereas total mineralization of OP can occur in less than 10 s at temperature higher than 500 °C[114]. Then, orthophosphates can react with metal cations (e.g. Ca^{2+}, Fe^{3+}, Al^{3+}, Mg^{2+}, Mn^{2+}) to form solid precipitates that are recovered in the solid product[10,77,114]. However, some studies[89,97,116,117] report a decrease in P recovery yield in solid product as temperature rises, thus suggesting that OP mineralization was not followed by orthophosphate precipitation, orthophosphate remaining dissolved in process water[48,71,80,81,118]. This was most probably due to a lack of metal cations or to pH values that did not favor metal phosphates precipitation. The effect of HT temperature increase on the increase in P, Ca, Fe, Al, and Mg contents of solid products has been observed in many studies[10,78,80,96,100,105,110,119]. The results confirm that temperature promotes P recovery in solid product via OP mineralization to orthophosphates followed by metal phosphate precipitation. Additionally, results from X-ray photoelectron spectroscopy (XPS) analysis also indicate that OP can hydrolyze into ortho-P/pyro-P during HT treatment[84,120], and that Fe^{3+} ions from iron oxides and Al^{3+} ions can combine with free orthophosphates to form $FePO_4$ and $AlPO_4$[120].

Among the studies analyzed in this review, there is a general agreement that the temperature increase favors the conversion from NAIP to AIP. Figure 1.13 shows the evolution of NAIP and AIP fractions as a function of the process severity. Although AIP is generally the minor inorganic fraction in SS (Figure 1.7), its content increases in the solid product after HT treatment, particularly at temperatures above 220 °C[78]. On the contrary the NAIP fraction tends to decrease with the increase in the HT severity factor f(T,t)[10,77–81,83,85–94].

As shown in Figure A.3, the temperature effect on NAIP and AIP speciation is more evident than reaction time effect. The addition of reagents, such as $FeCl_3$ or the presence of high Ca relative amounts can lead to experimental points inconsistent with the general trend (Figure 1.13). High temperature promotes the precipitation of inorganic orthophosphates into the form of Ca-phosphates, but it may also promote dissolution of NAIP complexes (such as Fe- and Al-phosphates) to Fe^{3+}, Al^{3+}, and orthophosphate ions, which may reprecipitate under the forms of stable Fe- and Al-(hydro)-oxides, and Ca-phosphates[37]. Similarly, longer reaction time has been found to promote AIP species in the inorganic fraction[77,78,81].

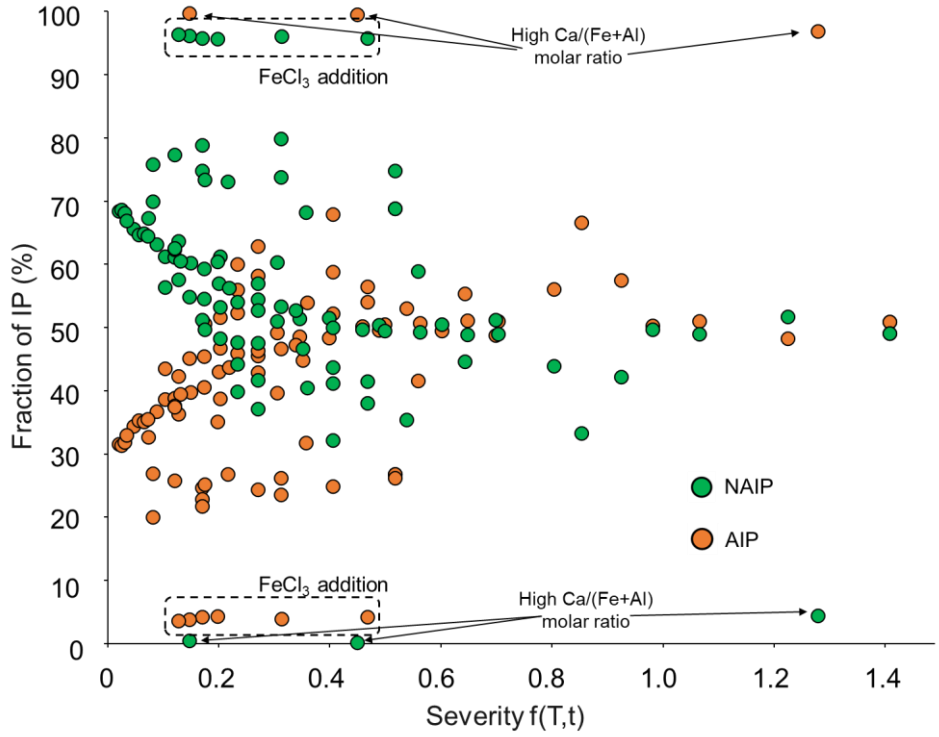

Figure 1.13 - Non-apatitic inorganic P (NAIP) (green points) and apatitic inorganic P (AIP) (orange points) fractions over total inorganic P (IP) as a function of the process severity expressed by the Ruyter severity factor f(T,t) (Equation 1.4). Data from [10,77–81,83,85–94]. Points in a dashed rectangle are related to a FeCl3-assisted process[86]. Points marked by arrows are characterized by a relatively high Ca/(Fe+Al) molar content[79,92].

Figure 1.14 shows the evolutions of the sum of H_2O-P and $NaHCO_3$-P fractions, and the sum of NaOH-P, HCl-P and residual-P fractions in the solid products, determined by the Hedley sequential fractionation method[121], as a function of process severity [62,71,82,103,105,106,109,110,118,122–124]. Figure A.4, Figure A.5 and Figure A.6 show respectively the individual trends of H_2O-P and $NaHCO_3$-P fractions, of NaOH-P and HCl-P fractions, and of residual-P fraction. According to the Hedley sequential fractionation method[121], H_2O-P corresponds to very weak bound P that is extracted by deionized water, $NaHCO_3$-P is exchangeable P that can be extracted by 0.5 M $NaHCO_3$, NaOH-P is generally associated with Fe- and Al-bound P that can be extracted by 0.1 M NaOH, HCl-P usually corresponds to Ca-bound P species that are extracted by 1 M HCl, while residual-P represents more stable recalcitrant P compounds that are not extracted or extracted by concentrated HCl (10-12 M) at high temperature (80 °C). The sum of H_2O-P plus $NaHCO_3$-P is often defined as readily available P. According to Figure 1.14, the sum of H_2O-P and $NaHCO_3$-P fractions decreases, while the sum of NaOH-P, HCl-P and residual-P fractions increases when increasing process severity. Figure A.7 shows that temperature effect on P fractionation is higher than reaction time. According to Figure A.5b, HCl-P fraction individually increases, while for the NaOH-P fraction there is no clear trend (Figure A.5a).

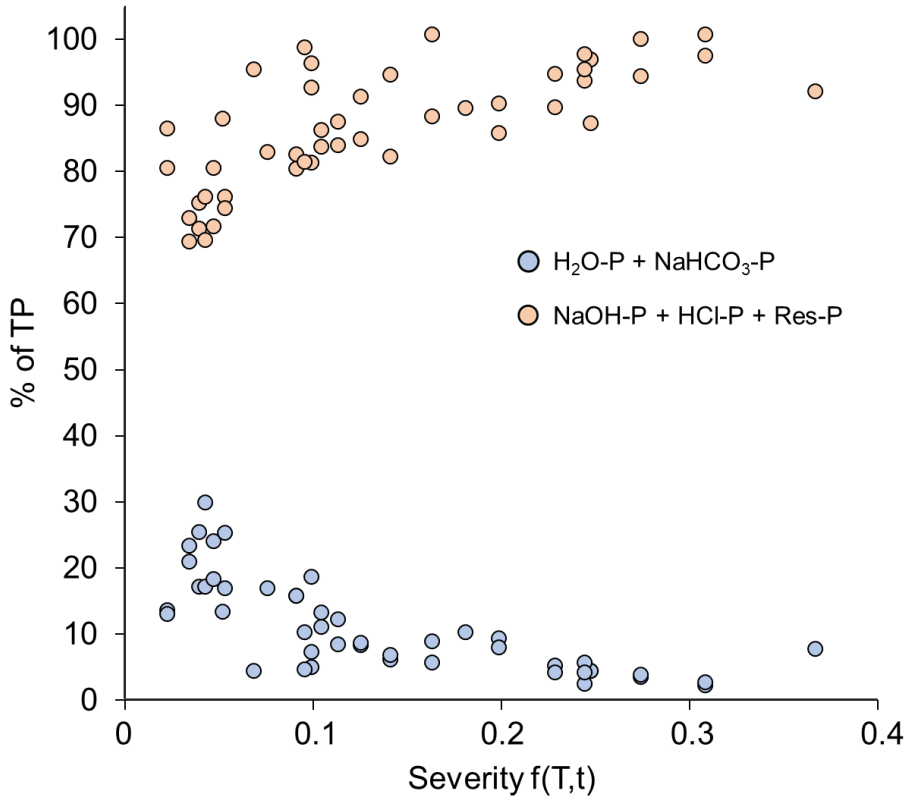

Figure 1.14 - Sum of the H_2O- and $NaHCO_3$- extracted P fractions (blue points), and the NaOH-, HCl- and residual- P fractions (orange points) as a function of the process severity expressed by the Ruyter severity factor f(T,t) (Equation 1.4). Data from [62,82,106,109,122,124].

These results suggest that, when increasing f(T, t), H_2O-P and $NaHCO_3$-P fractions are converted to the more stable NaOH-P and HCl-P fractions. However, at the same time, a fraction of NaOH-P may be converted to HCl-P by dissolution of Fe- and/or Al-phosphates followed by phosphate reprecipitation under the form of Ca phosphates. According to this hypothesis, Ca^{2+} content and pH values of the process water can play a key role on phosphate reprecipitation, thus affecting the P speciation of solid residues. Therefore, depending on which phenomenon is predominant, the NaOH-P fraction can increase or decrease, thus explaining the fluctuating values of NaOH-P fractions according to the increase in process severity.

Most of the studies in Table A.1 were performed under autogenous pressure conditions, and no additional gas was used. As pressure increases with increasing temperature, the effect on P speciation coincides with the influence of temperature increase. Zhu et al.[94] have investigated the effect of pressure (from 20.5 up to 23.5 MPa) on HTG of SS at 400 °C for 1 h of reaction time. They observed a decrease in P recovery yield in the solid product with increasing pressure, as well as a decrease in OP fraction of solid products, while no trend was observed for NAIP and AIP fractions. They also observed that soluble P concentration in process water increased with increasing pressure. These results suggest a link between pressure increase and solubility increase

of the main metal phosphates species. However, the scarcity of experimental results does not allow today to confirm this trend.

1.6.2. Solid-to-liquid ratio

The effect of different solid-to-liquid ratio (SLR) of the feed on HT treatment performance of SS was investigated by some of the studies listed in Table A.1[78,98,107,125]. Several authors have found that the solid product yield increases by increasing SLR, which correspond to a higher solid content in the feed[78,98,125], whereas higher water content of the feed can promote hydrolysis of high-molecular-weight compounds and dissolution of less stable solid phases, thus decreasing the solid product mass yield[98,125].

Moreover, a higher SLR has been found to promote P recovery yield in the solid product[78,98,125] and to decrease the P recovery yield in water[98,107,125]. Both He et al.[98] and Aragón-Briceño et al.[125] observed that a higher SLR leads to a higher P concentration in water, most probably because smaller water volumes resulted in higher P concentrated solutions. On the contrary, Hämäläinen et al.[107] found lower orthophosphate concentration in water at a higher SLR, and this was mainly attributed to a less efficient OP mineralization. Furthermore, Ovsyannikova et al.[78] observed an increase in AIP fraction recovery by increasing SLR, and this was primarily related to the high alkaline conditions of the samples which favored Ca phosphate precipitation. Indeed, the increase in the solid content often produces a higher alkaline reaction medium, which stabilizes Ca phosphates while mobilizing Fe and Al phosphates. Nevertheless, available data were not sufficient to clearly describe a global and unequivocal tendency correlating P speciation and content to solid-to-liquid ratio, thus requiring more specific studies on the subject.

1.6.3. Acidic and basic treatments

A large number of studies in Table A.1 have also investigated the effect of pH adjustment on P speciation and migration during HT treatments of SS[10,43,62,77,84,85,87,91,108,126]. Indeed, adsorption, precipitation, and other P-related chemical reactions are considerably affected by pH[127]. Different acidic or alkaline solutions can be used to adjust the pH of the feed, producing a significant effect on the product's properties and P speciation. NaOH is generally used to increase the medium pH[62,77,84,85,87,91,126]. Acid solutions used in the selected works include hydrochloric acid[10,62,84,87,91], nitric acid[43,77,128], sulfuric acid[108,126,129], formic acid[126], acetic acid[85,126], and citric acid[130].

The effect of pH on the solid product mass yield is not clear. Some authors correlated a pH increase with a higher solid product mass yield[43,91]. By contrast, Shettigondahalli Ekanthalu et al.[126] suggested that the solid product mass yield decreases at higher pH. Regardless of the initial feed pH, the reaction medium after the HT process presents an approximately neutral pH[62,85,126]. Indeed, the presence of dissolved organic compounds, carbonates, and colloids can produce a buffering effect that helps to shift the product's pH towards neutral values. The solid product can be slightly more acidic than

the liquid one due to the presence of organic acids resulting from the decomposition of carbohydrates[62].

Figure 1.15 shows all the collected experimental points that correlate the P recovery yield in the solid product with the feed pH, showing that the P recovery yield in the solid product increases with increasing pH, while for pH higher than 12 it decreases. This could be explained by considering that both Ca phosphate and Ca carbonate solubility decrease with increasing pH[131–133]. At pH higher than 12, CO_3^{2-} become the most prevalent carbonate species in solution. Therefore, the precipitation of $CaCO_3$ could become prevalent over that of Ca phosphates, thus leading to competition with phosphates for Ca^{2+} ions, resulting in a lower relative amount of Ca phosphates in the solid product.

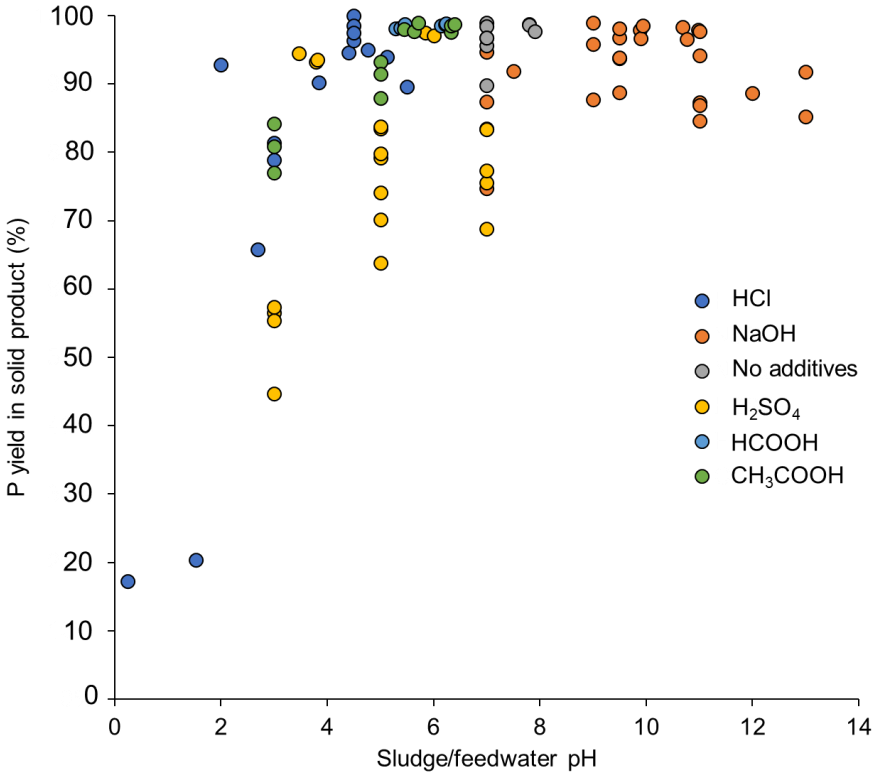

Figure 1.15 - P recovery yield in the solid product as a function of water process pH, each color represents a different acidic or basic species used to adjust the feed or feed water pH. Data from [10,62,84,85,87,91,108,126].

Several authors agree with the positive effect of the pH increase on the recovery of P in the solid product [10,43,85,87,91,108]. Higher pH promotes Ca phosphate precipitation[77], while a lower pH promotes P dissolution in water[10,129] as a more acidic medium can more easily dissolve inorganic P species as well as metal species[10], preventing their precipitation. McIntosh et al.[62] obtained the lowest P recovery yields in the solid products at the extreme range of the tested pH values (2 and 12), while the highest value is obtained at almost neutral pH. The use of two different acid solutions, organic and inorganic, to adjust the pH of the medium to the same value, leads to divergent results. Inorganic acids such as HCl and H_2SO_4 seem to favor P solubilization and recovery

in process water to a higher extent compared to organic acids (acetic and formic acid)[126].

In general, more acidic conditions have been associated with a decrease in OP content in the solid product[10,85,91], whereas pH increase usually leads to a decrease in NAIP and an increase in AIP fraction over the total P content[10,77,84,85,87,91]. This trend can be explained by observing the solubility trend of the main metal phosphates constituting the NAIP and AIP fractions: as shown in Figure 1.16, at low pH (1-2), the solubility of different Ca phosphate species (AIP) is higher compared to the solubility of Fe and Al phosphates. This trend is reversed at alkaline conditions (pH of 11-12), which favor the dissolution of Fe and Al phosphates (NAIP) and the precipitation of Ca phosphates (AIP).

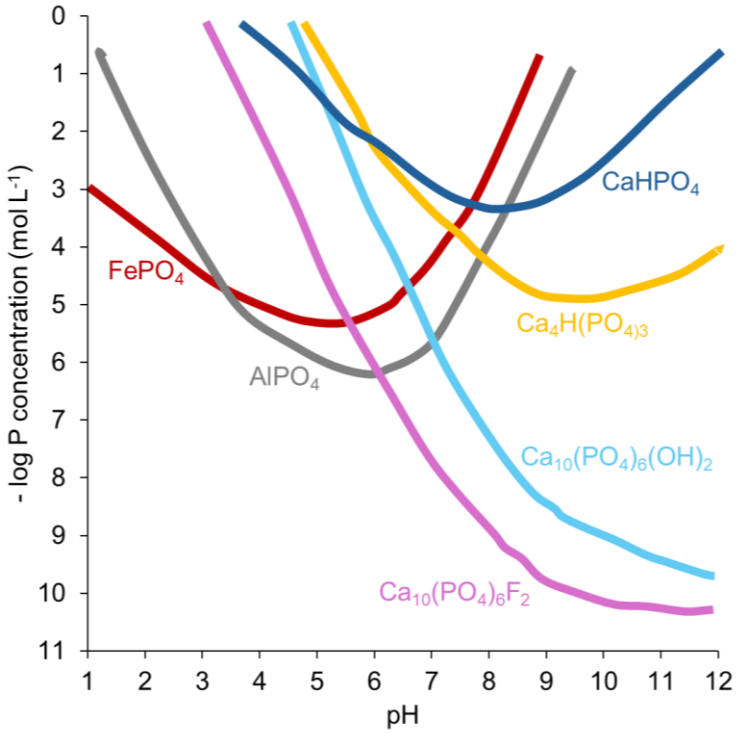

Figure 1.16 - Solubility of the metal phosphates. Adapted from [134] and [72].

It should be noticed that carbonate alkalinity plays an important role in Ca phosphate equilibrium: high carbonate alkalinity could lead to $CaCO_3$ precipitation at pH > 10[135], which can be in competition with Ca phosphate precipitation. Regarding P speciation in process water, more acidic conditions promote a higher orthophosphate content in process water, because low pH prevents precipitation of orthophosphate under the form of solid metal phosphates[84,129,130].

These results are coherent with the comprehensive results related to P availability in soils as a function of pH, which show that P fixation by Ca presents a maximum around pH 8, while P fixation by Al and Fe occurs at lower pH, presenting a maximum respectively around pH 5.5 and pH 3.5[136,137]. These trends are coherent with the solubilities of Ca, Fe and Al phosphates shown in Figure 1.16.

1.6.4. Use of additives

Recovering P under the form of AIP from SS is interesting to produce mineral fertilizers[138] as calcium phosphates salts are thermodynamically stable, making them optimal to produce slow-release fertilizers, limiting problems of leaching, runoff, P loss, and eutrophication[138,139], besides, AIP-based fertilizers can be used in particularly acidic soils, where Fe and Al phosphates are less effective[134]. Moreover, using sequential extraction, it is possible to separate Ca phosphates from Fe and al phosphates through controlled pH variation, by exploiting the different solubility of the various salts. This method allows for the recovery of precipitates with a high degree of purity.

The Ca/P molar ratio of the solution represents one of the most important parameters to improve AIP recovery from wastewater treatment systems. Indeed, Ca/P molar ratios of usual AIP minerals (e.g. dicalcium phosphate, tricalcium phosphate, octacalcium phosphate, hydroxyapatite) are comprised between 1 and 1.67, and often it is needed to add Ca-containing additive to have sufficient Ca^{2+} ions to convert all P into AIP. Different works investigate the effect of Ca addition on P fate and speciation during HT treatments of SS[77,83,84,87,88,98]. Free lime (CaO) represents the most used Ca-containing additive in the literature. Indeed, CaO dissolution in water results in an increase in Ca^{2+} ions and pH of the solutions, which are both two important parameters controlling Ca phosphate precipitation. To define the Ca addition effect alone, separated from the pH increase effect, and to avoid the problem of lime low solubility in water, Zheng et al.[87] proposed $CaCl_2$ as an alternative, which showed the same results as CaO in terms of conversion of NAIP to AIP, and allowed to recover almost all soluble P in the solid phase by Ca phosphate precipitation.

Figure 1.17 shows the collected experimental points which correlate process severity and Ca/P molar ratio with the relative amount of AIP in the hydrochar (expressed as % of total IP). The results in Figure 1.17 clearly show that AIP fraction increases by increasing process severity and by increasing Ca/P molar ratio of the feed. The results of Zheng et al.[83] have also indicated that Ca addition also promotes the increase in IP and the decrease in OP fractions in the solid products. Most probably, the alkaline conditions related to the Ca addition have promoted OP extraction from solid phase, followed by OP mineralization to orthophosphates, and then Ca phosphate precipitation. Overall, the results in the literature confirm that Ca addition leads to a significant AIP increase in the solid products, both in relative fraction and absolute concentration, which is accompanied by a NAIP decrease. Moreover, the results of some authors indicate that the NAIP conversion to AIP could be virtually complete when adding the correct amounts of CaO[77]. Indeed, the increase in pH due to CaO addition promotes Al and Fe phosphates dissolution to Al^{3+}, Fe^{3+}, and orthophosphate ions. Then, orthophosphates can react with Ca^{2+} ions and precipitate in the form of Ca phosphates at high pH[98].

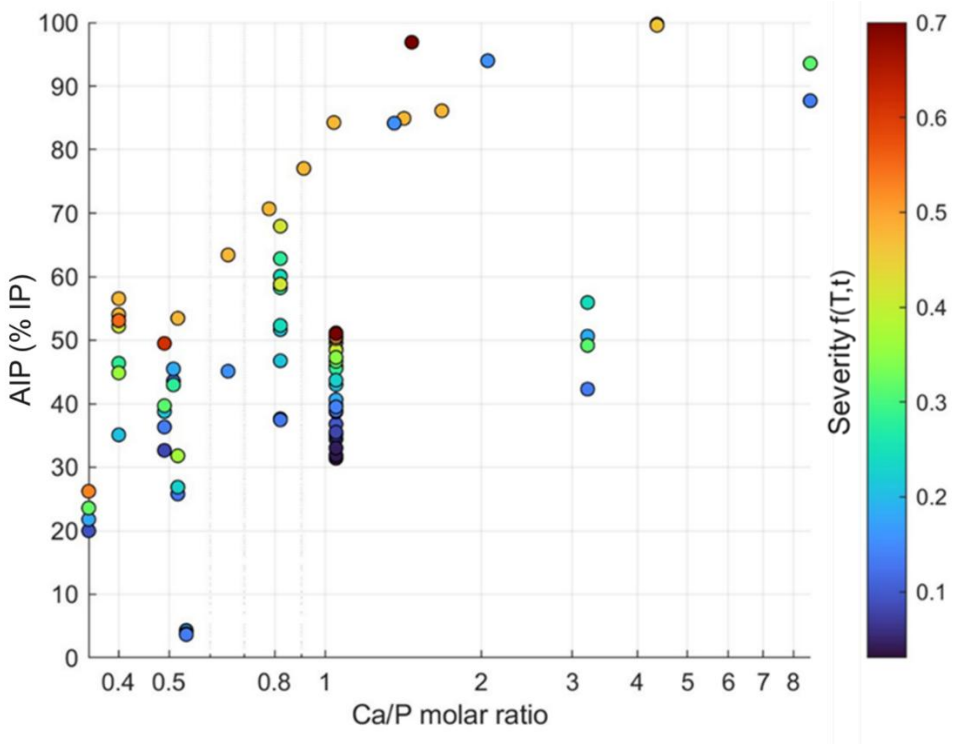

Figure 1.17 - Apatite inorganic P (AIP) fraction over total inorganic P (IP) as a function of the Ca/P molar ratio of the feedstock. Color represents process severity expressed by the Ruyter severity factor f(T,t) (Equation 1.4). Data from [10,77–81,86,88,89,91–93].

Other studies have examined the addition of different substances to the sludge feed to investigate their effects on P speciation and distribution. The nature of the selected additives is disparate, and all the selected substances have an industrial application. Table 1.1 lists the substances used in the selected works as additives, their main purposes and practical function and their effects on P speciation during HT process of SS.

Li et al.[86] studied P migration and distribution under $FeCl_3$-assisted HTC of secondary SS. $FeCl_3$ is a well-known and widely used P-removal agent. Its addition improved both the solid recovery yield and the P recovery in solid product. Besides, $FeCl_3$ promotes an acidic environment, allowing the dissolution of AIP in the liquid phase[74,93], releasing free orthophosphates which react with Fe^{3+} ions, and then leading to the precipitation of NAIP[140].

Yu et al.[93] investigated the effect of three different salts addition ($FeCl_3$, $AlCl_3$, and $CaCl_2$) during HTC of primary SS. The salts addition increased the P recovery yield in the solid product. Among the three salts, $AlCl_3$ fixed the largest P amount, followed by $CaCl_3$ and $FeCl_3$. During HT treatment with the addition of $AlCl_3$, the Al^{3+} ions concentration decreased sharply while the Fe^{3+} and Ca^{2+} ions concentration increased, indicating that P preferentially precipitated with Al under such experimental conditions[93]. Fe and Al phosphates constitute stable precipitates under slightly acid pH conditions, because Fe and Al phosphates have a solubility minimum between pH 5.5 and 6.5 (Figure 1.16), while at basic conditions they are replaced by Ca-containing compounds. HTC's process water is generally weakly acidic, and therefore Al and Fe are most effective for P fixation. $FeCl_3$ addition led to a NAIP concentration increase and to a AIP fraction decrease, indicating

that a robust presence of Fe^{3+} ions can break the Ca-containing P species and fix P[93]. $CaCl_2$ addition resulted in an AIP fraction increase[93]. $AlCl_3$ addition led to a strong NAIP fraction increase, while the AIP fraction almost totally disappeared.

Table 1.1 - Additives used in the selected works and their effects on solid recovery yield, P partition among solid product and process water, and P speciation in solid product.

Name	Formula	Purpose	Solid recovery yield	P recovery in solid product	P recovery in process water	AIP %	NAIP %	Ref.
Ferric chloride	$FeCl_3$	Fe^{3+} ions supplier	+	+	-	-	+	[86,93,99]
Calcium chloride	$CaCl_2$	Ca^{2+} ions supplier		+	-	+	-	[93]
Aluminum chloride	$AlCl_3$	Al^{3+} ions supplier		+	-	-	+	[93]
Sodium persulfate	$Na_2S_2O_8$	Improving sludge dewaterability		+	-			[122]
Polyacrylamide	$(C_3H_5NO)_n$	Flocculating agent	+	≈	≈			[99]
Poly aluminum chloride	$[Al_2(OH)_nCl^{6-n}]_m$	Flocculating agent	+	+	-			[99]
Sodium carbonate	Na_2CO_3	Improving H_2 production in HTG		-	+			[141]
Potassium carbonate	K_2CO_3	Improving H_2 production in HTG, alkalinity regulator, higher deoxygenation		-	+			[119,141]

Qi et al.[99] studied the effects of different additives, namely $FeCl_3$, polyacrylamide, and poly aluminum chloride. Solid product recovery yield increased following the use of all three additives, but this effect was more prominent for $FeCl_3$ and poly aluminum chloride, probably because Fe^{3+} and Al^{3+} ions were released into the medium and then they were available to precipitate with P. Beside the chemical effect of adding metal ions in the medium, these additives are generally used in coagulation-flocculation[142] processes, stabilizing the negative charged smaller particles and increasing the size of coagulated clumps. These properties can further explain the solid product recovery yield increase reported in Table 1.1.

Xiong et al.[122] studied the influence of sodium persulfate during a HT treatment of SS. The introduction of sodium persulfate led to a noticeable increase in P recovery in the solid product, most probably because $SO_4^{\bullet-}$ radicals attack OP[143] and decompose it into free orthophosphates, later fixed in the solid phase by metal species[144].

Wang et al.[141] realized a supercritical water gasification of SS, with and without the addition of two alkaline additives, Na_2CO_3 and K_2CO_3. The carbonates addition resulted in a 54-fold higher P concentration in process water, disengaging Ca from phosphates to form more stable Ca carbonates. K_2CO_3 seems to be more effective to increase the P concentration in process water[119]. K^+ has a higher capacity to combine with aluminum ions, releasing orthophosphates from aluminum-P species.

In summary, P precipitation in the solid product can be improved through the addition of different reagents and flocculant agents, including Fe, Al, and Ca chlorides, sodium persulfate, and poly aluminum chloride. Among the chlorides, $CaCl_2$ leads to an increase in the AIP fraction, while Fe and Al chlorides increase the NAIP fraction.

1.6.5. Proposed mechanism for phosphorus conversion

Overall, the experimental results collected from the literature indicate three main mechanisms involving P conversion during HT treatment of SS:

i) **OP mineralization** to soluble orthophosphates, thus leading to a decrease in OP content in the liquid and/or solid phases, and to an increase in P concentrations in the liquid phase. The kinetic of OP mineralization to orthophosphate is primarily controlled by the temperature according to a Arrhenius kinetic law[113], with longer time required for OP mineralization at lower HT temperature (< 180 °C). Acidic conditions and strong oxidizers further favor OP mineralization.

ii) **Dissolution of inorganic P** compounds to soluble orthophosphates, thus leading to a decrease in the inorganic P content of the solid phase, and to an increase in P concentrations of the liquid phase. Physical properties of HT water (e.g. dielectric constants, ionic product) appear to be the main parameters controlling the dissolution of the different inorganic P compounds (e.g. Fe-P, Al-P, Ca-P complexes), according to their relative temperature to dissolution dependence. High T, high pH and CaO addition favor Fe-P and Al-P species dissolution, while acidic conditions and $FeCl_3$ and $AlCl_3$ addition promote Ca-P complexes dissolution.

iii) **Orthophosphates (re)-precipitation** under the form of solid metal phosphates, thus leading to a decrease in P concentration of the liquid phase, and to an increase in the P recovery yield in the solid product[96,123]. The availability of metal cations (Ca^{2+}, Fe^{3+}, Al^{3+}, Mg^{2+}, and Mn^{2+}), as well as the temperature, pH, and alkalinity conditions of the water process, are the main physical-chemical parameters controlling metal phosphate precipitation and P speciation in the solid products. Slightly acidic conditions and $FeCl_3$ and $AlCl_3$ addition promote Fe-P and Al-P complexes precipitation, while basic conditions (pH ≈ 8) and CaO or $CaCl_2$ addition favor Ca-P species precipitation.

1.7. Perspectives and conclusions

P recovery from SS is a critical strategy to satisfy the growing food-production demand and to reduce eutrophication[2,18]. It is the object of increasing attention from the

scientific community, trying to find new value chains for SS disposal. From this perspective, thermal treatments have been extensively studied[33].

P and N can be recovered in the solid products (ashes and biochars) from the thermal treatments, which can be used directly as soil improvers or subjected to chemical extraction or other processes to recover the nutrients or remove heavy metals[6]. SS has a high-water content (> 95%), which leads to high energy costs related to pre-drying treatments[27,38]. However, HT treatments are carried out in a wet medium, and the water improves heat and matter diffusion and promotes polymerization, decarboxylation, and dehydration reactions[43,44].

P migration and speciation during SS HT treatments are the subjects of different studies. Through a critical analysis of the various variables that affect P migration in HT products, it is possible to better understand the mechanisms that regulate the nutrients' fate in these processes and the interactions between organic matter, nutrients, and metals.

The parameters that influence P speciation and recovery are various, but process severity is the one that has the largest impact on P migration and that has been extensively characterized. More specifically, the HT temperature is the factor that affects P conversion the most[59]: a temperature increase leads to a higher P recovery in the solid product, a lower P concentration in process water, the mineralization of OP, and the conversion of NAIP to AIP, although these assumptions can be made only for high enough temperatures that allow organic matter breakdown and metal compounds precipitation.

Reaction time also influences P speciation, but the temperature effect seems to be prevalent. The influence of temperature and reaction time are not independent: it has been observed that time influences P speciation differently at different HT temperatures. Even though it has been suggested that low temperatures with longer times may have the same effect as shorter times with higher temperatures, the collected results do not allow to build a definitive picture of residence time impact on P speciation. Future studies should further investigate residence time role on nutrients reaction paths, to explore P transformation kinetics, which today constitute an important knowledge gap: a relatively simple kinetic model has been proposed for organic P decomposition and orthophosphates precipitation[114], but it has been conceived for high temperatures and short durations, further efforts should be made to realize a kinetics model for other HT conditions.

Between the other parameters that influence P speciation, a higher SLR is correlated to an increased solid product recovery yield and an increased P recovery in the solid product[78,98,125]. However, collected data were not sufficient to show a definite trend correlating P pathways and distribution to solid-to-liquid ratio, thus requiring further studies on the topic.

P recovery in the solid product can be enhanced by increasing the medium alkalinity and by adding different additives, Ca-containing ones such as CaO, $CaCl_2$, and $Ca(OH)_2$[77,83,84,87,88,98], but also other metals chlorides, namely $FeCl_3$ and $AlCl_3$, sodium persulfate, and poly aluminum chloride.

By contrast, the dissolution of P in process water can be promoted by lower pH[84,129,130] and the addition of Na_2CO_3 or K_2CO_3[141]. Higher pH and the addition of Ca-containing species have been associated with higher AIP yields, while the NAIP fraction can be increased by lower pH, and the addition of Fe- and Al-containing species.

The AIP fraction appears to be quite interesting because it is less soluble and more thermodynamically stable than other P fractions at high temperatures. Considering HT products, P-containing species solubility needs to be fully investigated to study the viability of their valorization as fertilizers. Although a large percentage of soluble-P is interesting as it is readily available for plants, it is possible that unbalanced qualities of this nutrient are not absorbed in time and that they are lost because of erosion, runoff, weathering, and leaching. It has been shown that, since HT leads to the transformation of soluble and unstable P species into more stable and less soluble species, HT solid products present reduced P leaching rate compared to raw SS[49]. For this reason, the manufacture of products that contain less soluble and more slow-release P is often the object of investigation, with the aim of producing high-efficiency P soil amendments.

In this perspective, the P valorization by precipitation in the form of Ca-containing compounds, such as hydroxyapatite, is particularly interesting and it could be opposed to other industrial processes generally applied which precipitate P in the form of struvite, which however presents some complications including the incomplete N recovery and the necessary Mg addition.

Table 1.2 shows a list of the elements that have been already partially clarified in this chapter, and the elements on which more efforts must be made to obtain a comprehensive and detailed understanding of P behavior during SS HT treatment, and that will be the subjects of this work investigation.

Most of the reviewed studies operate at temperatures generally associated with HTC ($T < 280$ °C), and less experimental data are available for higher temperatures corresponding to HTL and HTG. For this reason, although the mechanisms related to P transformation during SS HT processes seem to be fundamentally the same above 300 °C, more effort is needed to better characterize P speciation during HTL and HTG. Moreover, bio-oil and syngas, the target products of HTL and HTG, constitute an interesting energy recovery from SS.

A complete characterization of the thermal profile of the SS HT treatment and a quantification of the reaction enthalpy would allow to estimate the process exothermicity and the associated energy gains to evaluate the whole cost-effectiveness of the SS HT treatment. It would be also interesting to assess the effect of some parameters that did not receive much attention in the reported works, such as pressure and solid loading, but it is also necessary to better investigate the possible interactions between the already investigated ones, such as temperature, time or feed composition (P, Ca, Fe contents).

Table 1.2 - State of knowledge on HT Treatment of SS for P Recovery. On the right there are the elements on which this work will focus, and the corresponding chapter(s) in which each element is discussed.

Elements that have been partially elucidated	**Elements that need further investigation**	
	Element	*Chapter(s)*
Effect of process severity on P speciation during HT treatment of SS, particularly under conditions associated with carbonization (T < 280 °C).	P speciation under more severe treatments (liquefaction T > 280 °C).	4
	Interaction between temperature and treatment duration on HT products characteristics and P speciation.	4
General mechanism of transformation among various P species (free orthophosphate, NAIP, AIP, OP).	Thermal profiling of the HT treatment.	4
	Effect of solid-to-liquid ratio (SLR) on product characteristics and P speciation.	5
Effect of pH variation on P speciation.	Interaction between sludge elemental stoichiometry (P, Ca, and Fe) and treatment parameters.	5, 6
Effect of calcium addition on P speciation.	Mechanisms governing organic phase and macronutrients (N, P, K) transformations.	4, 5, 6
Effect of various additives on P speciation.	Assessment of the environmental compatibility of HT products for potential use as fertilizers or soil amendments.	4, 5, 6

Moreover, a detailed assessment of pollutants in the HT products should be made (e.g. heavy metals, polycyclic aromatic hydrocarbons), in order to estimate the costs of their removal or the most suitable approaches to reduce their amount and hazard. All these elements would contribute to provide a complete and well-defined understanding of the mechanisms governing the transformations of organic matter and macronutrients during SS HT treatment.

The results of this first chapter have been used to select materials, methods and analytical techniques coherent with our experimental work plan, that will be comprehensively described in Chapter 2. These methods and techniques have been used to characterize both SS feeds and HT products. Chapter 2 will also present the origin of the sludges used as feed, followed by a description of the experimental setup for the hydrothermal treatment.

Chapter 3 will offer a detailed description of the digestate feeds used in this work, covering their physical properties, elemental composition, and phosphorus speciation. These characteristics will be compared with the distributions observed for sewage sludge in Chapter 1, providing insights into the transformations of organic and mineral phases during the hydrothermal process.

Chapter 4 will discuss the combined effect of temperature and treatment duration on the by-products characteristics, with a specific focus on P, examining its distribution in the by-products, its speciation, and the mechanisms that regulate its conversion. The investigated temperatures will be those typical of HTL, thus focusing on a range that has been little studied in previous research. Additionally, Chapter 4 will examine the pathways of organic species conversion and the thermal profile of the hydrothermal process, along with considerations for energy recovery.

Chapter 5 will provide the effect of feed characteristics and composition on HT by-products properties and P speciation. This analysis will be realized by comparing the results of a hydrothermal treatment realized under the same conditions on two sludges (comprehensively characterized in Chapter 3) with different properties.

The effect of feed composition will be further investigated in *Chapter 6*, centered on the role of Ca addition and Ca/P molar ratio on P speciation and, more generally, on the characteristics of the by-products, with the aim of producing a solid by-product with a high AIP fraction, which would enable its use as a slow-release fertilizer.

The results in Chapters 4, 5 and 6 will allow to develop a scheme of the general mechanisms regulating the organic and inorganic matter conversion and macronutrients distribution and speciation during the HT treatment of SS.

Finally, the HT by-products described in Chapters 4, 5, and 6 will also be characterized in terms of environmental compatibility, considering their potential use as fertilizers according to existing legislation, or their release into the environment.

2. Materials and methods

This chapter provides a detailed account of the materials and methods utilized in the experimental work that led to the results presented in Chapters 3 to 6. Initially, the origin of the sludges and the specific treatments they undergo at the WWTP are introduced. The experimental setup for the HT treatment is then described. Subsequently, the analytical techniques selected for the comprehensive characterization of the products are listed, along with the extraction methods for quantifying phosphorus (P), metals, and heavy metals, and for characterizing P speciation. The method for quantifying the enthalpy of reaction associated with the HT treatment is also presented. Finally, the systematic methodology behind the experimental plan's conception and the tools used for statistical analysis of the results are explained.

2.1. Sewage sludge digestate

2.1.1. Wastewater treatment plant

The SS digestate used in this work is collected from the Aix-La Pioline municipal WWTP, located in Aix-en-Provence (Bouches-du-Rhône, France, 175000 population equivalent). Figure 2.1 shows a scheme of the processes that urban wastewaters undergo in the Aix-La Pioline municipal treatment plant. Wastewater arriving at the treatment plant undergoes an initial degreasing pre-treatment. Afterwards, the wastewater is sent to the secondary treatment tank, for biological treatment. Here the organic contaminants degradation occurs due to the action of aerobic microorganisms.

The sludge produced from this step is then sent to a flotation cell where it is concentrated. The thickened sludge is then fed into the anaerobic digester along with the fats and oils separated in the initial degreasing phase. AD leads to the production of biogas and digested sludge, or digestate. The clarified water exiting the secondary treatment is sent to a tertiary treatment tank, where P removal occurs through the addition of an inorganic coagulant, $FeCl_3$, and an anionic organic flocculant. The sludge produced in this step is fed into an industrial centrifuge along with the digested sludge exiting the digester. Here, thanks to the addition of an additional cationic flocculant, the sludge is thickened to reach a solid content of around 20%.

The sludges collected from the treatment plant and used in this experimental work are:

i) the digested sludge exiting the anaerobic digester, that is further concentrated through a small-scale centrifuge without any additives at the laboratory, obtaining a thickened version (Sludge A)

ii) the thickened sludge exiting the industrial centrifuge, obtained from the mixing of digested sludge and tertiary sludge (Sludge B).

For a complete characterization, the respective aqueous phases related to the two sludges were also characterized: Centrate A is the supernatant from the laboratory centrifugation performed on the digested sludge exiting the digester, while Centrate B refers to the supernatant exiting the industrial centrifugation where Sludge B is produced.

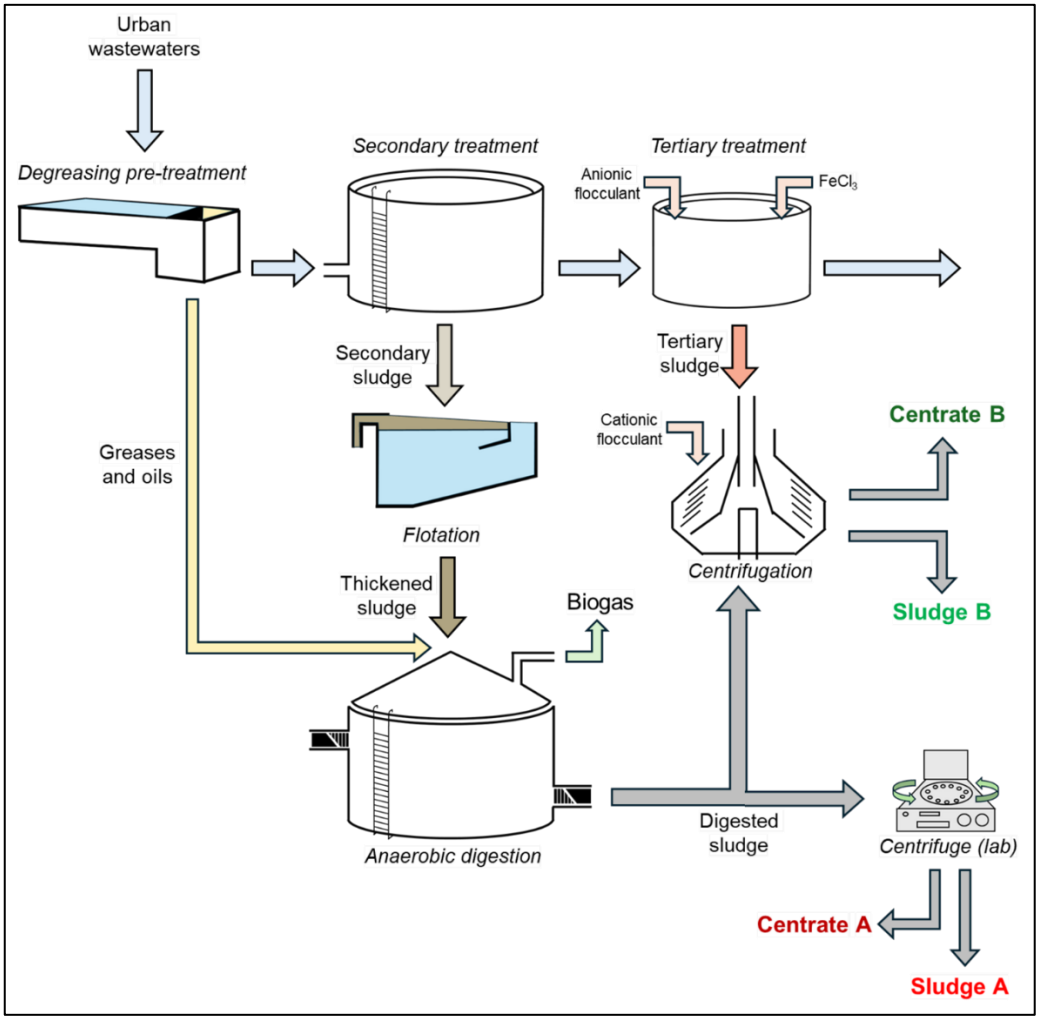

Figure 2.1 - Diagram of the physical, chemical, and biological processes that wastewater undergoes at the Aix-La Pioline wastewater treatment plant.

2.1.2. Digestate pre-treatment

The SS digestate exiting the anaerobic digester contains a low total solids (TS) content (2.5 %), which is not ideal for a small-scale HT treatment. Therefore, several methods have been considered to dewater the digestate and enhance its solid fraction.

In some works[39,77,83,96,97], digestate is completely dried at 105 °C to facilitate its preservation, and then water is reintegrated in the HT reactor. This allows to produce a reconstructed solution with a determined TS content by mixing known masses of water and SS powder. This is a practical method that allows easy control of the amount of water

introduced into the system. However, all thermal methods involving drying the digestate have been excluded, in order to preserve as much as possible the digestate original properties, to avoid organic fraction alteration, volatile components evaporation, and to prevent modification of P and other element speciation due to precipitation and/or crystallization processes coinciding with water evaporation.

Other methods involving the addition of inorganic and organic coagulants have been excluded to prevent alteration of the digestate composition. Besides, Sludge B was obtained following a tertiary treatment assisted by the addition of a coagulant and two flocculants. Therefore, the comparative analysis of the HT products of the two sludges allows to assess their effect (discussed in Chapter 5). Adding coagulants to Sludge A as well would prevent a clear assessment of their impact.

Vacuum Büchner filtration with 0.7 µm glass microfiber paper and manual filtration with 0.45 µm nylon membrane have been excluded due to the particularly lengthy processing times: the digestate liquid fraction is characterized by colloidal organic aggregates (see Section 3.3.2) which led to filter membrane fouling, thus significantly reducing the filters lifespan.

Centrifugation was conducted using a Sigma 2-16P centrifuge, operating at 4000 rpm (2504 g) for a duration of 20 min. This process effectively separated the SS digestate into two distinct fractions: a more aqueous-rich supernatant, labeled "Centrate A", and a more-solid rich pellet identified as "Sludge A". Both fractions were carefully collected in separate sealed plastic containers and then stored at 4 °C for future utilization and/or characterization. Sludge B and Centrate B are stored respectively in a 20 L and 2 L containers at the time of collection, and subsequently refrigerated at 4 °C.

The superior performance of centrifugation compared to alternative methods listed previously led to its selection as the preferred technique for SS digestate concentration in the experimental protocol.

2.2. Hydrothermal treatment

2.2.1. Experimental reactor

The HT treatment is realized in a 0.2 L (d: 50 mm, H: 100 mm) cylindrical austenitic chromium-nickel-stainless steel batch reactor shown in Figure 2.2. Figure 2.3 schematizes the whole experimental setup. The reactor is heated with a resistance wire system in the reactor jacket and cooled with the injection of pressurized air on the reactor external shell. Temperature regulation is automatized thanks to a proportional integral derivative (PID) controller. The pressurizing and inerting of the reaction medium is obtained with the injection of N_2 inside the reactor. N_2 is injected with a TOP Industrie (Vaux-le-Pénil, France) syringe pump (ref 608 91 00) to accurately regulate the gas flow and pressure. Mixing is provided with a Rushton turbine. Water cooling is used to keep the mixer turbine motor from overheating. Removable baffles are added to minimize the tangential component of velocity which causes vortex formation, and thus promoting mixing.

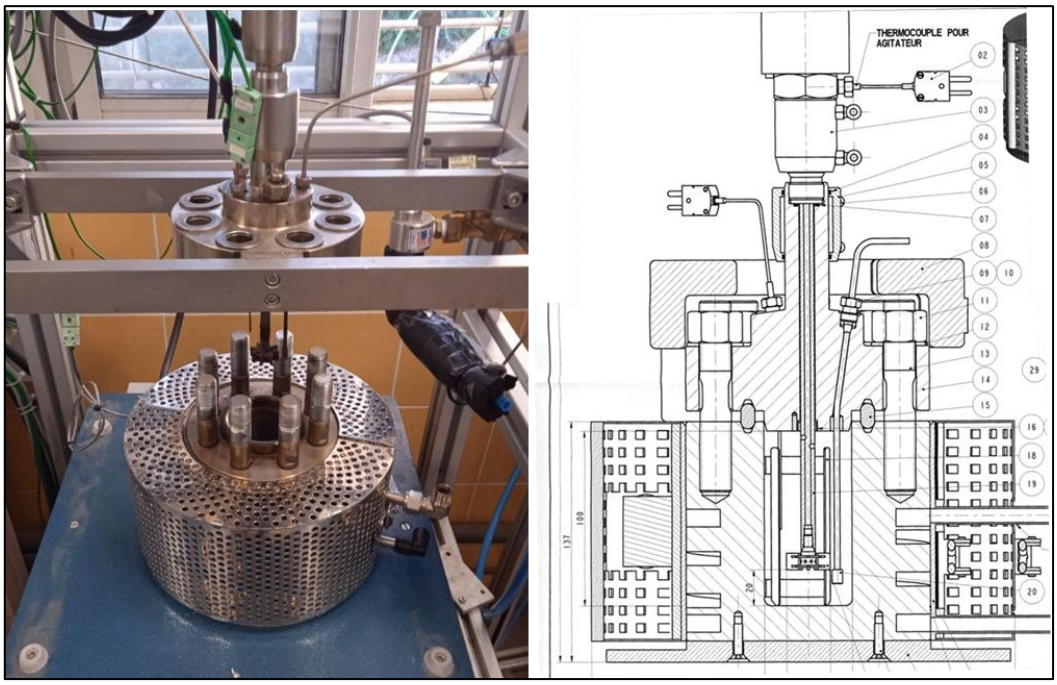

Figure 2.2 - Left: appearance of the small batch reactor used for the SS HT treatment. Right: technical scheme of the reactor body.

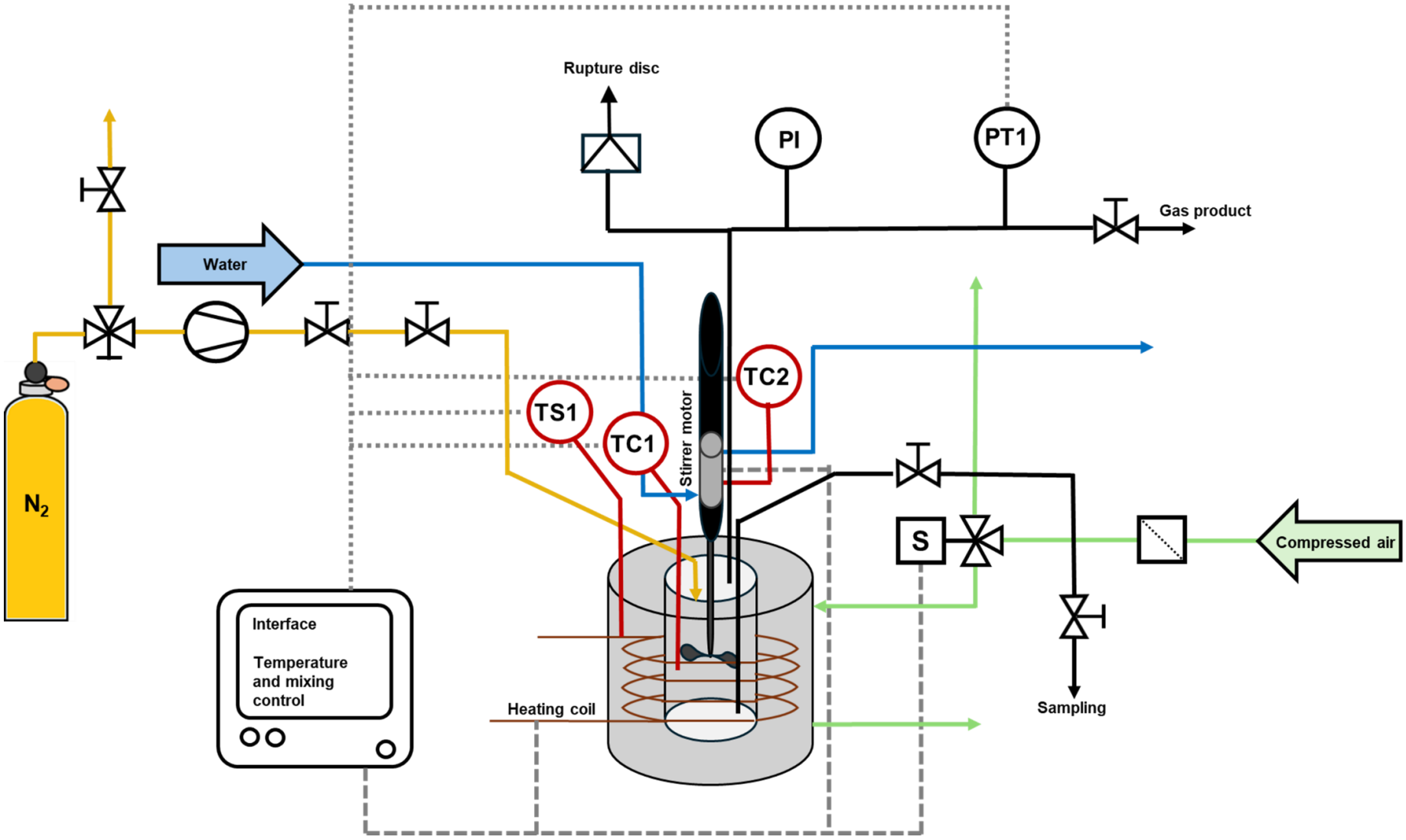

Figure 2.3 - Schematization of the experimental setup. PI: pressure indicator; PT1: pressure transmitter (P inside the reactor); TC1: reactor internal temperature; TS1: temperature of the heating coil; TS1: mixer motor temperature.

2.2.2. Reactor loading and reaction monitoring

Sludge A or Sludge B is taken from the refrigerated plastic container, transferred to a beaker, brought to room temperature, and mixed with a spatula to ensure homogeneity. The weight of the beaker filled with digestate is recorded. Using a spatula, a certain amount of digestate is carefully transferred inside the reactor, compacting it on the bottom and making sure to fill about 70% of the available volume. The beaker with the residual digestate is weighed and the digestate quantity loaded into the reactor is calculated by difference.

After sealing the reactor, N_2 is introduced via a syringe pump. The reactor is initially filled with low pressure of N_2, which is then gently evacuated to reduce as much as possible the amount of residual oxygen and ensure inerting. This process is repeated a couple of times. After that, the reactor is pressurized to the desired initial pressure. The desired temperature and mixing rate are selected, starting the heating and mixing processes. All measured reactor parameters (internal temperature TC1, heating coil temperature TS1, internal pressure PT1, turbine mixing rate v_{mix}, turbine motor temperature TC2) are continuously recorded every 2 s. When the reactor internal temperature reaches the set temperature (± 10 °C) the treatment starts. After the desired time is passed, room temperature (25 °C) is selected as the set temperature thus starting the cooling process. At the end of the cooling process, when the reactor internal temperature reaches about 35 °C, the reactor is gently depressurized. Cooling and mixing are stopped, and the reactor is opened to recover the HT treatment product.

2.2.3. By-products recovery and separation

The reactor content is mixed with a spatula to ensure homogenization and then recovered with a 100 mL syringe connected to a rubber tube to draw the product from the bottom of the reactor. The product is transferred to the centrifuge tube. Some of the product, especially the solid residues, remains on the bottom and walls of the reactor, on the baffles, on the turbine and on the thermocouple body. These residues are recovered with a spatula and transferred inside the centrifuge tube. A certain amount of residue is impossible to recover with the syringe or spatula. 100 ml of acetone are introduced in the reactor. The reactor is sealed, and the mixing is restarted for 5 min. Then the reactor is opened and the acetone with the dissolved and suspended residue is recovered with a syringe. All acetone is evaporated, allowing to estimate the amount of residue recovered with this technique, generally around 1-2% of the feed mass. A certain amount of product residues remains unrecoverable and may appear in the mass losses.

The recovered product is centrifuged at 4000 rpm for 20 min, allowing to obtain a liquid aqueous supernatant (process water) and a solid pellet. The process water is filtered using a 0.45 µm nylon syringe filter. Both the solid pellet and the filtered process water are then stored at 4 °C in sealed plastic containers.

The methods used for reactor loading and product recovery and separation are schematized in Figure 2.4.

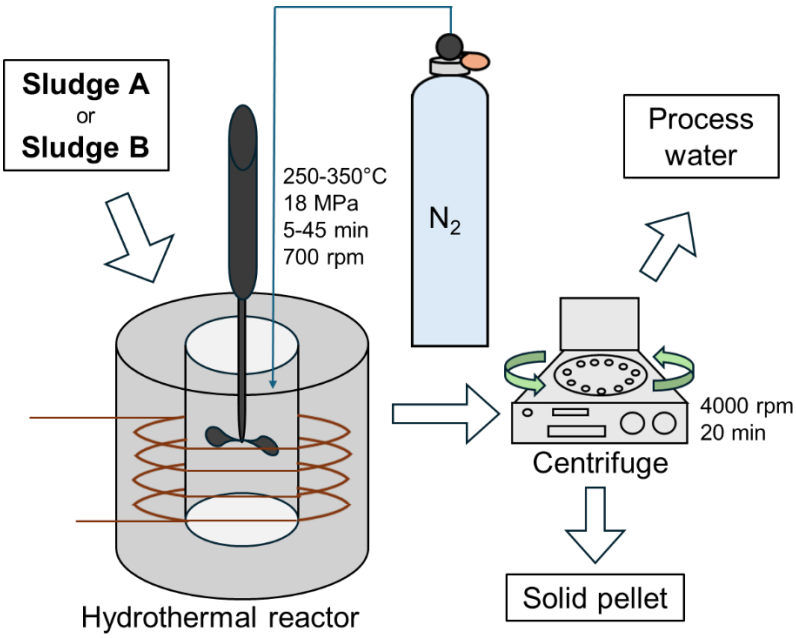

Figure 2.4 - Experimental protocol scheme for reactor loading and product recovery and separation.

The quantification of bio-oil yield is performed through acetone extraction. 1 g of dry solid pellet, ground into powder and sieved to 100 µm, is placed into a flask filled with 20 mL of acetone (PROLABO 0.792 g cm^{-3}) and stirred for 20 min. Subsequently, the contents of the flask are poured onto a Büchner funnel with a paper filter, connected to a vacuum pump. The solid collected on the filter is washed with an additional 80 mL of acetone. The filter with the solid residue is then dried completely, and the residual mass is measured. The fraction of pellet extracted with acetone is quantified according to Equation 2.1:

$$\%_{org} = 100 - \frac{m_{res}}{m_{pel}} \cdot 100 \qquad (2.1)$$

Where m_{res} is the residual mass after acetone extraction, washing and drying, and m_{pel} is the original pellet mass inserted in the flask. The bio-oil yield relative to feed dry mass is calculated according to Equation 2.2:

$$Oil\ (\%) = \frac{m_{S,dry} \cdot \%_{org}}{m_{D,dry}} \cdot 100 \qquad (2.2)$$

Where $m_{S,dry}$ and $m_{D,dry}$ are the dry masses of respectively the solid pellet and the digestate fed to the reactor, and $\%_{org}$ is the acetone-extractable fraction of the pellet, calculated according to Equation 2.1.

The extraction of the organic phase (bio-oil) was performed on the dried solid pellet solely for quantification purposes. Therefore, the results presented in this work concerning “process water” and “solid pellet” refer to the by-products separated by

centrifugation without any extraction of the organic phase. Although most of the organic phase is recovered in the solid pellet, it is important to emphasize that both by-products contain an organic phase.

2.3. Characterization of liquid phases

This section outlines the experimental protocols and methods chosen to thoroughly characterize all liquid phases within our experimental campaign, including the digestate **centrates** (Centrate A and B) and the HT treatment **process water**.

2.3.1. General characteristics

Optical microscopy has been used to characterize the digestate centrate to assess the size and nature of the organic matter aggregates present in the sludge. The filtered liquid phase density is measured with a density meter Anton Paar DMA 5000 M. Liquid phases pH is measured on filtered samples (0.45 µm nylon filter) using a multiparameter analyzer Consort C5020 (Turnhout, Belgium). For the HT process water, pH measurements are realized immediately after the product separation.

2.3.2. Total alkalinity

Total alkalinity is measured according to standard method ISO EN 9963-1, 1996. 5 mL of the filtered liquid sample are titrated with an HCl solution, and the pH is continuously measured up to pH 4.5. Total alkalinity (A_T), expressed as mg L^{-1} $CaCO_3$ equivalent, is calculated according to Equation 2.3:

$$A_T = \frac{C_{HCl} \cdot V_{HCl} \cdot 1000}{V_{liq}} \cdot 50 \qquad (2.3)$$

Where C_{HCl} is the HCl solution concentration expressed in mol L^{-1} (0.1 mol L^{-1}), V_{HCl} (mL) is the volume of HCl solution utilized for titrating the liquid sample up to pH 4.5, and V_{liq} (mL) is the volume of the filtered liquid sample. The 50-conversion factor allows to obtain the result in mg L^{-1} $CaCO_3$.

2.3.3. Solid content

4 g of liquid sample are placed in an aluminum crucible and dried at 105 °C overnight, allowing to measure its total solids (TS) content expressed in percentage (%) according to Equation 2.4:

$$TS\ (\%) = \frac{m_{dry}}{m_{liq}} \cdot 100 \qquad (2.4)$$

Where m_{liq} (g) is the liquid sample mass, and m_{dry} is the residual mass after drying (g).

The same technique is applied to the filtered liquid sample, measuring the total dissolved solids (TDS) content (%) (Equation 2.5):

$$TDS\ (\%) = \frac{m_{dry,\phi}}{m_{liq,\phi}} \cdot\ 100 \qquad (2.5)$$

Where $m_{liq,\Phi}$ (g) is the filtered liquid sample mass, and $m_{dry,\Phi}$ is the residual mass after drying (g).

Total suspended solids (TSS) content (%) is evaluated by difference according to Equation 2.6:

$$TSS\ (\%) = TS(\%) - TDS\ (\%) \qquad (2.6)$$

2.3.4. Total and ammonia nitrogen

Total bound N (TN) includes all inorganic forms (nitric N, nitrous N, ammoniacal N) and all organic forms of N in a liquid sample. The TN concentration in the filtered liquid phase is quantified using kit cell tests (Lovibond VARIO Total Nitrogen, Dortmund, Germany), based on standard method ISO 23697-2, 2023.

The liquid sample is digested with a heated alkaline K persulfate solution. Then, chromotropic acid is added to develop a color reaction. TN concentration is then read in an ultraviolet–visible (UV-VIS) spectrophotometer (Photolab 7100 UV-vis) at wavelength 410 nm.

Ammonium nitrogen (NH_4-N) contained in the filtered liquid phases is quantified using kit cell tests (Lovibond VARIO am Vial Test Reagent Set, Dortmund, Germany), based on standard method ISO 7150-1, 1984. It involves the reaction of ammonium with salicylate and hypochlorite ions in the presence of sodium nitrosopentacyanoferrate(lll), resulting in the formation of a blue compound. The absorbance of this compound is then measured using an ultraviolet-visible spectrophotometer (Photolab 7100 UV-vis) at a wavelength of 410 nm.

Nitrate-nitrogen (NO_3-N) in the filtered liquid phases has been quantified using kit cell tests (Spectroquant® Test Kits of Merck KGaA, Darmstadt, Germany), based on SM 4500 NO^{3-} E (1997/2011) and ISO Standard 7890-1. According to this method, nitrates react with 2,6-dimethylphenol in the presence of sulfuric and phosphoric acids to produce 4-nitro-2,6-dimethylPhenol. The concentration is quantified by spectrometric measurement of the absorbance of the reaction product at 324 nm.

2.3.5. Chemical Oxygen Demand

Chemical oxygen demand (COD mg O_2 L^{-1}) quantifies the quantity of oxygen that can be consumed in a solution by various reactions with oxidizable organic compounds. COD contained in the filtered liquid phases is quantified using kit cell tests (Supelco Spectroquant, Darmstadt, Germany), based on standard method ISO 15705, 2002.

According to this method, the liquid sample is oxidized with a hot sulfuric solution of potassium dichromate, with silver sulfate as catalyst. The concentration of green Cr^{3+} ions is then determined photometrically, by reading the absorbance at 600 nm using an ultraviolet-visible spectrophotometer (Photolab 7100 UV-vis).

2.3.6. Dissolved carbon

Total Carbon (TC) and Total Inorganic Carbon (TIC) contained in the filtered liquid phases are measured using a Shimadzu TOC-L Total Organic Carbon Analyzer. TC includes inorganic, organic, and volatile C. It is quantified with a catalytic combustion achieved by heating it up to 680 °C in an oxygen-rich environment. TIC includes all dissolved carbon dioxide, bicarbonate, and carbonate species. Its measurement involves converting these components to carbon dioxide after sample acidification. TC and TIC are expressed in g L^{-1}. Total Organic Carbon (TOC), expressed in g L^{-1}, includes all C present in organic compounds. It is calculated by difference according to Equation 2.7. TC and TIC are expressed in g L^{-1}.

$$TOC = TC - TIC \quad (2.7)$$

2.3.7. Free orthophosphates

Soluble orthophosphate phosphorus (PO_4-P) concentration in filtered liquid phases were determined according to the ammonium molybdate-ascorbic acid method from the standard method ISO EN 6878, 2004 (described in Annex B). PO_4^{3-} ions constituting PO_4-P react with a molybdate-antimony solution to form an antimony phosphomolybdate complex which is then reduced with ascorbic acid to form a strongly colored blue complex. PO_4-P concentration is then quantified by measuring the complex absorbance at 880 nm using an ultraviolet-visible spectrophotometer (Photolab 7100 UV-vis).

2.3.8. Inductively Coupled Plasma Atomic Emission Spectroscopy (ICP – AES)

Some elements present in the liquid phases can be detected and quantified by Inductively Coupled Plasma Atomic Emission Spectroscopy (ICP -AES). This analytical technique uses inductively coupled plasma (high temperature ionized gas) to produce excited ions that emit electromagnetic radiation at wavelengths characteristic of the specific investigated element. The ICP-AES analysis is realized with an Agilent 5800 VDV spectrometer, available at the LA-ICP-MS platform – CEREGE (Aix-Marseille Université). The technique has allowed to quantify P, Fe, Ca, Al, Mg and K contents in the liquid samples preemptively filtered (0.45 µm nylon filter) and appropriately diluted with a 1 M HCl solution to preserve metals in solution and avoid (re-)precipitation.

2.4. Characterization of solid phases

This section outlines the experimental protocols and methods used to thoroughly characterize all solid phases within the experimental campaign, including Sludge A and B, and the solid pellet by-products. The solid phases dry mass is evaluated by drying the sample at 105 °C overnight. Total Solid Recovery Yield (TSRY%) is defined by Equation 2.8:

$$TSRY\% = \frac{m_{S,dry} + m_{L,dry}}{m_{D,dry}} \quad (2.8)$$

Where $m_{S,dry}$, $m_{L,dry}$ and $m_{D,dry}$ are the dry masses of respectively the solid pellet, the process water and the digestate fed to the reactor.

2.4.1. Lyophilization

Lyophilization is a low-temperature drying process in which the sample is exposed to low temperatures and pressures, to freeze the sample's water content and to remove it by sublimation. Unlike conventional high temperature drying methods, this method allows to avoid altering or destroying thermolabile components in the sample.

Before lyophilization, solid samples are frozen at -20 °C for 24 h. Solid samples lyophilization has been realized in a lyophilizer SP Scientific VirTis Benchtop Pro. The lyophilizer condenser is kept at -60 °C and 6 -10 Pa. The frozen samples are kept in the chamber for 3-4 days. The lyophilized samples are finely ground and stored in sealed plastic tubes at 4 °C. This method has been employed to prepare the samples for the Nuclear Magnetic Resonance (NMR) Spectroscopy (Section 2.4.5).

2.4.2. Elemental CNHS analysis

Elemental CNHS analysis allows to determine the dried solid sample carbon (C), hydrogen (H), nitrogen (N) and sulfur (S) content. This analysis is realized with a Thermo Scientific FlashEA 1112 Elemental Analyzer, located at the Spectropole platform (Aix-Marseille Université). This technique consists of burning a small amount of powdered dried solid sample in a controlled atmosphere and then analyzing the produced gases. C in the sample is converted to CO_2, N into NO_x, H into H_2O and S into SO_2. The gas products pass over heated purity copper to remove oxygen and to convert NO_x into N_2. Product gas (CO_2, N_2, H_2O and SO_2) are then separated and detected by gas chromatography (GC). The ash content of solid phases is a measure of the mass of the sample residue after combustion. Ash content is determined by exposing the dried sample at 900 °C in a muffle furnace for 1 h. The sample is placed in a ceramic crucible without a cover, in order to allow oxidation. Ash (%), expressed on a dry basis, is calculated according to Equation 2.9:

$$Ash\ (\%) = \frac{m_{900}}{m_{dry}} \cdot 100 \quad (2.9)$$

Where m_{dry} is the dried solid phase sample mass before oxidation (g), and m_{900} is the residual mass after oxidation (g).

The oxygen (O) content (%) in the solid samples is calculated by difference according to Equation 2.10:

$$O\% = 100 - C\% - N\% - H\% - S\% - Ash\% \quad (2.10)$$

Where C%, H%, N% and S% are the relative C, N, H and S contents expressed on a dry basis, and Ash% is the ashes relative content as defined in Equation 2.9.

2.4.3. Aqua regia extraction

Aqua regia extraction can be used to digest a solid sample, in order to mineralize and solubilize various elements and then determine their content by analyzing the resultant solution by spectroscopic methods. Aqua regia is a mixture of nitric acid (HNO_3) and hydrochloric acid (HCl), generally in an optimal molar ratio of 1:3. The technique used in this work is based on standardized methods described in norm EN ISO 13346, 2000 (method B). 0.5 g of the dried solid sample are transferred in a 30 mL borosilicate glass test tube. 1 mL of deionized water is added to humidify the sample. Then 6 mL of hydrochloric acid and 2 mL of nitric acid are added to the sample. The tube is sealed and heated in a small heating reactor at 130°C for 2h. When the time has run out, the content of the test tube is transferred to a 250 mL volumetric flask, and then filtered with a 0.45 µm nylon filter. As explained in the norm, the utilization of this method is suggested for the determination of, P, As, Cd, Cr, Cu, Hg, Ni, Pb, Se and Zn. Other elements can be extracted and quantified with this method, but the fraction of the elements bonded or complexed with silicate species cannot be properly characterized as aqua regia is not able to extract silicates. Previous works have pointed out the possibility of having significantly low efficiency for the extraction of some elements[145,146]. Indeed, these elements could be found in silicates or other particularly refractory compounds such as crystalline Fe and Mn oxides.

2.4.4. Inductively Coupled Plasma Spectroscopy

Aqua regia extracts prepared as described in Section 2.4.3 have been appropriately diluted with deionized water and analyzed with Inductively Coupled Plasma Spectroscopy to quantify various elements. Inductively Coupled Plasma Atomic Emission Spectroscopy (ICP -AES), realized with an Agilent 5800 VDV spectrometer (LA-ICP-MS platform – CEREGE, Aix-Marseille Université), has allowed to quantify P, Fe, Ca, Al, Mg, K, Cu and Zn contents. Additionally, Inductively Coupled Plasma Mass Spectrometry (ICP – MS), realized with a Perkin Elmer NexIon 300X spectrometer (LA-ICP-MS platform – CEREGE, Aix-Marseille Université), has allowed to measure heavy metals traces (Cr, Pb, Ni, V, Ag, As, Cd and Hg). ICP-MS has been selected to quantify heavy metals because it is

a high-sensitivity method that allows to accurately detect trace elements at parts per trillion (ppt) levels.

2.4.5. Nuclear magnetic resonance spectroscopy

Nuclear magnetic resonance (NMR) spectroscopy allows to obtain information about specific functional groups present in the sample, leading to the identification of specific molecular structures and organic compounds. The lyophilized solid phase samples, prepared as described in Section 2.4.1, have been analyzed with solid state NMR spectroscopy. All solid-state cross polarization magic angle (CPMAS) NMR spectra were obtained on a Bruker Avance-400 MHz NMR spectrometer (Spectropole, Aix-Marseille Université) operating at a ^{13}C and ^{31}P resonance frequency of 101.6 MHz and 162.1MHz, respectively. ^{13}C and ^{31}P CPMAS experiments were performed with a commercial Bruker Double-bearing probe. About 100 mg of samples were placed in zirconium dioxide rotors of 4-mm outer diameter and spun at a magic angle spinning rate of 10 kHz. The CP technique[147] was applied with a ramped ^{1}H-pulse starting at 100% power and decreasing until 50% during the contact time in order to circumvent Hartmann-Hahn mismatches[148,149]. The contact time was 2 ms for ^{13}C CPMAS and 3ms for ^{31}P CPMAS. To improve the resolution, a dipolar decoupling GT8 pulse sequence[150] was applied during the acquisition time. To obtain a good signal-to-noise ratio, 10000 scans were accumulated using a delay of 2s in ^{13}C CPMAS experiment and 3000 scans with a delay of 3s in ^{31}P CPMAS experiment. The ^{13}C and ^{31}P chemical shifts were referenced to tetramethylsilane and H_3PO_4, respectively.

2.4.5.1. ^{13}C Spectral analysis

In typical ^{13}C solid state NMR spectra, the chemical shift range covers a broad region, from approximately 0 to 250 ppm. The chemical shift being the difference between the resonance frequency of the nucleus and a reference frequency. This shift is generated by the electronic environment surrounding the nucleus, modifying the local magnetic field. Specific shift values can be associated with classes of organic compounds, allowing for a qualitative and semi-quantitative analysis of the organic species that compose the analyzed samples.

1. The 0-45 ppm region is associated with alkyl carbons found in:
   - Short chain aliphatic carbons[151–153] constituting volatile fatty acids[151], branched chained molecules[153] and steroid-like molecules[151] (0-28 ppm).
   - Long chain aliphatic carbons from proteins, lipids[152] and plant biopolymers (waxes, fatty acids)[154] (28-45 ppm)
2. The 45-110 ppm region is associated with N- and O- alkyl carbons[155] contained in carbohydrates such as cellulose and hemicellulose, methoxyl groups and N-substituted alkyl species found in proteins[151,152] and lignin[151].
3. The 110-160 ppm region is ascribed to aromatic carbons:

- Non-substituted and C-substituted aromatic carbons are generally found in the 110-140 ppm region[152,155]
- Aromatic carbon linked to N or O found in lignin[151,152], phenols[152,155], polyphenols[156] and aromatic ethers[152,155] are detected in the 140-160 ppm region.

4. The 160-220 ppm region is associated with carboxylic and carbonylic carbons:
   - Between 160 ppm and 190 ppm we find the carboxyl carbon constituting free carboxylic acids[152], esters, and amides[151,152,155].
   - Between 190 and 220 ppm are found the carbonyl groups in aldehydes, ketones and organic acids[151–153]

These two last sub regions can overlap. Besides, slightly different ranges are indicated in literature, depending on the source. ^{13}C solid state NMR analysis is qualitative, as it allows to associate the presence of a certain peak to specific class of molecules, but it is also semi-quantitative, as the integration of the area of specific regions, expressed as fraction of total area can provide a general understanding of the organic C speciation and the relative amounts of different organic compounds families. Three quantities are used to realize this semi-quantitative analysis:

Aromaticity index (Equation 2.11) allows to determine the relative amount of aromatic structures; O-Alkyl/Alkyl (OA/A) ratio (Equation 2.12) provides an insight on the sample degradation state, as alkyl carbon are generally more stable than O-alkyl species, a lower OA/A ratio implies a more advanced decomposition; hydrophobicity index (Equation 2.13), which gives information about the hydrophobic/hydrophilic nature of the sample.

$$Aromaticity\ index\ (\%) = \frac{Area(110 - 160\ ppm)}{Area\ (0 - 160\ ppm)} \cdot 100 \tag{2.11}$$

$$\frac{OA}{A} ratio = \frac{Area(45 - 110\ ppm)}{Area(0 - 45\ ppm)} \tag{2.12}$$

$$Hydrophobicity\ index = \frac{Area(0 - 45) + Area(110 - 160)}{Area(45 - 110) + Area(160 - 220)} \tag{2.13}$$

2.4.6. Extraction methods for phosphorus speciation

Between the tools available to characterize P speciation in solid phases, lately, there has been a concerted effort to employ harmonized extraction schemes, in order to facilitate a consistent analysis of different results across the literature. Two extraction methods stand out in literature as the most frequently applied to characterize P speciation: Standard Measurement and Testing (SMT) method and Hedley sequential extraction method. Both have been employed in this work and are described in the following sections.

2.4.6.1. Standard Measurement and Testing method

Between all possible P speciation schemes, the SMT protocol[74] is the most applied one for P speciation characterization of SS and SS HT products, and it has been used in a large number of studies investigating P speciation during SS HT treatment[10,77–81,83,85–94]. A slightly revised version of the SMT protocol has been used in this work as a primary tool to characterize P speciation in the solid phases (Sludges A and B and solid pellet by-products). This method, resumed in Figure 2.5, allows to distinguish five different fraction of P species: total phosphorus (TP), organic phosphorus (OP), inorganic phosphorus (IP), non-apatite inorganic phosphorus (NAIP) and apatite inorganic phosphorus (AIP).

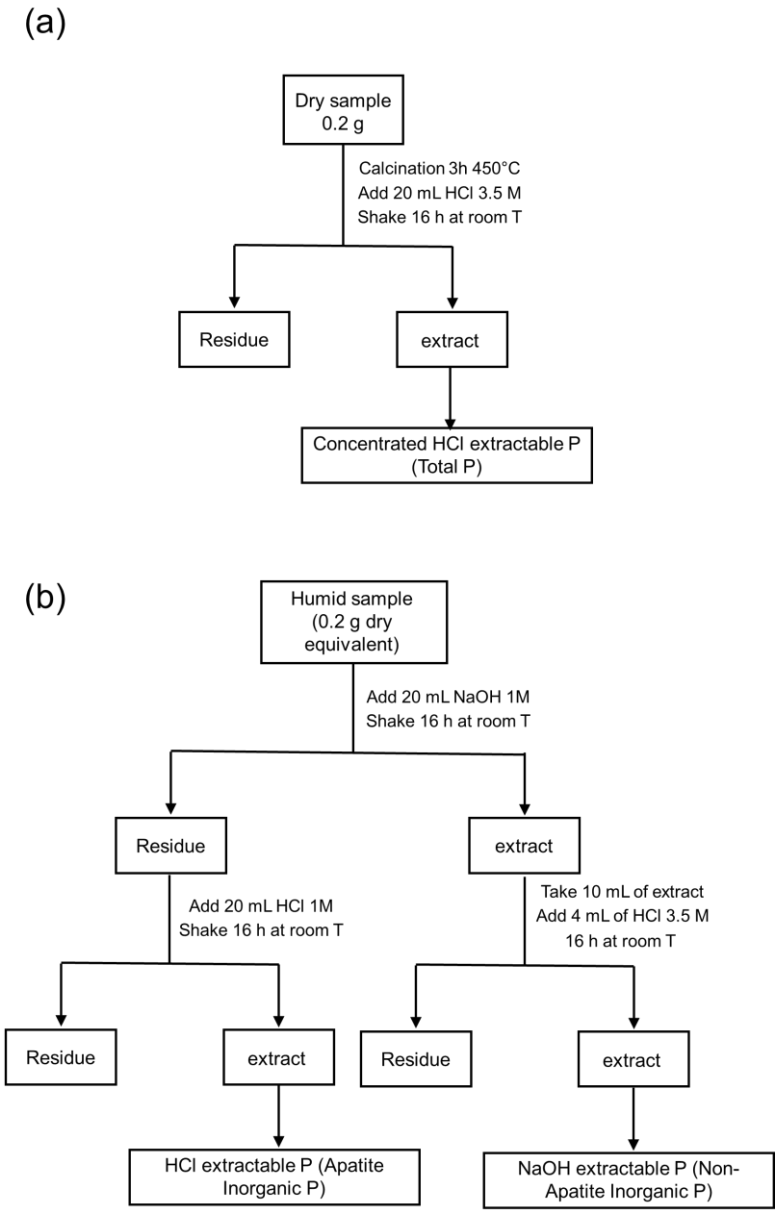

Figure 2.5 - The SMT extraction method for Total P (TP) quantification (a) and Non-Apatite Inorganic P (NAIP) and Apatite Inorganic P (AIP) quantification (b). Adapted from Ruban et al. [74].

TP extraction method is presented in Figure 2.5a and described below:

a) 0.2 g of dried solid sample are calcinated at 450 °C for 3 h in a muffle furnace. The sample is placed in a ceramic crucible closed with a cover, to create an inert atmosphere and prevent oxidation.
b) The ash residue is transferred to a centrifuge vial. 20 mL of HCl 3.5 are added to the vial, which is then subjected to 16 h of rotary agitation at 5 r min^{-1} at room temperature.
c) Supernatant (extract) and pellet (residue) are separated by centrifugation (2000 g, 15 min) with a Sigma 2-16P centrifuge.
d) The supernatant is collected and filtered (0.45 μm nylon filter) and its PO_4-P content is measured by the ammonium molybdate-ascorbic acid method (ISO EN 6878, 2004), described in Section 2.3.7, using an ultraviolet–visible (UV-VIS) spectrophotometry.

TP content (mg g^{-1} of dry solid) is calculated according to Equation 2.14:

$$TP = C_p \frac{0.02}{m_{dry}} \quad (2.14)$$

Where C_p (mg L^{-1}) is the PO_4-P concentration measured by UV-VIS spectroscopy and m_{dry} is the sample dry mass.

Another method to measure TP is aqua regia extraction combined with ICP-AES analysis, as illustrated in Sections 2.4.3 and 2.4.4.

The separation in NAIP and AIP is based on the different solubilities of Ca, Fe, and Al phosphates under various pH conditions. As shown in Figure 1.16, at low pH (1-2), the solubility of different Ca phosphate species (AIP) is higher compared to the solubility of Fe and Al phosphates. This trend is reversed at high pH (11-12), which favors the dissolution of Fe and Al phosphates (NAIP) and the precipitation of Ca phosphates (AIP).

NAIP fraction refers to IP not bonded to Ca compounds, more specifically P bound to Al and/or Fe compounds that are soluble at high pH or readily available phosphates that can be desorbed by OH- exchange. NAIP extraction method is shown in Figure 2.5b:

a) 20 mL of NaOH 1M are added to the humid solid sample (0.2 g of dried mass equivalent) and then subjected to 16 h of rotary agitation at 5 r min^{-1} at room temperature.
b) Supernatant (extract) and pellet (residue) are separated by centrifugation (2000 g, 15 min) with a Sigma 2-16P centrifuge.
c) 10 mL of the extract are transferred to another centrifuge vial, and 4 mL of HCl 3.5 M are added. The mix is left at rest for 16 h, and then centrifuged (2000 g, 15 min).
d) The supernatant is collected and filtered (0.45 μm nylon filter) and its PO_4-P content is measured by the ammonium molybdate-ascorbic acid method, using UV-VIS spectrophotometry.

NAIP content (mg g^{-1} of dry solid) is calculated according to Equation 2.15:

$$NAIP = C_p \frac{0.014}{0.01} \frac{V_{ext}}{m_{dry}} \quad (2.15)$$

Where C_p (mg L^{-1}) is the PO_4-P concentration measured by UV-VIS spectroscopy, V_{ext} is the volume of extracted solution and m_{dry} is the sample dry mass. The OP extractable in this step is unlikely to undergo mineralization into phosphate, thus it remains unquantified.

AIP fraction accounts for P associated with various Ca compounds generally soluble at low pH. AIP extraction method is shown in Figure 2.5b and described below:

a) 20 mL of HCl 1M are added to the solid pellet obtained in NAIP extraction step (b), and then subjected to 16 h of rotary agitation at 5 r min^{-1} at room temperature.
b) Supernatant (extract) and pellet (residue) are separated by centrifugation (2000 g, 15 min) with a Sigma 2-16P centrifuge.
c) The supernatant is collected and filtered (0.45 μm nylon filter) and its PO_4-P content is measured by the ammonium molybdate-ascorbic acid method, using UV-VIS spectrophotometry.

AIP content (mg g^{-1} of dry solid) is calculated according to Equation 2.16:

$$AIP = C_p \frac{V_{ext}}{m_{dry}} \quad (2.16)$$

Where C_p (mg L^{-1}) is the PO_4-P concentration measured by UV-VIS spectroscopy, V_{ext} is the volume of the extracted solution and m_{dry} (g) is the sample dry mass.

OP denotes P found in organic compounds like phospholipids, DNA, and ATP. OP content (mg g_{dry}^{-1}) is estimated by difference according to Equation 2.17, where TP, NAIP and AIP contents are expressed in mg g_{dry}^{-1}.

$$OP = TP - NAIP - AIP \quad (2.17)$$

2.4.6.2. Hedley method

Another method widely used to characterize P speciation in SS and its HT products is the Hedley method[121]. This method involves five sequential extractions designed to provide insights into P bioavailability for plant utilization. It has been conceived to distinguish different P forms in soil, and to assess their relative "bioavailability" for plants, but it has been successively applied on biomass samples and it has been largely used to characterize SS and HT treatment hydrochar in various studies reported in Chapter 1 [62,71,82,103,105,106,109,110,118,122–124].

A slightly revised version of the Hedley protocol has been used in this work to characterize exclusively the two sludges, in order to provide complementary information on P speciation. This method, resumed in Figure 2.6, allows to distinguish five different fraction of P species: H_2O-P, $NaHCO_3$-P, NaOH-P, HCl-P and Residual P, as described below:

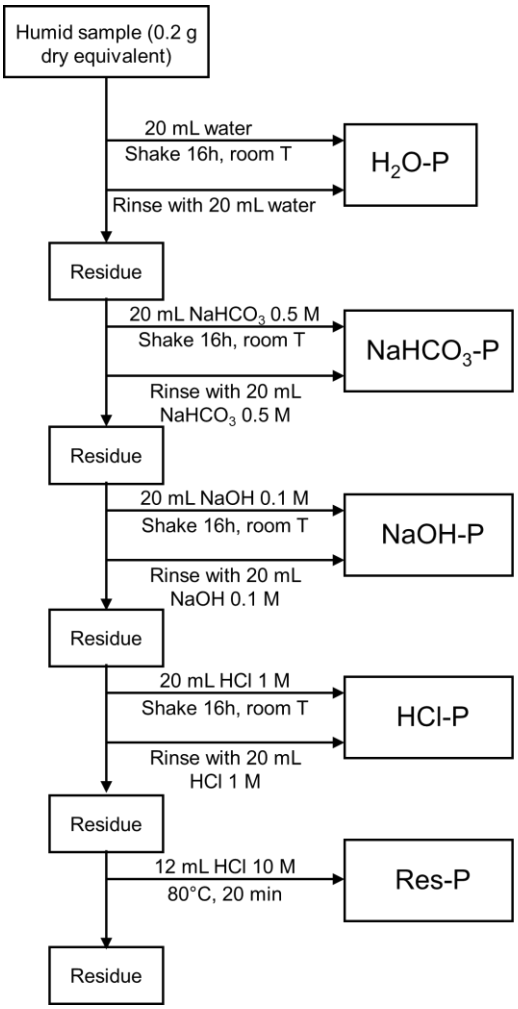

Figure 2.6 - Adjusted Hedley fractionation method. Adapted from [121].

A. 20 mL of deionized water are added to the solid phase sample (0.2 g dry matter equivalent), which is then subjected to 16 h of rotary agitation at 5 r min^{-1} at room temperature.
B. Supernatant (extract) and pellet (residue) are separated by centrifugation (2000 g, 15 min) with a Sigma 2-16P centrifuge.
C. The extract is collected.
D. The residue is rinsed with 20 mL of deionized water, which is added to the collected extract.
E. The extract is filtered (0.45 µm nylon filter) and its PO_4-P content is measured by the ammonium molybdate-ascorbic acid method, using UV-VIS spectrophotometry, measuring P water-soluble fraction (H_2O-P).

Step (a) to (e) are repeated for the three subsequent extractions, changing the extracting solution:

- 20 mL of $NaHCO_3$ 0.5 M are added to the H_2O-P extraction residue to extract $NaHCO_3$-P, which is defined as weakly bound P, as P extraction is mainly due to ion exchange.

- 20 mL of NaOH 0.1 M are added to the $NaHCO_3$-P extraction residue to extract NaOH-P. This fraction primarily involves the dissolution of Al- and Fe-bound P compounds that are soluble under high pH conditions.
- 20 mL of HCl 1 M are added to the NaOH-P extraction residue to extract HCl-P. This fraction is characterized as Ca-bound P, with P extraction primarily occurring through the dissolution of Ca-phosphate complexes under acidic conditions.
- Finally, 12 mL of HCl 10 M are added to the HCl-P extraction residue and heated at 80 °C for 20 minutes, the extract is collected and filtered, yielding the residual P fraction (Res-P). This fraction represents organic and inorganic P in stable residual compounds that need much more energy to be dissolved.

Each Hedley fraction described above, measured as mg g^{-1} of dry solid, is calculated according to Equation 2.18:

$$Extr - P = C_p \frac{V_{sol}}{m_{dry}} \quad (2.18)$$

Where C_p (mg L^{-1}) is the PO_4-P concentration measured by UV-VIS spectroscopy, m_{dry} (g) is the original sample dry mass, and V_{sol} is the volume of the extraction solution used in each step (L). In the case of the first step the total volume measured corresponds to the volume of water (0.02 L) + the water contained in the wet sample.

It is essential to critically analyze the results obtained from the application of this method on biomass samples, as it could lead to significant quantification errors for substantial amounts of P and for notable fractions of OP. A portion of the OP might be extracted in the third extraction with NaOH[157], and the spectrometric measurement would not allow for its quantification, leading to an underestimation of the OP quantity. Additionally, the solution used in the third phase (0.1 M NaOH) may not be sufficiently alkaline to fully solubilize Fe and Al phosphates. For these reasons, it is necessary to interpret the results of this method while considering its limitations and to integrate them with the results of other analytical techniques.

2.5. Hydrothermal treatment thermal profile investigation

This paragraph illustrates the experimental and analytical techniques used to qualitatively and quantitatively characterize the thermal profile of the HT treatment of SS.

A preliminary analysis of the thermal profile of Sludge A HT treatment was conducted by recording the reactor temperature TC1 and pressure PT1 values over time.

A more specific and accurate analysis was carried out by differential scanning calorimetry (DSC) using a calorimeter SETERAM C80. In this type of instrument, the heat required to raise the sample's temperature is measured by comparing it to the heat required to raise the temperature of a reference. This calorimeter allows to realize the

DSC measurement up to 300 °C, allowing the reproduction of subcritical HT conditions present inside the batch reactor. The accuracy for the temperature measurement with the high-pressure cell was calibrated using a known amount of Indium (melting point 156.6 °C). Figure 2.7 presents a scheme of the experimental setup for DSC analysis.

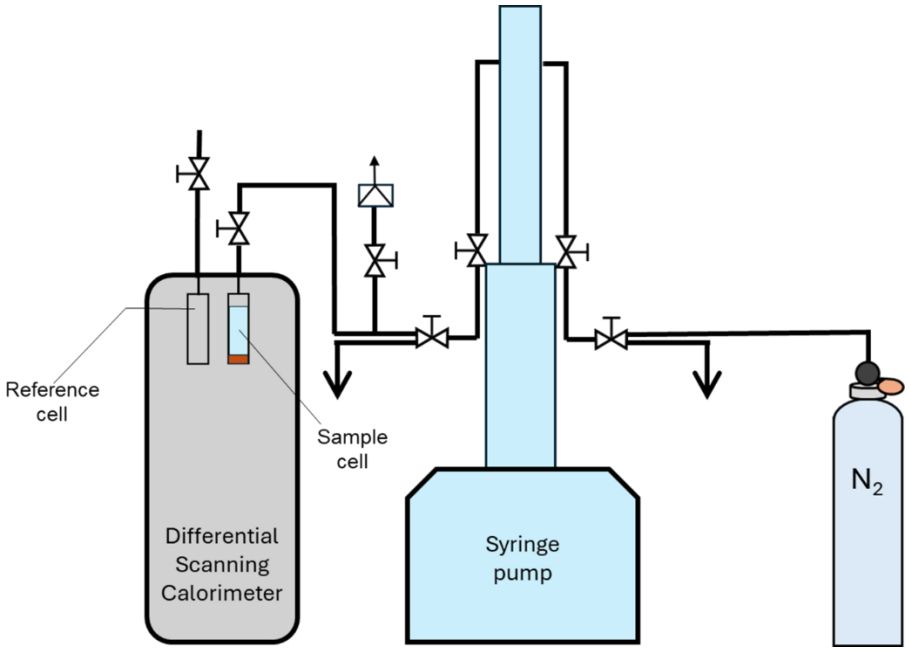

Figure 2.7 - Experimental setup used for high-pressure DSC analysis.

The sludge sample was prepared by drying it at 105 °C until complete water evaporation, and by grinding and sieving it at 100 µm to obtain a more homogenous sample. Between 200 and 600 mg of dried, grinded, sieved sludge were put in a 4 mL high-pressure stainless-steel cell, capable of resisting pressures up to 60 MPa. A volume of deionized water ranging from 1.4 to 1.8 mL was added to the dried solid, resulting in a final total mass of 2 g and thus, reproducing sludge samples with TS contents ranging from 10% to 30%. The cell was then sealed and inserted into the calorimeter body. Then, using a Teledyne Isco 100DX syringe pump connected to a N_2 gas bottle, the cell atmosphere was inerted and pressurized at a selected pressure value.

The thermal procedure is based on the one proposed by Pecchi et al.[158], consisting of a first stabilization phase at 50 °C for 180 min, followed by a linear heating phase at 1 °C min^{-1} up to 300 °C and then an isothermal phase at 300 °C for 120 minutes. The sample is then subjected to a slow cooling phase from 300 °C down to 50 °C at 0.3 °C min^{-1}. In order to specifically measure the HT reactions thermal profile and to separate it from the simple heating of water and solid matter in the cell, the so-called "exhaust" method[158,159] has been employed. According to this procedure, the thermal program is realized a first time on the water + dried sludge sample, and then a second time on the HT residues (consisting of water, hydrochar and gas), without opening the cell between the two runs as schematized in Figure 2.8:

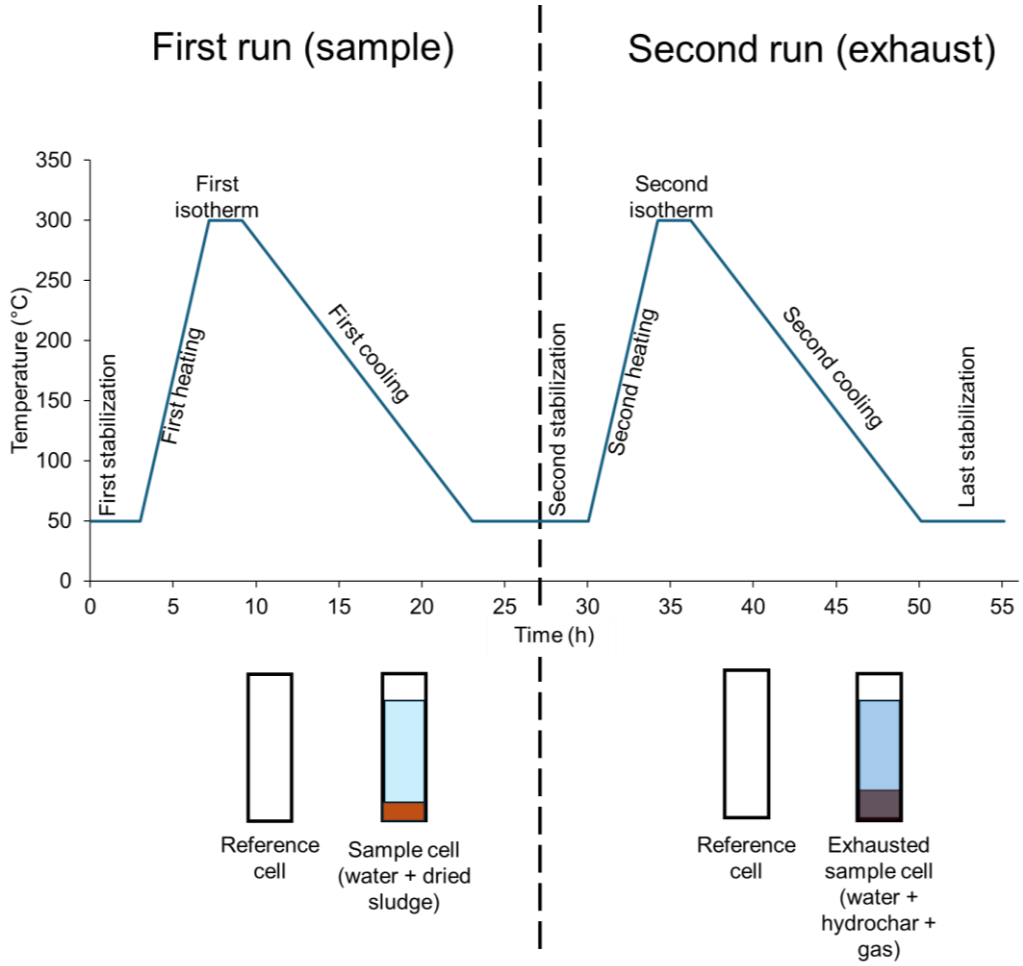

Figure 2.8 - DSC thermal procedure as proposed by Pecchi et al.[158], consisting of two consecutive runs realized without opening the cell.

The heat flux of the first heating phase q_1 corresponds to the thermal flux required to heat the dried sludge and the water and to achieve water saturation conditions $q_{heating1}$, plus the heat related to the HT reaction q_{HT}, according to Equation 2.19:

$$q_1 = q_{heating,1} + q_{HT} \quad (2.19)$$

The heat flux of the second heating phase q_2 (Equation 2.20) corresponds only to the thermal flux required to heat the exhaust HT products (hydrochar, process water and gas) and to achieve water saturation conditions $q_{heating2}$. Assuming that HT reactions have been completed in the first run, no heat is associated with HT reactions.

$$q_2 = q_{heating,2} \quad (2.20)$$

In "exhaust" method, the heat flux associated exclusively to the HT heat of reaction q_{HT} is calculated by subtracting the second heating flux from the first heating flux (Equation 2.21):

$$q_{HT} = q_1 - q_2 \quad (2.21)$$

An alternative to this method is the "water" method[159]. With this second method, the estimation of the heat required to heat up the water present in the initial sludge sample is done in a separate run with pure water, and the HT heat of reaction is calculated by subtracting the pure water heating flux from the first heating flux.

This extra run on a pure water sample q_{water} could assess the heat flux related exclusively to the heating and evaporation of water to achieve saturation conditions $q_{heating,water}$ (Equation 2.22):

$$q_{water} = q_{heating,water} \quad (2.22)$$

However, it has been observed that free water has a different specific heat compared to water in contact with solid material, to which it can bind through various physical and chemical interactions (solvation or adsorption)[160]. Therefore, there is an inherent error in the estimation of the heat flow fraction related to water with this second method since, in both the initial sludge sample and the exhaust sample, water is present along with a fine solid phase (<100 μm) of hydrochar.

The sludge HT treatment total enthalpy of reaction ΔH_{HT} has been estimated by integrating q_{HT} (Equation 2.21) between the instant t_1 corresponding to a temperature of 75 °C and the instant t_2 at the end of the isotherm phase at 300 °C as indicated in Equation 2.23:

$$\Delta H_{HT} = \int_{t_1}^{t_2} q_{HT}\, dt \quad (2.23)$$

The evaluation of HT reaction enthalpy is calculated starting from 75 °C and not from 50 °C in order to exclude initial heat flux fluctuations related to water thermal inertia. This does not affect the result as no HT reaction is expected in this temperature range.

To replicate HT batch reactor conditions, an initial analysis was conducted with a sample pressurized to 4.8 MPa of N_2, matching the starting pressure needed to reach 18 MPa at 300 °C. To evaluate the impact of initial pressure on reaction enthalpy during SS HT treatment, two additional N_2 pressures were tested: 0.1 MPa (autogenous conditions) and 9.5 MPa, doubling the standard 4.8 MPa.

To investigate the effect of SLR on SS HT reaction enthalpy, three different solid contents have been implemented, corresponding to 10%, 20% and 30% of total mass in the DSC cell.

2.6. Statistical analysis

2.6.1. Design of experiments methodology

Experimental design, or design of experiments (DOE) is a systematic methodology process used to organize and realize experiments in an efficient way, maximizing the output of useful information and ensuring that collected results are valid and can lead to

significant conclusions. This paragraph was developed based on the statistical elements provided by Cox and Reid, The Theory of the Design of Experiments, 2000[161].

Design of experiments can be used in different scenarios and for one or more purposes, notably to determine whether a factor affects the results, to assess the presence of possible interactions between different factors, to build a mathematical model that properly describes the relationship between factors and response, and to find the optimal set of factor value to obtain a specific desired response.

Both screening design and surface response design approaches (described in Annex C) have been used in this work. To evaluate the statistical significance of the obtained models the ANOVA (ANalysis Of VAriance) (Table C.2) has been implemented. The global variation related to the model can be quantified using the determination coefficient R^2 (equation C.10). The statistical significance of each coefficient of the obtained model is evaluated with Student t-test[162]. To study more responses at the same time, the desirability function approach is implemented.

The design of experiments definition, the design model selection, the linear regressions execution to obtain the predictive models, and the statistical analysis of the results were all performed using the AZURAD® software (Marseille, France).

2.6.1.1. Design of experiment to assess the effects of temperature and time

The first series of experiments investigate the role of temperature and treatment duration on HT by-products characteristics and P speciation (Chapter 4) after the hydrothermal treatment of Sludge A. For the design of the experiments (DOE) of this experimental step, it was not necessary to use a specific optimal DOE matrix to reduce the number of total experiments, as at this stage of the investigation the factors studied are only two (temperature and duration) and therefore the number of experiments required is relatively small. For each factor, three levels were selected so that responses could be used to obtain second-degree polynomial response surfaces.

As a result, the selected design for this investigation is a complete symmetric factorial design with two factors (temperature, duration) and three levels (250 °C, 300 °C, 350 °C for temperature; 5 min, 15 min, 45 min for duration), resulting in $3^2 = 9$ experiments of hydrothermal treatment realized on Sludge A. Each experiment has been repeated twice, resulting in a total of 18 experiments (Table 2.1).

The experimental plan results were utilized to conduct both a screening DOE and a response surface DOE. The screening DOE was employed to evaluate the relative effect of each factor independently of possible interactions, while the response surface DOE was used to model the response as a function of the two factors, predicting their behavior within the experimental domain.

Table 2.1 - List of the conditions selected for the temperature/time design of experiments.

n°	Repetitions	Temperature (°C)	Treatment duration (min)	Process severity f(T,t)
1	2	250	5	0.19
2	2	250	15	0.24
3	2	250	45	0.30
4	2	300	5	0.35
5	2	300	15	0.43
6	2	300	45	0.54
7	2	350	5	0.57
8	2	350	15	0.71
9	2	350	45	0.88

The screening design allows to obtain information about the effect of each factor in the form of coefficients of the following linear model (Equation 2.24):

$$y = b_0 + b_{1A}x_{1A} + b_{1B}x_{1B} + b_{2A}x_{2A} + b_{2B}x_{2B} \quad (2.24)$$

Where b_0, b_{1A}, b_{1B}, b_{2A}, b_{2B} are the model coefficients obtained as result of the linear regression, while x_{1A}, x_{1B}, x_{2A}, x_{2B} are discrete variables that can assume two values (0, 1). All the possible combinations of these variables correspond to a specific pair of parameters T, t, as indicated in Table 2.2:

Table 2.2 - Values assumed by the five coefficients constituting the screening design of experiments model described by Equation 2.24.

N°	Experimental plan		Model matrix				
	Factor		b_0	x_{1A}	x_{1B}	x_{2A}	x_{2B}
	Temperature (°C)	*Duration (min)*		b_1	b_2	b_2	b_2
1	250	5	1	1	0	1	0
2	250	15	1	1	0	0	1
3	250	45	1	1	0	0	0
4	300	5	1	0	1	1	0
5	300	15	1	0	1	0	1
6	300	45	1	0	1	0	0
7	350	5	1	0	0	1	0
8	350	15	1	0	0	0	1
9	350	45	1	0	0	0	0

The coefficients obtained from the screening analysis are then interpreted by evaluating their relative weight compared to the smallest significant effect.

Surface response design allows to obtain a second-degree polynomial function for each response, as described by Equation 2.25:

$$y = b_0 + b_1T + b_2t + b_{1-1}T^2 + b_{2-2}t^2 + b_{1-2}T \cdot t \quad (2.25)$$

Where b_0, b_1, b_2, $b_{1\text{-}1}$, $b_{2\text{-}2}$, $b_{1\text{-}2}$ are the coefficients of the polynomial model, T is temperature, and t is the treatment duration. Both temperature and duration are normalized to the experimental range according to Equations 2.26 and 2.27, converting the intervals to a range of -1 to 1, where -1 corresponds to the range minimum value and 1 to the maximum value.

$$T' = \frac{T - 300}{50} \quad (2.26)$$

$$t' = \frac{t - 25}{20} \quad (2.27)$$

Table 2.3 presents the temperature and duration values used in our model along with their corresponding normalized values.

Table 2.3 - Temperature and duration values used in the second-degree polynomial model along with their corresponding normalized values in the range -1 to 1.

Temperature (°C)	Corresponding value in the model	Time (min)	Corresponding value in the model
250	-1	5	-1
300	0	15	-0.5
350	1	45	1

2.6.1.2. Design of experiment to assess the effects of temperature, time, and Ca/P molar ratio

In a second series of experiments the role of Ca/P molar ratio is explored by studying its effect in relation to the previously characterized factors (temperature, time) on HT by-products characteristics and P speciation (Chapter 6) following HT treatment of Sludge B. For this purpose, the surface response of the Design of experiments (DOE) has been conceived by extending the DOE realized in Chapter 4 to study the effects of HT temperature and duration by adding a third factor (Ca/P molar ratio) with three levels (0.70, 1.15, 1.60). The minimum value (0.7) represents the Ca/P molar ratio in Sludge B without any addition of CaO. The selection of the other two levels was based on the molar ratio of the main P and Ca complexes found in HT treatment products (dicalcium phosphate, tricalcium phosphate, octacalcium phosphate, hydroxyapatite), which range between 1 and 1.67. The Ca/P molar ratios of 1.15 and 1.60 are attained by adding 0.67% and 1.33% CaO, respectively, relative to Sludge B mass in the reactor.

The overall DOE consists of three factors, each with three levels, resulting in a total of $3^3 = 27$ combinations. To reduce the number of experiments, an optimal-D matrix design

is proposed. The optimality criterion used in generating D-optimal designs aims to maximize |X'X|, where |X'X| denotes the determinant of the information matrix X'X.

The use of the D-optimal matrix allows to realize a minimal number of experiences equal to 10 generated by the Azurad software (Marseille, France). A central point is added (with the central levels of each factor, 300 °C, 15 min, Ca/P= 1.2). Additionally, three more experimental points that were previously conducted to achieve the results described in Chapter 5 were included in the matrix, resulting in a total of 14 experiments. Two experimental points were conducted twice, while the central point was conducted three times. Therefore, the final number of experiments conducted was 18. Table 2.4 presents the characteristics of these 18 experiments in the order of realization.

Table 2.4 - 18 experiments constituting the surface response DOE for studying temperature, duration and Ca/P molar ratio effects on HT by-products characteristics.

N°	Repetitions	Temperature (°C)	Duration (min)	Ca/P molar ratio
1	1	300	15	0.70
2	1	250	15	0.70
3	1	350	15	0.70
4	1	300	5	0.70
5	1	250	45	0.70
6	2	350	45	1.60
7	1	300	45	1.15
8	1	350	45	0.70
9	2	250	5	1.15
10	1	350	5	1.60
11	1	350	15	1.15
12	1	250	45	1.60
13	1	300	15	1.60
14	3	300	15	1.15

Surface response design allows to obtain a second-degree polynomial function for each response, as described by Equation 2.28:

$$y = b_0 + b_1 T + b_2 t + b_3 Ca + b_{1-1} T^2 + b_{2-2} t^2 + b_{3-3} Ca^2 + b_{1-2} T \cdot t + b_{1-3} T \cdot Ca + b_{2-3} t \cdot Ca \quad (2.28)$$

Where b_0, b_1, b_2, b_3, $b_{1\text{-}1}$, $b_{2\text{-}2}$, $b_{3\text{-}3}$, $b_{1\text{-}2}$, $b_{1\text{-}3}$, $b_{2\text{-}3}$ are the coefficients of the polynomial model, T is temperature (°C), t is the treatment duration (min), and Ca is Ca/P molar ratio.

Temperature, duration and Ca/P molar ratio are normalized to the experimental range according to Equations 2.26, 2.27 and 2.29 converting the intervals to a range of -1 to 1, where -1 corresponds to the range minimum value and 1 to the maximum value.

$$Ca' = \frac{Ca - 1.15}{0.35} \tag{2.29}$$

Table 2.5 presents the Ca/P molar ratio values used in our model along with their corresponding normalized values.

Table 2.5 - Ca/P molar ratio values used in the second-degree polynomial model along with their corresponding normalized values in the range -1 to 1.

Ca/P molar ratio	Corresponding value in the model
0.70	-1
1.15	0
1.60	1

The screening design allows to obtain information about the effect of each factor in the form of coefficients of the following linear model. It is realized by using the same matrix used for the surface response design. The coefficients obtained from the screening analysis are then interpreted by evaluating their relative weight compared to the smallest significant effect.

2.6.2. Error propagation

The evaluation of the propagation of systematic and random errors associated with the various experimental measurements conducted throughout this work is essential for a critical understanding of the results' statistical significance.

The results reported in the following chapters are often the product of a series of measurements. For a generic quantity, obtained by realizing and combining a series of measurements x_1, x_2, x_3, ..., each with a corresponding uncertainty Δx_1, Δx_2, Δx_3, ..., the final value of the quantity can be expressed as a generic function f of the various measurements made: $f(x_1, x_2, x_3, \ldots)$. In this case, the uncertainty relative to the calculated value can be quantified according to the relationship expressed in Equation 2.30:

$$\Delta f = \left|\frac{\partial f}{\partial x_1}\right| \Delta x_1 + \left|\frac{\partial f}{\partial x_2}\right| \Delta x_2 + \left|\frac{\partial f}{\partial x_3}\right| \Delta x_3 + \cdots \tag{2.30}$$

When a measure x is repeated N times, obtaining N different values x_i, the statistical mean of the measure can be expressed by Equation 2.31:

$$\bar{x} = \frac{1}{N} \sum_{i=1}^{N} x_i \tag{2.31}$$

The dispersion of a set of measures is provided by the statistical variance, corresponding to the average of the squared differences between each measure x_i and the mean $\bar{x}$ as described in Equation 2.32:

$$\sigma_x^2 = \frac{1}{N}\sum_{i=1}^{N}(x_i - \overline{x})^2 \quad (2.32)$$

Corresponding to the square of the standard deviation σ_x. Thus, the result of the repeated measurements is given in the form $\bar{x} \pm \sigma_x$.

For a generic quantity f, obtained by realizing and combining a series of measurements x_1, x_2, x_3, ..., each with a corresponding variance Δx_1, Δx_2, Δx_3, the variance of the final quantity is obtained according to the propagation law expressed in Equation 2.33:

$$\sigma_f^2 = \left(\frac{\partial f}{\partial x_1}\right)^2 \sigma_{x_1}^2 + \left(\frac{\partial f}{\partial x_2}\right)^2 \sigma_{x_2}^2 + \left(\frac{\partial f}{\partial x_3}\right)^2 \sigma_{x_3}^2 + \cdots \quad (2.33)$$

The final quantity standard deviation corresponds to the square root of the variance calculated with Equation 2.32.

All gravimetric measurements, quantifications using test kits and sequential extractions for P speciation have been realized in triplicates. For each set of analyses, limit of detection and limit of quantification were determined by analysis of blanks. All chemicals used were of analytical grade.

2.6.3. Ruyter severity function

The Ruyter[101] severity factor f(T,t) is a function of time and temperature, already used in previous works[11,81,102] to model some hydrochar characteristics and HT results. This function is described in Section 1.6.1 and recalled in Equation 2.34, where t represents the reaction time (s) and T is the temperature (K).

$$f(T,t) = 50\, t^{0.2}\, e^{-\frac{3500}{T}} \quad (2.34)$$

This function has been developed by modeling experimental kinetic data from HTC of various biowastes and subbituminous coal between 120 and 390 °C, and reaction time from 1 min to 6 months. This function assumes time-temperature equivalence, meaning that the same products' characteristics can be obtained with a shorter reaction time and higher temperature, or with a longer reaction time and lower temperature.

The model has been particularly successful because, as can be seen from the formula in Equation 2.34 and the visualization of the function in Figure 2.9, it includes an exponential effect of increasing temperature but a linear effect of increasing treatment duration, making the effect related to temperature predominant over time. As presented in Chapter 1, many properties of the HT treatment products and results associated with this type of process appear to follow this kind of law, where temperature seems to have a

greater impact on the outcomes. Therefore, using this parameter often allows for easier modeling of experimental results.

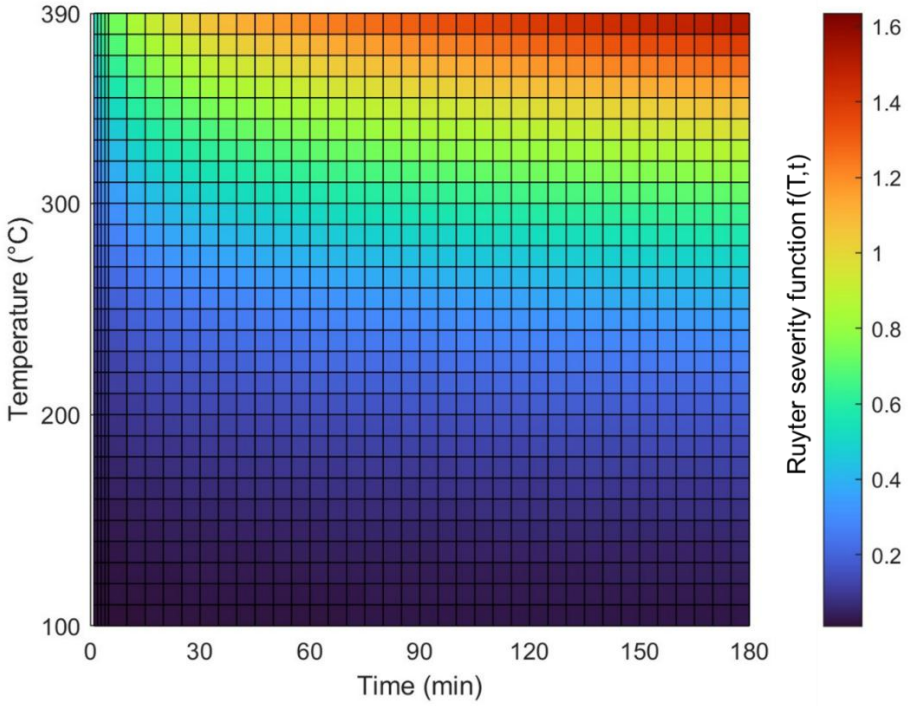

Figure 2.9 - Ruyter[101] severity function (Equation 2.34) as a function of temperature (°C) and treatment duration (min).

The Ruyter coalification model has been employed in our work in order to verify if the obtained results follow the trends already observed in the literature and described in Chapter 1, and to directly compare our results with those of similar studies.

2.7. Conclusions

This chapter has systematically illustrated the materials and methods used to realize the experimental work. The origin of the sludges and the specific treatments applied at the wastewater treatment station were first detailed. The hydrothermal treatment setup was then described, including the batch reactor configuration, sludge loading procedures, and the recovery and separation of by-products. Subsequently, the analytical techniques utilized for the comprehensive characterization of the products were listed, along with the extraction methods for quantifying phosphorus, metals, and heavy metals, as well as for characterizing P speciation. The method for determining the enthalpy of reaction associated with the HT treatment was also presented. Finally, the systematic approach to the development of the experimental plan and the statistical tools used for analyzing the results were elucidated. All these methods have been employed to obtain and analyze the results presented in Chapters 3 to 6.

3. Sewage sludge digestate feed characterization

3.1. Introduction

In this chapter, a detailed description of the characteristics of the digestate feeds used in this work is provided, covering general physical properties, elemental composition, and P speciation. A comprehensive analysis of both the sludges (A and B) and the centrates (A and B) will be presented to offer a thorough understanding of the solid and liquid phases that constitute the digestate used in the HT treatment.

A preliminary analysis of the feeds is necessary for various reasons:

- There is significant variability in SS composition based on geographical origin and the source of the wastewater (municipal or industrial). Therefore, it is necessary to clearly illustrate how the feeds compare to the value distributions reported in the literature and presented in Section 1.5.1, interpreting any discrepancies using the available information. Additionally, this analysis is crucial to understand the results in the following chapters (4-6), which will detail the products of the HT treatment of these feeds. Knowing the characteristics of both the feeds and the products is essential to understand the transformations that the organic and mineral phases undergo during the thermal process.
- The processes that wastewater undergoes in the treatment plant can influence the characteristics of the resulting sludge[9,11–15]. Although the two feeds sampled for this study originate from the same wastewater treatment plant (WWTP), and therefore should not exhibit significantly different characteristics, they are produced at different stages of the treatment process, as explained in Section 2.1.1 and illustrated in Figure 2.1. Thus, comparing their characteristics is necessary to understand the impact of these processes. Additionally, the two feeds were sampled at different times (Sludge A in March 2022 and Sludge B in May 2023), and seasonality could have significantly affected the characteristics of the urban wastewater arriving at the treatment plant.
- As already explained in Section 1.6.4, the presence and concentration of certain metals, such as Ca, Fe, and Al (and the molar ratios Ca/P, Fe/P and Al/P), have an important effect on P speciation. Therefore, it is necessary to quantify these elements to contextualize the results related to P sequential extraction for the feeds and their respective products.

In the final part of this chapter, we will analyze the environmental compatibility of these feeds, considering their potential disposal through agricultural field spreading and

use as organic fertilizers. This evaluation will include an assessment of their macronutrient, organic carbon, and heavy metals content, comparing these parameters with relevant European directives.

3.2. Materials and methods

The processes realized at the WWTP in which Sludge A, Sludge B, Centrate A and Centrate B are produced are described in Section 2.1.1 and in Figure 2.1.

Centrate A and Centrate B have been analyzed according to methods and techniques described in Section 2.3, characterizing their main physical properties, alkalinity, solid content, soluble N and PO_4-P concentration, dissolved C, COD, and metal contents. Sludge A and Sludge B were characterized as described in Section 2.4, quantifying their elemental composition, metal and heavy metal content, and P speciation.

In this chapter, the chemical and physical properties and results will be expressed in the form *a ± s (n)*, where *a* corresponds to the average of the different measurements, *s* is the standard deviation, calculated according to Equation 2.33, and *n* is the number of measurements.

3.3. Feed characterization

3.3.1. Sludges characterization

Figure 3.1 shows the appearance of the two sludges used as feed in this work (Sludge A and Sludge B). The two sludges main physico-chemical characteristics are resumed in Table 3.1.



Figure 3.1 - Visual presentation of Sludge A (left) and Sludge B (right).

As shown in Figure 2.1, Sludge A is obtained by dewatering the collected SS digestate, coming directly from the anaerobic digester (TS 2.5%) by centrifugation at 4000 rpm for 20 min. Sludge A appears as a relatively homogeneous and viscous black sludge and still retains an important amount of moisture, with a TS content of 6.7 ± 0.2% (18).

Sludge B, obtained from the industrial centrifugation of digested sludge mixed with tertiary sludge, presents a more opaque, cohesive and viscous consistency, and is characterized by a TS content of 18.89 ± 0.02 % (9). Both values are coherent with the values typically observed for SS used as feed in HT treatments, ranging from 2% to 30%[1].

Table 3.1 - Main physico-chemical characteristics for Sludge A and Sludge B obtained with methods and techniques described in Section 2.4. Reported values are in the form a ± s (n), where a is the average of the different measurements, s the standard deviation, and n the number of measurements.

	Sludge A	***Sludge B***
Moisture (%)	93.3 ± 0.2 (18)	81.11 ± 0.02 (9)
Total Solids (TS) %	6.7 ± 0.2 (18)	18.89 ± 0.02 (9)
Ashes %*	22.7 ± 0.2 (6)	24.78 ± 0.08 (6)
C (%)*	37.5 ± 0.6 (9)	37.5 ± 0.4 (3)
N (%)*	6.4 ± 0.2 (9)	6.3 ±0.2 (3)
H (%)*	5.84 ± 0.04 (9)	5.61 ± 0.04 (3)
S (%)*	1.10 ± 0.03 (9)	1.00 ± 0.01 (3)
O (%)**	26.4 ± 0.7 (6)	24.8 ± 0.1 (3)
P (mg g^{-1})*	32 ± 2 (9)	41.1 ± 0.8 (3)
Ca (mg g^{-1})*	29.0 ± 0.9 (9)	36.7 ± 0.5 (3)
Fe (mg g^{-1})*	23 ± 1 (9)	48.9 ± 0.8 (3)
K (mg g^{-1})*	7 ± 2 (9)	2.5 ± 0.4 (3)
Mg (mg g^{-1})*	6.7 ± 0.6 (9)	6.3 ± 0.1 (3)
Al (mg g^{-1})*	2.3 ± 0.3 (9)	2.02 ± 0.08 (3)
Zn (mg g^{-1})*	0.57 ± 0.02 (9)	0.7 ± 0.1 (3)
Cu (mg g^{-1})*	0.44 ± 0.02 (9)	0.399 ± 0.007 (3)
Pb (mg kg^{-1})*	25 ± 1 (9)	51 ± 2 (3)
Cr (mg kg^{-1})*	25 ± 1 (9)	25.0 ± 0.3 (3)
V (mg kg^{-1})*	19.2 ± 0.6 (9)	23.3 ± 0.2 (3)
Ni (mg kg^{-1})*	17.7 ± 0.7 (9)	19.0 ± 0.2 (3)
Ag (mg kg^{-1})*	6.3 ± 0.3 (9)	3.11 ± 0.08 (3)
As (mg kg^{-1})*	3.4 ± 0.2 (9)	3.0 ± 0.2 (3)
Cd (mg kg^{-1})*	0.96 ±0.03 (9)	0.85 ± 0.04 (3)
Hg (mg kg^{-1})*	0.15 ± 0.02 (9)	0.10 ± 0.02 (3)

*on dry mass basis; **on dry mass basis, obtained by difference

As shown in Figure 3.2, ultimate analysis revealed that Sludge A contains 22.7 ± 0.2 % (6) Ash, while Sludge B contains a slightly higher amount at 24.8 ± 0.1 % (6) Ash. Although these values align with typical distributions for sludges used in HT treatments, these two sludges are particularly rich in organic matter, presenting a relatively low ash content.

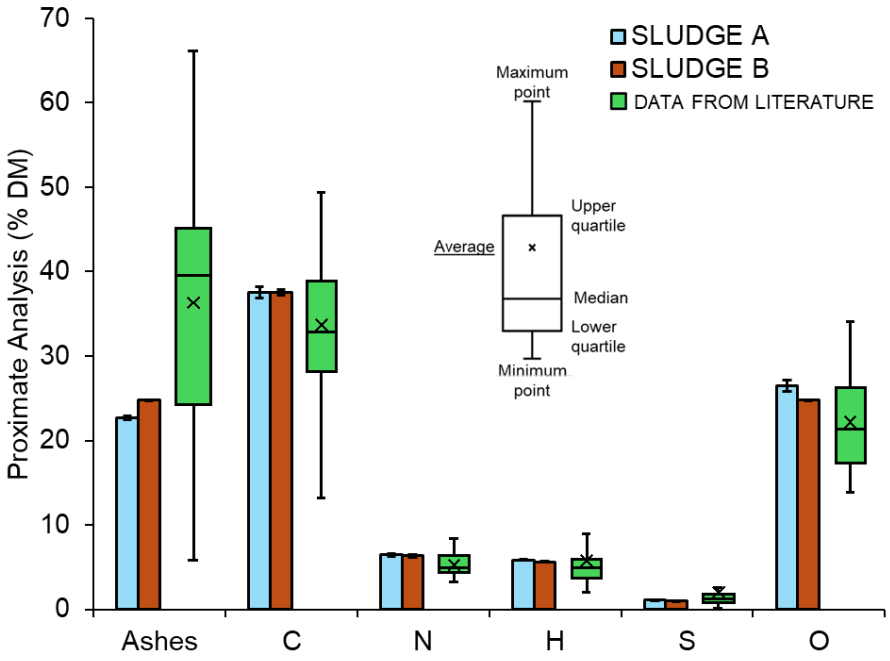

Figure 3.2 - Sludge A and Sludge B ultimate analysis results in terms of C, N, H, S, O and ash contents expressed as % of total dry matter. Error bars representing standard deviation. Box plots report distributions of the works listed in Table A.1.

The slightly higher ash content in Sludge B can be attributed to its origin, which partly consists of sludge from tertiary treatment where P removal is achieved through the addition of $FeCl_3$.

The ultimate analysis provided the composition of the two sludges in terms of carbon (C), hydrogen (H), nitrogen (N), sulfur (S), and oxygen (O). These results, depicted in Figure 3.2, are compared with ultimate analysis distributions observed for SS in works listed in Table A.1. Both sludges exhibit very similar compositions, which are also consistent with values reported in the literature.

Figure 3.3 shows the Van Krevelen diagram of the two sludges samples compared to results of available studies on SS HT treatments (Table A.1). When interpreting the Van Krevelen diagram in the context of organic matter maturation, various zones are depicted, in order to help visualize the organic matter transformation into different stages of coalification. The first zone associated with biomass (top right) is characterized by relatively high O/C and H/C ratios, related to the presence of large amounts of cellulose, lignin, and other organic compounds. The coalification process is associated with a reduction in H/C and O/C, leading to a shift downwards and to the left, towards the origin of the graph. This progression moves through zones with progressively lower values of O/C and H/C, passing to materials comparable to peat (partially decomposed organic matter generally found in wetlands), lignite (low rank coal, rich in moisture and volatile matter), coal, and finally anthracite (high-rank coal). These zones provide a general indication of the positioning of experimental results relative to these classes of materials, allowing for a more intuitive interpretation. The experimental O/C and H/C molar ratios of the two sludges are in line with the general distributions found for SS[163]. Both the

experimental points and the data collected from literature are in fact placed in the Van Krevelen diagram in an area generally associated with SS and biomass[163].

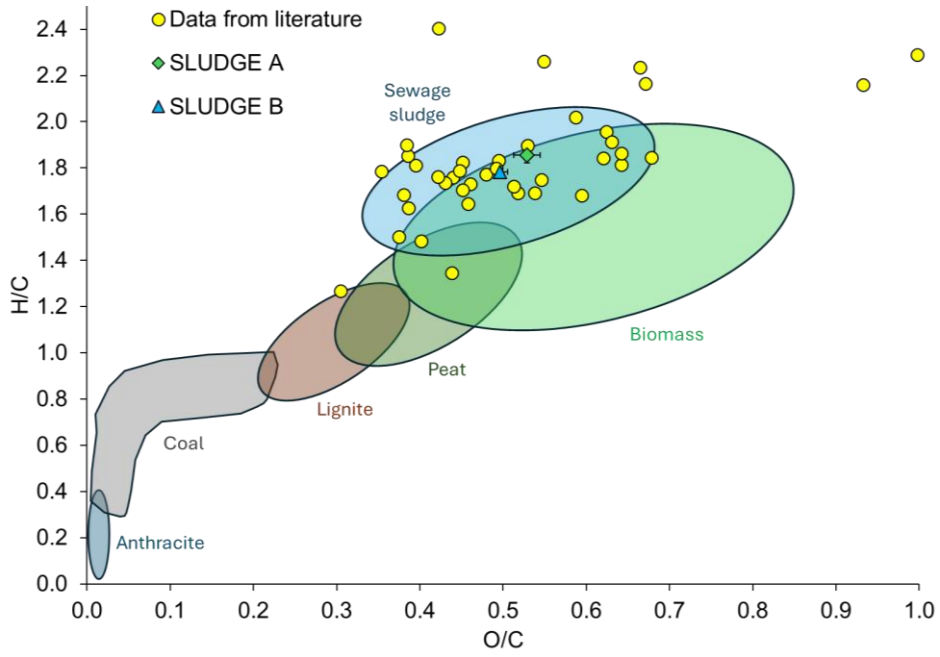

Figure 3.3 - Van Krevelen diagram for Sludge A and Sludge B, and for sludges used in works listed in Table A.1. Error bars representing standard deviation. Adapted from [163,164].

Figure 3.4 presents the content of P, Ca, Fe, Al, Mg and K in the two sludges expressed as mg g^{-1} on a dry basis, alongside the general content distributions observed for SS in Table A.1. Sludge A contains 32 ± 2 (9) mg g^{-1} of P, while Sludge B phosphorus content is higher, at 41.1 ± 0.8 (3) mg g^{-1}. This higher amount is coherent with the origin of Sludge B, obtained by mixing the SS digestate with sludge from P removal treatment. $FeCl_3$ addition may have promoted the precipitation of P, therefore enriching Sludge B P content. Among the metals found in P complexes and compounds in SS, Ca, Fe, Al, Mg and K are generally prevalent. Sludge A contains 29 ± 2 (9) mg g^{-1} of Ca, 23 ± 1 (9) mg g^{-1} of Fe, 2.3 ± 0.3 (9) mg g^{-1} of Al, 6.7 ± 0.6 (9) mg g^{-1} of Mg and 7 ± 2 (9) mg g^{-1} of K. In comparison, Sludge B has a higher Ca content at 36.7 ± 0.5 (3) mg g^{-1}, more than double the amount of Fe at 48.9 ± 0.8 (3) mg g^{-1}, comparable amounts of Al and Mg, respectively 2.02 ± 0.08 (3) mg g^{-1} and 6.3 ± 0.1 (3) mg g^{-1}, and a lower amount of K, at 2.5 ± 0.4 (3) mg g^{-1}.

The substantial higher Fe content in Sludge B can easily be attributed to the addition of $FeCl_3$ as an inorganic coagulant to promote dewatering, and which leads to P precipitation, while the differences in Ca and K contents can be attributed to seasonal fluctuations in water Ca^{2+} and K^+ contents. Sludge A has been collected in March 2022, while Sludge B has been collected in May 2023. An analysis of the measurements related to the chemical sanitary controls of the water distribution network in the section where the purification station is located, showed relatively significant fluctuations in the concentration of Ca^{2+} in the water, with values ranging from a minimum of 52.6 mg L^{-1} to

62.3 mg L^{-1} (a maximum variation of 16%)[165]. As shown in Section 3.3.2, Centrate B actually contains a higher concentration of Ca and a lower concentration of K compared to Centrate A. However, this gap is smaller compared to the difference observed for the respective sludges. The higher Ca content in Sludge B could be also explained by considering the possible participation of Ca^{2+} ions in the complexation of organic matter with ferric ions (Fe^{3+})[166], and therefore it could precipitate together with the organic matter-$Fe(OH)_3$ complexes.

For both sludges, P, Ca, Fe, Al, Mg and K contents are substantially comparable to the average values found in literature[1]. Sludges A and B have lower Al levels compared to literature values, likely because many WWTP use $AlCl_3$ for phosphates removal, while "*La Pioline*" WWTP uses $FeCl_3$. This could account for the generally higher Al content reported in most published studies.

Ca/P, Fe/P, and Al/P molar ratios are respectively 0.70, 0.40 and 0.08 for Sludge A and 0.69, 0.66 and 0.06 for Sludge B. For both sludges these ratios are lower than the values of the most commons Fe, Ca, and Al phosphates that can precipitate in water solutions ($FePO_4$, $CaHPO_4$, $Ca_5(PO_4)_3(OH)$, $AlPO_4$)[72]. If P were present in the sludges exclusively in the form of $CaHPO_4$ or $Ca_5(PO_4)_3$, the Ca/P molar ratio would be higher than 1. Similarly, if it were present exclusively in the form of $FePO_4$ or $AlPO_4$, the respective Fe/P and Al/P molar ratios would be higher than 1. Therefore, the fact that the actual molar ratios are lower than 1 for all three of these metals, indicates that P is present in different species and that it is not complexed exclusively with Ca, Fe, or Al.

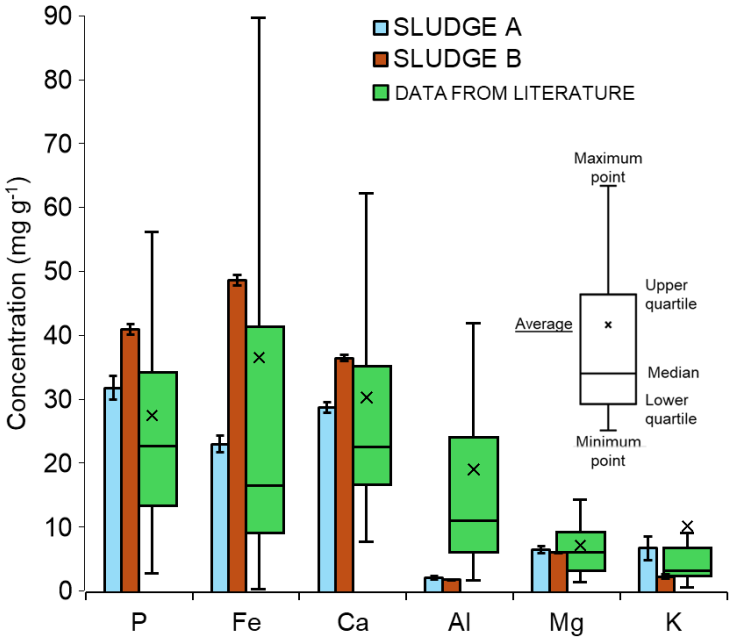

Figure 3.4 - P, Ca, Fe, Al, Mg and K content in Sludge A and B expressed as mg g^{-1} of dried sludge. Box plots represent the general content distributions observed for SS used in HT treatments and listed in Table A.1. Error bars represent standard deviation.

Both digestates contain some hundreds mg kg^{-1} of Cu and Zn, some dozens mg kg^{-1} of Pb, Cr, V and Ni, few mg kg^{-1} of Ag and As, and traces of Cd and Hg (< 1 mg kg^{-1}), expressed

on a dry basis (Figure 3.5). Except for Pb and Ag, Sludge B has comparable heavy metals contents with respect to Sludge A. Both Sludge A and B metals and heavy metals observed contents are consistent with the ranges reported in the literature[11].

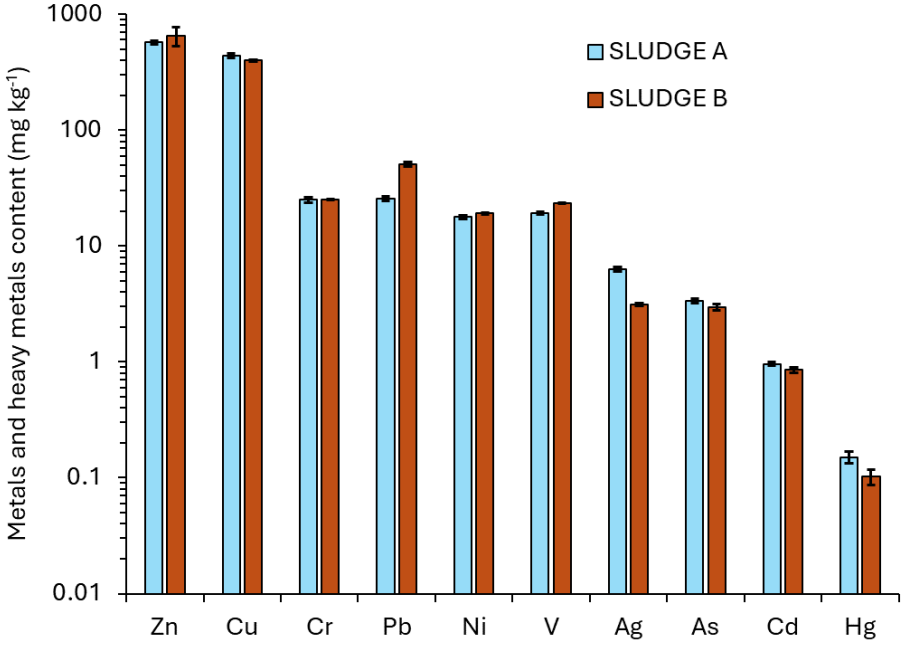

Figure 3.5 - Heavy metals contents in Sludge A and B expressed as mg kg^{-1} of dried sludge. Error bars represent standard deviation.

Figure 3.6 shows the results of SMT extraction method to assess P speciation, described in Section 2.4.6.1. Figure 3.6a reports the three P fractions absolute contents expressed as mg P g^{-1} on a dry basis, while Figure 3.6b shows the relative amounts as fractions of TP compared with general SS distributions from literature.

In Sludge A, P is mainly present as NAIP at 20.4 ± 0.6 (7) mg P g^{-1}, which is 61 ± 5% (7) of TP, followed by 8.4 ± 0.4 (7) mg P g^{-1} of AIP (25 ± 2% (7) of TP), and 5 ± 2 (7) mg P g^{-1} of OP (14 ± 5% (7) of TP). Sludge B has similar values: 22.3 ± 0.8 (3) mg P g^{-1} of NAIP (59 ± 2% (3) of TP), 11.8 ± 0.3 (3) mg P g^{-1} of AIP (30.9 ± 0.9% (3) of TP), and only 4 ± 1 (3) mg P g^{-1} of OP (10 ± 3% (3) of TP).

Sludge B has slightly less OP than Sludge A in both absolute and relative terms. At a first glance this could be attributed to the use of $FeCl_3$ in tertiary sludges that partially compose Sludge B, which precipitates phosphates as Fe phosphate, increasing the inorganic P fraction. However, although the absolute amount of NAIP is slightly higher in Sludge B, the AIP content is also higher, indicating that more P is present as Ca phosphate complexes.

Thus, adding $FeCl_3$ does not significantly increase NAIP in Sludge B. This may be due to $FeCl_3$ dissociating into Fe^{3+} and Cl^- ions in wastewater, which then quickly hydrolyze to form $Fe(OH)_3$ flocs. The primary suggested mechanism for organic matter removal during coagulation is the adsorption of natural organic matter onto these ferric hydroxide flocs. Fe^{3+} ions neutralize the negative charge of organic particles, allowing them to aggregate

into flocs that can decant. This mechanism would lead to a reduced availability of Fe^{3+} cations to interact with free PO_4^{3-} anions to form Fe phosphates, which would otherwise result in higher NAIP content[166].

These results are strongly consistent with the distributions observed in SS, for which the NAIP fraction is usually the prevalent one[1] (Figure 3.6b).

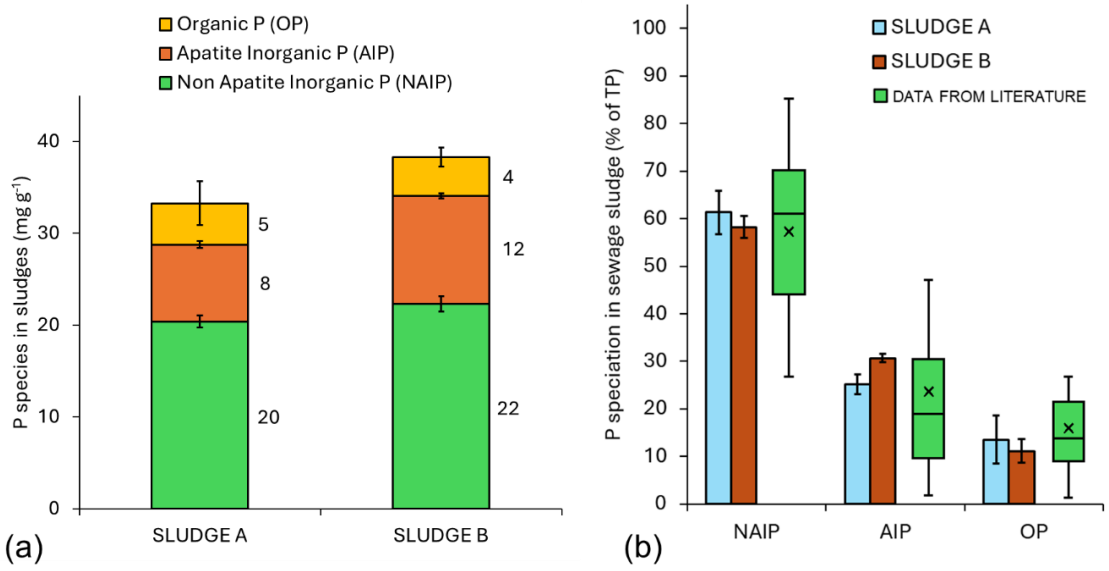

Figure 3.6 - (a) NAIP, AIP and OP absolute contents in Sludge A and B, expressed as mg P g^{-1} of dried sludge. (b) Relative NAIP, AIP and OP amounts as fraction of TP (SMT method)[74]. Error bars represent standard deviation. Box plots represent P speciation distribution in SS form previous studies[10,77–94].

The results of Hedley extraction method, described in Section 2.4.6.2, provide a complementary view of P speciation. SMT method is by far the most widely used for characterizing P speciation in SS and sludge HT products, as it allows to assess the relative amounts of OP and IP and to distinguish IP bound to Ca (apatitic) from IP complexed with Fe and Al (non-apatitic). However, the application of this method to SS and soils may not always provide comprehensive information on the specific nature of P-containing species.

For example, the NAIP fraction is described as NaOH-extractable P and consists of P bound to Al, Fe, and Mn oxides and hydroxides, but since it is the first extraction, it also contains weakly bound P recoverable through simple washing or ion exchange. Therefore, using the SMT method alone does not allow for a precise determination of how much of the extracted P comes from the dissolution of Fe- and Al- phosphates soluble at high pH, and how much is already extractable at neutral or weakly alkaline pH. To enable a more specific analysis in this regard, the Hedley method has been applied. This method is widely used to distinguish different P forms in soil, and to assess their relative "bioavailability" for plants, but it has been recurrently applied to determine P speciation in SS [62,82,106,109,122,124]. The results of Hedley method extraction for both sludges are shown in Figure 3.7.

The first notable result is the difference between Sludge A and Sludge B in terms of soluble and readily available P, corresponding to the P fractions extracted with water and $NaHCO_3$. In Sludge A, the sum of these fractions reaches 45%, whereas in Sludge B, it constitutes only a minor part of the total P, just over 10%. This suggests that in Sludge B, the addition of $FeCl_3$ leads to a more thermodynamically stable form of P. It also indicates that a significant portion of the free phosphates in solution and the easily exchangeable phosphates, weakly adsorbed on oxide/hydroxide surfaces[167], precipitates into more recalcitrant forms.

For Sludge A it is possible to observe a relatively accurate correspondence between the SMT method AIP fraction (25 ± 2% (7) of TP) and the Hedley method HCl-P fraction (21 ± 1% (3) of TP), confirming that more stable forms of Ca-P complexes constitute a minor fraction of TP present in the sludge.

The sum of the Hedley extracts of Sludge A makes up for 31.1 ± 0.6 (3) mg P g^{-1}, which corresponds to 97% of total P obtained with ICP-AES analysis, confirming that most P has been recovered in the five sequential extractions. Res-P obtained in the last step of the method can be partially linked to organic-P together with most recalcitrant inorganic species that HCl 1M could not dissolve. Res-P fraction (1.6 ± 0.1 (3) mg P g^{-1}) is lower than OP fraction obtained in the SMT extraction (5 ± 2 (7) mg P g^{-1}), suggesting that not all organic P species have been mineralized in the final concentered HCl extraction or that some organic P has been lost in previous extraction steps. Becker and Kruse[157] suggested that some organic P species, such as DNA or phosphate esters, could be extracted in the NaOH solution, which would lead to an underestimation of OP fraction in Hedley method, because any organic P species extracted in NaOH fraction would not be detected by the spectrometric method.

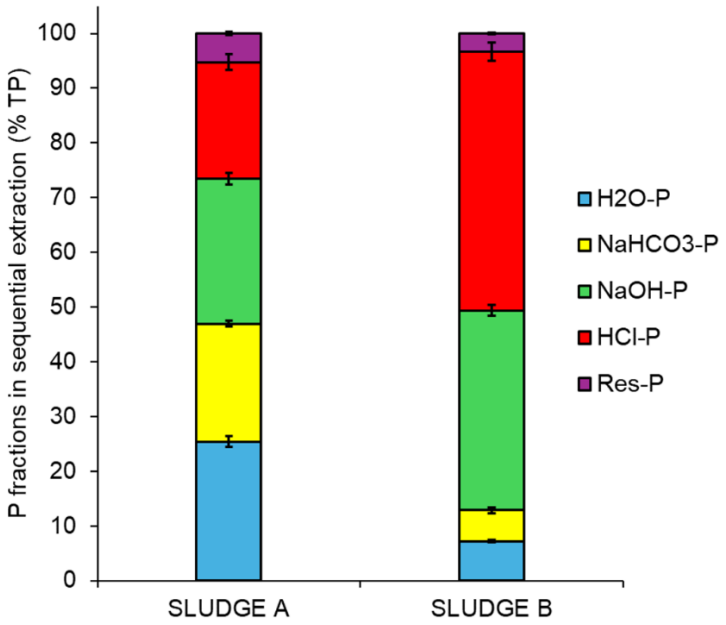

Figure 3.7 - Results of Hedley extraction method[121] for Sludge A and B. Each fraction is expressed as the ratio of the sum of all fractions. Error bars represent standard deviation.

For Sludge B, SMT method NAIP (22.3 ± 0.8 (3) mg P g^{-1}) and P in the sum of Hedley first three extracts (20.5 ± 0.4 (3) mg P g^{-1}) are comparable. However, in relative terms, NAIP (59 ± 2% (3) of TP) is higher than P in H_2O-P + $NaHCO_3$-P + NaOH-P extracts (49 ± 1% (3) of TP) because SMT total P, obtained by calcination and HCl extraction, equal to 38.0 ± 0.5 (6) mg P g^{-1}, is lower than the sum of P in all Hedley extracts (41.5 ± 0.7 (3) mg P g^{-1}). It has previously been observed that multiple-steps extraction methods can lead to an overestimation of TP[157,168]. Ammonium molybdate-ascorbic acid method used to quantify P in each step, can be in fact sensitive to P included in colloids[169], thus measuring an excess of P, higher than soluble P. Besides, the solid residue might retain some of the extraction solution, which can cause an overestimation of both the volume of the extraction solution and the extracted mass of P.

For Sludge B, SMT method AIP (11.8 ± 0.3 (3) mg P g^{-1}) is remarkably lower than the Hedley HCl-P fraction (19.6 ± 0.6 (3) mg P g^{-1}), meaning that a higher amount of P has been extracted in the Hedley extraction. It is necessary to consider that in the SMT extraction, the NAIP fraction is extracted using 1M NaOH, whereas in the Hedley sequential extraction, the solution used is 0.1 M NaOH. It can be assumed that the NaOH solution in the Hedley extraction is not sufficiently alkaline to completely solubilize Fe and Al phosphates. Therefore, the possible undissolved salts may be extracted in the subsequent step, resulting in a higher amount of HCl-P.

Figure 3.8 compares the total P values for both sludges, obtained with four different quantification techniques:

1. SMT method (calcination at 450 °C + extraction with HCl 3.5 + UV-vis spectroscopy)
2. Aqua regia digestion + UV-vis spectroscopy
3. Aqua regia digestion + ICP-AES
4. Sum of all Hedley extraction fractions

There is a certain discrepancy between the various quantification methods. Sludge A TP content ranges from a minimum of 31.1 ± 0.6 (3) mg P g^{-1} of dried sludge to a maximum of 33 ± 2 (3) mg P g^{-1}. Sludge B TP values range from 37.2 ± 0.3 (3) mg P g^{-1}, up to 41.5 ± 0.7 (3) mg P g^{-1}.

Although for Sludge A the differences fall between the standard deviation ranges, the discrepancy between the various values is not negligible and shows how the choice of a technique affects P quantification. It was not possible to observe a specific trend that suggests the superior performance of one method over another. This result indicates that the outcomes of these analyses should be interpreted with caution, and that there are limitations in comparing speciation evaluated with different techniques.

In conclusion, the comparison between the results of the Hedley extraction method mainly shows that the soluble- and easily extractable-P phases in Sludge B are significantly lower than in Sludge A. The discrepancies among the NAIP, AIP, NaOH-P, and HCl-P fractions are due to differences in the extraction solutions used, methodological differences, and discrepancies in the quantification of total P.

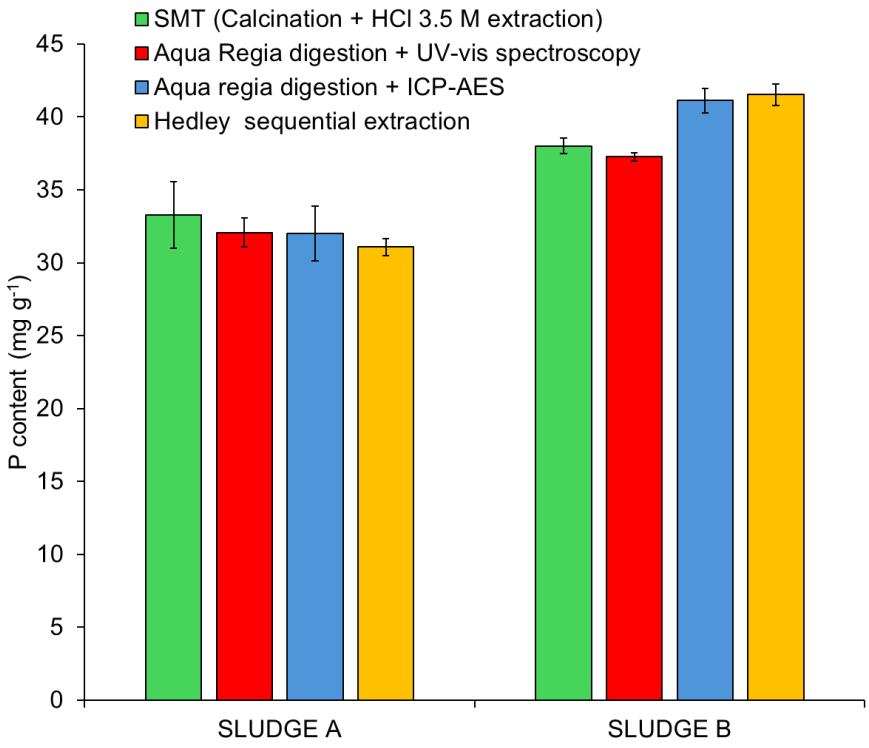

Figure 3.8 - Comparison between the total P values obtained with four different quantification techniques for Sludge A and B expressed as mg P g^{-1} of dried sludge. Error bars represent standard deviation.

3.3.2. Centrates characterization

The main physico-chemical characteristics of the two centrates are resumed in Table 3.2. As shown in Figure 2.1, Centrate A is obtained by dewatering the SS digestate coming directly from the anaerobic digester by centrifugation at 4000 rpm for 20 min. Centrate A appears as a homogeneous, colloidal, and opaque liquid. Centrate B is obtained from the industrial centrifugation of digested sludge mixed with tertiary sludge, and it appears lighter and clearer compared to Centrate A. The characterization of the two centrate samples is necessary as it provides information on the liquid fraction constituting the two sludges used as feed (Sludge A and Sludge B) and characterizes their composition in terms of soluble substances. Both centrates have a relatively low TDS, equal to 0.26 ± 0.01% (3) for Centrate A and 0.16 ± 0.01% (3) for Centrate B. The higher amount relative to Centrate A could be linked to the higher presence of organic matter and colloids in Centrate A compared to Centrate B. In fact, Centrate A offers strong resistance to filtration at 0.45 µm, leading to filter clogging after less than a millimeter of filtrate. A microscopic examination of Centrate A confirmed the presence of organic matter and aggregates with characteristic sizes ranging from tens to several hundreds of µm, as shown in Figure 3.9. The lower TDS rate in Centrate B could be attributed to the effect of the inorganic coagulant and the two polymeric flocculants added during tertiary treatment and centrifugation, leading to organic matter coagulation and precipitation.

Table 3.2 - Main physico-chemical characteristics for Centrate A and Centrate B. Reported values are in the form a ± s (n), where a corresponds to the average of the different measurements, s is the standard deviation, and n is the number of measurements.

	Centrate A	***Centrate B***
TDS (%)	0.26 ± 0.01 (3)	0.16 ± 0.01 (3)
Density (g L^{-1})	1001.913 ± 0.007[a]	1001.379 ± 0.007[a]
pH	8.12 ± 0.04 (6)	8.03 ± 0.01 (6)
Total alkalinity (g $CaCO_3$ L^{-1})	3.71 ± 0.04 (3)	2.75 ± 0.04 (3)
COD (gO_2 L^{-1})	0.39 ± 0.06 (3)	0.27 ± 0.01 (3)
TC (g C L^{-1})	0.87 ± 0.01 (3)	0.770 ± 0.003 (3)
TIC (g C L^{-1})	0.521 ± 0.002 (3)	0.499 ± 0.007 (3)
TOC (g C L^{-1})	0.35 ± 0.01 (3)	0.270 ± 0.008 (3)
TN (g N L^{-1})	1.10 ± 0.03 (3)	1.0 ± 0.2 (3)
NH_3-N (g N L^{-1})	1.00 ± 0.01 (3)	0.72 ± 0.05 (6)
TP (g P L^{-1})	0.34 ± 0.02[a]	0.199 ± 0.007[a]
PO_4-P (g P L^{-1})	0.31 ± 0.01 (3)	0.193 ± 0.003 (3)
Ca (mg L^{-1})	42 ± 2[a]	44.3 ± 0.7 [a]
Fe (mg L^{-1})	1.47 ± 0.04[a]	1.85 ± 0.08 [a]
Al (mg L^{-1})	< 0.06	< 0.06
Mg (mg L^{-1})	3.7 ± 0.2[a]	2.9 ± 0.1 [a]
K (g L^{-1})	0.26 ± 0.02[a]	0.21 ± 0.03 [a]

[a]Propagated uncertainty, calculated according to Equation 2.30

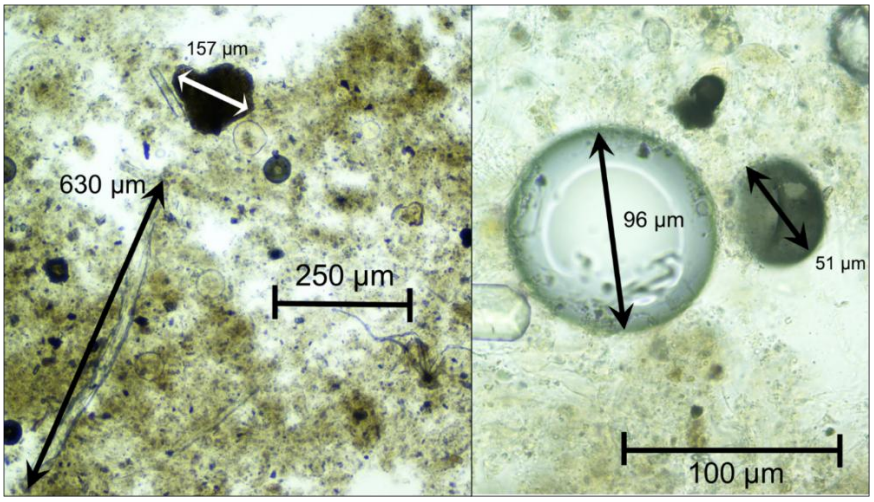

Figure 3.9 - Microscopic examination of Centrate A.

The pH range of a digestate may vary based on the biomass type fed into the anaerobic digester and the thermal, chemical, or biological processes it undergoes, as well as any additives used for improved dewatering. Centrate A and B are characterized by almost the same pH, respectively 8.12 ±0.04 (6) and 8.03 ±0.01 (6). The slightly lower pH of Sludge B could be linked to the $FeCl_3$ addition in the tertiary treatment tank, due to OH^- consumption by ferric ions[170]. The pH values of both centrates align with typical ranges reported in previous works[11].

Total alkalinity is influenced by both upstream processes and biomass origin. However, it is also connected to the quality and inherent characteristics of water entering the municipal water treatment station. Centrate A has a total alkalinity of 3.71 ± 0.04 (3) g L^{-1} $CaCO_3$, while Centrate B presents a lower value at 2.75 ± 0.04 (3) g L^{-1} $CaCO_3$. These values are higher than values generally associated with primary and secondary sludges, generally between 0.5 and 1.5 g L^{-1} $CaCO_3$[11,171] but are in line with observed values for digested sludge, between 2.5 and 3.5 g L^{-1} $CaCO_3$[11]. Increased alkalinity in an anaerobic digestion process is expected and linked to methanogenic bacteria activity which produce ammonia, carbon dioxide and bicarbonate[172]. The alkalinity of an optimized AD process ranges from 1 to 5 g L^{-1} $CaCO_3$[172]. Therefore, the value of Centrate A, which represents the sludge downstream of the digester, is perfectly consistent with a functional process. As for Centrate B, the reduced value could be attributed to the fact that Sludge B is obtained by mixing the digestate with the sludge from the tertiary treatment, which may have a lower alkalinity. Besides, addition of $FeCl_3$ may also have acidified the medium and consumed some alkalinity, leading to a lower value for Centrate B. Nevertheless, AD alkalinity can vary significantly with changes in several factors, including the quantity of solids loaded into the digester[14]. Therefore, the different Centrate B value could also be related to variations in certain conditions within the digester between the two digestate collections (March 2022 and May 2023).

COD content is respectively 0.39 ± 0.06 (3) g O_2 L^{-1} in Centrate A, and 0.27 ± 0.01 (3) g O_2 L^{-1} in Centrate B. The lower COD value in Centrate B could be due to the decrease in organic matter content as fine colloids, following the coagulation-flocculation process in the tertiary treatment, which can constitute an important fraction of total COD[173]. These results are consistent with TOC analysis results, which show a TC content of 0.87 ± 0.01 (3) g L^{-1} for Centrate A, and 0.770 ± 0.001 (3) for Centrate B. Centrate B has also lower TOC and TIC contents compared to Centrate A. However, if the TIC decreases by only 4% between one centrate and the other, the difference in TOC is 23%, confirming the hypothesis that Centrate B is characterized by a lower amount of organic matter.

TN concentrations in Centrate A and B are comparable around 1 g L^{-1}. Both TN values are in line with previously observed values for digestate liquid fraction[174]. Most of soluble N is found as NH_4-N (1.00 ± 0.01 (3) g L^{-1} in Centrate A, which corresponds to 91% of TN, and 0.72 ± 0.05 (6) g L^{-1} in Centrate B, which corresponds to 72% of TN). For both centrates ammonium-N constitute the main N source, as it was previously observed for digestate liquid fraction[173,175]. However, Centrate A contains more ammonium than Centrate B. This could be related to the AD process, in which NH_4-N concentration increases[176] due to N-organic species degradation[177]. Centrate A is directly produced from the digestate collected downstream of the digester, while Centrate B is obtained from a mix of digested Sludge and non-digested sludge which could contain a lower NH_4-N concentration.

A significant fraction of P in SS (22%-45%) ends-up in liquid fraction (centrate) after solid-liquid separation (centrifugation)[178]. Centrate A contains nearly 340 ± 20 mg L^{-1} of soluble P (Figure 3.10), while Centrate B presents a lower soluble P concentration, at

199 ± 7 mg L^{-1}. In both cases soluble P is present almost exclusively in the form of PO_4-P (Table 3.2).

K, Ca, Mg and Fe are present in a solubilized form in Centrate A respectively with 260 ± 20 mg L^{-1}, 42 ± 2 mg L^{-1}, 3.7 ± 0.2 mg L^{-1} and 1.47 ± 0.04 mg L^{-1} (Figure 3.10). Centrate B presents a slightly higher content of Ca, 44.3 ± 0.7 mg L^{-1}, higher Fe concentration at 1.85 ± 0.08 mg L^{-1}, and lower Mg and K contents, respectively at 2.9 ± 0.1 mg L^{-1} and 210 ± 30 mg L^{-1}. The lower soluble P and the higher soluble Fe concentrations in Centrate B compared to Centrate A can be easily explained by considering the $FeCl_3$-assisted coagulation realized to produce the tertiary sludges that partially compose Sludge B which promote phosphates precipitation. Differences in Ca, Mg and K concentration could be due to season fluctuations and are in line with the observed contents in the respective sludges. A higher amount of dissolved Ca^{2+} could have promoted Ca precipitation, thus increasing Ca content in the sludge.

Ca/P molar ratio in Centrate A and in Centrate B is respectively 0.09 ± 0.01 and 0.17 ± 0.01. The higher Ca/P ratio in Centrate B is directly related to the lower P concentration and the slightly higher Ca concentration. Fe/P molar ratios are remarkably lower at 0.0024 ± 0.0002 for Sludge A, and 0.0052 ± 0.0004 for Sludge B.

N/P, Mg/P and K/P molar ratios in Centrate A are respectively 7.2 ± 0.7, 0.014 ± 0.002 and 0.69 ± 0.09, while in Centrate B they are 11 ± 1, 0.019 ± 0.001 and 0.8 ± 0.1. Therefore, these effluents are not favorable candidates for nutrient recovery through struvite ($NH_4MgPO_4 \cdot 6\ H_2O$) precipitation. The process would require the addition of Mg to fully recover P, but it would hinder the retrieval of a significant portion of N. Alternatively, the K-struvite ($KMgPO_4 \cdot 6\ H_2O$) option would demand K integration to complete P recovery.

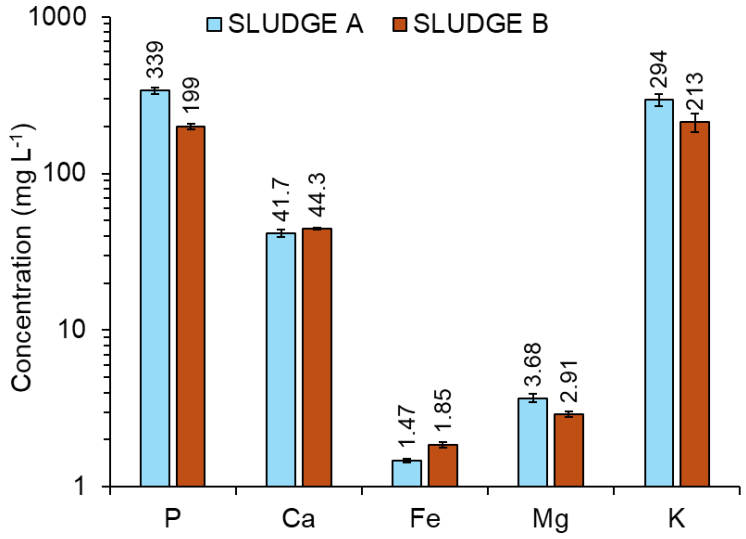

Figure 3.10 - P, Ca, Fe, Mg and K concentration in Centrate A and B. Error bars represent propagated uncertainty.

3.4. Environmental compatibility

The application of sludge in agriculture within the European Union (EU) is presently regulated solely by the heavy metal limits (Cd, Cu, Hg, Ni, Pb, and Zn) established in Council Directive 86/278/EEC[179] and the relative national transpositions of the directive. Table 3.3 shows the 86/278/EEC directive limits and the limits prescribed by the French legislation[180], together with the relative values measured for both Sludge A and Sludge B. Both sludges are compatible with prescribed limits, implying a possible utilization in agriculture by spreading them on the soil.

Table 3.3 - European[179] and French national[180] limits for heavy metals in sludge in the perspective of an agricultural application, compared to Sludge A and B actual values (on a dry basis).

	Heavy metals limits in sludges (mg kg^{-1})		Measured values (mg kg^{-1})	
	86/278/EEC	**Arrêté 08/01/1998**	**Sludge A**	**Sludge B**
Cd	20-40	20	0.96	0.85
Cu	1000-1750	1000	435	399
Ni	300-400	200	17.7	19
Pb	750-1200	800	25.5	50.6
Zn	2500-4000	3000	570	651
Hg	16-25	10	0.15	0.1
Cr	-	1000	25	25
Cr+Cu+Ni+Zn	-	4000	1048	1094

Another evaluation of the environmental compatibility of these sludges could be made by assessing their properties for potential use as organic fertilizers by comparing these properties with the 2019/1009 regulation on the market of EU fertilizing products and amending regulations[181].

Table 3.4 shows the macronutrients and organic carbon contents guidelines, and the heavy metals limits prescribed by the regulation, and the respective values for both Sludge A and B. It is evident that both sludges meet the guidelines for minimum macronutrients and organic carbon values.

Regarding heavy metals, both sludges meet all the limits suggested by the regulation, except for Cu. For the exploitation of the sludges as commercial organic fertilizers, it is necessary to reduce the amount of Cu in the sludges. Exceeding Cu content could be reduced by an upstream approach, limiting its dispersion into the environment in the first place. Besides, further investigations must be conducted to ensure that these two products are compatible for fertilizer use according to this regulation guidelines, specifically to assess biuret ($C_2H_5N_3O_2$), perchlorate (ClO^{4-}), hexavalent chromium (Cr VI), and pathogens (*Salmonella*, *Escherichia Coli*) contents.

Concerning Centrate A and B, both products are not compatible with discharge into the environment due to their high COD concentration, which is 390 ± 60 (3) mg O_2 L^{-1} for Centrate A and 270 ± 10 (3) mg O_2 L^{-1} for Centrate B, exceeding the limit prescribed by the European Council Directive of May 21, 1991[182], which is 125 mg L^{-1}. Furthermore,

the concentration of TP and TN is likely incompatible with direct discharge into the environment, as it could lead to eutrophication phenomena. The European Directive prescribes limit values for P and N only in the case of discharge into eutrophication-sensitive areas; these values are two orders of magnitude lower than those of our centrates. Therefore, additional treatments must be realized before releasing these centrates into the environment. Possible solutions could include recirculation in the anaerobic digester[183], wet oxidation[184], and, in order to reduce P and N contents, precipitation in the form of Ca phosphate and/or struvite[185].

Table 3.4 - Comparison between the macronutrients and organic carbon contents guidelines and the heavy metals limits prescribed by the 2019/1009 regulation[181], and the respective values for both Sludge A and B. X = it does not respect the guidelines. ✓ = it respects the guidelines.

		Guidelines	Sludge A (dry)		Sludge B (dry)	
		*minimum value %**	Composition %	Compatibility	Composition %	Compatibility
Macronutrients	N		6.4		6.3	
	P_2O_5		7.3		9.4	
	K_2O		0.8		0.3	
	Sum	4	14.6	✓	16	✓
Organic Carbon	C_{org}	15	43.3	✓	42.1	✓
Contaminants		*limit mg kg^{-1}**	Composition mg kg^{-1}	Compatibility	Composition mg kg^{-1}	Compatibility
	Cd	1.5	0.96	✓	0.85	✓
	Hg	1	0.15	✓	0.10	✓
	Ni	50	17.7	✓	19.0	✓
	Pb	120	25.5	✓	50.6	✓
	As	40	3.36	✓	2.95	✓
	Cu	300	440	X	390	X
	Zn	800	570	✓	650	✓

*guidelines and limits from [181]. P_2O_5 = P/0.436; K_2O = K/0.830; C_{org} = 0.56 · Organic Matter according to the regulation guidelines. Organic Matter (%DM) calculated as 100% - ash%.

3.5. Conclusion

In this chapter, a comprehensive characterization of the two sludges (Sludge A and Sludge B) and their respective centrates (Centrate A and Centrate B) is proposed. The goal was to provide a thorough understanding of both the solid and soluble species constituting the sludges. We focused on general physical properties, elemental composition, and more specifically P speciation, using two complementary extraction techniques to better understand the nature and bioavailability of P species in the two sludges. All the results were compared with the general properties of SS presented in Chapter 1.

By comparing the results of Sludge A and Sludge B, we identified the impact of different WWTP on the feeds. For instance, Sludge B contains a tertiary sludge rich in Fe, which significantly affects P speciation.

Additionally, the environmental compatibility of these feeds has been evaluated regarding their potential disposal through spreading in agricultural fields and their use as organic fertilizers. This evaluation included an assessment of their macronutrient, organic carbon, and heavy metal content, comparing these parameters with relevant European directives.

In conclusion, this chapter has provided a detailed foundation for understanding the digestate feeds used in our study. By thoroughly characterizing these feeds, we have laid the groundwork for interpreting the HT treatment results in the next three chapters.

4. Effect of temperature and treatment duration on by-products characteristics and phosphorus speciation

4.1. Introduction

The analysis of the literature that investigates P speciation during HT treatment of SS (Chapter 1) assesses that between the various influencing parameters, temperature and treatment duration were the most investigated. Consequently, the effect of these two parameters on the distribution and physicochemical properties of the by-products is deeply studied in this work, as well as their elemental composition, and more specifically, P conversion and speciation.

As explained in Section 1.5.2, nearly 80% of the studies available in the literature regarding the HT treatment of SS are conducted at temperatures below 280 °C, corresponding to HTC. Few studies provide information on the characteristics of the products under more severe conditions associated with HTL and HTG. For this reason, the investigations will be conducted within a temperature range from 250 °C to 350 °C.

250 °C is a temperature still associated with HTC, and evaluating the difference between the products obtained at this temperature and those resulting from more severe conditions will provide more detailed information regarding the transition between HTC and HTL. The maximum temperature value, 350 °C, was chosen to remain in sub-critical condition; besides, it corresponds to the operating limit temperature of the batch reactor used (Section 2.2.1).

As for the duration of the treatment, HTL generally has a relatively short residence time: from a few minutes to several tens of minutes. Initially, in some preliminary experiments, a range from 10 to 30 min has been selected, typical durations of HTL, but no substantial differences were observed, so the experimental investigation has been extended from 5 up to 45 min.

The feed selected for this first series of experiments is Sludge A. As explained in Section 2.1.1 this sludge is collected directly downstream of the anaerobic digester and thickened in the laboratory through centrifugation. We decided to focus only on this feed for this first experimental series to investigate specifically the effect of temperature and time, excluding the possible effect of additives, such as $FeCl_3$ and organic flocculants present in Sludge B. A specific analysis of the effects that the type of sludge used has on the characteristics of the products will be specifically addressed in the investigation discussed in Chapter 5.

This chapter begins with an overview of the by-products' distribution and mass balance, followed by an analysis of the process water and solid pellet by-products properties in relation to temperature and treatment duration, and as a function of process severity f(T,t). Special attention will be given to P, examining its distribution in the two by-products, its speciation in the solid pellet, and the mechanisms that regulate its conversion. Finally, in the last section, the thermal profile of the HT treatment will be discussed, along with some energy considerations.

4.2. Materials and methods

The HT treatment experiments have been realized by introducing 110 g of Sludge A in the 0.2 L batch reactor described in Section 2.2.1. The choice of this mass is a compromise, as lower masses did not allow obtaining enough solid product to perform all the planned analyses, while higher masses resulted in having too little headspace. 110 g corresponds to filling about 70% of the reactor available volume. All experiences have been realized with a N_2 pressure of 18 MPa in correspondence of the operative temperature, and with a mixing rate of 700 rpm.

The results presented in this work concerning “process water” and “solid pellet” refer to the by-products separated mechanically by centrifugation as explained in Section 2.2.3. without any extraction of the organic phase. "Process water” appears as a macroscopically single-phase aqueous liquid, and no separation of an oily phase occurs after mechanical separation. Therefore, although most of the organic phase is recovered in the solid pellet, it is important to emphasize that both by-products contain an organic phase. The separation and quantification of the organic phase were not performed in this phase due to the limited quantities of by-products.

The process water by-products have been analyzed according to methods and techniques described in Section 2.3, characterizing their main physical properties, alkalinity, solid content, soluble N and PO_4-P concentration, dissolved C, COD, and metal contents. The solid pellet by-products were characterized as described in Section 2.4, quantifying its elemental composition, organic profile, metal and heavy metal content, and P speciation. Finally, the HT treatment energetic profile has been investigated by Differential Scanning Calorimetry, as explained in Section 2.5. The HT severity factor (Section 2.6.3) has been used to better understand the synergistic impacts of temperature and reaction time and to easily compare the values with the results from available literature (Chapter 1).

The statistical analysis of the results was carried out following the methods described in Section 2.6.1 (ANOVA table and Student's t-test) with the experimental design described in Section 2.6.1.1. Error bars in this chapter’s figures represent the propagated uncertainty in measurements calculated with Equation 2.30. Experimental results reported in the discussion are accompanied by the respective propagated uncertainty. Proximate, pH, alkalinity, TN, NH_4-N, COD, TC, TIC, TOC, PO_4-P analysis and P sequential extractions were performed in triplicates. All reported results correspond to the weighted

average of duplicates. For each set of analyses, limit of detection and limit of quantification were determined by analysis of blanks. All chemicals used were of analytical grade.

4.3. Mass balances and by-products distribution

Figure 4.1 shows the global mass distributions as a function of process severity.

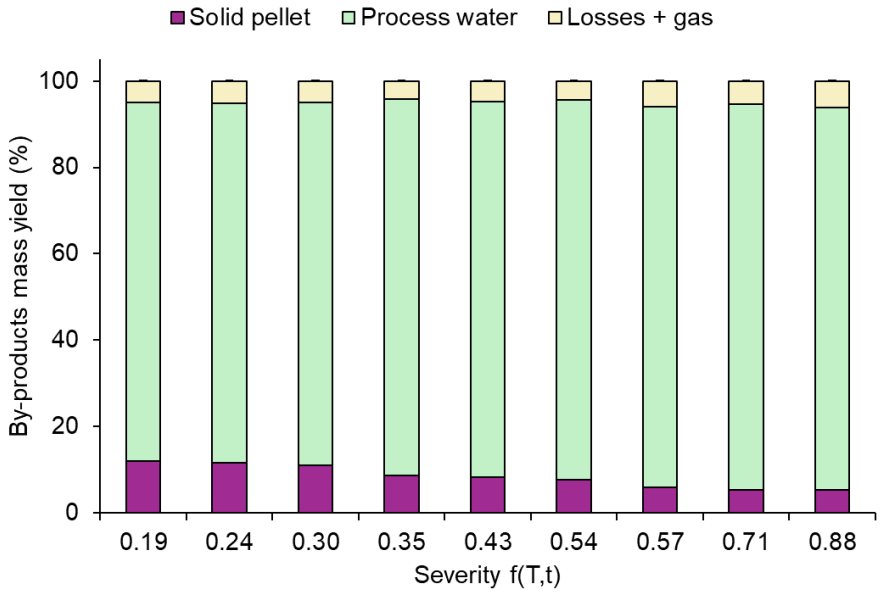

Figure 4.1 - Global mass yield as a function of severity f(T,t): Error bars representing propagated uncertainty.

Global mass losses constitute between 3% and 7% of the mass fed to the reactor. Mass losses could be linked to gas production and to small amounts of unrecoverable product remaining on the reactor walls and internal components.

An increase in process severity is associated with a reduction in the solid pellet and an increase in process water (Figure 4.1). This phenomenon is likely due to the degradation of biopolymers and organic matter, the solubilization of their fragments, and the dissolution of the inorganic salts in Sludge A. Figures 4.2a and 4.2b present the evolution of respectively the solid pellet dry weight and total dissolved solids (TDS) in process water, showing a clear trend with process severity. A more severe process leads to a reduction of TDS in process water (from 2.31 ± 0.03% down to 0.45 ± 0.03%) and to an increase of the solid pellet dry weight (from 25.5 ± 0.1% up to 41.9 ± 0.3%). Therefore, an increase in process severity leads to a better by-products separation which could be linked to colloids degradation and dissolved compounds precipitation in the solid by-product, but also to an increase in the organic species hydrophobicity.

Figure 4.2c shows a clear TSRY% reduction with increasing process severity, dropping from 77.4 ± 0.4% down to 41.0 ± 0.5% at most severe conditions. The reduction of TSRY%

with increasing process severity has been comprehensively described in previous works[81], confirming that a higher f(T,t) (> 0.5) is generally associated with low SRY (< 55%)[1].

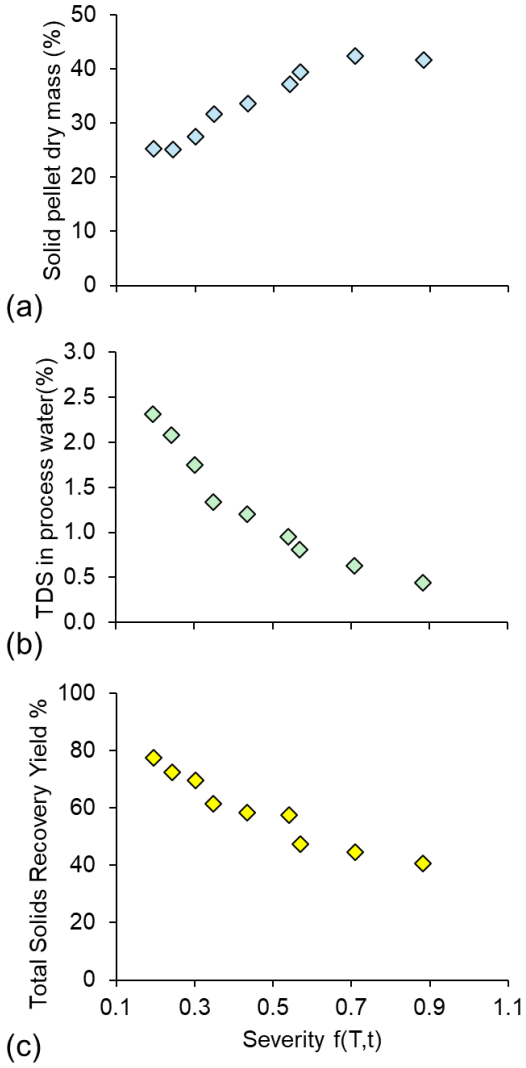

Figure 4.2 - (a) Solid pellet by-product dry mass (%) (b) Process water TDS (c) Total Solids Recovery Yield (as defined by Equation 2.8) evolutions as a function of HT severity f(T,t).

Figure 4.3 shows the mass balances for C, N, P, Ca, Fe, Mg and K, indicating the relative distribution of these elements in each of the two by-products, as well as the losses.

For C (Figure 4.3a) both mass yield in solid pellets and C recovered in process water decrease with increasing process severity, suggesting that an increasing amount of C is lost in the gas product as CO_2[11]. Besides, a certain amount of C is surely lost in the unrecoverable residue remaining at the reactor bottom and components.

N mass distribution (Figure 4.3b) shows that most N is recovered in the liquid product, as expected[186]. N relative amount in solid pellets decreases with increasing process severity, while N in process water increases, confirming that HT treatment enhances protein hydrolysis and the mineralization of amino acids fragments into soluble ammonia[81]. Curiously, the sum of N measured in the products is 10-20% higher than N measured in feed. This discrepancy is likely due to the relatively high experimental error

associated with measuring TN in the process water, which may have resulted in an overestimation.

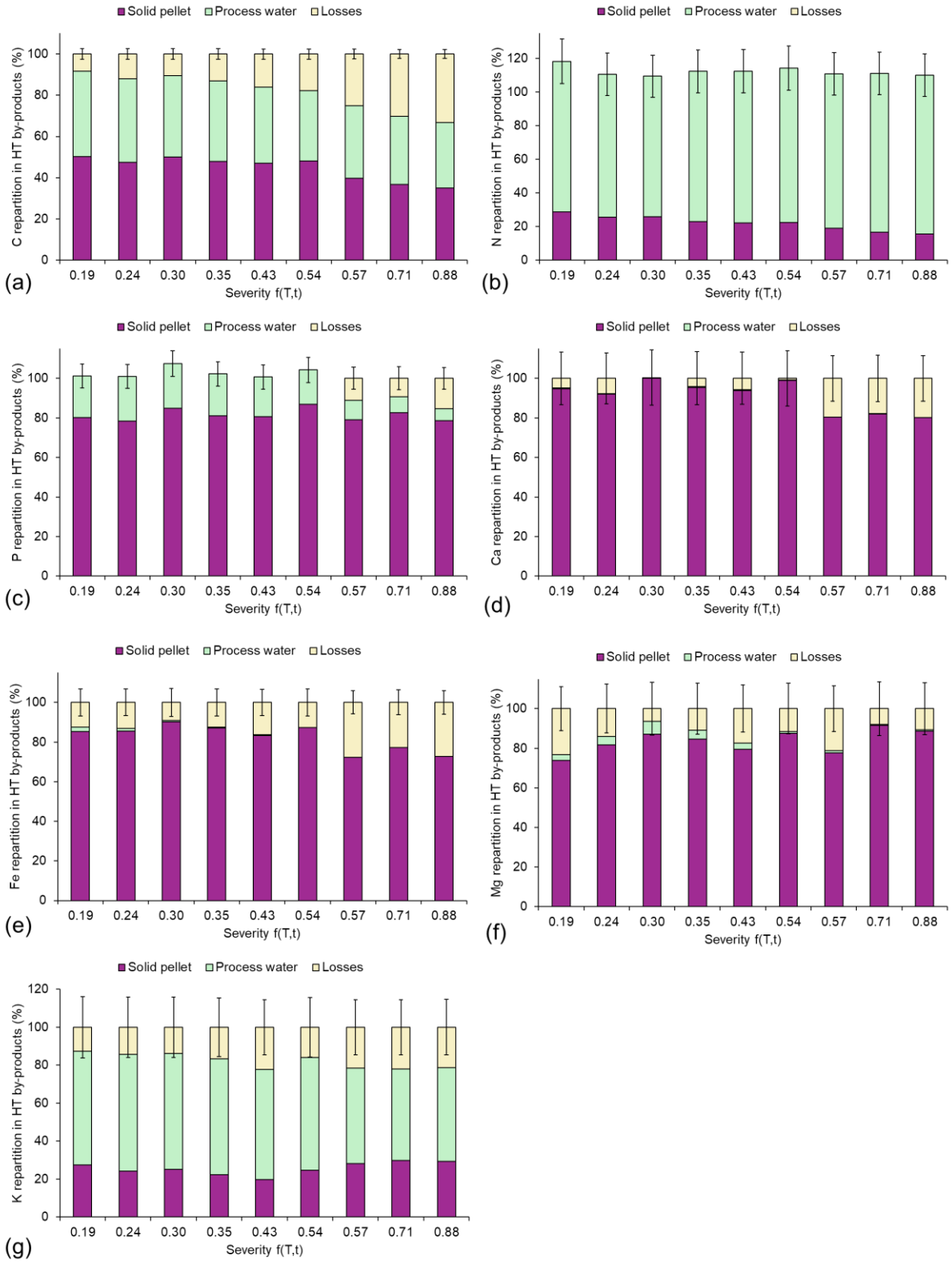

Figure 4.3 - Mass distribution in HT treatment by-product for carbon (a), nitrogen (b), phosphorus (c), calcium (d), iron (e), magnesium (f) and potassium (g). Error bars represent propagated uncertainty.

P distribution in by-products is shown in Figure 4.3c. P is mainly recovered in the solid product. Increasing process severity leads to a decrease in P yield in process water, particularly at 350 °C. However, this decrease is not accompanied by a corresponding increase in the solid pellet yield. Since P does not form gaseous species under these conditions[5,49], P losses must necessarily be attributed to the unrecovered solid product (residue left in the reactor) or to P that could not be effectively extracted using the aqua regia digestion method (Section 2.4.3).

Figures 4.3d and 4.3e respectively show Ca and Fe by products distribution. In both cases, the majority of Ca and Fe are recovered in the solid phase, with negligible fractions found in process water. Substantial losses occur, particularly at treatments conducted at 350 °C (process severity from 0.57 to 0.88). The distribution of Mg in the two by-products is shown in Figure 4.3f. Again, most of Mg is recovered in the solid phase, but a significant fraction is present in the process water under less severe conditions. There are substantial losses observed as well (up to 25%). Finally, Figure 4.3g illustrates K distribution in the two by-products. In this case, the majority of K is recovered in the liquid phase, consistent with findings from previous studies[187].

Table 4.1 presents part of the results from the screening analysis, providing a qualitative indication of the effect that the two factors (temperature and time) have on various parameters related to by-products distribution and mass balance.

Table 4.1 - Screening analysis results on by products distribution and mass balances based on the experimental design reported in Table 2.1. Statistical validation is reported in Table D.20 (Annex D). Positive effects are expressed through one or two positive signs (+), negative effects through one or two negative signs (-). Effects are indicated with a double sign if the effect is three times more significant than the smallest significant effect. The absence of symbols indicates that the effect is not significant.

Factor	**Temperature (°C)**			**Time (min)**		
from:	250	250	300	5	5	15
to:	300	350	350	15	45	45
Losses + gas		+	+			
Process water by-product (% total product)	++	++	++		+	
Solid pellet by-product (% total product)	- -	- -	- -		-	
Process water TDS (%)	- -	- -	-	-	-	-
Solid pellet by-product dry mass (%)	+	++	+		+	
TSRY (%)	- -	- -	- -	-	-	
C losses (% feed C)	+	++	++	+	+	
P losses (% feed P)		+	+			
Ca losses (% feed Ca)		+	+			
Fe losses (% feed Fe)		+	+			
K losses (% feed K)	+	+				

Temperature has a significant positive effect on the mass discrepancy between feed and recovered product (solid + liquid), specifically at 350 °C. A temperature increase has been associated to higher gas production[11], and a sharp increase in the gas yield during SS HT treatments has been specifically observed between 300 and 350 °C[188].This could be linked to the increased mass difference.

Higher temperature significantly enhances the amount of process water while reducing the amount of solid pellet. Similarly, longer treatment duration also positively affects process water amount, particularly when extended from 5 to 45 min, though this effect is less pronounced compared to that of temperature.

Both temperature and time have a significant negative effect on process water TDS, but temperature effect is prevalent: a temperature increase from 250 to 350 °C has an effect more than three times higher than an extension of the treatment duration from 5 to 45 min. Temperature exerts a significant positive influence on the solid pellet dry mass, prevailing over the time effect, which only becomes significant when extending the treatment from 5 to 45 min. Both temperature and time have a significant negative effect on TSRY%. The effect is particularly strong when passing from 250 to 350 °C. Table D.1 (Annex D) reports the ANOVA validation tool for the surface response second-degree polynomial model based on the TSRY% results. The second-degree polynomial model provided by the surface response is statistically significant, with a p-value less than 0.01% and an R^2 of 0.97. The model standard deviation is equal to 2.5%. Table D.2 reports the second-degree model coefficients of the surface response for TSRY%, with respective statistical validation. The coefficients for the linear effects of temperature (b_1) and time (b_2) are statistically significant, whereas the quadratic terms and the interaction term between the two factors are not. The linear coefficient for temperature is more than four times higher than the coefficient for the linear effect of time, suggesting a predominant effect of temperature over time. Equation 4.1 shows the corresponding second-degree polynomial model obtained for TSRY%:

$$\boldsymbol{TSRY}\% = \mathbf{56.54} - \mathbf{14.43}\boldsymbol{T} - \mathbf{3.11}\boldsymbol{t} - 0.44T^2 + 2.80t^2 + 0.11T \cdot t \qquad (4.1)$$

Where T and t are respectively temperature and treatment duration expressed as normalized values according to Equations 2.26 and 2.27. Statistically significant terms are in bold. The obtained surface response is visualized in Figure 4.4.

Previous works have already observed that an increase in temperature leads to TSRY% reduction: higher temperatures enhance the dissolution and degradation of organic matter through the solubilization of inorganic material and biopolymers[39,91], resulting from dehydration and decarboxylation reactions[80,81,97–99]. Although treatment duration also influences the decrease in TSRY%[71,81,82], this effect is less pronounced compared to that of temperature, as previously observed by Funke and Ziegler [65], confirming our model results. As shown in Table 4.1, a strong correlation exists between temperature and duration increase and C losses, further confirming that more severe treatments lead to higher CO_2 production.

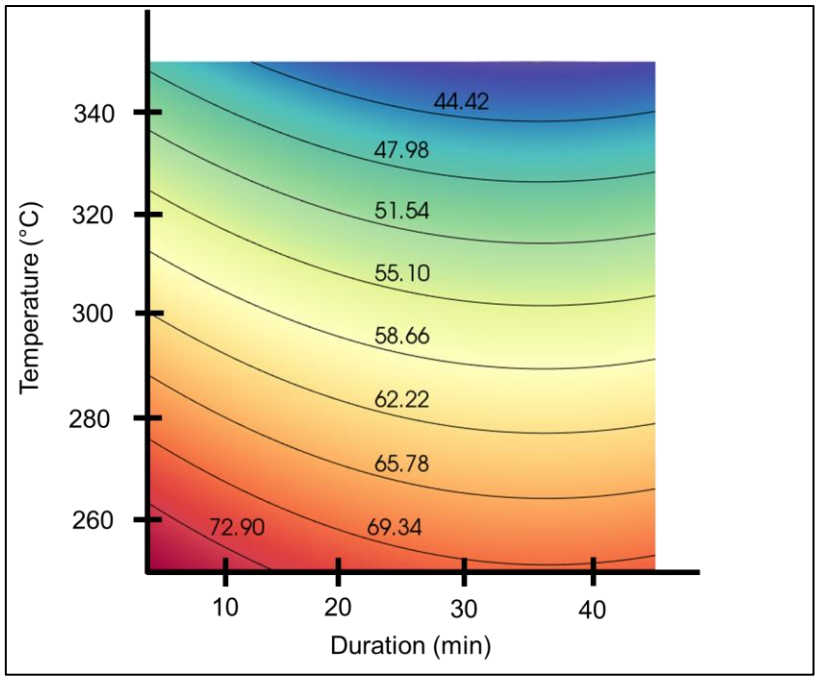

Figure 4.4 - Second-degree polynomial surface response for TSRY% based on the experimental design reported in Table 2.1, as a function of temperature (°C) and treatment duration (min) as expressed by Equation 4.1.

Regarding other elements, there is a significant correlation between losses of P, Ca, Fe, and K and temperature, particularly when passing from 300 to 350 °C. An initial hypothesis is linked to the unrecoverable solid residue left in the reactor. An alternative explanation could be related to the effectiveness of the extraction method used to prepare samples analyzed by ICP-AES for elemental quantification (aqua regia extraction). Higher temperatures may result in the formation of refractory and recalcitrant solid compounds that aqua regia is unable to fully extract or extracts less effectively, such as silicates or crystalline Fe[145,146]. This method is primarily designed for heavy metal extraction and may have limitations when applied to other elements. No significant correlation has been observed between P, Ca, Fe and K losses and treatment duration.

4.4. Process water characterization

Process severity does not have a significant effect on the filtered process water density, which is roughly constant and equal to 1008.2 ± 0.5 g L^{-1}. Figure 4.5 shows the evolution of pH and total alkalinity of the HT process water with increasing process severity. Both pH and alkalinity increase with increasing process severity. Following the least severe HT treatment, 250 °C, 5 min (severity = 0.19), process water shifts towards a more neutral pH (7.52 ± 0.02) compared to Centrate A pH (8.12 ± 0.01). This could be explained by considering the release of organic acids following carbohydrates breakdown[62]. In fact, the ^{13}C solid-state NMR results described in Section 4.5.2, show that at 250 °C carbohydrate hydrolysis is already observed. For longer treatment durations, process water pH increases: 7.82 ± 0.02 for the 250 °C, 45 min treatment (severity = 0.30), and for

higher temperature treatments it levels off at approximately 8.0. An interpretation of the observed pH evolution is provided in the next two sections.

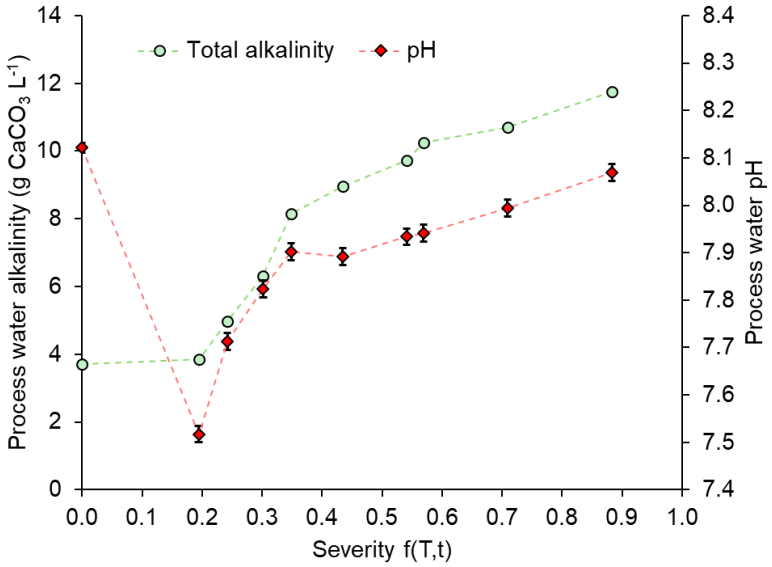

Figure 4.5 - Process water pH and total alkalinity evolutions as a function of HT severity f(T,t). Error bars represent propagated uncertainty. Dashed lines are included to help data interpretation.

4.4.1. Soluble nitrogen

In Figure 4.6, the concentration of NH_4-N in process water is shown alongside its relative proportion with TN. TN in process water exhibits no discernible trend, consistently maintaining an approximate value of 4.5 ± 0.2 g L^{-1}, irrespective of process severity. This value is more than 4 times compared to Centrate A concentration (1.1 g L^{-1}).

NH_4-N concentration in process water rises with increasing process severity, passing from 1.23 ± 0.07 g L^{-1} at 250 °C, 5 min (severity = 0.19) up to 2.8 ± 0.2 g L^{-1} at 350 °C, 45 min (severity = 0.88), indicating that a more severe HT treatment enhances organic N mineralization into ammonium. Previous works have already observed that a temperature increase leads to the recovery of soluble N mainly in process water, and primarily in the ammonium form[186]. A temperature increase has been correlated with protein and pyridine-N compounds hydrolysis and deamination, leading to the release of inorganic N (NH_4-N)[189].

The concentration of non-ammoniacal soluble N in process water, mainly composed of soluble organic N compounds (Org-N), decreases with increasing process severity, from 3.4 ± 0.4 g L^{-1} (73 ± 3% of TN) at 250 °C, 5 min (severity = 0.19), to 1.8 ± 0.4 g L^{-1} (39 ± 7% of TN) at 350 °C, 45 min (severity = 0.88). These values are significantly higher than the non-ammoniacal N in Centrate A, around 0.1 g L^{-1} (less than 10% of TN). This shift is linked to the rapid degradation of protein compounds that constitute the solid phase into soluble Org-N, which occurs at relatively low temperatures (150 °C)[81], leading to the release of soluble organic N in process water. The ^{13}C solid-state NMR results reported in

Section 4.5.2 show that the HT treatments lead to the disappearance of a peak at 54.9 ppm previously detected in Sludge A. This peak possibly corresponds to a CH-N group characteristic of certain proteins[151]. The HT treatment also leads to the rapid reduction of a peak at 173.3 ppm, which is related to carboxylic C often part of the amide group in peptide bonds[155,190]. The reduction of these two peaks is consistent with the suggested mechanism of protein hydrolysis and deamination.

Interestingly, the fact that total soluble N remains relatively constant above 250 °C suggests that the process of breaking down solid protein compounds into soluble N is complete at temperatures below 250 °C. Then, at temperatures above 250 °C, further degradation of soluble Org-N occurs, leading to a decrease in its concentration and an increase in NH_4-N concentration. These conclusions have been previously reported in various studies[81,191,192]. The proposed mechanism is further supported by N content in the solid pellet by-product, which decreases with increasing process severity (Section 4.5.1).

Higher amounts of ammonium in solution provide a buffer effect that counteract process water acidification following the organic acids release, which could explain the pH increase (Figure 4.5). The pH evolution of process water suggests that at 250 °C, for short durations, the hydrolysis of carbohydrates and the release of organic acids into solution are prominent, leading to the reaction medium acidification (Figure 4.5). Meanwhile, for longer durations and higher temperatures, the hydrolysis of proteins into ammonium counterbalances the effect of acids, resulting in an increase in pH[81].

pH, total soluble N and NH_4-N concentrations observed for HT process water are in line with the ranges associated with digestate HT aqueous products reported in literature[11].

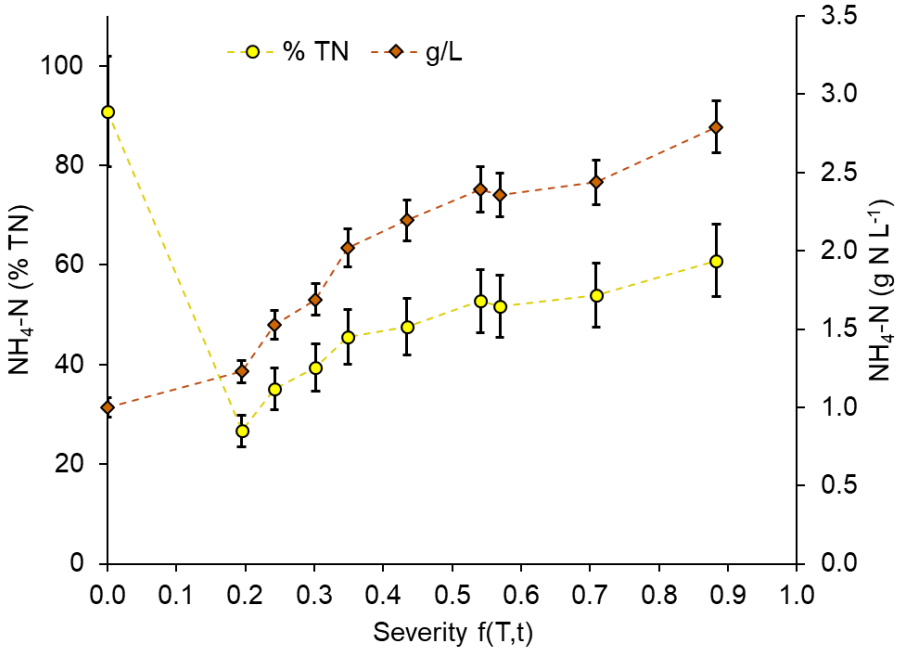

Figure 4.6 - Concentration of ammonium N (NH_4-N) in process water (g L^{-1}) and its relative proportion in relation to total soluble N. Error bars represent propagated uncertainty. Dashed lines are included to help data interpretation.

4.4.2. Soluble carbon

As shown in Figure 4.7a, process water shows high COD concentration (from 19 ± 1 g L^{-1} up to 31 ± 1 g L^{-1}) compared to Centrate A (0.39 ± 0.06 g L^{-1}). Indeed, COD in aqueous by-products has a concentration of two orders of magnitude higher than a typical wastewater treatment influent[193]. A more severe treatment leads to a COD content reduction (Figure 4.7a). Figure 4.7b shows TIC and TOC concentrations (g L^{-1}) in process water. The water phase after HT process shows relatively high TC content compared to digestate feed liquid fraction[11]. The HT treatment leads to biopolymers hydrolysis and the release of soluble organic fragments[54], contributing to the TOC and COD increase.

A process severity increase leads to a TC decrease: 12.4 ± 0.4 g L^{-1} for 250 °C, 5 min (severity = 0.19) against 9.0 ± 0.3 g L^{-1} for 350 °C, 45 min (severity = 0.88), corresponding to a 28% reduction. Besides, a process severity increase leads to higher TIC concentration and lower TOC concentration (Figure 4.7b).

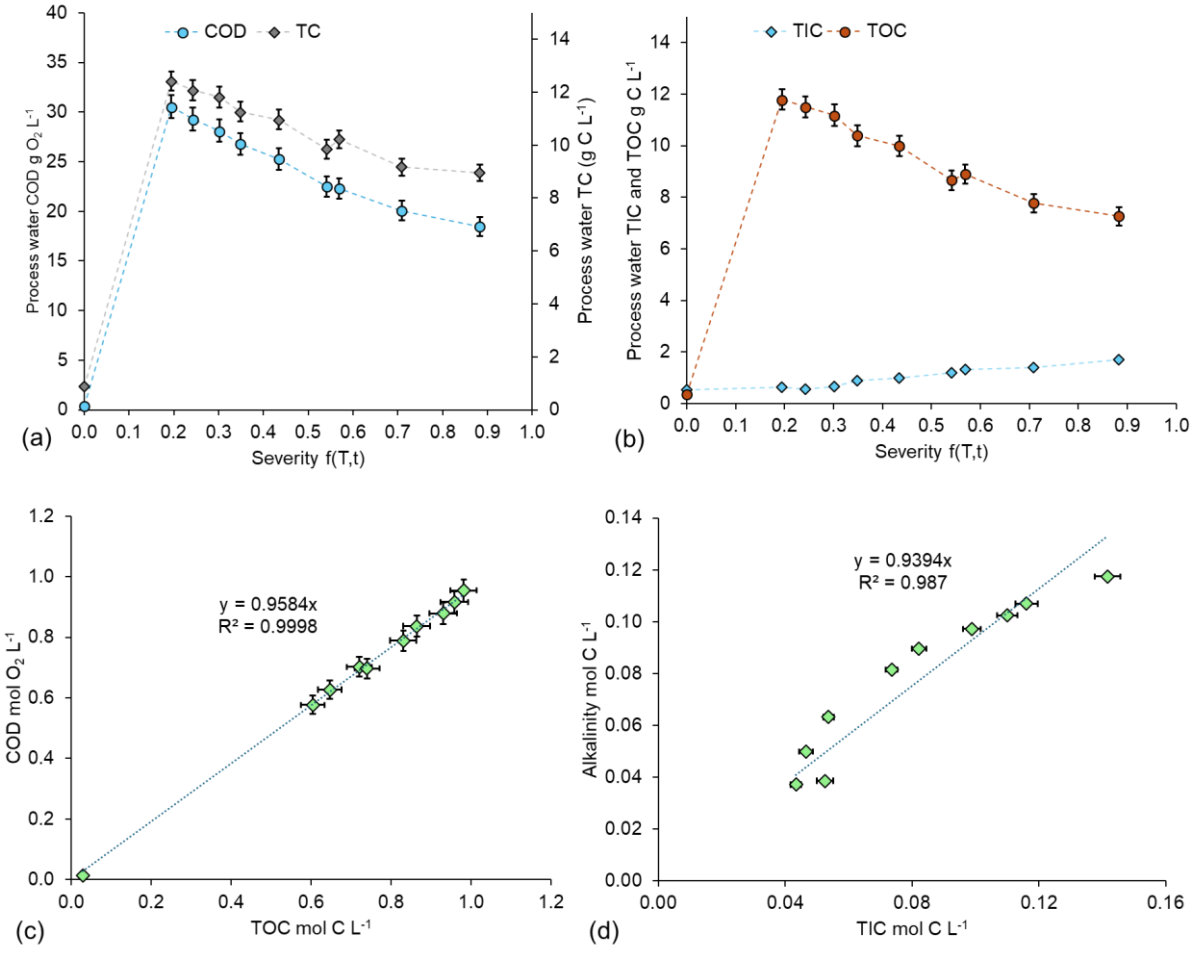

Figure 4.7 - (a) COD concentration (g O_2 L^{-1}) and TC concentration (g C L^{-1}) in process water by-product as a function of increasing severity. (b) TIC and TOC concentration (g C L^{-1}) in process water by-product as a function of increasing severity. (c)correlation between TOC concentration (mol C L^{-1}) and COD content (mol O_2 L^{-1}). (d) correlation between TIC concentration (mol C L^{-1}) and alkalinity expressed in mol C L^{-1}. Error bars represent propagated uncertainty. Dashed lines are included to help data interpretation.

These results seem to contradict various studies reporting that higher temperatures[194] and longer treatments[195] generally leads to a TOC concentration increase in water phase, suggesting that the solubilization of organic C compounds is the main cause. However, previous studies have observed that during SS HT treatments, TOC concentration can decrease with increasing temperature[188] , suggesting that part of water soluble organic compounds could move into other phases (ex. adsorbed in the solid by-product) or are converted into other species (ex. gas production). The reduction of soluble organic species concentration could be related to polymerization, condensation and aromatization mechanisms that lead to the formation of solid hydrochar clusters and the precipitation of C in the solid phase[52,60]. This hypothesis is supported by the increase in the solid by-product aromaticity with increasing process severity and by the overall increase in the hydrophobicity of the organic species, as illustrated in Section 4.5.2.

Figure 4.8 shows process water by-products under progressively more severe treatments. Process water obtained at 250 °C, 5 min (severity = 0.19) is black and opaque. However, increasing process severity results in clearer and more transparent products, suggesting a reduction in soluble C. Additionally, this change in color could be explained by a nucleation and growth mechanism of hydrochar microspheres resulting from the condensation and aromatization processes of organic intermediates[52,60]. Under milder conditions, hydrochar nuclei and microspheres are formed, and if they are smaller than 0.45 µm, they are not filtered out during process water by-product recovery. Increasing process severity leads to the growth of these spheres and the precipitation of hydrochar[58], leaving a clearer liquid. This would also explain TOC reduction.

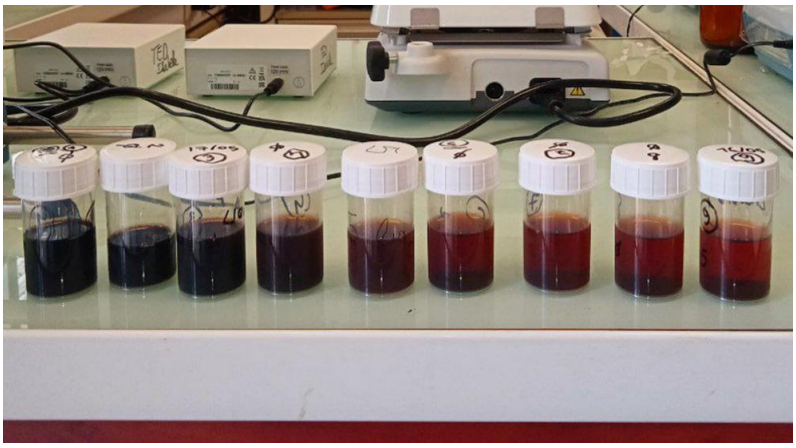

Figure 4.8 - Process water by-products under progressively more severe treatments.

As shown in Figure 4.7c, there is a strong correlation between TOC and COD results expressed respectively as mol O_2 L^{-1} and mol C L^{-1}. There is an almost 1:1 molar ratio between the two parameters. Thus, defining COD as the amount of oxygen consumed in the complete oxidation of organic C, the two quantities are directly related as described in the following reaction (Equation 4.2):

$$n\,C + n\,O_2 \rightarrow n\,CO_2 \qquad (4.2)$$

These results provide a global view that helps interpret previously reported pH and alkalinity results (Figure 4.5). The degradation of organic N and subsequent mineralization into NH_4-N releases NH_3 in the reaction medium. NH_3 reacts with a proton to form NH_4^+, as shown in Equation 4.3. This reaction reduces the concentration of H^+ ions, leading to an increase in OH- ions, which explains the increase of pH.

$$NH_3 + H^+ \leftrightarrow NH_4^+ \quad (4.3)$$

However, the increase in alkalinity cannot be directly linked to NH_4-N increase, because at pH 7.5-8.1, the equilibrium is shifted almost entirely to NH_4^+[196], which does not contribute to alkalinity. TIC includes dissolved CO_2, carbonic acid, bicarbonate, and carbonate ions, according to Equation 4.4.

$$CO_2 + H_2O \leftrightarrow H_2CO_3 \leftrightarrow H^+ + HCO_3^- \leftrightarrow 2H^+ + CO_3^{2-} \quad (4.4)$$

However, at pH 7.5-8.1, HCO_3^- ions predominate. Thus, TIC can be interpreted as a measure of bicarbonate ions in solution. An increase in process severity leads to an increase in TIC concentration, which corresponds to a higher content of dissolved HCO_3^-.

The increase of bicarbonate concentration can be effectively correlated to the rise in alkalinity, as shown in Figure 4.7d. Despite bicarbonate formation producing H^+ ions, NH_3's higher molar concentration provides a buffering effect, preventing medium acidification.

4.4.3. Dissolved metallic species

As shown in Figure 4.9a, the HT treatment leads to a strong reduction of soluble Ca and an increase of soluble Fe, Mg, P, and K concentration compared to the feed concentration. This suggests that Ca^{2+} precipitate in the solid pellet, and Fe^{3+} and Mg^{2+} are released in process water following the HT treatment, at least at less severe conditions. Soluble Fe and Ca concentration decrease with increasing process severity. The behavior of soluble Mg is less straightforward. For the reaction at 250 °C, Mg concentration increases when increasing treatment duration from 16 ± 1 mg L^{-1} at 5 min to 35 ± 2 mg L^{-1} at 45 min. For higher temperatures Mg concentration drops again and decreases with increasing reaction time (Figure 4.9a). This behavior has been already observed[81]. Nevertheless, the values reported in Figure 4.9a are obtained by calculating a weighted average of the duplicate process water products. Between two results of a duplicate, relatively high discrepancies were observed (up to 80% relative difference for the 250 °C, 15 min experimental points). Such a discrepancy between two results of the same experiment can have various causes. Although the experiments were conducted under the same conditions of pressure, temperature, and duration, slight differences in the cooling process duration may have influenced the precipitation phenomenon of Mg-containing compounds. This observation indicates that the careful control of the cooling process would be a key point for a continuous process development. Soluble Al is below the limit of detection, which means that less than 60 µg L^{-1} are present in process water. Soluble K concentration decreases for most severe treatments realized at 350 °C (Figure 4.9b).

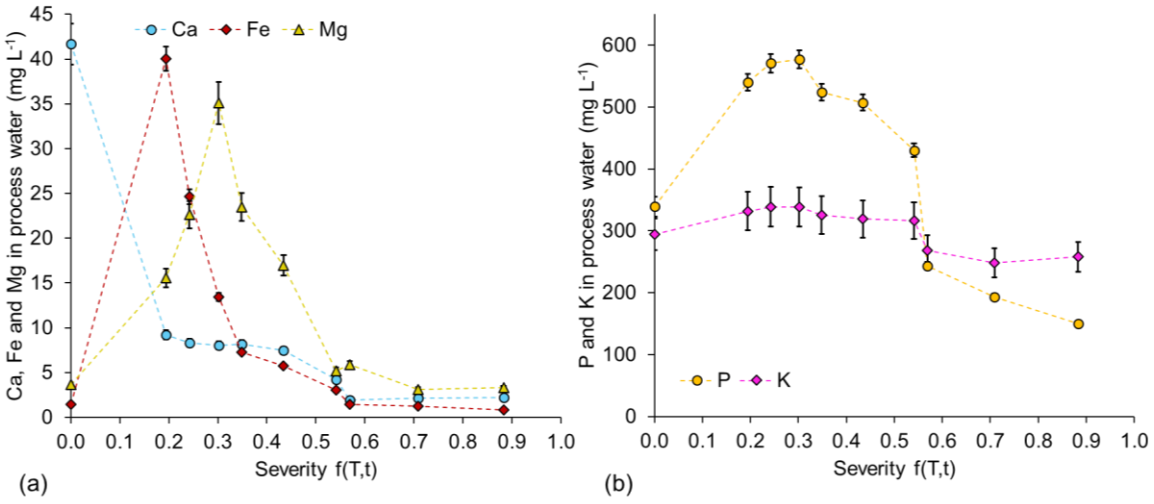

Figure 4.9 - Concentration of Ca, Fe, Mg (a), P and K (b) in process water by-products as a function of severity f(T,t). Error bars represent propagated uncertainty. Dashed lines are included to help data interpretation.

4.4.4. Experimental design analysis results

Table 4.2 shows the screening analysis results for the responses related to process water by-products.

Table 4.2 - Screening analysis results for process water properties based on the experimental design reported in Table 2.1. Statistical validation is provided in Table D.21 (Annex D). Positive effects are expressed through one or two positive signs (+), negative effects through one or two negative signs (-). Double sign means that the effect is three times more significant than the smallest significant effect. The absence of symbols indicates that the effect is not significant.

Factor	**Temperature (°C)**			**Time (min)**		
from:	250	250	300	5	5	15
to:	300	350	350	15	45	45
pH	+	+			+	
alkalinity (g_{CaCO3} L^{-1})	++	++	+	+	+	+
NH_3-N (g L^{-1})	++	++	+	+	+	+
COD (g L^{-1})	-	-	-		-	
TC (g L^{-1})	-	- -	-	-	-	-
TOC (g L^{-1})	-	- -	-	-	-	-
TIC (g L^{-1})	+	++	+		+	+
Ca (mg L^{-1})	-	-				
Fe (mg L^{-1})[a]	- -	- -	- -	-	-	-
Mg (mg L^{-1})		-				
K (mg L^{-1})	-	- -	- -			

[a]Result obtained using the logarithm of the response Y_i, $\log_{10}(Y_i)$, to prevent the model from returning negative values.

An increase in temperature from 250 to 300 °C significantly raises pH, but further raising the HT temperature to 350 °C has not been correlated to a significant effect. Extending treatment duration from 5 to 45 minutes also correlates with higher pH. When passing from 250 to 300 °C and/or for longer treatment durations, the hydrolysis of proteins into ammonium is enhanced, counterbalancing the effect of organic acids resulting from carbohydrates hydrolysis, resulting in an increase in pH[81].

Both temperature and treatment duration influence the increase in total alkalinity, with temperature having the predominant effect. This is directly linked to an increase in soluble inorganic carbon and more specifically in HCO_3^- ions concentration. They have also been correlated to an increase in NH_4-N concentration in process water, which enhances protein hydrolysis.

COD concentration decreases with both increasing temperature and HT duration, but the temperature effect is prevalent. Besides, a temperature increase has been correlated with a reduction of TC and TOC concentrations and with an increase of TIC content. This is interpreted considering that part of water-soluble organic compounds move into other phases (polymerization and condensation reactions leading to hydrophobic hydrochar cluster formation) or are converted into other species (gas or soluble inorganic C species) when temperature is increased[188]. An increase in treatment duration has once more the same effects of temperature, but to a lesser extent.

A temperature increase has been significantly correlated with Ca and Fe concentration decrease in process water, while a longer treatment duration has been correlated with a reduction in Fe concentration but to a lesser extent compared with temperature.

Table D.3 (Annex D) reports the ANOVA validation tool for the surface response model of the soluble Fe concentration (mg L^{-1}) in process water. The model has been obtained by using the logarithm of the soluble Fe concentration values to avoid obtaining negative values in the surface response. The second-degree polynomial model provided by the surface response is statistically significant, with a p-value less than 0.01% and an R^2 of 0.99. Table D.4 reports the second-degree model coefficients of the surface response for the base-10 logarithm of soluble Fe concentration (mg L^{-1}) in process water, with respective statistical validation. The linear coefficients for temperature (b_1) and time (b_2) are statistically significant, with a p-value lower than 0.01%. The quadratic coefficients are not statistically significant. The effect of temperature is more pronounced than the one of time, as the temperature linear coefficient is more than 3 times higher than the time linear coefficient. The obtained surface response model for soluble Fe concentration shows a significant interaction between temperature and duration, as the p-value for the interaction term is lower than 5%. The influence of duration on the concentration of soluble Fe is more pronounced at lower temperatures. For example, at 250 °C, extending the duration from 5 to 45 min leads to a reduction from 40 mg L^{-1} to 13 mg L^{-1}. Conversely, at 350 °C, prolonging the treatment duration only slightly reduces the already low concentration from 1.4 mg L^{-1} to 0.8 mg L^{-1}. This suggests that the kinetics of Fe precipitation increases with temperature, and that at 350 °C, most soluble Fe precipitates fully within 5 min. Equation 4.5 shows the corresponding second-degree polynomial model obtained for TSRY%:

$$\boldsymbol{log_{10}Fe} = \mathbf{0.629} - \mathbf{0.654}\boldsymbol{T} - \mathbf{0.182} + 0.011T^2 + 0.053t^2 + \mathbf{0.055}\boldsymbol{T \cdot t} \quad (4.5)$$

Where T and t are respectively temperature and treatment duration expressed as normalized values according to Equations 2.26 and 2.27. Statistically significant terms are in bold. The corresponding surface response is visualized in Figure 4.10.

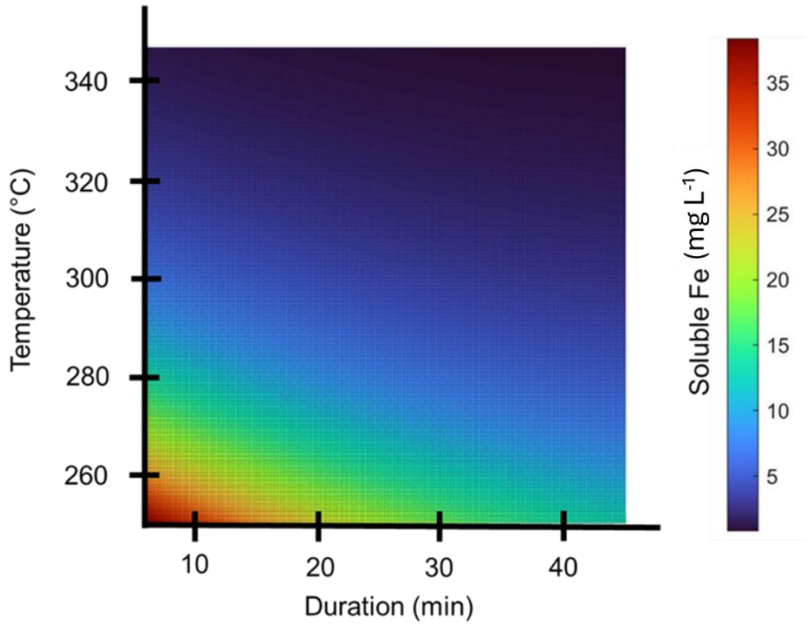

Figure 4.10 - Second-degree polynomial surface response for soluble Fe concentration (mg L^{-1}) in process water, based on the experimental design reported in Table 2.1, as a function of temperature (°C) and treatment duration (min) as expressed by Equation 4.5.

For Mg, screening analysis showed that only temperature has a significant effect: an increase in temperature from 250 to 350 °C leads to Mg precipitation in the solid product (Table 4.2). A decrease in soluble K concentration has been correlated with a temperature increase, especially from 300 to 350 °C. No significant duration effect was observed.

4.5. Solid by-product characterization

4.5.1. Ultimate analysis

Figure 4.11 shows ash, C, O (4.11a) and N, H, S (4.11b) contents in the solid pellet by-products. The solid resulting from HT treatment has a higher relative ash content compared to the initial digestate feed, with ash content increasing as process severity rises (Figure 4.11a). N, H and O contents in the solid by-products are lower than the digestate feed, and they decrease with increasing process severity. Instead, S and C contents fluctuate respectively around 1% and 38%.

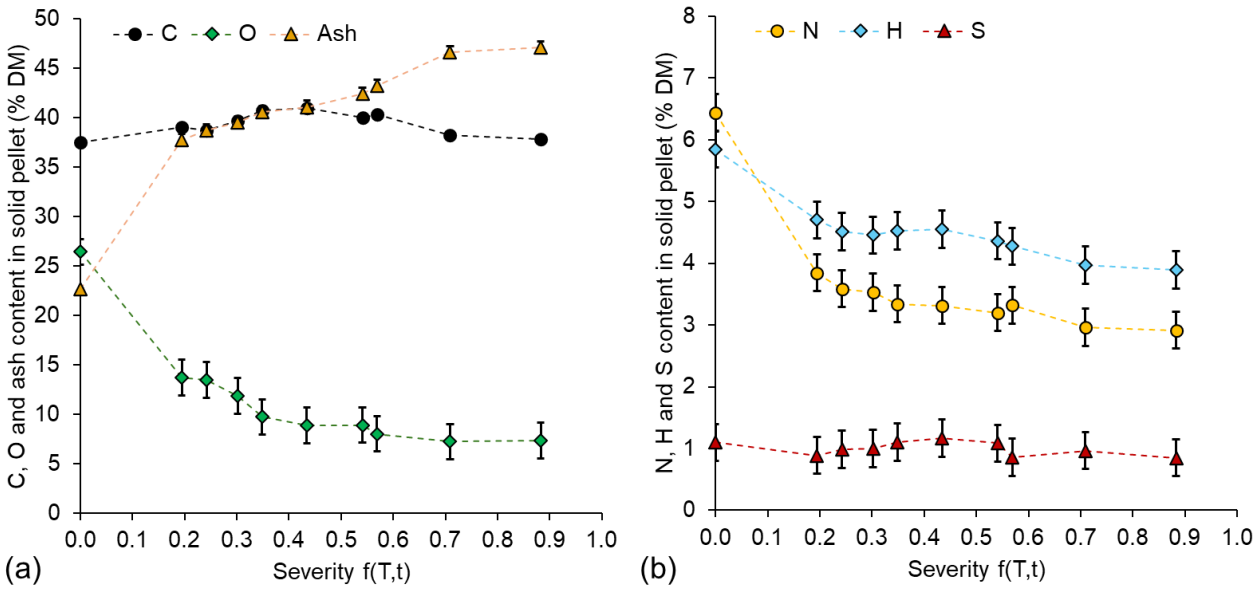

Figure 4.11 - Ultimate analysis results for solid pellet by products. (a) Ash, C, O (b) N, H, S contents as a function of HT severity f(T,t). Error bars represent propagated uncertainty. Dashed lines are included to help data interpretation.

More severe treatments enhance decarboxylation, dehydration, deamination, and organic decomposition reactions, thus explaining N, H, O reduction and ash content increase with higher process severity[11]. The consistent S content confirms previous findings[197] indicating that in the HTC of SS, the majority of S is retained in the solid product. The results of solid pellet ultimate analysis are in line with ranges observed in literature[11].

Figure 4.12 presents the Van Krevelen diagram of the HT treated solid pellets, illustrating the transformation of biomass through changes in O/C and H/C molar ratios. Reported results for solid products are in line with SS HT hydrochars values available in literature[11]. Both O/C and H/C ratios decrease as process severity increases. The transformation trend followed by the points on the diagram seems to suggest dehydration and decarboxylation as main reactions, with dehydration being the dominant one[59], as the rate of dehydration is always higher than the rate of decarboxylation[65]. The reduction in O/C and H/C also suggests an increase in the solid by-product aromaticity[198]. This trend has been already observed in previous works[10,91,130,199]. Table 4.3 shows the screening design results for the responses related to solid pellet by-product ultimate analysis.

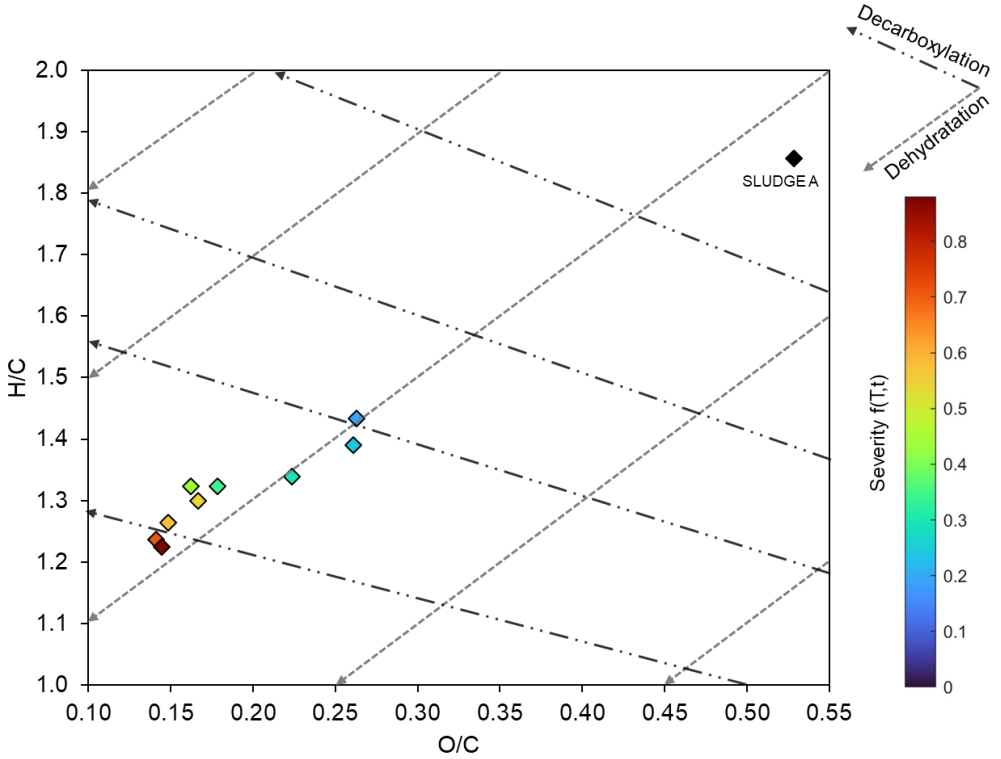

Figure 4.12 - Van Krevelen diagram for the solid pellet by-products. Color bar represent HT severity f(T,t).

Table 4.3 - Screening analysis results for solid by-product ultimate analysis based on the experimental design reported in Table 2.1. Statistical validation is provided in Table D.22 (Annex D). Positive effects are expressed through positive signs (+), negative effects through negative signs (-). Double sign indicates that the effect is three times more significant than the smallest significant effect. The absence of symbols indicates that the effect is not significant.

Factor	**Temperature (°C)**			**Time (min)**		
from:	250	250	300	5	5	15
to:	300	350	350	15	45	45
Ash content (% dry mass)	+	+	+		+	
Nitrogen (N) (% DM)	-	-	-	-	-	
Hydrogen (H) (% DM)		-	-		-	
Sulfur (S) (% DM)	+		-			
Oxygen (O) (% DM)	-	- -	-			
O/C molar ratio	-	-				
H/C molar ratio	-	-	-		-	

Both higher temperatures and longer treatment durations contribute to increase the ash content, with temperature having a predominant effect. An increase in temperature is linked to a decrease in N, H, and O content in the solid by-product. A longer treatment

duration is associated with lower levels of N and H. However, no significant correlation has been found between C content and either temperature or treatment duration increase. A HT temperature increase from 250 to 300 °C has been significantly correlated to an increase in S content in solid by-pellet products, confirming the tendency of S to be accumulated in the solid product following an HT treatment[197]. Additionally, the screening analysis revealed a decrease in S content when increasing the temperature from 300 to 350 °C, possibly due to the formation of gaseous S compounds (SO_2, H_2S).

An increase in temperature has been associated with a decrease in O/C and H/C ratios, whereas an increase in treatment duration has only been significantly correlated with a reduction in the H/C ratio.

4.5.2. Fate of organics

^{13}C solid-state NMR analysis results in Figure 4.13 provide a rich insight into the organic C species constituting Sludge A and the nine HT product pellets, obtained under increasingly severe conditions.

As for Sludge A spectrum, the 23.6, 30.8 and 40.8 ppm peaks are all associable to paraffinic C in alkyl chains[155]. More specifically, the 23.6 ppm peak corresponds to a branched aliphatic C[152], while the 30.8 ppm peak could be generated by methylenic carbons $(-CH_2-)_n$ in fatty acids chains[152], and the 40.8 ppm peak could be associated to carbons in methyl groups ($-CH_3$)[200]. The peak at 54.9 ppm could be associated with a methoxyl group ($-OCH_3$) in aromatic ethers constituting lignin[151,155,200,201]. CH-N groups in proteins may also contribute to the generation of this peak[151]. The 72.6 ppm peak is generated by groups in carbohydrates[155], more specifically by C2, C3, C5 in cellulose and carbon from xylan (hemicellulose)[151]. This signal could be also related to ether and secondary alcohol groups in lignin. The signal at 102.8 ppm could be also related to carbohydrates, in particular to C1 carbons in xylan[151]. Signals at 118.4 and 137.2 ppm are respectively generated by an unsubstituted aromatic carbon and a C-substituted aromatic carbon [155], while signal at 129.4 could be attributed to both[155,200]. Peak at 157.4 ppm could be associated with an aromatic carbon bonded with a hetero-element[202], and more specifically to a carbon in an aromatic ring of lignin[203]. Finally, the peak at 173.3 ppm is generated by carboxylic groups[155,200] in amide groups constituting peptide bonds in proteins[155,190,202,203].

Table 4.4 displays the integrated values corresponding to each family of organic compounds, providing a semi-quantitative indication of their relative amount.

The solid pellet resulting from the least severe treatment (250 °C, 5 min) presents three peaks in the 0-45 ppm region, corresponding to paraffinic C in alkyl chains[155], specifically at 23.2 ppm, 30.2 ppm (branched aliphatic C and methylenic C)[152] and at 14.7 ppm. The peaks at lower chemical shifts (0-28 ppm) could be associated with the presence of volatile fatty acids (acetic, propionic, butyric, valeric)[151].

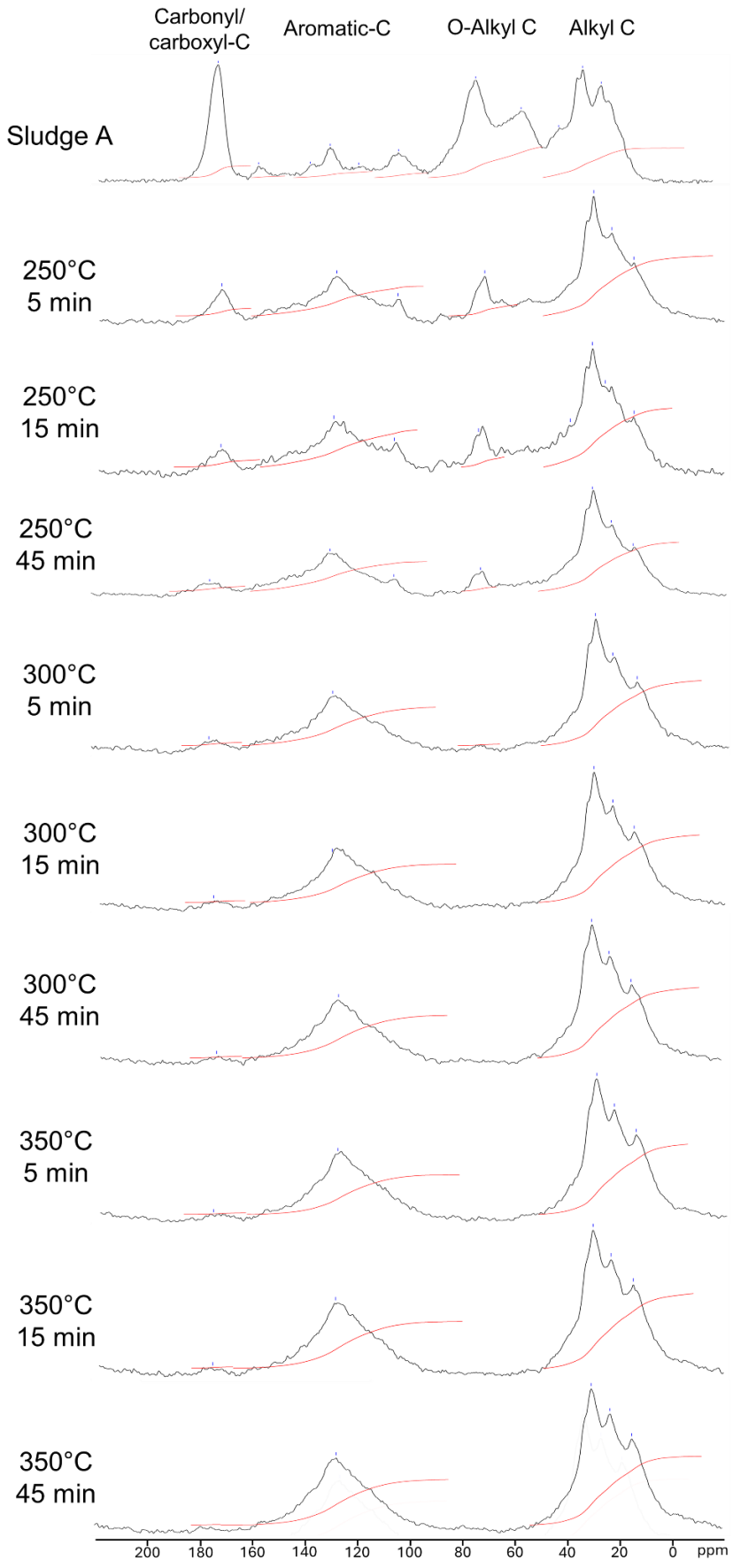

Figure 4.13 - ^{13}C solid-state NMR analysis results.

Between the peaks associated with groups found in carbohydrates (O-alkyl region at 45-110 ppm) two peaks (72.0 and 105.4 ppm) are found in the HT product solid pellet. Compared to the spectrum of Sludge A, the peaks in this region have decreased both in size and intensity, suggesting a generalized phenomenon of carbohydrate hydrolysis. The peak at 54.9 ppm detected in Sludge A is not present in the HT solid pellet. If this peak is associated with a methoxyl-C[151,155,200], its disappearance could suggest a degradation of the lignin structure. If it is instead linked to the presence of CH-N groups[151] in proteins, it would imply their degradation.

Table 4.4 - Integration values of peaks corresponding to each family of organic compounds (% of total area).

Chemical shift (ppm)				*0-45*	*45-110*	*110-160*	*160-210*
Sample	**Temperature (°C)**	**time (min)**	**Severity f(T,t)**	**Aliphatic C**		**Aromatic C**	**Carbonyl-carboxyl C**
				Alkyl-C	**O-alkyl C**		
Sludge A	-	-	0	34.8	41.9	9.3	14
				76.7			
Solid pellet by-product	250	5	0.19	55.3	10.5	27	6.9
				65.8			
	250	15	0.24	51.7	9	33	6.6
				60.7			
	250	45	0.30	55.6	5.1	34	5.8
				60.7			
	300	5	0.35	60.1	1.3	36	3.1
				61.4			
	300	15	0.43	62.8	0	36	1.6
				62.8			
	300	45	0.54	61.5	0	37	1.5
				61.5			
	350	5	0.57	63.1	0	36	1.4
				63.1			
	350	15	0.71	60.8	0	38	1.1
				60.8			
	350	45	0.88	59.9	0	40	0.4
				59.9			

The groups at 72.0 and 105.4 ppm, which can be associated with carbons in cellulose and hemicellulose[151], are reduced in intensity compared to those in Sludge A, once again suggesting the hydrolysis of these two biopolymers. The peak at 105.5 ppm could be associated with a dioxigenated anomeric C1[151], which can be found in both cellulose and xylan structures, as well as in smaller oligomers and simple monomers derived from the hydrolysis of biopolymers.

The presence of a peak at 128.9 ppm in the solid pellet suggests the presence of aromatic species[155,200]. Finally, the peak at 173.0 ppm, associated with carboxylic carbon[155,200], shows much lower intensity compared to that measured in Sludge A, suggesting a particularly extensive decarboxylation phenomenon already at 250 °C. Considering that during HT treatments decarboxylation occurs at relatively low

temperatures (150 °C) [51], this result is consistent. If this peak is associated with carboxylic groups in amides constituting protein peptide bonds, its reduction in intensity and area could imply the breaking of the peptide bond, thereby suggesting protein hydrolysis. Increasing the duration of the HT treatment conducted at 250 °C results in further reduction in the intensity of the peaks associated with carboxylic carbon and carbohydrates, suggesting a further biopolymers hydrolysis, and a continuation of the dehydration and decarboxylation reactions on the biopolymers fragments.

When the temperature is increased to 300 °C, the peaks at 72 and 105 ppm disappear. This suggests a complete cellulose and hemicellulose degradation below 300 °C[54]. With further increasing process severity, the area and intensity of the peak in the aromatic region increase, suggesting a significant aromatization phenomenon[52,60]. The group associated with carboxylic carbon becomes negligible already at 300 °C but disappears completely only under the most severe treatment (350 °C, 45 min).

Figure 4.14 illustrates the evolution of the aromaticity index, OA/A ratio, and hydrophobicity index with increasing process severity. An analysis of the aromaticity index of sludge and products (Figure 4.14a) shows that increasing process severity leads to an increase in the aromatic matrix in the solid product pellet. The increase in process severity also leads to a decrease in the O-alkyl/alkyl ratio (Figure 4.14b), which drops to zero already at 300 °C, 15 min, implying virtually complete hydrolysis of carbohydrates in favor of the production of small carbon chains with paraffinic C, volatile fatty acids, and organic acids[52,60,61]. Finally, the process severity increase results in the production of an increasingly hydrophobic product pellet (Figure 4.14c). Overall, the analysis of the ^{13}C NMR peaks suggests a phenomenon of carbohydrate and protein hydrolysis accompanied by decarboxylation and dehydration reactions, which leads to the production of organic acids and long chain fatty acids associated with the peaks in the lower shift region of the spectrum (0-28 ppm). Decarboxylation is particularly rapid and occurs at temperatures below 250 °C. Carbohydrate hydrolysis is complete at 300 °C. The presence of carboxylation and dehydration reactions is further supported by the O/C and H/C ratios reduction with increasing process severity described in Figure 4.12.

The hydrolysis, dehydration, and decarboxylation of lipids lead to the formation of long-chain fatty acids and intermediate alkanes and alkenes[60], which constitute the alkyl fraction at lower shifts. The fragments produced by hydrolysis, dehydration, and decarboxylation reactions undergo condensation and polymerization phenomena, and finally aromatization, which lead to an increase in the aromaticity of the product and the formation of hydrochar clusters. In treatments of higher process severity, the product is characterized by an aromatic fraction (the hydrochar) and an aliphatic fraction (the biofuel), both of which are highly hydrophobic, explaining the better separability of the bioproducts (Section 4.3). These results confirm the general organic species conversion mechanisms described in Section 1.4.

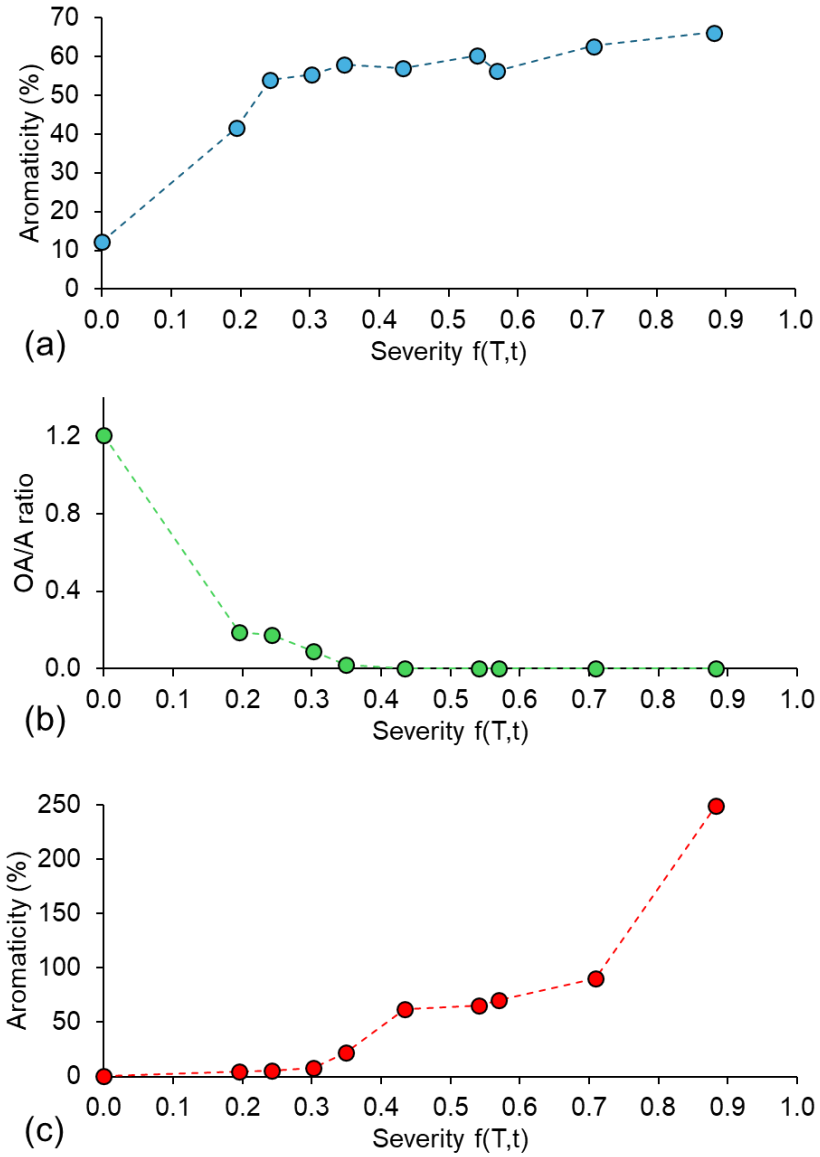

Figure 4.14 - (a) Organic C species aromaticity index, (b) O-Alkyl/alkyl ratio and (c) hydrophobicity index as a function of increasing HT severity f(T,t). Dashed lines are included to help data interpretation.

4.5.3. Metals and heavy metals

Figure 4.15 shows P, Ca, Fe, Mg (4.15a), Al, K, Zn, Cu (4.15b) content in solid pellet by-product (mg g^{-1} of dry solid) as a function of process severity. Figure 4.16 shows Cr, Pb, Ni, V, Ag (4.16a), As, Cd, Hg (4.16b) content in solid pellet by-product (mg kg^{-1} of dry solid) as a function of process severity. These contents are expressed on a dry basis.

After the HT treatment, Ca, Fe and Mg contents in the solid pellet increase with increasing process severity. These contents are doubled compared to the digestate feed (Figure 4.15a). Al content also increases with increasing process severity (Figure 4.15b). It has been previously shown that the solubilization and degradation of organic matter

leads to Ca, Fe, Al and Mg accumulation in the solid product[11]. K content in the solid pellet is generally lower than the feed digestate (Figure 4.15b), which could be explained by the solubilization of K compounds. Indeed, it has been observed that most of K is recovered in process water after the HT treatment[187]. For more severe conditions (T = 350 °C) K content in the solid pellet increases, suggesting a partial (re-) precipitation of solubilized K.

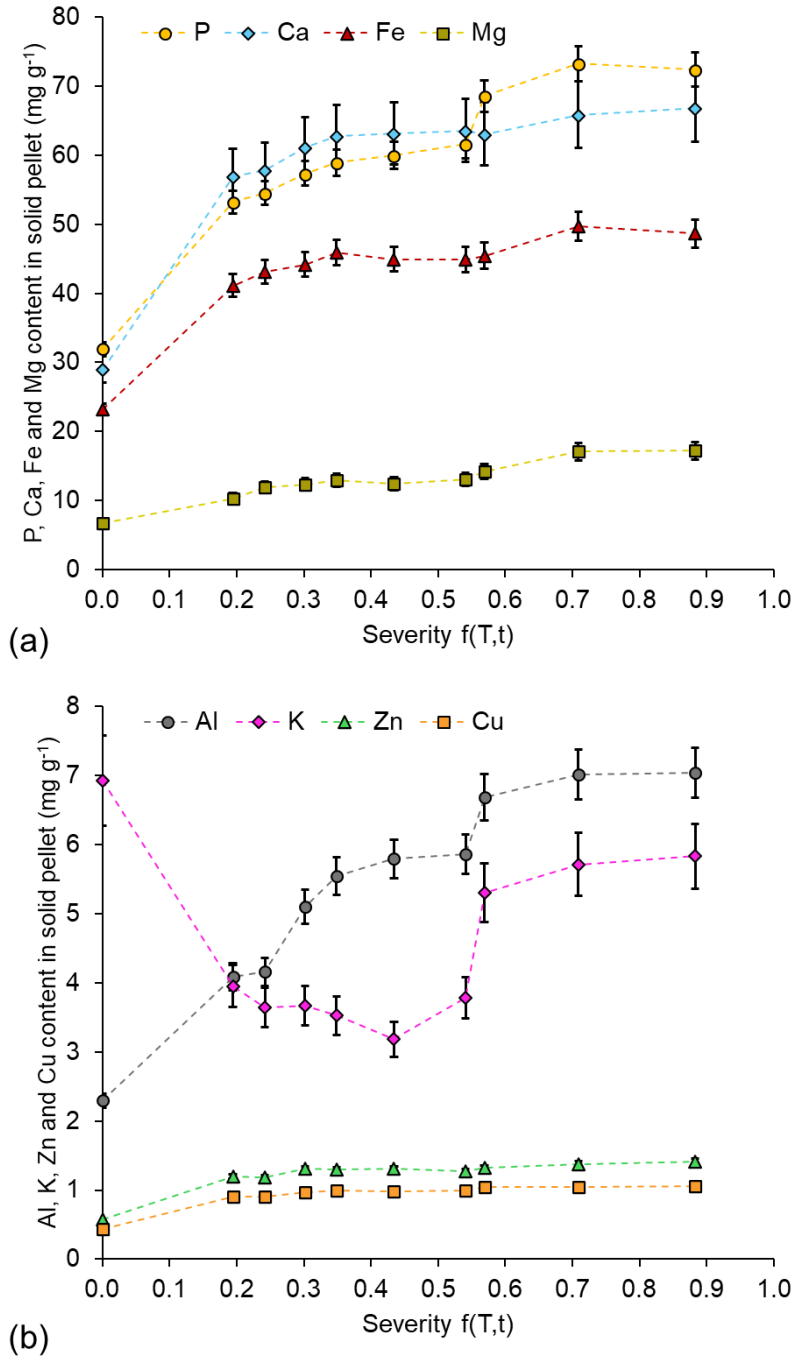

Figure 4.15 - (a) P, Ca, Fe, Mg, (b) Al, K, Zn, Cu content in solid pellet by-product, expressed as mg g^{-1} of dry solid, as a function of HT severity f(T,t). Error bars represent propagated uncertainty. Dashed lines are included to help data interpretation.

At 350 °C, 18 MPa water density is equal to 0.59 kg L^{-1}, while at 300 °C, 18 MPa is equal to 0.73 kg L^{-1}. It has been shown that in sub-critical conditions the solubility of K phosphates increases with increasing water density[204]. According to this, for the treatments realized at 350 °C, K phosphates solubility would be lower, explaining the partial reprecipitation of K.

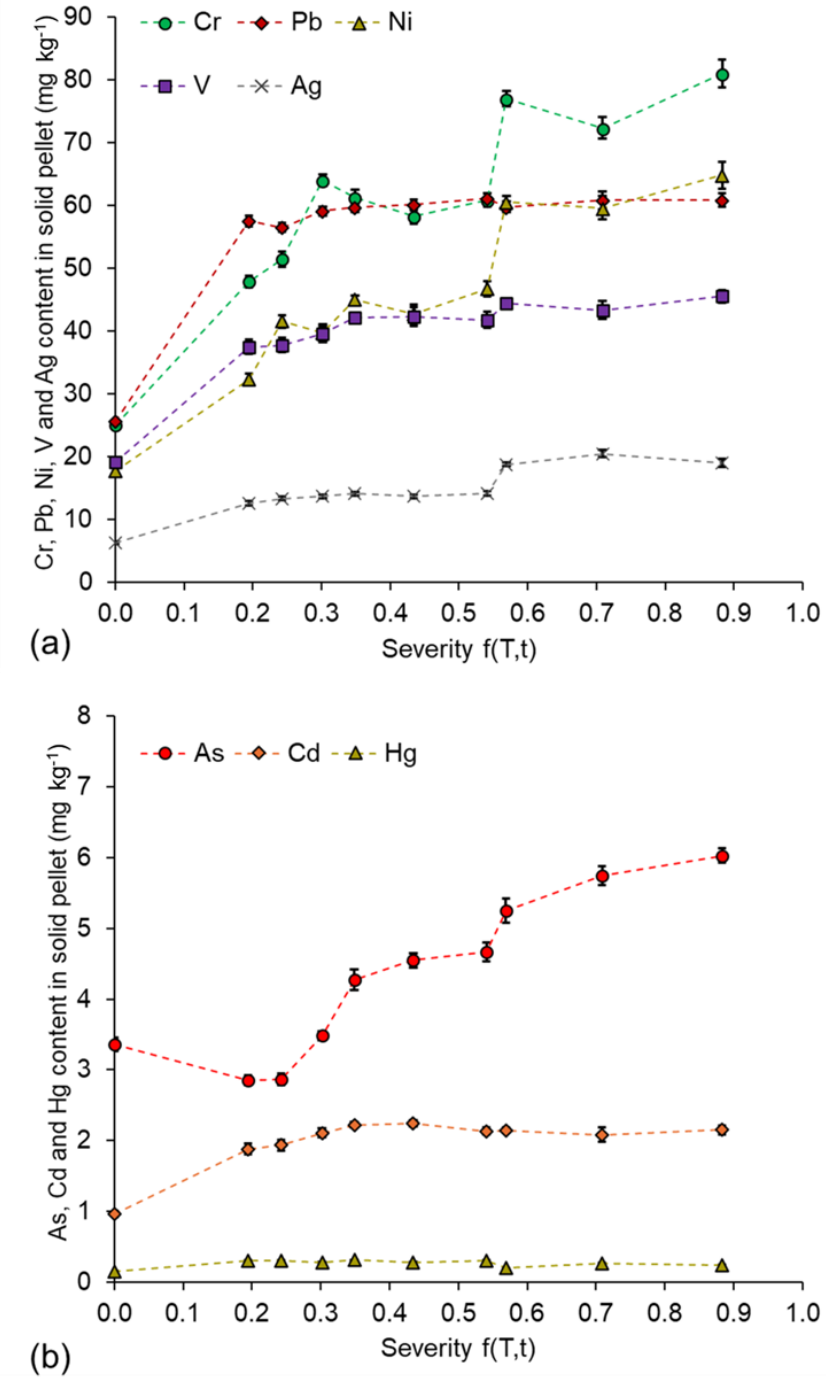

Figure 4.16 - (a) Cr, Pb, Ni, V, Ag, (b) As, Cd, Hg content in solid pellet by-product, expressed as mg kg^{-1} of dry solid, as a function of HT severity f(T,t). Error bars represent the propagated uncertainty combined with the relative standard deviation associated with the spectrometric intensity measurement (3). Dashed lines are included to help data interpretation.

Heavy metals content in solid products (Figure 4.16a and 4.16b) generally increases with increasing process severity, except for Hg which probably volatilizes at higher temperatures. When Hg is kept at a temperature between its melting point (-39 °C) and boiling point (357 °C), a fraction of it will volatilize. In fact, mercury is the metal with the highest observed volatility. The vapor pressure of Hg is 0.26 Pa at 25 °C and doubles every 10 °C[205]. Hg reaches a vapor pressure of 1 Pa at 42 °C, whereas other heavy metals are less volatile: Cd and As at 250-290 °C, Pb at 705 °C, Ag and Cr above 1000 °C, and Ni and V above 1500 °C[206]. This excludes the possibility of losses of these heavy metals due to volatilization during the reactor opening.

The content of metals and heavy metals in the solid product are of the same order of magnitude as the values observed in the digestate feed, but generally higher, confirming the heavy metals accumulation in the solid product. These contents are also in line with the ranges observed in literature, which are in the order of 0.1-1 mg g^{-1} for Cu and Zn, 10-1000 mg kg^{-1} for Ni, 10-100 mg kg^{-1} for Cr and As and 0.1 – 10 mg kg^{-1} for Cd and Hg [11].

Table 4.5 shows the screening design of experiments results for the responses related to the solid pellet by-product.

Table 4.5 - Screening analysis results for metals and heavy metals contents in solid pellet (expressed on a dry basis) based on the experimental design reported in Table 2.1. Statistical validation is provided in Table D.23 (Annex D). Positive effects are expressed through one or two positive signs (+), negative effects through one or two negative signs (-). Double effects are three times more significant than the smallest significant effect. The absence of symbols indicates that the effect is not significant.

Factor	**Temperature (°C)**			**Time (min)**		
from:	250	250	300	5	5	15
to:	300	350	350	15	45	45
Calcium (Ca) (mg g^{-1})	+	++	+		+	
Iron (Fe) (mg g^{-1})		+				
Aluminum (Al) (mg g^{-1})	+	+	+			
Magnesium (Mg) (mg g^{-1})	+	++	+	+	+	
Potassium (K) (mg g^{-1})		+	+			
Copper (Cu) (mg g^{-1})	+	+	+			
Zinc (Zn) (mg g^{-1})		+	+			
Mercury (Hg) (mg kg^{-1})		-	-			
Vanadium (V) (mg kg^{-1})	+	+				
Chrome (Cr) (mg kg^{-1})		+	+			
Nickel (Ni) (mg kg^{-1})	+	++	+			
Arsenic (As) (mg kg^{-1})	++	++	++	+	+	+
Silver (Ag) (mg kg^{-1})	+	++	++	+	+	
Cadmium (Cd) (mg kg^{-1})	+	+				

A temperature increase has been correlated with Ca, Fe, Al, Mg and K increase in the solid pellet. A longer treatment duration has been correlated only with Ca and Mg content increase in the solid pellet (Table 4.5). This increase has also been correlated with Cu, Zn, V, Cr, Ni, As, Ag, and Cd increase and with Hg decrease in the solid product. A longer treatment duration has been correlated only with As and Ag increase. No correlation has been observed for Pb (Table 4.5).

4.6. Phosphorus speciation and distribution

The HT treatment at 250 °C and 300 °C leads to an increase of soluble P concentration in process water compared to Centrate A concentration (Figure 4.9b). For the experiences realized at 250 °C (severity from 0.19 up to 0.30) Soluble P concentration slightly increases with increasing treatment duration at 250 °C, from 540 ± 14 mg P L^{-1} at 5 min up to 577 ± 15 mg P L^{-1} after 45 min. However, at 300 °C and 350 °C the trend is reversed, with a decreasing concentration for longer treatment. For the most severe treatments at 350 °C, soluble P concentration decreases below Centrate A original value.

Figure E.1 (Annex E) compares TP concentration in process water, obtained by ICP-AES spectroscopy (Section 2.3.8), with PO_4-P concentration, measured by ammonium molybdate-ascorbic acid method and UV-VIS spectroscopy (EN 6878, 2004) (Section 2.3.7). The two methods provide very similar results for all experimental points and the differences fall within the uncertainty intervals, suggesting that around 100% of soluble P in process water is present in the form of PO_4-P and that the presence of soluble organic P species is negligible. This result is in line with previous observations according to which OP is completely mineralized to PO_4-P in less than 60 min, when T is higher than 175 °C[10,77,78,82]. The low levels of soluble organic P in Sludge A, combined with the relatively high temperatures used in this study, explain why PO_4-P is present as the only form of soluble P found in process water by-product.

P content in the solid pellet (expressed on a dry basis) increases after the HT treatment and increase with increasing process severity (Figure 4.15a), from 53 ± 2 mg P g^{-1} at 250 °C, 5 min (severity = 0.19), up to 72 ± 2 mg P g^{-1} at 350 °C, 45 min (severity = 0.88). This result has been comprehensively described in previous works[1], showing that at more severe conditions, P tends to accumulate within the solid fraction despite the enhanced solubilization of solid organic matter and TSRY reduction.

Figure E.2 (Annex E) compares the TP contents in the solid by-product measured with two different methods:

1. Aqua Regia digestion and ICP-AES Spectroscopy (EN ISO 13346, 2000), the same methods used to quantify metal and heavy metal species (Section 2.4.3 and 2.4.4).
2. Calcination followed by HCl extraction technique as proposed in the SMT method[74] (Section 2.4.6.1).

The results from both methods are directly comparable, and all discrepancies fall within uncertainty bars. Therefore, it can be concluded that both methods can be used for the characterization of these samples.

Figure 4.17 shows P relative repartition in the two by-products (process water and pellet) as a fraction of the total feed. The P fraction in the solid pellet is calculated by difference under the hypothesis that no gaseous or volatile P species are formed during the SS HT treatment. In fact, if in some dry thermal processes, P can end up in the gaseous phase (pyrolysis and gasification)[49], in HT treatments, P is recovered exclusively in the solid and liquid by-products[5,49,207]. Both most common forms of elemental P (white phosphorus and red phosphorus) are solid under ambient conditions. In any case, the presence of elemental P in the reaction products is to be excluded due to their low stability and high reactivity. P oxides are also solid under ambient conditions. Although P_4O_{10} can sublimate into a gas, the presence of water in the reaction medium excludes the presence of this oxide, as it would undergo hydration. Phosphine (PH_3) is the most common gaseous phosphorus species under ambient conditions. However, any trace of phosphine would react with water at high temperature and pressure conditions, yielding orthophosphoric acid[208]. P present in the products of hydrothermal treatments is almost exclusively in the form of organic P or phosphates, in both cases appearing as solids or dissolved in aqueous solution.

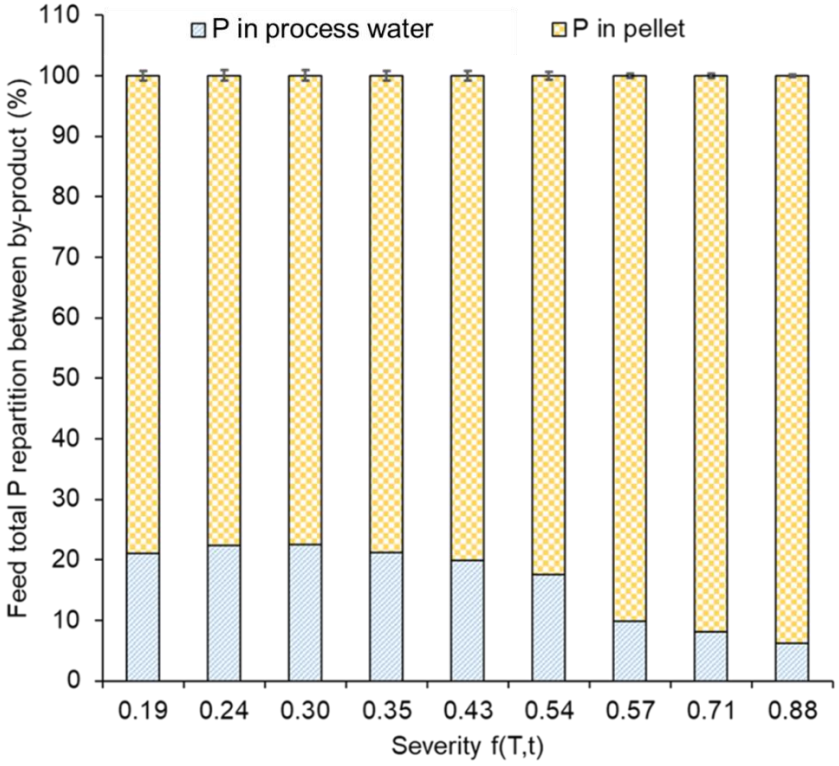

Figure 4.17 - P relative repartition in the two by-products (solid pellet and process water). P fraction in the solid pellet is calculated by difference under the hypothesis that no gaseous or volatile P species are formed during the SS HT treatment. Error bars represent propagated uncertainty.

For the treatments carried out at 250 °C (process severity from 0.19 to 0.30), increasing the treatment duration leads to an increase in the yield of P recovered in process water. However, this increase is very modest and falls within experimental uncertainty. Starting from 300 °C, increasing the process severity leads to a decrease in the yield of P in process water. Consequently, the fraction of P recovered in the product pellet is higher for more severe treatments (94% of P fed to the reactor is recovered in the pellet for the most severe treatment at 350 °C and 45 min). These results could be explained considering that at relatively low temperatures the mineralization kinetics of OP, following an Arrhenius kinetic law[113], is relatively slow, requiring several minutes to fully mineralize solid OP and release it into solution[82]. At higher temperatures the mineralization kinetics is much faster[114], the precipitation of PO_4^{3-} ions with metal cations is the dominant phenomenon that determines the P precipitation and accumulation in the solid product[10,77]. P contents in the solid and liquid by-products obtained for this work are in line with the ranges available in literature[1,11].

Figure 4.18 shows P speciation in the solid pellet. AIP is the prevalent P fraction in the solid pellet, in contrast to the digestate feed, for which the predominant fraction is NAIP. The most noticeable result is the increase of AIP and the decrease of NAIP as the process severity increases, when temperature increases from 300 to 350 °C. This phenomenon has been extensively observed in previous works[10,77–81,83,85–94].

These results appears to confirm that high temperatures lead to the precipitation of PO_4^{3-} with Ca^{2+} cations into the form of Ca-phosphates, with a concomitant dissolution of NAIP complexes (such as Fe- and Al-phosphates) into Fe^{3+}, Al^{3+}, and PO_4^{3-} ions, which could be then reprecipitated as stable Fe- and Al-(hydro)-oxides[37]. This mechanism is further supported by the results of ICP-AES of process water by-products (Figure 4.9a), which show a Fe release following the HT treatment under less severe conditions, and at the same time, precipitation of soluble Ca. Subsequently, increasing the process severity leads to a decrease in the concentration of both Fe (which would precipitate as Fe hydroxide) and Ca (which precipitates as Ca phosphate).

In contrast to the digestate feed, for which the OP has been estimated to be around 14% of TP, no statistically significant residual OP fraction has been reliably observed in the solid pellets. This is primarily due to the high uncertainty of the SMT method, which consists of a series of sequential extractions and can lead to a significant error propagation[157]. The amount of residual OP in solid pellet, if present, is therefore too small to be estimated with relative certainty. The OP amount in Sludge A is already relatively low (14%), besides, several studies indicate that OP can be completely mineralized to PO_4-P in less than 60 min, in particular at temperatures above 175 °C[10,77,78,82,114,115].

^{31}P solid-state NMR results, reported in Figure E.3, show a main peak centered around 0 ppm with an amplitude of about 20 ppm. This type of peak is present in Sludge A and solid pellets, with no significant effect of temperature and duration. This signal is most likely attributable to orthophosphates [15] (9-13 ppm), although the sludge signal may include contributions from some OP species (monoesters and diesters) within the -10 to 10 ppm range[209]. These OP contributions should not be significant in the solid pellet

signals. These observations suggest that P in the solid phase is almost exclusively in the form of PO_4-P bound to metal cations, forming salts such as Fe, Al, and Ca phosphates. The increased signal intensity observed at 350 °C may be related to a higher presence of phosphate salts in the pellet due to enhanced precipitation of PO_4-P with Ca.

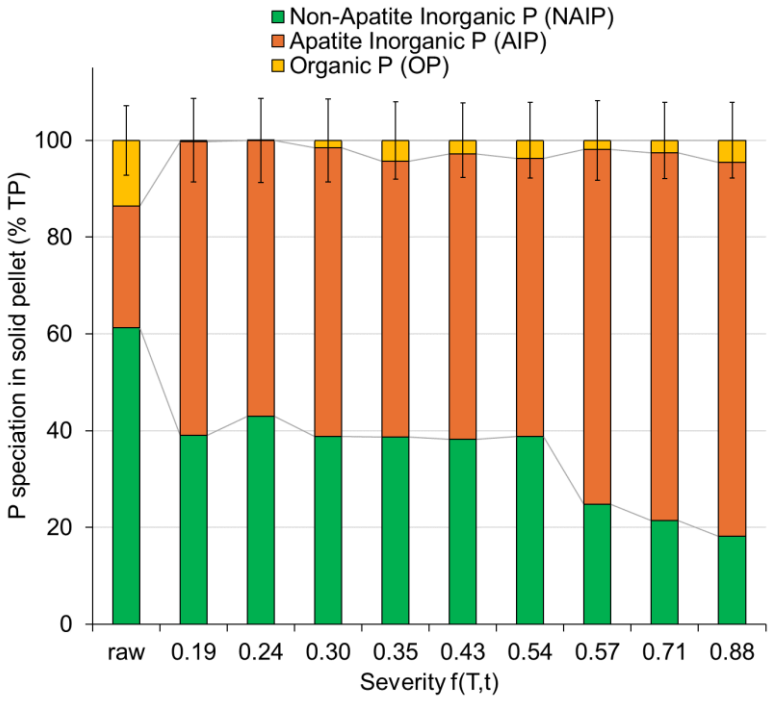

Figure 4.18 - P speciation in the solid pellet as a function of HT severity f(T,t). Error bars represent propagated uncertainty.

Figure 4.19a shows the Ca/P, Fe/P and Mg/P molar ratios in process water by-products. Ca/P, Fe/P and Mg/P molar ratios in process water are always lower than 1. This clearly shows that Ca, Fe or Mg are limiting for P precipitation. Ca/P molar ratio in Centrate A is equal to 0.09, but for HT process water it sharply decreases to values around 0.01. Although at 250 °C soluble P concentration remains roughly constant with increasing treatment duration, both soluble P and soluble Ca concentrations decrease with increasing process severity (Figure 4.9). However, Ca/P molar ratio remains more and less constant as process severity increases. These results could suggest that the decrease in soluble Ca is correlated with the decrease in soluble P according to a specific molar proportion, confirming the precipitation of Ca phosphates.

Fe/P molar ratio in Centrate A is equal to 0.002, but the process water obtained in the least severe HT treatment (severity = 0.19) is more than 17 times higher. A process severity increase leads to a sharp Fe/P molar ratio decrease, until returning to values close to those of Centrate A. Fe/P molar ratio reduction with process severity is directly associated with soluble Fe concentration decrease (Figure 4.9a). This result supports the hypothesis that a HT treatment realized at lower temperatures (250 °C) leads to the dissolution of NAIP and the subsequent release of Fe^{3+} ions into solution. Higher severities could cause the reprecipitation of Fe as $Fe(OH)_3$ [37]. Mg/P molar ratio in

process water is generally higher compared to Centrate A value. At 250 °C (severity from 0.19 to 0.30), longer treatment duration leads to a higher Mg/P molar ratio, while for higher temperature (300-350 °C) Mg/P ratio decreases with increasing process severity. This trend follows the same evolution of soluble Mg concentration (Figure 4.9a), as discussed in Section 4.4.3.

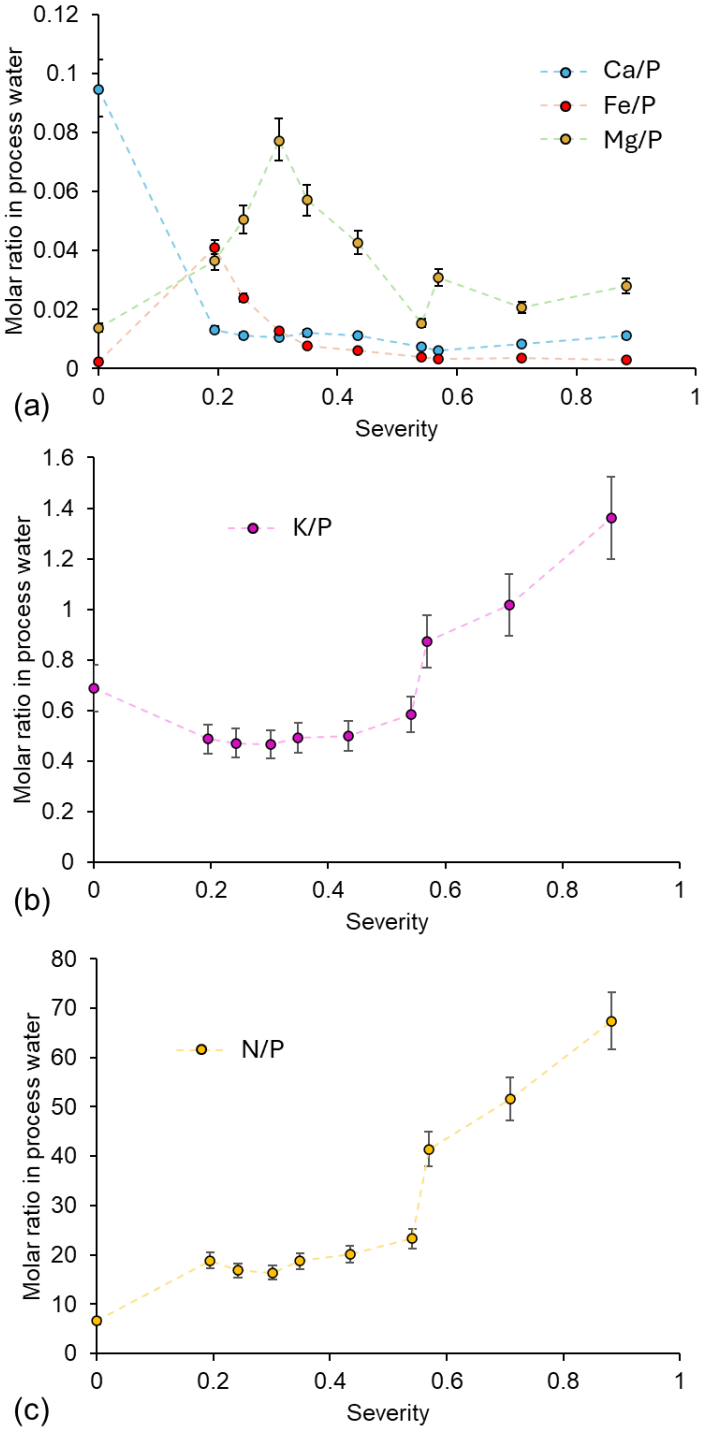

Figure 4.19 - Ca/P, Fe/P and Mg/P (a) K/P (b) and N/P (c) molar ratios in process water by-product as a function of severity f(T,t). Error bars represent propagated uncertainty. Dashed lines are included to help data interpretation.

Figure 4.19a shows that the available Ca^{2+}, Fe^{3+}, and Mg^{2+} concentrations in solution are insufficient for complete orthophosphate precipitation. Under milder conditions, up to 10% of phosphorus could precipitate, dropping to less than 4% under more severe conditions. Figure 4.19b shows the K/P molar ratio in process water. Initially around 0.7 in Centrate A, it drops to 0.5 at 250 °C due to significant PO_4-P release. Higher process severity increases the K/P ratio, due to reduced PO_4-P levels and a slight rise in soluble K at 350°C (Figure 4.9b). This trend suggests that P precipitation is not accompanied by K precipitation, ruling out potassium phosphate formation, which is consistent with its relatively high solubility[210].

Figure 4.19c shows the N/P molar ratio in process water, which increases with increasing process severity. This trend is specifically related to PO_4-P concentration decrease with increasing process severity, as soluble N concentration remains relatively constant regardless of process severity (Section 4.4.1). This result shows that P precipitation is not accompanied by N precipitation, ruling out the significant recovery of these two nutrients as struvite.

Figure 4.20 shows Ca/P, Fe/P, Mg/P, Al/P, K/P and N/P molar ratios in HT treatment solid pellets.

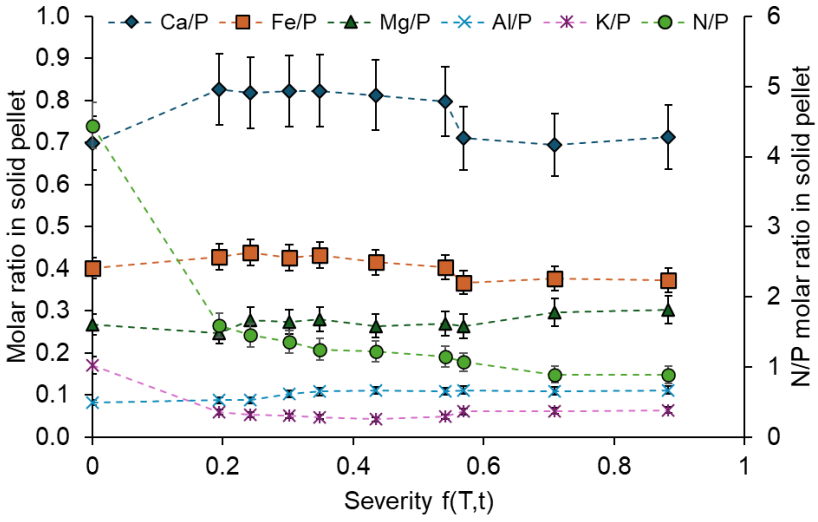

Figure 4.20 - Ca/P, Fe/P, Mg/P, K/P and N/P molar ratios in solid pellet by-product as a function of severity f(T,t). Error bars represent propagated uncertainty. Dashed lines are included to help data interpretation.

In Sludge A, the Ca/P molar ratio is 0.7. For HT treatments at 250-300 °C, the ratio increases to approximately 0.8 due to the majority of Ca being recovered in the solid pellet, while about 20% of P remains in the process water. At 350 °C, the ratio reverts to around 0.7, as an increased fraction of P is recovered in the solid pellet. A Ca/P molar ratio of approximately 0.7 in the solid pellet indicates that even if all Ca precipitates as dicalcium phosphate ($CaHPO_4$), only about 70% of P in Sludge A could be recovered as calcium phosphate. This is consistent with the AIP fraction in the solid pellets, which is around 70% under the most severe conditions (Figure 4.18). Consequently, to further increase the AIP fraction, additional Ca needs to be added to the sludge.

Fe/P, Mg/P and Al/P molar ratios in solid pellets remain roughly constant respectively around 0.4, 0.3 and 0.1. There is no direct relationship between Fe/P and Al/P molar ratios and the NAIP fraction in the solid pellets, as not all Fe and Al are necessarily in the form of phosphates; they may also be present as other compounds (e.g., hydroxides or oxides). K/P molar ratio in Sludge A is approximately 0.17. This ratio decreases in the solid pellets (around 0.06). This is due to a partial dissolution of K-containing compounds, while P tends to accumulate in the solid pellet. N/P ratio (Figure 4.20) sharply decreases after the hydrothermal treatment, as a consistent fraction of N is released in process water following protein and pyridine-N compounds hydrolysis and deamination, leading to the release of inorganic N (NH_4-N)[189]. N/P molar ratio in solid pellet decreases with increasing process severity as N content increases and P content decreases.

Table 4.6 shows the screening design trends obtained with results for P distribution and speciation discussed in this section.

Table 4.6 - Screening analysis results for P distribution and speciation based on the experimental design reported in Table 2.1. Statistical validation is provided in Table D.24 (Annex D). Positive effects are expressed with positive signs (+), negative effects with negative signs (-). Double effects are three times more significant than the smallest significant effect. The absence of symbols indicates that the effect is not significant. Contents in pellets are expressed on a dry basis.

Factor	**Temperature (°C)**			**Time (min)**		
from:	250	250	300	5	5	15
to:	300	350	350	15	45	45
Soluble P in process water (mg P L^{-1})	-	- -	- -		-	-
PO_4-P in process water (mg P L^{-1})	-	- -	- -		-	-
TP in pellet (AR extraction + ICP)(mg P g^{-1})	+	++	++	+	+	
TP in pellet (SMT) (mg P g^{-1})	+	++	+		+	
NAIP in pellet (mg P g^{-1})		-	-			
NAIP in pellet (% TP)		-	-			
AIP in pellet (mg P g^{-1})		+	+			
AIP in pellet (% TP)		+	+			

A temperature increase has been correlated to a decrease of soluble P concentration. Moreover, the screening analysis allowed to define a significant correlation between soluble P reduction and longer treatment duration, specifically between 15 and 45 min.

Table D.5 (Annex D) reports the ANOVA validation table for the second-degree polynomial model obtained with soluble P concentration in process water results. The obtained model is statistically significant, with a p-value lower than 0.01% and an R^2 of 0.98. The model standard deviation is equal to 27.5 mg L^{-1}. Table D.6 reports the coefficients of the second-degree model surface response for P concentration in process water (mg P L^{-1}), with respective statistical validation. The coefficients for the linear effects of temperature (b_1) and time (b_2) are statistically significant, together with the

temperature quadratic term ($b_{1\text{-}1}$). As shown in Table D.6, the linear coefficient for temperature is more than 7 times higher than the coefficient for the linear effect of time, confirming the predominant influence of temperature on soluble P concentration compared to time. Besides, the coefficient $b_{1\text{-}2}$ is statistically significant, allowing to highlight the presence of an interaction between temperature and time. According to this model, for low temperature (250 °C), a longer duration leads to a slight increase in soluble P concentration, from 559 mg L^{-1} at 5 min, to 567 mg L^{-1} at 45 min. However, this increase is not significant as the model standard deviation is equal to 27.5 mg L^{-1}. For the highest temperature (350 °C) the trend is reversed, as the model suggests that a longer treatment leads to a decrease in soluble P concentration, from 240 mg L^{-1} at 5 min, down to 132 mg L^{-1} at 45 min. In general, the model shows that time influence is not significant at 250 °C, but becomes more important when T ≥ 300 °C. Equation 4.6 shows the corresponding second-degree polynomial model obtained for P concentration in process water (mg P L^{-1}).

$$\boldsymbol{P_{soluble}}\left(\frac{\boldsymbol{mg}}{\boldsymbol{L}}\right) = \mathbf{483.3} - \mathbf{188.4}\boldsymbol{T} - \mathbf{25.1}\boldsymbol{t} - \mathbf{108.1}\boldsymbol{T^2} - 0.54t^2 - \mathbf{29.0}\boldsymbol{T}\cdot\boldsymbol{t} \quad (4.6)$$

Where T and t are respectively temperature and treatment duration expressed as normalized values according to Equations 2.26 and 2.27. Statistically significant terms are in bold.

Figure 4.21 shows the response surface obtained for P concentration in process water (mg L^{-1}) as a function of temperature (°C) and treatment duration (min). Screening analysis results show a correlation between both temperature and treatment duration and the TP content in the solid by-products (Table 4.6).

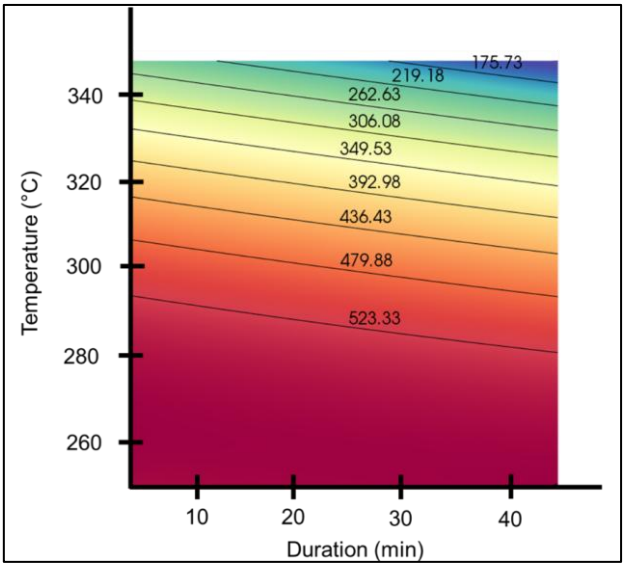

Figure 4.21 - Second-degree polynomial surface response for P concentration in process water (mg P L^{-1}), based on the experimental design reported in Table 2.1, as a function of temperature (°C) and treatment duration (min) as expressed by Equation 4.6, with the coefficients reported in Table D.6.

However, temperature effect is prevalent over treatment duration, a trend that had already been observed in other works[78,81]. Table D.7 reports the ANOVA validation tool for the second-degree polynomial model obtained with P recovery yield in solid pellet (% of total feed P) results. In this model, solid pellet P fraction is calculated by difference under the hypothesis that no gaseous or volatile P species are formed during the SS HT treatment. The obtained model is statistically significant, with a p-value lower than 0.01% and an R^2 of 0.98. The model standard deviation is equal to 0.98 %. Table D.8 reports the second-degree model coefficients of the surface response for P recovery yield in solid pellet (%), with respective statistical validation. The coefficients for the linear effects of temperature (b_1) and time (b_2) are statistically significant, together with the temperature quadratic term ($b_{1\text{-}1}$) and the interaction term ($b_{1\text{-}2}$). The obtained surface response confirms once more the predominant influence of temperature compared to time and a significant interaction between temperature and time effects. For treatments realized at 250 °C, a longer treatment does not lead to a significant effect on P recovered in the solid pellet. At 300 °C and 350 °C, a longer treatment is associated with an increase in P yield in the solid pellet. The effect of time becomes more significant at higher temperatures. Equation 4.7 shows the corresponding second-degree polynomial model obtained for P recovery yield in solid pellet (%).

$$\boldsymbol{P\ yield\ in\ solid\ pellet}\ (\%) = \mathbf{80.7} + \mathbf{7.17}\boldsymbol{T} + \mathbf{0.96}\boldsymbol{t} + \mathbf{4.51}\boldsymbol{T^2} - 0.12t^2 + \mathbf{1.15}\boldsymbol{T}\cdot\boldsymbol{t} \qquad (4.7)$$

Where T and t are respectively temperature and treatment duration expressed as normalized values according to Equations 2.26 and 2.27. Statistically significant terms are in bold. Figure 4.22 shows the response surface obtained for P recovery yield in solid pellet (%) as a function of temperature (°C) and treatment duration (min).

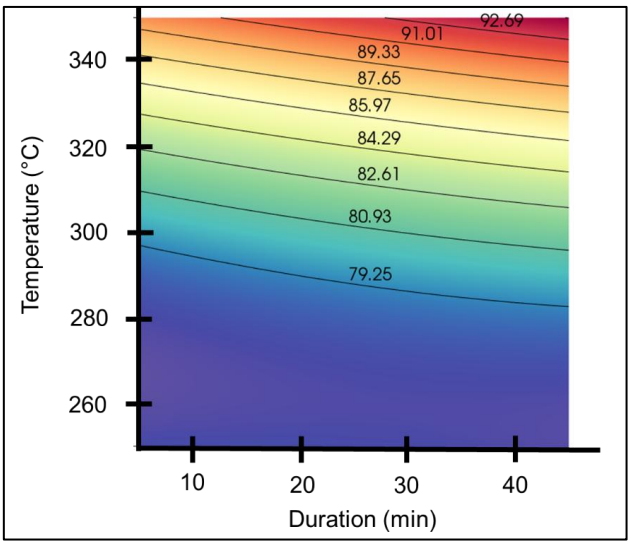

Figure 4.22 - Second-degree polynomial surface response for P recovery yield in solid pellet (%), based on the experimental design reported in Table 2.1, as a function of temperature (°C) and treatment duration (min) as expressed by Equation 4.7, with the coefficients reported in Table D.8. Solid pellet P fraction is calculated by difference under the hypothesis that no gaseous or volatile P species are formed during the SS HT treatment.

Table D.9 reports the ANOVA validation tool for the second-degree polynomial model obtained with AIP fraction (% of TP) results. The obtained model is statistically significant, with a p-value lower than 1% and an R^2 of 0.98. The model standard deviation is equal to 1.7 %. Table D.10 reports the second-degree model coefficients of the surface response for AIP in solid pellet (% TP), with respective statistical validation. The coefficients for the linear and quadratic effects of temperature (b_1) and ($b_{1\text{-}1}$) are statistically significant, while no significance has been observed for treatment duration, thus confirming once more the predominant influence of temperature over time. The statistically significant effect of the quadratic temperature term indicates a particularly notable increase in AIP% at the highest temperature (350 °C), while it is statistically less relevant between 250 °C and 300 °C. Equation 4.8 shows the corresponding second-degree polynomial model obtained for AIP in solid pellet (% TP).

$$\boldsymbol{AIP}\ (\%) = \mathbf{57.67} + \mathbf{8.22}\boldsymbol{T} + 0.57t + \mathbf{9.46}\boldsymbol{T^2} - 0.23t^2 + 1.22T \cdot t \qquad (4.8)$$

Where T and t are respectively temperature and treatment duration expressed as normalized values according to Equations 2.26 and 2.27. Statistically significant terms are in bold. Figure 4.23 shows the response surface obtained for AIP (% TP) as a function of temperature (°C) and treatment duration (min).

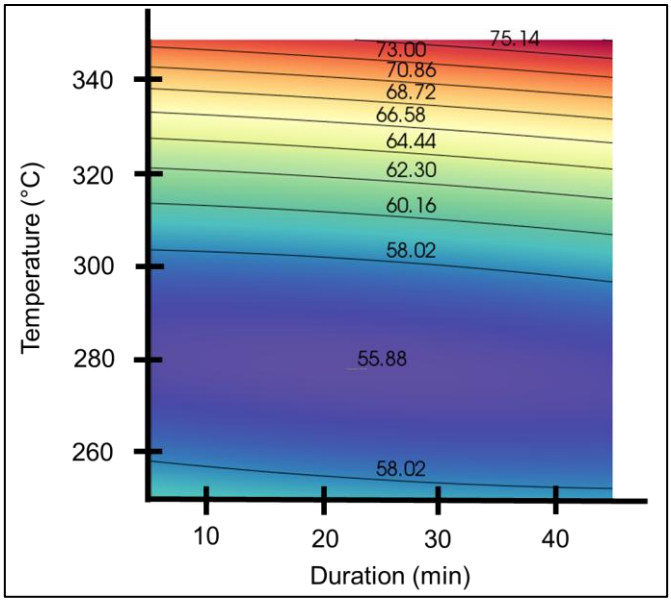

Figure 4.23 - Second-degree polynomial surface response for AIP in solid pellet (% TP), based on the experimental design reported in Table 2.1, as a function of temperature (°C) and treatment duration (min), expressed by Equation 4.8 (coefficients reported in Table D.10).

The set of results presented in this section allows to support the proposition for an overall mechanism for P conversion during HT of SS illustrated in Section 1.6.5. P speciation is controlled by the relative significance of three different group of reactions:

I. **OP mineralization** to soluble PO_4^{3-}, which leads to OP content decrease in the liquid and/or solid phases, and to an increase in P concentration in the liquid phase.

II. **Dissolution of IP** compounds to soluble PO_4^{3-}, which leads to a decrease in the IP content of the solid phase, and to an increase in P concentration of the liquid phase.

III. **PO_4^{3-} (re)-precipitation** under the form of solid metal phosphates, leading to a decrease in P concentration in the liquid phase, and to an increase in the P recovery yield in the solid product[96,123].

Figure 4.24 resumes the mechanism for P conversion developed with the results presented in this section.

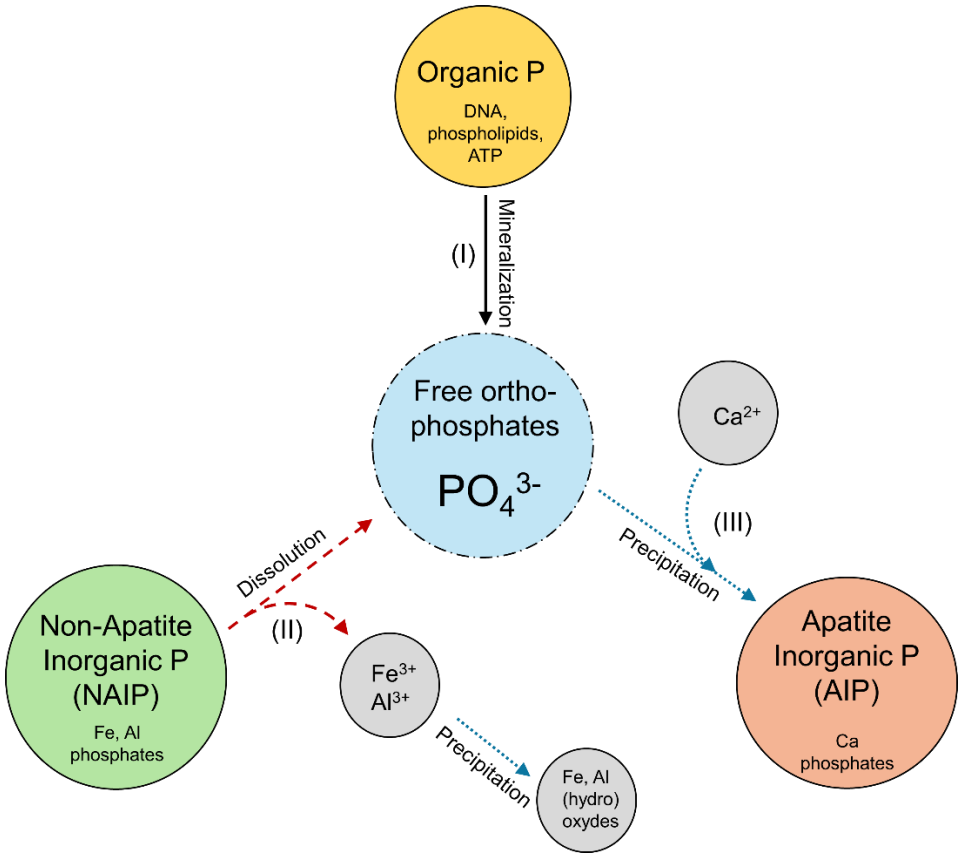

Figure 4.24 - Proposed P mechanism. (I) OP mineralization to soluble PO_4^{3-} (II) Dissolution of Fe and Al P phosphates to soluble PO_4^{3-} (III) PO_4^{3-} (re)-precipitation with Ca^{2+} cations under the form of Ca phosphates. For less severe reactions (250 °C) (I) and (II) are prevalent. At more severe conditions (350 °C) reaction (III) is prevalent.

At 250 °C the product process water has a higher soluble P concentration compared to the digestate feed (from 320 mg L^{-1} to almost 600 mg L^{-1}), indicating that HT at relatively low severities favors OP mineralization (I) and IP dissolution (II) into free phosphates. However, the product pellet, despite being obtained at relatively low temperatures (250 °C), predominantly consists of AIP, contrasting with the P speciation of the feed digestate, whose prevailing P-form is NAIP. This implies that NAIP has been converted to AIP, and thus a partial re-precipitation of phosphates with Ca cations (III). This result is in line with the variations in concentration of soluble Ca and Fe between Centrate A and process water

by-products (Figure 4.9a): the concentration of soluble Ca steeply decrease after the HT treatment, which can be explained with P-Ca compounds precipitation, and the concentration of soluble Fe increases, which is due to NAIP Fe-P complexes dissolution. Longer durations at 250 °C led to a slight increase in soluble PO_4-P, suggesting the prevalence of OP mineralization (I) and NAIP dissolution (II) over AIP precipitation.

At 300 °C PO_4-P concentration starts decreasing, showing that the phosphates precipitation with metallic cations is becoming prevalent. Finally, at 350 °C, reaction (III), is the predominant one, specifically phosphates precipitation with Ca^{2+} cations. This is confirmed by the lower PO_4-P process water concentration, the decrease in soluble Ca concentration and the strong increase in the AIP relative fraction. Another element that confirms calcium phosphate precipitation as the prevalent reaction mechanism, is the Ca/P molar ratio in process water (Figure 4.19), which remains constant around 0.1 regardless of process severity, despite decreases in both soluble P and Ca concentrations. This suggests a correlation between the precipitation of the two elements, following a specific molar ratio.

4.7. Options for products valorization and disposal

As already discussed in Section 3.4 for Sludge A and B, an evaluation of the environmental compatibility of the solid pellet by-products could be made by assessing their properties for potential use as macronutrient inorganic fertilizers by comparing these properties with the 2019/1009 regulation on the market of EU fertilizing products and amending regulations[181].

Table 4.7 shows the macronutrients contents guidelines and the heavy metals limits from the regulation, and the respective ranges measures in the solid pellets. All solid pellet by-products meet the guidelines for minimum macronutrients values. Regarding heavy metals, all pellets meet all the limits suggested by the regulation, except for Cu. For the exploitation of the solid pellets as commercial macronutrient inorganic fertilizers, it is necessary to reduce the amount of Cu. It can be realized by reducing Cu amount already in the sludges as suggested in Section 3.4: exceeding Cu content could be reduced by an upstream approach, limiting its dispersion into the environment in the first place. Further investigations must be conducted to ensure that the solid pellet by-products are compatible for fertilizer use according to this regulation guidelines, specifically to assess biuret ($C_2H_5N_3O_2$), perchlorate (ClO_4^-) and hexavalent chromium (Cr VI). Pathogens (*Salmonella*, *Escherichia Coli*) content should not be a problem as the high temperatures and pressures in the HT treatment should have resulted in complete microorganisms' sterilization. Concerning process water, the obtained by-products are not compatible with discharge into the environment due to their high COD concentration, which ranges from 18 g O_2 L^{-1} to 31 g O_2 L^{-1}, exceeding the limit prescribed by the European Council Directive of May 21, 1991[182], which is 0.125 g O_2 L^{-1}. Furthermore, the concentration of TP and

TN is likely incompatible with direct discharge into the environment, as it could lead to eutrophication phenomena.

Table 4.7 - Comparison between the macronutrients guidelines and the heavy metals limits prescribed by the 2019/1009 regulation[181], and the respective ranges observed for solid pellet by-products. **X** = it does not respect the guidelines. ✓ = it respects the guidelines. Compositions in solid pellets are expressed on a dry basis.

		Guidelines	**Solid pellet by-products**	
		*minimum value %**	Composition %	Compatibility
Macronutrients	N		2.9 - 3.9	
	P_2O_5		12.2 - 16.6	
	K_2O		0.4 - 0.7	
	MgO		1.7 - 2.9	
	CaO		8.0 - 9.4	
	SO_3		2.1 - 2.9	
	Sum	18	27.3 - 36.3	✓
Contaminants		*limit mg kg^{-1}**	Composition mg kg^{-1}	Compatibility
	Cd	60**	13.5 - 15.4**	✓
	Hg	1	0.2 - 0.3	✓
	Ni	100	32.3 - 64.8	✓
	Pb	120	56.5 - 61.1	✓
	As	40	2.6 - 6.0	✓
	Cu	600	907 - 1056	X
	Zn	1500	1184 - 1407	✓

*guidelines and limits from [181]. P_2O_5 = P/0.436; K_2O = K/0.830; MgO = Mg/0.603; CaO = Ca/0.715; SO3 = S/0.4. **expressed as mg kg^{-1} P_2O_5.

Additional treatments to reduce these contents must be realized before releasing the process water into the environment. Possible solutions could include wet oxidation[184] and precipitation in the form of Ca phosphate, struvite[185] and/or K-struvite[211].

However, struvite precipitation requires equimolar quantities of N, P and Mg to be effective. N/P molar ratio in process water ranges from 19 up to 67 (Figure 4.19c), meaning that even if all P is precipitated as struvite, a large amount of N would remain in solution. Besides, Mg/P molar ratio range is 0.02 - 0.07 (Figure 4.19a), meaning that additional Mg should be added to precipitate all P. An alternative would be to precipitate K-struvite, characterized by a K atom in place of the ammonium ion. The K/P molar ratio ranges from 0.5 to 1.4 (Figure 4.19b), so not all P would be precipitated, and Mg would still need to be added. Another disadvantage of this method is that it does not allow for N precipitation. Furthermore, the precipitation of Ca phosphate is also challenging because the moles of Ca in process water are two orders of magnitude lower than the moles of P (Figure 4.19a). Alternatively, process water can be recirculated in the anaerobic digester[212–214] or used as a medium for microalgae cultivation[215].

4.8. Thermal profile investigation

A preliminary simple analysis of the thermal profile of the HT treatment is given by examining the variation in process parameters (temperature and pressure) over time. Figures F.1, F.2, and F.3 (Annex F) show the evolution of key temperatures (reactor internal temperature, heating coil temperature, and set temperature) and pressure recorded during the experiments conducted respectively at 250 °C, 300 °C, and 350 °C, for a duration of 15 min. The reactor internal temperature shows an initial slow increase due to the feed and the reactor's metal body thermal inertia, followed by a linear phase. Then, specifically for experiments conducted at T_{set} of 250 °C and 300 °C, an exothermic phenomenon is detected, as a sharp temperature rise occurs around 165-170 °C, resulting in a 30-40 °C jump within a few seconds, before returning to a relatively linear trend. Finally, as the target temperature is approached, the rate of temperature increase slows down and it stabilizes around the set value.

In Figures F.1b, F.2b and F.3b the temperature profile is shown in detail within the exothermic phenomenon region, where the sharp temperature increase was observed, alongside with the heating rate, defined by Equation 4.9:

$$\frac{dT}{dt}\left(\frac{°C}{min}\right) = \frac{\Delta T}{\Delta t} \tag{4.9}$$

Where ΔT (°C) corresponds to the difference in the reactor internal temperature values registered at two consecutive instants t_i and t_{i-1} (min), which constitute the time step Δt = 2 s. This quantity can be interpreted as the discretization of the first derivative of temperature with respect to time.

For the T_{set} of 250 °C and 300 °C experiences (Figures F.1b and F.2b), the heating rate is initially low and roughly constant (6 ± 4 °C min^{-1} for T_{set} of 250 °C, and 5 ± 4 °C min^{-1} for T_{set} of 300 °C). Around 165-170 °C, there is a peak of several hundred °C min^{-1} that lasts a few seconds, before stabilizing again to values around 0-10 °C min^{-1}. This behavior denotes an instantaneous exothermic phenomenon. Interestingly, in the experiment conducted at 350 °C (Figure F.3), this phenomenon exhibits different characteristics. There isn't a sharp temperature increase around 165 -170 °C, but a disturbance in the linear temperature increase trend has been observed between 130 °C and 180 °C. The heating rate, initially comprised between 0-10 °C min^{-1}, increases up to 60 °C min^{-1}, and then oscillates between positive and negative values around 170-190 °C, before stabilizing again around 0-10 °C min^{-1}. Under these conditions, the exothermic phenomenon is therefore less abrupt. It occurs over a longer period (4 min). Additionally, there is a mechanism that dampens the generated heat, as indicated by the oscillation of the heating rate between positive and negative values.

The three experiences have been realized using the same amount (110 g) of feed (Sludge A) and the same mixing rate (700 rpm), the main difference being the initial pressure, varied in order to obtain a working pressure of 18 MPa in correspondence of set temperature. The reactor is in fact pressurized with 7.4 MPa of N_2 for the 250 °C treatment, with 4.7 MPa of N_2 for the 300 °C one, while for the 350 °C treatment the

reactor is simply inertized with N_2 without further pressurization. The initial pressure is therefore the parameter that plays a central role in influencing these exothermic phenomenon characteristics.

Since these three experiments are characterized by different target temperatures, the PID controller responds differently to the sudden temperature increase. For example, in the case of T_{set} equal to 250 °C, since the exothermic phenomenon approaches the target temperature, the controller responds with a sharp cooling by injecting air in the reactor jacket: this can be observed in the heating coil temperature decrease. This cooling also occurs for T_{set} of 300 °C, but it is less abrupt, while it is not observed for the 350 °C treatment. To compare the effect of pressure while excluding the influence of different thermal power provided to the reactor, three experiments are conducted with the same feed mass (110 g), same mixing rate (700 rpm), same initial temperature (17 °C) and same target temperature (250 °C), varying only the initial pressure (0 MPa, 2 MPa, and 7 MPa). The thermal profiles of these experiments are available in Figure 4.25.

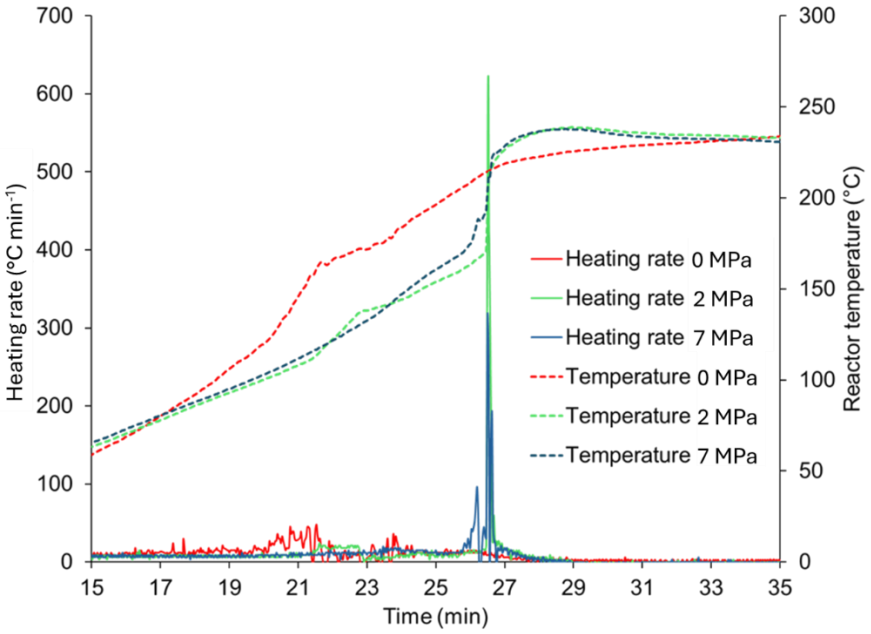

Figure 4.25 - Reactor internal temperature and heating rate (as defined in Equation 4.9) for three HT treatments realized with the same feed mass (110 g), same mixing rate (700 rpm), same initial temperature (17 °C) and same target temperature (250 °C), at three increasing initial pressures (0 MPa, 2 MPa, 7 MPa).

These profiles confirm that pressurizing the reactor results in a more abrupt exothermic phenomenon, characterized by a sharp temperature increase in the 2 MPa and 7 MPa experiments. In contrast, the non-pressurized experiment shows a milder response, distributed over a longer duration.

To characterize this exothermic phenomenon more accurately, Sludge A behavior has been analyzed with differential scanning calorimetry (DSC) (Section 2.5). The digestate was first dried at 105 °C, ground, and sieved to obtain a more homogeneous sample. Subsequently, 200 to 600 mg of dry sludge were placed into the calorimeter cell, with the

necessary amount of water added to achieve the desired % of dry matter, resulting in a total mass of approximately 2000 mg.

The technique used, the "exhaust method", is detailed in Section 2.5 and involves subjecting the sample twice to the same program. Figure 4.26 shows an example of a DSC experience realized on a 20% DM sample (400 mg dried sludge + 1600 mg water) with an initial pressure of 4.7 MPa. As it can be clearly seen, the heat flux (W kg^{-1}) associated with the first run (q_1) is higher than the one related to the second run (q_2), confirming the presence of an exothermic (set of) reaction(s) that does not take place in the second run on the exhaust sample.

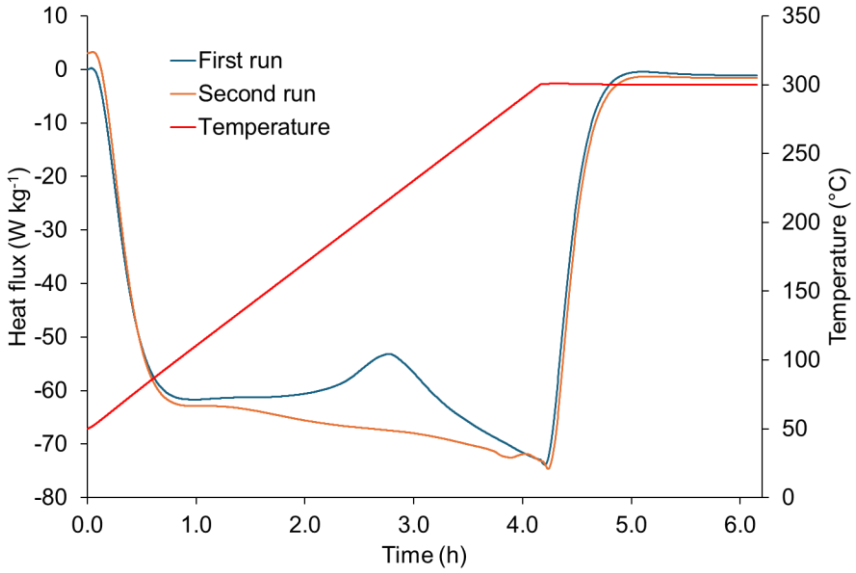

Figure 4.26 - Heat flux (W kg^{-1}) of a DSC experience realized on a 20% DM sample (400 mg dried sludge + 1600 mg water) with an initial pressure of 4.7 MPa, using the "exhaust method" described in Section 2.5.

The quantification of the heat flux purely associated to the exothermic reaction (q_{HT}) is realized by subtracting the thermal profile of the second run from the one of the first run (Equation 2.21). Figure 4.27 shows the different q_{HT} for three DSC analysis realized using 2 g of sludge 20% DM with respectively no pressurization, 4.7 MPa and 9.4 MPa of N_2. q_{HT} is expressed as W kg^{-1} of dry matter.

As shown in Figure 4.27, the two experiments conducted under pressure exhibit very similar curves, peaking at 205 °C with a maximum heat flow rate of 68 W kg^{-1} for the sample at P_{start} = 4.7 MPa, and 75 W kg^{-1} for the sample pressurized at 9.4 MPa. The DSC analysis of the non-pressurized sample yields a curve with a similar shape to the others (peaking at 207 °C), but with lower heat flow values (maximum of 44 W kg^{-1}). This curve also shows more pronounced oscillations, suggesting thermal fluctuations within this temperature range.

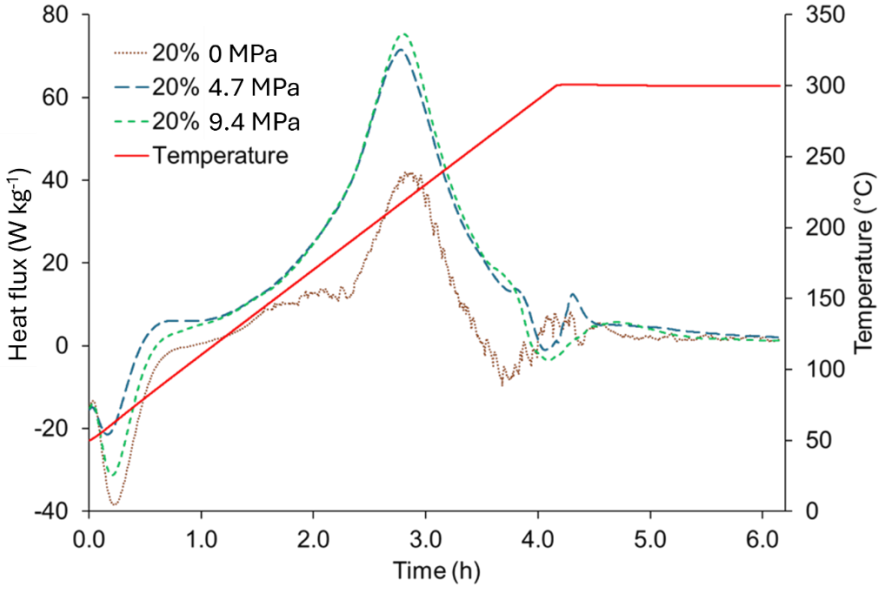

Figure 4.27 – Heat flux of three DSC analysis realized using 2 g of sludge 20% DM with respectively no pressurization, 4.7 MPa and 9.4 MPa of N_2. q_{HT} is expressed as W kg^{-1} of dry matter.

An additional investigation has been conducted by performing a DSC analysis on three samples with the same initial pressure (9.4 MPa) but increasing solid-to-water ratio. The results, shown in Figure 4.28, suggest an absolute heat of reaction which is directly proportional to the amount of solid matter inserted into the cell, therefore the curves representing the evolution over time of the thermal flow expressed in W kg^{-1} of dry matter are relatively similar, showing more or less the same amplitude, peak position and peak height.

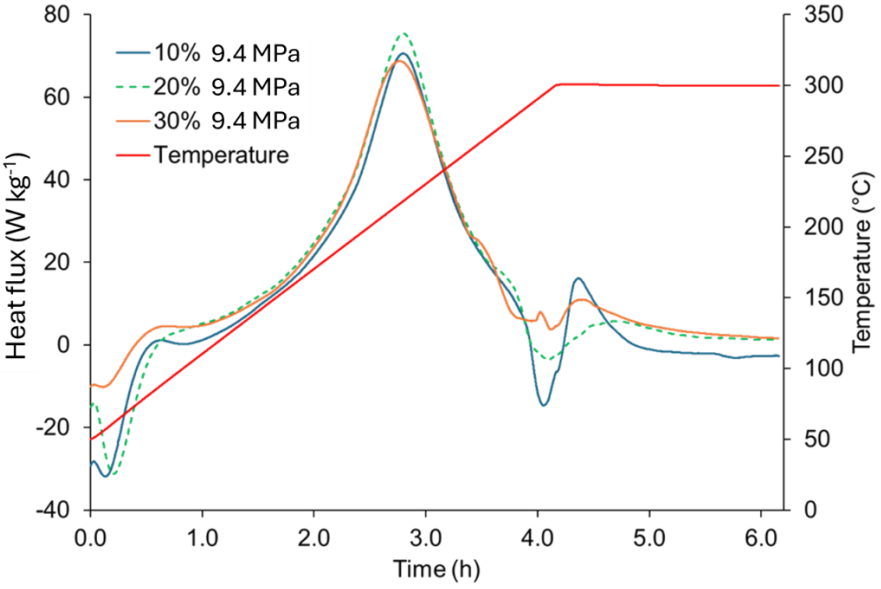

Figure 4.28 - Results of three DSC analysis realized using 2 g of sludge with varying solid loading (10%, 20%, 30% DM) with 9.4 MPa of N_2. q_{HT} is expressed as W kg^{-1} of dry matter.

Notably, while these curves peak around 205 °C (the temperature where the exothermic phenomenon was detected in the reactor), no sudden temperature spike linked to rapid reactions was observed, unlike in the batch reactor. Instead, the reactions driving the exothermic phenomenon occur gradually over a prolonged period, lasting more than 3 hours. However, it's crucial to highlight that the conditions in the batch reactor and those in the calorimeter are not equivalent. Primarily because the reactor's heating rate is more than 10 times faster. Moreover, DSC analysis does not allow mixing conditions that could influence the thermal profile and kinetics of the exothermic phenomenon in the batch reactor.

The enthalpies associated with the described DSC experiences are reported in Table 4.8, together with the peak heat flux (W kg^{-1}) and the temperature and time associated with the peak.

The enthalpies of HT treatments realized on the 20% DM Sludge A sample increase with increasing initial pressure, with 191 kJ kg^{-1} (in dry basis) of produced heat in autogenous conditions, 287 kJ kg^{-1} with an initial pressure of 4.7 MPa, and 337 kJ kg^{-1} in double the pressure. If expressed on dry ash-free basis, these values are respectively 246 kJ kg^{-1}, 372 kJ kg^{-1} and 436 kJ kg^{-1}. The peak position is always around 205-207 °C, but the maximum heat flux also increases with a greater pressurization, passing from 44.3 W kg^{-1} with no pressurization, up to 75.1 W kg^{-1} with Pstart = 9.4 MPa.

Changing the solid loading from 10% to 30% does not lead to a significative trend: measured enthalpies are measured to be around 300-340 kJ kg^{-1} (380-440 kJ kg^{-1} on a dry ash-free basis), and the peak is always observed around 206 °C. The results suggest that the 20 %DM HT treatment allows to maximize both the enthalpy and the maximum heat flux, but there is not enough data to assess the significance of this result.

Table 4.8 - Enthalpy, peak temperature, time and intensity for the DSC experiences realized at three different initial pressures (0, 4.7, 9.4 MPa) and solid loading (10%, 20%, 30%). Enthalpy and heat flux are expressed as kJ kg^{-1} and W kg^{-1} of dry matter.

Sludge A 20 % DM (400 mg dry sludge + 1600 mg water)					
Initial pressure (MPa)	**Reaction enthalpy (kJ kg^{-1})**		**Peak temperature (°C)**	**Peak time (h)**	**Heat flux peak (W kg^{-1})**
	Dry basis	**Dry ash-free basis**			
0	-191	-246	207.5	2.82	44.3
4.7	-287	-372	205.1	2.78	67.8
9.4	-337	-436	206.4	2.80	75.1
Sludge A 9.4 MPa N_2					
Dry matter (%)	**Reaction enthalpy (kJ kg^{-1})**		**Peak temperature (°C)**	**Peak time (h)**	**Heat flux peak (W kg^{-1})**
	Dry basis	**Dry ash-free basis**			
10	-310	-401	206.5	2.80	71.7
20	-337	-436	206.4	2.80	75.1
30	-297	-384	204.5	2.77	65.5

Previous works have already examined the thermal profile and kinetics of sludge/digestate HTC. In particular, Pecchi et al.[158] have investigated the heat release rate profile of digestate HTC using High Pressure Differential Scanning Calorimetry. HTC

has been realized with a maximum temperature of 250 °C in autogenous inert conditions. Solid loading corresponds to 11%. The analysis allowed to characterize an exothermic reaction lasting for more than 2 h, with a peak in correspondence of the maximal temperature (250 °C) of around 200 W kg^{-1}, notably higher than the values obtained in this work, which could be explained by the higher heating rate (5 °C min^{-1}). The total enthalpy is however equal to 490 kJ kg^{-1} of dry digestate (670 kJ kg^{-1} on dry ash-free basis), comparable to the results of this work.

The exothermicity of biomass HTC has been related to the complex scheme of reactions which the organic matter undergoes, described in Section 1.4 (hydrolysis, dehydration, decarboxylation, polymerization, and condensation)[65]. Ischia et al.[159] suggests that the overall exothermicity could result from the balance of endothermic reactions (isomerization and dehydration to 5-HMF) and exothermic reactions (5-HMF degradation into lactic and formic acid and aromatization). Titirici et al.[216] attribute the exothermicity to carbohydrates dehydration.

In our work, the hydrolysis of biopolymers was observed as early as 250 °C, and at 300 °C, the hydrolysis of carbohydrates is virtually complete (Section 4.5.2). The oligomers resulting from this hydrolysis undergo dehydration, decarboxylation[52,60], polymerization[52], and aromatization[52,60] reactions, leading to the production of aromatic clusters and an increase in light aliphatic fractions, as demonstrated by the results of the ^{13}C solid-state NMR analysis and explained in Section 4.5.2. The overall set of these reactions is therefore likely at the basis of the overall HTC exothermicity.

No studies have specifically investigated the effect of pressure on HTC thermal profile. Preliminary results suggest that pressurizing the system increases the thermal energy generated by the HT treatment.

Altering the pressure obviously modifies the thermal conductivity and ionic product of subcritical water, significantly increasing the reaction rate[217]. Moreover, some authors[60,218] propose that using higher pressure enhances the kinetics of certain reactions occurring during the HT treatment of biomass, as higher water pressure increases the impact of the aqueous environment on the thermochemical decomposition of biopolymers[218]. In two different works Yu et al.[218,219] showed that high-pressure water promotes the breaking of hydrogen bonds and the activation of C-H bonds in cellulose, catalyzing dehydration, and facilitates the HT transformation of pectin, enhancing carbonization, dehydration, and aromatization reactions.

Another phenomenon that should not be excluded or underestimated is related to the reduced amount of water evaporation under pressurized conditions in batch systems. When HT treatment is conducted under autogenous conditions, the liquid-vapor system is at saturation, and the developed pressure is close to the saturation pressure of water at the corresponding temperature. In these conditions, a portion of the thermal energy produced is used to vaporize some of the water until vapor saturation is reached. This phenomenon could explain why the thermal flux obtained under autogenous conditions shows more pronounced fluctuations (Figure 4.27), which would be associated with local phenomena of water evaporation and condensation. Pressurizing the system allows for a

greater amount of water to remain in the liquid state, thereby preventing thermal energy from being used for phase change.

To characterize the relative importance of the observed exothermic phenomenon in order to assess whether it can actually lead to a considerable energy saving, it is necessary to quantify the energy required to perform the hydrothermal treatment on the sludge sample. A rough estimate of this quantity is provided by equation 4.10.

$$Q_{req} = (1 - w_{solid})Q_{water} + w_{solid} Q_{solid} \quad (4.10)$$

Where Q_{req} is the energy required to heat the sludge sample from 50 to 300 °C (kJ kg^{-1}), Q_{water} is the energy required to heat the water (kJ kg^{-1}), Q_{solid} is the energy required to heat the dried sludge (kJ kg^{-1}) and w_{solid} is the mass fraction of solid matter in the sludge sample. Q_{water} can be calculated according to equation 4.11:

$$Q_{water} = \left(U_{water,300°C} - U_{water,50°C}\right) \quad (4.11)$$

Where $U_{water,50°C}$ is the massic internal energy of liquid water at 50 °C and atmospheric pressure (kJ kg^{-1}) and $U_{water,300°C}$ is the internal energy of liquid water at 300 °C and saturation pressure (kJ kg^{-1}). The water massic internal energies are calculated using the National Institute of Standards and Technology (NIST) Thermophysical Properties of Fluid Systems database[220]. Q_{water} can be calculated according to equation 4.12:

$$Q_{water} = \int_{50\,°C}^{300\,°C} c_v \, dT \quad (4.12)$$

Where c_v is the specific heat capacity at constant volume of the dried sludge (kJ kg^{-1}K^{-1}), which is a function of temperature, according to the linear relation[221] reported in equation 4.13:

$$c_v = 1077 + 3.2\,T \quad (4.13)$$

Using these equations, it is possible to estimate that the energy required to heat Sludge A with 10%, 20%, and 30% dry matter content is respectively 1052 kJ kg^{-1}, 981 kJ kg^{-1}, and 909 kJ kg^{-1}. As shown in Table 4.9, Using the mass reaction enthalpies obtained with an initial pressure of 9.4 MPa, it can be estimated that the energy generated by the exothermic reaction during the hydrothermal treatment of Sludge A corresponds to 3%, 7%, and 10% of the energy required to heat the system from 50 to 300 °C.

Table 4.9 - Energy analysis of DSC experiments. First column: total energy required to heat the sample. second column: reaction enthalpy; third column: energy supplied to the system in the form of reaction heat (%).

Solid loading	Energy required to heat the sludge (kJ kg^{-1})	Reaction enthalpy at initial pressure of 9.4 MPa (kJ kg^{-1} of dry matter)	Thermal energy generated by the exothermic reaction (%)
10%	1052	310	2.9 %
20%	981	337	6.9 %
30%	909	297	9.8 %

Although the result suggests the possibility of a significant energy saving (up to 10% of the energy supplied to the system for sludge with 30% dry matter), it is important to note that this value corresponds to specific initial pressurization conditions. In cases where the treatment is conducted under saturated conditions, the thermal phenomenon is less intense, as previously explained in this section. While pressurization allows for an intensification of the thermal energy recovered, it comes with a considerable cost and is not always technically feasible, especially in continuous-flow systems. Moreover, this energy recovery in the form of heat could come at the expense of the properties of the reaction products and their calorific value.

4.9. Conclusion

In this chapter the effect of temperature and treatment duration on HT by-products characteristics and P speciation have been exposed.

Screening DOE shows that increasing temperature and treatment duration reduce the solid pellet mass, increase process water amount, but also reduce process water TDS (%) and increase solid pellet dry mass (%), effectively leading to a better by-products separation and increased product hydrophobicity.

Response surface DOE shows that higher temperatures have a prevalent effect over treatment duration, leading to a TSRY% reduction by enhancing inorganic material dissolution and organic matter degradation.

The fate of organic species has been specifically characterized by ^{31}C solid-state NMR spectroscopy, showing a complete biopolymers degradation already at 300 °C, through hydrolysis, dehydration, and decarboxylation reactions, producing small carbon chains with paraffinic C, volatile fatty acids, and organic acids. A process severity increase has been also associated with an improved aromatization and the formation of hydrochar clusters.

The HT product obtained at higher process severity consists of an aromatic fraction (the hydrochar) and an alkyl fraction (the biofuel), which are highly hydrophobic, explaining the improved by-products separability.

The organic species conversion mechanism is further supported by the reduction of solid pellet O/C and H/C molar ratio, confirming the role of dehydration and decarboxylation reactions in HT treatment.

This set of reactions is also at the basis of HT treatment overall exothermicity. DSC of the HT treatment has in fact allowed to quantify the global HT enthalpy of reaction between 190 and 340 kJ kg^{-1} of dry sludge (250 – 440 kJ kg^{-1} on a dry ash-free basis), depending on solid loading and initial pressure. The pressurization of the system has indeed been correlated with a higher reaction enthalpy, due to the improved impact of water pressure on the thermochemical decomposition of biopolymers and/or the reduced water evaporation. It has been estimated that in a HT treatment conducted under high initial pressure and high solid loading conditions, up to 10% of the required energy can be self-generated by the exothermic reaction.

Hydrolysis of carbohydrates releases organic acids into the process water, causing a pH decrease in milder treatments (250 °C). Conversely, at higher temperatures, protein degradation releases NH_3, which protonates to NH_4^+, thereby increasing pH. Increased process severity is also linked to higher alkalinity, attributed to raised HCO_3^- concentration in the solution.

A temperature and duration increase has been correlated with a N, H and O content decrease in the HT solid pellet by-product, accompanied by an ash content increase, explained by organic matter degradation and a concomitant accumulation of mineral matter in the solid product. Coherently, metals and heavy metals contents in the solid pellet generally increase with increasing process severity.

A comprehensive analysis of both process water and solid pellet by-products allowed to define a P conversion mechanism scheme. HT at relatively low severities favors OP mineralization and IP dissolution into free phosphates, leading to higher soluble P concentration compared to the digestate feed. The product pellet predominantly consists of AIP, while P in Sludge A is mainly NAIP. This implies that there has been a conversion from NAIP to AIP, and a re-precipitation of phosphates with Ca cations. Soluble Ca concentration steeply decreases after the HT treatment at 250 °C, which can be explained with P-Ca compounds precipitation, while soluble Fe concentration increases, due to NAIP Fe-P complexes dissolution.

At 300 °C PO_4-P concentration starts decreasing, showing that the phosphates precipitation with metallic cations is becoming prevalent. Finally, at 350 °C, phosphates precipitation with Ca^{2+} cations becomes the prevalent reaction, as confirmed by the low PO_4-P concentration and the strong increase in the AIP fraction.

Ca/P molar ratio in process water remains roughly constant around 0.1 regardless of process severity, despite decreases in both soluble P and Ca concentrations. This suggests a correlation between the precipitation of the two elements, following a specific molar ratio, further confirming that P precipitation with Ca to form Ca phosphate is the predominant mechanism at more severe conditions.

Regarding potential use as macronutrient inorganic fertilizers, all solid pellet by-products meet minimum macronutrient value guidelines and, except for Cu content, generally comply with heavy metal limits. However, further investigations are needed to confirm that the solid pellet by-products meet regulatory guidelines for fertilizer use, assessing biuret, perchlorate, and hexavalent chromium contents. The process water by-product is unsuitable for environmental discharge due to high concentrations of TN, TP, and COD, indicating the need for additional treatments.

In the context of this work, which aims to integrate energy recovery and mineral fraction recuperation, the results of this chapter show that employing a more severe HT process facilitates P recovery in the solid product and produces hydrochar with higher aromaticity and lower H/C and O/C ratios, resembling higher rank chars. However, the solid product cannot be simultaneously utilized for energy valorization and as a fertilizer product.

In the perspective of HTL, extracting the biofuel from the by-products by using an organic solvent is the first interest, but this additional step revealed to be impractical due

to Sludge A low solid loading, resulting in insufficient solid product quantities for both biofuel extraction and comprehensive solid characterization.

To evaluate bio-oil yield and complement P recovery in the solid phase, a higher dry mass sludge (Sludge B) was selected. This choice aligns with literature results indicating that higher solid loading ratios enhance P yield in the solid phase[78,98,125]. Results comparing the use of Sludge B versus Sludge A are therefore discussed in Chapter 5.

It is important to note that in the experiments conducted in this chapter, complete P precipitation was not achieved even under the most severe conditions. For instance, at 350 °C for 45 min, a residual concentration of P remained in the process water at 150 mg L^{-1}, corresponding to 6% of feed P. For all process water by-products, Ca/P, Fe/P and Mg/P molar ratios are always lower than 1, indicating that the available Ca^{2+}, Fe^{3+}, and Mg^{2+} concentrations in solution are insufficient for complete orthophosphate precipitation.

Our goal is to recover all P in the solid phase for optimal valorization. As explained in Section 1.6.4, a critical parameter influencing P precipitation is the stoichiometric amount of certain metals, particularly Fe and Ca, which form stable complexes and precipitates.

Sludge B contains a higher amount of Fe compared to Sludge A, as detailed in Section 3.3.1, thus the effect of increasing the Fe/P molar ratio can be examined by comparing results between Sludge A and B products (Chapter 5).

Ca/P molar ratio in solid pellet by-products is roughly 0.7, meaning that not more than 70% of total P can precipitate with the available Ca, assuming the formation of dicalcium phosphate ($CaHPO_4$). Under the most severe conditions, it was indeed observed that AIP corresponds to about 70% of the TP. To achieve higher amounts of AIP, it is therefore necessary to introduce additional Ca into the sludge, to increase the molar ratio of Ca/P to at least 1. This means that the stoichiometry of the key metals involved in P speciation is a crucial parameter in defining the conversion pathway of P during HT treatments. For this reason, in Chapter 6, the effect of increasing the Ca/P molar ratio by adding an additive (CaO) directly into the HT reactor will be specifically investigated. Additionally, the biofuel yield will be quantified, offering a comprehensive perspective on the potential synergy between energy and mineral recovery.

5. Effect of feed characteristics on by-products characteristics and phosphorus speciation

5.1. Introduction

This chapter presents how feed characteristics and composition affects HT by-products and P speciation by comparing the HT products from Sludge A (Chapter 4) with those from Sludge B under the same temperature and duration conditions. Sludge A and B's characteristics are thoroughly described in Chapter 3. After an initial presentation of the by-products' distribution and general characteristics, the detailed properties of the process water and solid pellet by-products will be interpreted. P conversion results are compared based on the sludge used as feed and interpreting them according to the sludge composition in terms of P, Fe, Ca, and other metals that may play a role in P speciation.

As shown in Figure 2.1, Sludge B is obtained in the WWTP by mixing SS digestate and a tertiary sludge from a dephosphatation tank where $FeCl_3$ and an organic flocculant are added. Therefore, Sludge B is richer in P, Ca, and Fe compared to Sludge A (Section 3.3.1). It will therefore be interesting to evaluate the effect of these additives on P conversion, residual P quantity in process water, and relative amounts of NAIP and AIP in the solid pellet.

5.2. Materials and methods

Six HT treatments for Sludge B using six different combinations of temperature and duration were realized as indicated in Table 5.1. The objective is to compare these results with the respective experiments conducted under the same conditions on Sludge A (experiments 2,3,4,5,8,9 from Table 2.1).

Table 5.1 - HT parameters for Sludge B treatments selected to compare the results with Sludge A products.

Temperature (°C)	Treatment duration (min)	Severity (-)
250	15	0.24
250	45	0.30
300	5	0.35
300	15	0.43
350	15	0.71
350	45	0.88

The HT treatment experiments have been realized by introducing around 85 g of Sludge B in the same small volume (0.2 L) batch described in Section 2.2.1. A smaller mass than the experiments conducted with Sludge A is introduced, as Sludge B has a lower density and higher porosity than Sludge A. 85 g approximately occupied the same volume (70% of the internal reactor volume) as 110 g of Sludge A. The compacting of the sludge has been tested to include a larger volume, but overly compacted sludge caused mixing control issues in the initial treatment phase. All experiences have been realized with a N_2 pressure of 18 MPa in correspondence of the operative temperature, and with a mixing rate of 700 rpm. The results presented in this work concerning "process water" and "solid pellet" refer to the by-products separated mechanically by centrifugation as explained in Section 2.2.3 without any extraction of the organic phase. The separation and quantification of the organic phase were not performed in this phase due to the limited quantities of by-products.

The process water by-products have been analyzed according to methods and techniques described in Section 2.3, characterizing their main physical properties, alkalinity, solid content, soluble N and PO_4-P concentration, dissolved C, COD, and metal contents. The solid pellet by-products were characterized as described in Section 2.4, quantifying its elemental composition, metal and heavy metal content, and P speciation. The HT severity factor (Section 2.6.3) has been used to better understand the synergistic impacts of temperature and reaction time. Experimental results reported in the discussion are accompanied by the respective propagated uncertainty. Proximate, pH, alkalinity, TN, NH_4-N, COD, PO_4-P analysis and P sequential extractions were performed in triplicates. For each set of analyses, limit of detection and limit of quantification were determined by analysis of blanks. All chemicals used were of analytical grade.

5.3. By-products distribution and general characteristics

Figure 5.1 shows the mass balances distributions for the HT treatments of Sludge A and B, relative to total mass, P, Ca, Fe, Mg and K.

For Sludge B, the total mass loss between the feed and the recovered product is between 5-8%, while it is 3-7% for Sludge A. Therefore, the use of one sludge rather than the other has not been associated with significant difference in the global mass balance.

Concerning mass balances for specific elements, for Sludge B, 84-104% of P is recovered in products with respect to feed P, 85-103% of Ca, 76-100% of Fe, 88-117% of Mg and 71-98% of K. Sludge A presents similar values: 85-108% of P, 80-100% of Ca, 72-91% of Fe, 77-94% of Mg and 78-87% of K.

For both sludges, global mass losses could be linked to gas production, to the evaporation of water and volatile products at the reactor opening, and to the small amounts of non-recoverable product remaining inside the reactor. By correlating the global mass losses with gas production, as already discussed in Section 4.3, the slightly

higher losses observed in Sludge B compared to Sludge A can be interpreted as a result of increased gas production, which would be directly linked to Sludge B higher solid loading.

As already observed in Section 4.3, the observed discrepancies in P, Ca, Fe, Mg and K mass balances are related to the unrecoverable solid residue left in the reactor and to the relative performance of the aqua regia digestion in extracting these elements from the sludges and the HT pellets.

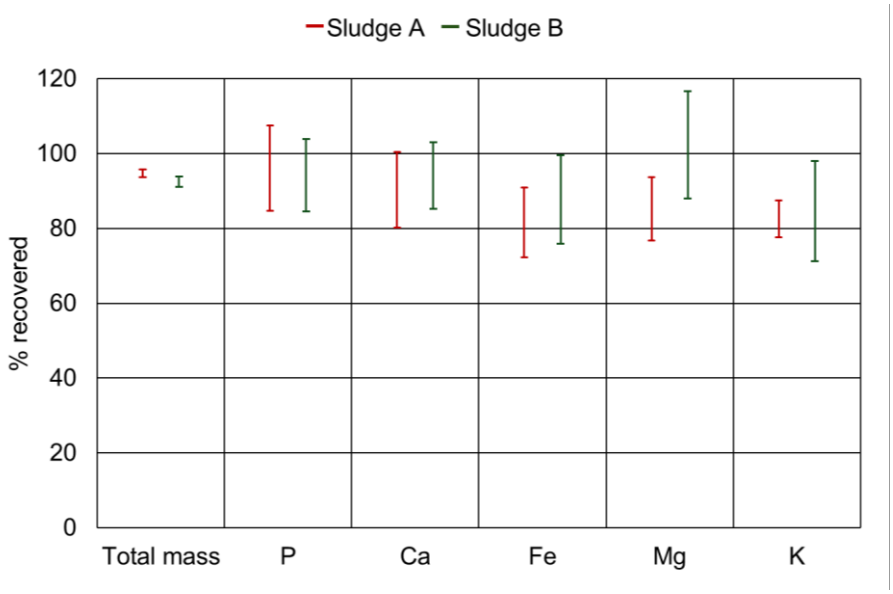

Figure 5.1 - Balances for total mass and P, Ca, Fe, Mg and K, for Sludge A and B HT treatments.

Following the centrifugation of the HT product, process water and a solid pellet are produced. Sludge A has a TS content (7%) that is approximately three times lower than Sludge B (19%). Figure 5.2 illustrates the mass distribution of the HT products from Sludge A and Sludge B, showing the repartition of water and TS between the pellet and the process water after centrifugation. In the case of Sludge B, the centrifugation of the product results in a greater amount of pellet and a smaller amount of process water compared to Sludge A. Nevertheless, in both cases, increasing the process severity leads to an increase in the amount of process water and a decrease in the amount of pellet. Additionally, for both sludges, a more severe process results in a decrease of dissolved solids in the process water and an increase in the TS present in the pellet.

It is evident that for both sludges, the relative amount of TS in process water and TS in pellet decreases with increasing process severity, while the water relative content slightly increases. The TS in the process water decreases significantly with the increase in process severity, while the relative amount of solids in the pellet remains relatively stable. This indicates concurrent biopolymer degradation, salt dissolution, and soluble species precipitation. Additionally, there is a noticeable transfer of water from the pellet to the process water, suggesting more effective separation by centrifugation following more severe treatments. This is also explained by an improved hydrophobicity of HT products with increasing process severity (Section 4.5.2). These effects are apparently more pronounced in Sludge B, likely due to higher solid loading. Figure 5.3 shows the HT

products TSRY% (Equation 2.8) for both sludges, compared with results from literature (listed in Table A.1).

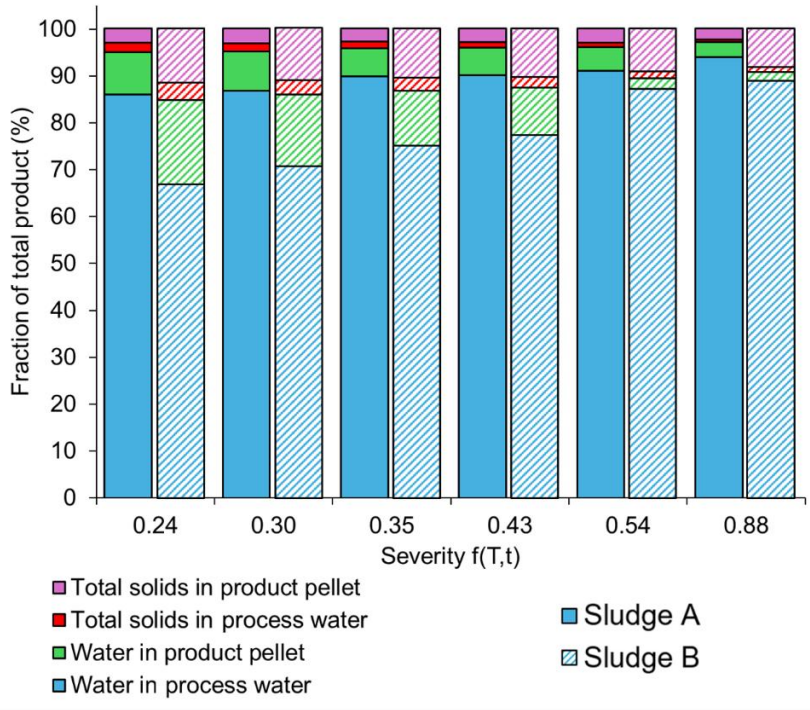

Figure 5.2 - Mass distribution of the HT products from Sludge A and Sludge B showing the repartition of water and TS between the pellet and the process water after centrifugation.

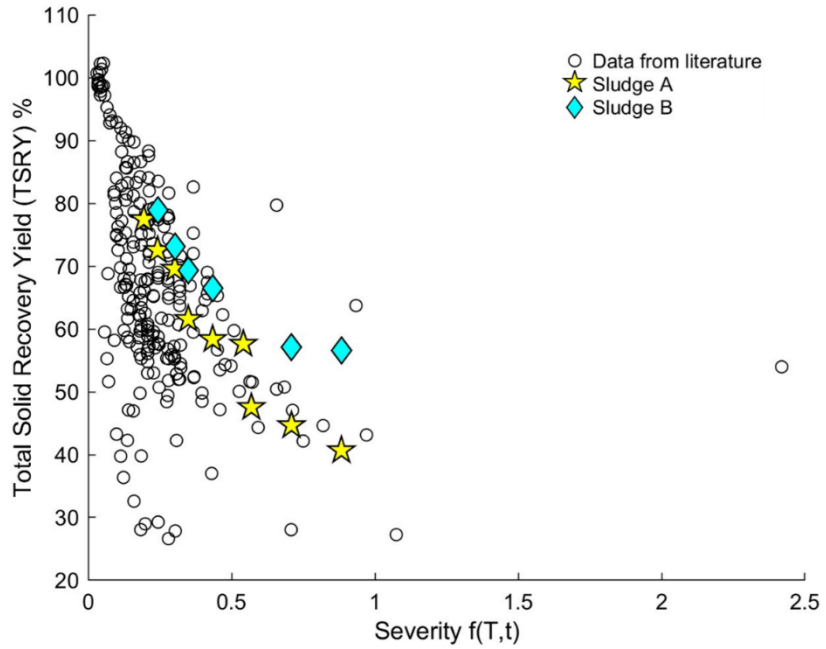

Figure 5.3 - HT products TSRY (Equation 2.8) for both sludges, compared with SS HT treatments Solid Recovery Yield (SRY) results from literature (works listed in Table A.1).

A process severity increase is clearly correlated with a decrease in TSRY%. Products of both sludges follow the general trend observed in literature. However, TSRY% is

higher for Sludge B products compared to Sludge A, probably because Sludge B contains more solid matter[78,98,125]. It has been suggested that the higher water content in Sludge A can promote biopolymers hydrolysis and dissolution, leading to a lower TSRY%[98,125].

The HT treatments of Sludge A and B exhibit a comparable thermal profile, as shown by the heat fluxes in Figure F.4 (Annex F). Two DSC experiences have been realized with the same amount of dried sludge and water, and the same initial pressure, changing only the sludge type. Clearly, the two curves exhibit a very similar shape, with a peak at 205 °C. The curve associated with Sludge B has a slightly higher peak (113 W kg^{-1} on dry ash-free basis instead of 98 W kg^{-1}) and a higher reaction enthalpy at -502 kJ kg^{-1} on dry ash-free basis (in Sludge A it was -436 kJ kg^{-1}). The lack of replication does not allow for the evaluation of the statistical validity of these results, but the similarities in shape, position, and magnitude of the curve suggest that the measured heat flow are related to the same group of reactions or related classes of reactions (hydrolysis, dehydration, decarboxylation).

5.4. Process water characterization

Figure 5.4 compares the main physico-chemical properties of the two sludges HT process waters, specifically pH, alkalinity, NH_4-N content, total soluble N, COD, Total, inorganic and organic soluble C. As seen in Figure 5.4a, for both sludges, process water presents comparable pH values between 7.2 and 8.2. In both cases HT treatment produce a process water with a lower pH compared to the original sludge feed, but for lower severities Sludge B products present a lower pH than Sludge A products, probably due to the release of a greater amount of organic acids following carbohydrates breakdown[62]. Then, for both sludges, higher severities lead to a pH increase until stabilization at around 8, due to nitrogenous organic species degradation into ammonia[81], which counteracts the acidification effect produced by the organic acids release.

For both sludges, increased process severity leads to higher alkalinity in process water (Figure 5.4b). Sludge B process water has higher alkalinity than Sludge A, likely due to a higher concentration of HCO_3^- ions resulting from the greater TS content in Sludge B. This is reflected in the higher TIC concentration (Figure 5.4g) in Sludge B products. Sludge B process water also shows higher concentrations of both TN (Figure 5.4d) and NH_4-N (Figure 5.4c) compared to Sludge A products. Given that both sludges have similar N content (Section 3.3.1), this difference is again attributed to the higher TS content in Sludge B. However, both sludges exhibit similar trends with increasing process severity: TN remains roughly constant (4.5 ± 0.2 g L^{-1} for Sludge A, and 10.8 ± 0.4 g L^{-1} for Sludge B), while NH_4-N increases. This indicates that protein hydrolysis is nearly complete at 250 °C for both sludges and that there is a direct correlation between process severity and the mineralization of N-containing organic fragments (peptides and amino acids) into ammonia. COD (Figure 5.4e) and soluble TC (Figure 5.4f) in process water decrease with increasing process severity for both sludges. The values for Sludge B products are about 2.8 times higher than those for Sludge A, reflecting the higher TS content in Sludge B

(which is also 2.8 times higher than Sludge A's). This pattern is also observed in the TOC concentration (Figure 5.4h).

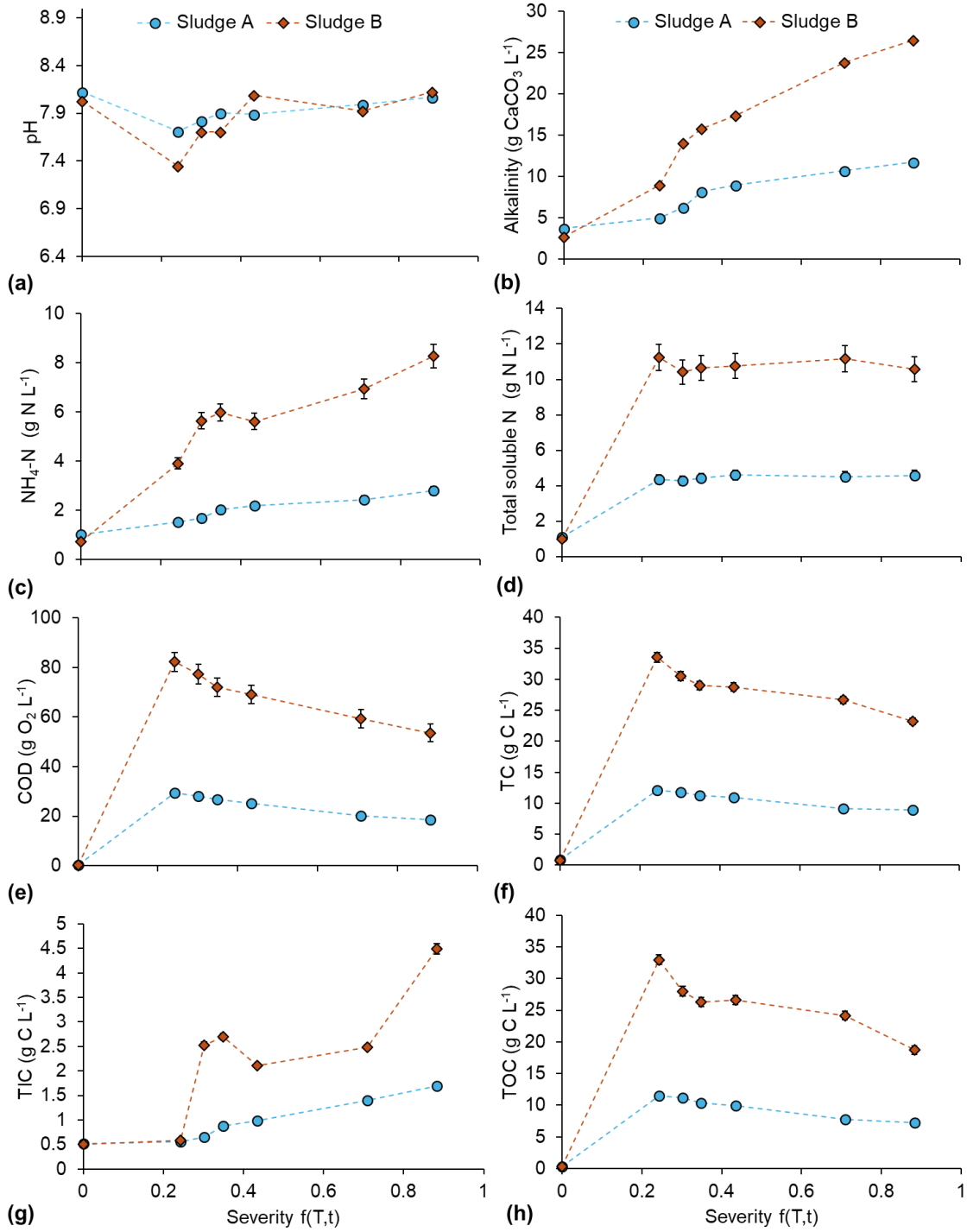

Figure 5.4 - Main physico-chemical properties of the two sludges HT process waters (a) pH, (b) alkalinity (g $CaCO_3$ L^{-1}), (c) NH_3-N (g N L^{-1}), (d) Total soluble N (g N L^{-1}), (e) COD (g O_2 L^{-1}), (f) Total soluble C (g C L^{-1}), (g) TIC (g C L^{-1}), (h) TOC (g C L^{-1}). pH measurement accuracy: ±0.01. Dashed lines are included to facilitate data interpretation. Error bars represent propagated uncertainty.

It is possible to correlate COD, expressed in mol O_2 L^{-1}, with TOC (mol C L^{-1}) for both sludges, revealing a 1:1 ratio between the two parameters (Figure G.1).

Figure 5.5 shows the concentrations of soluble P, Ca, Fe, Mg and K in the HT process water of Sludge A and B, while Figure G.2 (Annex G) shows P, Ca, Fe, Mg and K yields in process water relative to total amounts in the sludge feed. Dissolved P in Sludge B products follows the same trend as Sludge A, with a release of soluble P species into the liquid phase following milder HT treatments (250-300 °C), and a sharp decrease in dissolved P for more severe treatments (350 °C) (Figure 5.5a). At lower severities (0.24-0.43), products from Sludge B show higher concentrations of soluble P than Sludge A (Figure 5.5a), possibly due to lower water content resulting in more P concentrated process water. Additionally, there is a greater absolute amount of OP available for mineralization[98,125]. Nevertheless, at higher severities (0.71-0.88), the concentration of soluble P is lower in Sludge B compared to Sludge A. The presence of higher concentrations of metal cations (mainly Ca^{2+} and Fe^{3+}) allows for a more complete PO_4^{3-} precipitation in the form of inorganic salts. Despite the process water from Sludge B showing a higher concentration of soluble P compared to Sludge A, less than 6% of Sludge B's P is recovered in the process water. In contrast, the process water from Sludge A yields over 20% of P at lower process severities (Figure G.2a). Previous studies have already reported that an increase in the solid-to-liquid-ratio (SLR) leads to less P recovered in process water [97,107,125]. Regardless, for both sludges, an increase in process severity leads to P transfer from process water to solid pellet.

For both sludges, soluble Fe and Ca species follow the same trend: a process severity increase leads to a decrease both in concentration (Figure 5.5b and 5.5c) and in relative amount, compared to the total Ca and Fe present in the feed (Figure G.2b and G.2c). Fe and Ca concentration is higher for the products of Sludge B, once again due to the lower SLR, and the greater amount of Ca and Fe in the feed. A negligible fraction of Ca and Fe is present in soluble form in the products of both sludges (< 1.5%). Under the most severe conditions, corresponding to a temperature of 350 °C, less than 0.2% of Ca and Fe are present in soluble form in process water.

Mg behavior is less straightforward. Although the concentration of soluble Mg in the two sludges is comparable (Figure 5.5d), the HT treatment of Sludge A leads to an initial release of Mg in process water, followed by reprecipitation under more severe conditions. In contrast, for Sludge B, the phenomenon of soluble Mg release was not observed, and the amounts of soluble Mg remain negligible, only slightly increasing at higher temperatures, but remaining lower than those of Sludge A (Figure 5.5d). The same trend was observed for Mg yield in process water (Figure G.2d). Evidently, the smaller amount of water in Sludge B and the presence of higher concentrations of other cations do not favor the dissolution of Mg-containing compounds in process water at milder severities.

K concentrations in the two sludges process water are comparable (Figure 5.5e). In both cases, most of K present in the feed is recovered in process water (Figure G.2e). Due to the high uncertainty of the experimental measurement, it was not possible to suggest specific trends for soluble K for both sludges.

Figure G.3 (Annex G) shows Ca/P molar ratio and Fe/P molar ratio in the process water obtained as a product of the HT treatment of Sludge A and Sludge B.

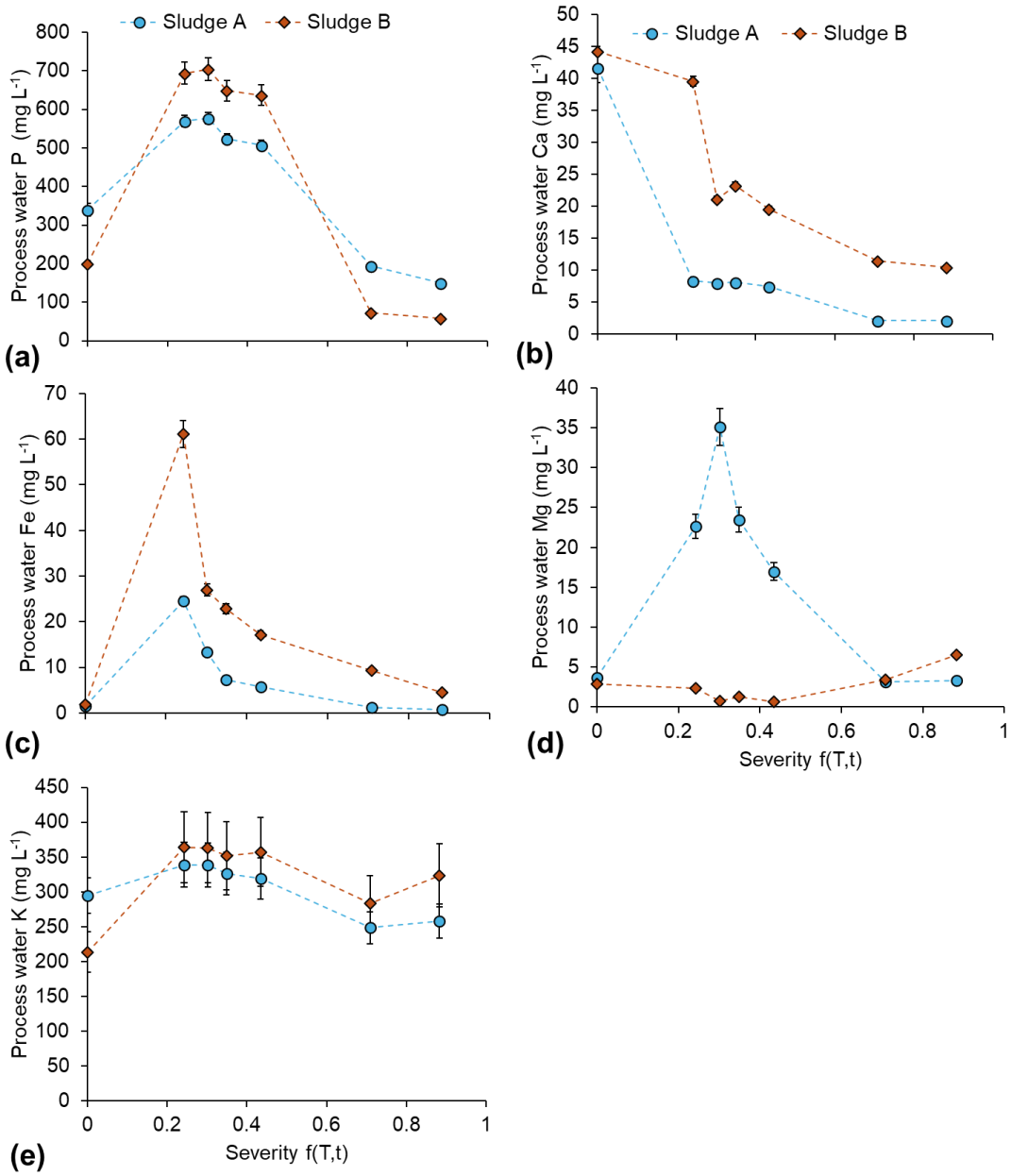

Figure 5.5 – Concentration (mg L^{-1}) of soluble P (a), Ca (b), Fe (c), Mg (d) and K (e) after HT process water of Sludge A and B. Error bars represent propagated uncertainty.

The molar ratios Ca/P and Fe/P are always lower than 1 in the process waters of both sludge types, regardless of process severity. This indicates that Ca and Fe are limiting factors for the precipitation of P present in the solution: even if all the Ca and Fe present in the solution were to bind with the free PO_4-P to precipitate as Ca and Fe phosphates, only a fraction of the P in solution would precipitate, leaving a non-negligible amount of P in the process water. Interestingly, in the case of Sludge A, the Ca/P molar ratio remains roughly constant in the process waters, with values around 0.1. This could indicate a specific molar correlation between the precipitation of P and Ca, suggesting a significant precipitation of P in the form of Ca phosphates. A similar phenomenon is observed for the Fe/P molar ratio, which is around 0.02 for less severe treatments but then decreases to stabilize around 0.004. However, this phenomenon is not observed in the case of Sludge

B. Specifically, the two experimental points corresponding to the most severe conditions (severity 0.71-0.88) show a higher Ca/P and Fe/P molar ratio than the points related to milder treatments. At these points, the concentration of soluble P is significantly lower than in less severe treatments (Figure 5.5), indicating substantial P precipitation. However, this sharp decrease in P concentration is not accompanied by a proportional precipitation of Ca and Fe. This result does not allow us to conclude with certainty that P primarily precipitates with Ca and/or Fe to form Ca and Fe phosphates.

Nevertheless, the concentration values and molar ratios could be the result of a complex set of thermodynamic equilibria; for example, the concentrations of Ca and Fe could be higher than expected, due the (re-)dissolution of other species containing these metals. In conclusion, the only element that can be deduced from the evolution of these molar ratios (Figure G.3) is the limiting role of Ca and Fe in the precipitation of P. More precise details on the specific products that precipitate can only be determined through the complete characterization of the solid pellet.

5.5. Solid by-products characterization

The ultimate analysis of product pellets determined that Sludge B products have a slightly higher ash content than those of Sludge A, consistent with the characteristics of their respective feed. The relative amounts of C, H, N, S, and O are comparable, and there are no significant differences in the evolution trends with increasing process severity. For both sludges, an increase in process severity has been correlated with N, H and O reduction and with an increase in ash content. No particular trend is observed for C.

Figure 5.6 shows Van Krevelen diagram for the pellets of Sludge A and B after HT treatments.

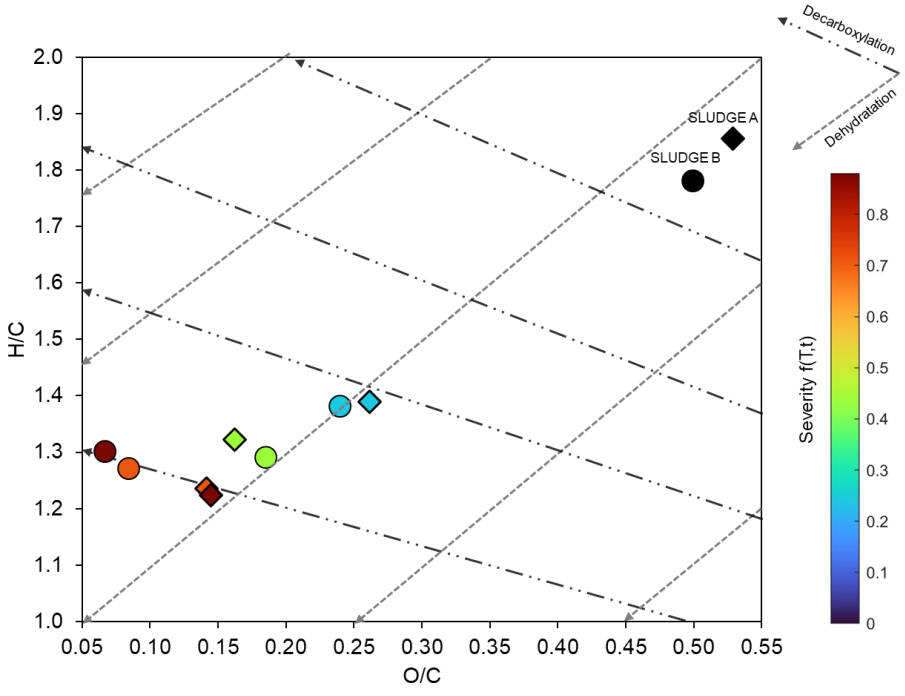

Figure 5.6 - Van Krevelen diagram for Sludge A (◆)and Sludge B (●) HT pellets.

At lower process severities, both sludges follow a similar dehydration trend during HT treatment. However, at higher process severities, Sludge B undergoes significant decarboxylation, approaching the characteristics of a high H/C bio-oil, typical product of HTL. This is not observed for Sludge A under the same temperature and duration conditions. Previous studies[222,223] have reported that higher solid loading can in fact increase the bio-oil yield. Because of reduced water content and higher organic matter, a higher amount of low-water-solubility organic compounds like fatty acids and phenolics migrate and merge into the recovered organic phase within the pellet[222]. Figure 5.7 shows P, Ca, Fe, Al, Mg and K contents in solid pellets (mg g^{-1} of dry matter) after HT treatment of Sludge A and B as function of process severity. P content in solid pellets of both sludges follow the same trend, increasing for more severe treatments (Figure 5.7a). P content in the products derived from Sludge B is consistently higher than that in the products from Sludge A, as Sludge B contains more P. Ca, Fe, Al, and Mg levels show similar trends, indicating metal accumulation in the product pellets. The metal content in solid products is strongly influenced by the initial concentrations in the sludges. Sludge B, being richer in Ca and Fe and poorer in Al and Mg than Sludge A, results in product pellets with higher Ca and Fe and lower Al and Mg. These results show how the initial composition of the feed in a HT treatment is the parameter that most influences the products characteristics. Additionally, Sludge A products present a higher increase in Mg and K contents for the most severe treatments, conducted at 350 °C, which suggests a precipitation of Mg and K at these conditions, coherently with soluble Mg and K decrease presented in Figure 5.5. This behavior has not been observed for Sludge B products.

Concerning heavy metals, the original content in the sludge used as feed seems to be the parameter that most affects the heavy metals content in the solid pellet. In general, for both sludges, heavy metals tend to accumulate in the solid pellet, leading to a generally higher content compared to the feeds.

Figure 5.8 shows the recovery yield of P in solid product for both Sludge A and B, compared to experimental results available in literature. The recovery yield of P in solid product is evaluated by subtracting P recovered in process water from total P introduced with the feed digestate. Most P is recovered in solid form within the product pellets. Higher process severity improves solid P recovery yield for both sludges. Sludge B pellets contain over 94% of feed P, while for Sludge A, between 78% and 94% of P is recovered in the product pellet. A higher SLR has already been correlated with an increase in P yield in solid products by previous studies[78,98,125]. However, the increase in P recovered in solid form may also be linked to Sludge B higher Ca and Fe content, which bind to PO_4-P in solution and precipitate to form stable compounds.

SMT extraction method[74] (Section 2.4.6.1) has been utilized to characterize P speciation in both sludges solid products. These results are compared with TP results from aqua regia extraction (Section 2.4.3) followed by ICP-AES analysis (Section 2.4.4), founding relatively satisfactory experimental agreement: as shown in Figure G.4, products from Sludge A have an extraction yield slightly above 100%, while those from Sludge B have a lower yield, around 90%.

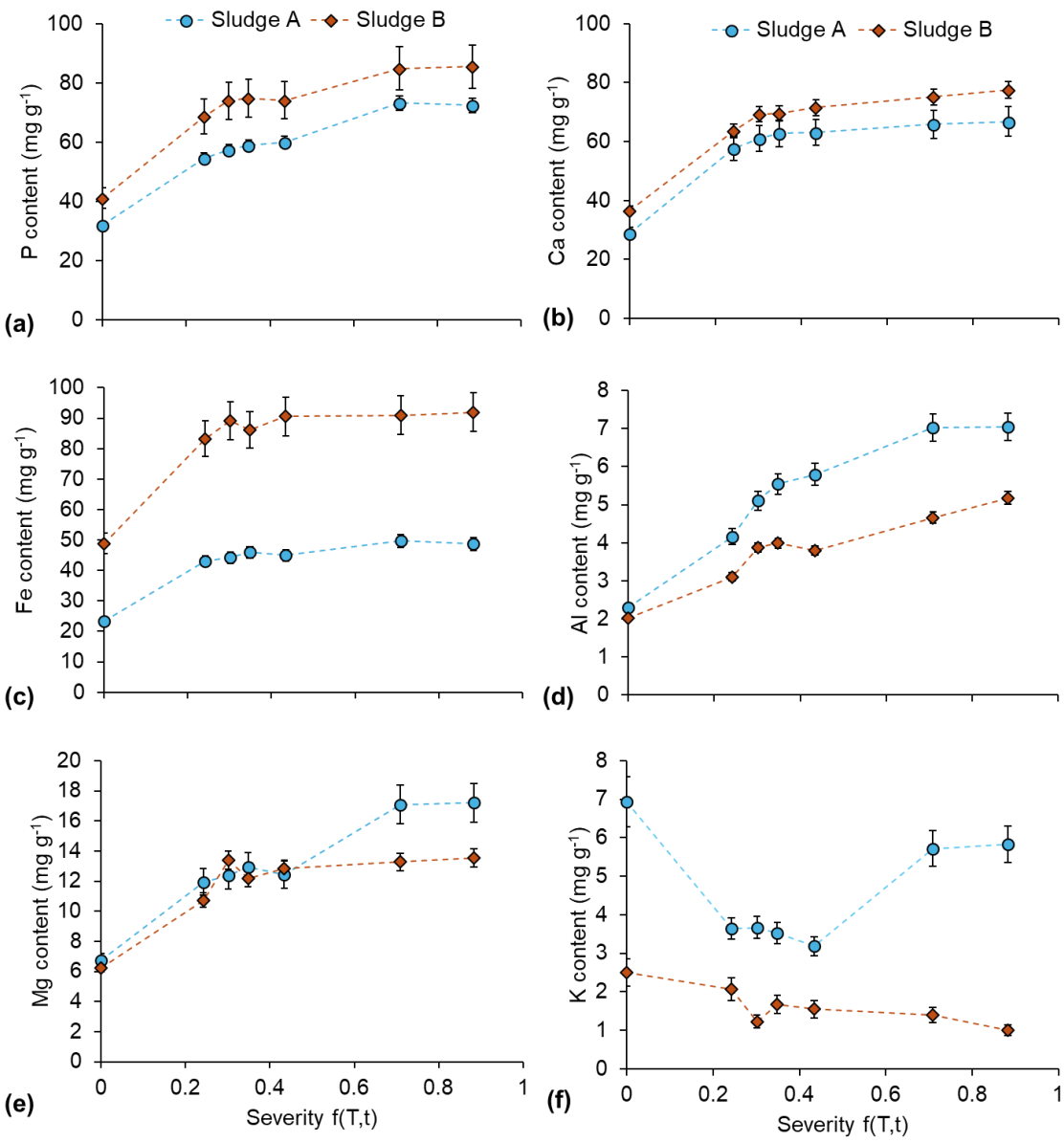

Figure 5.7 - P(a), Ca (b), Fe (c), Al (d), Mg (e) and K (f) contents (mg g^{-1} of dry matter) in Sludge A and B HT solid pellets as function of severity. Error bars represent propagated uncertainty.

This could suggest that HT products from Sludge B contain more recalcitrant P species which are not extracted by the SMT method. However, this hypothesis does not fully explain why a lower yield has been observed for Sludge B feed too, implying the presence of these recalcitrant species in the sludge too. The most likely explanation is a P overestimation by ICP-AES analysis. Both methods show relatively high experimental error, primarily due to the selected analytical method and the extraction phases, which may not be fully effective, as well as the representativeness and heterogeneity of the sample. In this context, the results align with the particularly high relative uncertainty of each measurement. SMT extracts analysis allowed to quantify NAIP and AIP relative fraction, which are expressed as fraction of TP in Figure 5.9, alongside a box distribution of the respective experimental results already available in literature.

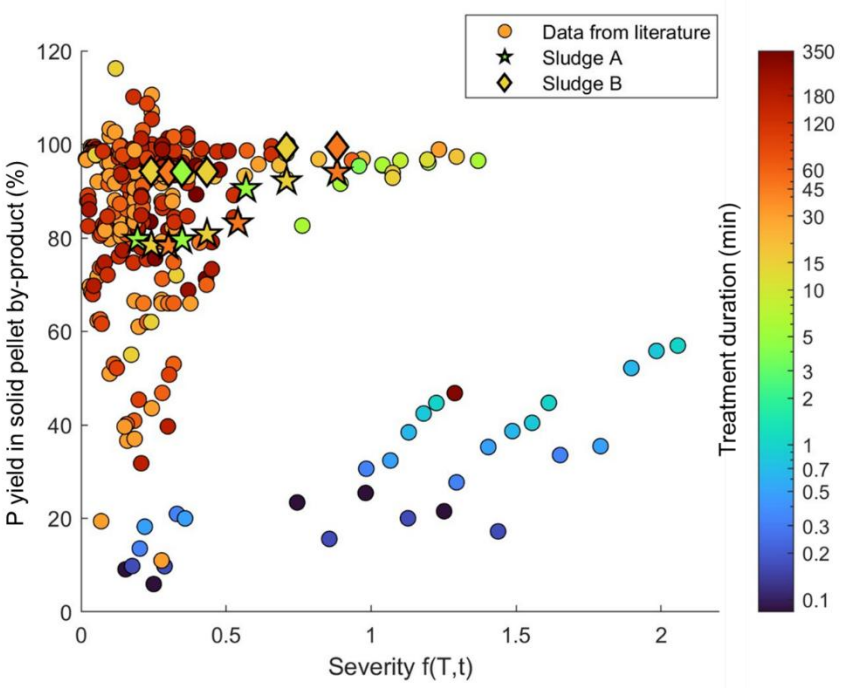

Figure 5.8 - P recovery yield in solid pellet by-product for both Sludge A and Sludge B, compared to experimental results available in literature (from studies listed in Table A.1).

For both sludges, it is possible to observe that more severe treatments (severity = 0.71 - 0.88) lead to an increase in the AIP fraction and a decrease in NAIP fraction compared to milder treatments (severity = 0.24 - 0.43). Interestingly, under less severe conditions (250-300 °C), Sludge B products present higher NAIP, and lower AIP relative fraction compared to Sludge A. This phenomenon can be easily explained by the greater Fe amount present in Sludge B, which has a Fe/P molar ratio of 0.66 compared to 0.40 in Sludge A.

The fractions of NAIP and AIP obtained for the two sludges at 350 °C (last two points) are comparable. At this temperature, the conversion from NAIP to AIP is favored, and the Ca/P molar ratio becomes the parameter that mostly defines the speciation. As both sludge samples exhibit a very similar Ca/P molar ratio, close to 0.7, it makes sense that the two AIP fractions are comparable under these conditions.

The NAIP and AIP values are in line with experimental results available in literature[1]. However, for the most severe treatments at 350 °C, the products show relatively low NAIP, and high AIP quantities compared to the values reported in the literature. OP relative quantities are evaluated by subtracting NAIP and AIP from TP. OP fractions are in the range of 1-5 %TP, but these results are not statistically significant and fall within the uncertainty range. Therefore, selected methods did not allow to observe any specific trend in OP for the two sludges products, and they did not detect any OP significant quantity in any of the products. This suggests that most of OP is already mineralized at 250 °C, 5 min, for both feeds. Figure G.5 shows Ca/P, Fe/P and Al/P molar ratio in the solid pellet product of the HT treatment of Sludge A and Sludge B. The Ca/P molar ratio (Figure G.5a) in both sludges is approximately 0.7.

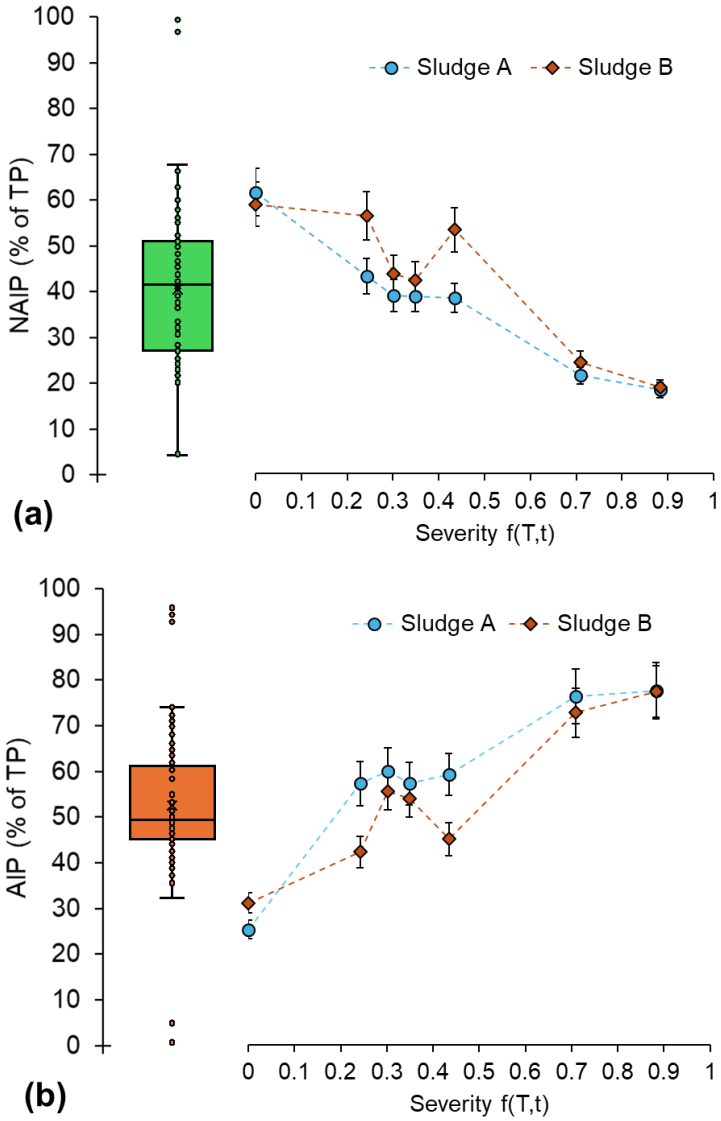

Figure 5.9 - SMT method NAIP and AIP relative fractions, expressed as fraction of TP, alongside the box distribution of the experimental results available in literature for NAIP (green) and AIP (orange) fractions distributions [10,77–94]. Error bars represent propagated uncertainty.

The Ca/P molar ratio in the solid pellets resulting from the HT treatment of Sludge A is slightly higher (around 0.8) for treatments realized at 250 and 300 °C, since a substantial amount of P is transferred to the process water following the mineralization of OP and the dissolution of some IP. However, at higher process severity, the molar ratio returns to 0.7, implying that most of the P and Ca are recovered in the solid pellets. The same applies to the solid pellets of Sludge B, where the Ca/P molar ratio remains around 0.7. The Fe/P molar ratio (Figure G.5b) also remains constant across the values for the two sludges, again suggesting that most of the Fe and P are recovered in the solid pellets.

A Ca/P molar ratio of 0.7 in the solid pellets (Figure G.5a) implies that no more than 70% of the P present in the solid phase could be present as calcium phosphates, assuming a calcium phosphate with a unimolar Ca/P stoichiometric ratio (e.g., dicalcium phosphate

$CaHPO_4$). This is indeed consistent with P speciation results (Figure 5.9), which show that under the most severe conditions, AIP constitutes around 70% of the TP in the solid pellets. This would imply that most of Ca present in the solid pellets is effectively bound to P. This means that the stoichiometry composition of the feed is a central parameter for P speciation in the solid products of the HT treatment. To further increase the P apatite fraction in the solid product, additional Ca must be added to raise the Ca/P molar ratio above 1. The sum of the Fe/P molar ratio (Figure G.5b) and the Al/P molar ratio (Figure G.5c) is equal to 0.4-0.5 for Sludge A and 0.6-0.7 for Sludge B. This suggests that, assuming precipitation of P in the form of stoichiometric unimolar Fe and Al phosphates (e.g., $FePO_4$ and $AlPO_4$), P could be obtained as NAIP, up to 50% for Sludge A and up to 70% for Sludge B. However, as seen in Figure 5.9, the relative NAIP fractions are generally lower, especially for higher severities. This would confirm the hypothesis that Fe and Al are present in the solid pellets in forms other than phosphates, such as hydroxides.

5.6. Conclusions

Figure 5.10 summarizes the chapter's results on how using Sludge B instead of Sludge A as HT feed affects the characteristics and properties of the by-products. The figure is divided into two columns. The left column shows results mainly interpreted as consequences of the higher solid-to-liquid ratio of Sludge B compared to Sludge A. The right column displays effects generally linked to the different composition of Sludge B, such as higher contents of P, Ca, and Fe, and a higher Fe/P molar ratio. Results attributable to both properties of Sludge B are placed between the two columns.

HT treatment of Sludge B leads to higher amounts of solid pellet and lower amounts of process water compared to Sludge A, which is a direct effect of the amount of solid matter initially present in Sludge B (three times that of Sludge A). This also affects the dry mass of solid pellet and the suspended solids in the process water (higher for Sludge B products). Consequently, TSRY is higher in Sludge B after HT treatments. The solid-to-liquid ratio higher for Sludge B has also been correlated with higher alkalinity and TN, NH_4-N, COD, TC, TIC and TOC concentrations in HT process water. This is a direct result of the higher amount of organic matter (carbohydrates and proteins) and the lower amount of water. Products obtained after the HT of sludge are characterized by higher concentration of soluble P for milder treatments (250 – 300 °C), which can be explained both by the higher amount of P in Sludge B, and the lower amount of water, leading to a more concentrated HT process water. Conversely, at 350 °C, treatments using Sludge B result in lower concentrations of soluble P compared to those using Sludge A. This is attributed to higher levels of Fe and Ca in Sludge B, which enhance the precipitation of free PO_4-P. For the same reasons, soluble Ca and Fe concentrations are higher in Sludge B HT treatments. For milder treatments, soluble Mg is notably lower in Sludge B HT process water, due to reduced water volume and possibly higher concentrations of other cations, which inhibit the dissolution of Mg-containing compounds. Lower water amount of Sludge B is also directly related to lower P, Ca, Fe and Mg yields in HT process water. Ca/P and

Fe/P molar ratio in both sludges HT treatment process water are always lower than 1, confirming the limiting role of Ca and Fe in the precipitation of P.

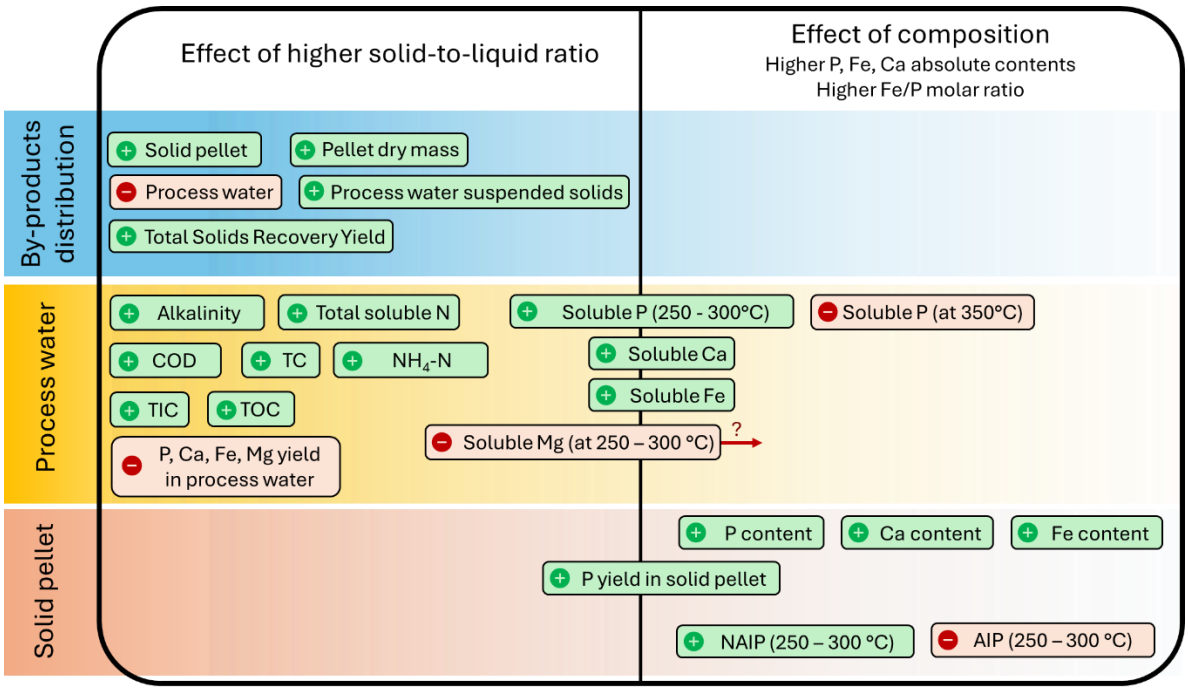

Figure 5.10 - Effects of using Sludge B instead of Sludge A on by-products physico-chemical characteristics.

Higher P, Fe and Ca contents for Sludge B is directly correlated with higher P, Fe and Ca contents in HT solid pellets. Higher P yield in the solid pellet by-product from Sludge B has been correlated with higher SLR[78,98,125], but the higher Fe and Ca quantities may have also contributed to precipitate more P. For milder treatments (250 -300 °C), the use of Sludge B leads to more NAIP and less AIP, due to the higher Fe/P molar ratio.

These results provide a general understanding of the effects of increased solid loading and different feed composition (P, Ca, and Fe) on HT treatment products.

At 350 °C, using a feed with higher solid loading and a higher Fe/P molar ratio can reduce the concentration of soluble P in process water by about three times compared to Sludge A. Using Sludge B also increases the P recovery yield in solid products from 94% to 99.4%. However, at lower temperatures (250– 300 °C), approximately 5% of P still remains in the liquid phase. Sludge A and Sludge B present an initial Ca/P molar ratio of 0.7, and solid pellets obtained from the HT treatment of both Sludge A and B have a Ca/P molar ratio of 0.7. This suggests that up to 70% of P in the solid phase could exist as calcium phosphates. This aligns with P speciation results, indicating that under severe conditions, about 70% of the total phosphorus is in the form of AIP. This also implies that most Ca in the pellets is bound to P, highlighting the importance of feed stoichiometry in determining P speciation. To further increase AIP fraction, additional Ca is needed to raise the Ca/P molar ratio to values above 1. In this perspective, Chapter 6 will examine the impact of increasing the Ca/P molar ratio on P distribution. Specifically, it will be explored if adding Ca can precipitate nearly all P in the solid phase, even at lower temperatures, and enhance its recovery primarily as Ca phosphates (AIP).

6. Effect of Calcium oxide addition on by-products characteristics and phosphorus speciation

6.1. Introduction

In various studies available in literature[77,83,84,87,88,98], Ca-containing additives are added to SS during HT treatment, primarily to enhance P recovery in the solid product in the form of AIP, generally with the purpose of producing a "slow-release P fertilizer with high bioavailability"[138,139]. The correlation between P speciation determined by sequential extraction techniques and the bioavailability of their respective fractions is not always clear and it is somewhat ambiguous. P bio-available species correspond to fractions that are readily assimilable or easily exchangeable by plants. These include fully dissociated PO_4^{3-} ions in solution, as well as weakly bound PO_4-P on Fe and Al compounds that become available after washing and ion exchange[37,224]. These species can be associated with the first two fractions extracted using the Hedley method[121], as described in Section 2.4.6.2 or with the Olsen-P, extracted with $NaHCO_3$ 0.5 M [225].

In soils, concentrations of soluble P are relatively low[224], instead, P is found as Ca, Al and Fe phosphate salts, which are quite insoluble in water in neutral pH conditions, thus they have low bioavailability because plants cannot assimilate them until they are dissolved [224]. Fe and Al phosphates are solubilized at low or high pH values, and are generally associated with NAIP fraction, while Ca phosphates are included in AIP fraction and extracted in acidic conditions[76]. These fractions should therefore indicate the P species that are less accessible for plant assimilation, or in any case, species whose availability is not direct but requires slow release due to gradual weathering and acidic leaching.

However, some studies available in literature identify the bioavailable P fraction as the sum of NAIP + OP[81,84,226], while other studies suggest that the AIP fraction has higher bioavailability compared to NAIP[77,83,87,138,227]. The sum of NAIP + OP is associated with bioavailable P likely because the NAIP fraction includes P species that are readily-available and loosely sorbed on metal (hydro)oxide surfaces[37,228]. Under alkaline pH in fact, the P-binding capacity of Fe and Al oxides decreases due to ligand exchange reactions, where PO_4^{3-} ions are replaced by OH^-[229]. Some OP species are soluble and can be included in water extracted-P, however, they cannot be directly assimilated by plants as they need to be firstly mineralized into PO_4-P by various species of bacteria and fungi[230]. Besides, Fe and Al phosphates are extracted at high pH but could not be considered as readily bio-available in all soils' conditions.

On the other hand, when AIP is indicated as a more bioavailable fraction compared to NAIP, the assessment is based on a bioavailability measurement technique according to Directive 77/535/EEC method 3.1.3[231], which uses a 2% citric acid solution (pH ≈ 2.1). In these conditions, compounds such as chlorapatite, farringtonite, stanfieldite[227], hydroxyapatite, and calcium pyrophosphate[83], generally recoverable in the AIP fraction, are soluble. Obviously, it is unlikely for soil to have such a low pH; therefore, a solid product containing a high content of AIP cannot be considered a source of soluble and rapidly assimilable P. Instead, it will tend to retain P in relatively stable Ca and Mg salts, releasing it slowly through natural acid leaching processes.

Furthermore, another important factor in evaluating the bioavailability of a phosphorus-based fertilizer is the degree of crystallinity of the phosphates it contains. It is well known that calcium phosphates with a high degree of crystallinity have a much lower solubility compared to amorphous calcium phosphates[73]. Therefore, a fertilizer based on calcium phosphates with a low degree of crystallinity could represent an ideal solution and a compromise between a source of P that is sufficiently soluble to be easily assimilated by plants, but not too soluble to cause runoff, leaching, and eutrophication.

Therefore, the appeal of producing a HT solid pellet with a high percentage of AIP is not linked to the production of easily and quickly assimilable P, but rather to a variety of reasons:

- To explore the possibility of achieving complete precipitation of soluble PO_4-P, not necessarily at high temperatures (already at 250 °C - 300 °C), in the form of Ca phosphates, thus producing a P-free process water.
- The solid pellet rich in AIP could be used as a fertilizer in particularly acidic soils where Fe and Al phosphates are less effective[134].
- The high thermodynamic stability of these salts makes them slow-release fertilizers, limiting problems of leaching, runoff, P loss, and eutrophication[138,139].
- Ca phosphates produced from HT treatments of SS have a content comparable to phosphate ore, making them more versatile products[232].
- Fertilizers containing Fe and Al could lead to excessively high concentrations of these metals in the soil, causing toxicity issues for crops[233,234].

For these reasons, in this Chapter the possibility of adding Ca during the HT treatment of Sludge B is investigated to study its effects on the by-products' properties, with a particular focus on P speciation.

After an initial presentation of the by-products general characteristics and distribution, the properties of process water and solid pellet by-products will be interpreted, particularly with respect to the Ca/P molar ratio. It will also be discussed how the addition of CaO affects the yield of bio-oil. Then, the analysis will focus on how the addition of CaO and the modification of the feed Ca/P molar ratio influences the distribution of P in the by-products, the concentration of soluble P in the process water, and, most importantly, P speciation in the solid pellet and its distribution between NAIP and AIP. Finally, a

desirability study will be conducted to determine the optimal process parameters that maximize both the bio-oil yield and P recovery in the solid as AIP.

6.2. Materials and methods

In previous works, Ca has been added in the forms of $CaCl_2$[87,93], $Ca(OH)_2$[84], and CaO[77,83,88,98]. $CaCl_2$ has been excluded to prevent acidification of the reaction medium, which could inhibit the precipitation of Ca phosphate, and to protect the reactor's internal wall, sensitive to high Cl concentrations. After several attempts, $Ca(OH)_2$ was also excluded due to difficulties in fully solubilizing it in the reaction medium. Consequently, CaO as a Ca-containing additive has been selected.

For this investigation, the HT treatment experiments have been realized by introducing around 85 g of Sludge B in the batch reactor (0.2 L) described in Section 2.2.1. A certain amount of CaO (Fisher Scientific, >97% purity) was added into the reactor between two layers of digestate to ensure homogeneity and prevent accumulation at the bottom. All experiences have been realized with a N_2 final pressure of 18 MPa in correspondence of the operative temperature, and with a mixing rate of 700 rpm. The results presented in this work concerning "process water" and "solid pellet" refer to the by-products separated mechanically by centrifugation as explained in Section 2.2.3 before any extraction of the organic phase. The extraction of the organic phase (bio-oil) was conducted on the dried solid pellet for quantification purposes only. All characteristics and measurements conducted on the solid pellet, as described in Section 2.4, were performed before the bio-oil extraction, in order to better compare these values with the results presented in Chapter 4 and 5.

The process water by-products have been analyzed according to methods and techniques described in Section 2.3, characterizing their main physical properties, alkalinity, solid content, soluble N and PO_4-P concentrations, dissolved C, COD, and metal contents. The solid pellet by-products were instead characterized as described in Section 2.4, quantifying its metal and heavy metal content, and P speciation.

The statistical analysis of the results is carried out following the methods described in Section 2.6.1 (ANOVA table and Student's t-test), with the experimental design described in Section 2.6.1.2. Experimental results reported in the discussion are accompanied by the respective propagated uncertainty. Proximate, pH, alkalinity, TN, NH_4-N, COD, PO_3-P analysis and P sequential extractions were performed in triplicates. Experimental results reported in the discussion are accompanied by the respective propagated uncertainty. For each set of analyses, limit of detection and limit of quantification were determined by analysis of blanks. All chemicals used were of analytical grade.

6.3. By-products distribution and mass balances

Figure 6.1a shows the global mass distributions as a function of process severity, for the three investigated Ca/P molar ratios. Figures 6.1b and 6.1c depict the mass balances for P and Ca, while Figures 6.2a, 6.2b and 6.2c show respectively Fe, Mg and K mass balances, indicating the relative distribution of these elements in the two by-products, as well as the losses.

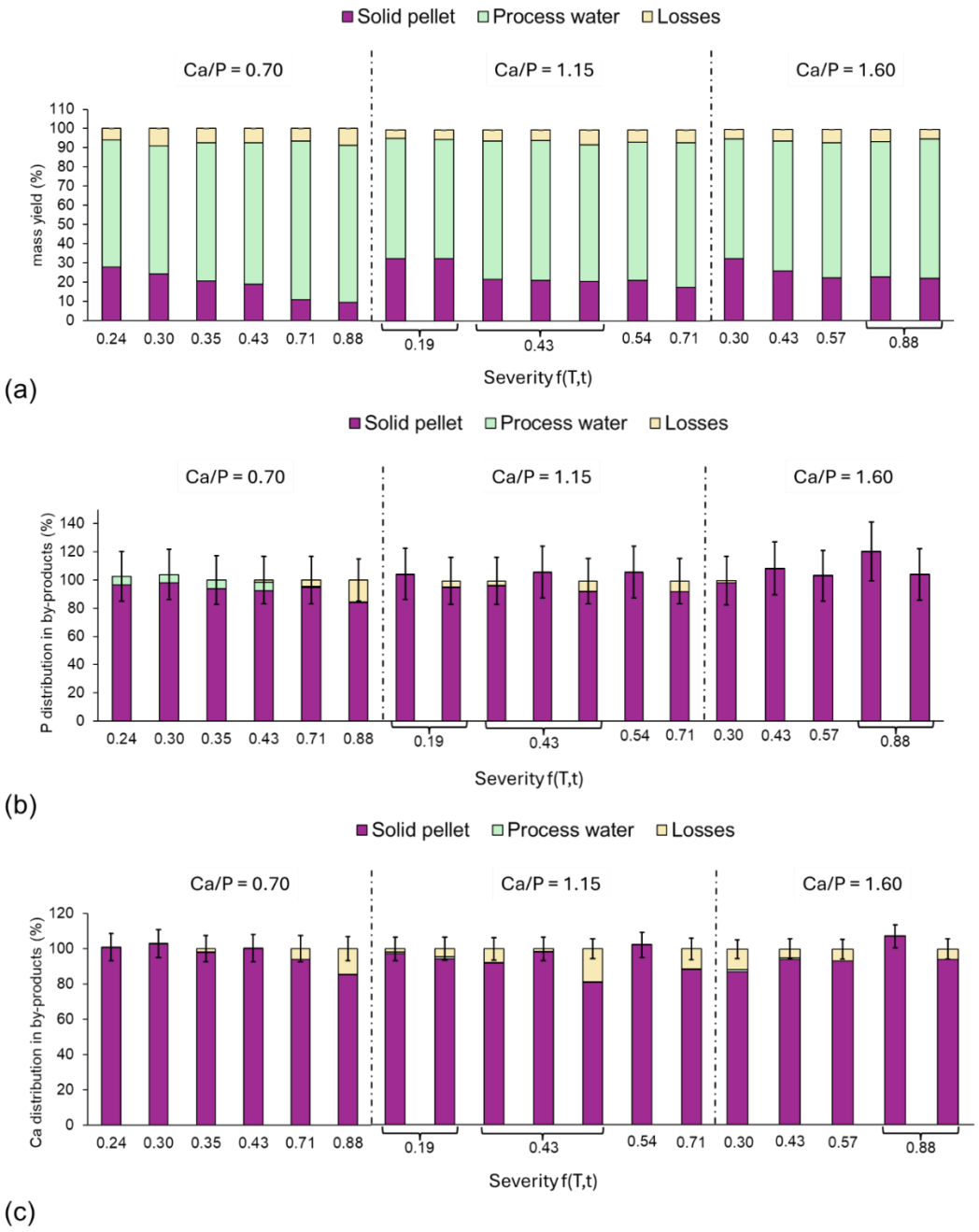

Figure 6.1 - Global mass (a), P (b) and Ca (c) mass distribution as a function of HT severity f(T,t), for the three investigated Ca/P molar ratios. Error bars represent propagated uncertainty.

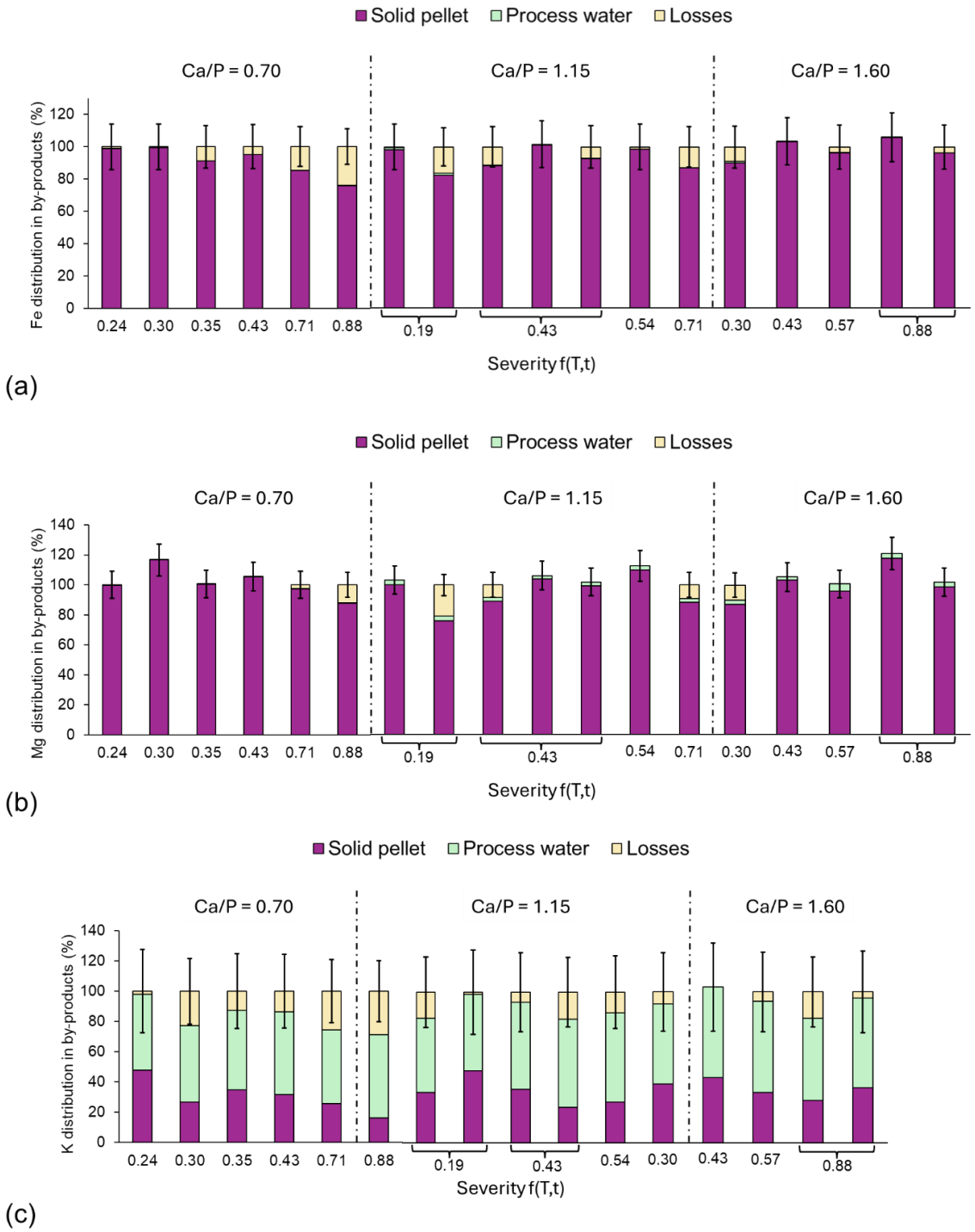

Figure 6.2 - Fe (a), Mg (b) and K (c) mass distribution as a function of HT severity f(T,t), for the three investigated Ca/P molar ratios. Error bars represent propagated uncertainty.

The recovered product accounts for 91 to 97% of the feed mass (Figure 6.1a). As shown in Figure 6.1a, a process severity increase leads to an increase in process water and a decrease in solid pellet absolute amounts for all Ca/P molar ratios. This is consistent with the results of the HT treatments realized on Sludge A (Section 4.3).

The addition of CaO results in an increase in solid pellet formation and a reduction in process water. Specifically, in HT treatments conducted at process severities of 0.30, 0.43,

and 0.88, the addition of 1.33% CaO (relative to sludge mass) increases the solid pellet yield respectively by 8%, 7%, and 14% relative to total feed mass. Furthermore, adding 0.67% CaO at process severities of 0.43 and 0.71 leads to a 3% and 6% increase in solid pellet yield relative to total feed mass. The screening design of these results shows that higher temperatures and longer treatment durations increase process water while reducing solid pellet yield. In contrast, adding CaO significantly increases solid pellet mass and reduces process water. No significant correlation was found between overall mass losses and the experimental parameters.

As shown in Figure 6.1 and Figure 6.2, P, Ca, Fe and Mg are mostly exclusively recovered in the solid pellet, while most of K is recovered in the process water (Figure 6.2c). The amounts of P, Ca, Fe, Mg and K recovered in by-products expressed as % of the amounts introduced in the feed, are 85-121% for P (Figure 6.1b), 81-107% for Ca (6.1c), 76-108% for Fe (6.2a), 79-121% for Mg (6.2b) and 71-103% for K (6.2c). The screening analysis of these results did not allow to find any statistically significant correlation between the recovery of these elements and the three factors (temperature, time, Ca/P molar ratio) investigated in this experimental plan. This is likely because the discrepancies in the mass balances of P, Ca, Fe, Mg, and K are related to the unrecoverable solid residue in the reactor and the relative performance of aqua regia digestion in extracting these elements from Sludge B and solid pellets (Section 2.4.3), which are independent of the HT treatment parameters.

As shown in Figure 6.3, an increase in process severity reduces process water TDS, suggesting the precipitation of inorganic species and an increase in the hydrophobicity of organic species (Section 4.5.2).

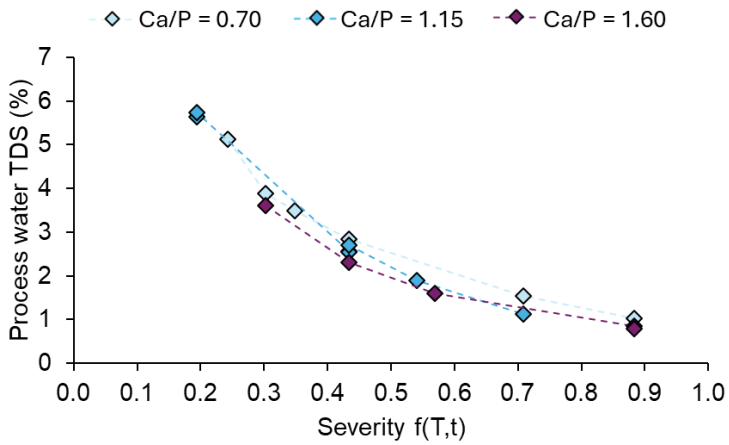

Figure 6.3 - Total dissolved solids in process water as a function of HT severity f(T,t), for the three investigated Ca/P molar ratios. Error bars represent propagated uncertainty. Dashed lines are included to help data interpretation.

Screening analysis of TDS results confirms that process water TDS significantly decreases with increasing temperature and treatment duration. Besides, the addition of CaO has been correlated with a further reduction in process water TDS. This can be

explained by examining the hydration reaction involving CaO in an aqueous environment (Equation 6.1):

$$CaO + H_2O \rightarrow Ca(OH)_2 \quad (6.1)$$

Then, calcium hydroxide dissociates according to Equation 6.2:

$$Ca(OH)_2 \rightarrow Ca^{2+} + 2(OH)^- \quad (6.2)$$

The release of Ca^{2+} and OH^- ions in the reaction medium could promote the precipitation of various soluble ionic species (including PO_4^{3-}), thereby reducing the amount of TDS.

Figure 6.4 shows the bio-oil yield as a function of process severity for the three investigated Ca/P molar ratios.

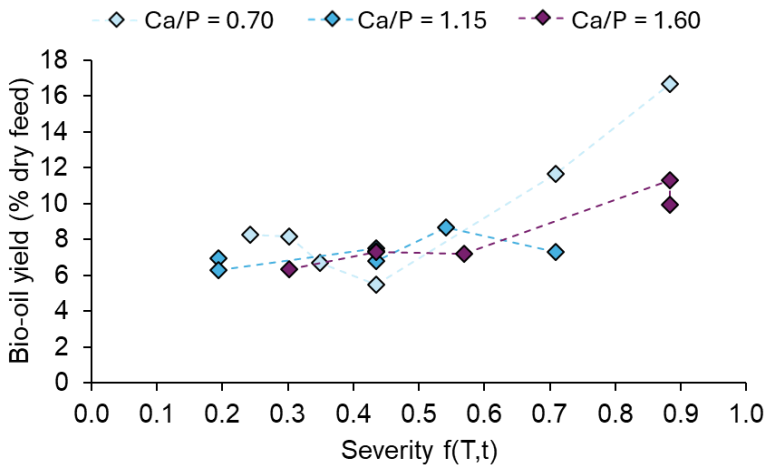

Figure 6.4 - Bio-oil yield (calculated according to Equation 2.2) expressed as % of total dry feed mass, as a function of HT severity f(T,t), for the three investigated Ca/P molar ratios. Error bars represent propagated uncertainty. Dashed lines are included to help data interpretation.

For the treatments realized without CaO addition (Ca/P= 0.70), increasing process severity clearly leads to a higher bio-oil yield, particularly for HT treatments at 350 °C. Indeed, treatments at 250 °C and 300 °C (severity 0.19 - 0.54) produce a bio-oil yield between 6% and 8%, while those at 350 °C (severity 0.7-0.9) yield between 12% and 17%.

When CaO is added (Ca/P= 1.15 and 1.60), the bio-oil yield at 250 °C and 300 °C remains similar to the treatments realized without CaO, ranging from 6% to 7%. However, at 350 °C, CaO addition significantly reduces the bio-oil yield. For example, at a process severity of 0.71, the bio-oil yield is 11.7 ± 0.1% without CaO but drops to 7.3 ± 0.1% with CaO addition (Ca/P= 1.15). This effect is even more pronounced at a process severity of 0.88, where the yield decreases from 16.7 ± 0.1% without CaO, to a minimum of 9.9 ± 0.1% with CaO (Ca/P = 1.60). Therefore, CaO addition appears to reduce bio-oil yield in treatments at 350°C. This phenomenon has a noticeable impact on the appearance and characteristics of the HT product. The product obtained without Ca addition presents

bituminous agglomerates at the bottom of the reactor, which did not need to be mechanically separated by centrifugation. The process water from this treatment has a light orange and transparent color. The dried solid pellet appears as a dark, hard, and shiny solid. The product obtained following the addition of CaO, on the other hand, results in a biphasic suspension, and there are no large solid agglomerates that spontaneously separate from the liquid. After centrifugation, the process water appears as an opaque black liquid. The dried solid pellet appears as a powdery and fragile solid. The screening analysis of bio-oil yield results confirmed that the bio-oil yield is significantly favored by increasing temperatures (in particular when passing from 300 to 350 °C) and longer treatment durations. Besides, CaO addition has been significantly correlated to a decrease in the amount of bio-oil extracted from the solid pellets.

Table D.11 reports the ANOVA validation tool for the second-degree polynomial model surface response for the bio-oil yield, expressed as fraction of dry feed. The second-degree polynomial model provided by the surface response is statistically significant, with a p-value less than 0.01% and an R^2 of 0.90. The model standard deviation is equal to 0.61%.

Table D.12 reports the second-degree model coefficients of the surface response for bio-oil yield, expressed as % of dry feed matter, with respective statistical validation. The coefficients for the linear effects of temperature (b_1), time (b_2) and Ca/P molar ratio (b_3) are statistically significant, with a p-value less than 5%. The obtained surface response confirms the positive effect of temperature and time on bio-oil yield, and the negative effect of CaO addition (b_3 is negative). The quadratic temperature term ($b_{1\text{-}1}$) is also significant, indicating that the effect of temperature becomes particularly significant at the upper end of the experimental range (350 °C). All the interaction terms are significant too. $b_{1\text{-}2}$ is positive, indicating that the effect of time becomes stronger at higher temperatures. $b_{1\text{-}3}$ and $b_{2\text{-}3}$ are negative, indicating that at high Ca/P molar ratio the effects of temperature and time are weaker.

Equation 6.3 shows the corresponding second-degree polynomial model obtained for bio-oil yield (% feed dry matter).

$$bio\ oil\ (\%\ feed\ dry) = \mathbf{7.46} + \mathbf{1.51}\boldsymbol{T} + \mathbf{1.37}\boldsymbol{t} - \mathbf{0.81}\boldsymbol{Ca} + \mathbf{1.17}\boldsymbol{T^2} - 0.41t^2 + 0.91Ca^2 + \mathbf{1.61}\boldsymbol{T}\cdot\boldsymbol{t} - \mathbf{1.01}\,\boldsymbol{T}\cdot\boldsymbol{Ca} - \mathbf{1.14}\cdot\boldsymbol{Ca}\cdot\boldsymbol{t} \quad (6.3)$$

Where T, t and Ca are respectively temperature, treatment duration and Ca/P molar ratio expressed as normalized values according to Equations 2.26, 2.27 and 2.29. Statistically significant terms are in bold.

Figure 6.5 shows the response surface obtained for bio -oil yield (% dry feed) as a function of temperature (°C), treatment duration (min) and feed Ca/P molar ratio.

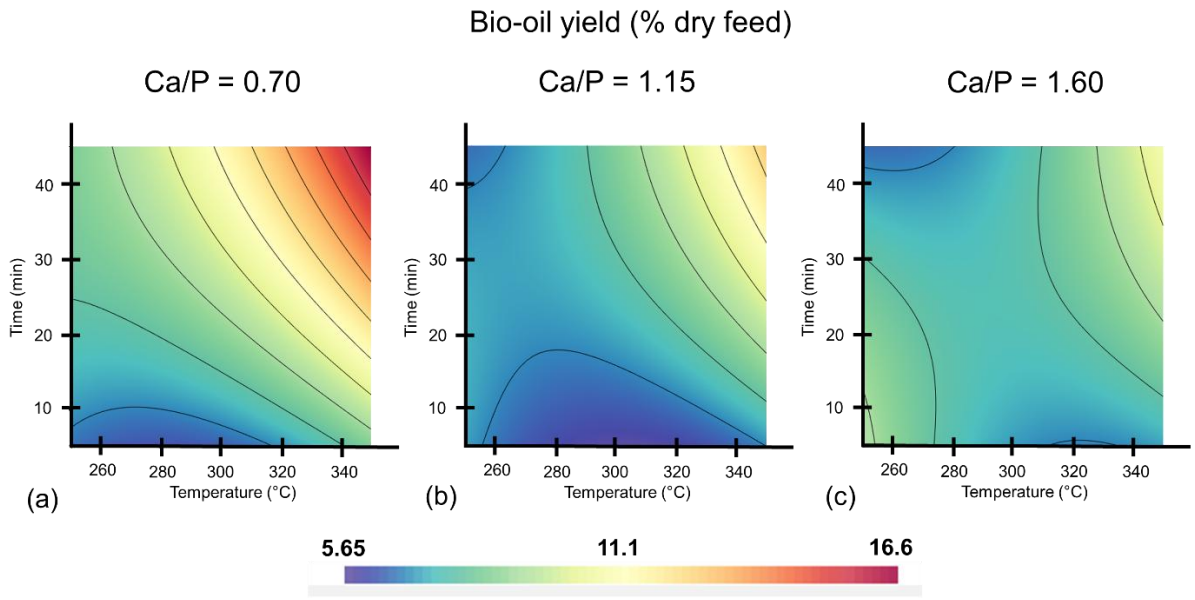

Figure 6.5 - Second-degree polynomial surface response for bio-oil yield expressed as % of dry feed matter, based on the experimental design reported in Table 2.4, as a function of temperature (°C) and treatment duration (min), for Ca/P molar ratio of 0.70 (a), 1.15 (b) and 1.60 (c), as expressed by Equation 6.3 with the coefficients reported in Table D.12.

The surface response presented in Figure 6.5 clearly shows that the addition of CaO inhibits the formation and/or recovery of the oily product under the most severe conditions.

A possible interpretation of this phenomenon requires defining the chemical species that typically make up the bio-oils produced during HTL. It has been showed that bio-oil is a complex product composed of various chemical species:

- Fatty acids[66,67] (resulting from lipids hydrolysis).
- Aldehydes and ketones[67] (produced by monosaccharides decarboxylation and dehydration).
- Phenols[66,67] (generated by lignin degradation).
- Alkenes[66] (from fatty acids decarboxylation).
- Esters[66,67] (generated by the interaction between fatty acids and various oxygenated intermediaries[235] coming from monosaccharides dehydration and aldol splitting, such as glyceraldehyde and glycolaldehyde[236]).

$Ca(OH)_2$ produced by CaO hydration might have reacted with the fatty acids and esters present in the bio-oil to produce soaps, alcohols, and water according to the saponification reactions described in Equations 6.4 and 6.5.

$$2(R-COOH) + Ca(OH)_2 \rightarrow 2(R-COO)^{-}Ca^{2+} + 2\,H_2O \quad (6.4)$$

$$2(R-COO-R') + Ca(OH)_2 \rightarrow 2(R-COO)^{-}Ca^{2+} + 2\,R'-OH \quad (6.5)$$

The resulting soaps would significantly reduce the hydrophobicity of the bio-oil phase, potentially forming micellar structures that could disperse some of the oily phase into the

process water (thus explaining the lower amount of bio-oils extracted from the solid pellet and hence the lower bio-oil yield in Figure 6.5) and introduce more water into the pellet, which explains why an increase in CaO has been correlated with an increase in water content in the solid pellet, as shown in Figure 6.6. At high temperatures and pressure, water's dielectric constant is significantly lower than at ambient conditions[237]. As a result, the biomolecules in the bio-oil are likely at least partially solubilized under sub-critical conditions during the HT treatment. Therefore, the proposed micelle-formation mechanism would occur only as the temperature approaches ambient levels. Other possible explanations to bio-oil yield reduction following CaO addition could include a possible catalytic effect of Ca in certain reactions involving organic molecules constituting the bio-oil, or the introduction of oxygen through CaO, leading to partial or complete oxidation of the bio-oil components.

In a previous study, CaO addition during HTL of biomass has been already correlated with a reduction in bio-oil yield and an increase in process water and solid pellet yield[238].

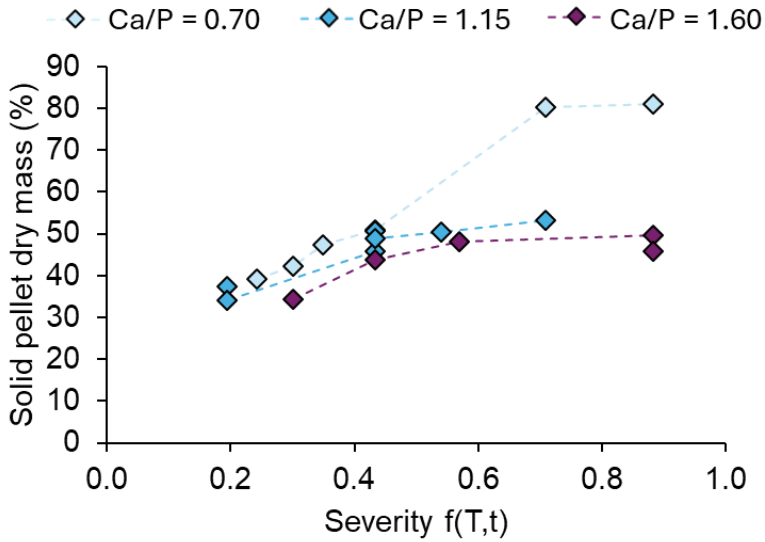

Figure 6.6 - Solid pellet by-product dry mass (%) as a function of severity f(T,t) for different Ca/P molar ratios. Error bars represent propagated uncertainty. Dashed lines are included to help data interpretation.

The proposed mechanism is also consistent with the differences in the appearance of by-products with and without CaO addition. The addition of CaO could lead to the saponification of certain species constituting the bio-oil and to the reduction of the hydrophobicity of the HT product. In fact, if the standard HT product presents a well-separated aqueous phase and solid-oily phase, when CaO is added, the solid and oily phases are dispersed in the liquid and are only partially separated following centrifugation. The ultimate analysis showed that both solid pellets from the HT treatments (350 °C, 45 min, without and with CaO) have the same H/C molar ratio of 1.3. However, the pellet with CaO has a higher O/C molar ratio (0.77 vs. 0.67). This increase

in O content is likely due to the addition of O as metal oxide. Table 6.1 resumes the screening analysis results about temperature, duration and Ca/P molar ratio effects on by-products distribution and mass balances discussed in this section.

Table 6.1 - Screening analysis results on by products distribution and mass balance based on the experimental design reported in Table 2.4. Statistical validation is provided in Table D.25 (Annex D). Positive effects are expressed through one or two positive signs (+), negative effects through one or two negative signs (-). Double effects are three times more significant than the smallest significant effect. The absence of symbols indicates that the effect is not significant.

Factor	Temperature (°C)			Time (min)			Ca/P molar ratio		
from:	250	250	300	5	5	15	0.70	0.70	1.15
to:	300	350	350	15	45	45	1.15	1.60	1.60
Process water (% total product)	++	++	+	+	+		-	- -	-
Solid pellet (% total product)	- -	- -	-	-	-		+	++	+
Bio-oil yield (% dry feed)		++	+		+	+	-	-	-
Process water TDS (%)	- -	- -	- -	- -	- -	- -	-	-	-
Solid pellet dry mass (%)	+	++	+		+		-	- -	-
TSRY (%)	-	-	-						

6.4. Process water characterization

Figure 6.7 presents the main process water physico-chemical properties as a function of process severity for the three different Ca/P molar ratios. Many of the process water physico-chemical properties follow the same trends described in Section 4.4 with respect to process severity. As shown in Figure 6.7a, pH for the least severe treatments is between 7.3 and 7.8, lower than pH of Centrate B (8.03 ± 0.01), denoting an acidification of the reaction medium due to the release of organic acids following carbohydrates breakdown[62]. A process severity increase leads to an increase in process water pH, which is probably due to proteins hydrolysis into ammonium, which reduces the concentration of H^+ ions, leading to an increase in OH^- ions, counterbalancing the effect of acids[81]. This is confirmed by the process water NH_4-N concentration which increases with increasing process severity (Figure 6.7c). Process water alkalinity (Figure 6.7b) increases with increasing process severity, which correlates directly with the concentration of HCO_3^- ions (Figure 6.7f), also increasing for more severe treatments. Finally, COD and TOC concentration in process water (Figure 6.7d and 6.7f) both decrease with increasing process severity, which could be related to polymerization, condensation and aromatization mechanisms leading to the precipitation of C in the solid phase[52,60] or to the conversion of organic C into other species (ex. gas production) [188]. The effect of Ca/P molar ratio adjustment on these process water physico-chemical properties is less straightforward, as the experimental points distribution for these parameters do not reveal any distinct trend.

The screening analysis of these results, shown in Table 6.2, confirmed that an increase in both temperature and treatment duration is correlated with an increase in pH, alkalinity, NH_4-N concentration, and TIC concentration, and with a decrease in COD, TC and TOC. On the other hand, the increase in Ca/P molar ratio does not have a significant effect on any of these parameters, except for alkalinity: the addition of CaO leads to an increase in the alkalinity of the process water, probably due to the dissociation of $Ca(OH)_2$ into Ca^{2+} and OH^- (hydroxide ions contribute to the total alkalinity).

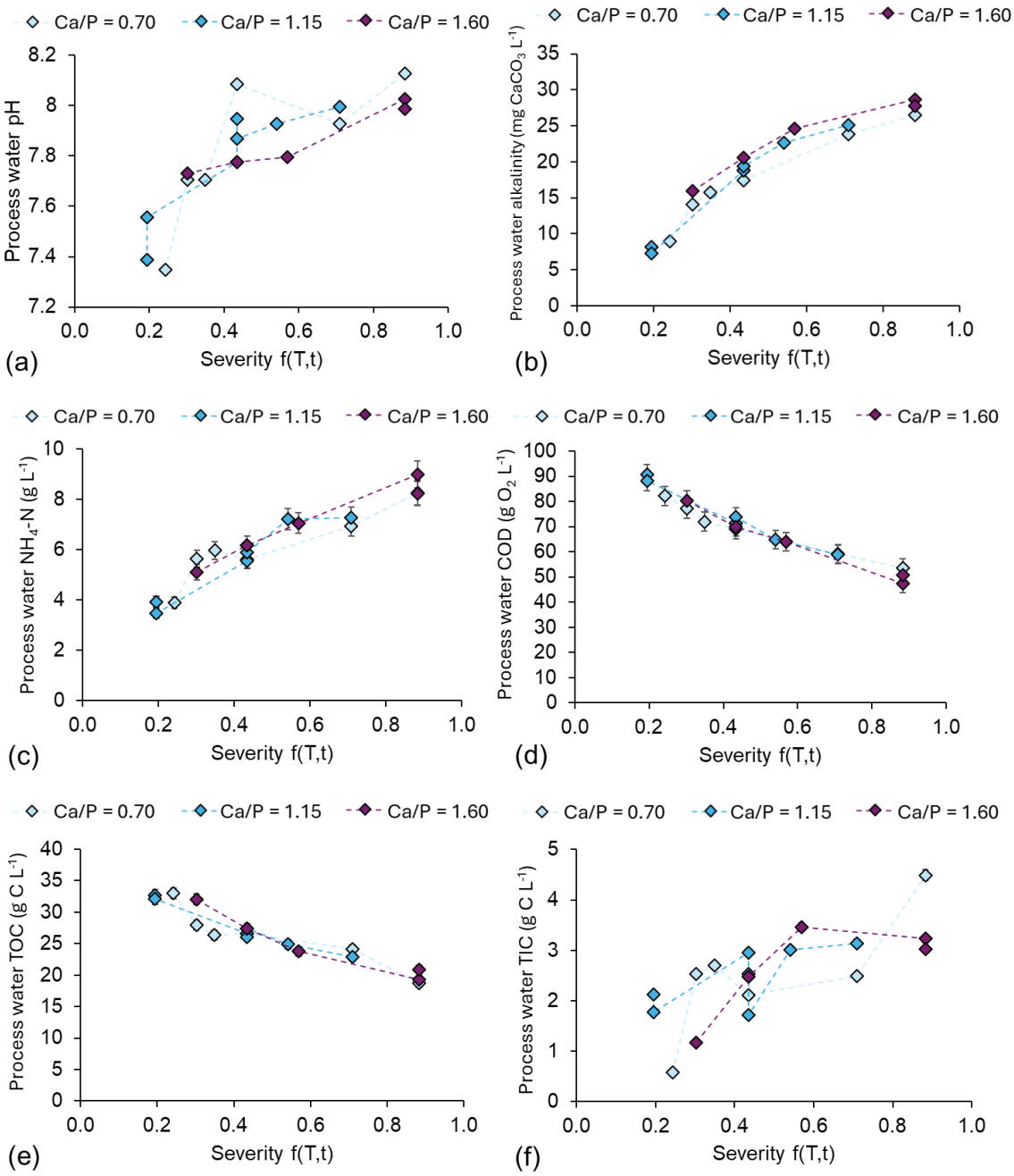

Figure 6.7 - Process water pH (a), alkalinity (b), NH_4-N (c), COD (d), TOC (e) and TIC (f) as a function of severity f(T,t) for different Ca/P molar ratios. Error bars represent propagated uncertainty. Dashed lines are included to help data interpretation.

Table 6.2 - Results of the screening analysis on process water characteristics based on the experimental design reported in Table 2.4. Statistical validation is provided in Table D.26 (Annex D). Positive effects are expressed through one or two positive signs (+), negative effects through one or two negative signs (-). Double effects are three times more significant than the smallest significant effect. The absence of symbols indicates that the effect is not significant.

Factor	Temperature (°C)			Time (min)			Ca/P molar ratio		
from:	250	250	300	5	5	15	0.70	0.70	1.15
to:	300	350	350	15	45	45	1.15	1.60	1.60
pH	+	+			+				
alkalinity ($gCaCO_3\ L^{-1}$)	++	++	++	+	++	+		+	+
NH_4-N ($g\ L^{-1}$)	+	+	+		+	+			
COD ($g\ L^{-1}$)	- -	- -	- -	-	-	-			
TC ($g\ L^{-1}$)	-	- -	-		-	-			
TOC ($g\ L^{-1}$)	-	- -	-		-	-			
TIC ($g\ L^{-1}$)	+	+		-		+			

Figure 6.8 shows soluble P, Ca, Fe, Mg and K concentration in process water as a function of severity f(T,t) for the three different Ca/P molar ratios.

As shown in Figure 6.8a, for HT treatments realized without the addition of CaO (Ca/P = 0.70), soluble P concentration decreases with increasing process severity. More specifically, for HT treatments realized at 250 – 300 °C (severity 0.24 – 0.43) soluble P is in the range 637 – 694 mg P L^{-1}, while at 350 °C (severity 0.71 – 0.88) the concentration falls to 57–73 mg P L^{-1}, which is a tenfold reduction. Ca/P molar ratio adjustment has a clear effect on soluble P concentration, as treatments realized with CaO addition yield significantly low soluble P concentration in process water (12-52 mg L^{-1}). For a Ca/P molar ratio of 1.15, the increase in process severity is still associated with a decrease in soluble P, going from an average value of 47 ± 2 mg P L^{-1} at a process severity of 0.19, down to 12.8 ± 0.5 at a process severity of 0.71. For a Ca/P ratio of 1.60, there is no longer a clear trend in the effect of process severity on the concentration of soluble P.

The screening analysis of soluble P results showed that an increase in temperature and treatment duration decreases the concentration of soluble P in process water, causing it to precipitate as a solid. Adding CaO further enhances P precipitation. Interestingly, when Ca/P molar ratio increases from 1.2 to 1.6, which involves doubling the CaO addition from 0.7% to 1.4% (relative to the feed mass), soluble P content does not decrease further, showing that a Ca/P molar ratio of 1.15 is sufficient for almost complete precipitation of soluble P, and suggesting that most of the phosphates binding to calcium precipitate in the form of dicalcium phosphate ($CaHPO_4$), which has a Ca/P molar ratio of 1. Indeed, it is less likely that under these conditions, most of P precipitates in the form of tricalcium phosphate ($Ca_3(PO_4)_2$), octacalcium phosphate ($Ca_8H_2(PO_4)_6$), or hydroxyapatite ($Ca_{10}(PO_4)_6(OH)_2$), which have molar ratios of 1.5, 1.33, and 1.67. Table D.13 reports the ANOVA validation tool for the process water soluble P second-degree polynomial surface response obtained with these results. To prevent the model from returning negative

concentration values, we fed the experimental matrix with the logarithm of the soluble P concentration, $\log_{10}(C_P)$, instead of the raw C_P values. The second-degree polynomial model provided by the surface response is statistically significant, with a p-value less than 0.01% and an R^2 of 0.99. Table D.14 reports the second-degree model coefficients of the response surface of soluble P (mg L^{-1}), with respective statistical validation. The coefficients for the linear effects of temperature (b_1), time (b_2) and Ca/P molar ratio (b_3) are statistically significant, with p-values lower than 1%. The obtained surface response confirms the negative effect of temperature, time and CaO addition on soluble P concentration. The quadratic temperature term (b_{1-1}) and quadratic Ca/P term (b_{3-3}) are also significant. The temperature-Ca/P interaction term (b_{1-3}) is significant and positive.

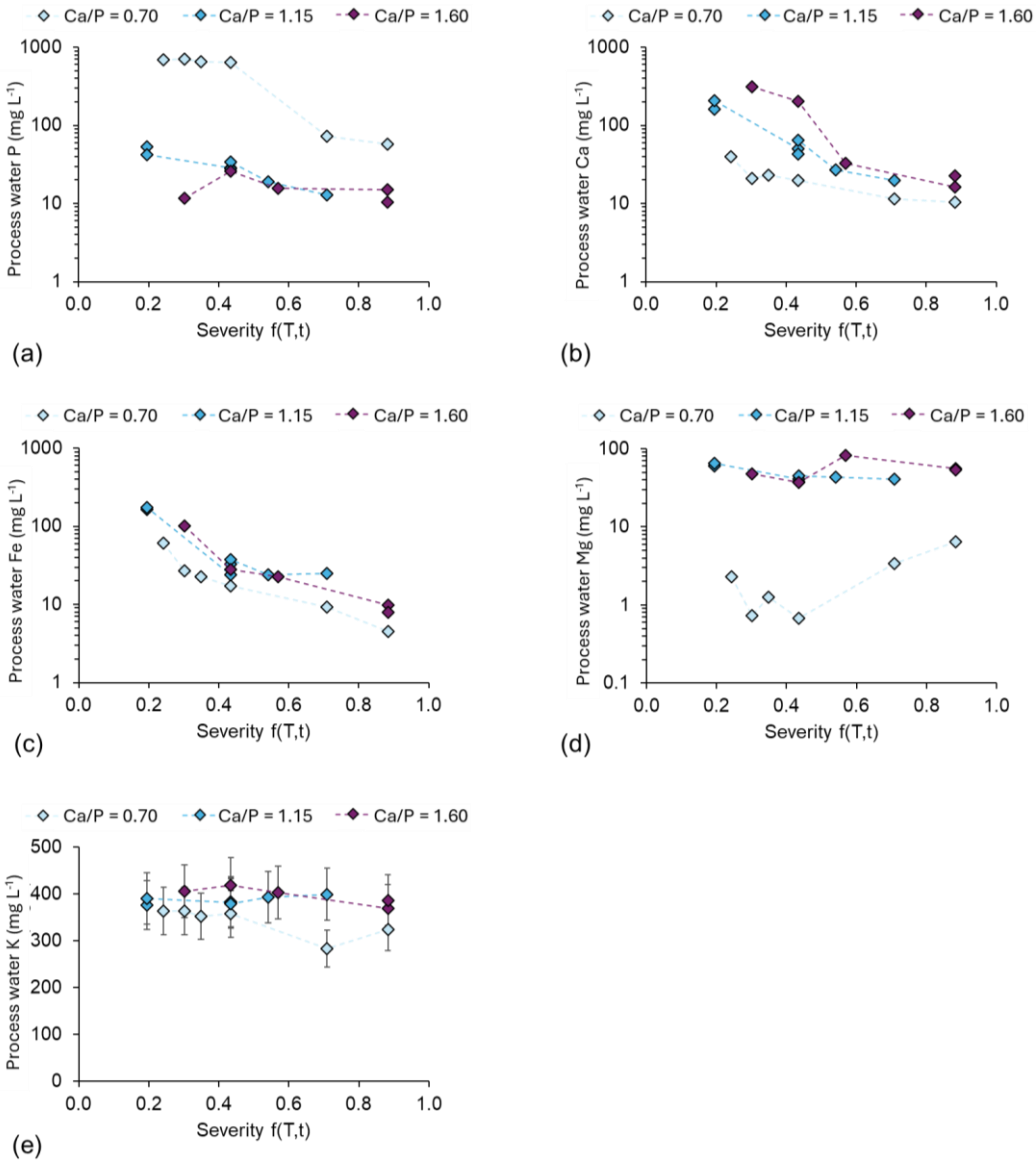

Figure 6.8 - Process water soluble P (a), Ca (b), Fe (c), Mg (d) and K (e) concentrations (mg L^{-1}) as a function of severity f(T,t) for different Ca/P molar ratios. Error bars represent propagated uncertainty. Dashed lines are included to help data interpretation.

This adds an additional effect of reducing soluble P concentration, specifically at low temperatures but higher Ca/P ratios, and at high temperatures but lower Ca/P ratios, indicating that the effect of temperature is less significant for high Ca/P ratios. Equation 6.6 shows the corresponding second-degree polynomial model obtained for soluble P concentration C_P (mg L^{-1}) as a function of temperature (°C), treatment duration (min) and feed Ca/P molar ratio:

$$\log_{10} C_P = \mathbf{1.42} - \mathbf{0.26}\boldsymbol{T} - \mathbf{0.12}\boldsymbol{t} - \mathbf{0.63}\boldsymbol{Ca} - \mathbf{0.23}\boldsymbol{T^2} + 0.07t^2 + \mathbf{0.54}\boldsymbol{Ca^2} + 0.01T \cdot t + \mathbf{0.26}\boldsymbol{T} \cdot \boldsymbol{Ca} + 0.03t \cdot Ca \quad (6.6)$$

where T, t and Ca are respectively temperature, treatment duration and Ca:P molar ratio expressed as normalized values according to Equations 2.26, 2.27 and 2.29. Statistically significant terms are in bold.

Figure 6.9 shows three response surfaces illustrating the variation in soluble P concentration with changes in temperature and Ca/P molar ratio for three different treatment durations. Since the differences between the three surfaces are minimal, the duration effect can be considered less impactful compared to the other two parameters.

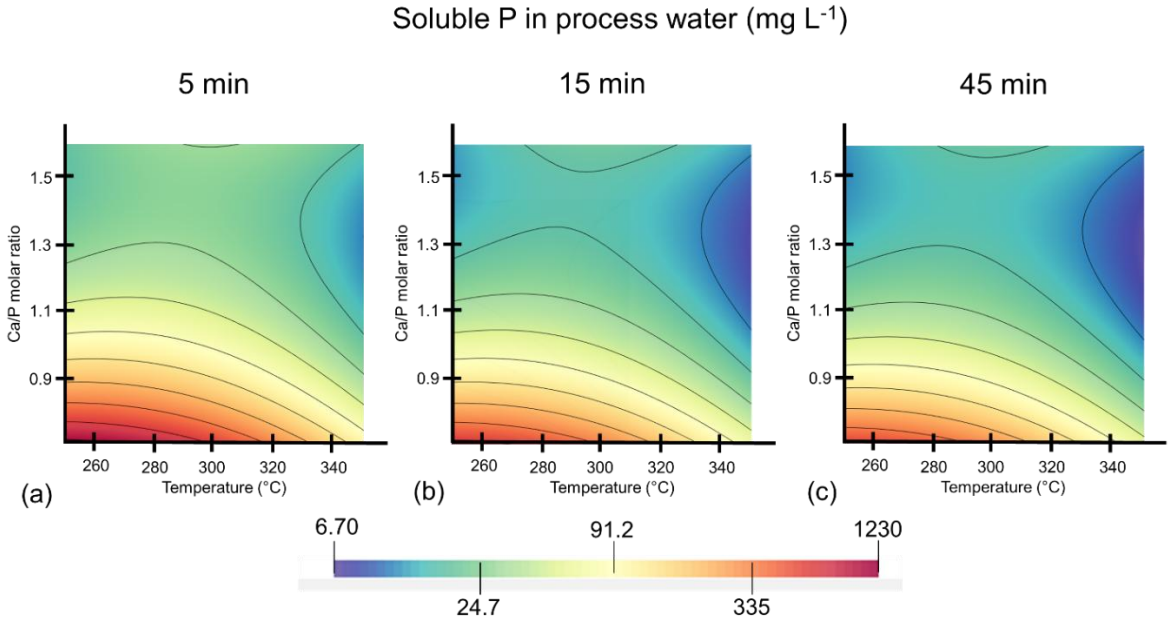

Figure 6.9 - Second-degree polynomial surface response for soluble P in process water (mg L^{-1}), based on the experimental design reported in Table 2.4, as a function of temperature (°C) and Ca/P molar ratio (-), for treatment duration of 5 min(a), 15 min(b) and 45 min (c), as expressed by Equation 6.6 with the coefficients reported in Table D.14.

Both higher temperatures and Ca/P molar ratio result in a decrease in soluble P, with the addition of CaO having the most significant impact.

Without any CaO addition, the temperature needs to be raised to 350 °C to achieve a soluble P concentration on the order of tens of mg L^{-1} (Figure 6.9a). However, the same result can be achieved by maintaining the temperature as low as 250 °C and adjusting the Ca/P molar ratio to 1 (adding approximately 2% of CaO relative to the dry feed mass).

This result is particularly surprising as it shows how CaO enables P precipitation without the need for excessively high temperatures, thereby saving energy.

Soluble Ca concentration (Figure 6.8b) clearly decreases with increasing process severity, while an increase in Ca/P molar ratio intuitively leads to a soluble Ca increase. The addition of CaO increases the concentration of soluble Ca by an order of magnitude, raising it from tens to hundreds of mg Ca L^{-1}.

Soluble Fe concentration (Figure 6.8c) decreases with increasing process severity. CaO addition leads to a significant increase in soluble Fe concentration, specifically when increasing Ca/P molar ratio from 0.70 to 1.15. Further increasing CaO ratio does not have a clear effect on soluble Fe concentration.

Soluble Mg concentration (Figure 6.8d) does not present a clear trend when increasing process severity. CaO addition, on the other hand, leads to substantial increase in Mg concentration, specifically when Ca/P molar ratio is increased from 0.70 to 1.15.

Soluble K concentration (Figure 6.8e) varies between 283 ± 39 and 418 ± 58 mg K L^{-1}. Based on the experimental results alone, it is not possible to identify any specific trend with increasing process severity or with the addition of CaO.

Screening analysis of soluble Ca, Fe, Mg and K results has allowed to assess that an increase in temperature is correlated with a general decrease in soluble Ca, Fe and K concentration, while longer treatments lead to a decrease in Ca, Mg and Fe soluble contents. These trends are similar to those observed for Sludge A, as described in Section 4.4.3.

Intuitively, CaO addition leads to an increase in the concentration of soluble Ca in process water. Curiously, Ca addition to the system has also been significantly correlated with an increase in soluble Fe, Mg, and K concentrations. Ca introduction into the system appears to lead to the precipitation of Ca^{2+} cations with the anions available in the aqueous medium (including free PO_4^{3-}), thus replacing other cations such as K^+, Mg^{2+}, and Fe^{3+}. Moreover, the addition of CaO, and the subsequent formation of $Ca(OH)_2$, would lead to an increase in the pH of the reaction medium, which could explain the greater dissolution of Fe phosphates. However, this pH increase was not observed in the process water, likely due to the buffering effect of organic acids released from the hydrolysis of carbohydrates.

The particularly pronounced effect observed for Mg could be related to the fact that Ca^{2+} and Mg^{2+} are both bivalent and therefore might be characterized by the same complexation affinity. Curiously, an increase in temperature from 300 to 350 °C has been correlated with an increase in the concentration of Mg in solution, contrary to the trend observed for the other cations. In this case too, the role of Ca^{2+} ions could central: it has already been observed that higher temperatures favor Ca precipitation (for Sludge A, a significant increase in AIP was observed precisely at 350 °C, as explained in Section 4.6), which could take the place of Mg^{2+} ions, leaving them in solution.

Table D.15 reports the ANOVA validation tool for the process water soluble Ca, Fe, Mg and K second-degree polynomial surface response obtained with soluble Ca, Fe, Mg and K results. In the case of Ca, Fe and Mg, in order to prevent the model from returning negative concentration values, we fed the experimental matrix with the 10-logarithm of the soluble

Ca, Fe and Mg concentration, $\log_{10}(C)$, instead of the raw concentration values. All obtained models are statistically significant as corresponding p-values are lower than 0.01% and R^2 coefficient is higher than 0.97 for Ca, Fe and Mg. K model on the other hand, allows for a less accurate fitting of the experimental data, with a R^2 of 0.82.

Equations 6.7, 6.8, 6.9 and 6.10 show the second-degree polynomial models obtained respectively for Ca, Fe, Mg and K concentration in process water as a function of temperature, treatment duration and feed Ca/P molar ratio.

$$\log_{10} C_{Ca} = \mathbf{1.67} - \mathbf{0.45}\boldsymbol{T} - \mathbf{0.14}\boldsymbol{t} + \mathbf{0.43}\boldsymbol{Ca} - 0.003T^2 - 0.08t^2 + 0.07Ca^2 + \mathbf{0.08}\boldsymbol{T}\cdot\boldsymbol{t} - \mathbf{0.23}\boldsymbol{T}\cdot\boldsymbol{Ca} - 0.06t\cdot Ca \quad (6.7)$$

$$\log_{10} C_{Fe} = \mathbf{1.42} - \mathbf{0.42}\boldsymbol{T} - \mathbf{0.19}\boldsymbol{t} + \mathbf{0.15}\boldsymbol{Ca} + \mathbf{0.19}\boldsymbol{T^2} + 0.07t^2 - \mathbf{0.22}\boldsymbol{Ca^2} - 0.05T\cdot t - 0.04T\cdot Ca + 0.06t\cdot Ca \quad (6.8)$$

$$\log_{10} C_{Mg} = \mathbf{1.51} + \mathbf{0.09}\boldsymbol{T} - \mathbf{0.05}\boldsymbol{t} + \mathbf{0.75}\boldsymbol{Ca} + \mathbf{0.22}\boldsymbol{T^2} + 0.04t^2 - \mathbf{0.68}\boldsymbol{Ca^2} + 0.13T\cdot t - 0.15T\cdot Ca + 0.08t\cdot Ca \quad (6.9)$$

$$K\left(\frac{mg}{L}\right) = \mathbf{390} - \mathbf{13.5}\boldsymbol{T} + 0.0005t + \mathbf{30.2}\boldsymbol{Ca} - 12.7T^2 - 0.24t^2 - 10.95Ca^2 - 5.09T\cdot t + \mathbf{10.4}\boldsymbol{T}\cdot\boldsymbol{Ca} - 6.36t\cdot Ca \quad (6.10)$$

Where T, t and Ca are respectively temperature, treatment duration and Ca/P molar ratio expressed as normalized values, according to Equations 2.26, 2.27 and 2.29. Statistically significant terms are in bold.

Coefficients related to the linear effect of temperature, time and Ca/P molar ratio are significant for all four models (except for time in the K concentration model). Quadratic temperature and Ca/P effect is significant for Fe and Mg surface response models. Both Ca and K model have a significant temperature - Ca/P interaction term: in the first case the term is negative, meaning that at higher temperatures the Ca/P ratio effect is less influent, while in the case of K concentration the interaction term is positive, meaning that at higher temperature the effect of CaO addition is stronger.

Figure 6.10 provides a visualization of the response surfaces for soluble Ca, Fe, Mg and K concentrations in process water as a function of temperature and Ca/P molar ratio, with a fixed treatment duration of 15 min. These surfaces confirm the trend just presented. Figures 6.10a, 6.10b and 6.10d show that an increase in temperature leads to a decrease in soluble Ca, soluble Fe and soluble K, while an increase in Ca/P molar ratio results in higher concentrations of Ca, Fe and K in the process water. In the case of Fe, the influence of CaO addition is more noticeable at lower temperatures (Figure 6.10b), for K it is more pronounced at 350 °C (Figure 6.10d). Soluble Mg (Figure 6.10c) follows the same general trends, but temperature influence is significant only at lower Ca/P ratios.

Figure H.1 (Annex H) shows P, Ca, Fe, Mg and K yield in process water expressed as % of total P, Ca, Fe, Mg and K introduced in the reactor. When no CaO is added to the system, P yield in process water is about 6% for 250 °C-300 °C treatments, but it falls at less than

1% for treatments realized at 350 °C. CaO addition further decreases P yield in process water, ranging from 0.09% to 0.41%.

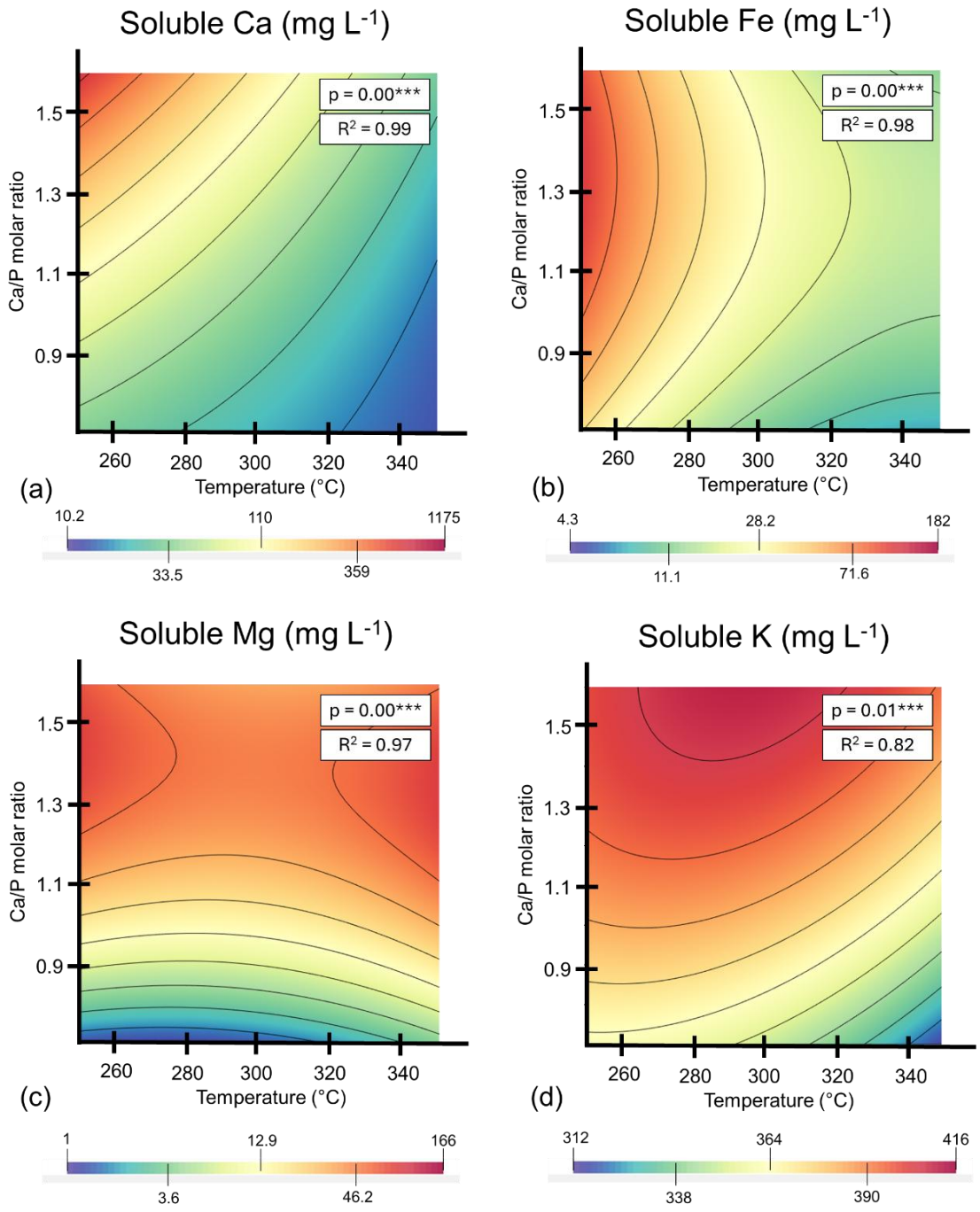

Figure 6.10 - Response surfaces for soluble Ca (a), Fe (b), Mg (c) and K (d) concentrations in process water based on the experimental design reported in Table 2.4, as a function of temperature and Ca/P molar ratio. Treatment duration is fixed at 15 min. Ca, Fe and Mg color scales are logarithmic.

Ca, Fe, Mg, and K yields in process water follow the same trends observed for their respective concentrations (Figure 6.8). For Ca and Fe, the amounts recovered in the process water are lower than 1%. For Mg, less than 1% is generally recovered in the process water under standard conditions, while around 3-4% is recovered when CaO is

added. Finally, between 50 and 60% of the total K is recovered in the aqueous phase. The trends obtained with screening analysis of these results follow the same trends observed for P, Ca, Fe, Mg and K concentration already discussed.

Table D.16 reports the ANOVA validation tool of the surface response model for P yield in process water (%). To prevent the model from returning negative yield values, we fed the experimental matrix with the logarithm of the soluble P yield, $\log_{10}$(P %), instead of the raw yield values. The second-degree polynomial model provided by the surface response is statistically significant, with a p-value less than 0.01% and an R^2 of 0.99.

Table D.17 reports the second-degree model coefficients of the response surface for P yield in process water (%), with respective statistical validation. The coefficients for the linear effects of temperature (b_1), time (b_2) and Ca/P molar ratio (b_3) are statistically significant. The obtained surface response confirms the negative effect of temperature, time and CaO addition on P yield in process water. The quadratic temperature term ($b_{1\text{-}1}$) and quadratic Ca/P term ($b_{3\text{-}3}$) are also significant. The temperature - Ca/P interaction term ($b_{1\text{-}3}$) is significant and positive. This adds an additional effect of reducing the concentration of soluble P, specifically at low temperatures but higher Ca/P ratios, and at high temperatures but lower Ca/P ratios, indicating that the effect of temperature is less significant for high Ca/P ratios.

Equation 6.11 shows the corresponding second-degree polynomial model obtained for P yield in process water (%) as a function of temperature (°C), treatment duration (min) and feed Ca/P molar ratio.

$$\begin{aligned}\log_{10} P\% = \ & \mathbf{-0.63 - 0.22T - 0.12t - 0.66Ca - 0.24T^2} + 0.06t^2 \\ & \mathbf{+ 0.53Ca^2} + \ 0.004T \cdot t + \mathbf{0.25T \cdot Ca} + 0.03t \cdot Ca\end{aligned} \tag{6.11}$$

Where T, t and Ca are respectively temperature, treatment duration and Ca/P molar ratio expressed as normalized values, according to Equations 2.26, 2.27 and 2.29. Statistically significant terms are in bold.

Figure 6.11 offers a visualization of the response surface for P yield in process water defined by Equation 6.11 as a function of temperature and Ca/P molar ratio for three values of time (5, 15 and 45 min). P recovered in the aqueous product is relatively low (<10%), and an increase in temperature and treatment duration leads to its reduction.

It is interesting to note that the P yield in process water decreases quite steeply with respect to the increase in Ca/P molar ratio. In fact, even after 5 minutes, over 99% of feed P has precipitated in the solid pellet when Ca/P molar ratio is approximately 1. Further CaO addition has a relatively negligible effect on P recovery in the solid pellet. If the primary goal of adding CaO is to precipitate P from process water, further CaO additions beyond a Ca/P molar ratio of 1 may not be considerable and might not provide any significant benefit.

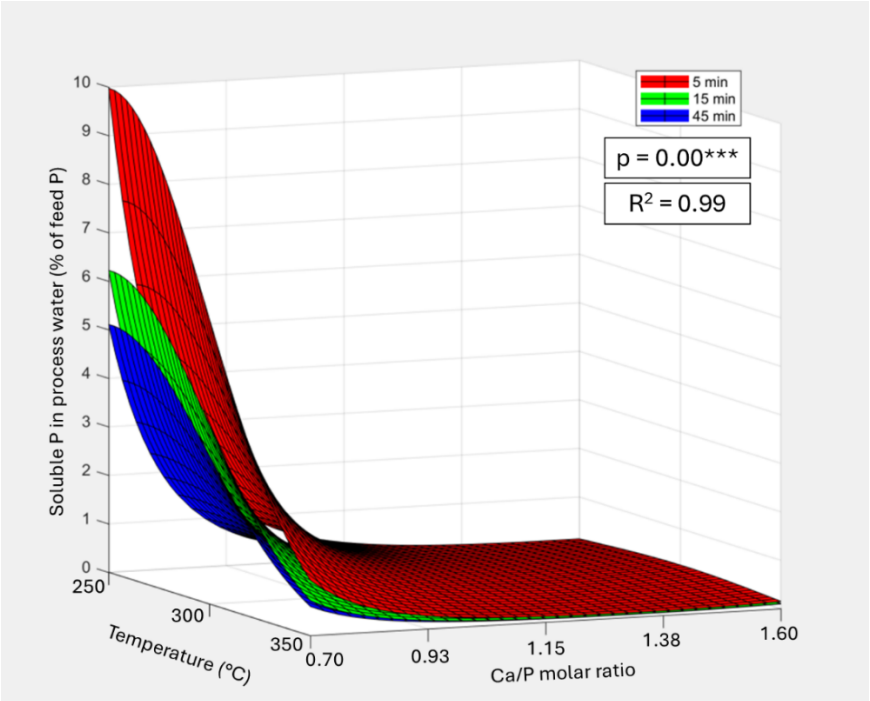

Figure 6.11 - Response surface for P yield in process water based on the experimental design reported in Table 2.4, as a function of Temperature and Ca/P molar ratio for three treatment durations (5, 15, 45 min).

Figure 6.12 shows Ca/P molar ratio and Fe/P molar ratio in the process water as a function of process severity for the three different feed Ca/P molar ratios.

The Ca/P molar ratio in the process water (Figure 6.12a) for treatments conducted without CaO addition, is always below 1, confirming the limiting role of Ca in the precipitation of P. For treatments with a feed Ca/P molar ratio of 1.15, the Ca/P ratio in process water under milder conditions ranges between 2.4 and 3.9, indicating that Ca is no longer a limiting factor, and that the precipitation of Ca phosphates could continue. However, for more severe treatments, Ca/P ratio decreases to values slightly above 1.

Similarly, for treatments with a feed Ca/P molar ratio of 1.60, the Ca/P ratio in process water under the least severe conditions is greater than 20 but increasing process severity leads to a decrease to values close to 1, suggesting that most of the Ca has precipitated.

In the process waters obtained at 300 °C and 350 °C with CaO addition, the Ca/P ratio ranges between 0.8 and 1.8, a range corresponding to the stoichiometry of the main calcium phosphates salts, suggesting a predominant presence of these compounds within the solid pellet.

The Fe/P molar ratio (Figure 6.12b) is below 1 for treatments conducted without the addition of CaO. Here too, Fe plays a limiting role in the precipitation of P. For treatments conducted with the addition of CaO, the Fe/P ratio is greater than 1 at 250 °C. However, in treatments conducted at higher temperatures Fe becomes limiting again. This suggests that for treatments conducted at 250 °C, Fe contained in Sludge B is released, following the dissolution of inorganic Fe salts. In the case of HT treatment without additives, Fe^{3+} ions would re-precipitate with P as Fe phosphates. The presence of CaO, however, releases a large amount of Ca^{2+} ions, which precipitate with the free PO_4^{3-}. Fe^{3+} ions would then

remain in solution, leading to higher Fe/P ratios compared to treatments without CaO. Further increase in process severity would then lead to Fe re-precipitation.

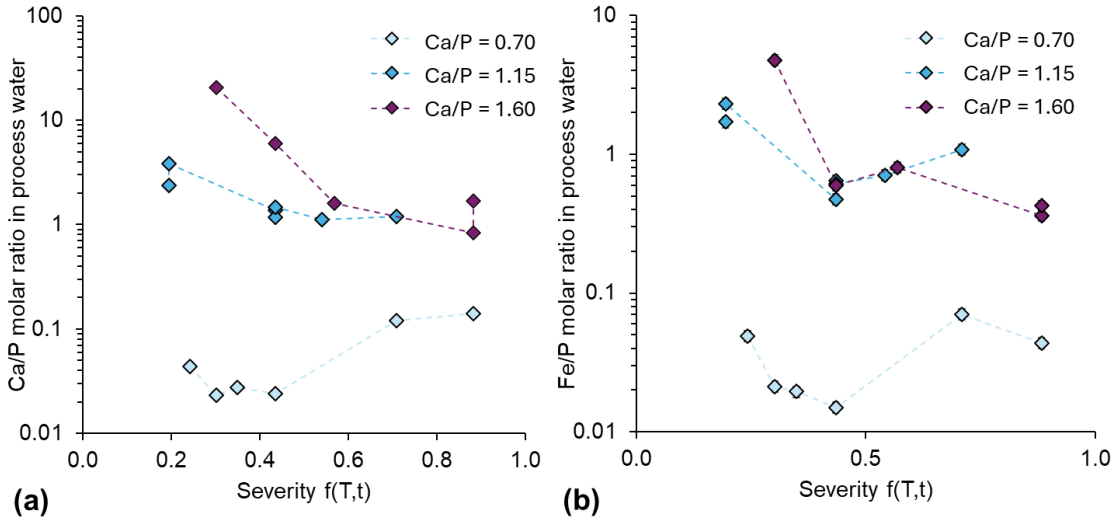

Figure 6.12 – Ca/P molar ratio (a) and Fe/P molar ratio (b) in process water as a function of severity f(T,t) for the three different feed Ca/P molar ratios (0.70, 1.15, 1.60). Error bars represent propagated uncertainty. Dashed lines are included to help data interpretation.

Table 6.3 resumes the results of screening design of experiments for the responses related to process water P, Ca, Fe, Mg and K discussed in this section.

Table 6.3 - Results of the screening analysis on process water composition based on the experimental design reported in Table 2.4. Statistical validation is provided in Table D.27 (Annex D). Positive effects are expressed through one or two positive signs (+), negative effects through one or two negative signs (-). Double effects are three times more significant than the smallest significant effect. The absence of symbols indicates that the effect is not significant.

Factor	Temperature (°C)			Time (min)			Ca/P molar ratio		
from:	250	250	300	5	5	15	0.70	0.70	1.15
to:	300	350	350	15	45	45	1.15	1.60	1.60
P (mg L^{-1})[a]		- -	- -	-	-	-	- -	- -	
Ca (mg L^{-1})[a]	-	- -	-		-	-	+	++	+
Fe (mg L^{-1})[a]	-	- -	-		-	-	+	+	
Mg (mg L^{-1})[a]	-	++	++	-	-		++	++	-
K (mg L^{-1})		-	-				+	+	+
P (% feed P)[a]		- -	- -	-	-	-	- -	- -	
Ca (% feed Ca)[a]	-	- -	-		-	-		+	
Fe (% feed Fe)[a]	-	- -	-		-	-	+	+	
Mg (% feed Mg)[a]	-	++	++	-	-		++	++	-

[a]Result obtained using the logarithm of the response Y_i, $\log_{10}(Y_i)$, to prevent the model from returning negative values.

6.5. Solid by-products characterization

Figure 6.13 shows P, Ca, Fe, Al, Mg and K contents in solid pellet, expresses as mg g^{-1} of dry matter, as a function of process severity and for the three different Ca/P molar ratios.

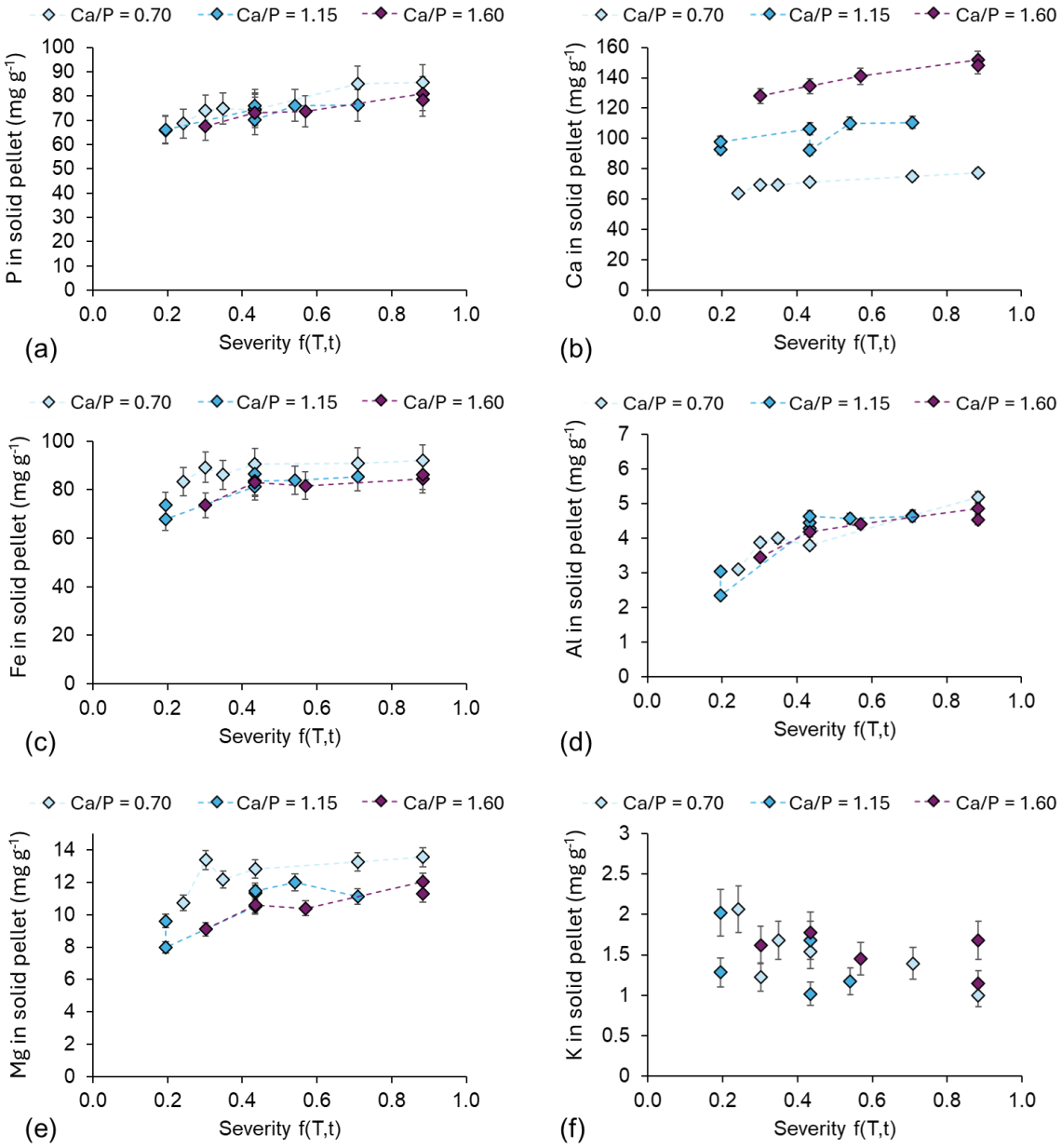

Figure 6.13 - P (a), Ca (b), Fe (c), Al (d), Mg (e) and K (f) contents in solid pellet expressed as mg g^{-1} (on a dry basis) as a function of severity f(T,t) for different Ca/P molar ratios. Error bars represent propagated uncertainty. Dashed lines are included to help data interpretation.

An increase in process severity leads to an increase in the content of P, Ca, Fe, Al, and Mg in the solid pellet. This is due to solubilization and degradation of organic matter, leading to the accumulation of the mineral fraction in the solid pellet. This has already

been observed for Sludge A (Section 4.5.3) and in previous works[11]. Process severity does not have a clear effect on K content in solid pellet (Figure 6.13f).

Ca/P molar ratio increase leads to a strong increase in Ca content, but it also results in a reduction in the content of P, Fe and Mg, probably because the addition of a substantial mass of Ca leads to a "dilution" of the amount of these two metals in the solid product. The adjustment of the Ca/P molar ratio is in fact achieved through the addition of CaO in amounts ranging from 3.5% to 7% of the dry mass present in the sludge feed. At severities of 0.30, 0.43 and 0.88, increasing Ca/P ratio from 0.70 to 1.60 leads to an increase of total dry solids recovered in the solid pellet of respectively 12.6%, 19.9% and 49.4%.

Fe and Mg content decrease in solid pellet is also consistent with the increase in soluble Fe and Mg in the process water, described in Section 6.4. CaO addition does not have a clear effect on Al an K content in solid pellet (Figure 6.13d and 6.13f).

The screening analysis of these results allowed to assess that P, Ca, Fe, Mg and K contents in HT solid by-products increase with increasing temperature and longer treatments. Once more this was already observed for Sludge A (Section 4.5.3). CaO addition has been correlated to a strong increase in Ca content, but it also results in a reduction in the content of P, Fe and Mg. While the addition of CaO promotes P precipitation, as discussed in Section 6.4, the overall increase in pellet dry mass results in a lower P content expressed as mg P g^{-1}.

Figure 6.14 shows NAIP and AIP fractions expressed as % of TP in solid pellet, as a function of process severity for the three different Ca/P molar ratios.

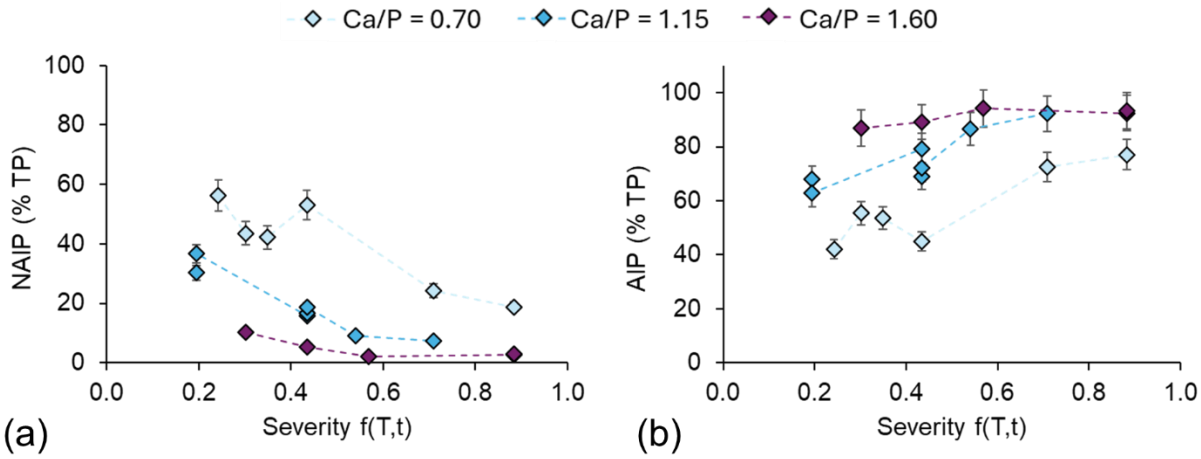

Figure 6.14 - NAIP (a) and AIP (b) fractions expressed as % of TP in solid pellet, as a function of severity f(T,t) for the three different Ca/P molar ratios. Error bars represent propagated uncertainty. Dashed lines are included to help data interpretation.

The results in Figure 6.14 show that a process severity increase leads to an increase in AIP fraction and a decrease in NAIP fraction. The effect of CaO addition is however more apparent, leading to a strong NAIP reduction and AIP increase. With no CaO addition AIP ranges from 42-55% of the TP for treatments carried out at 250 °C and 300 °C, up to 72-77% at 350 °C. Conversely, the NAIP decreases from 42-56% at 250 – 300 °C, down to 19-24% at 350 °C. When the Ca/P ratio is increased to 1.15, the AIP increases to values

ranging from 63% to 92%, and the NAIP falls within a range between 7% and 37% of the TP. When Ca/P molar ratio is 1.60, AIP fraction is not lower than 87% of TP. The NAIP, on the other hand, is very low, with values not exceeding 10%.

Screening analysis of these results shows that a temperature increase is correlated with NAIP reduction and AIP increase. This was observed for Sludge A products too (Section 4.6). Besides, a longer treatment has been correlated with lower NAIP fraction.

As expected, P speciation is affected by CaO addition: a Ca/P molar ratio increase has been correlated with NAIP decrease and AIP increase.

Table D.18 reports the ANOVA validation tool for the second-degree polynomial surface response for AIP, expressed as fraction of TP. The second-degree polynomial model provided by the surface response is statistically significant, with a p-value less than 0.01% and an R^2 of 0.96. The model standard deviation is equal to 5%.

Table D.19 reports the second-degree model coefficients of the response surface for AIP, expressed as a fraction of solid pellet TP, with respective statistical validation. The coefficients for the linear effects of temperature (b_1) and Ca/P molar ratio (b_3) are statistically significant. The obtained surface response confirms the positive effect of temperature and Ca/P molar ratio on AIP yield. The quadratic Ca/P term ($b_{3\text{-}3}$) is also significant. The T - Ca/P interaction term is significant and negative, this adds a positive contribution for low temperatures and high Ca/P ratios, and for high temperatures and low Ca/P ratios, indicating that at high Ca/P molar ratio the effect of temperature is less impactful.

Equation 6.12 shows the corresponding second-degree polynomial model obtained for AIP fraction (% of TP) as a function of temperature (°C), treatment duration (min) and feed Ca/P molar ratio.

$$AIP\ (\%TP) = \mathbf{76.6} + \mathbf{9.68}\boldsymbol{T} + 3.90t + \mathbf{14.84}\boldsymbol{Ca} + 3.27T^2 + 2.38t^2 \\ -\mathbf{7.33}\boldsymbol{Ca}^{\mathbf{2}} - 2.80T \cdot t - \mathbf{4.49}\boldsymbol{T} \cdot \boldsymbol{Ca} - 2.64t \cdot Ca \quad (6.12)$$

Where T, t and Ca are respectively temperature, treatment duration and Ca/P molar ratio expressed as normalized values according to Equations 2.26, 2.27 and 2.29. Statistically significant terms are in bold.

Figure 6.15 shows the response surface obtained for AIP, expressed as a fraction of solid pellet TP, as a function of temperature (°C), treatment duration (min) and feed Ca/P molar ratio. For a 15 min treatment at 250 °C, increasing the Ca/P molar ratio to 1.15 allows for a 20% increase in the AIP fraction (from around 45% to 65%). To achieve the same relative amount of AIP without the addition of CaO, it is necessary to reach at least 310 °C.

Increasing the Ca/P molar ratio to 1.6 allows for more than 80% of P to be in AIP form in the solid product already at 250 °C, 5 min, while a maximum of around 95% can be obtained at 350 °C and Ca/P= 1.6. This result demonstrates that the addition of CaO allows to precipitate nearly all P in the sludge in the solid pellet by-product, mainly as AIP, even at relatively low temperatures (250 °C).

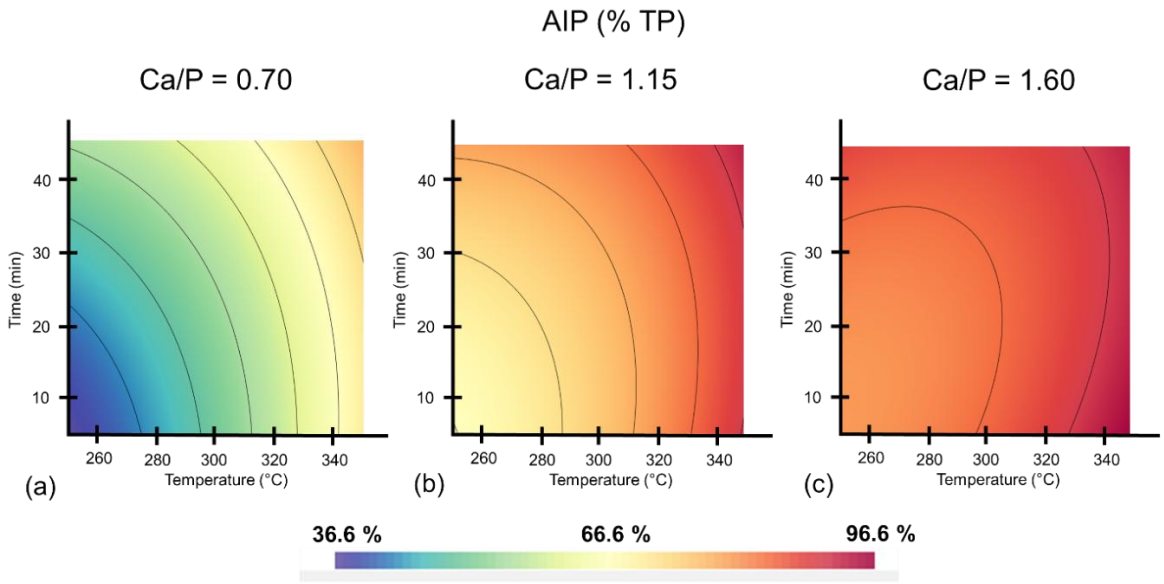

Figure 6.15 - AIP fraction expressed as % of total P in solid pellet by-product based on the experimental design reported in Table 2.4, as a function of temperature and treatment duration for three Ca/P molar ratios (0.70, 1.15, 1.60).

Figure 6.16 compares the experimental results for AIP fraction expressed as % of solid pellet IP, with results from various studies available in literature. The obtained results clearly follow the same general trend suggested by existing data: an increase in process severity and in the Ca/P molar ratio leads to an increase in the AIP fraction (and conversely, a decrease in NAIP). For the treatments carried out with a Ca/P molar ratio lower than 1.5, a higher AIP fraction is obtained in this study compared to literature data, probably because relatively high temperatures and thus higher severities than those in the available studies are proposed.

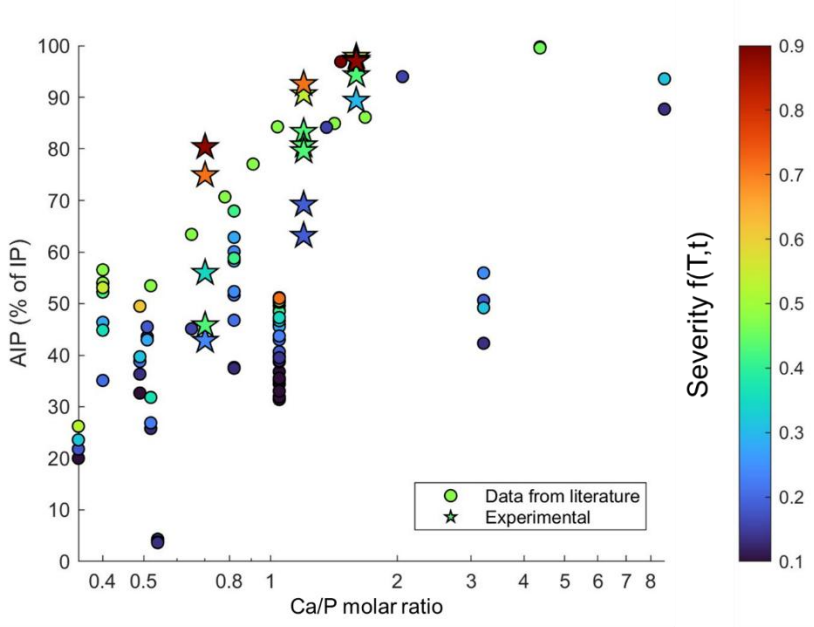

Figure 6.16 - Comparison between AIP fraction (% of IP) in this study (★), with data points from various studies available in literature(●) [10,77–81,86,88,89,91–93].

Figure H.2 (Annex H) shows the Cu, Zn, Pb, V, Cr, Ni, As, Ag, Cd, Hg content in the solid pellet, expressed as mg g^{-1} or mg kg^{-1} on a dry basis, as a function of process severity for the three Ca/P molar ratios. The screening analysis of these results allowed to assess that an increase in temperature leads to Cu, Zn, Pb, V, Cr, Ni, As and Cd accumulation in the solid pellet. An increase in treatment duration has been correlated with an increase of Pb, V, Cr, As and Cd content in solid pellet. This has been already observed for Sludge A (Section 4.5.3). The increase in the Ca/P molar ratio through the addition of CaO, on the other hand, results in a decrease in Cu, Zn, V, Cr and Ni content in the solid pellet, since a substantial amount of mineral solid matter is added to the final solid product. The only heavy metal that has been positively correlated with the addition of CaO is As: an increase in the Ca/P molar ratio leads to an increase in the As content in the solid pellet. This could be related to the precipitation of compounds such as Ca arsenites ($Ca(AsO_2)_2$, and $CaAsO_2OH{\cdot}½H_2O$) and arsenates ($Ca_5(AsO_4)_3OH$)[239].

Figure 6.17 shows Ca/P, Fe/P and Al/P molar ratios in the solid pellet product as a function of process severity for the three Ca/P molar ratios. The Ca/P ratio in the solid pellets remains roughly constant and independent of process severity, maintaining roughly the same value initially present in the feed (0.70, 1.15, and 1.60). This suggests that nearly all P and Ca are recovered in the solid pellet. In treatments conducted without the addition of CaO, the Ca/P ratio in solid pellet is around 0.70, as in Sludge B. For the more severe treatments, AIP constitutes about 70% of TP (Figure 6.14b), suggesting that all Ca has precipitated with P, supposing the precipitation of a phosphate with unimolar stoichiometry ($CaHPO_4$).

In the case of a Ca/P ratio of 1.15 in the feed, under the highest severities (0.54-0.71), Ca/P ratio is about 1.10 in both the process water (Figure 6.12a) and the solid pellet (Figure 6.17a). Less than 0.2% of the P remains in process water (Figure H.1a). Around 90% of the P recovered in the solid pellet is AIP (Figure 6.14b). This suggests that P precipitation is complete, with P precipitating with Ca, predominantly in the form of dicalcium phosphate ($CaHPO_4$) with a Ca/P stoichiometry of 1, and possibly octacalcium phosphate ($Ca_8H_2(PO_4)_6$) with a Ca/P stoichiometry of 1.33.

For treatments with an Ca/P ratio of 1.60 in the feed, under the highest severities (0.57-0.88), the solid pellet Ca/P ratio is roughly 1.5 (Figure 6.17a), while it is around 1 in the process water (Figure 6.12a). Less than 0.2% of P remains as soluble P in the process water (Figure H.1a). Over 90% of the P recovered in the solid pellet is AIP (Figure 6.14b). Again, the results suggest complete P precipitation with Ca, primarily in the form of dicalcium phosphate ($CaHPO_4$) with a Ca/P stoichiometry of 1, and possibly with compounds with higher Ca/P stoichiometry such as octacalcium phosphate ($Ca_8H_2(PO_4)_6$, Ca/P = 1.33), tricalcium phosphate ($Ca_3(PO_4)_2$, Ca/P = 1.5), and hydroxyapatite ($Ca_{10}(PO_4)_6(OH)_2$, Ca/P = 1.66). However, the fact that P precipitation is already complete with a Ca/P molar ratio in the feed of 1.15 suggests a more likely precipitation of dicalcium phosphate and octacalcium phosphate. However, it should be noted that this analysis based on molar ratios is purely speculative, and to confirm it, it would be necessary to analyze P speciation with analytical techniques such as X-ray diffraction or X-ray

absorption near edge structure, which would allow the identification of specific compounds and track their evolution during the HT treatment.

Fe/P and Al/P molar ratio in solid pellets (Figure 6.17b and 6.17c) maintain roughly the same molar ratio initially present in Sludge B. The sum of Fe/P and Al/P ratios is lower than 0.8, suggesting that at most 80% of P could precipitate in the form of $FePO_4$ and $AlPO_4$. However, as shown in Figure 6.14a, NAIP fraction is always lower than 60%, and for the treatments realized with the highest Ca/P ratio, it is lower than 10%, suggesting that most Fe and Al in solid pellet is present in other compounds such as Fe and Al hydroxides.

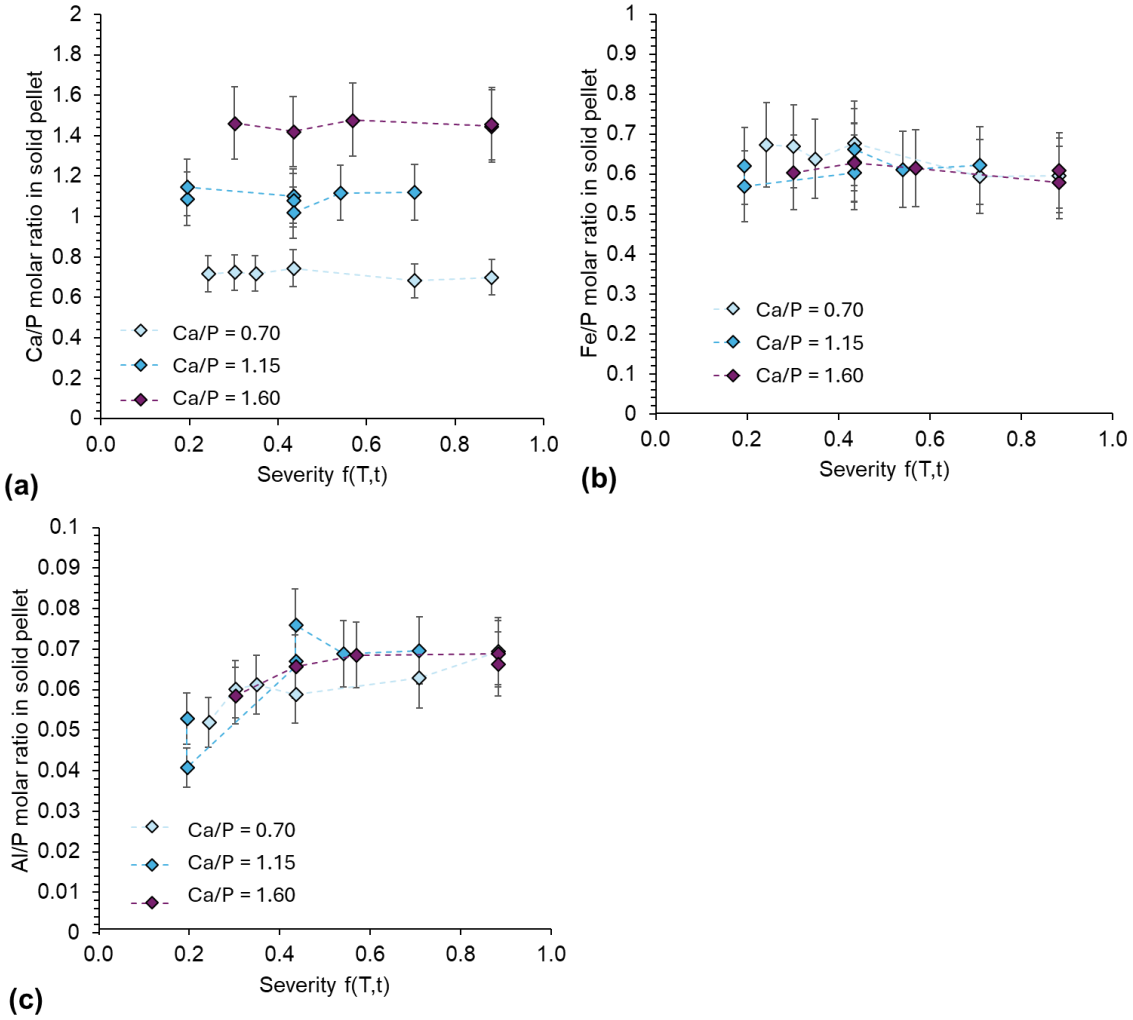

Figure 6.17 – Ca/P (a), Fe/P (b), and Al/P (c) molar ratio in solid pellet as a function of severity f(T,t) for the three different feed Ca/P molar ratios (0.70, 1.15, 1.60). Error bars represent propagated uncertainty. Dashed lines are included to help data interpretation.

Table 6.4 resumes the screening results for the responses related to the solid pellet by-products characteristics.

Table 6.4 - Screening analysis results on solid pellet by-products characteristics based on the experimental design reported in Table 2.4. P, metals and heavy metals contents are expressed on a dry basis. Statistical validation is provided in Table D.28 (Annex D). Positive effects are expressed through one or two positive signs (+), negative effects through one or two negative signs (-). Double effects are three times more significant than the smallest significant effect. The absence of symbols indicates that the effect is not significant.

Factor	Temperature (°C)			Time (min)			Ca/P molar ratio		
from:	*250*	*250*	*300*	*5*	*5*	*15*	*0.7*	*0.7*	*1.2*
to:	*300*	*350*	*350*	*15*	*45*	*45*	*1.2*	*1.6*	*1.6*
P (mg g^{-1})	+	++	+		+	+	-	-	
NAIP (% TP)	-	- -	-		-	-	- -	- -	-
AIP (%TP)		+	+				+	+	
Ca (mg g^{-1})	+	+	+				++	++	++
Fe (mg g^{-1})	+	+		+	+		-	-	
Al (mg g^{-1})	+	+			+				
Mg (mg g^{-1})	+	+			+	+	-	-	
Cu (mg g^{-1})	+	+	+				-	- -	-
Zn (mg g^{-1})	+	+					-	-	-
Pb (mg g^{-1})			+	+		-			
V (mg g^{-1})	+	+				+		-	
Cr (mg g^{-1})	+	+			+		-	-	
Ni (mg g^{-1})	+	+	+				-	-	
As (mg g^{-1})	++	++				+	++	++	+
Cd (mg g^{-1})		+	+	+					

As shown in Table 6.5, the recovered solid pellets obtained with both no additives and with CaO addition could potentially be used as macronutrient inorganic fertilizers according to 2019/1009 regulation on the market of EU fertilizing products [181], as they all meet the guidelines for minimum macronutrients values and respect the prescribed heavy metals limits, except for Cu, which could be reduced by an upstream approach, limiting its dispersion into the environment it the first place. Further investigations must be conducted to ensure that the solid pellet by-products are compatible for fertilizer use according to this regulation guidelines, specifically to assess biuret ($C_2H_5N_3O_2$), perchlorate (ClO_4^-) and hexavalent chromium (Cr VI) contents. The obtained pellets could be then exploited as Ca-rich slow-release P inorganic fertilizers.

Table 6.5 - Comparison between the macronutrients guidelines and the heavy metals limits prescribed by the 2019/1009 regulation[181], and the respective ranges observed for solid pellet by-products. *guidelines and limits from [181]. P_2O_5 = P/0.436; K_2O = K/0.830; MgO = Mg/0.603; CaO = Ca/0.715; SO_3 = S/0.4. **expressed as mg kg^{-1} P_2O_5. Composition expressed on a dry basis.

		Guidelines	Without CaO	With CaO
Macronutrients		*minimum value %**	Composition %	
	Sum	18	31.8 - 39.1	> 29.5
Contaminants		*limit mg kg^{-1}**	Composition mg kg^{-1}	
	Cd	60**	8.5 - 8.7**	9.05 - 9.09**
	Hg	1	0.13 - 0.22	0.09 - 0.17
	Ni	100	33.8 - 45.6	28.0 - 40.0
	Pb	120	53.9 - 97.0	58.3 - 76.6
	As	40	2.8 - 4.0	3.6 - 5.5
	Cu	600	710 - 831	614 - 787
	Zn	1500	1049 - 1197	940 - 1131

6.6. Integration of bio-oil production and solid pellet exploitation as fertilizer

The addition of CaO leads to the release of Ca^{2+} ions in the reaction medium, which have a dual effect on both the inorganic and organic phases: the high amount of Ca^{2+} ions leads to the almost complete precipitation of PO_4^{3-} as Ca phosphates (AIP). At the same time, $Ca(OH)_2$ derived from the hydration of CaO may lead to the saponification of some bio-oil components, reducing its yield.

Therefore, while the addition of CaO is beneficial for the complete recovery of P in the solid phase as AIP, it may significantly reduce the extractable bio-oil quantity and thus its potential energy valorization. Hence, it is necessary to find an optimal Ca/P molar ratio that allows sufficient P recovery without excessively reducing the extractable bio-oil quantity.

To achieve this, the desirability function approach is applied. In a first attempt, global desirability is calculated from the combination of the following factors:

1. Bio-oil yield above 15%, with a target of 16.6% (the maximum observed value).
2. A residual P fraction in the process water below 1%, with a target of 0.06% (the minimum observed value).
3. An AIP fraction in the solid pellet above 70% of TP, with a target of 96.6% (the maximum observed value).

Table 6.6 presents the specifics of this desirability study and the relative results.

Table 6.6 - Specifics of the first desirability study and relative results.

Specifics					
Response	**Type of desirability function**	**Target (%)**	**Limit**		
Bio-oil yield (% dry feed)	Maximization	16.6	Lower limit	15	
P in process water (% feed P)	Minimization	0.06	Upper limit	1	
AIP (% TP)	Maximization	96.6	Lower limit	70	
Optimum					
Factor		**Response (%)**		**Desirability (%)**	**Global desirability (%)**
Temperature (°C)	350	Bio-oil yield (% dry feed)	15.9	56.2	**43.4**
Time (min)	45	P in process water (% feed P)	0.4	34.7	
Ca/P molar ratio	0.76	AIP (% TP)	80.9	41.8	

The computed optimum corresponds to a global desirability of 43%. The optimum corresponds to the highest temperature and duration conditions (350 °C, 45 min). The severity of the HT treatment has in fact been correlated to a higher bio-oil yield, greater precipitation of soluble PO_4-P, and conversion of NAIP to AIP. The optimal Ca/P molar ratio of 0.76 allows for the precipitation of over 99.5% of the total feed P in solid form, with more than 80% in AIP form, achieving a bio-oil yield of 15.9%. Higher Ca/P molar ratio values would lead to more AIP, but a significant reduction in bio-oil yield. A Ca/P molar ratio of 0.76 corresponds to adding slightly more than 0.5% of CaO, expressed as a percentage of the dry mass of sludge introduced into the reactor.

In this first approach, the focus of the optimization is primarily on the bio-oil yield, which has a lower limit (15%) particularly close to the target value (16.6%). Another approach involves applying less stringent specifications for the bio-oil yield, aiming to further maximize the AIP% fraction. In this second approach, the global desirability is calculated by combining the following factors:

1. Bio-oil yield above 10%, with a target of 16.6% (the maximum observed value).
2. A residual P fraction in the process water below 1%, with a target of 0.06% (the minimum observed value).
3. An AIP fraction in the solid pellet above 90% of TP, with a target of 96.6% (the maximum observed value).

Table 6.7 presents the specifics of this second desirability study and the relative results.

Table 6.7 - Specifics of the second desirability study and relative results.

Specifics					
Response	**Type of desirability function**	**Target (%)**	**Limit**		
Bio-oil yield (% dry feed)	Maximization	16.6	Lower limit	10	
P in process water (% feed P)	Minimization	0.06	Upper limit	1	
AIP (% TP)	Maximization	96.6	Lower limit	90	
Optimum					
Factor		**Response (%)**		**Desirability (%)**	**Global desirability (%)**
Temperature (°C)	350	Bio-oil yield (% dry feed)	12.1	32.35	**59.4**
Time (min)	45	P in process water (% feed P)	0.06	99	
Ca/P molar ratio	1.24	AIP (% TP)	94.3	65.6	

In this case, the computed optimum corresponds to a higher global desirability, equal to 59%. The optimum corresponds once more to the highest temperature and duration conditions (350 °C, 45 min). The optimal Ca/P molar ratio of 1.24 allows for the precipitation of over 99.9% of the total feed P in solid form, with more than 94% in AIP form, achieving a bio-oil yield of 12.1%. Lower Ca/P molar ratio values would lead to a higher bio-oil yield, but also to reduction in AIP%. A Ca/P molar ratio of 1.24 corresponds to adding more than 0.8% of CaO, expressed as a percentage of the dry mass of sludge introduced into the reactor.

Figure 6.18 compares the global desirability responses for the two discussed approaches.

The comparison between the two figures confirms that, for both approaches, the desirability is greater than zero near the regions corresponding to the more severe conditions (350 °C, 45 min). The main difference between the two approaches lies only in the feed Ca/P molar ratio. In the approach aimed at maximizing bio-oil yield, Ca/P is between 0.7 and 0.85, whereas in the approach aimed at maximizing AIP, Ca/P is higher, ranging from 1 to 1.8. Therefore, the choice of a Ca/P molar ratio must be made considering the parameter of main concern, without forgetting the cost of the selected additive.

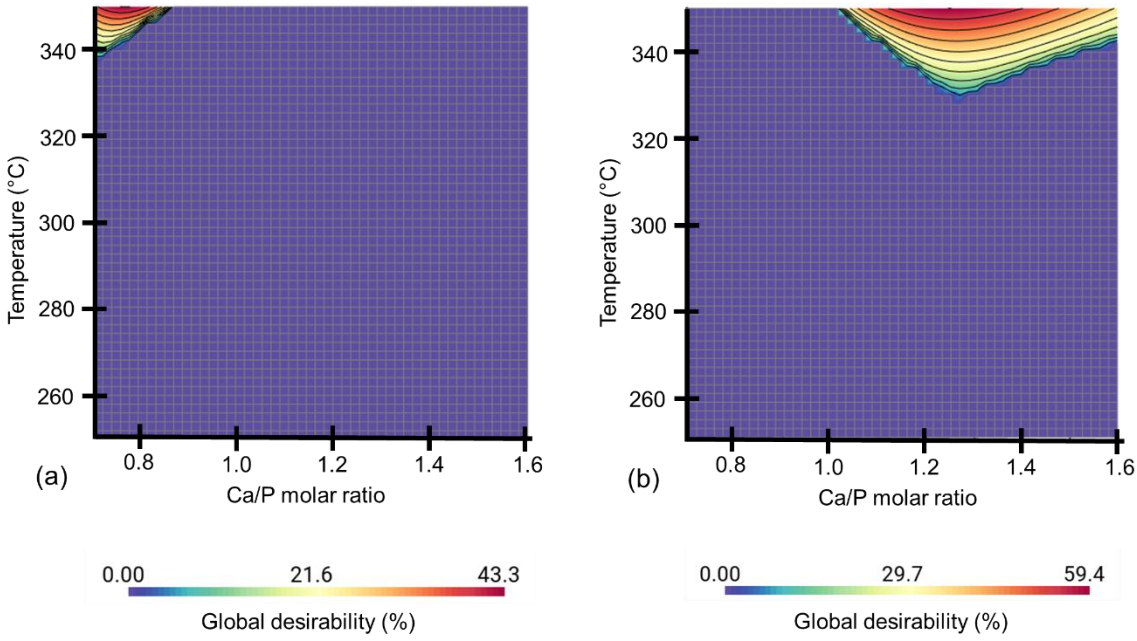

Figure 6.18 - (a) Global desirability color map obtained with specification described in Table 6.6 (bio-oil yield oriented). (b) global desirability color map obtained with specification described in Table 6.7 (AIP oriented). Desirability expressed as function of feed Ca/P molar ratio and temperature. Treatment duration is fixed at 45 min.

6.7. Conclusions

In this final Chapter 6, it was examined how modifying the Ca/P molar ratio with CaO addition during HT treatment of SS digestate may affect HT by-products and P speciation. To conduct the investigation, a D-optimal matrix experimental plan with three factors (temperature, time, and Ca/P molar ratio) was implemented and their relative effects in the form of second-degree polynomial response surfaces was evaluated. The results of the experimental plan showed that the addition of CaO leads to a noticeable decrease in bio-oil yield, which might be due to possible saponification reactions of some bio-oil components (esters and fatty acids) with $Ca(OH)_2$. This results in a decrease in the overall hydrophobicity of the product and thus an increase in the water content in the solid pellet.

The increase in the Ca/P molar ratio through the addition of CaO increases the alkalinity of the process water due to the release of OH^- ions into the reaction medium. The addition of CaO has also a very strong effect on the precipitation of soluble P. Adding just over 2% CaO (of the dry feed mass) reduces residual soluble P to a few tens of mg L^{-1}, even at 250 °C, precipitating over 99% of the feed P in the solid phase with a Ca/P molar ratio of about 1.

The increase in the molar ratio of Ca leads to an increase in the concentrations of Ca, Fe, Mg, and K in the process water, probably because the added Ca^{2+} ions displace other metal ions in the precipitation mechanisms. The addition of CaO is correlated with an increase in the Ca content in the solid pellet, and a decrease in the content of all other

measured elements, due to the addition of a substantial mass of inert material that is recovered in the pellet. An exception was observed for As, which can form precipitates with Ca.

The increase in the molar ratio of Ca is correlated with an increase in AIP and a decrease in NAIP, obtaining up to 90% of P in the AIP form.

Following CaO addition, Ca is no longer a limiting factor for P precipitation for milder treatments (250 °C), however, for more severe treatments, Ca/P ratio decreases to values slightly above between 0.8 and 1.8, suggesting that most of the Ca has precipitated. Interestingly, this Ca/P range corresponds to the stoichiometry of the main calcium phosphates salts (dicalcium phosphate, tricalcium phosphate, octacalcium phosphate and hydroxyapatite), suggesting a predominant presence of these compounds within the solid pellet.

When CaO is added, nearly 100 % of P and Ca are recovered in the solid pellet. Ca/P molar ratio in solid pellet and in process water are of the same order of magnitude, and most P in solid pellet is AIP. These observations suggest that P precipitation is complete, and that P precipitates predominantly with Ca. The fact that P precipitation is already complete with a Ca/P molar ratio in the feed of 1.15 suggests a more likely precipitation of dicalcium phosphate and maybe octacalcium phosphate. Further analysis with -ray diffraction or X-ray absorption near edge structure would be necessary to confirm this hypothesis.

This result shows that the stoichiometry of P with the principal metals capable of forming precipitates (Ca, Fe, Al, Mg) is essential for accurately predicting or controlling P precipitation as a specific or desired compound.

Analyzing the overall process desirability helped us to identify the optimal combination of factors to minimize P in process water, maximize AIP fraction, while avoiding significant reduction of bio-oil yield. According to the results of the analysis, an HT treatment conducted at 350 °C for 45 min, with a Ca molar ratio of about 0.76 If the priority is to maximize bio-oil production while obtaining less AIP. Conversely, if the focus is on maximizing AIP at the expense of bio-oil production, the optimal ratio is 1.24. Both approaches result in an interesting compromise, thereby allowing for the integration of energy recovery in the form of bio-oil, with the complete recovery of P in the solid phase as particularly stable Ca phosphates. The solid pellet thus produced would be compatible with agricultural use as an inorganic fertilizer rich in Ca and with slow-release P, particularly suitable for acidic soils or soils sensitive to eutrophication or Fe/Al bioaccumulation. More detailed studies on the solid pellet bioavailability for plants can be made by assessing the degree of crystallinity of Ca phosphates: a very low degree of crystallinity, indicating a predominance of amorphous Ca phosphates, would imply higher solubility and therefore better bioavailability.

Future studies should focus on a more in-depth characterization of the bio-oil, including its organic components and fuel properties. This characterization would also allow us to precisely understand the mechanism behind the reduction in bio-oil yield following the addition of CaO and confirm whether it is indeed due to saponification. Another crucial aspect to characterize is the amount of P lost along with the organic phase

after extraction with acetone. It is necessary to ensure that excessive amounts of P are not lost in the organic phase to optimally valorize the two by-products separately. Acetone is an organic solvent in which phosphates are not soluble. Nevertheless, if the extraction is performed on pellets containing a lot of soluble P, a part might end up in the extract, which also contains the water from the pellet. For this reason, it is essential to produce solid pellets in which P is thermodynamically stable and fixed in solid form. Additionally, the use of other organic solvents could be investigated.

General conclusion

The discussion presented in this work has allowed to understand how the main parameters of HT treatment influence P fate and repartition among the by-products, allowing to outline a general mechanism that can describe the chemical and physical pathways that P-containing species undergo during the HT process.

This type of analysis has allowed the definition of optimal parameters to valorize SS both from an energy perspective (bio-oil production) and for the recovery of the mineral fraction, in the form of a solid product rich in Ca phosphate that could be used as a slow-release fertilizer. A not exhaustive analysis of the current legislative limits in force, has shown that the solid product meets most of the established limits.

According to previous studies, temperature is the factor with the most significant impact. Higher temperatures result in increased P recovery in solid products and influence the conversion of organic phosphorus (OP) into inorganic phosphorus (IP), and non-apatite inorganic phosphorus (NAIP) into apatite inorganic phosphorus (AIP). Reaction time also affects P speciation, but temperature remains the dominant factor.

The analysis of these studies has also identified several unclear areas that warrant further research, which have been addressed in this work. Most studies reviewed focus on temperatures typical of HT carbonization ($T < 280$ °C), with limited experimental data available for higher temperatures associated with liquefaction and gasification. Additionally, further investigation is needed to better understand the interaction between temperature and treatment duration.

The experimental campaign results allowed to highlight the impact of temperature and time on by-products distribution: increasing temperature and treatment duration leads to a better by-products separation, to inorganic material dissolution and organic matter degradation. ^{31}C solid-state NMR spectroscopy results showed a complete biopolymers degradation already at 300 °C, through hydrolysis, dehydration, and decarboxylation reactions. Higher temperatures lead to aromatization and the formation of hydrochar clusters. This set of reactions contributes to the overall exothermic nature of the HT treatment, which has been characterized by differential scanning calorimetry. The global enthalpy of reaction is quantified between 190 and 340 kJ kg^{-1} of dry matter. This exothermic reaction can potentially generate up to 10% of the energy required for the HT treatment.

P, calcium (Ca), iron (Fe), magnesium (Mg) and heavy metals contents in the solid pellet generally increase with increasing temperature and treatment duration. At lower temperatures (250 °C), OP mineralization and NAIP dissolution lead to a release of free orthophosphates in the reaction medium. At higher temperatures (300 – 350 °C) the re-precipitation of orthophosphates with Ca is the dominant mechanism, leading to a product with a prevalent AIP fraction. Interestingly, complete P precipitation was not

achieved even under the most severe conditions. For all process water by-products, Ca/P, Fe/P and Mg/P molar ratios are always lower than 1, indicating that the available Ca^{2+}, Fe^{3+}, and Mg^{2+} concentrations in solution are insufficient for complete orthophosphate precipitation. Besides, Ca/P molar ratio in solid pellet by-products is at most 0.7, meaning that not more than 70% of total P can precipitate with the available Ca, assuming the formation of dicalcium phosphate ($CaHPO_4$). Under the most severe conditions, it was indeed observed that AIP corresponds to about 70% of total P. To achieve higher amounts of calcium phosphate, it is therefore necessary to introduce additional Ca into the sludge. This indicates that the stoichiometry of the key metals involved in P speciation is a crucial parameter in defining the conversion pathway of P during HT treatments.

To explore the effects of solid loading and feedstock composition, factors often overlooked in previous studies, a comparison was conducted on the HT treatment of two sludges from the same wastewater treatment plant. These sludges differed in key characteristics, including total solids content and composition, particularly Fe content.

Using sludge with higher solid loading resulted in greater total solids recovery yield, increased alkalinity, and higher concentrations of TN, NH_4-N, COD, TC, TIC, and TOC in the process water. This is attributed to the higher organic matter content (carbohydrates and proteins) and lower water content. Higher solid loading also led to increased soluble P concentration in process water for milder treatments. However, higher levels of Fe and Ca in the sludge were associated with lower soluble P concentrations, especially for more severe treatments.

Sludges with higher P, Fe, and Ca contents result in higher levels of these elements in the solid pellets, while increased Fe leads to more P recovered in the non-apatite inorganic fraction. A sludge with high solid loading (20 %) and a higher Fe/P molar ratio (0.7) can enhance P recovery in solid products. However, at lower temperatures (250–300 °C), a significant amount of P can remain in process water.

To optimize P recovery as Ca phosphate in solid products, the final section of this study explored the impact of adding CaO during HT treatment of SS on by-product characteristics and P speciation. The addition of CaO significantly reduces bio-oil yield, likely due to saponification reactions of bio-oil components (esters and fatty acids) with $Ca(OH)_2$. However, CaO addition strongly promotes the precipitation of soluble P, enabling the recovery of over 99% of the feed P in the solid product with a Ca/P molar ratio of approximately 1. This addition also increases the AIP content, up to 90% of total P. For more severe treatments (300 °C – 350 °C), the Ca/P molar ratio in both the solid pellet and process water ranges from 0.8 to 1.8, indicating that most of Ca has precipitated. P precipitation is nearly complete with a feed Ca/P molar ratio of 1.15, suggesting the formation of dicalcium phosphate and possibly octacalcium phosphate.

An optimal HT treatment that minimizes P recovered in process water, maximize the AIP fraction, and avoid significant reductions in bio-oil yield would be conducted at 350 °C for 45 minutes, with a Ca/P molar ratio comprised between 0.76 and 1.24, depending on whether the priority is to maximize bio-oil yield or the AIP fraction. The resulting solid pellet could serve as an effective inorganic fertilizer, rich in Ca and offering slow-release

P, making it particularly suitable for acidic soils or those prone to eutrophication or Fe/Al bioaccumulation.

Figure 7.1 proposed a schematic summary of all the chemical reactions and physical mechanisms undergone by the organic components of the biomass, along with the general pathways related to P conversion and speciation that have been defined and discussed in this work.

The biopolymers constituting the organic matter undergo hydrolysis, dehydration, decarboxylation, condensation, and aromatization reactions, producing solid hydrochar and bio-oil. The OP, mainly contained in phospholipids, undergoes rapid mineralization. P contained in inorganic phosphates and adsorbed onto metal hydroxides is released as PO_4-P, which combines with available metal cations in solution to precipitate as metal phosphates.

Although this work has provided many elements to understand the mechanisms behind the conversion and speciation of P during the HT treatment of SS, it is possible to propose some general perspectives and directions for upcoming research on the subject.

Future studies should focus on a more in-depth characterization of the bio-oil, including its organic and inorganic components and fuel properties. This characterization would also allow to precisely understand the mechanism behind the reduction in bio-oil yield following the addition of CaO and confirm if the saponification reaction can explain this evolution. Another crucial aspect is the amount of P lost along with the organic phase after extraction with acetone for bio-oil extraction. It is necessary to ensure that excessive amounts of P are not lost in the organic phase to optimally valorize the two by-products separately. Acetone is an organic solvent in which phosphates are not soluble. Nevertheless, if the extraction is performed on pellets containing a lot of soluble P, a part might end up in the extract, which also contains the water from the pellet. For this reason, it is essential to produce solid pellets in which P is thermodynamically stable and fixed in solid form. Additionally, the use of other organic solvents could be investigated.

Future investigations should also focus on the specific characterization of P-containing compounds (both organic and inorganic) present in SS and HT solid product. Analytical techniques such as X-ray diffraction or X-ray absorption near edge structure allow the identification of specific compounds and can track their evolution during the HT treatment. A more detailed investigation on the solid pellet bioavailability for crops can be made by assessing the degree of crystallinity of Ca phosphates with X ray diffraction: a very low degree of crystallinity, indicating a predominance of amorphous Ca phosphates, would imply higher solubility and therefore better bioavailability.

Another unclear aspect concerns the kinetics of OP mineralization, which is not characterized due to the relative high temperatures, resulting in apparently too fast kinetics, and due to P speciation techniques (sequential extraction) with high experimental error, which does not allow precise quantification of OP. Further research is needed to explore the role of treatment duration on OP mineralization. To achieve this, one could consider implementing a continuous process to treat an effluent particularly rich in OP. Using a continuous reactor would allow for more precise control of the residence time in the order of seconds or minutes, facilitating the development of a kinetic

model for OP mineralization under varying HT conditions. An implementation of continuous HT treatment could also be applied to SS to produce bio-oil and solid products for mineral phase valorization. This approach would allow for greater process automation. This would be, together with a cost-effectiveness analysis of the process, the next required step in the perspective of an industrial application.

The solid products resulting from the HT treatment seem to be compatible with European and French regulations for use as fertilizers in agriculture, but some analyses are still required to complete the characterization of environmental compatibility, including the quantification of biuret, perchlorate, and hexavalent Cr. Furthermore, with a view to industrial scale-up of the process, it is necessary to understand how to treat or valorize the process water, whose COD and N, P content may be too high for release in the environment and thus would require more treatments, leading to additional costs. Alternatively, it would be interesting to study in detail a process that integrates anaerobic digestion of SS and HT treatment of the digestate, where the HT process water is recirculated into the digester. Some studies exist on this topic, but they are not in-depth.

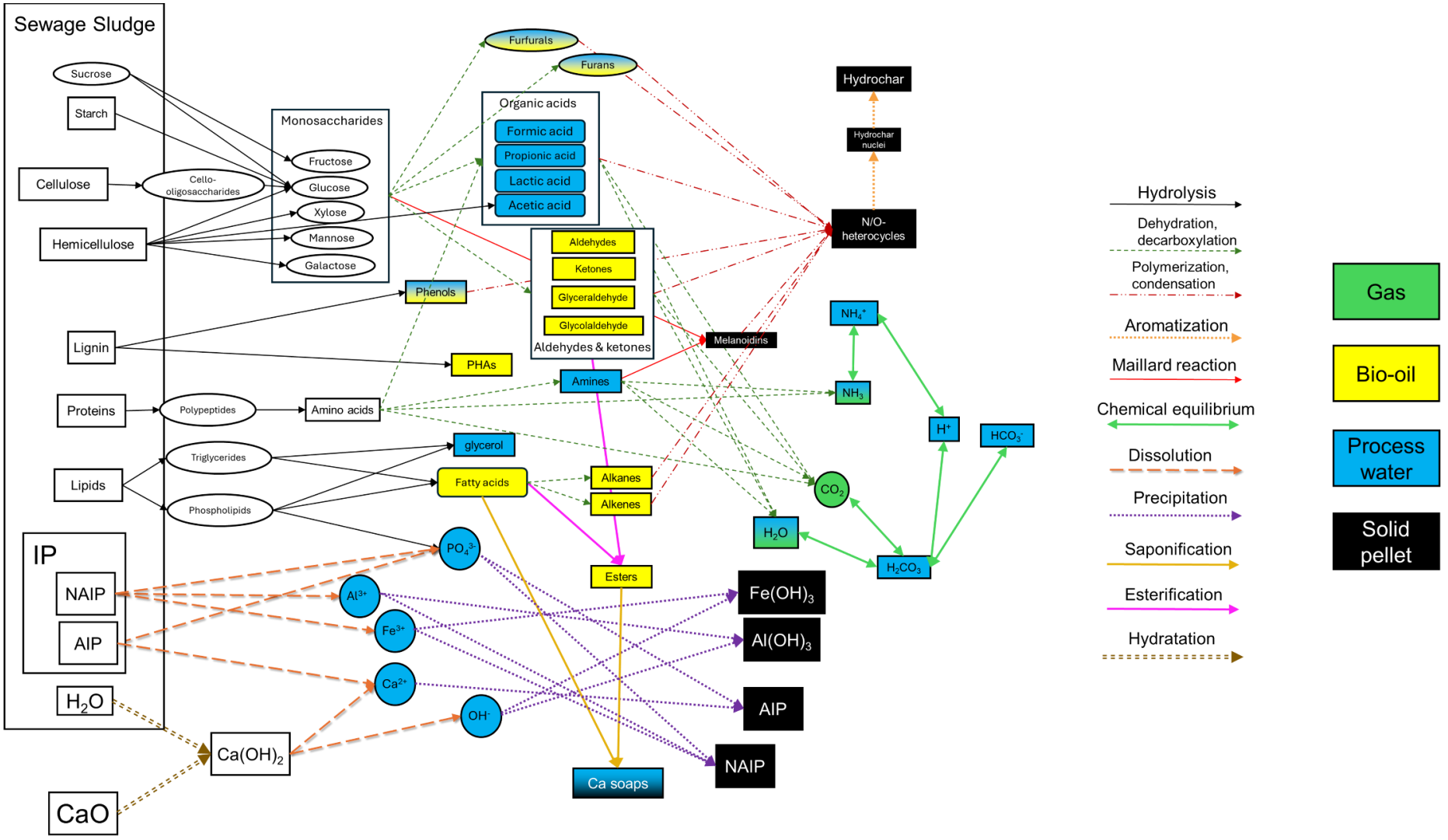

Figure 7.1 - Schematic summary of the chemical reactions and physical mechanisms interesting the organic components of the biomass, along with the general pathways related to P conversion and speciation.

Résumé en français

I. Etat de l'Art

Le phosphore (P) est un nutriment essentiel à l'agriculture moderne[2]. La demande d'engrais contenant P, liée à la croissance démographique, entraînera une raréfaction des réserves en apatite[7,8], menaçant la production alimentaire mondiale. Il est donc crucial de récupérer et valoriser le P à grande échelle à partir de déchets riches en P.

Les boues de station d'épuration sont un mélange liquide-solide produit en continu dans les stations d'épuration (STEP). Elles contiennent principalement de l'eau[6], de la matière organique, des métaux lourds, des pathogènes[9] et des nutriments essentiels comme le P, l'azote (N) et le potassium (K)[10]. Face à l'augmentation de la production mondiale de boues de STEP, leur valorisation pour récupérer le P devient cruciale pour soutenir l'approvisionnement alimentaire et limiter l'eutrophisation[2,18]. Des traitements thermiques (incinération, pyrolyse, gazéification) permettent d'éliminer les polluants organiques et pathogènes, tout en produisant des sous-produits intéressants comme du biochar, du biocarburant et du syngas[32].

Au cours de la dernière décennie, de nombreuses études internationales ont exploré l'applicabilité des traitements hydrothermaux (HT) pour valoriser la biomasse[39–42]. Ces procédés transforment la biomasse humide sans étape de séchage préalable, via des réactions favorisées par l'eau[46]. La carbonisation hydrothermale (HTC) produit du hydrochar à 180-280 °C avec un chauffage lent[49]. La liquéfaction hydrothermale (HTL) se fait à 250-400 °C avec un chauffage rapide pour obtenir du biohuile comme produit principal[49]. La gazéification hydrothermale (HTG), réalisée à des températures supérieures à 400 °C, en eau supercritique, génère un syngas riche en H_2[45,50].

Une analyse critique des études disponibles en littérature a permis de sélectionner plus de 65 travaux sur la conversion du P lors des traitements HT des boues de STEP.

La teneur en P des boues utilisées dans les études sélectionnées varie de 2,8 à 56,2 mg P g^{-1}, avec une moyenne de 27,4 mg P g^{-1}. Les teneurs moyennes en fer (Fe), calcium (Ca), aluminium (Al) et magnésium (Mg) sont respectivement de 36,5, 30,3, 19,0 et 7,1 mg g^{-1}. Les rapports molaires Fe/P, Ca/P et Al/P sont proches de ceux des phosphates de Ca, Fe, Al et Mg les plus courants[72], ce qui suggère que ces éléments ne sont pas limitants pour la précipitation du P. La Figure I montre la spéciation du P suivant la méthode *Standard Measuring and Treatment* (SMT) [74,75], selon laquelle le P total (TP) est fractionné en P organique (OP) et P inorganique (IP). Ce dernier peut être encore fractionné en P inorganique apatitique (AIP), constitué principalement de phosphates de calcium, et P inorganique non-apatitique (NAIP), désignant le P inorganique non lié au Ca[76].

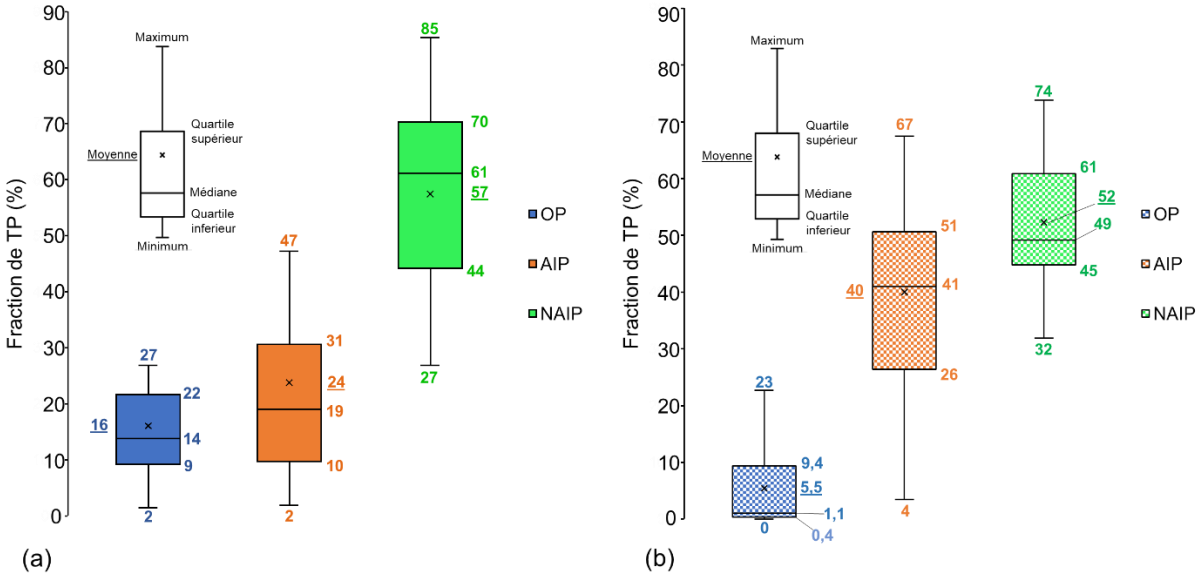

Figure I - Distribution en boîte à moustache des quantités relatives de P inorganique apatitique (AIP), de P inorganique non apatitique (NAIP) et de P organique (OP) dans les boues de STEP (a) et dans les produits solides du traitement HT (b), exprimées en fraction de la teneur totale en P (%TP). Les valeurs moyennes sont soulignées. [10,77–94].

La Figure Ia indique que dans les boues de STEP le NAIP représente 57% du TP, suivi par le AIP à 24%, et le OP à 16%.

Les principaux paramètres du procédé HT étudiés sont la température, la durée et le taux en solides totaux (ST) des boues. Sur 580 points expérimentaux, la majorité des études (78%) se situent entre 80 et 280 °C.

Les concentrations moyennes de P, Fe, Ca, Al, Mg dans les produit solides des traitements HT des boues de STEP sont respectivement de 41,1 mg P g^{-1}, 51,3 mg Fe g^{-1}, 39,8 mg Ca g^{-1}, 19,7 mg Al g^{-1} et 7,1 mg Mg g^{-1}, généralement plus élevées par rapport aux teneurs moyennes dans les boues de STEP, indiquant un phénomène d'accumulation de ces éléments dans le produit solide[5].

Comme indiqué par la Figure Ib, dans le produit solide du traitement HT, le NAIP représente 52 % du P total, suivi de l'AIP (40 %) et de l'OP (5,5 %). Les fractions de NAIP et d'OP sont plus faibles après HT, tandis que l'AIP augmente.

La température et le temps de réaction sont les paramètres les plus étudiés pour leurs effets sur les produits et la spéciation du P. Le facteur de sévérité HT f(T,t), basé sur ces deux variables, est couramment utilisé, notamment via le modèle de carbonisation de Ruyter[101] (équation I).

$$f(T,t) = 50\, t^{0.2}\, e^{-\frac{3500}{T}} \qquad \text{(I)}$$

avec t le temps (s) et T la température (K).

Le rendement en produit solide est défini par l'équation II :

$$Rendement\ en\ produit\ solide\ (\%) = \frac{m_{PS,sec}}{m_{BSE,sec}} \cdot 100 \qquad \text{(II)}$$

avec $m_{PS,sec}$ la masse sèche du produit solide (g), et $m_{BSE,sec}$ la masse sèche de la boue utilisée comme substrat du procédé HT(g).

Un f(T,t) élevé (> 0,5) réduit le rendement en produit solide (< 55 %) en raison de la dégradation et solubilisation des biopolymères[9,11].

Le contenu en P (mg P g^{-1}) augmente avec la température[62,77,79–82,89,91,98,105–109] et le temps[71,77,81,82,100,107,110], la température ayant un impact plus fort[78,81].

Le rendement de récupération du P dans le produit solide (%) est défini par l'équation III :

$$Rendement\ de\ P\ dans\ le\ produit\ solide\ (\%) = \frac{C_{P,PS}}{C_{P,BSE}} \cdot 100 \qquad \text{(III)}$$

avec $C_{P,PS}$ et $C_{P,BSE}$ les contenus en P total dans le produit solide et dans la boue (mg P g^{-1}).

La Figure II montre une corrélation positive entre l'augmentation de f(T,t) et le rendement de P dans le produit solide, indiquant qu'une température plus élevée et/ou un temps de réaction prolongé favorise cette récupération[10,39,77,80,81,85,88,96,98,99,103,111,112].

L'effet du temps de réaction est plus pertinent à basse température (< 180 °C), influençant la minéralisation des OP en orthophosphates. L'OP est complètement minéralisé en moins de 60 min à une température supérieure à 175 °C[10,77,78,82,114,115], et en moins de 10 s à > 500 °C[114]. L'augmentation de f(T,t) favorise la conversion de NAIP en AIP, avec une hausse d'AIP après traitement et une diminution de NAIP[10,77–81,83,85–94].

Une augmentation du taux en solides totaux des boues utilisées comme alimentation du procédé HT est corrélée à un rendement de récupération de produit solide plus élevé et à une meilleure récupération de P dans le produit solide[78,98,125]. Cependant, les données disponibles ne suffisent pas à établir une corrélation claire entre les voies de conversion du P et le taux en solides totaux, ce qui souligne la nécessité de poursuivre les recherches sur ce sujet.

Un grand nombre d'études sélectionnées ont examiné l'effet de l'ajustement du pH sur la spéciation et la migration du P lors des traitements HT des boues de STEP[10,43,62,77,84,85,87,91,108,126]. Le rendement de récupération du P dans le produit solide augmente avec l'augmentation du pH. Un pH élevé favorise la précipitation des phosphates de Ca[77], tandis qu'un pH plus bas favorise la dissolution du P dans l'eau[10,129], car un milieu plus acide dissout plus facilement les espèces inorganiques du P ainsi que les espèces métalliques[10].

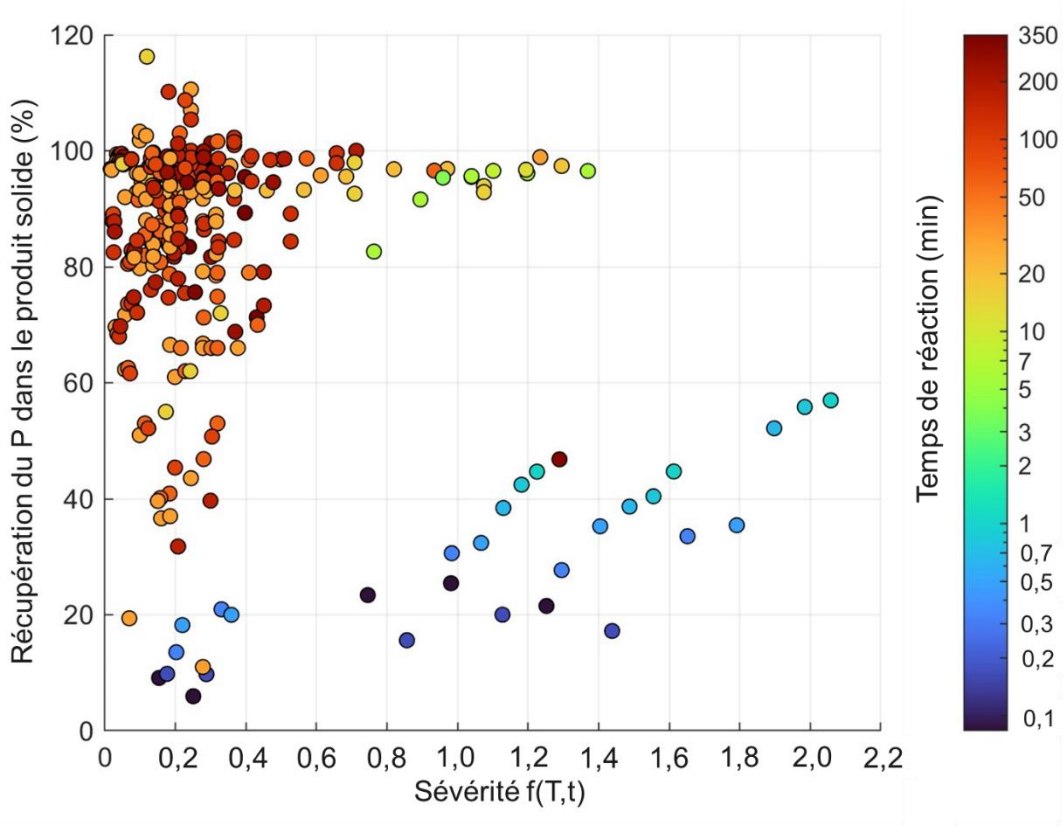

Figure II - Rendement de récupération du P dans le produit solide en fonction de f(T,t) (équation I). L'échelle de couleurs représente la durée du traitement exprimée en min[1].

Différents travaux étudient l'effet de l'ajout de Ca sur la migration et la spéciation du P lors des traitements HT des boues de STEP [77,83,84,87,88,98]. L'oxyde de Ca (CaO) est l'additif contenant du Ca le plus utilisé dans la littérature. La Figure III présente les points expérimentaux recueillis qui mettent en relation la sévérité du procédé et le rapport molaire Ca/P de l'intrant avec la quantité relative d'AIP dans le produit solide (exprimée en % de l'IP total). Les résultats montrent clairement que la fraction d'AIP augmente avec l'augmentation de la sévérité du procédé et du rapport molaire Ca/P.

D'autres additifs peuvent être ajoutés pour améliorer la récupération du P dans le produit solide, comme les chlorures de calcium[87], de fer[93], d'aluminium[93], de polyaluminium[99] et le persulfate de sodium[122].

L'analyse de l'état de l'art de la recherche sur ce sujet a également permis d'identifier les points qui nécessitent des recherches plus approfondies. Ainsi, des recherches supplémentaires sont nécessaires pour mieux caractériser la spéciation du P pour des températures > 280°C (HTL et HTG). Une caractérisation complète du profil thermique du traitement HT et une quantification de l'enthalpie de réaction permettraient d'estimer l'exothermicité du procédé et les gains énergétiques associés afin d'évaluer l'efficacité économique globale du traitement HT des boues de STEP.

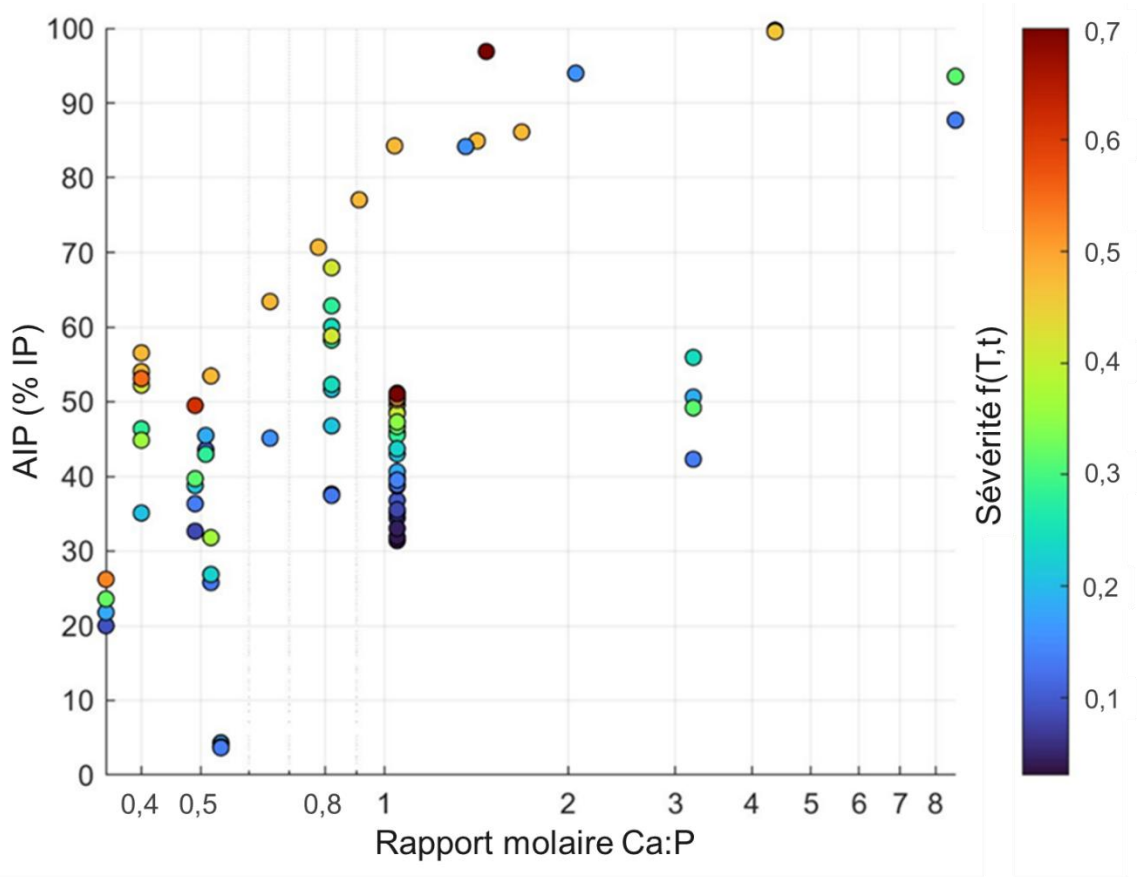

Figure III - Fraction de P inorganique apatitique (AIP) sur le P inorganique total(IP) en fonction du rapport molaire Ca/P du substrat. La couleur représente la sévérité du traitement (équation I.1) [10,77–81,86,88,89,91–93].

Il serait également intéressant d'évaluer l'effet de certains paramètres qui n'ont pas reçu beaucoup d'attention dans les travaux rapportés, tels que la pression et le taux en solides totaux, et également plus en détail les interactions possibles entre ceux déjà étudiés, tels que la température, le temps ou la composition de l'alimentation (contenu en P, Ca, Fe). De plus, une évaluation détaillée des polluants dans les produits HT devrait être réalisée afin d'estimer les coûts de leur élimination ou les approches les plus appropriées pour réduire leur quantité et leur dangerosité. Tous ces éléments contribueraient à fournir une compréhension complète et bien définie des mécanismes régissant les transformations de la matière organique et des macronutriments lors du traitement HT des boues de STEP.

II. Matériel et méthodes

Le digestat de boues secondaires utilisé dans ce travail est collecté à partir de la station d'épuration municipale d'Aix-La Pioline, située à Aix-en-Provence (Bouches-du-Rhône, France) (175 000 équivalents habitants).

Les boues utilisées sont :

I. Boues sortant du digesteur anaérobie, épaissies par centrifugation au laboratoire (Sigma 2-16P centrifuge, 4000 rpm, 20 min) (**Boues A**),
II. Mélange de boues digérées et tertiaires, épaissi par centrifugation industrielle au sein de la STEP (**Boues B**).

Les phases aqueuses associées, sortant des respectives centrifugations ont été également caractérisées, en distinguant **Surnageant A** et **Surnageant B**.

Le traitement HT est réalisé dans un réacteur cylindrique en acier inoxydable austénitique au chrome-nickel de 0,2 L (d : 50 mm, H : 100 mm), présenté en Figure IV. Le réacteur est chauffé grâce à une résistance électrique et refroidi par injection d'air comprimé. La régulation de la température est automatisée grâce à un contrôleur PID. La pressurisation du milieu de réaction est obtenue par injection d'azote (N_2), effectuée par une pompe à seringue TOP Industrie (Vaux-le-Pénil, France). L'agitation est assurée par une turbine de type Rushton à 6 pâles.

La boue est d'abord transférée dans un bécher, portée à température ambiante, puis mélangée avec une spatule pour garantir son homogénéité avant d'être introduite dans le réacteur. Celui-ci est ensuite scellé et pressurisé. Une fois que la température interne atteint la valeur cible (± 10 °C), le traitement débute. Après la durée de traitement définie, la phase de refroidissement est enclenchée. Lorsque la température interne descend à environ 35 °C, le réacteur est dépressurisé puis ouvert.

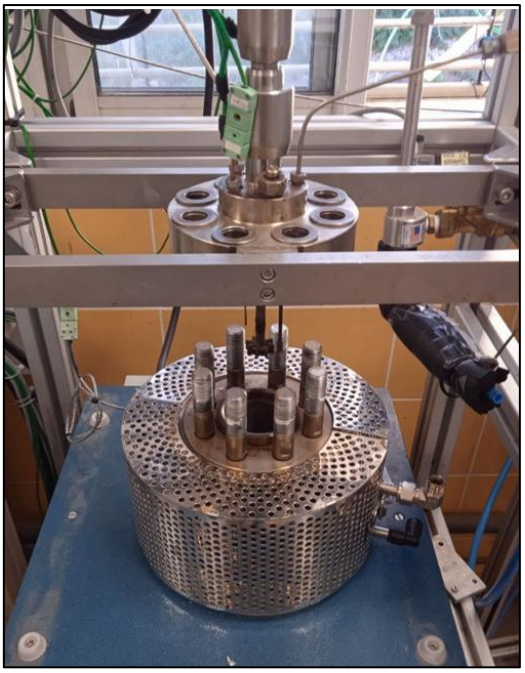

Figure IV - Réacteur utilisé pour le traitement HT des boues de STEP.

Le contenu du réacteur est récupéré puis centrifugé à 4000 tr min^{-1} pendant 20 min, permettant ainsi d'obtenir un surnageant aqueux liquide (eau de procédé) et une pastille solide. L'eau de procédé est filtrée à l'aide d'un filtre à seringue en nylon de 0,45 µm.

La quantification du biohuile est réalisée par extraction à l'acétone. 1 g de pastille solide séché, broyée et tamisée à 100 µm, est placé dans un flacon rempli de 20 mL d'acétone (PROLABO 0,792 g cm^{-3}) et agité pendant 20 min. Ensuite, le contenu du flacon est versé sur un entonnoir Büchner avec un filtre en papier, connecté à une pompe à vide. Le solide collecté sur le filtre est lavé avec 80 mL supplémentaires d'acétone. Le filtre avec le résidu solide est ensuite complètement séché, et la masse résiduelle mesurée.

La densité des phases liquides est mesurée à l'aide d'un densimètre Anton Paar DMA 5000 M. Le pH est mesuré sur des échantillons filtrés (filtre en nylon de 0,45 µm) à l'aide d'un analyseur multi-paramètres Consort C5020 (Turnhout, Belgique). L'alcalinité totale est mesurée conformément à la méthode standard EN 9963-1, 1998. La teneur en solides totaux dissous (STD) des phases liquides est mesurée en séchant l'échantillon liquide filtré (0,45 µm) à 105 °C pour 16h, puis en mesurant la masse résiduelle.

La concentration en azote total (TN) dans la phase liquide filtrée est quantifiée à l'aide de tests de cellule de kit (Lovibond VARIO Total Nitrogen, Dortmund, Allemagne), selon la méthode standard ISO 23697-2, 2023. L'azote ammoniacal (NH_4-N) contenu dans les phases liquides filtrées est quantifié à l'aide de tests de cellule de kit (Lovibond VARIO am Vial Test Reagent Set, Dortmund, Allemagne), selon la méthode standard ISO 7150-1, 1984.

La demande chimique en oxygène (DCO) (mg O_2 L^{-1}) contenue dans les phases liquides filtrées est quantifiée à l'aide de tests de cellule de kit (Supelco Spectroquant, Darmstadt, Allemagne), selon la méthode standard ISO 15705, 2002.

Le Carbone Total (TC) et le Carbone Inorganique Total (TIC) contenus dans les phases liquides sont mesurés à l'aide d'un analyseur de Carbone Organique Total Shimadzu TOC-L. Le Carbone Organique Total (TOC) est calculé par différence.

La concentration du P sous forme d'orthophosphates (PO_4-P) dans les phases liquides filtrées a été déterminée selon la méthode standard EN 6878, 2004. La concentration de PO_4-P est ensuite quantifiée à l'aide d'un spectrophotomètre ultraviolet-visible (Photolab 7100 UV-vis).

L'analyse spectrométrique d'émission atomique à plasma à couplage inductif (ICP-AES) est réalisée avec un spectromètre Agilent 5800 VDV, disponible sur la plateforme LA-ICP-MS du laboratoire CEREGE (Aix-Marseille Université). La technique a permis de quantifier les concentrations de P, Fe, Ca, Al, Mg et K dans les échantillons liquides préalablement filtrés (filtre en nylon de 0,45 µm) et dilués avec une solution de HCl à 1 M pour préserver les métaux en solution et éviter leur (re)précipitation.

La masse sèche des phases solides est évaluée en séchant l'échantillon à 105 °C pendant 16h. Le Rendement de Récupération des Solides Totaux (TSRY%) est défini par l'Équation IV:

$$TSRY\% = \frac{m_{S,sec} + m_{L,sec}}{m_{B,sec}} \quad \text{(IV)}$$

avec $m_{S,sec}$, $m_{L,sec}$ et $m_{B,sec}$ les masses sèches respectivement de la pastille solide, de l'eau de procédé et du digestat introduit dans le réacteur.

L'analyse élémentaire CNHS est réalisée avec un analyseur élémentaire Thermo Scientific FlashEA 1112, situé sur la plateforme Spectropole (Aix-Marseille Université). La

teneur en cendres des phases solides est déterminée en exposant l'échantillon séché à 900 °C dans un four à moufle pendant 1 heure. La teneur en oxygène (O) (%) dans les échantillons solides est calculée par différence.

L'extraction à l'eau régale est utilisée pour digérer un échantillon solide, afin de minéraliser et de solubiliser divers éléments, puis de déterminer leur teneur en analysant la solution résultante par des méthodes spectroscopiques. L'eau régale est un mélange d'acide nitrique (HNO_3) et d'acide chlorhydrique (HCl), dans un rapport molaire optimal de 1:3. La technique utilisée dans ce travail est basée sur la méthode normée décrite dans la norme EN ISO 13346, 2000 (méthode B). Les extraits d'eau régale sont analysés par ICP-AES pour quantifier divers éléments : P, Fe, Ca, Al, Mg, K, Cu et Zn. La spectrométrie de masse à plasma à couplage inductif (ICP-MS), réalisée avec un spectromètre Perkin Elmer NexIon 300X (plateforme LA-ICP-MS – CEREGE, Aix-Marseille Université), a permis de mesurer les traces de métaux lourds (Cr, Pb, Ni, V, Ag, As, Cd et Hg).

Le protocole SMT (Standard Measurement and Testing)[74] est utilisé pour quantifier cinq fractions différentes de phosphore : le phosphore total (TP), le phosphore organique (OP), le phosphore inorganique (IP), le phosphore inorganique non apatitique (NAIP) et le phosphore inorganique apatitique (AIP).

Les expériences ont été réalisées en suivant un « *plan d'expériences* » à l'aide du logiciel Azurad (France)[161] avec à la fois une étude de criblage et une étude de surface de réponse. Le plan de criblage permet d'évaluer l'effet relatif de chaque facteur sans considérer les interactions possibles, tandis que le plan de surface de réponse a servi à modéliser la réponse en fonction des facteurs, en prédisant leur comportement dans le domaine expérimental. La pertinence statistique du modèle obtenu est évaluée à l'aide de l'outil ANOVA (Analyse de la variance), tandis que la signification de chaque coefficient est évaluée à l'aide du test t de Student[162].

Une première série d'expériences (voir la section IV) étudie le rôle de la température et de la durée du traitement sur les caractéristiques des sous-produits du traitement HT. Le plan sélectionné pour cette étude est un plan factoriel symétrique complet avec deux facteurs (température, durée) et trois niveaux (250 °C, 300 °C, 350 °C pour la température ; 5 min, 15 min, 45 min pour la durée), ce qui aboutit à $3^2 = 9$ expériences. Chaque expérience a été répétée deux fois, soit un total de 18 expériences (Tableau I).

Dans une deuxième série d'expériences (voir la section VI), le rôle du rapport molaire Ca/P est exploré en étudiant son effet par rapport aux facteurs précédemment caractérisés. Le plan d'expériences global se compose de trois facteurs (température, durée, rapport Ca/P), chacun avec trois niveaux, ce qui donne un total de $3^3 = 27$ combinaisons. Afin de réduire le nombre d'expériences, un plan de matrice D-optimal est proposé, ce qui permet de réaliser un nombre minimal d'expériences égal à 10, généré par le logiciel Azurad. Le Tableau II présente les caractéristiques des 14 expériences réalisées pour ce plan d'expérience dans l'ordre de réalisation.

Tableau I - Conditions sélectionnées pour le plan d'expériences considérant la température et le temps.

N°	Répétitions	Température (°C)	Durée du traitement (min)	Sévérité du procédé f(T,t)
1	2	250	5	0,19
2	2	250	15	0,24
3	2	250	45	0,30
4	2	300	5	0,35
5	2	300	15	0,43
6	2	300	45	0,54
7	2	350	5	0,57
8	2	350	15	0,71
9	2	350	45	0,88

Tableau II - Conditions sélectionnées pour le plan d'expériences étudiant la température, le temps et le rapport molaire Ca/P.

N°	Répétitions	Température (°C)	Durée du traitement (min)	Rapport molaire Ca/P
1	1	300	15	0,70
2	1	250	15	0,70
3	1	350	15	0,70
4	1	300	5	0,70
5	1	250	45	0,70
6	2	350	45	1,60
7	1	300	45	1,15
8	1	350	45	0,70
9	2	250	5	1,15
10	1	350	5	1,60
11	1	350	15	1,15
12	1	250	45	1,60
13	1	300	15	1,60
14	3	300	15	1,15

Les résultats rapportés dans ce travail sont accompagnés de l'incertitude relative propagée. Toutes les mesures gravimétriques, les quantifications utilisant des kits de test et les extractions séquentielles pour la spéciation du P ont été réalisées en triplicata. Pour chaque série d'analyses, les limites de détection et de quantification ont été déterminées par l'analyse des blancs. Tous les produits chimiques utilisés étaient de grade analytique.

III. Caractérisation des boues

Dans cette section, les propriétés chimiques et physiques ainsi que les résultats seront exprimés sous la forme m ± e (n), où a correspond à la moyenne des différentes mesures, e à l'écart type, et n au nombre de mesures.

Les principales caractéristiques physico-chimiques des deux Boues A et B sont résumées dans le Tableau III.

Tableau III - Caractéristiques physico-chimiques des Boues A et B. Les valeurs reportées sont sous la forme m ± e (n), où a correspond à la moyenne des différentes mesures, e est l'écart type, et n est le nombre de mesures. [a]Incertitude propagée.
*sur base sèche; **sur base sèche, obtenu par différence.

	Boue A	***Boue B***
Humidité (%)	93,3 ± 0,2 (18)	81,11 ± 0,02 (9)
Solides totaux (ST) %	6,7 ± 0,2 (18)	18,89 ± 0,02 (9)
Cendres %*	22,7 ± 0,2 (6)	24,78 ± 0,08 (6)
C (%)*	37,5 ± 0,6 (9)	37,5 ± 0,4 (3)
N (%)*	6,4 ± 0,2 (9)	6,3 ±0,2 (3)
H (%)*	5,84 ± 0,04 (9)	5,61 ± 0,04 (3)
S (%)*	1,10 ± 0,03 (9)	1,00 ± 0,01 (3)
O (%) **	26,4 ± 0,7 (6)	24,8 ± 0,1 (3)
P (mg g^{-1})*	32 ± 2 (9)	41,1 ± 0,8 (3)
Ca (mg g^{-1})*	29,0 ± 0,9 (9)	36,7 ± 0,5 (3)
Fe (mg g^{-1})*	23 ± 1 (9)	48,9 ± 0,8 (3)
K (mg g^{-1})*	7 ± 2 (9)	2,5 ± 0,4 (3)
Mg (mg g^{-1})*	6,7 ± 0,6 (9)	6,3 ± 0,1 (3)
Al (mg g^{-1})*	2,3 ± 0,3 (9)	2,02 ± 0,08 (3)
Zn (mg g^{-1})*	0,57 ± 0,02 (9)	0,7 ± 0,1 (3)
Cu (mg g^{-1})*	0,44 ± 0,02 (9)	0,399 ± 0,007 (3)
Pb (mg kg^{-1})*	25 ± 1 (9)	51 ± 2 (3)
Cr (mg kg^{-1})*	25 ± 1 (9)	25,0 ± 0,3 (3)
V (mg kg^{-1})*	19,2 ± 0,6 (9)	23,3 ± 0,2 (3)
Ni (mg kg^{-1})*	17,7 ± 0,7 (9)	19,0 ± 0,2 (3)
Ag (mg kg^{-1})*	6,3 ± 0,3 (9)	3,11 ± 0,08 (3)
As (mg kg^{-1})*	3,4 ± 0,2 (9)	3,0 ± 0,2 (3)
Cd (mg kg^{-1})*	0,96 ±0,03 (9)	0,85 ± 0,04 (3)
Hg (mg kg^{-1})*	0,15 ± 0,02 (9)	0,10 ± 0,02 (3)

La Boue A conserve encore une quantité importante d'humidité, avec un taux de matière sèche (ST) de 6,7 ± 0,2 % (18). La Boue B présente une consistance plus opaque, cohésive et visqueuse, et est caractérisée par un taux en solides totaux (ST) de 18,89 ± 0,02 % (9). Les boues sont riches en matière organique, avec une faible teneur en cendres (< 25%). La teneur légèrement plus élevée en cendres dans la Boue B pourrait être due à l'ajout de $FeCl_3$ lors du traitement tertiaire. Les compositions des deux boues en cendres et en C, N, H, S, O sont similaires et conformes aux données de la littérature[11].

La Boue A contient 32 ± 2 mg g^{-1} de P, tandis que la Boue B, issue du mélange de boues digérées et de boues tertiaires de dephosphatation, en contient 41,1 ± 0,8 mg g^{-1}. L'ajout de $FeCl_3$ et des floculants organiques a probablement favorisé la précipitation du P, enrichissant ainsi la Boue B. La Boue B présente une teneur en Ca supérieure (+24%) à la

boue A, plus de deux fois la quantité de Fe (lié à l'ajout de $FeCl_3$), des niveaux similaires d'Al et de Mg, et une teneur en K réduite.

Les deux boues contiennent plusieurs centaines de mg kg^{-1} de Cu et Zn, des dizaines de mg kg^{-1} de Pb, Cr, V et Ni, quelques mg kg^{-1} d'Ag et As, ainsi que des traces de Cd et Hg (< 1 mg kg^{-1}). Ces valeurs sont cohérentes avec la littérature[11].

La Figure V illustre les résultats de la méthode d'extraction SMT pour la spéciation du P, montrant les quantités relatives en fractions de TP par rapport aux distributions générales des boues secondaires reportées dans la littérature[10,77–94].

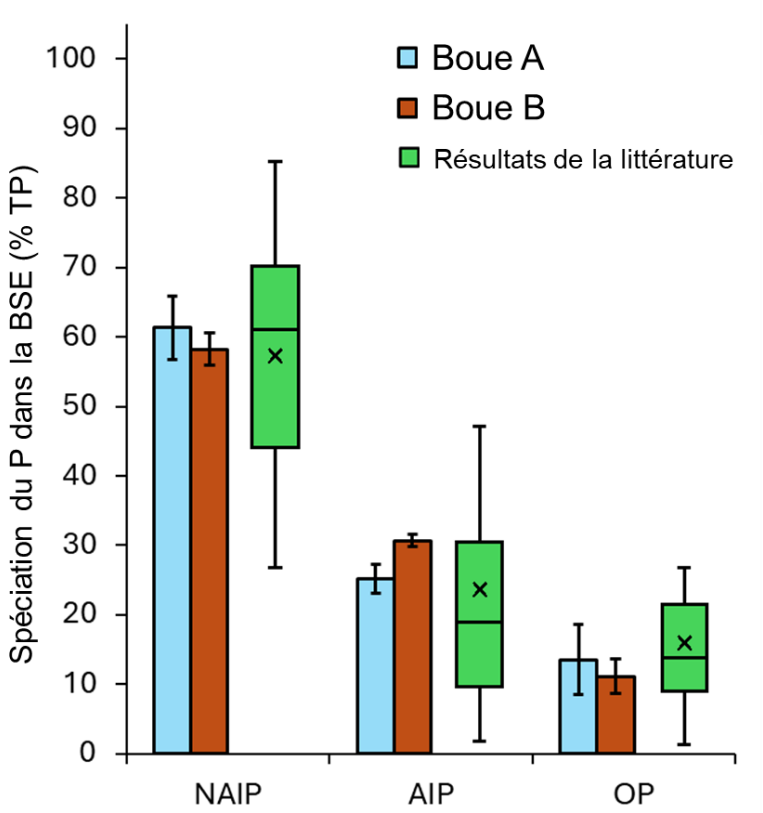

Figure V - Quantités relatives de NAIP, AIP et OP (%TP) (méthode SMT[134]). Les barres d'erreur représentent l'écart-type. Les graphiques en boîte à moustache représentent les résultats des études antérieures[10,77–94].

Dans la Boue A, le P est principalement présent sous forme de NAIP à 61 ± 5 % (7) du TP, suivi par l'AIP (25 ± 2 % (7) du TP) et l'OP (14 ± 5 % (7) du TP). La Boue B présente des valeurs similaires : NAIP : 59 ± 2 % (3) du TP, AIP : 30,9 ± 0,9 % (3) du TP, et OP : 10 ± 3 % (3) du TP. La teneur plus élevée en AIP dans la Boue B pourrait être liée à sa plus grande teneur en Ca. L'ajout de $FeCl_3$ n'a pas amené à une augmentation de la quantité de NAIP, car le $FeCl_3$ se dissocie en Fe^{3+} et Cl^-, puis forme rapidement des flocons de $Fe(OH)_3$. Les ions Fe^{3+} neutralisent les particules organiques, formant des flocs décantables, ce qui limite leur interaction avec le PO_4^{3-} pour former des phosphates de fer[166].

Les principales caractéristiques physico-chimiques des surnageants A et B sont résumées dans le Tableau IV. Le surnageant A provient de la centrifugation de boues digérées à 4000 tr min^{-1} pendant 20 min. Le surnageant B est obtenu par centrifugation industrielle de boues digérées mélangées à des boues tertiaires.

Tableau IV - Caractéristiques physico-chimiques des surnageants A et B. Les valeurs reportées sont sous la forme m ± e (n), où a correspond à la moyenne des différentes mesures, e est l'écart type, et n est le nombre de mesures. [a]Incertitude propagée.

	Surnageant A	***Surnageant B***
STD (%)	0,26 ± 0,01 (3)	0,16 ± 0,01 (3)
Densité (g L^{-1})	1001,913 ± 0,007[a]	1001,379 ± 0,007[a]
pH	8,12 ± 0,04 (6)	8,03 ± 0,01 (6)
Alcalinité totale (g $CaCO_3$ L^{-1})	3,71 ± 0,04 (3)	2,75 ± 0,04 (3)
DCO (gO_2 L^{-1})	0,39 ± 0,06 (3)	0,27 ± 0,01 (3)
TC (mg C L^{-1})	0,87 ± 0,01 (3)	0,770 ± 0,003 (3)
TIC (mg C L^{-1})	0,521 ± 0,002 (3)	0,499 ± 0,007 (3)
TOC (mg C L^{-1})	0,35 ± 0,01 (3)	0,270 ± 0,008 (3)
TN (g N L^{-1})	1,10 ± 0,03 (3)	1,0 ± 0,2 (3)
NH_4-N (g N L^{-1})	1,00 ± 0,01 (3)	0,72 ± 0,05 (6)
TP (g P L^{-1})	0,34 ± 0,02[a]	0,199 ± 0,007[a]
PO_4-P (g P L^{-1})	0,31 ± 0,01 (3)	0,193 ± 0,003 (3)
Ca (mg L^{-1})	42 ± 2[a]	44,3 ± 0,7 [a]
Fe (mg L^{-1})	1,47 ± 0,04[a]	1,85 ± 0,08 [a]
Al (mg L^{-1})	< 0,06	< 0,06
Mg (mg L^{-1})	3,7 ± 0,2[a]	2,9 ± 0,1 [a]
K (g L^{-1})	0,26 ± 0,02[a]	0,21 ± 0,03 [a]

Les deux surnageants ont une faible teneur en STD, avec des niveaux plus élevés dans le surnageant A, probablement dus à une plus grande présence de matière organique et de colloïdes. Les pH des surnageants A et B sont légèrement au-dessus de 8, en accord avec les données de la littérature[11]. Le surnageant B montre une alcalinité plus faible, probablement à cause de l'ajout de $FeCl_3$, qui a acidifié le milieu et consommé une partie de l'alcalinité. La DCO plus faible du surnageant B pourrait s'expliquer par la diminution de la matière organique après le processus de coagulation-floculation du traitement tertiaire[173]. Les concentrations en TN sont similaires dans les deux surnageants, autour de 1 g L^{-1}, avec l'ammonium comme principale source de N[173,175]. L'ajout de $FeCl_3$ dans la Boue B favorise la précipitation des phosphates, expliquant les concentrations plus faibles en P soluble et plus élevées en Fe soluble dans le surnageant B.

IV. Effet de la température et du temps

Les expériences ont été réalisées en introduisant 110 g de Boue A dans le réacteur discontinu de 0,2 L, avec une pression de 18 MPa d'azote (N_2), à la température opératoire

et une vitesse d'agitation de 700 tr min^{-1}. Le plan d'expérience suivi est décrit dans le Tableau I.

Les pertes de masse globales, comprises entre 3 % et 7 %, sont dues à la production de gaz[11] et aux résidus non récupérables sur les parois et éléments internes du réacteur. Une augmentation de la sévérité du procédé réduit la masse de la pastille solide et augmente celle de l'eau de procédé. Elle diminue également les STD de l'eau et accroît la masse sèche de la pastille, ce qui améliore la séparation des sous-produits. Le TSRY% diminue avec l'augmentation de la sévérité du procédé, passant de 77,4 ± 0,4 % à 41,0 ± 0,5 % dans les conditions les plus sévères.

Ces effets sont dus à la dégradation des biopolymères et à la dissolution des sels inorganiques dans la Boue A[39,91]. La répartition du carbone montre qu'une part croissante de C est perdue en CO_2 dans le produit gazeux avec l'augmentation de la sévérité du procédé[11]. La majorité du N est récupérée dans l'eau de procédé[186], tandis que sa proportion dans la pastille solide diminue avec la sévérité, indiquant une hydrolyse des protéines et une minéralisation en ammoniac[81]. Le P est principalement récupéré dans la pastille, avec un rendement en P dans l'eau de procédé qui diminue avec la sévérité. Le Ca, Fe, et Mg sont majoritairement récupérés dans la phase solide, bien que le Mg soit plus présent dans l'eau sous des conditions moins sévères. Le K est principalement récupéré dans la phase liquide, ce qui est cohérent avec les résultats d'études antérieures[187].

Le pH et l'alcalinité augmentent avec la sévérité du procédé. Après un traitement HT à 250 °C pendant 5 min (sévérité = 0,19), le pH de l'eau de procédé se rapproche plus de la neutralité (7,52 ± 0,02) que celui du surnageant A (8,12 ± 0,01), probablement en raison de la libération d'acides organiques[62]. À des températures plus élevées et des durées plus longues, le pH se stabilise autour de 8,0. La concentration de TN dans l'eau de procédé reste stable à environ 4,5 ± 0,2 g L^{-1}, indépendamment de la sévérité. En revanche, le NH_4-N augmente avec la sévérité, ce qui, en fournissant un effet tampon, compense l'acidification due à la libération d'acides organiques et explique l'augmentation du pH[81]. L'eau de procédé présente une concentration élevée en DCO (19 ± 1 g L^{-1} à 31 ± 1 g L^{-1}) comparée au surnageant A (0,39 ± 0,06 g L^{-1})[193]. Un traitement plus sévère diminue la DCO[188], ce qui suggère que les composés organiques solubles sont soit transférés vers d'autres phases, soit transformés (ex. production de gaz) [52,60]. Cette réduction peut être due à la polymérisation et à la formation de clusters solides de hydrochar, entraînant la précipitation du carbone dans la phase solide.

Comme le montre la Figure VI, le traitement HT réduit fortement le Ca soluble et augmente les concentrations de Fe, Mg, P, et K solubles, indiquant que le Ca^{2+} précipite, tandis que le Fe^{3+} et le Mg^{2+} sont partiellement transférés dans l'eau de procédé, surtout à des conditions moins sévères. Une augmentation de la sévérité réduit les concentrations de Ca, Fe, Mg et K dans l'eau de procédé.

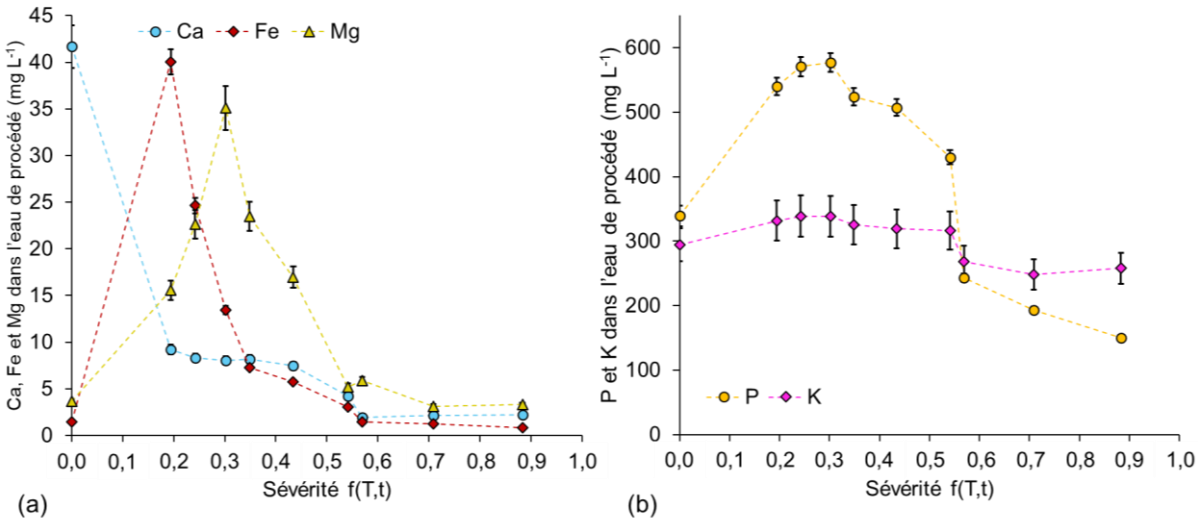

Figure VI - Concentration de Ca, Fe, Mg (a), P et K (b) dans l'eau de procédé en fonction de la sévérité f(T,t). Les barres d'erreur représentent l'incertitude.

La pastille solide du traitement HT présente une teneur en cendres plus élevée que le digestat initial, cette teneur augmentant avec la sévérité. Les concentrations de N, H et O diminuent avec la sévérité, en raison des réactions de décarboxylation, de déshydratation et de décomposition organique[11], tandis que celles de S et C restent constantes.

La Figure VII montre les concentrations de P, Ca, Fe, Mg (VIIa), et Al, K, Zn, Cu (VIIb) dans la pastille solide en fonction de la sévérité. Après le traitement HT, les contenus en Ca, Fe, Al et Mg augmentent avec la sévérité, en raison de la solubilisation et de la dégradation de la matière organique[11]. En revanche, la teneur en K est généralement plus faible dans la pastille solide, probablement à cause de la solubilisation des composés de K[187]. Les niveaux de métaux lourds (Cu, Zn, V, Cr, Ni, As, Ag, et Cd) dans le produit solide augmentent également avec la sévérité.

Le traitement HT à 250 °C et 300 °C entraîne une augmentation de la concentration en P soluble dans l'eau de procédé par rapport à la concentration du surnageant A (Figure VIIb). Pour les expériences réalisées à 250 °C (sévérité de 0,19 à 0,30), la concentration en P soluble augmente légèrement avec la durée du traitement, passant de 540 ± 14 mg P L^{-1} après 5 min à 577 ± 15 mg P L^{-1} après 45 min. Cependant, à 300 °C et 350 °C, la tendance s'inverse, avec une diminution de la concentration pour des durées de traitement plus longues. Pour les traitements les plus sévères à 350 °C, la concentration en P soluble tombe en dessous de la valeur originale du surnageant A. Pour tous les sous-produits d'eau de procédé, les rapports molaires Ca/P, Fe/P et Mg/P sont toujours inférieurs à 1, indiquant que les concentrations disponibles de Ca^{2+}, Fe^{3+} et Mg^{2+} en solution sont insuffisantes pour une précipitation complète des orthophosphates.

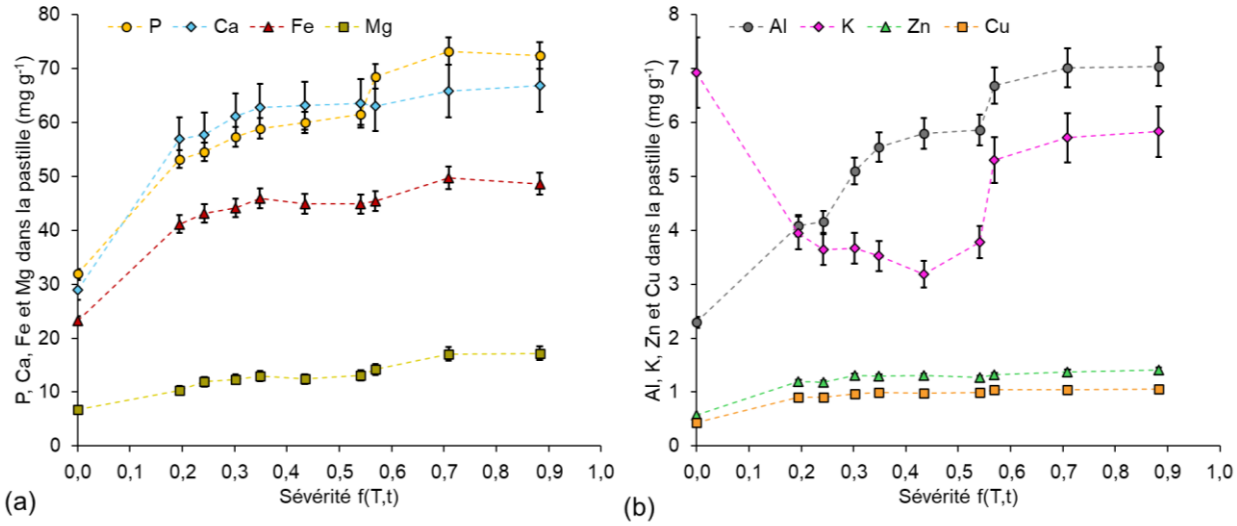

Figure VII - (a) Teneur en P, Ca, Fe, Mg, (b) Al, K, Zn, Cu dans la pastille solide en fonction de la sévérité f(T,t). Les barres d'erreur représentent l'incertitude.

La teneur en P dans la pastille solide augmente après le traitement HT et avec la sévérité du procédé (Figure VIIa), passant de 53 ± 2 mg P g^{-1} à 250 °C, 5 min (sévérité = 0,19) à 72 ± 2 mg P g^{-1} à 350 °C, 45 min (sévérité = 0,88). Ces résultats, décrits en détail dans des travaux précédents[1], montrent que, dans des conditions plus sévères, le P tend à s'accumuler dans la fraction solide. L'analyse de criblage de ces résultats montre une corrélation entre la température, la durée du traitement et la teneur en TP dans les sous-produits solides. Cependant, l'effet de la température prédomine sur la durée du traitement, une tendance déjà observée dans d'autres études[78,81].

La Figure VIII montre que l'AIP est la fraction principale de P dans la pastille solide, contrairement à la boue A, où c'est le NAIP. Avec l'augmentation de la sévérité, en particulier en passant de 300 °C à 350 °C, l'AIP augmente et le NAIP diminue, tendance déjà observée dans des études antérieures[10,77–81,83,85–94]. L'analyse de criblage montre une corrélation entre la température et la quantité relative de AIP (% TP) dans le produit solide.

Le Tableau D.9 (Annexe D) présente l'outil de validation ANOVA pour le modèle polynômial de second degré obtenu avec les résultats de la fraction AIP (% de TP). Le modèle obtenu est statistiquement significatif, avec une p-value inférieure à 1 % et un R^2 de 0,98. L'écart-type du modèle est de 1,7 %. Le Tableau D.10 présente les coefficients du modèle polynômial de second degré pour la réponse de surface de l'AIP dans le produit solide (% TP), accompagnés de leur validation statistique. Les coefficients pour les effets linéaires et quadratiques de la température (b_1) et ($b_{1\text{-}1}$) sont statistiquement significatifs, ce qui n'est pas le cas pour la durée du traitement, confirmant ainsi l'influence prépondérante de la température sur le temps. L'effet statistiquement significatif du terme quadratique de la température indique une augmentation particulièrement marquée du % AIP à la température la plus élevée (350 °C), tandis qu'il est statistiquement moins pertinent entre 250 °C et 300 °C.

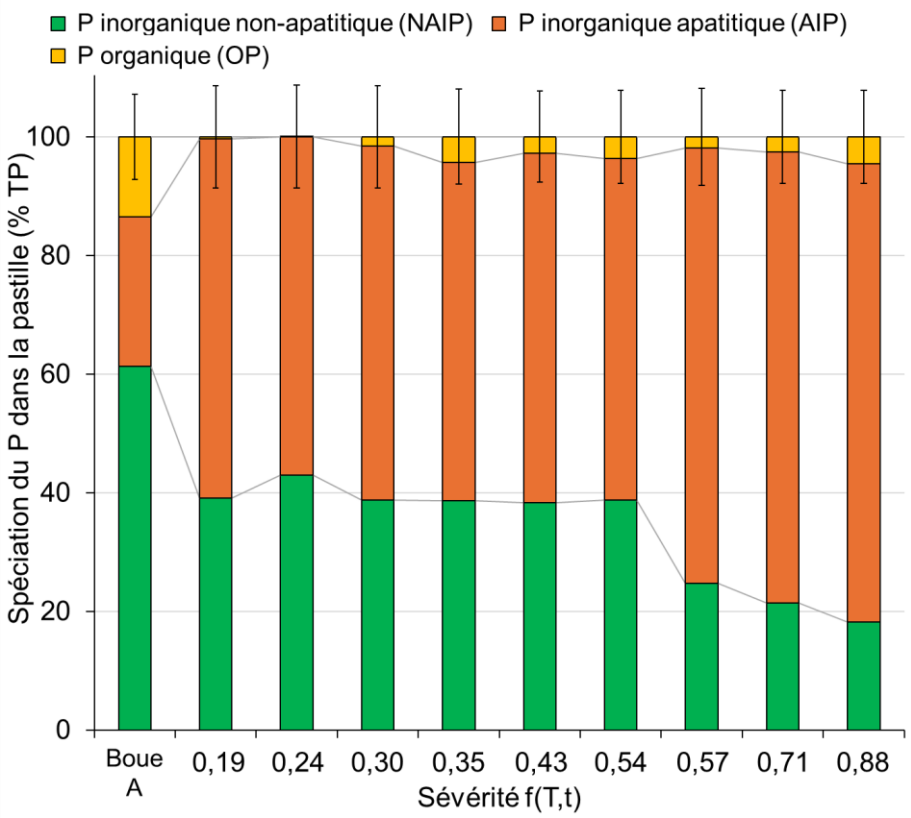

Figure VIII - Spéciation du P dans la pastille solide en fonction de la sévérité f(T,t). Les barres d'erreur représentent l'incertitude.

Le rapport molaire Ca/P dans les sous-produits solides est d'environ 0,7, ce qui signifie que pas plus de 70 % du P total ne peut précipiter avec le Ca disponible, en supposant la formation de phosphate dicalcique ($CaHPO_4$). Dans les conditions les plus sévères, l'AIP représente environ 70 % du P total. Pour obtenir des quantités plus élevées d'AIP, il est donc nécessaire d'ajouter du Ca à la boue pour porter le ratio molaire Ca/P à au moins 1. Ainsi, la stœchiométrie des métaux clés impliqués dans la spéciation du P est un paramètre crucial pour définir le mécanisme de conversion du P lors des traitements HT.

Ces résultats suggèrent un mécanisme global de conversion du P lors du HT des SS, illustré dans la Figure IX. La spéciation du P est contrôlée par trois groupes de réactions :

(i) La *minéralisation* de l'OP en orthophosphates solubles, réduisant le contenu en OP dans les phases solide et liquide et augmentant la concentration d'orthophosphates dans la phase liquide. Ce processus est principalement contrôlé par la température, par une loi cinétique de type Arrhenius[113].

(ii) La *dissolution* des composés inorganiques de P en orthophosphates solubles, réduisant le contenu en IP de la phase solide et augmentant la concentration en orthophosphates dans la phase liquide. La dissolution dépend des propriétés physiques de l'eau dans des conditions HT. Des températures élevées, un pH élevé et l'ajout de CaO favorisent la dissolution des espèces Fe-P et Al-P, tandis que des conditions acides et l'ajout de $FeCl_3$ ou $AlCl_3$ favorisent celle des complexes Ca-P.

(iii) La *précipitation* des orthophosphates en phosphates solides, diminuant la concentration de P dans la phase liquide et augmentant la récupération de P dans le solide[96,123]. Ce processus est influencé par la disponibilité des cations métalliques et par les conditions de pH et d'alcalinité.

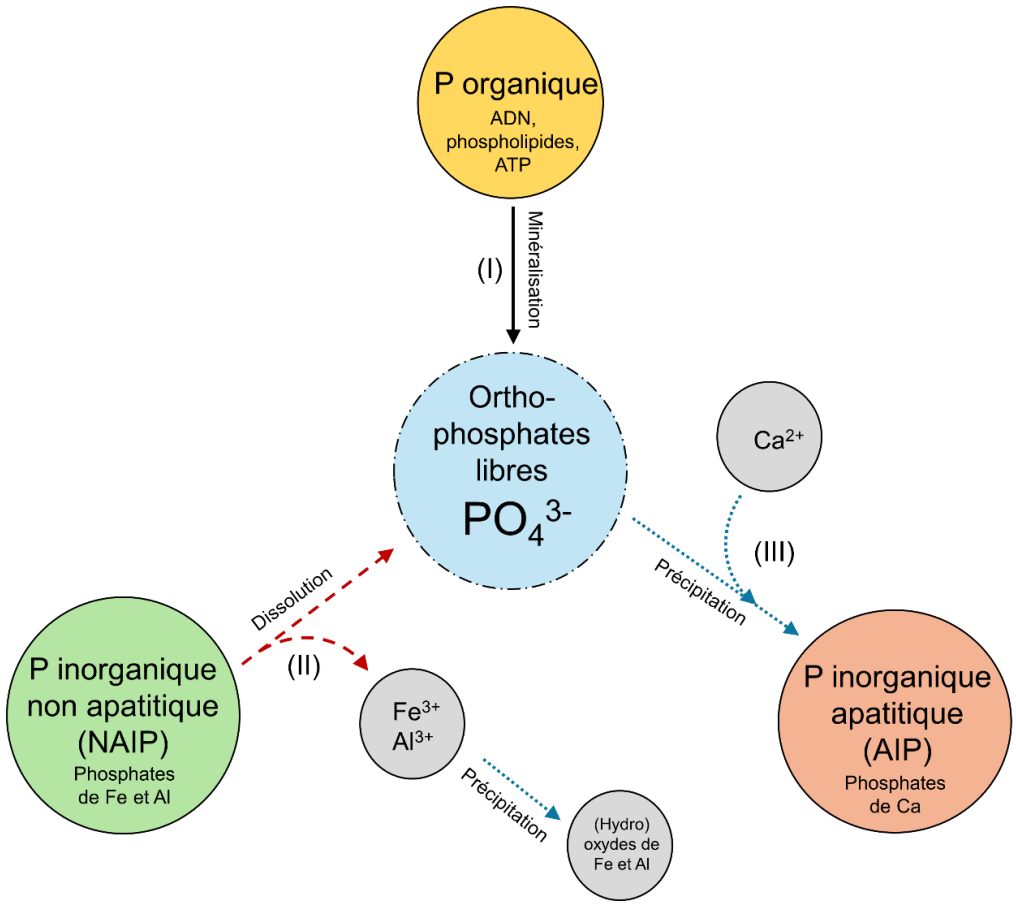

Figure IX - Mécanisme proposé pour la conversion du P. (I) Minéralisation de OP en PO_4^{3-} (II) Dissolution des phosphates de Fe et d'Al en PO_4^{3-} (III) (Re)précipitation de PO_4^{3-} avec Ca^{2+} sous forme de phosphates de Ca. Pour des traitements moins sévères (250 °C) (I) et (II) sont prédominants. Dans des conditions plus sévères (350 °C), la réaction (III) est prédominante.

À 250 °C, l'eau de procédé présente une concentration en P soluble plus élevée par rapport à la boue d'origine (de 320 mg L^{-1} à env. 600 mg L^{-1}), ce qui indique que le procédé HT à des sévérités relativement faibles favorise la minéralisation des OP (I) et la dissolution des IP (II) en PO_4-P.

Le produit solide, obtenu à une température relativement basse (250 °C), est principalement composé d'AIP, contrairement à la spéciation du P du digestat d'origine, où la forme prédominante est NAIP. Cela suggère que le NAIP a été converti en AIP, entraînant ainsi une précipitation partielle des PO_4^{3-} avec des cations Ca^{2+} (III). Ce résultat est cohérent avec les variations de concentration en Ca et Fe (Figure VI) : la concentration en Ca soluble diminue fortement après le traitement HT, ce qui peut s'expliquer par la précipitation des composés P-Ca, et la concentration en Fe soluble augmente, en raison de la dissolution des complexes Fe-P (NAIP). Des durées plus longues à 250 °C entraînent

une légère augmentation de PO_4-P, suggérant la prévalence de la minéralisation des OP (I) et de la dissolution des NAIP (II) par rapport à la précipitation de l'AIP (III).

À 300 °C, la concentration de PO_4-P commence à diminuer, montrant que la précipitation des phosphates avec des cations métalliques devient prépondérante. Enfin, à 350 °C, la précipitation de PO_4^{3-} avec les cations Ca^{2+} (III) est prédominante. Cela est confirmé par la concentration plus faible de PO_4-P dans l'eau de procédé, la diminution de la concentration en Ca soluble et l'augmentation marquée de la fraction relative d'AIP. Un autre élément confirmant que la précipitation des phosphates de calcium est le mécanisme de réaction prédominant est le ratio molaire Ca/P dans l'eau de procédé, qui reste constant autour de 0,1 indépendamment de la sévérité du procédé, malgré les diminutions des concentrations en P et Ca solubles. Cela suggère une corrélation entre la précipitation des deux éléments, suivant un ratio molaire spécifique.

V. Effet des caractéristiques de l'alimentation

Six traitements HT de la Boue B utilisant six combinaisons différentes de température et de durée ont été réalisés (correspondant aux expériences 2, 3, 4, 5, 8 et 9 du plan d'expérience présenté dans le Tableau I), en comparant ces résultats avec les expériences respectives effectuées dans les mêmes conditions sur la Boue A.

Pour la Boue B, la perte totale de masse entre le substrat et le produit récupéré est de 5 à 8 %, tandis que pour la Boue A, elle est de 3 à 7 %. Ainsi, l'utilisation d'une boue plutôt que de l'autre n'est associée à une différence significative dans le bilan de masse global. Pour la Boue B, 84 à 104 % du P total est récupéré dans les produits, 85 à 103 % du Ca, 76 à 100 % du Fe, 88 à 117 % du Mg et 71 à 98 % du K. La Boue A présente des valeurs similaires : 85 à 108 % du P, 80 à 100 % du Ca, 72 à 91 % du Fe, 77 à 94 % du Mg et 78 à 87 % du K.

La Boue A a une teneur en ST (7 %) environ trois fois inférieure à celle de la Boue B (19 %). Dans le cas de la Boue B, la centrifugation du produit entraîne une plus grande quantité de pastille solide et une moindre quantité d'eau de procédé par rapport à la Boue A. Néanmoins, dans les deux cas, une augmentation de la sévérité du procédé conduit à une augmentation de la quantité d'eau de procédé et à une diminution de la quantité de pastille solide.

Le TSRY% est plus élevé pour les produits de la Boue B par rapport à la Boue A, probablement en raison de la teneur plus élevée en matière solide de la Boue B[98,125].

Pour les deux boues, l'eau de procédé présente un pH comparable, entre 7,2 et 8,2. Le traitement HT réduit le pH par rapport au substrat d'origine. À sévérités plus faibles, l'eau de procédé de la Boue B a un pH plus bas que celle de la Boue A, probablement en raison de la libération accrue d'acides organiques après la décomposition des glucides[62]. Pour les deux boues, une sévérité plus élevée augmente le pH jusqu'à environ 8, grâce à la dégradation des composés azotés en ammoniaque[81], qui compense l'acidification due aux acides organiques. L'eau de procédé de la Boue B présente des concentrations plus élevées de TN et de NH_4-N que celle de la Boue A, en raison de sa teneur plus élevée en ST.

Cependant, dans les deux cas, le TN reste stable, tandis que le NH_4-N augmente avec la sévérité. La DCO et le TC soluble dans l'eau de procédé diminuent avec la sévérité pour les deux boues. Les valeurs pour la Boue B sont environ 2,8 fois plus élevées que pour la Boue A, en raison de sa teneur en ST plus élevée.

Le P dissous dans l'eau de procédé de la Boue B suit la même évolution que dans la Boue A, avec une augmentation à des traitements plus doux (250-300 °C) et une diminution marquée à des traitements plus sévères (350 °C). À faibles sévérités (0.24-0.43), l'eau de procédé de la Boue B montre des concentrations plus élevées de P soluble, probablement en raison de sa moindre teneur en eau. À des sévérités plus élevées (0.71-0.88), le P soluble est plus bas dans l'eau de procédé de la Boue B, grâce à une meilleure précipitation du PO_4-P due à des concentrations plus élevées de cations métalliques.

Pour les deux boues, les concentrations de Fe et Ca solubles diminuent avec l'augmentation de la sévérité du procédé. Les produits de la Boue B présentent des concentrations plus élevées de Fe et Ca, en raison de son moindre taux en solides totaux et de sa teneur initiale plus élevée pour ces éléments. Les rapports molaires Ca/P et Fe/P sont toujours inférieurs à 1 dans les eaux de procédé des deux types de boues, quelle que soit la sévérité du procédé. Cela indique que le Ca et le Fe sont des facteurs limitants pour la précipitation du P soluble.

La teneur en P des produits solides des deux boues suit la même tendance, augmentant avec la sévérité du traitement. Les produits de la Boue B présentent systématiquement une teneur en P plus élevée que ceux de la Boue A, en raison de la plus grande quantité de P dans la Boue B. Les niveaux de Ca, Fe, Al et Mg montrent des tendances similaires, indiquant une accumulation de métaux dans les pastilles solides. La composition initiale des boues influence fortement la teneur en métaux des produits solides. La Boue B, plus riche en Ca et Fe mais plus pauvre en Al et Mg que la Boue A, produit des pastilles avec des teneurs plus élevées en Ca et Fe et plus faibles en Al et Mg. Cela montre que la composition initiale de la boue est le principal facteur influençant la composition des produits.

La majorité du P est récupérée dans les produits solides, avec un rendement accru pour des traitements plus sévères. Les pastilles solides de Boue B contiennent plus de 94 % du P, contre 78-94 % pour la Boue A. L'augmentation du P solide est liée au taux en solides totaux plus élevée[97,107,125] et à la présence de Ca et Fe qui favorisent la précipitation des PO_4^{3-}.

Pour les deux boues, les traitements plus sévères augmentent la fraction d'AIP et réduisent celle de NAIP. À 250-300 °C, les produits de la Boue B présentent une fraction plus élevée de NAIP et plus faible d'AIP que la Boue A, en raison de la teneur plus élevée en Fe de cette boue. À 350 °C, les fractions de NAIP et d'AIP sont similaires pour les deux boues, car la conversion de NAIP en AIP est favorisée et le rapport molaire Ca/P, similaire pour les deux boues, détermine la spéciation. En effet, les Boues A et B présentent un rapport molaire Ca/P de 0,7, et les produits solides ont un rapport molaire Ca/P de 0,7. Cela suggère que jusqu'à 70 % du P dans la phase solide pourrait exister sous forme de phosphates de Ca. Cela est en accord avec les résultats de la spéciation du P, indiquant qu'en conditions plus sévères, environ 70 % du TP est sous forme de AIP. Cela implique

également que la plupart du Ca dans les pastilles est lié au P, soulignant l'importance de la stœchiométrie du substrat dans la détermination de la spéciation du P.

VI. Effet de l'ajout d'oxyde de calcium

Pour cette partie de l'étude, les expériences de traitement hydrothermal (HT) ont été réalisées en introduisant environ 85 g de Boue B dans le réacteur batch avec une certaine quantité de CaO (Fisher Scientific, >97 % de pureté) dans le réacteur discontinu de 0,2 L, avec une pression de 18 MPa d'azote (N_2) à la température opératoire et une vitesse d'agitation de 700 tr min^{-1}, en suivant le plan d'expériences présenté dans le tableau II.

Le produit récupéré représente 91 à 97 % de la masse d'alimentation. L'ajout de CaO augmente la masse de pastilles solides et réduit l'eau de procédé, sans corrélation significative avec les pertes massiques globales. P, Ca, Fe et Mg sont principalement récupérés dans la pastille solide, tandis que K l'est dans l'eau de procédé. Aucune corrélation significative n'a été trouvée avec les facteurs (température, temps, rapport Ca/P) et les pertes en P, Ca, Fe, Mg et K, probablement en raison des écarts liés à la performance relative de la digestion à l'eau régale[145,146].

L'ajout de CaO réduit les STD dans l'eau de procédé, grâce à la libération de Ca^{2+} qui favorise la précipitation d'espèces ioniques solubles comme PO_4^{3-}.

Sans ajout de CaO, une plus grande sévérité augmente le rendement en biohuile, surtout à 350 °C. Avec ajout de CaO, le rendement en biohuile à 350 °C diminue significativement[238]. Le biohuile, composé de divers produits chimiques (acides gras, aldéhydes, cétones, phénols, alcènes, esters)[66,67], peut réagir avec le $Ca(OH)_2$ formé par l'hydratation du CaO, produisant des savons qui réduisent l'hydrophobicité de la phase biohuile. Ce phénomène conduit à la formation de structures micellaires qui dispersent une partie de la phase huileuse dans l'eau de procédé et introduisent plus d'eau dans la pastille, expliquant ainsi la corrélation entre l'augmentation de CaO et l'augmentation de la teneur en eau de la pastille solide.

L'analyse des résultats du criblage des analyses réalisées sur l'eau de procédé a montré que l'augmentation de la température et de la durée du traitement augmente le pH, l'alcalinité, la concentration en NH_4-N , et en TIC, tout en réduisant le COD, le TC et le TOC. L'augmentation du ratio molaire Ca/P n'affecte significativement que l'alcalinité, qui augmente avec l'ajout de CaO en raison de la dissociation de $Ca(OH)_2$ en Ca^{2+} et OH^- (les ions hydroxyles contribuent à l'alcalinité totale).

L'ajustement du rapport molaire Ca/P influence fortement la concentration en P soluble. Les traitements avec ajout de CaO montrent une concentration significativement plus faible en P soluble dans l'eau de procédé. Lorsque le ratio Ca/P passe de 1,15 à 1,60 la concentration en P soluble ne diminue plus de manière significative, indiquant qu'un ratio de 1,15 est suffisant pour une précipitation presque complète du P. L'étude de criblage des concentrations de Ca, Fe, Mg et K solubles a permis de constater que l'ajout de CaO augmente la concentration en Ca soluble dans l'eau de procédé. Curieusement, l'ajout de Ca a également été significativement corrélé avec une augmentation des

concentrations de Fe, Mg et K solubles. L'introduction de Ca dans le système semble entraîner la précipitation des cations Ca^{2+} avec les anions disponibles dans le milieu aqueux (y compris les PO_4^{3-} libres), remplaçant ainsi d'autres cations tels que K^+, Mg^{2+} et Fe^{3+}. L'augmentation du rapport Ca/P entraîne une forte augmentation du contenu en Ca dans la pastille solide, mais elle réduit également les contenus en P, Fe et Mg, probablement parce que l'ajout d'une masse importante de Ca sous forme minérale entraîne une « dilution » de ces métaux dans le produit solide.

L'ajout de CaO entraîne une forte réduction du NAIP et une augmentation de l'AIP[10,77–81,86,88,89,91–93]. Plus précisément, avec l'ajout de CaO, près de 100 % du P et du Ca sont récupérés dans la pastille solide, et la majorité du P dans la pastille solide est de l'AIP. La précipitation du P est complète et le P précipite principalement avec Ca. Le fait que la précipitation du P soit déjà complète avec un ratio molaire Ca/P de 1,15 suggère une précipitation prévalente de phosphate de dicalcium ($CaHPO_4$).

L'analyse de la désirabilité globale du processus a permis d'identifier la combinaison optimale de facteurs pour minimiser le P dans l'eau de procédé, maximiser la fraction d'AIP, tout en évitant une réduction significative du rendement en biohuile. Selon les résultats de l'analyse, un traitement HT à 350 °C pendant 45 min, avec un ratio molaire de Ca d'environ 0,76, est optimal si la priorité est de maximiser la production de biohuile tout en obtenant moins d'AIP. En revanche, si l'objectif est de maximiser l'AIP au détriment de la production de biohuile, le ratio optimal est de 1,24. Les deux approches offrent un compromis intéressant, permettant d'intégrer la récupération énergétique sous forme de biohuile, avec la récupération complète du P sous forme de phosphates de Ca particulièrement stables. La pastille solide ainsi produite serait compatible avec une utilisation agricole en tant qu'engrais minéral riche en Ca et en P à libération lente, particulièrement adapté aux sols acides ou sensibles à l'eutrophisation ou à la bioaccumulation de Fe/Al. Des études plus détaillées sur la biodisponibilité de la pastille solide pour les plantes pourraient être réalisées en évaluant le degré de cristallinité des phosphates de Ca : un très faible degré de cristallinité, indiquant une prédominance de phosphates de Ca amorphes, impliquerait une solubilité plus élevée et donc une meilleure biodisponibilité.

References

[1] A. Tangredi, C. Barca, J.-H. Ferrasse, O. Boutin, Effect of process parameters on phosphorus conversion pathways during hydrothermal treatment of sewage sludge: A review, Chem. Eng. J. 463 (2023) 142342. https://doi.org/10.1016/j.cej.2023.142342.

[2] H. Liu, G. Hu, I.A. Basar, J. Li, N. Lyczko, A. Nzihou, C. Eskicioglu, Phosphorus recovery from municipal sludge-derived ash and hydrochar through wet-chemical technology: A review towards sustainable waste management, Chem. Eng. J. 417 (2021) 129300. https://doi.org/10.1016/j.cej.2021.129300.

[3] Encyclopedia of Ocean Sciences, ScienceDirect (n.d.). http://www.sciencedirect.com:5070/referencework/9780122274305/encyclopedia-of-ocean-sciences (accessed June 18, 2024).

[4] C. général au développement durable, Disruption of nitrogen and phosphorus biogeochemical cycles, Fr. Face Aux Neuf Lte. Planétaires (n.d.). https://www.statistiques.developpement-durable.gouv.fr/edition-numerique/la-france-face-aux-neuf-limites-planetaires/en/6-disruption-of-nitrogen-and-phosphorus.php (accessed June 18, 2024).

[5] C.I. Aragón-Briceño, A.K. Pozarlik, E.A. Bramer, L. Niedzwiecki, H. Pawlak-Kruczek, G. Brem, Hydrothermal carbonization of wet biomass from nitrogen and phosphorus approach: A review, Renew. Energy 171 (2021) 401–415. https://doi.org/10.1016/j.renene.2021.02.109.

[6] Y. Zhu, Y. Zhai, S. Li, X. Liu, B. Wang, X. Liu, Y. Fan, H. Shi, C. Li, Y. Zhu, Thermal treatment of sewage sludge: A comparative review of the conversion principle, recovery methods and bioavailability-predicting of phosphorus, Chemosphere 291 (2022) 133053. https://doi.org/10.1016/j.chemosphere.2021.133053.

[7] Phosphate Rock Statistics and Information | U.S. Geological Survey, (n.d.). https://www.usgs.gov/centers/national-minerals-information-center/phosphate-rock-statistics-and-information (accessed December 13, 2022).

[8] U.S.G. Survey, Mineral commodity summaries 2020, U.S. Geological Survey, 2020. https://doi.org/10.3133/mcs2020.

[9] A.L. Tasca, M. Puccini, R. Gori, I. Corsi, A.M.R. Galletti, S. Vitolo, Hydrothermal carbonization of sewage sludge: A critical analysis of process severity, hydrochar properties and environmental implications, Waste Manag. 93 (2019) 1–13. https://doi.org/10.1016/j.wasman.2019.05.027.

[10] Y. Shi, G. Luo, Y. Rao, H. Chen, S. Zhang, Hydrothermal conversion of dewatered sewage sludge: Focusing on the transformation mechanism and recovery of phosphorus, Chemosphere 228 (2019) 619–628. https://doi.org/10.1016/j.chemosphere.2019.04.109.

[11] H. Liu, I.A. Basar, A. Nzihou, C. Eskicioglu, Hydrochar derived from municipal sludge through hydrothermal processing: A critical review on its formation, characterization, and valorization, Water Res. 199 (2021) 117186. https://doi.org/10.1016/j.watres.2021.117186.

[12] R.D. Tyagi, R.Y. Surampalli, S. Yan, T.C. Zhang, C.M. Kao, B.N. Lohani, Sustainable Sludge Management, American Society of Civil Engineers, 2009. https://doi.org/10.1061/9780784410516.
[13] N. Mahmoud, G. Zeeman, H. Gijzen, G. Lettinga, Interaction between digestion conditions and sludge physical characteristics and behaviour for anaerobically digested primary sludge, Biochem. Eng. J. 28 (2006) 196–200. https://doi.org/10.1016/j.bej.2005.11.004.
[14] G. Tchobanoglous, F.L. Burton, H.D. Stensel, M.& E. Inc, F. Burton, Wastewater Engineering: Treatment and Reuse, McGraw-Hill Education, 2003.
[15] Q. Wang, C.S. Raju, N. Almind-Jørgensen, M. Laustrup, K. Reitzel, U.G. Nielsen, Variation in Phosphorus Speciation of Sewage Sludge throughout Three Wastewater Treatment Plants: Determined by Sequential Extraction Combined with Microscopy, NMR Spectroscopy, and Powder X-ray Diffraction, Environ. Sci. Technol. 56 (2022) 8975–8983. https://doi.org/10.1021/acs.est.2c01815.
[16] J. Feng, I. Burke, X. Chen, D. Stewart, Assessing metal contamination and speciation in sewage sludge: implications for soil application and environmental risk, Rev. Environ. Sci. Biotechnol. 22 (2023). https://doi.org/10.1007/s11157-023-09675-y.
[17] Statistics | Eurostat, (n.d.). https://ec.europa.eu/eurostat/databrowser/view/ten00030/default/map?lang=en (accessed June 18, 2024).
[18] D. Cordell, A. Rosemarin, J.J. Schröder, A.L. Smit, Towards global phosphorus security: A systems framework for phosphorus recovery and reuse options, Chemosphere 84 (2011) 747–758. https://doi.org/10.1016/j.chemosphere.2011.02.032.
[19] D. Bixio, C. Thoeye, J. Koning, D. Joksimovic, D. Savic, T. Wintgens, T. Melin, Wastewater reuse in Europe, Desalination 187 (2006) 89–101. https://doi.org/10.1016/j.desal.2005.04.070.
[20] P. Kehrein, M. van Loosdrecht, P. Osseweijer, M. Garfí, J. Dewulf, J. Posada, A critical review of resource recovery from municipal wastewater treatment plants – market supply potentials, technologies and bottlenecks, Environ. Sci. Water Res. Technol. 6 (2020) 877–910. https://doi.org/10.1039/C9EW00905A.
[21] J. Edwards, M. Othman, S. Burn, A review of policy drivers and barriers for the use of anaerobic digestion in Europe, the United States and Australia, Renew. Sustain. Energy Rev. 52 (2015) 815–828. https://doi.org/10.1016/j.rser.2015.07.112.
[22] R. 03 US EPA, Basic Information about Anaerobic Digestion, (2015). https://www.epa.gov/anaerobic-digestion/basic-information-about-anaerobic-digestion (accessed June 18, 2024).
[23] Solving the bottleneck in biogas production, CORDIS Eur. Comm. (n.d.). https://cordis.europa.eu/article/id/36083-solving-the-bottleneck-in-biogas-production (accessed June 18, 2024).
[24] A. Murray, A. Horvath, K.L. Nelson, Hybrid Life-Cycle Environmental and Cost Inventory of Sewage Sludge Treatment and End-Use Scenarios: A Case Study from China, Environ. Sci. Technol. 42 (2008) 3163–3169. https://doi.org/10.1021/es702256w.
[25] O. Krüger, C. Adam, Recovery potential of German sewage sludge ash, Waste Manag. 45 (2015) 400–406. https://doi.org/10.1016/j.wasman.2015.01.025.
[26] L. Fang, Q. Wang, J. Li, C.S. Poon, C.R. Cheeseman, S. Donatello, D.C.W. Tsang, Feasibility of wet-extraction of phosphorus from incinerated sewage sludge ash

(ISSA) for phosphate fertilizer production: A critical review, Crit. Rev. Environ. Sci. Technol. 51 (2021) 939–971. https://doi.org/10.1080/10643389.2020.1740545.
[27] L. Wang, Y. Chang, A. Li, Hydrothermal carbonization for energy-efficient processing of sewage sludge: A review, Renew. Sustain. Energy Rev. 108 (2019) 423–440. https://doi.org/10.1016/j.rser.2019.04.011.
[28] F. Guilayn, J. Jimenez, M. Rouez, M. Crest, D. Patureau, Digestate mechanical separation: Efficiency profiles based on anaerobic digestion feedstock and equipment choice, Bioresour. Technol. 274 (2019) 180–189. https://doi.org/10.1016/j.biortech.2018.11.090.
[29] P. Wang, C. Xu, X. Zhang, Q. Yuan, Performance evaluation of a solar evaporation system for liquid digestate concentration, Water Res. 211 (2022) 118056. https://doi.org/10.1016/j.watres.2022.118056.
[30] F. Román, J. Adolph, O. Hensel, Hydrothermal treatment of biogas digestate as a pretreatment to reduce fouling in membrane filtration, Bioresour. Technol. Rep. 13 (2021) 100638. https://doi.org/10.1016/j.biteb.2021.100638.
[31] N. Di Costanzo, A. Cesaro, F. Di Capua, G. Esposito, Exploiting the Nutrient Potential of Anaerobically Digested Sewage Sludge: A Review, Energies 14 (2021) 8149. https://doi.org/10.3390/en14238149.
[32] M. Schnell, T. Horst, P. Quicker, Thermal treatment of sewage sludge in Germany: A review, J. Environ. Manage. 263 (2020) 110367. https://doi.org/10.1016/j.jenvman.2020.110367.
[33] N. Gao, K. Kamran, C. Quan, P.T. Williams, Thermochemical conversion of sewage sludge: A critical review, Prog. Energy Combust. Sci. 79 (2020) 100843. https://doi.org/10.1016/j.pecs.2020.100843.
[34] B. Galey, M. Gautier, B. Kim, D. Blanc, V. Chatain, G. Ducom, N. Dumont, R. Gourdon, Trace metal elements vaporization and phosphorus recovery during sewage sludge thermochemical treatment – A review, J. Hazard. Mater. 424 (2022) 127360. https://doi.org/10.1016/j.jhazmat.2021.127360.
[35] Y. Zhu, Q. Zhao, D. Li, J. Li, W. Guo, Performance comparison of phosphorus recovery from different sludges in sewage treatment plants through pyrolysis, J. Clean. Prod. 372 (2022) 133728. https://doi.org/10.1016/j.jclepro.2022.133728.
[36] E. Bloem, A. Albihn, J. Elving, L. Hermann, L. Lehmann, M. Sarvi, T. Schaaf, J. Schick, E. Turtola, K. Ylivainio, Contamination of organic nutrient sources with potentially toxic elements, antibiotics and pathogen microorganisms in relation to P fertilizer potential and treatment options for the production of sustainable fertilizers: A review, Sci. Total Environ. 607–608 (2017) 225–242. https://doi.org/10.1016/j.scitotenv.2017.06.274.
[37] C. Barca, M. Martino, P. Hennebert, N. Roche, Kinetics and capacity of phosphorus extraction from solid residues obtained from wet air oxidation of sewage sludge, Waste Manag. 89 (2019) 275–283. https://doi.org/10.1016/j.wasman.2019.04.024.
[38] X. Zhang, X. Li, R. Li, Y. Wu, Hydrothermal Carbonization and Liquefaction of Sludge for Harmless and Resource Purposes: A Review, Energy Fuels 34 (2020) 13268–13290. https://doi.org/10.1021/acs.energyfuels.0c02467.
[39] U. Ekpo, A.B. Ross, M.A. Camargo-Valero, P.T. Williams, A comparison of product yields and inorganic content in process streams following thermal hydrolysis and hydrothermal processing of microalgae, manure and digestate, Bioresour. Technol. 200 (2016) 951–960. https://doi.org/10.1016/j.biortech.2015.11.018.

[40] N. Doassans-Carrère, J.-H. Ferrasse, O. Boutin, G. Mauviel, J. Lédé, Comparative Study of Biomass Fast Pyrolysis and Direct Liquefaction for Bio-Oils Production: Products Yield and Characterizations, Energy Fuels 28 (2014) 5103–5111. https://doi.org/10.1021/ef500641c.
[41] K. Tekin, S. Karagöz, S. Bektaş, A review of hydrothermal biomass processing, Renew. Sustain. Energy Rev. 40 (2014) 673–687. https://doi.org/10.1016/j.rser.2014.07.216.
[42] D.C. Elliott, P. Biller, A.B. Ross, A.J. Schmidt, S.B. Jones, Hydrothermal liquefaction of biomass: Developments from batch to continuous process, Bioresour. Technol. 178 (2015) 147–156. https://doi.org/10.1016/j.biortech.2014.09.132.
[43] R. Huang, Y. Tang, Speciation Dynamics of Phosphorus during (Hydro)Thermal Treatments of Sewage Sludge, Environ. Sci. Technol. 49 (2015) 14466–14474. https://doi.org/10.1021/acs.est.5b04140.
[44] J.A. Libra, K.S. Ro, C. Kammann, A. Funke, N.D. Berge, Y. Neubauer, M.-M. Titirici, C. Fühner, O. Bens, J. Kern, K.-H. Emmerich, Hydrothermal carbonization of biomass residuals: a comparative review of the chemistry, processes and applications of wet and dry pyrolysis, Biofuels 2 (2011) 71–106. https://doi.org/10.4155/bfs.10.81.
[45] H. Huang, X. Yuan, The migration and transformation behaviors of heavy metals during the hydrothermal treatment of sewage sludge, Bioresour. Technol. 200 (2016) 991–998. https://doi.org/10.1016/j.biortech.2015.10.099.
[46] P. Biller, A.B. Ross, Hydrothermal processing of algal biomass for the production of biofuels and chemicals, Biofuels 3 (2012) 603–623. https://doi.org/10.4155/bfs.12.42.
[47] K.-Q. Tran, Fast hydrothermal liquefaction for production of chemicals and biofuels from wet biomass – The need to develop a plug-flow reactor, Bioresour. Technol. 213 (2016) 327–332. https://doi.org/10.1016/j.biortech.2016.04.002.
[48] P. Kritzer, Corrosion in high-temperature and supercritical water and aqueous solutions: a review, J. Supercrit. Fluids 29 (2004) 1–29. https://doi.org/10.1016/S0896-8446(03)00031-7.
[49] R. Huang, C. Fang, X. Lu, R. Jiang, Y. Tang, Transformation of Phosphorus during (Hydro)thermal Treatments of Solid Biowastes: Reaction Mechanisms and Implications for P Reclamation and Recycling, Environ. Sci. Technol. 51 (2017) 10284–10298. https://doi.org/10.1021/acs.est.7b02011.
[50] M. Park, N. Kim, S. Lee, S. Yeon, J.H. Seo, D. Park, A study of solubilization of sewage sludge by hydrothermal treatment, J. Environ. Manage. 250 (2019) 109490. https://doi.org/10.1016/j.jenvman.2019.109490.
[51] K.I. John, M.O. Omorogie, Biomass-based hydrothermal carbons for catalysis and environmental cleanup: a review, Green Chem. Lett. Rev. 15 (2022) 162–186. https://doi.org/10.1080/17518253.2022.2028017.
[52] A.L. Pauline, K. Joseph, Hydrothermal carbonization of organic wastes to carbonaceous solid fuel – A review of mechanisms and process parameters, Fuel 279 (2020) 118472. https://doi.org/10.1016/j.fuel.2020.118472.
[53] G. Ischia, L. Fiori, Hydrothermal Carbonization of Organic Waste and Biomass: A Review on Process, Reactor, and Plant Modeling, Waste Biomass Valorization (2021). https://doi.org/10.1007/s12649-020-01255-3.
[54] M.T. Reza, J. Andert, B. Wirth, D. Busch, J. Pielert, J.G. Lynam, J. Mumme, Hydrothermal Carbonization of Biomass for Energy and Crop Production, Appl. Bioenergy 1 (2014). https://doi.org/10.2478/apbi-2014-0001.

[55] M. Sasaki, Z. Fang, Y. Fukushima, T. Adschiri, K. Arai, Dissolution and Hydrolysis of Cellulose in Subcritical and Supercritical Water, Ind. Eng. Chem. Res. 39 (2000) 2883–2890. https://doi.org/10.1021/ie990690j.
[56] Y. Ogihara, R.L. Smith, H. Inomata, K. Arai, Direct observation of cellulose dissolution in subcritical and supercritical water over a wide range of water densities (550–1000 kg/m3), Cellulose 12 (2005) 595–606. https://doi.org/10.1007/s10570-005-9008-1.
[57] K. Mochidzuki, N. Sato, A. Sakoda, Production and Characterization of Carbonaceous Adsorbents from Biomass Wastes by Aqueous Phase Carbonization, Adsorption 11 (2005) 669–673. https://doi.org/10.1007/s10450-005-6004-6.
[58] M. Sevilla, A.B. Fuertes, Chemical and Structural Properties of Carbonaceous Products Obtained by Hydrothermal Carbonization of Saccharides, Chem. – Eur. J. 15 (2009) 4195–4203. https://doi.org/10.1002/chem.200802097.
[59] T. Wang, Y. Zhai, Y. Zhu, C. Li, G. Zeng, A review of the hydrothermal carbonization of biomass waste for hydrochar formation: Process conditions, fundamentals, and physicochemical properties, Renew. Sustain. Energy Rev. 90 (2018) 223–247. https://doi.org/10.1016/j.rser.2018.03.071.
[60] S. Wu, Q. Wang, M. Fang, D. Wu, D. Cui, S. Pan, J. Bai, F. Xu, Z. Wang, Hydrothermal carbonization of food waste for sustainable biofuel production: Advancements, challenges, and future prospects, Sci. Total Environ. 897 (2023) 165327. https://doi.org/10.1016/j.scitotenv.2023.165327.
[61] M. Sevilla, A.B. Fuertes, The production of carbon materials by hydrothermal carbonization of cellulose, Carbon 47 (2009) 2281–2289. https://doi.org/10.1016/j.carbon.2009.04.026.
[62] S. McIntosh, R.V. Padilla, T. Rose, A.L. Rose, E. Boukaka, D. Erler, Crop fertilisation potential of phosphorus in hydrochars produced from sewage sludge, Sci. Total Environ. 817 (2022) 153023. https://doi.org/10.1016/j.scitotenv.2022.153023.
[63] X. Lu, J.R.V. Flora, N.D. Berge, Influence of process water quality on hydrothermal carbonization of cellulose, Bioresour. Technol. 154 (2014) 229–239. https://doi.org/10.1016/j.biortech.2013.11.069.
[64] X. Zhuang, H. Zhan, Y. Song, C. He, Y. Huang, X. Yin, C. Wu, Insights into the evolution of chemical structures in lignocellulose and non-lignocellulose biowastes during hydrothermal carbonization (HTC), Fuel 236 (2019) 960–974. https://doi.org/10.1016/j.fuel.2018.09.019.
[65] A. Funke, F. Ziegler, Hydrothermal carbonization of biomass: A summary and discussion of chemical mechanisms for process engineering, Biofuels Bioprod. Biorefining 4 (2010) 160–177. https://doi.org/10.1002/bbb.198.
[66] F. Di Lauro, M. Balsamo, R. Solimene, M.L. Alfieri, P. Manini, R. Migliaccio, P. Salatino, F. Montagnaro, Characterization of Biocrude Produced by Hydrothermal Liquefaction of Municipal Sewage Sludge in a 500 mL Batch Reactor, Ind. Eng. Chem. Res. 63 (2024) 955–967. https://doi.org/10.1021/acs.iecr.3c03058.
[67] R. Ghadge, N. Nagwani, N. Saxena, S. Dasgupta, A. Sapre, Design and scale-up challenges in hydrothermal liquefaction process for biocrude production and its upgradation, Energy Convers. Manag. X 14 (2022) 100223. https://doi.org/10.1016/j.ecmx.2022.100223.
[68] B.M. Kabyemela, T. Adschiri, R.M. Malaluan, K. Arai, Glucose and Fructose Decomposition in Subcritical and Supercritical Water: Detailed Reaction Pathway, Mechanisms, and Kinetics, Ind. Eng. Chem. Res. 38 (1999) 2888–2895. https://doi.org/10.1021/ie9806390.

[69] D.A. Nelson, P.M. Molton, J.A. Russell, R.T. Hallen, Application of direct thermal liquefaction for the conversion of cellulosic biomass, Ind. Eng. Chem. Prod. Res. Dev. 23 (1984) 471–475. https://doi.org/10.1021/i300015a029.
[70] W. Kwapinski, I. Kolinovic, J.J. Leahy, Sewage Sludge Thermal Treatment Technologies with a Focus on Phosphorus Recovery: A Review, Waste Biomass Valorization 12 (2021) 5837–5852. https://doi.org/10.1007/s12649-020-01280-2.
[71] R. Huang, Y. Tang, Evolution of phosphorus complexation and mineralogy during (hydro)thermal treatments of activated and anaerobically digested sludge: Insights from sequential extraction and P K-edge XANES, Water Res. 100 (2016) 439–447. https://doi.org/10.1016/j.watres.2016.05.029.
[72] W. Stumm, J.J. Morgan, Aquatic Chemistry: Chemical Equilibria and Rates in Natural Waters, John Wiley & Sons, 2012.
[73] E. Valsami-Jones, Mineralogical controls on phosphorus recovery from wastewaters, Mineral. Mag. - Min. MAG 65 (2001) 611–620. https://doi.org/10.1180/002646101317018433.
[74] V. Ruban, J.F. López-Sánchez, P. Pardo, G. Rauret, H. Muntau, Ph. Quevauviller, Harmonized protocol and certified reference material for the determination of extractable contents of phosphorus in freshwater sediments - A synthesis of recent works, Fresenius J. Anal. Chem. 370 (2001) 224–228. https://doi.org/10.1007/s002160100753.
[75] V. Ruban, J.F. López-Sánchez, P. Pardo, G. Rauret, H. Muntau, P. Quevauviller, Selection and evaluation of sequential extraction procedures for the determination of phosphorus forms in lake sediment, J. Environ. Monit. 1 (1999) 51–56. https://doi.org/10.1039/A807778I.
[76] C. Wang, Y. Zhang, H. Li, R. Morrison, Sequential extraction procedures for the determination of phosphorus forms in sediment, Fac. Sci. Med. Health - Pap. Part A (2013) 147–157. https://doi.org/10.1007/s10201-012-0397-1.
[77] Y. Xu, F. Yang, L. Zhang, X. Wang, Y. Sun, Q. Liu, G. Qian, Migration and transformation of phosphorus in municipal sludge by the hydrothermal treatment and its directional adjustment, Waste Manag. 81 (2018) 196–201. https://doi.org/10.1016/j.wasman.2018.10.011.
[78] E. Ovsyannikova, P.J. Arauzo, G.C. Becker, A. Kruse, Experimental and thermodynamic studies of phosphate behavior during the hydrothermal carbonization of sewage sludge, Sci. Total Environ. 692 (2019) 147–156. https://doi.org/10.1016/j.scitotenv.2019.07.217.
[79] W. Shi, C. Feng, W. Huang, Z. Lei, Z. Zhang, Study on interaction between phosphorus and cadmium in sewage sludge during hydrothermal treatment by adding hydroxyapatite, Bioresour. Technol. 159 (2014) 176–181. https://doi.org/10.1016/j.biortech.2014.02.108.
[80] C. Pérez, J.-F. Boily, S. Jansson, T. Gustafsson, J. Fick, Acid-Induced Phosphorus Release from Hydrothermally Carbonized Sewage Sludge, Waste Biomass Valorization 12 (2021) 6555–6568. https://doi.org/10.1007/s12649-021-01463-5.
[81] L. Wang, Y. Chang, Q. Liu, Fate and distribution of nutrients and heavy metals during hydrothermal carbonization of sewage sludge with implication to land application, J. Clean. Prod. 225 (2019) 972–983. https://doi.org/10.1016/j.jclepro.2019.03.347.

[82] Q. Wang, H. Jung, B. Wan, P. Liu, P. Yang, Y. Tang, Transformation Kinetics of Phosphorus and Nitrogen in Iron-Rich Sewage Sludges during Hydrothermal Treatment and Recovery of Nutrients from Process Water, ACS Sustain. Chem. Eng. 9 (2021) 10630–10641. https://doi.org/10.1021/acssuschemeng.1c03452.
[83] X. Zheng, Y. Ye, Z. Jiang, Z. Ying, S. Ji, W. Chen, B. Wang, B. Dou, Enhanced transformation of phosphorus (P) in sewage sludge to hydroxyapatite via hydrothermal carbonization and calcium-based additive, Sci. Total Environ. 738 (2020) 139786. https://doi.org/10.1016/j.scitotenv.2020.139786.
[84] Y. Shi, Z. Chen, Y. Cao, J. Fan, J.H. Clark, G. Luo, S. Zhang, Migration and transformation mechanism of phosphorus in waste activated sludge during anaerobic fermentation and hydrothermal conversion, J. Hazard. Mater. 403 (2021) 123649. https://doi.org/10.1016/j.jhazmat.2020.123649.
[85] T. Wang, Y. Zhai, Y. Zhu, C. Peng, T. Wang, B. Xu, C. Li, G. Zeng, Feedwater pH affects phosphorus transformation during hydrothermal carbonization of sewage sludge, Bioresour. Technol. 245 (2017) 182–187. https://doi.org/10.1016/j.biortech.2017.08.114.
[86] S. Li, W. Zeng, Z. Jia, G. Wu, H. Xu, Y. Peng, Phosphorus species transformation and recovery without apatite in FeCl3-assisted sewage sludge hydrothermal treatment, Chem. Eng. J. 399 (2020) 125735. https://doi.org/10.1016/j.cej.2020.125735.
[87] X. Zheng, Z. Jiang, Z. Ying, Y. Ye, W. Chen, B. Wang, B. Dou, Migration and Transformation of Phosphorus during Hydrothermal Carbonization of Sewage Sludge: Focusing on the Role of pH and Calcium Additive and the Transformation Mechanism, ACS Sustain. Chem. Eng. 8 (2020) 7806–7814. https://doi.org/10.1021/acssuschemeng.0c00031.
[88] Y. Feng, K. Ma, T. Yu, S. Bai, D. Pei, T. Bai, Q. Zhang, L. Yin, Y. Hu, D. Chen, Phosphorus Transformation in Hydrothermal Pretreatment and Steam Gasification of Sewage Sludge, Energy Fuels 32 (2018) 8545–8551. https://doi.org/10.1021/acs.energyfuels.8b01860.
[89] J.D. Marin-Batista, A.F. Mohedano, J.J. Rodríguez, M.A. de la Rubia, Energy and phosphorous recovery through hydrothermal carbonization of digested sewage sludge, Waste Manag. 105 (2020) 566–574. https://doi.org/10.1016/j.wasman.2020.03.004.
[90] X. Zhang, L. Zhang, A. Li, Hydrothermal co-carbonization of sewage sludge and pinewood sawdust for nutrient-rich hydrochar production: Synergistic effects and products characterization, J. Environ. Manage. 201 (2017) 52–62. https://doi.org/10.1016/j.jenvman.2017.06.018.
[91] X. Zheng, M. Shen, Z. Ying, Y. Feng, B. Wang, B. Dou, Correlating phosphorus transformation with process water during hydrothermal carbonization of sewage sludge via experimental study and mathematical modelling, Sci. Total Environ. 807 (2022) 150750. https://doi.org/10.1016/j.scitotenv.2021.150750.
[92] E. Ovsyannikova, A. Kruse, G.C. Becker, Feedstock-Dependent Phosphate Recovery in a Pilot-Scale Hydrothermal Liquefaction Bio-Crude Production, Energies 13 (2020) 379. https://doi.org/10.3390/en13020379.
[93] Y. Yu, X. Yang, Z. Lei, R. Yu, K. Shimizu, N. Chen, C. Feng, Z. Zhang, Effects of three macroelement cations on P mobility and speciation in sewage sludge derived hydrochar by using hydrothermal treatment, Bioresour. Technol. Rep. 7 (2019) 100231. https://doi.org/10.1016/j.biteb.2019.100231.

[94] W. Zhu, Z.R. Xu, L. Li, C. He, The behavior of phosphorus in sub- and super-critical water gasification of sewage sludge, Chem. Eng. J. 171 (2011) 190–196. https://doi.org/10.1016/j.cej.2011.03.090.
[95] J.B.J. Jr, Plant Nutrition and Soil Fertility Manual, 2nd ed., CRC Press, Boca Raton, 2012. https://doi.org/10.1201/b11577.
[96] X. Han, F. Wang, B. Zhou, H. Chen, R. Yuan, S. Liu, X. Zhou, L. Gao, Y. Lu, R. Zhang, Phosphorus complexation of sewage sludge during thermal hydrolysis with different reaction temperature and reaction time by P K-edge XANES and 31P NMR, Sci. Total Environ. 688 (2019) 1–9. https://doi.org/10.1016/j.scitotenv.2019.06.017.
[97] A.M. Smith, S. Singh, A.B. Ross, Fate of inorganic material during hydrothermal carbonisation of biomass: Influence of feedstock on combustion behaviour of hydrochar, Fuel 169 (2016) 135–145. https://doi.org/10.1016/j.fuel.2015.12.006.
[98] C. He, K. Wang, A. Giannis, Y. Yang, J.-Y. Wang, Products evolution during hydrothermal conversion of dewatered sewage sludge in sub- and near-critical water: Effects of reaction conditions and calcium oxide additive, Int. J. Hydrog. Energy 40 (2015) 5776–5787. https://doi.org/10.1016/j.ijhydene.2015.03.006.
[99] G. Qi, X. Wang, Y. Shen, X. Liu, M. Asraful Alam, B. Liu, Y. Chen, Effect of different flocculants on the characteristics of hydrochar and hydroliquid derived from the hydrothermal treated active sludge. A comparative study, J. Environ. Chem. Eng. 10 (2022) 107514. https://doi.org/10.1016/j.jece.2022.107514.
[100] D. Bhatt, A. Shrestha, R.K. Dahal, B. Acharya, P. Basu, R. MacEwen, Hydrothermal Carbonization of Biosolids from Waste Water Treatment Plant, Energies 11 (2018) 2286. https://doi.org/10.3390/en11092286.
[101] H.P. Ruyter, Coalification model, Fuel 61 (1982) 1182–1187. https://doi.org/10.1016/0016-2361(82)90017-5.
[102] R. Yahav Spitzer, V. Mau, A. Gross, Using hydrothermal carbonization for sustainable treatment and reuse of human excreta, J. Clean. Prod. 205 (2018) 955–963. https://doi.org/10.1016/j.jclepro.2018.09.126.
[103] Y. Fei, D. Zhao, Y. Liu, W. Zhang, Y. Tang, X. Huang, Q. Wu, Y. Wang, T. Xiao, C. Liu, Feasibility of sewage sludge derived hydrochars for agricultural application: Nutrients (N, P, K) and potentially toxic elements (Zn, Cu, Pb, Ni, Cd), Chemosphere 236 (2019) 124841. https://doi.org/10.1016/j.chemosphere.2019.124841.
[104] L. Qian, S. Wang, P.E. Savage, Fast and isothermal hydrothermal liquefaction of sludge at different severities: Reaction products, pathways, and kinetics, Appl. Energy 260 (2020) 114312. https://doi.org/10.1016/j.apenergy.2019.114312.
[105] Q. Wang, X. Liu, H. Jung, S. Zhao, S.G. Pavlostathis, Y. Tang, Effect of Prestage Hydrothermal Treatment on the Formation of Struvite vs Vivianite during Semicontinuous Anaerobic Digestion of Sewage Sludge, ACS Sustain. Chem. Eng. 9 (2021) 9093–9105. https://doi.org/10.1021/acssuschemeng.1c02638.
[106] Q. Wang, C. Zhang, P. Liu, H. Jung, B. Wan, D. Patel, S.G. Pavlostathis, Y. Tang, Effect of Interstage Hydrothermal Treatment on Anaerobic Digestion of Sewage Sludge: Speciation Evolution of Phosphorus, Iron, and Sulfur, ACS Sustain. Chem. Eng. 8 (2020) 16515–16525. https://doi.org/10.1021/acssuschemeng.0c05544.
[107] A. Hämäläinen, M. Kokko, V. Kinnunen, T. Hilli, J. Rintala, Hydrothermal carbonisation of mechanically dewatered digested sewage sludge—Energy and nutrient recovery in centralised biogas plant, Water Res. 201 (2021) 117284. https://doi.org/10.1016/j.watres.2021.117284.

[108] P. Knötig, H. Etzold, B. Wirth, Model-Based Evaluation of Hydrothermal Treatment for the Energy Efficient Dewatering and Drying of Sewage Sludge, Processes 9 (2021) 1346. https://doi.org/10.3390/pr9081346.
[109] Q. Wang, C. Zhang, D. Patel, H. Jung, P. Liu, B. Wan, S.G. Pavlostathis, Y. Tang, Coevolution of Iron, Phosphorus, and Sulfur Speciation during Anaerobic Digestion with Hydrothermal Pretreatment of Sewage Sludge, Environ. Sci. Technol. 54 (2020) 8362–8372. https://doi.org/10.1021/acs.est.0c00501.
[110] M. Paneque, J.M. de la Rosa, A.F. Patti, H. Knicker, Changes in the Bio-Availability of Phosphorus in Pyrochars and Hydrochars Derived from Sewage Sludge after Their Amendment to Soils, Agronomy 11 (2021) 623. https://doi.org/10.3390/agronomy11040623.
[111] G. Weijin, Z. Zizheng, L. Yue, W. Qingyu, G. Lina, Hydrogen production and phosphorus recovery via supercritical water gasification of sewage sludge in a batch reactor, Waste Manag. 96 (2019) 198–205. https://doi.org/10.1016/j.wasman.2019.07.023.
[112] T.M. Aida, T. Nonaka, S. Fukuda, H. Kujiraoka, Y. Kumagai, R. Maruta, M. Ota, I. Suzuki, M.M. Watanabe, H. Inomata, R.L. Smith, Nutrient recovery from municipal sludge for microalgae cultivation with two-step hydrothermal liquefaction, Algal Res. 18 (2016) 61–68. https://doi.org/10.1016/j.algal.2016.06.009.
[113] D. Feng, L. Malleret, A. Soric, O. Boutin, Kinetic study of glyphosate degradation in wet air oxidation conditions, Chemosphere 247 (2020) 125930. https://doi.org/10.1016/j.chemosphere.2020.125930.
[114] A. Amrullah, Y. Matsumura, Sewage Sludge Gasification under a Hydrothermal Condition: Phosphorus Behavior and Its Kinetics, Energy Fuels 33 (2019) 2301–2307. https://doi.org/10.1021/acs.energyfuels.8b04289.
[115] Y. Yu, Z. Lei, T. Yuan, Y. Jiang, N. Chen, C. Feng, K. Shimizu, Z. Zhang, Simultaneous phosphorus and nitrogen recovery from anaerobically digested sludge using a hybrid system coupling hydrothermal pretreatment with MAP precipitation, Bioresour. Technol. 243 (2017) 634–640. https://doi.org/10.1016/j.biortech.2017.06.178.
[116] L. Pola, L. Fernández-García, S. Collado, P. Oulego, M. Díaz, Macronutrient solubilisation during hydrothermal treatment of sewage sludge, J. Water Process Eng. 43 (2021) 102270. https://doi.org/10.1016/j.jwpe.2021.102270.
[117] C. Aragón-Briceño, A.B. Ross, M.A. Camargo-Valero, Evaluation and comparison of product yields and bio-methane potential in sewage digestate following hydrothermal treatment, Appl. Energy 208 (2017) 1357–1369. https://doi.org/10.1016/j.apenergy.2017.09.019.
[118] C. Fang, R. Huang, C.M. Dykstra, R. Jiang, S.G. Pavlostathis, Y. Tang, Energy and Nutrient Recovery from Sewage Sludge and Manure via Anaerobic Digestion with Hydrothermal Pretreatment, Environ. Sci. Technol. 54 (2020) 1147–1156. https://doi.org/10.1021/acs.est.9b03269.
[119] F. Conti, S.S. Toor, T.H. Pedersen, T.H. Seehar, A.H. Nielsen, L.A. Rosendahl, Valorization of animal and human wastes through hydrothermal liquefaction for biocrude production and simultaneous recovery of nutrients, Energy Convers. Manag. 216 (2020) 112925. https://doi.org/10.1016/j.enconman.2020.112925.
[120] J. Li, J. Jin, Y. Zhao, Z. Zou, Y. Wu, J. Sun, J. Xia, Enhancing phosphorus bioavailability in sewage sludge through co-hydrothermal treatment with biomass, J. Water Process Eng. 51 (2023) 103448. https://doi.org/10.1016/j.jwpe.2022.103448.

[121] M.J. Hedley, J.W.B. Stewart, B.S. Chauhan, Changes in Inorganic and Organic Soil Phosphorus Fractions Induced by Cultivation Practices and by Laboratory Incubations, Soil Sci. Soc. Am. J. 46 (1982) 970–976. https://doi.org/10.2136/sssaj1982.03615995004600050017x.
[122] Q. Xiong, J. Xia, X. Wu, X. Wu, H. Hou, H. Lv, Influence of persulfate on transformation of phosphorus and heavy metals for improving sewage sludge dewaterability by hydrothermal treatment, Environ. Sci. Pollut. Res. 29 (2022) 33252–33262. https://doi.org/10.1007/s11356-022-18624-1.
[123] A. Matayeva, S.R. Rasmussen, P. Biller, Distribution of nutrients and phosphorus recovery in hydrothermal liquefaction of waste streams, Biomass Bioenergy 156 (2022) 106323. https://doi.org/10.1016/j.biombioe.2021.106323.
[124] Y. Fei, D. Zhao, Y. Cao, H. Huot, Y. Tang, H. Zhang, T. Xiao, Phosphorous Retention and Release by Sludge-Derived Hydrochar for Potential Use as a Soil Amendment, J. Environ. Qual. 48 (2019) 502–509. https://doi.org/10.2134/jeq2018.09.0328.
[125] C.I. Aragón-Briceño, O. Grasham, A.B. Ross, V. Dupont, M.A. Camargo-Valero, Hydrothermal carbonization of sewage digestate at wastewater treatment works: Influence of solid loading on characteristics of hydrochar, process water and plant energetics, Renew. Energy 157 (2020) 959–973. https://doi.org/10.1016/j.renene.2020.05.021.
[126] V. Shettigondahalli Ekanthalu, S. Narra, J. Sprafke, M. Nelles, Influence of Acids and Alkali as Additives on Hydrothermally Treating Sewage Sludge: Effect on Phosphorus Recovery, Yield, and Energy Value of Hydrochar, Processes 9 (2021) 618. https://doi.org/10.3390/pr9040618.
[127] Y. Xu, H. Hu, J. Liu, J. Luo, G. Qian, A. Wang, pH dependent phosphorus release from waste activated sludge: contributions of phosphorus speciation, Chem. Eng. J. 267 (2015) 260–265. https://doi.org/10.1016/j.cej.2015.01.037.
[128] G.C. Becker, D. Wüst, H. Köhler, A. Lautenbach, A. Kruse, Novel approach of phosphate-reclamation as struvite from sewage sludge by utilising hydrothermal carbonization, J. Environ. Manage. 238 (2019) 119–125. https://doi.org/10.1016/j.jenvman.2019.02.121.
[129] V.S. Ekanthalu, S. Narra, T. Ender, E. Antwi, M. Nelles, Influence of Post- and Pre-Acid Treatment during Hydrothermal Carbonization of Sewage Sludge on P-Transformation and the Characteristics of Hydrochar, Processes 10 (2022) 151. https://doi.org/10.3390/pr10010151.
[130] M. Escala, T. Zumbühl, Ch. Koller, R. Junge, R. Krebs, Hydrothermal Carbonization as an Energy-Efficient Alternative to Established Drying Technologies for Sewage Sludge: A Feasibility Study on a Laboratory Scale, Energy Fuels 27 (2013) 454–460. https://doi.org/10.1021/ef3015266.
[131] L.C. Chow, Solubility of Calcium Phosphates, in: L.C. Chow, E.D. Eanes (Eds.), Monogr. Oral Sci., KARGER, Basel, 2001: pp. 94–111. https://doi.org/10.1159/000061650.
[132] H. McDowell, T.M. Gregory, W.E. Brown, Solubility of Ca5(PO4)3OH in the System Ca(OH)2-H3PO4-H2O at 5, 15, 25, and 37 °C, J. Res. Natl. Bur. Stand. Sect. Phys. Chem. 81A (1977) 273–281. https://doi.org/10.6028/jres.081A.017.
[133] P. Hart, G. Colson, J. Burris, Application of Carbon Dioxide to reduce water side lime scale in heat exchanges, J Sci. Technol. For. Prod. Process. 1 (2012) 67–70.
[134] A.J. Erickson, J.S. Gulliver, P.T. Weiss, Enhanced Sand Filtration for Storm Water Phosphorus Removal, J. Environ. Eng. 133 (2007) 485–497. https://doi.org/10.1061/(ASCE)0733-9372(2007)133:5(485).

[135] S. Aghajanian, H. Nieminen, T. Koiranen, Precipitation of calcium carbonate in highly alkaline solution through carbonated water, in: 2019. https://www.semanticscholar.org/paper/Precipitation-of-calcium-carbonate-in-highly-water-Aghajanian-Nieminen/d8f20dec4bece3a86d1603aef2ecd2625d7dce1a (accessed January 31, 2023).
[136] C. PUBLISHING, Australian Soil Fertility Manual, n.d. https://www.publish.csiro.au/book/5338 (accessed November 15, 2022).
[137] N.J. Barrow, The effects of pH on phosphate uptake from the soil, Plant Soil 410 (2017) 401–410. https://doi.org/10.1007/s11104-016-3008-9.
[138] R. Li, Z. Zhang, Y. Li, W. Teng, W. Wang, T. Yang, Transformation of apatite phosphorus and non-apatite inorganic phosphorus during incineration of sewage sludge, Chemosphere 141 (2015) 57–61. https://doi.org/10.1016/j.chemosphere.2015.05.094.
[139] Q. Liu, Z. Fang, Y. Liu, Y. Liu, Y. Xu, X. Ruan, X. Zhang, W. Cao, Phosphorus speciation and bioavailability of sewage sludge derived biochar amended with CaO, Waste Manag. 87 (2019) 71–77. https://doi.org/10.1016/j.wasman.2019.01.045.
[140] L. Li, H. Pang, J. He, J. Zhang, Characterization of phosphorus species distribution in waste activated sludge after anaerobic digestion and chemical precipitation with Fe3+ and Mg2+, Chem. Eng. J. 373 (2019) 1279–1285. https://doi.org/10.1016/j.cej.2019.05.146.
[141] C. Wang, W. Zhu, C. Chen, H. Zhang, Y. Fan, B. Mu, J. Zhong, Behavior of Phosphorus in Catalytic Supercritical Water Gasification of Dewatered Sewage Sludge: The Conversion Pathway and Effect of Alkaline Additive, Energy Fuels 33 (2019) 1290–1295. https://doi.org/10.1021/acs.energyfuels.8b04054.
[142] H.K. Agbovi, L.D. Wilson, Flocculation Optimization of Orthophosphate with $FeCl_3$ and Alginate Using the Box–Behnken Response Surface Methodology, Ind. Eng. Chem. Res. 56 (2017) 3145–3155. https://doi.org/10.1021/acs.iecr.6b04765.
[143] G. Zhen, X. Lu, Y. Zhao, X. Chai, D. Niu, Enhanced dewaterability of sewage sludge in the presence of Fe(II)-activated persulfate oxidation, Bioresour. Technol. 116 (2012) 259–265. https://doi.org/10.1016/j.biortech.2012.01.170.
[144] L. Appels, J. Baeyens, J. Degrève, R. Dewil, Principles and potential of the anaerobic digestion of waste-activated sludge, Prog. Energy Combust. Sci. 34 (2008) 755–781. https://doi.org/10.1016/j.pecs.2008.06.002.
[145] R. Taraškevičius, R. Zinkutė, R. Stakėnienė, M. Radavičius, Case Study of the Relationship between *Aqua Regia* and *Real Total* Contents of Harmful Trace Elements in Some European Soils, J. Chem. 2013 (2012) e678140. https://doi.org/10.1155/2013/678140.
[146] J. Ščančar, R. Milacic, M. Horvat, Comparison of Various Digestion and Extraction Procedures in Analysis of Heavy Metals in Sediments, Water. Air. Soil Pollut. 118 (2000) 87–99. https://doi.org/10.1023/A:1005187602820.
[147] J. Schaefer, E.O. Stejskal, Carbon-13 nuclear magnetic resonance of polymers spinning at the magic angle, J. Am. Chem. Soc. 98 (1976) 1031–1032. https://doi.org/10.1021/ja00420a036.
[148] O.B. Peersen, X.L. Wu, I. Kustanovich, S.O. Smith, Variable-Amplitude Cross-Polarization MAS NMR, J. Magn. Reson. A 104 (1993) 334–339. https://doi.org/10.1006/jmra.1993.1231.

[149] R.L. Cook, C.H. Langford, R. Yamdagni, C.M. Preston, A Modified Cross-Polarization Magic Angle Spinning 13C NMR Procedure for the Study of Humic Materials, Anal. Chem. 68 (1996) 3979–3986. https://doi.org/10.1021/ac960403a.
[150] G. Gerbaud, F. Ziarelli, S. Caldarelli, Increasing the robustness of heteronuclear decoupling in magic-angle sample spinning solid-state NMR, Chem. Phys. Lett. 377 (2003) 1–5. https://doi.org/10.1016/S0009-2614(03)01056-X.
[151] S. Pizzanelli, L. Calucci, C. Forte, S. Borsacchi, Studies of Organic Matter in Composting, Vermicomposting, and Anaerobic Digestion by 13C Solid-State NMR Spectroscopy, Appl. Sci. 13 (2023) 2900. https://doi.org/10.3390/app13052900.
[152] A.V. Piterina, J. Barlett, J.T. Pembroke, C-NMR assessment of the pattern of organic matter transformation during domestic wastewater treatment by autothermal aerobic digestion (ATAD), Int. J. Environ. Res. Public. Health 6 (2009) 2288–2306. https://doi.org/10.3390/ijerph6082288.
[153] C. Keeler, E.F. Kelly, G.E. Maciel, Chemical–structural information from solid-state 13C NMR studies of a suite of humic materials from a lower montane forest soil, Colorado, USA, Geoderma 130 (2006) 124–140. https://doi.org/10.1016/j.geoderma.2005.01.015.
[154] M. a. Pereira, O. c. Pires, M. Mota, M. m. Alves, Anaerobic biodegradation of oleic and palmitic acids: Evidence of mass transfer limitations caused by long chain fatty acid accumulation onto the anaerobic sludge, Biotechnol. Bioeng. 92 (2005) 15–23. https://doi.org/10.1002/bit.20548.
[155] S. Amir, M. Hafidi, G. Merlina, H. Hamdi, J.-C. Revel, Elemental analysis, FTIR and 13C-NMR of humic acids from sewage sludge composting, Agronomie 24 (2004) 13–18. https://doi.org/10.1051/agro:2003054.
[156] D.A.N. Ussiri, C.E. Johnson, Characterization of organic matter in a northern hardwood forest soil by 13C NMR spectroscopy and chemical methods, Geoderma 111 (2003) 123–149. https://doi.org/10.1016/S0016-7061(02)00257-4.
[157] G.C. Becker, A. Kruse, Discussion of Classical Phosphate Extraction Schemes to Identify Speciation in (Hydro-) Thermochemically Treated Sewage Sludge, ACS Sustain. Chem. Eng. 11 (2023) 15841–15850. https://doi.org/10.1021/acssuschemeng.3c03720.
[158] M. Pecchi, F. Patuzzi, V. Benedetti, R. Di Maggio, M. Baratieri, Thermodynamics of hydrothermal carbonization: Assessment of the heat release profile and process enthalpy change, Fuel Process. Technol. 197 (2020) 106206. https://doi.org/10.1016/j.fuproc.2019.106206.
[159] G. Ischia, M. Cazzanelli, L. Fiori, M. Orlandi, A. Miotello, Exothermicity of hydrothermal carbonization: Determination of heat profile and enthalpy of reaction via high-pressure differential scanning calorimetry, Fuel 310 (2022) 122312. https://doi.org/10.1016/j.fuel.2021.122312.
[160] N. Deliiski, Transient Heat Conduction in Capillary Porous Bodies, in: Convect. Conduct. Heat Transf., IntechOpen, 2011. https://doi.org/10.5772/21424.
[161] D.R. Cox, N. Reid, The theory of the design of experiments, Chapman & Hall/CRC, Boca Raton, 2000.
[162] P. Armitage, G. Berry, J.N.S. Matthews, Statistical Methods in Medical Research, Wiley, 2001.
[163] K. Król, K. Iskra, W. Ferens, J.M. Miodoński, Testing properties of sewage sludge for energy use, Environ. Prot. Eng. 45 (2019). https://doi.org/10.37190/epe190405.

[164] S. Mazumder, P. Saha, M.T. Reza, Co-hydrothermal carbonization of coal waste and food waste: fuel characteristics, Biomass Convers. Biorefinery 12 (2022). https://doi.org/10.1007/s13399-020-00771-5.
[165] Contrôle sanitaire des EDCH, (n.d.). https://orobnat.sante.gouv.fr/orobnat/rechercherResultatQualite.do (accessed June 25, 2024).
[166] C.C. Davis, M. Edwards, Role of Calcium in the Coagulation of NOM with Ferric Chloride, Environ. Sci. Technol. 51 (2017) 11652–11659. https://doi.org/10.1021/acs.est.7b02038.
[167] M.R. Carter, Soil Sampling and Methods of Analysis, CRC Press, 1993.
[168] K. Dinkler, B. Li, J. Guo, B. Hülsemann, G.C. Becker, J. Müller, H. Oechsner, Adapted Hedley fractionation for the analysis of inorganic phosphate in biogas digestate, Bioresour. Technol. 331 (2021) 125038. https://doi.org/10.1016/j.biortech.2021.125038.
[169] F.H. Rigler, Further Observations Inconsistent with the Hypothesis That the Molybdenum Blue Method Measures Orthophosphate in Lake Water1, Limnol. Oceanogr. 13 (1968) 7–13. https://doi.org/10.4319/lo.1968.13.1.0007.
[170] X. Jingliang, S. Yuanjie, P. Anran, F. Kateb, H.M.A. Aldeeb, Research on the effects of ferric salt added into aeration tank for phosphorus removal on biochemical system, Appl. Math. Nonlinear Sci. 6 (2021) 281–290. https://doi.org/10.2478/amns.2021.2.00041.
[171] M.Y. Jat Baloch, W. Zhang, T. Sultana, M. Akram, B.A.A. Shoumik, Md.Z. Khan, M.A. Farooq, Utilization of sewage sludge to manage saline–alkali soil and increase crop production: Is it safe or not?, Environ. Technol. Innov. 32 (2023) 103266. https://doi.org/10.1016/j.eti.2023.103266.
[172] G. S., A. Pugazhendi, S. Kavitha, S. Kumar, R. Banu, Evaluation of operational parameters for semicontinuous anaerobic digester treating pretreated waste activated sludge, Desalination Water Treat. 57 (2016) 9093–9100. https://doi.org/10.1080/19443994.2015.1029526.
[173] A. Akhiar, A. Battimelli, M. Torrijos, H. Carrere, Comprehensive characterization of the liquid fraction of digestates from full-scale anaerobic co-digestion, Waste Manag. 59 (2017) 118–128. https://doi.org/10.1016/j.wasman.2016.11.005.
[174] A. Xia, J.D. Murphy, Microalgal Cultivation in Treating Liquid Digestate from Biogas Systems, Trends Biotechnol. 34 (2016) 264–275. https://doi.org/10.1016/j.tibtech.2015.12.010.
[175] I. Krzemińska, M. Oleszek, D. Wiącek, Liquid Anaerobic Digestate as a Source of Nutrients for Lipid and Fatty Acid Accumulation by Auxenochlorella Protothecoides, Molecules 24 (2019) 3582. https://doi.org/10.3390/molecules24193582.
[176] J. Suschka, K. Grübel, Nitrogen in the Process of Waste Activated Sludge Anaerobic Digestion, Arch. Environ. Prot. 40 (2014) 123–136. https://doi.org/10.2478/aep-2014-0021.
[177] M. Kayhanian, Ammonia Inhibition in High-Solids Biogasification: An Overview and Practical Solutions, Environ. Technol. 20 (1999) 355–365. https://doi.org/10.1080/09593332008616828.
[178] B. Drosg, W. Fuchs, S.T. Al, M. Madsen, B. Linke, Nutrient Recovery by Biogas Digestate Processing, JRC Publ. Repos. (2015). https://publications.jrc.ec.europa.eu/repository/handle/JRC97163 (accessed May 31, 2024).

[179] Council Directive 86/278/EEC of 12 June 1986 on the protection of the environment, and in particular of the soil, when sewage sludge is used in agriculture, 1986. http://data.europa.eu/eli/dir/1986/278/oj/eng (accessed June 26, 2024).
[180] Arrêté du 08/01/98 fixant les prescriptions techniques applicables aux épandages de boues sur les sols agricoles pris en application du décret n° 97-1133 du 08/12/97 relatif à l'épandage des boues issues du traitement des eaux usées | AIDA, (n.d.). https://aida.ineris.fr/reglementation/arrete-080198-fixant-prescriptions-techniques-applicables-epandages-boues-sols (accessed June 26, 2024).
[181] Regulation (EU) 2019/1009 of the European Parliament and of the Council of 5 June 2019 laying down rules on the making available on the market of EU fertilising products and amending Regulations (EC) No 1069/2009 and (EC) No 1107/2009 and repealing Regulation (EC) No 2003/2003, 2023. http://data.europa.eu/eli/reg/2019/1009/2023-03-16/eng (accessed March 3, 2024).
[182] Council Directive 91/271/EEC of 21 May 1991 concerning urban waste-water treatment, 1991. http://data.europa.eu/eli/dir/1991/271/oj/eng (accessed June 26, 2024).
[183] D. Yang, C. Hu, L. Dai, Z. Liu, B. Dong, X. Dai, Post-thermal hydrolysis and centrate recirculation for enhancing anaerobic digestion of sewage sludge, Waste Manag. 92 (2019) 39–48. https://doi.org/10.1016/j.wasman.2019.04.044.
[184] L.B. Silva Thomsen, K. Anastasakis, P. Biller, Wet oxidation of aqueous phase from hydrothermal liquefaction of sewage sludge, Water Res. 209 (2022) 117863. https://doi.org/10.1016/j.watres.2021.117863.
[185] M.T. Munir, B. Li, I. Boiarkina, S. Baroutian, W. Yu, B.R. Young, Phosphate recovery from hydrothermally treated sewage sludge using struvite precipitation, Bioresour. Technol. 239 (2017) 171–179. https://doi.org/10.1016/j.biortech.2017.04.129.
[186] A. Urbanowska, M. Kabsch-Korbutowicz, C. Aragon-Briceño, M. Wnukowski, A. Pożarlik, L. Niedzwiecki, M. Baranowski, M. Czerep, P. Seruga, H. Pawlak-Kruczek, E. Bramer, G. Brem, Cascade Membrane System for Separation of Water and Organics from Liquid By-Products of HTC of the Agricultural Digestate—Evaluation of Performance, Energies 14 (2021) 4752. https://doi.org/10.3390/en14164752.
[187] M.-J. Alhnidi, D. Wüst, A. Funke, L. Hang, A. Kruse, Fate of Nitrogen, Phosphate, and Potassium during Hydrothermal Carbonization and the Potential for Nutrient Recovery, ACS Sustain. Chem. Eng. 8 (2020) 15507–15516. https://doi.org/10.1021/acssuschemeng.0c04229.
[188] Y. Su, D. Liu, M. Gong, W. Zhu, Y. Yu, H. Gu, Investigation on the decomposition of chemical compositions during hydrothermal conversion of dewatered sewage sludge, Int. J. Hydrog. Energy 44 (2019) 26933–26942. https://doi.org/10.1016/j.ijhydene.2019.08.182.
[189] T. Wang, Y. Zhai, Y. Zhu, C. Peng, B. Xu, T. Wang, C. Li, G. Zeng, Influence of temperature on nitrogen fate during hydrothermal carbonization of food waste, Bioresour. Technol. 247 (2018) 182–189. https://doi.org/10.1016/j.biortech.2017.09.076.
[190] O.W. Howarth, D.M.J. Lilley, Carbon-13-NMR of peptides and proteins, Prog. Nucl. Magn. Reson. Spectrosc. 12 (1978) 1–40. https://doi.org/10.1016/0079-6565(78)80001-6.

[191] F. Yin, H. Chen, G. Xu, G. Wang, Y. Xu, A detailed kinetic model for the hydrothermal decomposition process of sewage sludge, Bioresour. Technol. 198 (2015) 351–357. https://doi.org/10.1016/j.biortech.2015.09.033.
[192] X. Zhuang, Y. Huang, Y. Song, H. Zhan, X. Yin, C. Wu, The transformation pathways of nitrogen in sewage sludge during hydrothermal treatment, Bioresour. Technol. 245 (2017) 463–470. https://doi.org/10.1016/j.biortech.2017.08.195.
[193] L.B. Silva Thomsen, P.N. Carvalho, J.S. dos Passos, K. Anastasakis, K. Bester, P. Biller, Hydrothermal liquefaction of sewage sludge; energy considerations and fate of micropollutants during pilot scale processing, Water Res. 183 (2020) 116101. https://doi.org/10.1016/j.watres.2020.116101.
[194] X.-P. Zhang, C. Zhang, X. Li, S.-H. Yu, P. Tan, Q.-Y. Fang, G. Chen, A two-step process for sewage sludge treatment: Hydrothermal treatment of sludge and catalytic hydrothermal gasification of its derived liquid, Fuel Process. Technol. 180 (2018) 67–74. https://doi.org/10.1016/j.fuproc.2018.08.012.
[195] Z. Cao, B. Hülsemann, D. Wüst, H. Oechsner, A. Lautenbach, A. Kruse, Effect of residence time during hydrothermal carbonization of biogas digestate on the combustion characteristics of hydrochar and the biogas production of process water, Bioresour. Technol. 333 (2021) 125110. https://doi.org/10.1016/j.biortech.2021.125110.
[196] R.E. Zeebe, D. Wolf-Gladrow, CO2 in Seawater: Equilibrium, Kinetics, Isotopes, Gulf Professional Publishing, 2001.
[197] H. Wang, Z. Yang, X. Li, Y. Liu, Distribution and transformation behaviors of heavy metals and phosphorus during hydrothermal carbonization of sewage sludge, Environ. Sci. Pollut. Res. 27 (2020) 17109–17122. https://doi.org/10.1007/s11356-020-08098-4.
[198] X. Zhuang, H. Zhan, Y. Huang, Y. Song, X. Yin, C. Wu, Conversion of industrial biowastes to clean solid fuels via hydrothermal carbonization (HTC): Upgrading mechanism in relation to coalification process and combustion behavior, Bioresour. Technol. 267 (2018) 17–29. https://doi.org/10.1016/j.biortech.2018.07.002.
[199] M. Malhotra, A. Garg, Hydrothermal carbonization of centrifuged sewage sludge: Determination of resource recovery from liquid fraction and thermal behaviour of hydrochar, Waste Manag. 117 (2020) 114–123. https://doi.org/10.1016/j.wasman.2020.07.026.
[200] B. Chefetz, Y. Hader, Y. Chen, Dissolved Organic Carbon Fractions Formed during Composting of Municipal Solid Waste: Properties and Significance, Acta Hydrochim. Hydrobiol. 26 (1998) 172–179. https://doi.org/10.1002/(SICI)1521-401X(199805)26:3<172::AID-AHEH172>3.0.CO;2-5.
[201] A. Piccolo, L. Campanella, B.M. Petronio, Carbon-13 Nuclear Magnetic Resonance Spectra of Soil Humic Substances Extracted by Different Mechanisms, Soil Sci. Soc. Am. J. 54 (1990) 750–756. https://doi.org/10.2136/sssaj1990.03615995005400030021x.
[202] M.-F. Dignac, P. Ginestel, A. Bruchet, J.-M. Audic, S. Derenne, C. Largeau, Changes in the organic composition of wastewater during biological treatment as studied by NMR and IR spectroscopies, Water Sci. Technol. 43 (2001) 51–58. https://doi.org/10.2166/wst.2001.0072.
[203] D. Martinez-Balmori, R. Spaccini, N.O. Aguiar, E.H. Novotny, F.L. Olivares, L.P. Canellas, Molecular Characteristics of Humic Acids Isolated from Vermicomposts and Their Relationship to Bioactivity, J. Agric. Food Chem. 62 (2014) 11412–11419. https://doi.org/10.1021/jf504629c.

[204] X. Ding, J.D. Sheehan, T. Zhang, Z. Shen, Y. Wang, Z. Jiang, T. Fang, Experimental-computational approach for elucidating the dissolution behavior of potassium phosphates in near- and supercritical water, J. Supercrit. Fluids 181 (2022) 105488. https://doi.org/10.1016/j.supflu.2021.105488.
[205] J.S. Gaffney, N.A. Marley, In-depth review of atmospheric mercury: sources, transformations, and potential sinks, Energy Emiss. Control Technol. 2 (2014) 1–21. https://doi.org/10.2147/EECT.S37038.
[206] C.B. Alcock, V.P. Itkin, M.K. Horrigan, Vapour Pressure Equations for the Metallic Elements: 298–2500K, Can. Metall. Q. 23 (1984) 309–313. https://doi.org/10.1179/cmq.1984.23.3.309.
[207] R. Huang, C. Fang, B. Zhang, Y. Tang, Transformations of Phosphorus Speciation during (Hydro)thermal Treatments of Animal Manures, Environ. Sci. Technol. 52 (2018) 3016–3026. https://doi.org/10.1021/acs.est.7b05203.
[208] J. Rabinowitz, F. Woeller, J. Flores, R. Krebsbach, Electric Discharge Reactions in Mixtures of Phosphine, Methane, Ammonia and Water, Nature 224 (1969) 796–798. https://doi.org/10.1038/224796a0.
[209] B.J. Cade-Menun, Characterizing phosphorus in environmental and agricultural samples by 31P nuclear magnetic resonance spectroscopy, Talanta 66 (2005) 359–371. https://doi.org/10.1016/j.talanta.2004.12.024.
[210] B. Han, Z. Sha, J.I. Partanen, M. Louhi-Kultanen, Solubility of potassium dihydrogen phosphate in aqueous solutions of acetone, ethyl acetate, and thiourea from T = (298.15–313.15) K, Fluid Phase Equilibria 336 (2012) 16–21. https://doi.org/10.1016/j.fluid.2012.08.031.
[211] A. Yesigat, A. Worku, A. Mekonnen, W. Bae, G.L. Feyisa, S. Gatew, J.-L. Han, W. Liu, A. Wang, A. Guadie, Phosphorus recovery as K-struvite from a waste stream: A review of influencing factors, advantages, disadvantages and challenges, Environ. Res. 214 (2022) 114086. https://doi.org/10.1016/j.envres.2022.114086.
[212] M. Shao, C. Zhang, X. Wang, N. Wang, Q. Chen, G. Cui, Q. Xu, Co-digestion of food waste and hydrothermal liquid digestate: Promotion effect of self-generated hydrochars, Environ. Sci. Ecotechnology 15 (2023) 100239. https://doi.org/10.1016/j.ese.2023.100239.
[213] E. Nyktari, E. Danso-Boateng, A. Wheatley, R. Holdich, Anaerobic digestion of liquid products following hydrothermal carbonisation of faecal sludge at different reaction conditions, DESALINATION WATER Treat. 91 (2017) 245–251. https://doi.org/10.5004/dwt.2017.20782.
[214] R.P. Ipiales, M.A. de la Rubia, E. Diaz, A.F. Mohedano, J.J. Rodriguez, Integration of Hydrothermal Carbonization and Anaerobic Digestion for Energy Recovery of Biomass Waste: An Overview, Energy Fuels 35 (2021) 17032–17050. https://doi.org/10.1021/acs.energyfuels.1c01681.
[215] A.T. Koçer, B. İnan, D. Özçimen, İ. Gökalp, A study of microalgae cultivation in hydrothermal carbonization process water: Nutrient recycling, characterization and process design, Environ. Technol. Innov. 30 (2023) 103048. https://doi.org/10.1016/j.eti.2023.103048.
[216] M.-M. Titirici, A. Thomas, M. Antonietti, Back in the black: hydrothermal carbonization of plant material as an efficient chemical process to treat the CO2 problem?, New J. Chem. 31 (2007) 787–789. https://doi.org/10.1039/B616045J.
[217] X. Zhuang, J. Liu, Q. Zhang, C. Wang, H. Zhan, L. Ma, A review on the utilization of industrial biowaste via hydrothermal carbonization, Renew. Sustain. Energy Rev. 154 (2022) 111877. https://doi.org/10.1016/j.rser.2021.111877.

[218] S. Yu, X. Dong, P. Zhao, Z. Luo, Z. Sun, X. Yang, Q. Li, L. Wang, Y. Zhang, H. Zhou, Decoupled temperature and pressure hydrothermal synthesis of carbon sub-micron spheres from cellulose, Nat. Commun. 13 (2022) 3616. https://doi.org/10.1038/s41467-022-31352-x.
[219] S. Yu, P. Zhao, X. Yang, Q. Li, B.A. Mohamed, J.M. Saad, Y. Zhang, H. Zhou, Low-temperature hydrothermal carbonization of pectin enabled by high pressure, J. Anal. Appl. Pyrolysis 166 (2022) 105627. https://doi.org/10.1016/j.jaap.2022.105627.
[220] Propriétés thermophysiques des systèmes fluides, (n.d.). https://webbook.nist.gov/chemistry/fluid/index.html.fr (accessed September 1, 2024).
[221] P. Arlabosse, S. Chavez, D. Lecomte, Method for Thermal Design of Paddle Dryers: Application to Municipal Sewage Sludge, Dry. Technol. 22 (2004) 2375–2393. https://doi.org/10.1081/DRT-200040041.
[222] R.B. Madsen, M. Glasius, How Do Hydrothermal Liquefaction Conditions and Feedstock Type Influence Product Distribution and Elemental Composition?, Ind. Eng. Chem. Res. 58 (2019) 17583–17600. https://doi.org/10.1021/acs.iecr.9b02337.
[223] A. Mathanker, S. Das, D. Pudasainee, M. Khan, A. Kumar, R. Gupta, A Review of Hydrothermal Liquefaction of Biomass for Biofuels Production with a Special Focus on the Effect of Process Parameters, Co-Solvents, and Extraction Solvents, Energies 14 (2021) 4916. https://doi.org/10.3390/en14164916.
[224] C.S. Reynolds, P.S. Davies, Sources and bioavailability of phosphorus fractions in freshwaters: a British perspective, Biol. Rev. 76 (2001) 27–64. https://doi.org/10.1111/j.1469-185X.2000.tb00058.x.
[225] S.R. Olsen, Estimation of Available Phosphorus in Soils by Extraction with Sodium Bicarbonate, U.S. Department of Agriculture, 1954.
[226] Z.-W. He, W.-Z. Liu, L. Wang, C.-C. Tang, Z.-C. Guo, C.-X. Yang, A.-J. Wang, Clarification of phosphorus fractions and phosphorus release enhancement mechanism related to pH during waste activated sludge treatment, Bioresour. Technol. 222 (2016) 217–225. https://doi.org/10.1016/j.biortech.2016.10.010.
[227] C. Adam, B. Peplinski, M. Michaelis, G. Kley, F.-G. Simon, Thermochemical treatment of sewage sludge ashes for phosphorus recovery, Waste Manag. 29 (2009) 1122–1128. https://doi.org/10.1016/j.wasman.2008.09.011.
[228] F. Andrieux-Loyer, A. Aminot, Phosphorus Forms Related to Sediment Grain Size and Geochemical Characteristics in French Coastal Areas, Estuar. Coast. Shelf Sci. 52 (2001) 617–629. https://doi.org/10.1006/ecss.2001.0766.
[229] N.X.Q. Vo, Y. Ji, T.V. Doan, H. Kang, Distribution of Inorganic Phosphorus Fractions in Sediments of the South Han River over a Rainy Season, Environ. Eng. Res. 19 (2014) 229–240. https://doi.org/10.4491/eer.2014.026.
[230] L.I. da Silva, M.C. Pereira, A.M.X. de Carvalho, V.H. Buttrós, M. Pasqual, J. Dória, Phosphorus-Solubilizing Microorganisms: A Key to Sustainable Agriculture, Agriculture 13 (2023) 462. https://doi.org/10.3390/agriculture13020462.
[231] Commission Directive 77/535/EEC of 22 June 1977 on the approximation of the laws of the Member States relating to methods of sampling and analysis for fertilizers, 1977. http://data.europa.eu/eli/dir/1977/535/oj/eng (accessed July 6, 2024).

[232] L. Deng, B.R. Dhar, Phosphorus recovery from wastewater via calcium phosphate precipitation: A critical review of methods, progress, and insights, Chemosphere 330 (2023) 138685. https://doi.org/10.1016/j.chemosphere.2023.138685.
[233] V. Harish, S. Aslam, S. Chouhan, Y. Pratap, S. Lalotra, Iron toxicity in plants: A Review, Int. J. Environ. Clim. Change 13 (2023) 1894–1900. https://doi.org/10.9734/IJECC/2023/v13i82145.
[234] R. Ofoe, R.H. Thomas, S.K. Asiedu, G. Wang-Pruski, B. Fofana, Lord Abbey, Aluminum in plant: Benefits, toxicity and tolerance mechanisms, Front. Plant Sci. 13 (2023). https://doi.org/10.3389/fpls.2022.1085998.
[235] D. López Barreiro, M. Beck, U. Hornung, F. Ronsse, A. Kruse, W. Prins, Suitability of hydrothermal liquefaction as a conversion route to produce biofuels from macroalgae, Algal Res. 11 (2015) 234–241. https://doi.org/10.1016/j.algal.2015.06.023.
[236] Z. Srokol, A.-G. Bouche, A. van Estrik, R.C.J. Strik, T. Maschmeyer, J.A. Peters, Hydrothermal upgrading of biomass to biofuel; studies on some monosaccharide model compounds, Carbohydr. Res. 339 (2004) 1717–1726. https://doi.org/10.1016/j.carres.2004.04.018.
[237] O. Yakaboylu, J. Harinck, K.G. Smit, W. Jong, Supercritical Water Gasification of Biomass: A Literature and Technology Overview, Energies 8 (2015) 859–894. https://doi.org/10.3390/en8020859.
[238] B. Motavaf, S.H. Capece, P.E. Savage, Screening Potential Catalysts for the Hydrothermal Liquefaction of Food Waste, Energy Fuels 35 (2021) 9437–9449. https://doi.org/10.1021/acs.energyfuels.1c00672.
[239] E.F. Zama, G. Li, Y.-T. Tang, B.J. Reid, N.M. Ngwabie, G.-X. Sun, The removal of arsenic from solution through biochar-enhanced precipitation of calcium-arsenic derivatives, Environ. Pollut. 292 (2022) 118241. https://doi.org/10.1016/j.envpol.2021.118241.
[240] E. Song, S. Park, H. Kim, Upgrading Hydrothermal Carbonization (HTC) Hydrochar from Sewage Sludge, Energies 12 (2019) 2383. https://doi.org/10.3390/en12122383.
[241] M. Lucian, F. Merzari, M. Gubert, A. Messineo, M. Volpe, Industrial-Scale Hydrothermal Carbonization of Agro-Industrial Digested Sludge: Filterability Enhancement and Phosphorus Recovery, Sustainability 13 (2021) 9343. https://doi.org/10.3390/su13169343.
[242] G. Gerner, L. Meyer, R. Wanner, T. Keller, R. Krebs, Sewage sludge treatment by hydrothermal carbonization : feasibility study for sustainable nutrient recovery and fuel production, Energies 14 (2021) 2697. https://doi.org/10.3390/en14092697.
[243] A. Amrullah, Y. Matsumura, Supercritical water gasification of sewage sludge in continuous reactor, Bioresour. Technol. 249 (2018) 276–283. https://doi.org/10.1016/j.biortech.2017.10.002.
[244] P. Das, S. Khan, M. AbdulQuadir, M. Thaher, M. Waqas, A. Easa, E.S.M. Attia, H. Al-Jabri, Energy recovery and nutrients recycling from municipal sewage sludge, Sci. Total Environ. 715 (2020) 136775. https://doi.org/10.1016/j.scitotenv.2020.136775.
[245] R. Ferrentino, R. Ceccato, V. Marchetti, G. Andreottola, L. Fiori, Sewage Sludge Hydrochar: An Option for Removal of Methylene Blue from Wastewater, Appl. Sci. 10 (2020) 3445. https://doi.org/10.3390/app10103445.

[246] F. Merzari, J. Goldfarb, G. Andreottola, T. Mimmo, M. Volpe, L. Fiori, Hydrothermal Carbonization as a Strategy for Sewage Sludge Management: Influence of Process Withdrawal Point on Hydrochar Properties, Energies 13 (2020) 2890. https://doi.org/10.3390/en13112890.
[247] P. Saetea, N. Tippayawong, Recovery of Value-Added Products from Hydrothermal Carbonization of Sewage Sludge, Int. Sch. Res. Not. (2013). https://doi.org/10.1155/2013/268947.
[248] A.L. Tasca, E. Stefanelli, A.M. Raspolli Galletti, R. Gori, G. Mannarino, S. Vitolo, M. Puccini, Hydrothermal Carbonization of Sewage Sludge: Analysis of Process Severity and Solid Content, Chem. Eng. Technol. 43 (2020) 2382–2392. https://doi.org/10.1002/ceat.202000095.
[249] F. Lai, Y. Chang, H. Huang, G. Wu, J. Xiong, Z. Pan, C. Zhou, Liquefaction of sewage sludge in ethanol-water mixed solvents for bio-oil and biochar products, Energy 148 (2018) 629–641. https://doi.org/10.1016/j.energy.2018.01.186.
[250] A.A. Shah, S.S. Toor, F. Conti, A.H. Nielsen, L.A. Rosendahl, Hydrothermal liquefaction of high ash containing sewage sludge at sub and supercritical conditions, Biomass Bioenergy 135 (2020) 105504. https://doi.org/10.1016/j.biombioe.2020.105504.
[251] R.A. Fisher, Statistical Methods for Research Workers, in: S. Kotz, N.L. Johnson (Eds.), Breakthr. Stat. Methodol. Distrib., Springer, New York, NY, 1992: pp. 66–70. https://doi.org/10.1007/978-1-4612-4380-9_6.
[252] Q. Wang, U.G. Nielsen, Applications of solid-state NMR spectroscopy in environmental science, Solid State Nucl. Magn. Reson. 110 (2020) 101698. https://doi.org/10.1016/j.ssnmr.2020.101698.

ANNEXES

A. Supplementary Figures and Tables: State of the Art

Table A.1 - Results from studies that have investigated P conversion during hydrothermal treatment of sewage sludge. HT = hydrothermal treatment; HTC = hydrothermal carbonization; HTL = hydrothermal liquefaction; HTG = hydrothermal gasification; PSS = primary sewage sludge; SSS = secondary sewage sludge; DSS = digested sewage sludge; M/NS = mixed or not specified sludge.

Reference	Hydrothermal treatment	Type of sludge	Sludge origin	Temperature (°C)	Reaction time (min)	Solid-to-liquid ratio (Kg L^{-1})	P content in sludge (mg P g^{-1} dry SS)	Solid product recovery yield (%)	P recovery yield in the solid product (%)	P content in the solid product (mg P g^{-1} dry char)	P concentration in process water (mg P L^{-1})
[81]	HTC	PSS	China	120-300	30-180	0.16	26.8	47.7-101	69.6-100 [a]	27.1-81	0-4570
[82]	HT	M/NS	USA	125-225	30-270	0.11	19	42.3-102	92.6-99.5 [a]	18.4-42	98-224
[82]	HT	DSS	USA	125-225	30-270	0.11	33	52.8-100	95.4-98.3 [a]	33.5-62	64-127
[116]	HT	SSS	Spain	100-200	15-210	0.035	16		80.5-97.8 [a]	12.9-15.64[e]	
[10]	HTC	SSS	China	170-320	30	0.23	25.4		17.25-95.8	27.65-47.8	
[105]	HT	M/NS	USA	90-155	240	0.07	12.1[b]			13.32-18.6	12.3-44.6
[105]	HT	M/NS	USA	90-155	240	0.05	12.7[b]			13.63-21.1	12.3-38
[83]	HTC	M/NS	China	160-280	120	0.11			72.1-89.1	28.4-40.5	129-485
[62]	HTC	SSS	Australia	180-240	30-150	0.25	14	68.6-75.7	92.8-102 [a]	19	
[62]	HTC	PSS	Australia	180-240	30	0.25	7	77.4-84	96-111 [a]	8-10	
[62]	HTC	SSS	Australia	180-240	30	0.25	21	68.1-74.8	103-107 [a]	29-33	
[77]	HTC	SSS	China	200-260	60-480	0.17	43			25.8-41.3	54-72
[103]	HTC	SSS	China	150-300	120	0.31	17.9	79.7-92.8	97.9-105 [a]	19-22.5	
[106]	HT	DSS	USA	90-185	240	0.06	34.2[b]			34.2-59	7.7-27.6 [a]
[43]	HTC	SSS	USA	225	1440	0.11	41	31.7-37.1	55.3-71.8 [a]	71-79	
[84]	HTC	DSS	China	170	30	0.18-0.23	23.1-30.5		88.8-99.1	31.5-40.9	39-415
[71]	HTC	SSS	USA	225	240-960	0.18	41	48.5-55.2	89.3-101	76-81	
[71]	HTC	DSS	USA	225	240-960	0.18	33	49.8-55.6	81.7-95.5	49-61	
[193]	HTL	PSS	Denmark	300-350	11.6-21						2.3-7.6[c]
[126]	HTC	M/NS	Germany	200-240	120	0.11	36.1	53.8-69	93.2-99		58-326
[78]	HTC	DSS	Germany	180-260	60-240	0.11-0.25	32	64.9-80.5	87.5-100	38.6-48.5	
[96]	HT	M/NS	China	140-200	10-60	0.10	96.2			113.9-178.6	
[107]	HTC	DSS	Finland	210-250	30-120	0.17-0.34	37.2	72-88.3	83.6-101 [a]	37.4-56.7	330-1130

Reference	Hydrothermal treatment	Type of sludge	Sludge origin	Temperature (°C)	Reaction time (min)	Solid-to-liquid ratio (Kg L^{-1})	P content in sludge (mg P g^{-1} dry SS)	Solid product recovery yield (%)	P recovery yield in the solid product (%)	P content in the solid product (mg P g^{-1} dry char)	P concentration in process water (mg P L^{-1})
[118]	HT	SSS	USA	125-225	240	0.20	56.2				159-163 [a]
[97]	HTC	M/NS	UK	200-250	240	0.11	2.8	63.7-73.8	53-92	2.3-3.5	
[98]	HTC	DSS	Singapore	200-380	20	0.05-0.21	13	35-76	91.6-99.4 [a]	17-35 [a]	16-229
[39]	HTC,HTL,HTG	DSS	Belgium	170-500	30-60	0.06-0.11	16.4	54-80	91.52-96.6 [a]		560-1360[d]
[85]	HTC	DSS	China	200-260	120	0.11	13.6	61.14-70.6	76.99-99	16.18-20.8	
[86]	HTC	SSS	China	200-260	30-240	0.03	117.8	42.27-54.8	93.4-96.2 [a]	36.59-37.4[e]	
[87]	HTC	M/NS	China	280	120	0.11	22.7	46.6-54.8	81.4-95.4 [a]	38.7-42.2	1-114
[240]	HTC	M/NS	South Korea	200	120		79.3	65.8	110 [a]	132.8 [a]	
[88]	HT	SSS	China	200-260	30	0.24	10.2	52-66.4	80.3-94.1 [a]	12.45-16.2	
[79]	HT	DSS	Japan	200-280	60	0.18	26.2			32.37-38.4	
[241]	HTC	M/NS	Italy	190	60		23	71.8 [a]	94.0 [a]	30.3 [a]	76.5
[89]	HTC	DSS	Spain	180-240	60	0.20	45.8	51.8-74.2	75.5-88.9 [a]	52.8-63	
[128]	HTC	DSS	Germany	190-220	120	0.18	31		91.3-102	42-45	74-173[c]
[242]	HTC	DSS	Switzerland	200	240	0.25	34.1	68.0	98.6 [a]	49.5	208
[129]	HTC	DSS	Germany	220	120	0.11	34.4				180-306
[90]	HTC	M/NS	China	220	30	0.13	24.8	39.8	66.6 [a]	41.5	
[111]	HTG	M/NS	China	380-460	6-18	0.03	38.1		82.6-97.1		
[122]	HT	M/NS	China	145	120	0.11	25.4			40.1-52.9	
[91]	HTC	M/NS	China	160-280	120	0.11	27.1	41.9-58.2	78.9-91.8	38.9-57.4	
[199]	HTC	M/NS	India	200	60-480	0.09		80.8-84.2			372-632[c]
[114,243]	HTG	SSS	Japan	300-600	0.08-1	0.26	13		6-57		
[100]	HTC	DSS	Canada	180-220	15-60	0.30	13.7	63.2-90.5	81.8-116 [a]	16.25-19	86-207[d]
[80]	HTC	DSS	Sweden	180-250	120	0.12	45	59.5-67.1	75.5-84.6 [a]	51-64	
[108]	HTC	DSS	Germany	180-240	85-439	0.33	47	52.4-84.9	44.7-83.7 [a]	30.7-57.6	134-2410
[99]	HTC	SSS	China	150-240	30-90	0.11	12.9	26.6-59.5	36.6-91.7 [a]	13.5-34.1	
[115]	HTC	DSS	Japan	120-240	30	0.02	44.9				373-580[c]
[110]	HTC	PSS	Spain	200-260	30-180		12.3	65-87 [a]	79.1-97.9	13.9-15.4	
[110]	HTC	SSS	Spain	200-260	30-180		16.7	57-83 [a]	73.3-99.7	20-21.6	
[141]	HTG	M/NS	China	400	30	0.12			44.3-98.9 [a]		41-2215
[109]	HT	M/NS	USA	90-185	240	0.06	19.2[b]			29.1-47.1	5.9-10.5
[123]	HTL	DSS	Denmark	300-350	20	0.20	7.8	42.2-47.2	128-132 [a]	21.16-24.4	
[119]	HTL	SSS	Denmark	350-400	15	0.27	9.6	27.3-28.1	92.6-93.9	24.2-27.2	131-186

Reference	Hydrothermal treatment	Type of sludge	Sludge origin	Temperature (°C)	Reaction time (min)	Solid-to-liquid ratio (Kg L^{-1})	P content in sludge (mg P g^{-1} dry SS)	Solid product recovery yield (%)	P recovery yield in the solid product (%)	P content in the solid product (mg P g^{-1} dry char)	P concentration in process water (mg P L^{-1})
[244]	HTL	M/NS	Qatar	350	30-120	0.14	12.3			3.3-8.9	
[92]	HTL	PSS	Denmark	350	300	0.04	21.2		46.8	99.2	15.8
[117]	HT	DSS	UK	160-250	30	0.05		56.8-73.4	11-37		73-104
[125]	HTC	DSS	UK	250	30	0.03-0.43		68-76	66.8-75.7 [a]		66-168
[112]	HT	M/NS	Japan	225-275	15-60	0.04	7		55-79		
[130]	HTC	DSS	Switzerland	205	420	0.25					14.3-17.8
[130]	HTC	PSS	Switzerland	190-220	300-420	0.10	25.2		97	28.1	72.7-159.6
[124]	HTC	M/NS	China	150-250	120	0.25	17.9	82.6-92.8	98-102 [a]	19.0-22.0	
[245]	HTC	DSS	Italy	190-250	180	0.14	22	62.9-83.3		42.0-47.0	
[246]	HTC	M/NS	Italy	190-250	30-60	0.03	5.22 [b]	49.4-77.2	87-103 [a]	6.2-10.2	11.1-38.4
[246]	HTC	DSS	Italy	190-250	30-60	0.03	5.81 [b]	64.6-82.8	75-103 [a]	6.7-7.5	12.2-22.7
[246]	HTC	DSS	Italy	190-250	30-60	0.17	9.22 [b]	66.8-88.2	79-88 [a]	9.2-10.9	0.2-0.4
[93]	HT	PSS	Japan	200	60	0.03	35	65-73.1	40.1-96.4	18.3-47.5	39.0-704
[94]	HTG	M/NS	China	350-500	5-60	0.05-0.20	14.1			19.7-22.6	43.8-70.8
[247]	HTC	DSS	Thailand	200	60-360	0.33		73.6-81.2			804-813
[248]	HTC	SSS	Italy	190-220	85-240	0.03-0.17	22.79	53.0-68.1	31.8-108.1 [a]	12.3-43.5	
[249]	HTL	M/NS	China	220	30	0.10-0.13	77.6	55.3-66.3	70-113 [a]	97.9-138.5	
[250]	HTL	SSS	Denmark	350-400	15	0.37	22.34		93-98	37.4-43.0	179-1503 [d]

[a] Calculated from paper data
[b] Does not consider dissolved P
[c] Orthophosphate (PO_4-P) concentration
[d] Expressed in mg kg^{-1}
[e] Expressed on a dry raw sludge basis

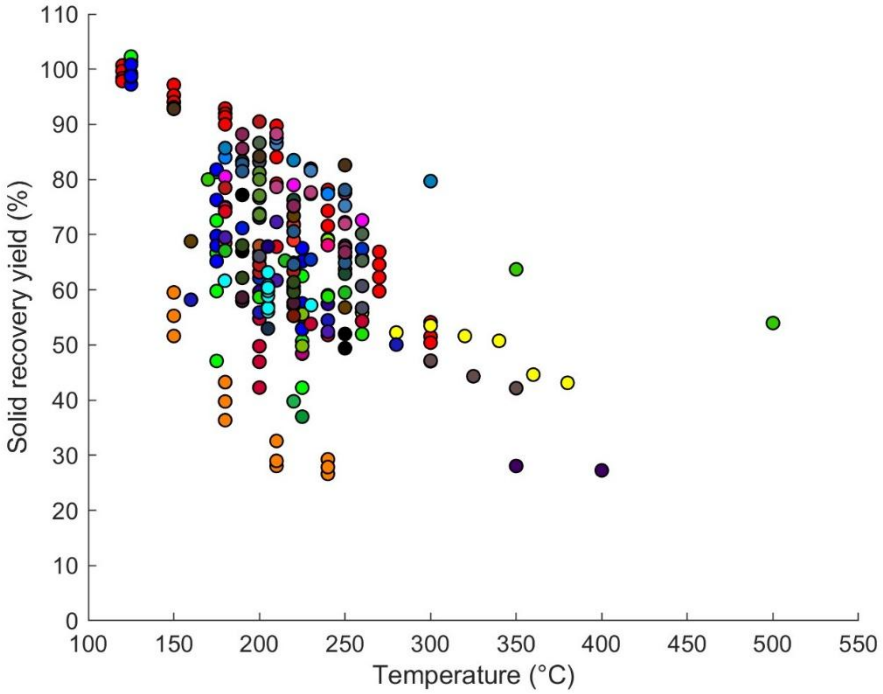

Figure A.1 - Solid product mass yield as a function of Temperature. Each color represents a different study listed in Table A.1.

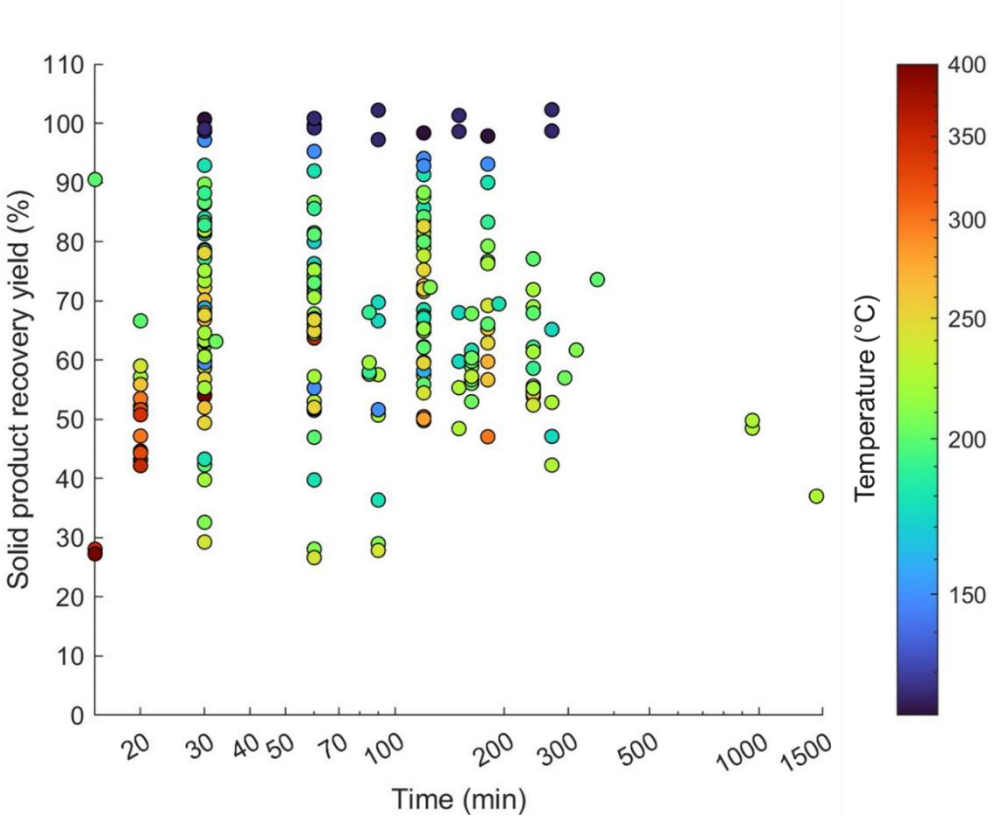

Figure A.2 - Solid product mass yield as a function of Time. Color scale represents treatment temperature. Data from works listed in Table A.1.

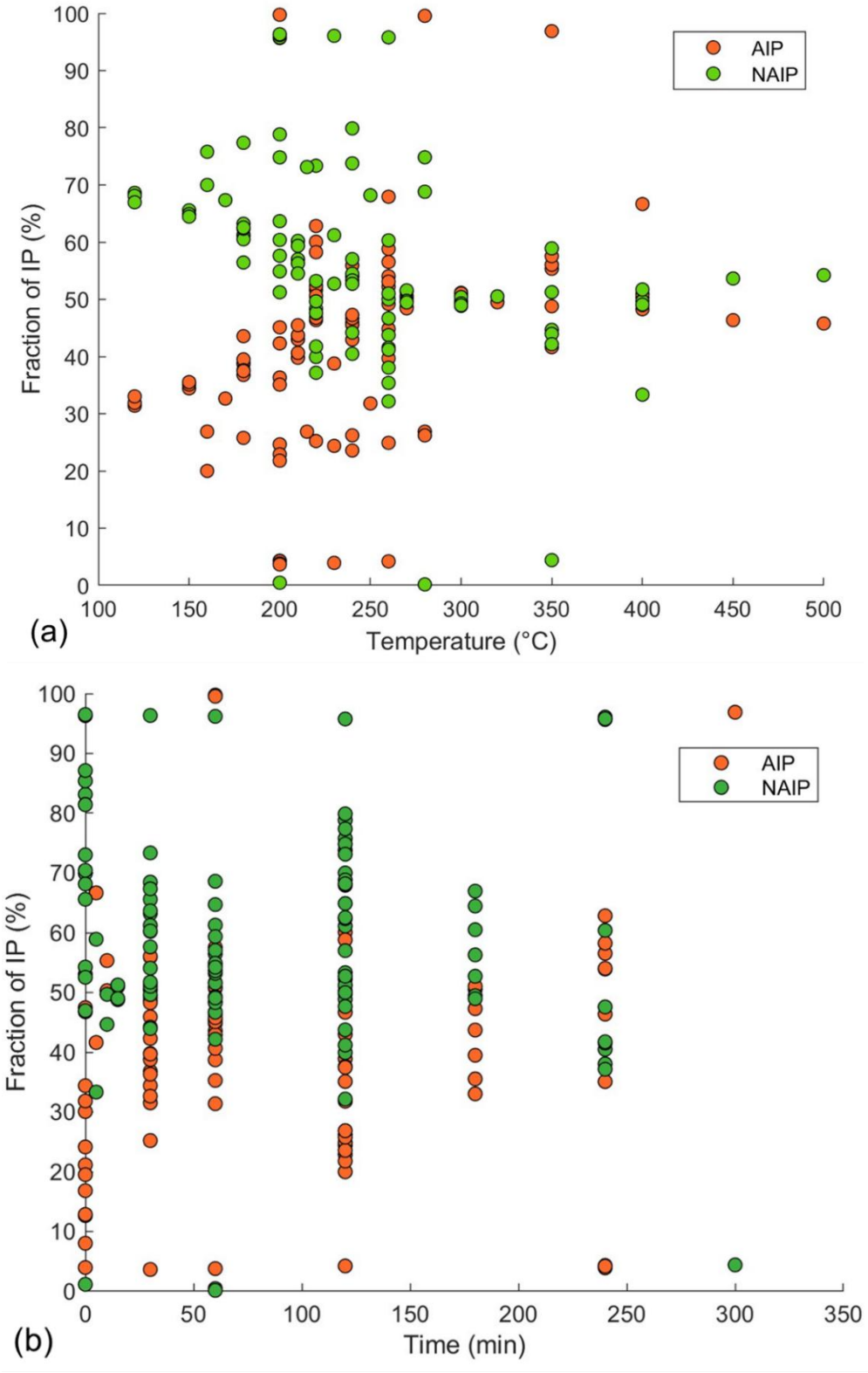

Figure A.3 - Evolution of non-apatitic inorganic P (NAIP) (green points) and apatitic inorganic P (AIP) (orange points) as a function of temperature (a) and treatment duration (b). Data from [10,77–81,83,85–94].

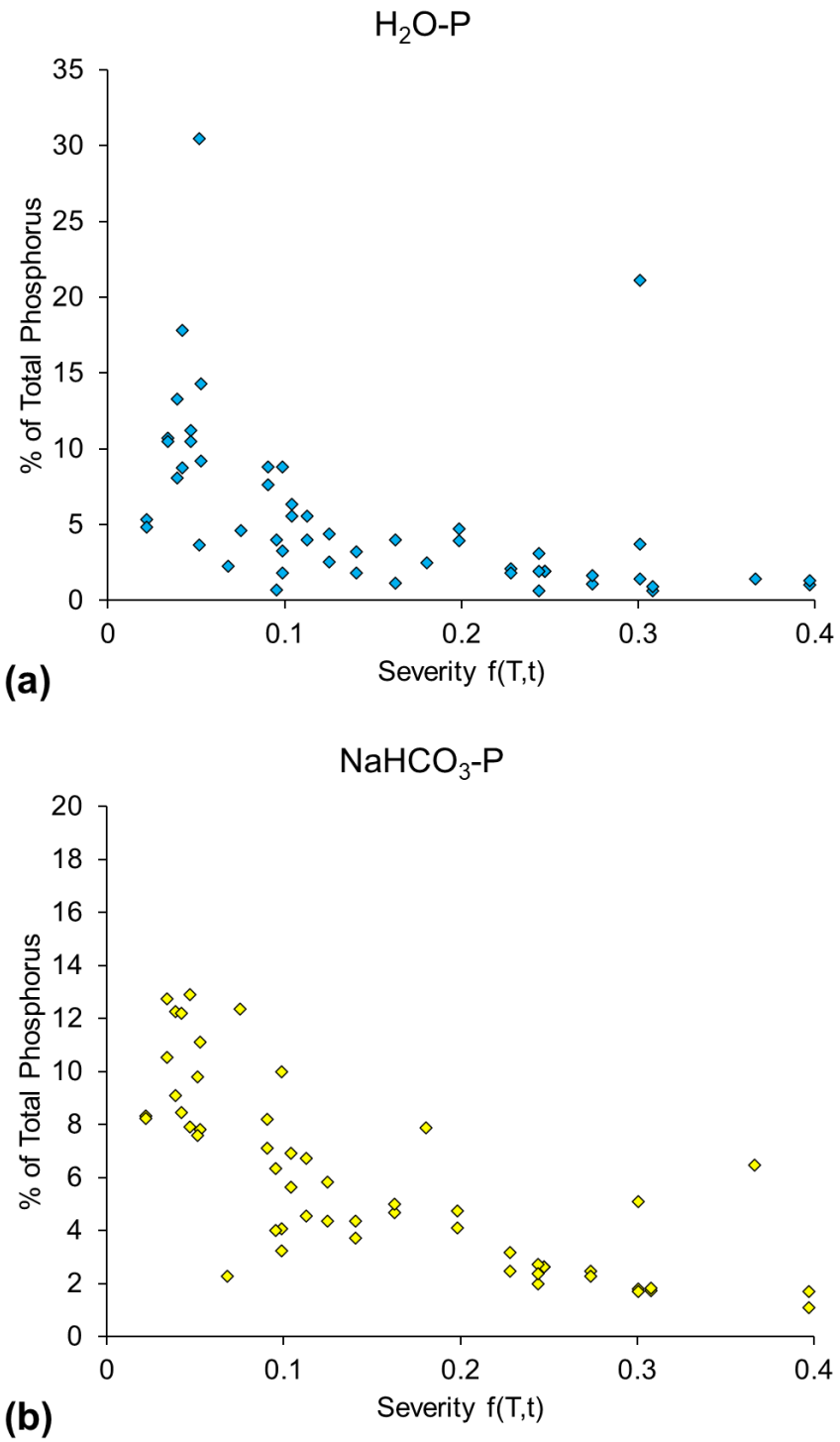

Figure A.4 - H_2O-P (a) $NaHCO_3$-P (b) fractions as a function of the process severity expressed by the Ruyter severity factor f(T,t). Data from [62,71,82,103,105,106,109,110,118,122–124].

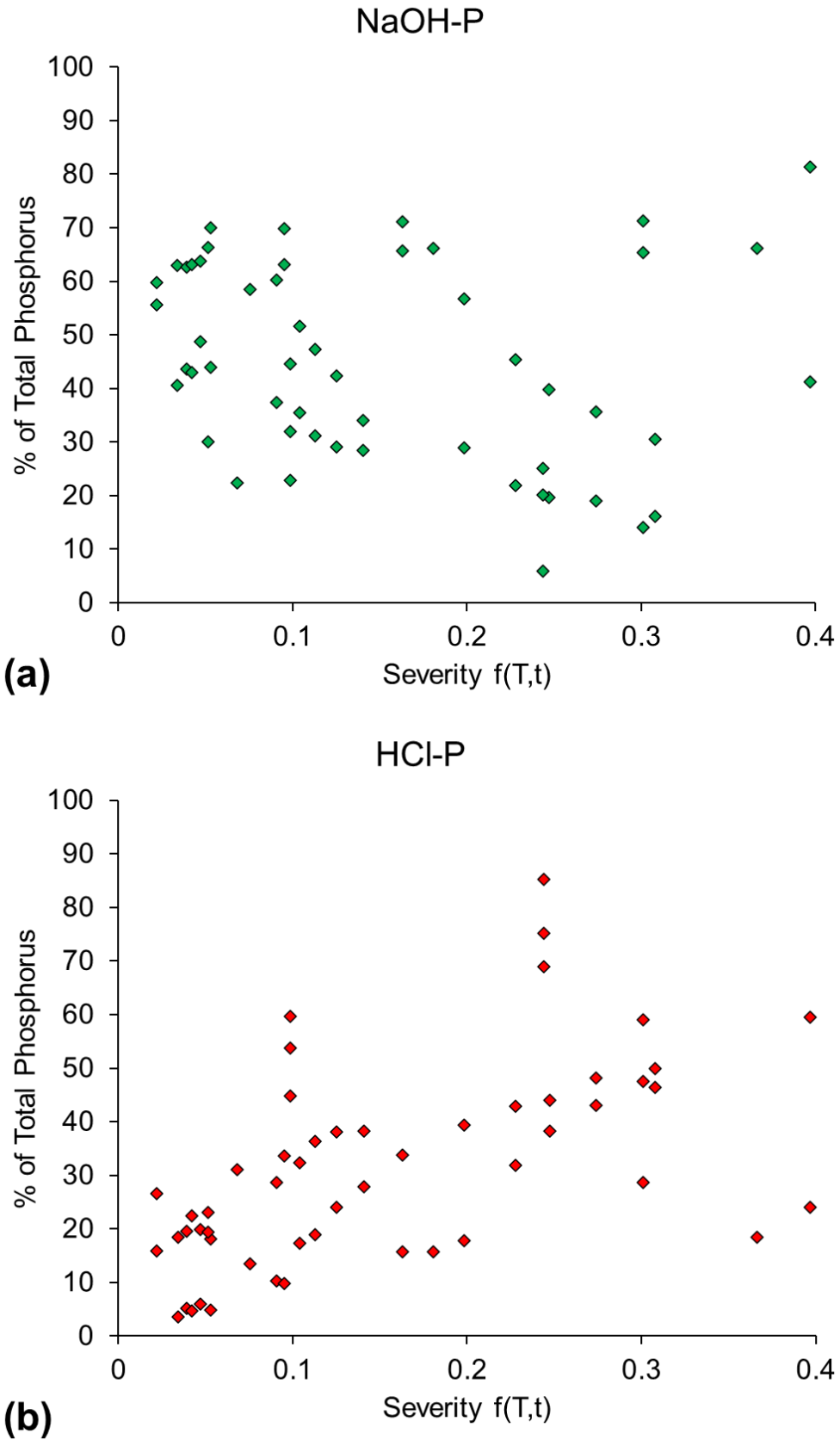

Figure A.5 - NaOH-P (a) HCl-P (b) fractions as a function of the process severity expressed by the Ruyter severity factor f(T,t). Data from [62,71,82,103,105,106,109,110,118,122–124].

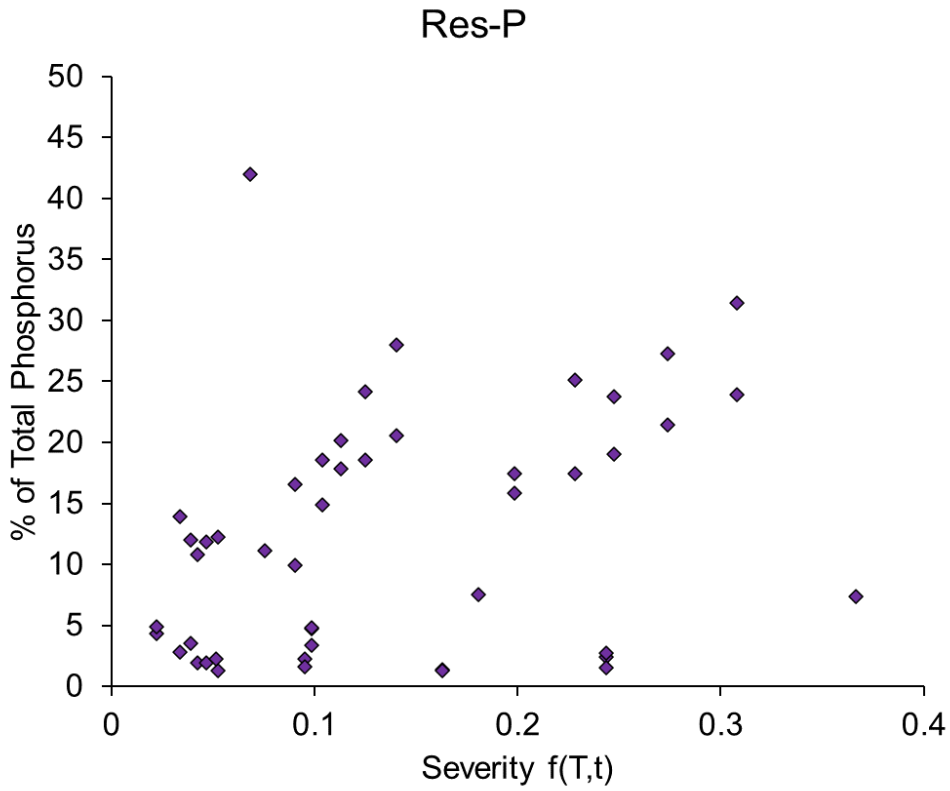

Figure A.6 - Residual P fraction as a function of the process severity expressed by the Ruyter severity factor f(T,t). Data from [62,71,82,103,105,106,109,110,118,122–124].

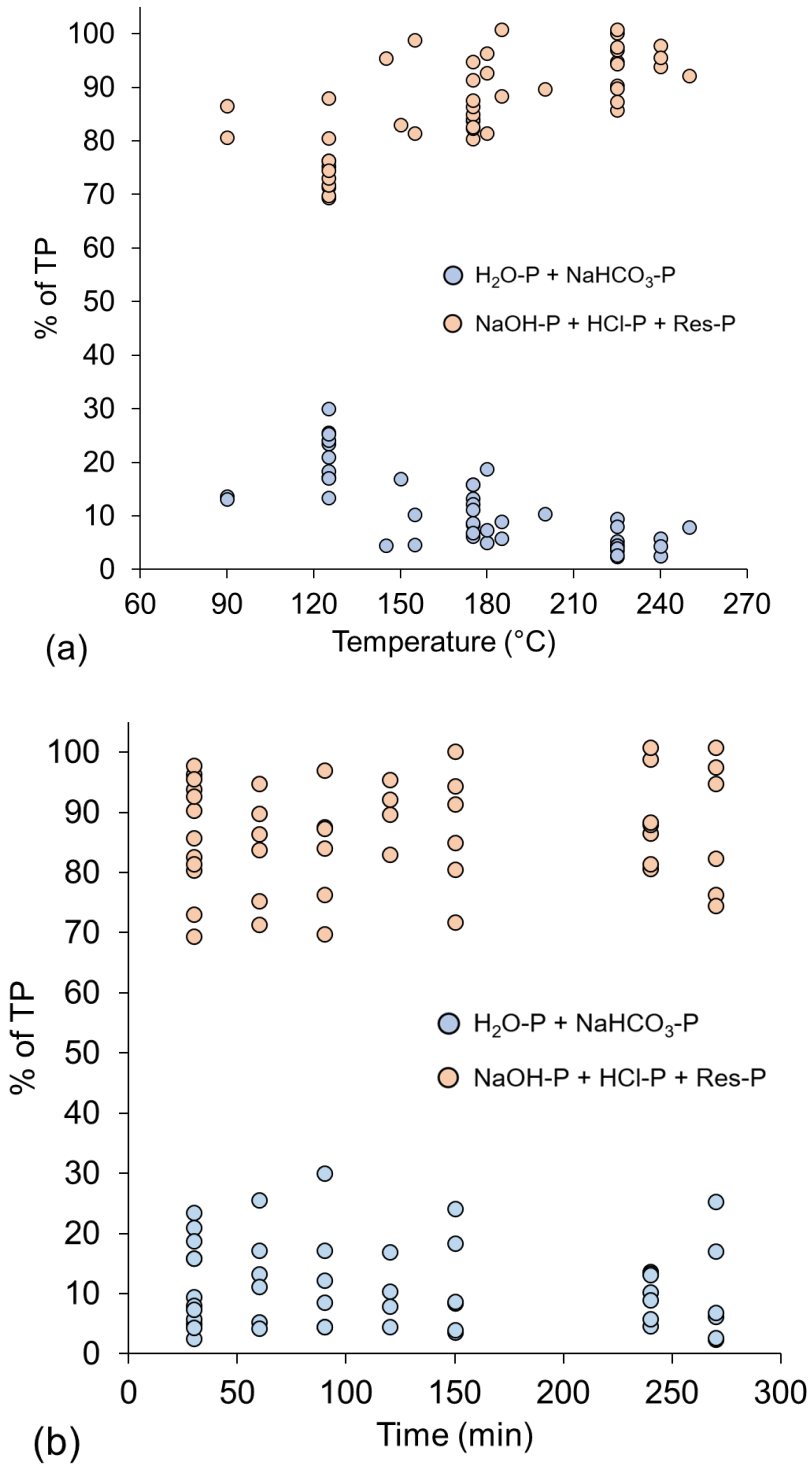

Figure A.7 - Sum of the H_2O- and $NaHCO_3$- extracted P fractions (blue points), and the NaOH-, HCl- and residual- P fractions (orange points) as a function of temperature(a) and treatment duration (b). Data from [62,82,106,109,122,124].

B. Ammonium molybdate-ascorbic acid method for orthophosphate concentration

12 mL of the chemical solution reacting with the liquid sample is prepared by adding the following chemical species in the following order:

- 4.8 mL of sulphuric acid (H_2SO_4) 9 mol L^{-1}
- 1.6 mL of ammonium heptamolybdate tetrahydrate ($(NH_4)_6Mo_7O_{24}$) 100g L^{-1}
- 1.6 mL of antimony potassium tartrate hemihydrate ($K(SbO)C_4H_4O_6 \cdot ½H_2O$) 3.5 g L^{-1}
- 4 mL of ascorbic acid ($C_6H_8O_6$) 100 g L^{-1}

Then, 0.3 mL of this solution are added to 4 mL of the liquid sample to be characterized. 0.3 mL of the solution are also added to 4 mL of deionized water to obtain a reference blank. A strong blue coloration will start to develop. After 10 to 30 min the absorbance at 880 nm of the reacted solution can be measured. To define a relationship between the absorbance and PO_4-P concentration, it is possible to build a calibration curve applying the ammonium molybdate-ascorbic acid method on various solution with known and progressively increasing concentrations of KH_2PO_4 (potassium dihydrogen phosphate) and then reading their absorbance at 880 nm. It is necessary to prepare KH_2PO_4 solution with a concentration under 1 mg L^{-1}. Under these conditions, the relation between PO_4-P concentration and absorbance at 880 nm is linear.

Five KH_2PO_4 solutions with progressively lower concentrations (1 mg L^{-1}, 0.5 mg L^{-1}, 0.25 mg L^{-1}, 0.125 mg L^{-1} and 0.0625 mg L^{-1}) were prepared to obtain the calibration curve. The respective absorbances at 880 nm, and the relative calibration curve was obtained by fitting the five experimental points with a linear trendline.

Using the trendline Equation it is possible to establish a linear relation between the PO_4-P concentration (C_P), measured in mg L^{-1}, and the absorbance at 880 nm (A), (Equation B.1):

$$A = k \cdot C \tag{B.1}$$

Where k is the slope of the trendline.

This method presents some limitations related to possible interferences. Suspended matter in the liquid sample can scatter the light passing through the cuvette. However, if the prepared samples are filtered (0.45 μm nylon filter), this problem can be avoided. Moreover, high silica concentrations can cause positive interferences and lead to a misleading reading. Between the chemical species that can cause interference there are iron (Fe), with a limit of 50 mg L^{-1}, copper (Cu) (max 10 mg L^{-1}), and SiO_2 (max 10 mg L^{-1}).

C. Methods for design of experiments

Alternatives to design of experiments approach are trial and error and one-factor-at-time method:

- Trial and error consists in testing different sets of selected factors, evaluating the effect on the response, adjusting the factors value accordingly and repeating until reaching the desired result.
- One-factor-at-time method consists in assessing the effect of all values for one factor, choosing the optimal value that most closely aligns the response with the desired result, fixing this factor to the optimal value, and then changing the focus on another factor, testing all its values to optimize the response.

Compared to these two methods, design of experiments approach is more effective, reducing the number of required experiments, effectively assessing the significance of possible interactions between factors and, more importantly, allowing to define a mathematical model to allow response prediction as a function of the selected factors.

Between the various possible design of experiments, factorial experimental designs are the simplest ones, consisting of testing all possible combinations. In symmetric full experimental design, all factors have the same number of levels (possible value that a factor can assume). In this case, as shown in Equation C.1, the number of required experiences n is equal to:

$$n = M^k \tag{C.1}$$

Where M is the number of levels and k is the number of factors.

This type of design of experiments can be used when the number of factors and levels is relatively low, because adding more factors or levels leads to an exponential growth of the sample size making the design of experiments generally too expensive to run.

Various design strategies can reduce the number of experiments needed to obtain a statistically significant model of the response, such as:

- Central composite design: includes three sets of experimental points: a standard factorial design with factors at high and low levels, additional points outside the experimental domain to test extreme values, and multiple repetitions at the central point.
- Box–Behnken design: This design combines factors at high and low levels while keeping the other factors at the central level, avoiding the extremes of the experimental domain and reducing the number of required experiments. Repetitions at the central point are included to evaluate experimental error.
- Optimal experimental design: this class of design of experiments are characterized by the optimality with respect to a specific statistical criterion. It allows to estimate a great number of parameters with fewer experiments, thus reducing the cost of the experimentation and minimizing variance. More

specifically, a D-optimal design maximizes the determinant of the information matrix of the design.

In the initial stages of experimentation, when it is not yet clear which factor has a significant effect on the response, a **screening** design is often implemented. This type of design of experiments focuses on finding the selected factors' main effects, testing their significance, but does not model the interactions between factors. This approach assesses the effects of a big number of factors by running a relatively small number of experiences.

In a 2^2 screening design, each of the two factors (x_1, x_2) can assume 2 different levels (levels A and B for factor x_1, and levels a and b for factor x_2) (Table C.1). This leads to four different combinations of factors that correspond to four experiments. The response of each experience is then used in a linear regression to obtain the coefficients of a simple linear model that describes the effect of each factor.

Table C.1 - Possible values assumed by the two factors (x_1, x_2) in a 2^2 screening DOE.

N°	Experimental plan		Model matrix		
	Factor		b_0	x_1	x_2
	x_1	x_2		b_1	b_2
1	A	a	1	-1	-1
2	A	b	1	-1	1
3	B	a	1	1	-1
4	B	b	1	1	1

The model obtained for the screening design of experiments is described by Equation C.2:

$$y = b_0 + b_1 x_1 + b_2 x_2 \quad \text{(C.2)}$$

Where b_0, b_1, b_2 are the coefficients of the linear model and x_1, x_2 are the variables representing the two factors x_1, x_2 when they assume one of the two possible values.

Another design of experiments approach is the **response surface design**, which allow to describe the relationship between response and factors in a polynomial regression model, generally second order, that includes linear, quadratic and interaction terms. The response surface design is realized to understand the local shape of the response when the factors assume the selected values and to find the optimal set of factors that maximize one or more responses.

A general form for a two factors second-degree polynomial surface response assumes the form described in Equation C.3:

$$y = b_0 + b_1 x_1 + b_2 x_2 + b_{1-1} x_1^2 + b_{2-2} x_2^2 + b_{1-2} x_1 x_2 \quad \text{(C.3)}$$

Where x_1, x_2 are the two factors, and b_0, b_1, b_2, $b_{1\text{-}1}$, $b_{2\text{-}2}$, $b_{1\text{-}2}$ are the coefficients of the linear model, with b_0, b_1, b_2 being the linear terms, $b_{1\text{-}1}$, $b_{2\text{-}2}$ the quadratic terms, and $b_{1\text{-}2}$ the interaction term.

Lastly it is necessary to evaluate the statistical significance of obtained results and to assess the model relevance. Various approaches exist for this step, but a popular choice consists in the ANOVA (ANalysis Of Variance) tool. A generalized form of the ANOVA table is shown in Table C.2:

Table C.2 - ANOVA table.

Source of variation	Sum of squares	Degrees of freedom	Mean square	F test	P-value
Regression	SSB	m -1	MSB = $\frac{SSB}{m-1}$	$\frac{MSB}{MSW}$	p
Residual	SSW	n - m	MSW = $\frac{SSW}{n-m}$		
Total	SST	n - 1			

Each table row expresses a different source of variation. First row corresponds to the variability due to the factor(s) of interest, which corresponds to the error related to the model itself. Second row corresponds to the variability that cannot be explained by the model, also indicated as residual or error variation. Finally, the third row describes total variation in data, and it is the combination of the two previous sources of variation.

First column contains sum of squares terms:

- SSB is defined as the sum of the squares of the difference between the model's estimated responses and the average of the measured responses, according to Equation C.4:

$$SSB = \sum_{i=1}^{n} (\hat{y}_i - \overline{y})^2 \tag{C.4}$$

- SSW is defined as the sum of the squares of the difference between the measured responses and the model's estimated responses, as shown in Equation C.5:

$$SSW = \sum_{i=1}^{n} (y_i - \hat{y}_i)^2 \tag{C.5}$$

- SST is the sum of the previous two terms, corresponding to the sum of the squares of the difference between the measured responses and their average (Equation C.6):

$$SST = \sum_{i=1}^{n} (y_i - \overline{y})^2 \tag{C.6}$$

Second column lists the degrees of freedom associated with each variation effect. The degrees of freedom associated with the regression variation is equal to m – 1, where m is the number of groups of the model (which corresponds to the number of coefficients). The degrees of freedom of residuals corresponds to n – m, where n is the number of experiences. Total degrees of freedom correspond to the total number of experiments – 1.

Third column lists mean squares, calculated dividing the respective sum of squares by the corresponding degrees of freedom, as indicated in Equations C.7 and C.8:

$$MSB = \frac{SSB}{m-1} \tag{C.7}$$

$$MSW = \frac{SSW}{n-m} \tag{C.8}$$

F-test (Fisher-Snedecor test) in column four allow to compare the two mean squares values defined above (Equation C.9):

$$f = \frac{MSB}{MSW} \tag{C.9}$$

This value is then compared to a critical value $f_{crit} = f(\alpha,m-1,n-m)$ obtained in a Fisher-Snedecor table, where α is the significance level, generally set at 0.05[251].

If $f > f_{crit}$ at $\alpha = 0.05$, or, in other words, if $p > 0.05$, the model is valid, and the regression significantly describes the measured response.

Finally, the global variation related to the model can be quantified using the determination coefficient R^2, as indicated in Equation C.10:

$$R^2 = \frac{SSB}{SST} = 1 - \frac{SSW}{SST} \tag{C.10}$$

A final validation test allows to check the significance of each coefficient of the model. To do so, the Student t-test is generally implemented[162].

For each coefficient effect β_i, the standard error $SE(\beta_i)$ is calculated, which measures the uncertainty of the coefficient estimation. The coefficient and its standard error are then compared using the t-statistic (Equation C.11):

$$t = \frac{\beta_i}{SE(\beta_i)} \tag{C.11}$$

Finally, knowing the degrees of freedom of the model (n-m), the t-distribution (Student's table) is used to find the p-value corresponding to the calculated t-statistic. If the p-value is lower than the significance level α (0.05), then the coefficient can be considered statistically significant.

In order to study more responses at the same time, it is possible to use the desirability function approach, that allows to optimize a process by maximizing or minimizing a set of

responses. To each response $Y_i(x)$ corresponds a desirability function $d_i(x)$ which can assume a value between 0 and 1, where 0 represents an unacceptable value and 1 is the ideal value. Global desirability is defined as the geometric mean of the individual desirabilities, as described is Equation C.12:

$$D = \left(\prod_{i=1}^{k} d_i\right)^{\frac{1}{k}} = (d_1 \cdot d_2 \cdot d_3 \cdot \ldots \cdot d_k)^{\frac{1}{k}} \qquad \text{(C.12)}$$

When the purpose is to maximize an individual response $Y_i(x)$ to a target value T_i, with a minimum acceptable value L_i, the related individual desirability $d_i(Y_i)$ is defined as indicated in Equation C.13:

$$d_i(Y_i) = \begin{cases} 0 & if\ Y_i(x) < L_i \\ \left(\dfrac{Y_i(x) - L_i}{T_i - L_i}\right) & if\ L_i \leq Y_i(x) \leq T_i \\ 1 & if\ Y_i(x) > T_i \end{cases} \qquad \text{(C.13)}$$

When the purpose is to minimize an individual response $Y_i(x)$ to a target value T_i, with a maximum acceptable value U_i, the related individual desirability $d_i(Y_i)$ is defined as indicated in Equation C.14:

$$d_i(Y_i) = \begin{cases} 0 & if\ Y_i(x) > U_i \\ \left(\dfrac{Y_i(x) - U_i}{T_i - U_i}\right) & if\ T_i \leq Y_i(x) \leq U_i \\ 1 & if\ Y_i(x) < T_i \end{cases} \qquad \text{(C.14)}$$

When only one individual desirability is equal to 0, global desirability is equal to 0. The global desirability is equal to 1 only if all individual desirabilities are equal to 1.

D. Statistical validation of experimental design models

Table D.1 - ANalysis Of VAriation (ANOVA) validation table for TSRY% second-degree polynomial surface response shown in Figure 4.4.

Source of variation	Sum of squares (SS)	Degrees of freedom	Mean square	F test	P-value (%)
Regression	2624.4	5	524.88	82.84	0.00***
Residual	76.04	12	0.5		
Total	2700.46	17			

Response's standard deviation	2.52
R^2	0.972
R^2A	0.960
Degrees of freedom	12

Table D.2 - Second-degree polynomial model coefficients for the TSRY% surface response shown in Figure 4.4.

Coefficients		Standard deviation	t-statistic	p-value (%)
b_0	56.54	1.7	33.34	
b_1	-14.43	0.74	-19.49	0***
b_2	-3.11	0.73	-4.28	0.11**
$b_{1\text{-}1}$	-0.44	1.26	0.35	73.25
$b_{2\text{-}2}$	2.8	1.75	1.6	13.48
$b_{1\text{-}2}$	0.11	0.86	0.13	89.92

Table D.3 - ANalysis Of VAriation (ANOVA) validation table for the second-degree polynomial surface response of soluble Fe concentration (mg L^{-1}) shown in Figure 4.10. Polynomial surface response models the base-10 logarithm of the soluble Fe concentration.

Source of variation	Sum of squares (SS)	Degrees of freedom	Mean square	F test	P-value (%)
Regression	5.713	5	1.143	260.6	0.00***
Residual	0.045	12	0.004		
Total	5.766	17			

Response's standard deviation	0.066
R^2	0.991
R^2A	0.987
Degrees of freedom	12

Table D.4 - Second-degree polynomial model coefficients for the surface response of the soluble Fe concentration (mg L^{-1}) in process water shown in Figure 4.10.

Coefficients		Standard deviation	t-statistic	p-value (%)
b_0	0.629	0.045	14.10	
b_1	-0.654	0.019	-33.58	0.00***
b_2	-0.182	0.019	-9.535	0.00***
$b_{1\text{-}1}$	0.011	0.033	0.337	74.17
$b_{2\text{-}2}$	0.053	0.046	1.162	26.78
$b_{1\text{-}2}$	0.055	0.022	2.433	3.16*

Table D.5 - ANalysis Of VAriation (ANOVA) validation table for process water P concentration (mg L^{-1}) second-degree polynomial surface response shown in Figure 4.21.

Source of variation	Sum of squares (SS)	Degrees of freedom	Mean square	F test	P-value (%)		Response's standard deviation	27.51
Regression	466402	5	93280	123.22	0.00***		**R^2**	0.981
Residual	9084.4	12	757.03				**R^2A**	0.973
Total	475486.5	17					**Degrees of freedom**	12

Table D.6 - Second-degree polynomial model coefficients for process water P concentration (mg L^{-1}) surface response shown in Figure 4.21.

Coefficients		standard deviation	t-statistic	p-value (%)
b_0	483.32	18.53	26.08	
b_1	-188.35	8.09	-2327	0.00***
b_2	-25.12	7.94	-3.16	0.82**
$b_{1\text{-}1}$	-108.09	13.76	-7.86	0.00***
$b_{2\text{-}2}$	-0.54	19.09	-0.03	97.8
$b_{1\text{-}2}$	-28.95	9.35	-3.1	0.92**

Table D.7 - Analysis Of Variation (ANOVA) validation table for P recovery yield in solid pellet (%) second-degree polynomial surface response shown in Figure 4.22.

Source of variation	Sum of squares (SS)	Degrees of freedom	Mean square	F test	P-value (%)		Response's standard deviation	0.98
Regression	689.97	5	137.99	142.78	0.00***		R^2	0.983
Residual	11.6	12	0.97				R^2A	0.977
Total	701.56	17					Degrees of freedom	12

Table D.8 - Second-degree polynomial model coefficients for P recovery yield in solid pellet (%) surface response shown in Figure 4.22.

Coefficients		standard deviation	t-statistic	p-value (%)
b_0	80.7	0.66	121.87	
b_1	7.17	0.29	24.8	0.00***
b_2	0.96	0.28	3.51	0.43**
$b_{1\text{-}1}$	4.51	0.49	9.18	0.00***
$b_{2\text{-}2}$	-0.12	0.68	-0.18	85.84
$b_{1\text{-}2}$	1.15	0.33	3.44	0.49**

Table D.9 - ANalysis Of VAriation (ANOVA) validation table for AIP in solid pellet (% TP) second-degree polynomial surface response shown in Figure 4.23.

Source of variation	Sum of squares (SS)	Degrees of freedom	Mean square	F test	P-value (%)	Response's standard deviation	1.732
Regression	592.55	5	118.51	39.5	0.61**	R^2	0.985
Residual	9	3	3			R^2A	0.960
Total	601.55	8				Degrees of freedom	3

Table D.10 - Second-degree polynomial model coefficients for AIP in solid pellet (% TP) surface response shown in Figure 4.23.

Coefficients		standard deviation	t-statistic	p-value (%)
b_0	57.67	1.29	44.47	
b_1	8.22	0.71	11.63	0.14**
b_2	0.57	0.71	0.81	47.58
$b_{1\text{-}1}$	9.46	1.22	7.72	0.45**
$b_{2\text{-}2}$	0.23	1.22	0.19	86.26
$b_{1\text{-}2}$	1.22	0.87	1.41	25.26

Table D.11 - ANalysis Of VAriation (ANOVA) validation table for bio-oil yield (% dry feed) second-degree polynomial surface response shown in Figure 6.5.

Source of variation	Sum of squares (SS)	Degrees of freedom	Mean square	F test	P-value (%)
Regression	108.58	9	12.06	32.95	0.00***
Residual	11.86	8	1.48		
Total	120.44	17			

Response's standard deviation	0.605
R^2	0.901
R^2A	0.791
Degrees of freedom	4

Table D.12 - Second-degree polynomial model coefficients for the bio-oil yield (% dry feed) surface response shown in Figure 6.5.

Coefficients		Standard deviation	t-statistic	p-value (%)
b_0	7.46	0.378	19.74	
b_1	1.51	0.200	7.52	0.17**
b_2	1.37	0.206	6.65	0.27**
b_3	- 0.81	0.207	- 3.91	1.75*
$b_{1\text{-}1}$	1.17	0.337	3.48	2.52*
$b_{2\text{-}2}$	- 0.41	0.490	- 0.84	44.68
$b_{3\text{-}3}$	0.91	0.353	2.56	6.24
$b_{1\text{-}2}$	1.61	0.230	7.02	0.22**
$b_{1\text{-}3}$	- 1.01	0.232	- 4.35	1.22*
$b_{2\text{-}3}$	- 1.14	0.236	- 4.86	0.83**

Table D.13 - ANalysis Of VAriation (ANOVA) validation table for process water soluble P second-degree polynomial surface response shown in Figure 6.9.

Source of variation	Sum of squares (SS)	Degrees of freedom	Mean square	F test	P-value (%)
Regression	7.170	9	0.797	72.546	0.00***
Residual	0.088	8	0.011		
Total	7.258	17			

Response's standard deviation	0.105
R^2	0.99
R^2A	0.97
Degrees of freedom	8

Table D.14 - Second-degree polynomial model coefficients for the process water soluble P surface response shown in Figure 6.9.

Coefficients		Standard deviation	t-statistic	p-value (%)
b_0	1.42	0.07	21.69	
b_1	-0.26	0.03	-7.43	0.00***
b_2	-0.12	0.04	-3.43	0.89**
b_3	-0.63	0.04	-17.52	0.00***
$b_{1\text{-}1}$	-0.23	0.06	-3.97	0.41**
$b_{2\text{-}2}$	0.07	0.08	0.85	41.93
$b_{3\text{-}3}$	0.54	0.06	8.76	0.00***
$b_{1\text{-}2}$	0.005	0.04	0.13	90.31
$b_{1\text{-}3}$	0.255	0.04	6.36	0.00***
$b_{2\text{-}3}$	0.03	0.04	0.69	51.03

Table D.15 - Second-degree model statistical validation of the response surface obtained for Ca, Fe, Mg and K concentration (mg L^{-1}) in process water. Ca, Fe and Mg model has been obtained by feeding the experimental matrix with the 10-logarithm of concentration results, to prevent the model from returning negative concentration values.

	Ca	Fe	Mg	K
Model p-value (%)	0.00***	0.00***	0.00***	0.01***
Model standard deviation	0.077	0.083	0.032	8.22
R^2	0.99	0.98	0.97	0.82
R^2A	0.97	0.96	0.94	0.63

Table D.16 - ANalysis Of VAriation (ANOVA) validation table for P yield in process water (%) second-degree polynomial surface response shown in Figure 6.11.

Source of variation	Sum of squares (SS)	Degrees of freedom	Mean square	F test	P-value (%)
Regression	7.36	9	0.818	81.98	0.00***
Residual	0.08	8	0.010		
Total	7.44	17			

Response's standard deviation	0.0999
R^2	0.989
R^2A	0.977
Degrees of freedom	8

Table D.17 - Second-degree polynomial model coefficients for P yield in process water (%) surface response shown in Figure 6.11.

Coefficients		Standard deviation	t-statistic	p-value (%)
b_0	-0.62	0.06	-10.04	
b_1	-0.22	0.03	-6.63	0.00***
b_2	-0.12	0.03	-3.40	0.94**
b_3	-0.66	0.04	-19.33	0.00***
$b_{1\text{-}1}$	-0.24	0.06	-4.31	0.26**
$b_{2\text{-}2}$	0.06	0.08	0.74	48.21
$b_{3\text{-}3}$	0.53	0.06	9.15	0.00***
$b_{1\text{-}2}$	0.004	0.04	0.10	92.55
$b_{1\text{-}3}$	0.25	0.04	6.48	0.00***
$b_{2\text{-}3}$	0.03	0.04	0.67	52.21

Table D.18 - ANalysis Of VAriation (ANOVA) validation table for AIP (%TP) second-degree polynomial surface response shown in Figure 6.15.

Source of variation	**Sum of squares (SS)**	**Degrees of freedom**	**Mean square**	**F test**	**P-value (%)**		**Response's standard deviation**	5.020
Regression	4664.8	9	518.3	20.6	0.01***		**R^2**	0.959
Residual	201.6	8	25.2				**R^2A**	0.912
Total	4866.4	17					**Degrees of freedom**	8

Table D.19 - Second-degree polynomial model coefficients for the AIP (%TP) surface response shown in Figure 6.15.

Coefficients		**Standard deviation**	**t-statistic**	**p-value (%)**
b_0	76.6	3.14	24.4	
b_1	9.68	1.66	5.83	0.00***
b_2	3.91	1.71	2.28	5.16
b_3	14.8	1.72	8.64	0.00***
$b_{1\text{-}1}$	3.27	2.80	1.17	27.52
$b_{2\text{-}2}$	2.38	4.06	0.59	57.45
$b_{3\text{-}3}$	-7.32	2.93	-2.50	3.69*
$b_{1\text{-}2}$	-2.80	1.91	-1.47	17.97
$b_{1\text{-}3}$	-4.49	1.92	-2.33	4.78*
$b_{2\text{-}3}$	-2.64	1.96	-1.35	21.37

Table D.20 –ANalysis Of VAriation (ANOVA) validation table for screening analysis results on by products distribution and mass balances in Table 4.1.

Response	Regression squares sum	Residuals squares sum	Regression mean square	Residuals mean square	f-test	p-value %	Response standard deviation	R^2	R^2A	degrees of freedom
Losses + gas	5.234	4.362	1.309	0.336	3.9	2.70*	0.579	0.545	0.406	13
Process water by-product (% total product)	123.439	3.63	30.86	0.279	110.502	0.00***	0.528	0.971	0.963	13
Solid pellet by-product (% total product)	123.439	3.63	30.86	0.279	110.502	0.00***	0.528	0.971	0.963	13
Process water TDS (%)	6.753	0.029	1.688	0.002	4782.025	0.00***	0.019	0.996	0.994	9
Solid pellet by-product dry mass (%)	731.952	36.977	182.989	2.844	64.333	0.00***	1.687	0.952	0.937	13
TSRY (%)	2624.316	76.144	656.079	5.857	112.012	0.00***	2.42	0.972	0.963	13
C losses (% feed C)	636.159	11.02	159.04	2.755	57.729	0.09***	1.66	0.983	0.966	4
P losses (% feed P)	437.711	49.334	109.428	12.333	8.872	2.87*	3.512	0.899	0.797	4
Ca losses (% feed Ca)	487.841	26.745	121.96	6.686	18.24	0.78**	2.586	0.948	0.896	4
Fe losses (% feed Fe)	359.164	31.118	89.791	7.78	11.542	1.81*	2.789	0.92	0.841	4
K losses (% feed K)	113.445	13.29	28.361	3.322	8.536	3.07*	1.823	0.895	0.79	4

Table D.21 –ANalysis Of VAriation (ANOVA) validation table for screening analysis results on process water properties in Table 4.2.

Response	Regression squares sum	Residuals squares sum	Regression mean square	Residuals mean square	f-test	p-value %	Response standard deviation	R^2	R^2A	degrees of freedom
pH	0.391	0.1	0.098	0.008	12.776	0.02***	0.088	0.797	0.735	13
alkalinity (g $CaCO_3$ L^{-1})	116.736	1.594	29.184	0.123	238.059	0.00***	0.35	0.987	0.982	13
NH_3-N (g L^{-1})	3.972	0.247	0.993	0.019	52.233	0.00***	0.138	0.941	0.923	13
COD (g L^{-1})	284.9	46.908	71.225	3.608	19.739	0.00***	1.9	0.859	0.815	13
TC (g L^{-1})	24.774	1.639	6.193	0.126	49.125	0.00***	0.355	0.938	0.919	13
TOC (g L^{-1})	42.403	2.206	10.601	0.17	62.457	0.00***	0.412	0.951	0.935	13
TIC (g L^{-1})	2.404	0.163	0.601	0.013	47.887	0.00***	0.112	0.936	0.917	13
Ca (mg L^{-1})	64.13	98.088	16.033	7.545	4.902	1.24*	1.808	0.395	0.209	9
Fe (mg L^{-1})[a]	5.684	0.079	1.421	0.006	233.41	0.00***	0.078	0.986	0.982	13
Mg (mg L^{-1})	1243.025	1265.888	310.756	97.376	3.191	4.95*	9.868	0.495	0.34	13
K (mg L^{-1})	20764.232	1581.35	5171.058	121.642	42.675	0.00***	11.029	0.929	0.907	13

Table D.22 –ANalysis Of VAriation (ANOVA) validation table for Screening analysis results on solid by-product ultimate analysis in Table 4.3.

Response	Regression squares sum	Residuals squares sum	Regression mean square	Residuals mean square	f-test	p-value %	Response standard deviation	R^2	R^2A	degrees of freedom
Ash content (% dry mass)	84.338	2.659	21.085	0.665	31.716	0.27**	0.815	0.969	0.939	4
Nitrogen (N) (% DM)	0.666	0.033	0.167	0.008	19.994	0.66**	0.091	0.952	0.905	4
Hydrogen (H) (% DM)	0.562	0.031	0.14	0.008	18.334	0.77**	0.088	0.948	0.897	4
Sulfur (S) (% DM)	0.097	0.007	0.024	0.002	14.013	1.27*	0.042	0.933	0.867	4
Oxygen (O) (% DM)	49.487	1.023	12.372	0.256	48.352	0.12**	0.506	0.98	0.959	4
O/C molar ratio	0.018	0.001	0.005	0.0002	28.114	0.35**	0.013	0.966	0.931	4
H/C molar ratio	0.036	0.001	0.009	0.0003	27.05	0.37**	0.018	0.964	0.929	4

Table D.23 –ANalysis Of VAriation (ANOVA) validation table for Screening analysis results on metals and heavy metals contents in solid pellet (expressed on a dry basis) in Table 4.5.

Response	Regression squares sum	Residuals squares sum	Regression mean square	Residuals mean square	f-test	p-value %	Response standard deviation	R^2	R^2A	degrees of freedom
Calcium (Ca) (mg g^{-1})	165.165	31.844	41.291	2.45	16.857	0.00***	1.565	0.838	0.789	13
Iron (Fe) (mg g^{-1})	87.668	79.183	21.917	6.091	3.598	3.47*	2.468	0.525	0.379	13
Aluminum (Al) (mg g^{-1})	19.034	6.093	4.758	0.469	10.152	0.06***	0.685	0.758	0.683	13
Magnesium (Mg) (mg g^{-1})	77.114	10.881	19.279	0.837	43.724	0.00***	0.664	0.876	0.838	9
Potassium (K) (mg g^{-1})	16.541	4.52	4.135	0.348	11.894	0.03***	0.59	0.785	0.719	13
Copper (Cu) (mg g^{-1})	45054.684	10699.194	11263.671	823.015	13.686	0.01***	28.688	0.808	0.749	13
Zinc (Zn) (mg g^{-1})	65453.077	32172.825	16363.269	2474.833	6.612	0.39**	49.748	0.67	0.569	13
Mercury (Hg) (mg kg^{-1})	0.014	0.009	0.003	0.0007	10.45	0.05***	0.018	0.611	0.491	9
Vanadium (V) (mg kg^{-1})	119.034	55.404	29.759	4.262	6.983	0.31**	2.064	0.682	0.585	13
Chrome (Cr) (mg kg^{-1})	1832.707	839.278	458.177	64.56	7.097	0.29**	8.035	0.686	0.589	13
Nickel (Ni) (mg kg^{-1})	1862.584	204.22	465.646	15.709	29.642	0.00***	3.963	0.901	0.871	13
Arsenic (As) (mg kg^{-1})	21.621	0.483	5.405	0.037	145.489	0.00***	0.193	0.978	0.971	13
Silver (Ag) (mg kg^{-1})	140.033	4.502	35.008	0.346	273.111	0.00***	0.358	0.969	0.959	9
Cadmium (Cd) (mg kg^{-1})	0.161	0.127	0.04	0.01	4.133	2.24*	0.099	0.56	0.424	13

Table D.24 –ANalysis Of VAriation (ANOVA) validation table for screening analysis results on P distribution and speciation in Table 4.6.

Response	Regression squares sum	Residuals squares sum	Regression mean square	Residuals mean square	f-test	p-value %	Response standard deviation	R^2	R^2A	degrees of freedom
Soluble P in process water (mg P L^{-1})	459141.104	16345.411	114785.276	1257.339	240.569	0.00***	21.844	0.966	0.955	9
PO_4-P in process water (mg P L^{-1})	454290.79	17203.29	113572.697	1323.33	196.557	0.00***	24.038	0.964	0.952	9
TP in pellet (AR extraction + ICP)(mg P g^{-1})	878.438	41.428	219.609	3.187	68.713	0.00***	1.785	0.955	0.941	13
TP in pellet (SMT) (mg P g^{-1})	451.111	9.4	112.778	2.35	47.99	0.12**	1.533	0.98	0.959	4
NAIP in pellet (mg P g^{-1})	123.441	10.839	30.86	2.71	11.388	1.85*	1.646	0.919	0.839	4
NAIP in pellet (% TP)	660.543	22.291	165.136	5.573	29.633	0.31**	2.361	0.967	0.935	4
AIP in pellet (mg P g^{-1})	857.159	16.521	214.29	4.13	51.883	0.11**	2.032	0.981	0.962	4
AIP in pellet (% TP)	586.566	14.987	146.641	3.747	39.139	0.18**	1.935	0.975	0.95	4

Table D.25 –ANalysis Of VAriation (ANOVA) validation table for screening analysis on by products distribution and mass balance results in Table 6.1.

Response	Regression squares sum	Residuals squares sum	Regression mean square	Residuals mean square	f-test	p-value %	Response standard deviation	R^2	R^2A	degrees of freedom
Process water (% total product)	732.75	32.043	122.125	2.913	465.441	0.00***	0.512	0.958	0.935	4
Solid pellet (% total product)	732.75	32.043	122.125	2.913	465.441	0.00***	0.512	0.958	0.935	4
Bio-oil yield (% dry feed)	84.102	36.34	14.017	3.304	38.282	0.00***	0.605	0.698	0.534	4
Process water TDS (%)	41.633	0.73	6.939	0.066	1587.411	0.00***	0.066	0.983	0.973	4
Solid pellet dry mass (%)	2246.885	539.538	374.481	49.049	62.861	0.00***	2.441	0.806	0.701	4
TSRY (%)	747.957	174.486	124.66	15.862	7.859	0.18**	3.983	0.811	0.708	11

Table D.26 –ANalysis Of VAriation (ANOVA) validation table for screening analysis on process water characteristics results in Table 6.2.

Response	Regression squares sum	Residuals squares sum	Regression mean square	Residuals mean square	f-test	p-value %	Response standard deviation	R^2	R^2A	degrees of freedom
pH	0.682	1.145	0.114	0.013	8.617	0.12**	0.115	0.825	0.729	11
alkalinity (g CaCO3 L^{-1})	729.62	7.922	121.603	0.72	168.843	0.00***	0.849	0.989	0.983	11
NH_4-N (g L^{-1})	38.844	1.041	6.474	0.095	68.385	0.00***	0.308	0.974	0.96	11
COD (g L^{-1})	2473.982	50.195	412.33	4.563	90.361	0.00***	2.136	0.98	0.969	11
TC (g L^{-1})	212.283	7.662	35.381	0.697	50.795	0.00***	0.835	0.965	0.946	11
TOC (g L^{-1})	307.162	11.901	51.194	1.082	47.316	0.00***	1.04	0.963	0.942	11
TIC (g L^{-1})	10.484	2.997	1.747	0.272	6.413	0.41**	0.522	0.778	0.656	11

Table D.27 –ANalysis Of VAriation (ANOVA) validation table for screening analysis on process water composition results in Table 6.3.

Response	Regression squares sum	Residuals squares sum	Regression mean square	Residuals mean square	f-test	p-value %	Response standard deviation	R^2	R^2A	degrees of freedom
P (mg L^{-1})[a]	6.711	0.547	1.119	0.05	199.297	0.00***	0.075	0.925	0.884	4
Ca (mg L^{-1})[a]	3.021	0.43	0.504	0.039	59.713	0.00***	0.092	0.875	0.808	4
Fe (mg L^{-1})[a]	3.008	0.104	0.501	0.009	53.075	0.00***	0.097	0.967	0.948	11
Mg (mg L^{-1})[a]	8.707	0.504	1.451	0.046	1452.27	0.00***	0.032	0.945	0.915	4
K (mg L^{-1})	12822.238	4408.459	2137.04	400.769	31.656	0.00***	8.216	0.744	0.605	4
P (% feed P)[a]	6.926	0.512	1.154	0.047	236.179	0.00***	0.07	0.931	0.894	4
Ca (% feed Ca)[a]	1.878	0.449	0.313	0.041	36.149	0.00***	0.093	0.807	0.702	4
Fe (% feed Fe)[a]	2.575	0.105	0.429	0.01	45.053	0.00***	0.098	0.961	0.94	11
Mg (% feed Mg)[a]	8.291	0.527	1.382	0.048	1841.107	0.00***	0.027	0.94	0.908	4

Table D.28 –ANalysis Of VAriation (ANOVA) validation table for screening analysis on solid pellet by-products results in Table 6.4.

Response	Regression squares sum	Residuals squares sum	Regression mean square	Residuals mean square	f-test	p-value %	Response standard deviation	R^2	R^2A	degrees of freedom
P (mg g^{-1})	490.33	54.109	81.722	4.919	16.614	0.01***	2.218	0.901	0.846	11
NAIP (% TP)	4839.571	480.087	806.595	43.644	128.949	0.00***	2.501	0.91	0.861	4
AIP (%TP)	4367.043	499.341	727.84	45.395	16.034	0.01***	6.738	0.897	0.841	11
Ca (mg g^{-1})	13837.188	226.736	2306.198	20.612	111.884	0.00***	4.54	0.984	0.975	11
Fe (mg g^{-1})	612.001	70.773	102	6.434	15.853	0.01***	2.537	0.896	0.84	11
Al (mg g^{-1})	8.058	0.987	1.343	0.09	14.972	0.01***	0.3	0.891	0.831	11
Mg (mg g^{-1})	33.721	4.64	5.62	0.422	13.324	0.02***	0.649	0.879	0.813	11
Cu (mg g^{-1})	59166.36	6686.249	9861.06	607.841	16.223	0.01***	24.654	0.898	0.843	11
Zn (mg g^{-1})	88135.392	13851.658	14689.232	1259.242	11.665	0.03***	35.486	0.864	0.79	11
Pb (mg g^{-1})	1578.427	680.576	263.071	61.871	4.252	1.85*	7.866	0.699	0.534	11
V (mg g^{-1})	141.022	42.575	23.504	3.87	6.073	0.51**	1.967	0.768	0.642	11
Cr (mg g^{-1})	407.064	51.719	67.844	5.747	11.806	0.08***	2.397	0.887	0.812	9
Ni (mg g^{-1})	259.416	44.407	43.236	4.934	8.763	0.24**	2.221	0.854	0.756	9
As (mg g^{-1})	6.932	1.887	1.155	0.21	98.602	0.00***	0.108	0.786	0.643	4
Cd (mg g^{-1})	0.169	0.055	0.028	0.005	5.685	0.65**	0.07	0.756	0.623	11

E. Supplementary figures: phosphorus quantification and speciation

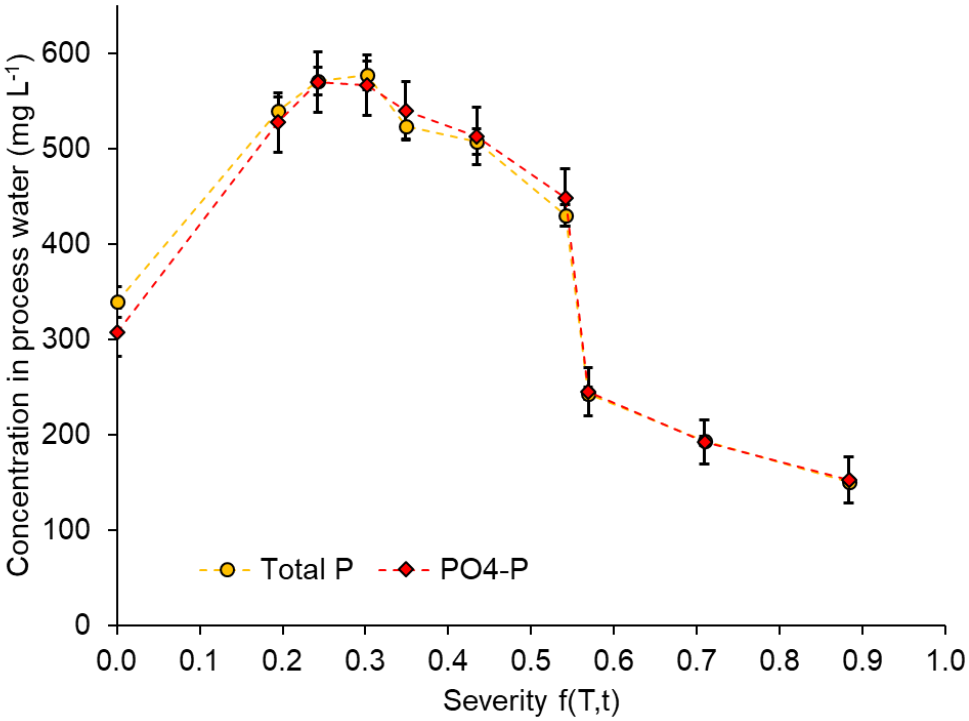

Figure E.1 - Comparison between TP concentration in process water, obtained by ICP-AES spectroscopy (Section 2.3.8), with PO_4-P concentration, measured by ammonium molybdate-ascorbic acid method and UV-vis spectroscopy (EN 6878, 2004) (Section 2.3.7). Error bars represent propagated uncertainty. Dashed lines are included to help data interpretation.

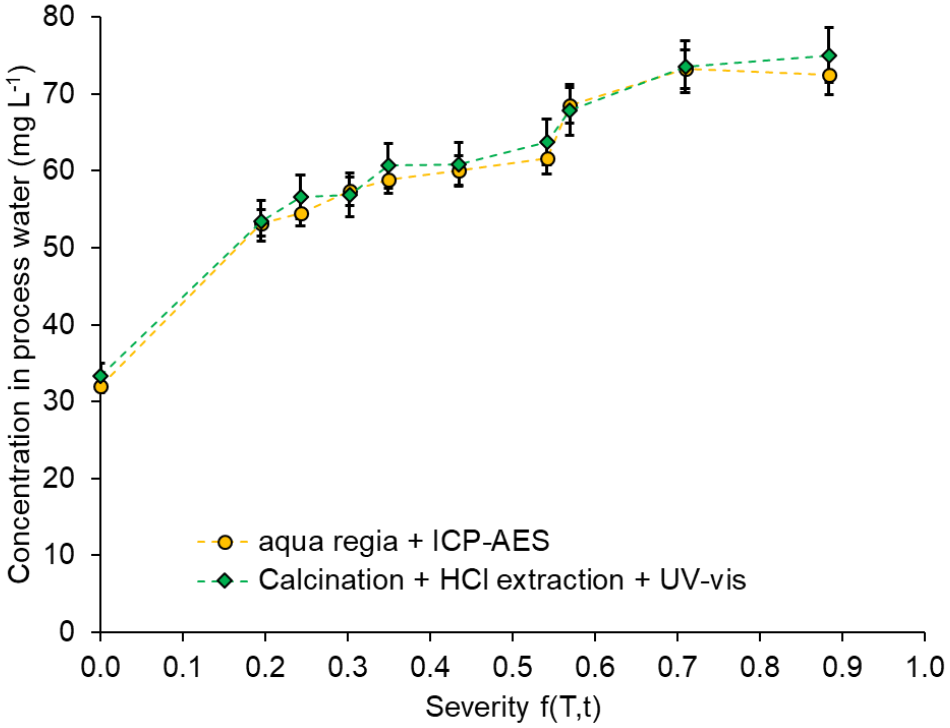

Figure E.2 - Comparison between TP content in solid pellet obtained Aqua Regia digestion and ICP-AES Spectroscopy (EN ISO 13346, 2000), the same methods used to quantify metal and heavy metal species (Section 2.4.3 and 2.4.4). Calcination + HCl extraction technique proposed by the SMT method[74] (Section 2.4.6.1). TP content expressed on a dry basis. Error bars represent propagated uncertainty. Dashed lines are included to help data interpretation.

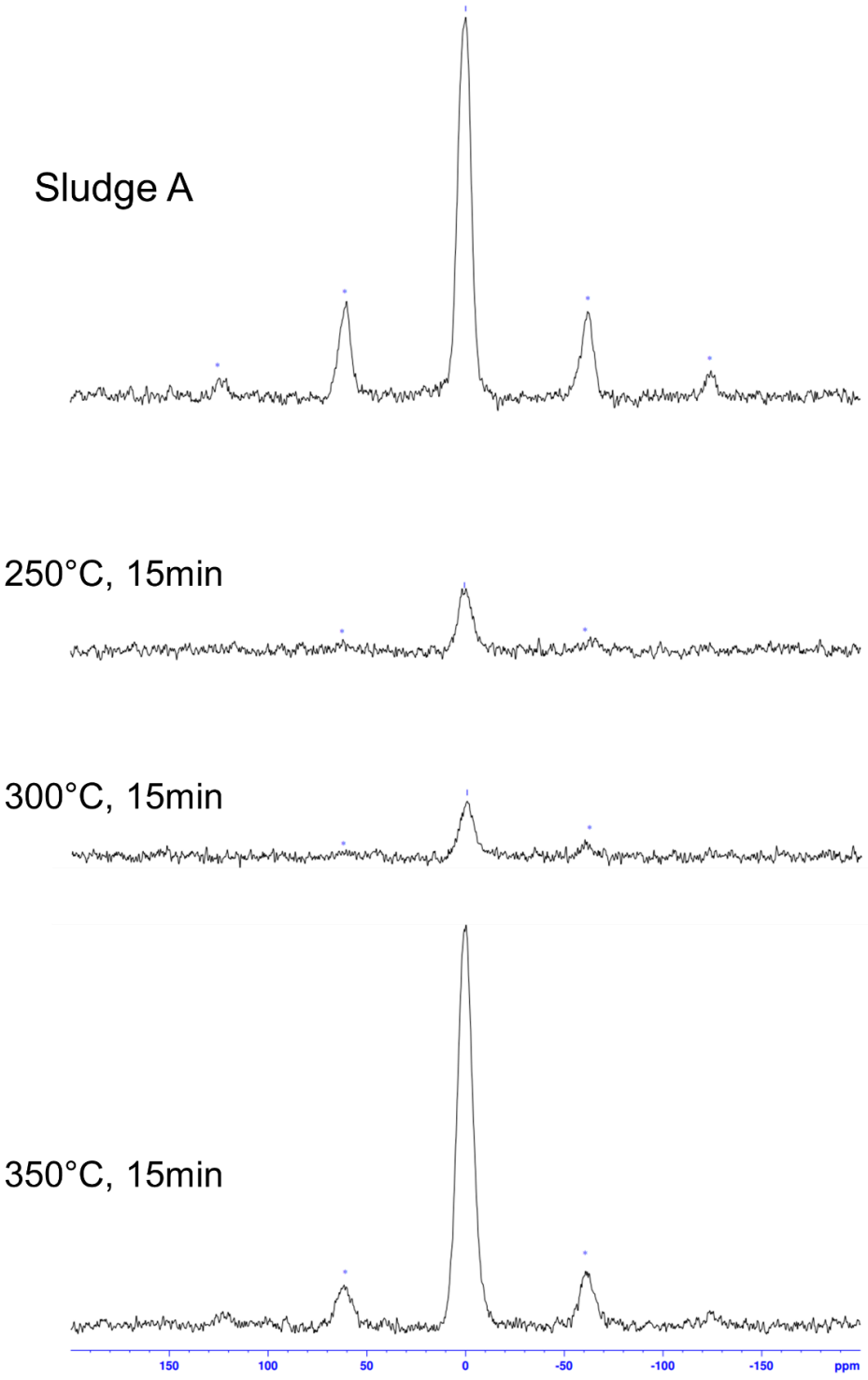

Figure E.3 - ^{31}P solid state NMR analysis results for Sludge A and hydrothermal solid pellet by-product obtained respectively at 250°C, 300°C and 350°C for a 15-minutes treatment. Peaks at ± 60 ppm and ± 120 ppm are related to spinning side bands from paramagnetic effects caused by Fe[252].

F. Supplementary elements for thermal profile investigation

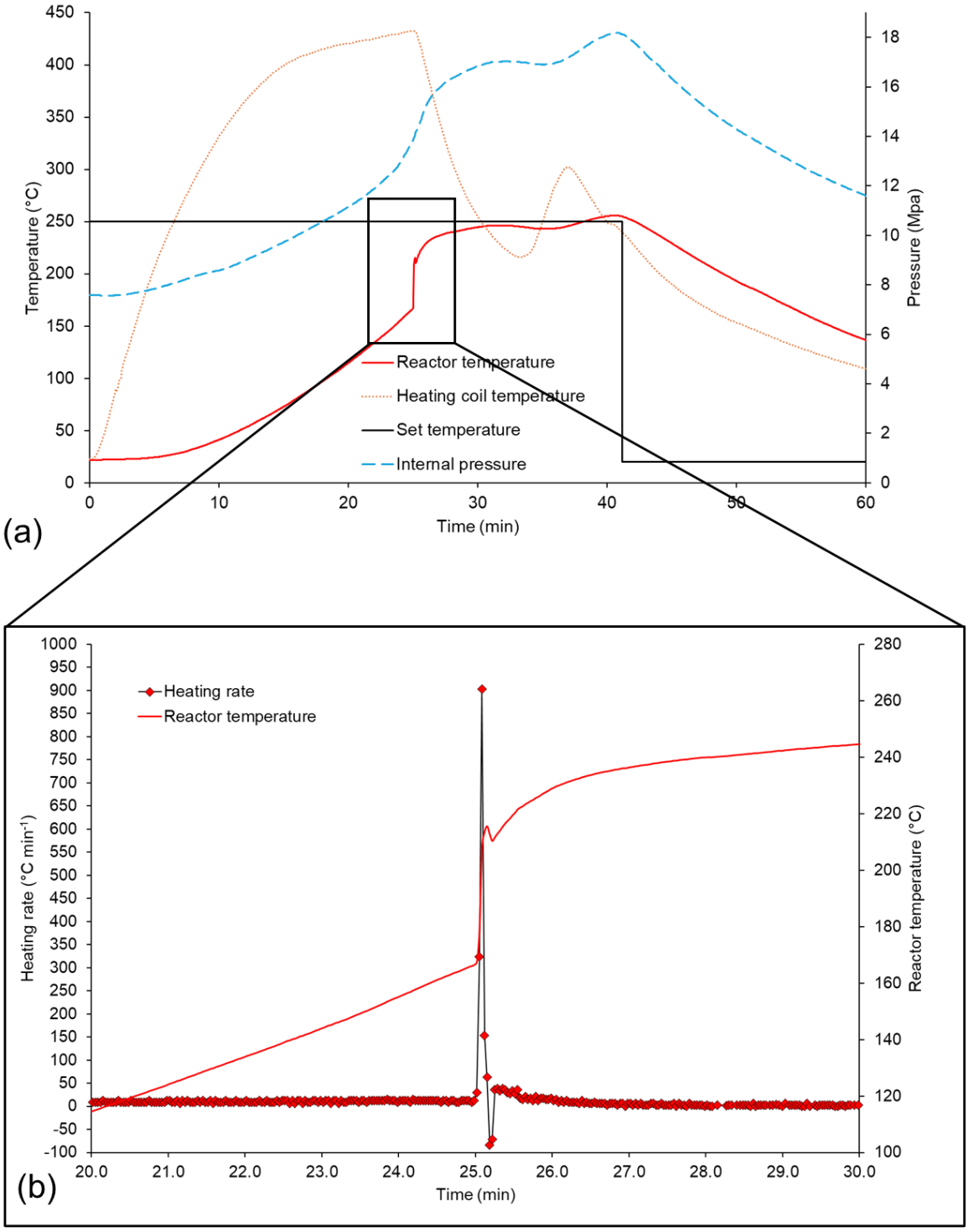

Figure F.1 - (a) Reactor internal temperature, heating coil temperature, set temperature and reactor internal pressure recorded during the experiments conducted at 250 °C for 15 min. (b) detail of reactor internal temperature and heating rate (as defined in Equation 4.9) in the time range in which the exothermic phenomenon has been observed.

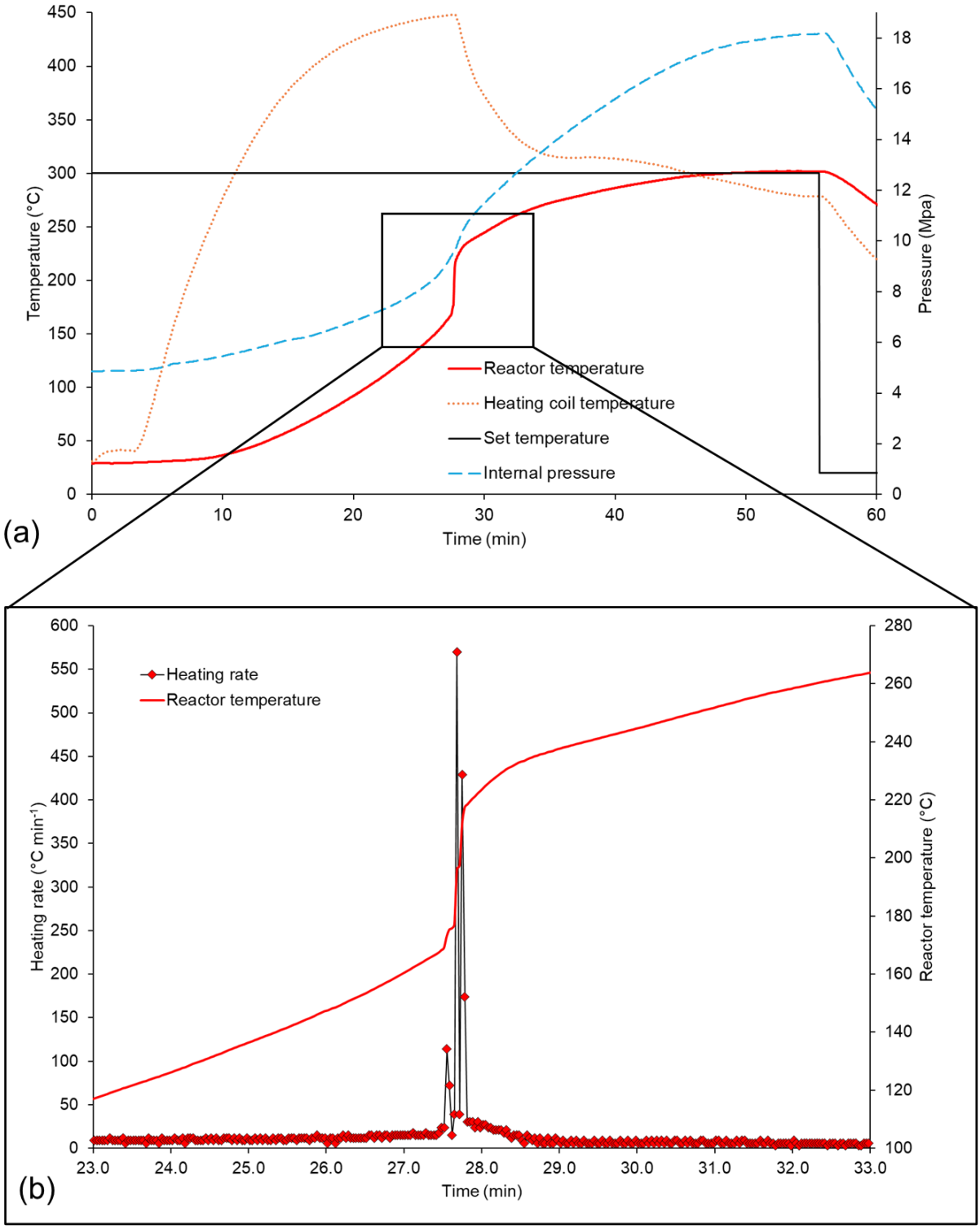

Figure F.2 - (a) Reactor internal temperature, heating coil temperature, set temperature and reactor internal pressure recorded during the experiments conducted at 300 °C for 15 min. (b) detail of reactor internal temperature and heating rate (as defined in Equation 4.9) in the time range in which the exothermic phenomenon has been observed.

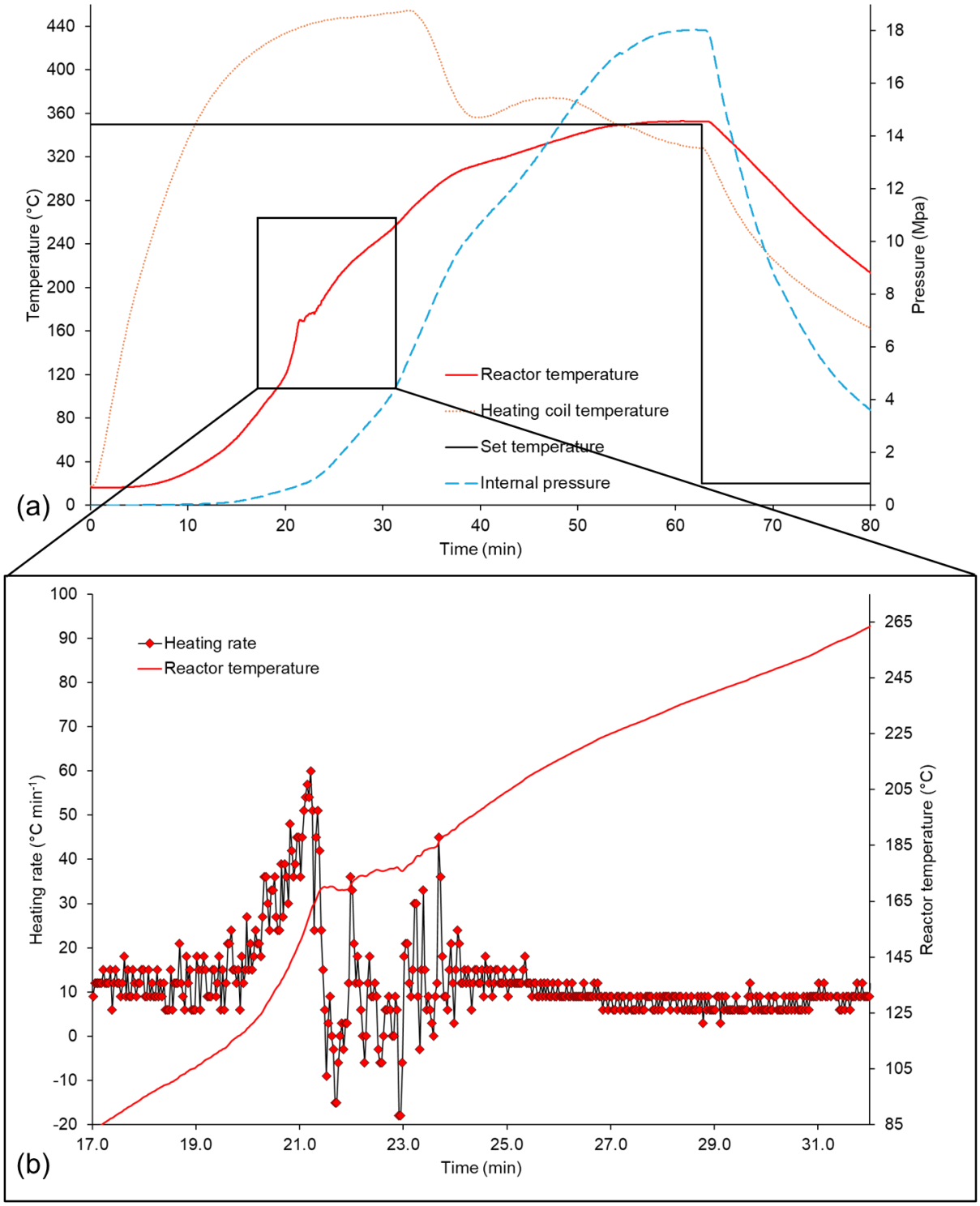

Figure F.3 - (a) Reactor internal temperature, heating coil temperature, set temperature and reactor internal pressure recorded during the experiments conducted at 350 °C for 15 min. (b) detail of reactor internal temperature and heating rate (as defined in Equation 4.9) in the time range in which the exothermic phenomenon has been observed.

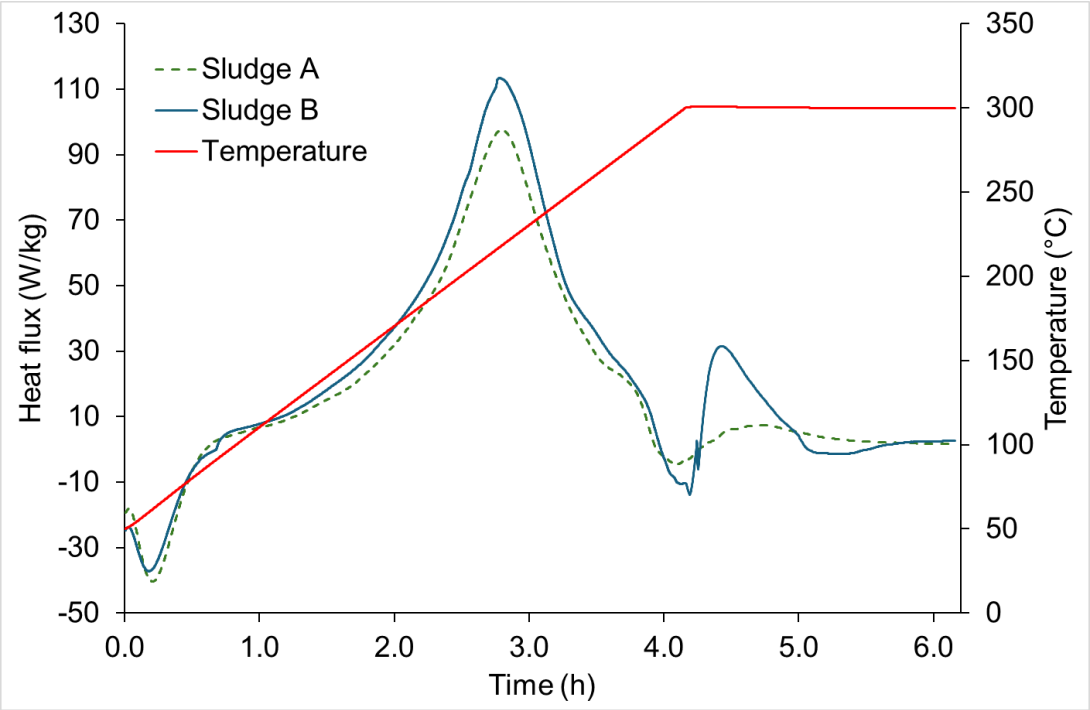

Figure F.4 – Heat flux of DSC analysis realized using 2 g of Sludge A and B (20% of dry matter) with an initial pressure of 9.4 MPa of N_2. q_{HT} is expressed as W kg^{-1} on a dry ash-free basis.

G. Supplementary elements for the investigation of feed properties on HT products

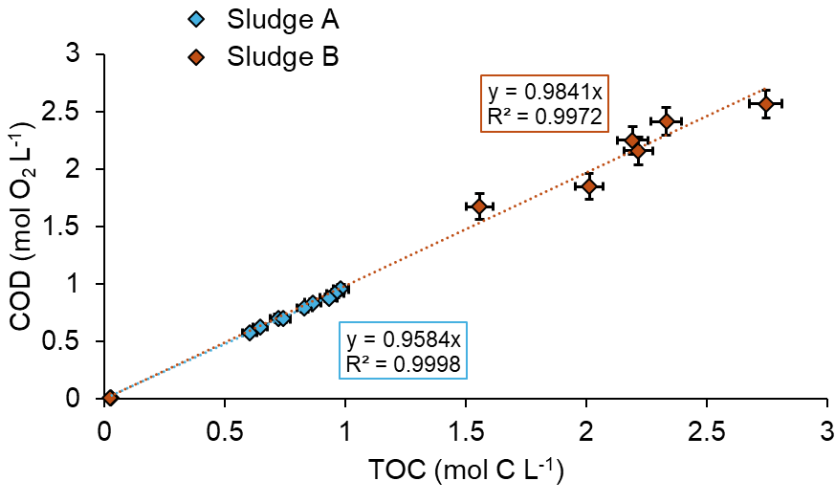

Figure G.1 - Correlation between TOC concentration (mol C L^{-1}) and COD content (mol O_2 L^{-1}) in Sludge A and Sludge B HT process water. Error bars represent propagated uncertainty.

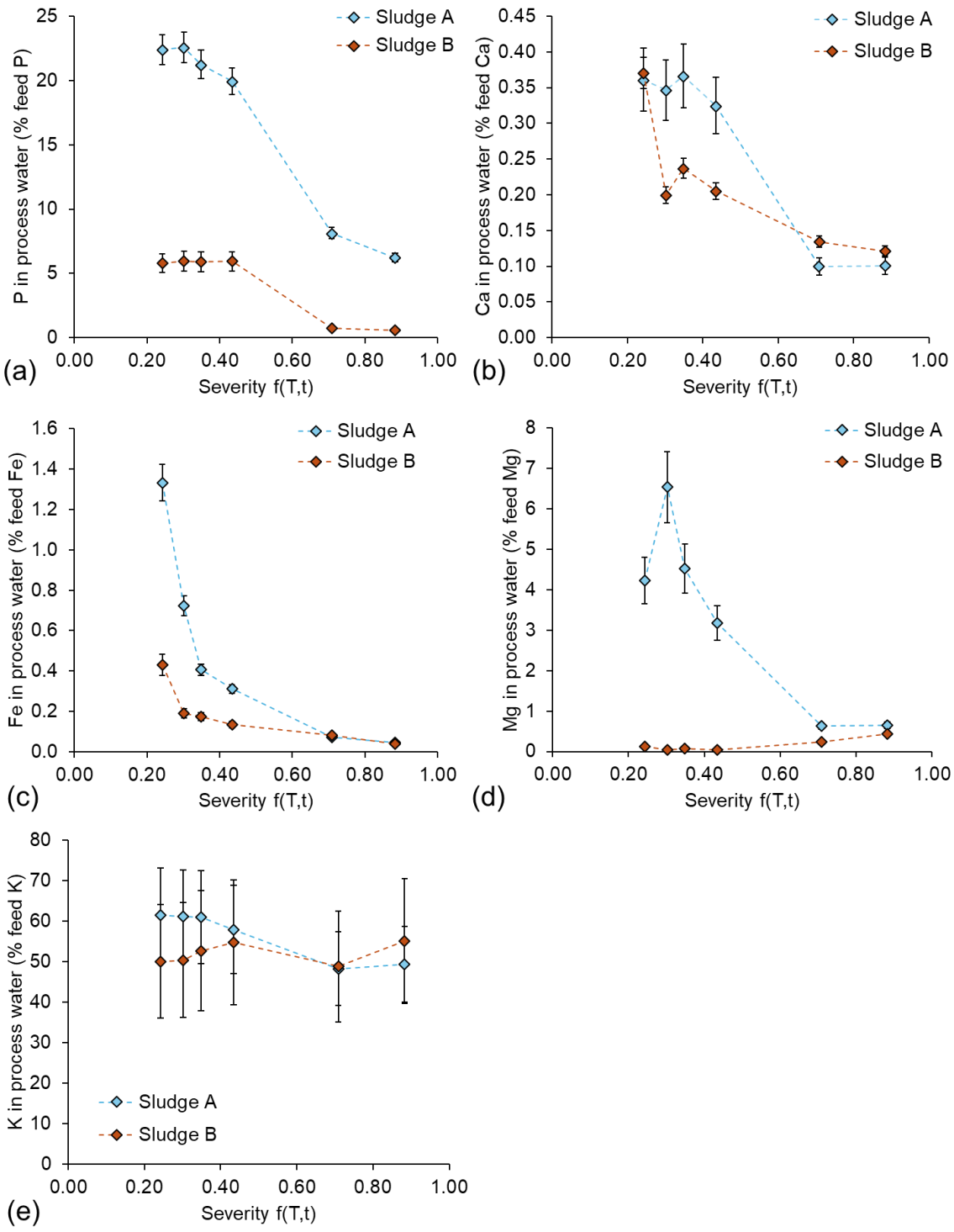

Figure G.2 - P (a), Ca (b), Fe (c), Mg (d) and K (e) yields in process water relative to total amounts in sludge feed. Dashed lines are included to facilitate data interpretation. Error bars represent propagated uncertainty.

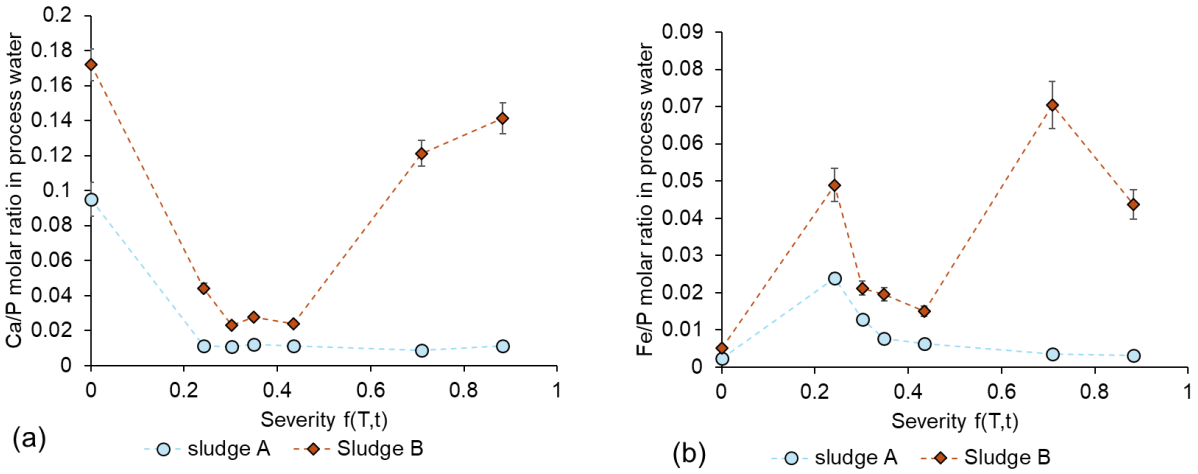

Figure G.3 - Ca/P (a) and Fe/P (b) molar ratio in process water as a function of severity f(T,t) for Sludge A and Sludge B. Dashed lines are included to facilitate data interpretation. Error bars represent propagated uncertainty.

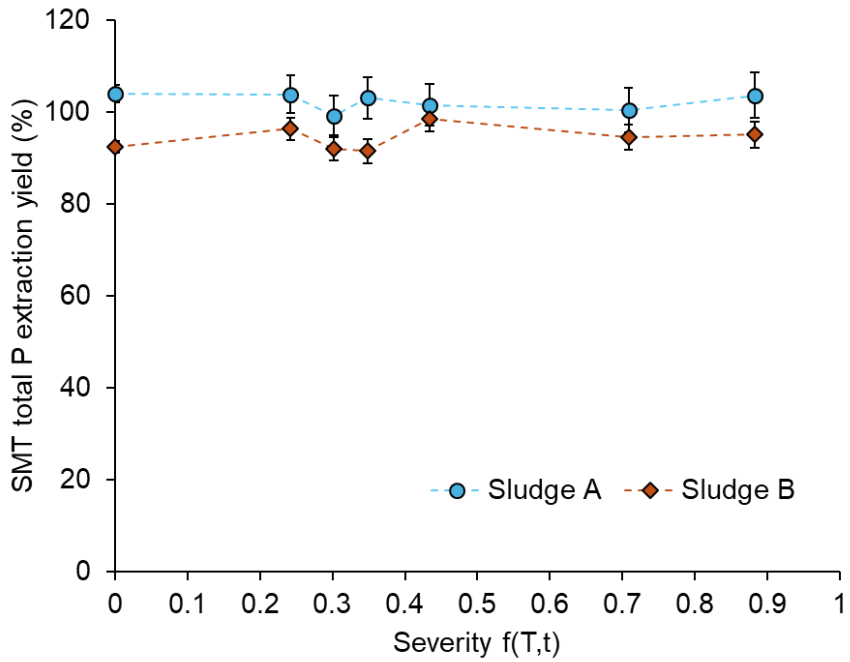

Figure G.4 - Ratio between SMT method TP results (calcination + leaching 3.5 M HCl) and TP results from aqua regia extraction + ICP-AES. Error bars represent propagated uncertainty.

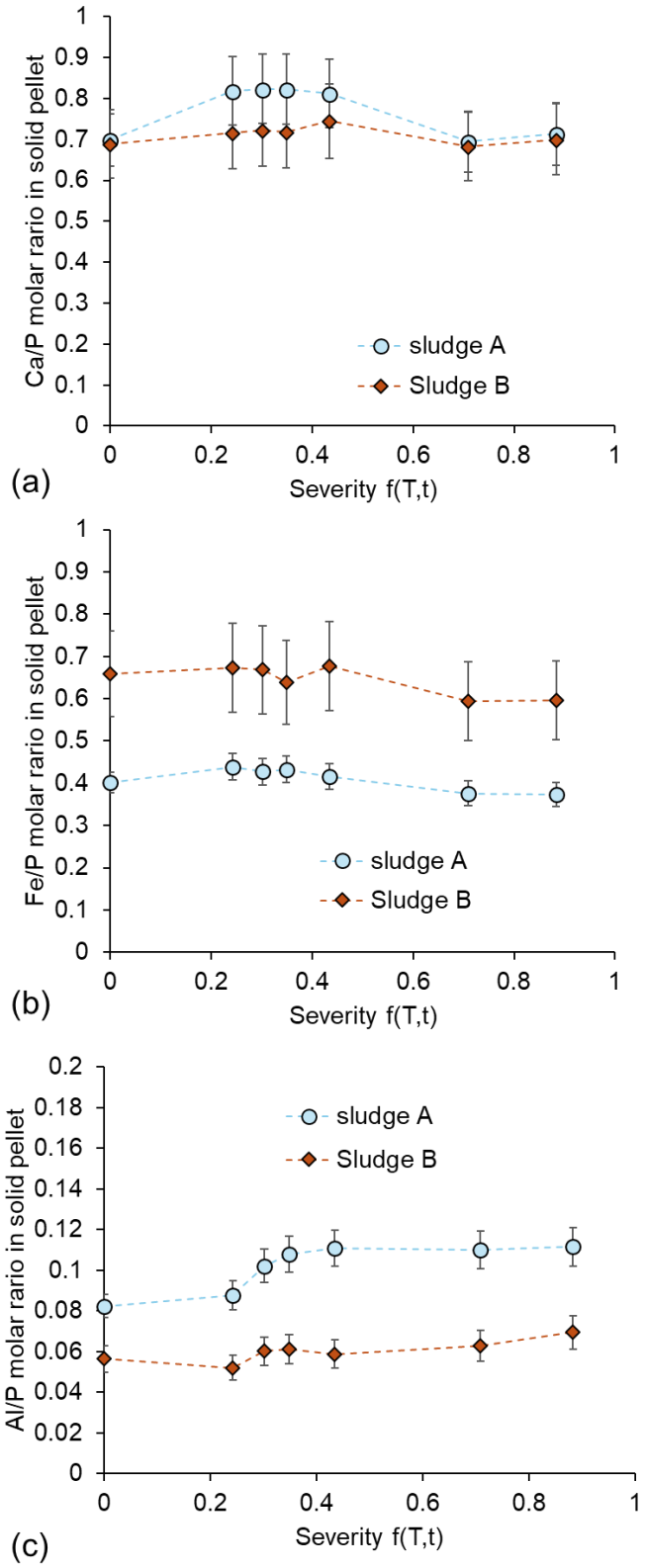

Figure G.5 - Ca/P (a), Fe/P (b) and Al/P (c) molar ratio in solid pellet by-products as a function of severity f(T,t) for Sludge A and Sludge B. Dashed lines are included to facilitate data interpretation. Error bars represent propagated uncertainty.

H. Supplementary elements for the investigation of CaO addition on HT products

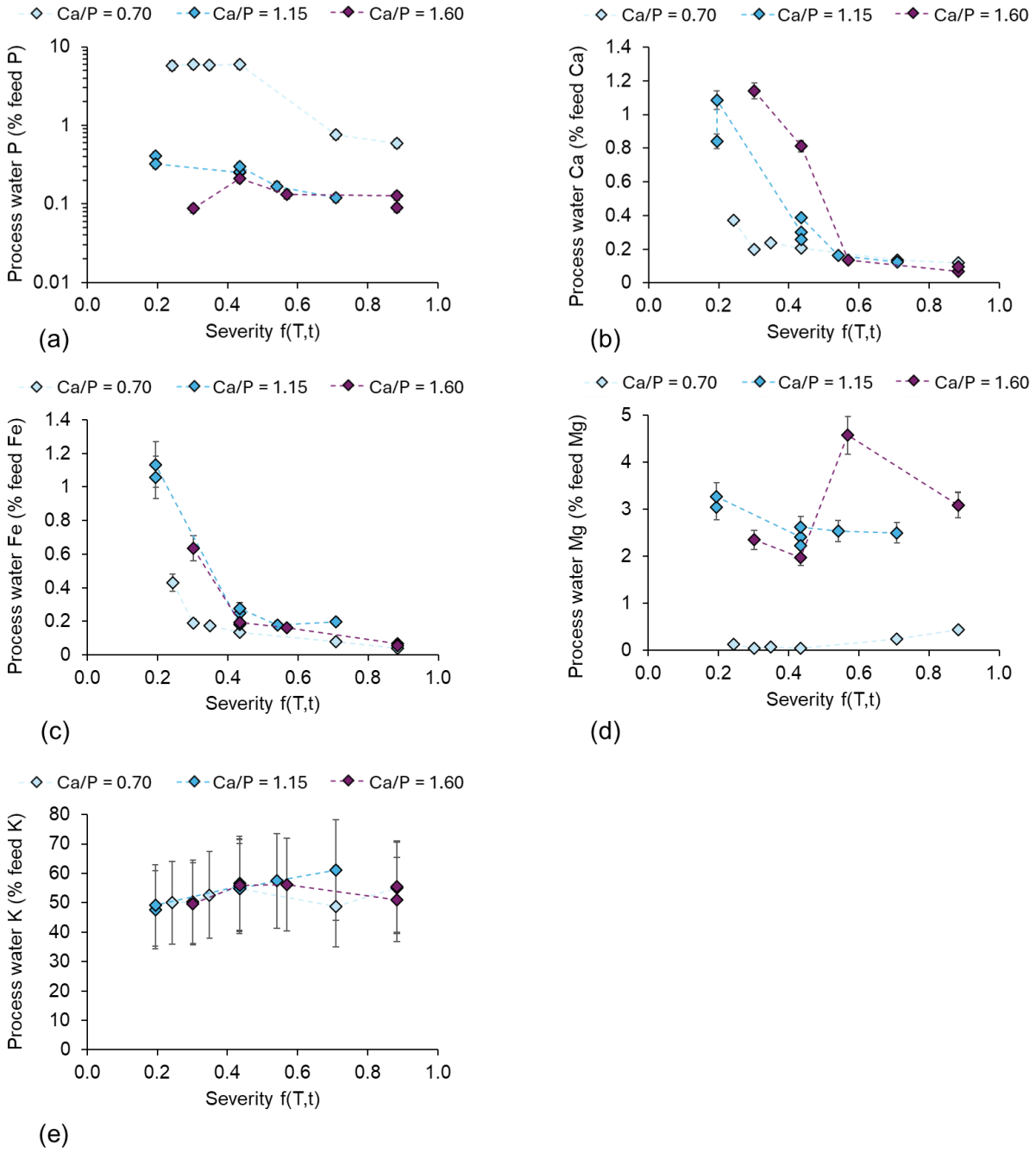

Figure H.1 - Soluble P (a), Ca (b), Fe (c), Mg (d) and K (e) yield in process water expressed as % of total feed P, Ca, Fe, Mg and K, as a function of severity f(T,t) for different Ca/P molar ratios. Error bars represent propagated uncertainty. Dashed lines are included to help data interpretation.

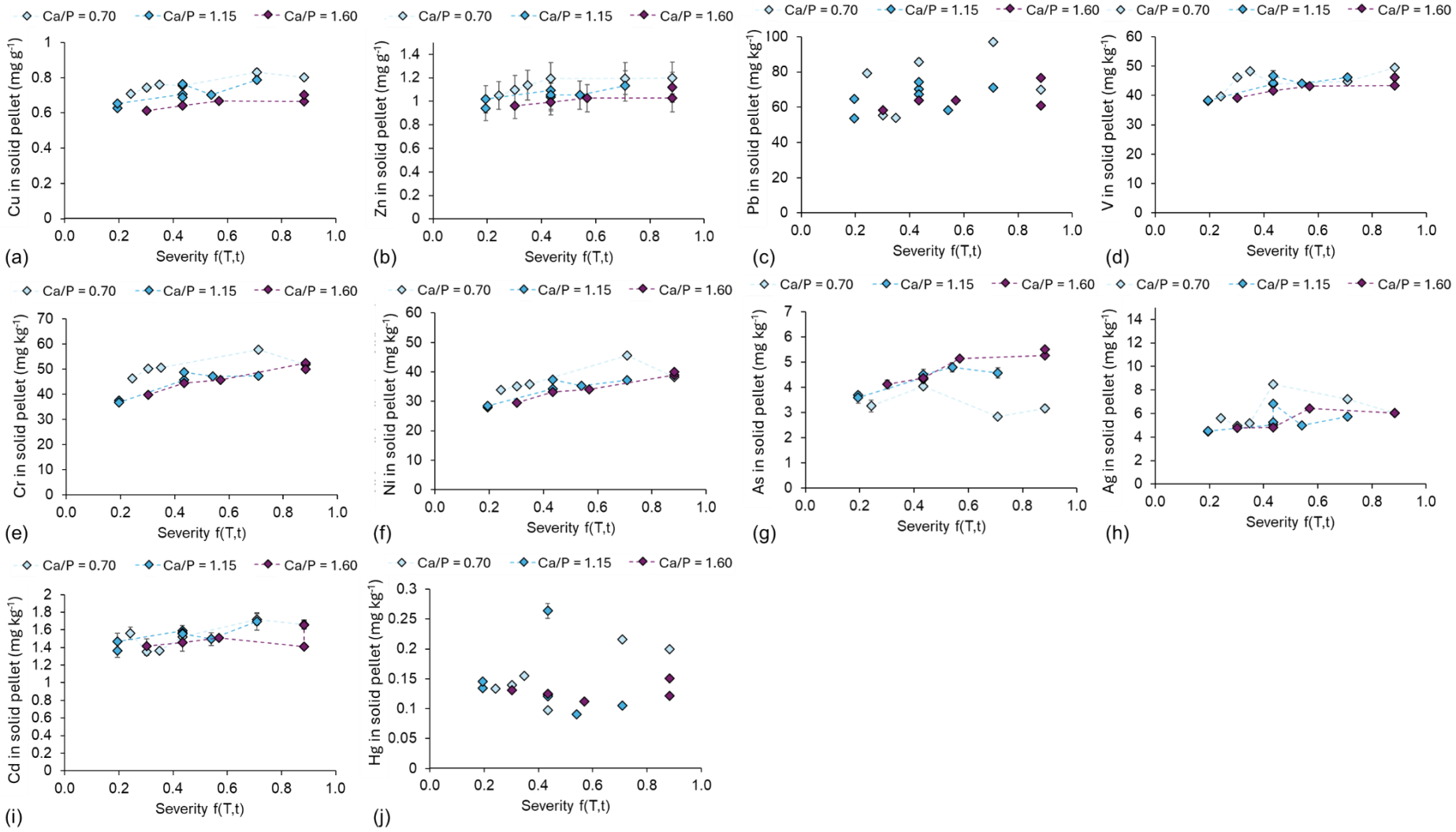

Figure H.2 - Cu (a), Zn (b), Pb (c), V (d), Cr (e), Ni (f), As (g), Ag (h), Cd (i), Hg (j) contents in solid pellet expressed as mg g^{-1} or mg kg^{-1} (on a dry basis), as a function of severity for different Ca/P molar ratios. Error bars represent the propagated uncertainty combined with the relative standard deviation associated with the spectrometric intensity measurement (3). Dashed lines are included to help data interpretation.